

Understanding
Ligand-Directed Heterogeneous Catalysis
on Model Surfaces

Dissertation

zur Erlangung des Doktorgrades
der Mathematisch-naturwissenschaftlichen Fakultät
der Christian-Albrechts-Universität zu Kiel

vorgelegt von
Carsten Schröder, M. Sc.
Kiel, 2022

Erste Gutachterin: Prof. Dr. Swetlana Schauer mann

Zweite Gutachterin: Prof. Dr. Melanie Schnell

Dritte Gutachterin: Prof. Dr. Katharina Al-Shamery

Tag der mündlichen Prüfung: 21. Juni 2022

Wem es vergönnt ist, an dem Aufbau der exakten Wissenschaften mitzuarbeiten, der wird sein Genügen und sein innerliches Glück finden in dem Bewusstsein, das Erforschliche erforscht zu haben und das Unerforschliche ruhig zu verehren.
(Max Planck)

Erklärung

Hiermit erkläre ich, dass die vorliegende Abhandlung, abgesehen von der wissenschaftlichen Beratung durch meine Betreuerin Frau Prof. Dr. Svetlana Schaueremann, nach Inhalt und Form meine eigene Arbeit ist. In dieser Dissertation werden die Ergebnisse zweier Forschungsprojekte zur Untersuchung heterogener Katalyse auf Metalloberflächen vorgestellt, deren Messungen im Institut für physikalische Chemie der Universität Kiel im Zeitraum von Dezember 2016 bis Dezember 2021 durchgeführt wurden. Diese Arbeit hat weder in Auszügen noch in ganzer Form einer anderen Stelle im Rahmen eines Prüfungsverfahrens vorgelegen. Teile dieser Arbeit wurden in fachwissenschaftlichen Zeitschriften veröffentlicht:

1. **Carsten Schröder**, Ann-Katrin Baumann, Marvin C. Schmidt, Jan Smyczek, Philipp A. Haugg, Ole-Christian Graap and Svetlana Schaueremann, *J. Phys. Chem. C* **2022**, 126, 4907–4920.
2. Christopher Witt, Marvin C. Schmidt, **Carsten Schröder**, Svetlana Schaueremann and Bernd Hartke, *J. Phys. Chem. C* **2021**, 125, 26167–26179.
3. **Carsten Schröder**, Philipp A. Haugg, Ann-Katrin Baumann, Marvin C. Schmidt, Jan Smyczek and Svetlana Schaueremann, *Chem. Eur. J.* **2021**, 27, 17240–17254.
4. Marvin Schmidt, Smadar Attia, **Carsten Schröder**, Ann-Katrin Baumann and Svetlana Schaueremann, *J. Phys. Chem. C* **2021**, 125, 19311–19324.
5. **Carsten Schröder**, Marvin C. Schmidt, Philipp A. Haugg, Ann-Katrin Baumann, Jan Smyczek and Svetlana Schaueremann, *Angew. Chem. Int. Ed.* **2021**, 60, 16349–16354.
6. **Carsten Schröder**, Marvin C. Schmidt, Christopher Witt, Smadar Attia, Jann Weber, Ann-Katrin Baumann, Bernd Hartke and Svetlana Schaueremann, *J. Phys. Chem. C* **2020**, 124, 28159–28168.
7. Marvin C. Schmidt, Smadar Attia, **Carsten Schröder**, Ann-Katrin Baumann, Svetlana Schaueremann, *J. Phys. Chem. C* **2020**, 124, 14262–14271.
8. Smadar Attia, Evan J. Spadafora, Marvin C. Schmidt, **Carsten Schröder**, Ann-Katrin Baumann and Svetlana Schaueremann, *Phys. Chem. Chem. Phys.* **2020**, 22, 15696–15706.
9. Smadar Attia, Marvin C. Schmidt, **Carsten Schröder**, Jann Weber, Ann-Katrin Baumann, Svetlana Schaueremann, *J. Phys. Chem. C* **2019**, 123, 29271–29277.
10. Smadar Attia, Marvin C. Schmidt, **Carsten Schröder**, Svetlana Schaueremann, *ACS Catal.* **2019**, 9, 6882–6889.
11. Smadar Attia, Marvin-Christopher Schmidt, **Carsten Schröder**, Pascal Pessier, Svetlana Schaueremann, *Angew. Chem. Int. Ed.* **2018**, 57, 16659–16664.

Die Arbeit ist unter Einhaltung der Regeln guter wissenschaftlicher Praxis der Deutschen Forschungsgemeinschaft entstanden und mir wurde zuvor kein akademischer Grad entzogen.

Kiel, im März 2022

Carsten Schröder

Abstract

One of the key challenges in chemistry is imparting selectivity to a multi-pathway reaction. Slight differences in the activation barriers often result in kinetic control over a chemical reaction – regardless of the thermodynamic stability of the products. By employing a suitable catalyst, the outcome of a chemical reaction may be promoted toward the desired product. Nowadays, heterogeneous catalysts are preferred over their homogeneous counterparts in most industrial processes because they offer a number of advantages for in-process application. However, heterogeneous catalysts are usually less selective as compared to homogeneous catalysts. A novel strategy in the research of catalysis is to combine the advantages of both heterogeneous and homogeneous catalysis functionalized with organic compounds on metal surfaces. The resulting hybrid materials thus provide both the capability to establish lateral interactions between adsorbates as well as the direct interaction of reaction intermediates with the metal surface. For the development of new catalysts, it is important to understand the fundamental processes at the catalyst surfaces. However, both the structural complexity as well as the dynamic transformation of a catalyst under operational conditions hinder the detailed structural investigation of the active surface. A strategy to overcome this deficit is to study chemical reactions on model systems under well-defined and reproducible conditions to obtain a fundamental-level understanding on the processes at the catalytic interface.

Toward this goal, the model catalyst approach was employed in this work to investigate the processes on the catalytic surfaces on microscopic scale. We employ a combination of surface-sensitive tools along with the molecular beam techniques to obtain detailed information on the mechanisms and kinetics of surface reactions. Specifically, infrared reflection absorption spectroscopy (IRAS) is employed to identify and follow the evolution of the surface species, including the preadsorbed ligands and the reaction intermediates, under the reaction conditions. Complementary, their spacial distribution on the catalytic surface is monitored by scanning tunneling microscopy (STM). In this thesis, the results of different mechanistic studies are presented that address the role of intermolecular interactions in chemical reactions in terms of promoting selectivity in multi-pathway reactions, weakening of specific chemical bonds by coadsorbates and stabilizing unstable surface species via lateral interactions. First, we investigated the formation of a ligand layer that promotes the chemoselective partial hydrogenation of α,β -unsaturated aldehyde acrolein toward the unsaturated alcohol propenol. Specifically, we created ligand-overlayers containing different types of organic adsorbates on Pd(111) to address the electronic and the geometric effects as well as the effects induced by formation of enol-containing ligand complexes, which play a crucial role in rendering the catalytic surface highly selective toward the hydrogenation of the C=O entity. In the second study, we investigated the adsorption and lateral interaction of an α -ketoester, ethyl pyruvate, on Pt(111) under different surface conditions. We could show a strong weakening of the ester bond due to intermolecular interactions that is potentially capable of affecting the reactivity of α -ketoesters. And finally, we demonstrate by the example of acetophenone that the formation of ketone–enol dimers, in which the unstable enol form is stabilized by the neighboring ketone molecule, is the first step of the low-barrier hydrogenation reaction of acetophenone. The results of these studies provide atomistic-level insights in the mechanisms of surface processes mediated by coadsorbed ligand molecules that give a starting idea of how lateral interactions can be employed as useful tools for the rational design of new catalytic materials with tailor-made catalytic properties.

Kurzzusammenfassung

Eine der größten Herausforderungen in der Chemie besteht darin, einer Reaktion mit mehreren Reaktionswegen Selektivität zu verleihen. Geringe Unterschiede in den Aktivierungsbarrieren führen oft zu einer kinetischen Kontrolle über eine chemische Reaktion – unabhängig von der thermodynamischen Stabilität der Produkte. Durch den Einsatz eines geeigneten Katalysators kann das Resultat einer chemischen Reaktion in Richtung des gewünschten Produkts verändert werden. Heutzutage werden heterogene Katalysatoren in den meisten industriellen Prozessen gegenüber homogener Katalysatoren bevorzugt, da diese eine Reihe von Vorteilen für die Prozessführung bieten. Allerdings ist die Selektivität heterogener Katalysatoren in der Regel geringer als bei homogenen Katalysatoren. Eine neue Strategie in der Katalysatorforschung besteht darin, die Vorteile sowohl der heterogenen als auch der homogenen Katalyse durch den gezielten Einsatz organischer Moleküle auf Metalloberflächen zu kombinieren. Die so entstehenden Hybridmaterialien ermöglichen sowohl laterale Wechselwirkungen zwischen Adsorbaten als auch die direkte Wechselwirkung von Reaktionszwischenprodukten mit der Metalloberfläche. Für die Entwicklung neuer Katalysatoren ist es wichtig, die grundlegenden Prozesse an den Katalysatoroberflächen zu verstehen. Allerdings erschweren sowohl die strukturelle Komplexität als auch die dynamische Veränderung eines Katalysators unter Betriebsbedingungen die detaillierte strukturelle Untersuchung der aktiven Oberfläche. Eine Strategie zur Überwindung dieses Defizits besteht darin, chemische Reaktionen an Modellsystemen unter genau definierten und reproduzierbaren Bedingungen zu untersuchen, um ein grundlegendes Verständnis der Vorgänge an der katalytischen Grenzfläche zu erlangen.

Um dieses Ziel zu erreichen, wurde in diesen Studien der Modellkatalysator-Ansatz verwendet, um die Prozesse auf den katalytischen Oberflächen auf mikroskopischer Ebene zu untersuchen. Wir verwenden eine Kombination von oberflächensensitiven Werkzeugen zusammen mit Molekularstrahltechniken, um detaillierte Informationen über die Mechanismen und die Kinetik von Oberflächenreaktionen zu erhalten. Insbesondere wird die Infrarot-Reflexions-Absorptionsspektroskopie (IRAS) eingesetzt, um die Entwicklung der Oberflächenspezies, einschließlich der vorab adsorbierten Liganden sowie der Reaktionszwischenprodukte, unter den Reaktionsbedingungen zu identifizieren und zu verfolgen. Ergänzend dazu wird ihre räumliche Verteilung auf der katalytischen Oberfläche mit Hilfe der Rastertunnelmikroskopie (RTM) abgebildet. In dieser Arbeit werden die Ergebnisse verschiedener mechanistischer Studien vorgestellt, die sich mit der Rolle intermolekularer Wechselwirkungen bei chemischen Reaktionen befassen und zwar in Bezug auf die Förderung der Selektivität bei parallel ablaufenden Reaktionen, die Schwächung spezifischer chemischer Bindungen durch Coadsorbat sowie die Stabilisierung instabiler Oberflächenspezies durch laterale Wechselwirkungen. Zunächst untersuchten wir die Bildung einer Ligandenschicht, die die chemoselektive partielle Hydrierung von α,β -ungesättigtem Aldehyd Acrolein zu dem ungesättigten Alkohol Propenol fördert. Konkret haben wir verschiedene Liganden-Überstrukturen mit unterschiedlichen Arten von organischen Adsorbaten auf Pd(111) erzeugt, um die elektronischen und geometrischen Effekte sowie die durch die Bildung von enolhaltigen Ligandenkomplexen induzierten Effekte zu untersuchen, die eine entscheidende Rolle dabei spielen die katalytische Oberfläche hochselektiv für die Hydrierung der C=O-Bindung zu machen. In der zweiten Studie untersuchten wir die Adsorption und laterale Wechselwirkung eines α -Ketoesters, Ethylpyruvat, auf Pt(111) unter verschiedenen Oberflächenbedingungen. Wir konnten eine starke Schwächung der Esterbindung durch intermolekulare Wechselwirkungen

nachweisen, die höchstwahrscheinlich die Reaktivität von α -Ketoestern maßgeblich beeinflusst. Und schließlich zeigten wir am Beispiel von Acetophenon, dass die Bildung von Keton–Enol–Dimeren, in denen das instabile Enol durch das benachbarte Keton stabilisiert wird, der erste Schritt der Hydrierungsreaktion von Acetophenon ist. Die Ergebnisse dieser Studien liefern tiefe Einblicke in die Mechanismen von Oberflächenprozessen, die durch coadsorbierte Ligandenmoleküle vermittelt werden, und geben eine erste Vorstellung davon, wie laterale Wechselwirkungen als nützliche Werkzeuge für die rationelle Entwicklung neuer katalytischer Materialien mit maßgeschneiderten katalytischen Eigenschaften eingesetzt werden können.

Contents

| | | |
|----------|---|------------|
| 1 | List of Publications | XII |
| 2 | Introduction | 1 |
| 3 | Theoretical Background | 10 |
| 3.1 | Scattering | 10 |
| 3.2 | Physisorption and Chemisorption | 11 |
| 3.3 | Hydrogen Adsorption on Pd and Pt | 15 |
| 3.4 | Adsorption and Sticking | 16 |
| 3.5 | Desorption | 20 |
| 3.6 | Diffusion | 21 |
| 3.7 | Lateral Interactions | 22 |
| 3.8 | Reaction Mechanisms at Gas–Solid Interfaces | 23 |
| 4 | Experimental Techniques | 25 |
| 4.1 | Molecular Beam Techniques | 25 |
| 4.1.1 | Supersonic Molecular Beams (SMB) | 26 |
| 4.1.2 | Effusive Molecular Beams (EB) | 28 |
| 4.2 | Quadrupole Mass Spectrometry (QMS) | 29 |
| 4.3 | Scanning Tunneling Microscopy (STM) | 31 |
| 4.4 | Infrared Spectroscopy | 32 |
| 4.4.1 | Detectors in Infrared Spectroscopy | 34 |
| 4.4.2 | Fourier Transform Infrared Spectroscopy (FTIR) | 34 |
| 4.4.3 | Infrared Reflection Absorption Spectroscopy (IRAS) | 37 |
| 4.5 | UHV IRAS/Molecular Beam Setup | 38 |
| 5 | Selective Partial Hydrogenation of Acrolein over Functionalized Pd(111) | 41 |
| 5.1 | Experimental Design | 51 |
| 5.1.1 | Analysis of the IR Spectra of Acrolein under Reactive Conditions | 51 |
| 5.1.2 | Parameters that Affect the Hydrogenation of Acrolein over Pd(111): Reaction Temperature | 53 |
| 5.1.3 | Parameters that Affect the Hydrogenation of Acrolein over Pd(111): Flux Rates of the Reactants Acrolein and Hydrogen | 54 |
| 5.1.4 | Parameters that Affect the Hydrogenation of Acrolein over Pd(111): Hydrogen Pretreatment of the Catalyst | 56 |
| 5.1.5 | Parameters that Affect the Hydrogenation of Acrolein over Pd(111): Artificial Ligand Layer | 58 |
| 5.2 | Hydrogenation of Acrolein over 2-Methyl-2-Pentenal-Functionalized Pd(111) | 62 |
| 5.3 | Hydrogenation of Acrolein over Allyl Cyanide-Functionalized Pd(111) | 66 |
| 5.4 | Hydrogenation of Acrolein over Acetophenone-Functionalized Pd(111) | 74 |
| 5.5 | Microscopic Model in Ligand-Directed Catalysis | 78 |

| | | |
|----------|--|------------|
| 6 | Lateral Interactions of Prochiral Adsorbates on Simple Crystalline Pt(111) Surfaces | 81 |
| 6.1 | Adsorption Geometry and Lateral Interaction of Ethyl Pyruvate on Pt(111) | 86 |
| 6.2 | Adsorption Study of Acetophenone on Pristine Pt(111) | 94 |
| 6.3 | Adsorption Study of Acetophenone on Hydrogen-covered Pt(111) | 99 |
| 7 | Conclusions | 105 |
| 8 | Reprints of Publications | 107 |
| 8.1 | Understanding Ligand-Directed Heterogeneous Catalysis: When the Dynamically Changing Nature of the Ligand Layer Controls the Hydrogenation Selectivity | 107 |
| 8.2 | Competing Reaction Pathways in Heterogeneously Catalyzed Hydrogenation of Allyl Cyanide: The Chemical Nature of Surface Species | 114 |
| 8.3 | Mechanisms Acting in Ligand-Directed Heterogeneous Catalysis: Electronic, Geometric and Enol-Induced Effects | 130 |
| 8.4 | Tuning the Strength of Molecular Bonds in Oxygenates via Surface-Assisted Intermolecular Interactions: Atomistic Insights | 145 |
| 8.5 | Disordered Two-Dimensional Self-Organization of Ethyl Pyruvate Molecules on the Pt(111) Surface | 156 |
| 8.6 | Surface-Driven Keto-Enol Tautomerization: Atomistic Insights into Enol Formation and Stabilization Mechanisms | 170 |
| 8.7 | Formation and Stabilization Mechanisms of Enols on Pt through Multiple Hydrogen Bonding | 177 |
| 8.8 | Keto-Enol Tautomerization as a First Step in Hydrogenation of Carbonyl Compounds | 186 |
| 8.9 | Temperature-Dependent Formation of Acetophenone Oligomers Accompanied by Keto-Enol Tautomerism: Real Space Distribution | 194 |
| 8.10 | Formation and Real-Space Distribution of Acetophenone Dimers on H-containing Pt(111) | 205 |
| 8.11 | Adsorption geometry and self-assembling of chiral modifier (R)-(+)-1-(1-naphthylethylamine) on Pt(111) | 220 |

List of Figures

| | | |
|------|--|----|
| 2.1 | Energy Diagram for Heterogeneous Catalysis | 1 |
| 2.2 | Trial-and-Error vs. Surface Science Approach | 2 |
| 2.3 | Model Catalyst Approach | 3 |
| 2.4 | Energy Diagram for Heterogeneous Catalysis | 4 |
| 2.5 | Hydrogenation Products of Acrolein over Pd-NP and Pd(111) | 6 |
| 2.6 | Experimental Approach | 7 |
| 2.7 | The Orito Reaction | 8 |
| | | |
| 3.1 | Simple Model for the Scattering Process | 10 |
| 3.2 | Lennard-Jones(12,6) Potential | 12 |
| 3.3 | Visualization of Different Types of Chemisorption | 13 |
| 3.4 | Visualization of Chemisorbed and Physisorbed Hydrogen | 14 |
| 3.5 | Model of the Precursor-Mediated Adsorption | 18 |
| 3.6 | Sticking Coefficient as a Function of Surface Coverage | 19 |
| 3.7 | Reaction Mechanisms in Heterogeneous Catalysis | 24 |
| | | |
| 4.1 | Schematic Drawing of a Supersonic Molecular Beam | 26 |
| 4.2 | Continuum Free-Jet Expansion | 27 |
| 4.3 | Schematic Drawing of an Effusive Molecular Beam | 28 |
| 4.4 | QMS Measurement Principle | 30 |
| 4.5 | STM Measurement Principle | 31 |
| 4.6 | Schematic Drawing of the Bruker Vertex 80v | 35 |
| 4.7 | Illustration of the Fourier Transformation in Infrared Spectroscopy | 36 |
| 4.8 | Metal Surface Selection Rule | 37 |
| 4.9 | Schematic Drawing of the Functional Parts of the Experimental Setup | 39 |
| 4.10 | Technical Drawing of the Experimental Setup | 40 |
| | | |
| 5.1 | Enzyme-Derived Catalysts | 42 |
| 5.2 | Hydrogenation Study on Substituted α,β -Unsaturated Aldehydes | 43 |
| 5.3 | Feasible Hydrogenation Products of Acrolein | 43 |
| 5.4 | Hydrogenation of Oxopromegestone over Different Transition Metals | 44 |
| 5.5 | Ligand-Directed Heterogeneous Catalysis | 45 |
| 5.6 | Temperature-Dependent Kinetic Study on Acrolein Hydrogenation over Pristine Pd(111) and Pd Nanoparticles | 46 |
| 5.7 | Kinetic and Spectroscopic Study on Acrolein Hydrogenation over Pristine Pd(111) at 270 K | 47 |
| 5.8 | Acting Surface Species in the Hydrogenation Reaction of Acrolein over Pristine Pd(111) | 48 |
| 5.9 | Chemical Structures of Molecules to Investigate Geometric and Electronic Effects of Preadsorbed Ligands | 49 |
| 5.10 | IR Spectra of Acrolein on H/Pd(111) at 250 K | 53 |

| | | |
|------|---|-----|
| 5.11 | Formation Rates of Propenol over H/Pd(111) at 250 K as a Function of Acrolein Flux | 55 |
| 5.12 | Formation Rates of Propenol over H/Pd(111) at 250 K as a Function of Hydrogen Pretreatment Time | 57 |
| 5.13 | Model of the Dense Oxopropyl Ligand Layer | 58 |
| 5.14 | Artificial Ligands for the Selective Partial Hydrogenation of Acrolein | 59 |
| 5.15 | Suggested η_1 and η_2 Geometry for Adsorbed Nitriles | 60 |
| 5.16 | Experimental Design for Investigating Ligand-Directed Catalysis | 61 |
| 5.17 | Kinetic Study on Acrolein Hydrogenation over MP/Pd(111) at 250 K | 63 |
| 5.18 | Hydrogenation of Acrolein over MP/Pd(111) at 250 K | 64 |
| 5.19 | Artificial Ligands: Geometric Effects | 65 |
| 5.20 | Kinetic Study on Acrolein Hydrogenation over AC/Pd(111) at 250 K | 66 |
| 5.21 | Hydrogenation of Acrolein over AC/Pd(111) at 250 K | 67 |
| 5.22 | Artificial Ligands: Electronic Effects | 68 |
| 5.23 | Microscopic Investigation of the Active AC Layer | 69 |
| 5.24 | Adsorption Study on AC on Pristine Pd(111) as a Function of Temperature | 70 |
| 5.25 | Chemical Transformation of AC on H/Pd(111) | 71 |
| 5.26 | Identification of the Active Ligand Species in AC/Pd(111) | 72 |
| 5.27 | Dynamic Transformation of AC under Operational Conditions | 73 |
| 5.28 | Kinetic Study on Acrolein Hydrogenation over AP/Pd(111) at 250 K | 74 |
| 5.29 | Kinetic Study on Acrolein Hydrogenation over AP/Pd(111) at 250 K at Different Coverages of AP | 75 |
| 5.30 | Hydrogenation of Acrolein over AP/Pd(111) at 250 K | 76 |
| 5.31 | Artificial Ligands: Enol-Induced Stabilization of the Oxopropyl Ligand | 78 |
| 5.32 | Summary of Different Effects in Ligand-Directed Hydrogenation of Acrolein | 79 |
| 6.1 | The Orito Reaction | 83 |
| 6.2 | Natural and Synthetic Chiral Modifiers | 84 |
| 6.3 | Proposed Adsorption Geometries of α -Ketoesters | 86 |
| 6.4 | IR Spectra of ^{12}C -EP and ^{13}C -EP on Pristine Pt(111) at 100 K | 87 |
| 6.5 | Combined IRAS and STM Study on EP Adsorbed on Pt(111) at 100 K | 88 |
| 6.6 | Statistic of EP Surface Species on Pt(111) Obtained by STM | 90 |
| 6.7 | Proposed Models for the Formation of EP Oligomers on Pt(111) | 91 |
| 6.8 | Simulated IR Spectrum of EP Adsorbed on Pt(111) | 92 |
| 6.9 | Real-Space STM Images of AP Adsorbed on Pt(111) at 200 K | 95 |
| 6.10 | IRAS Study on AP Adsorbed on Pt(111) as a Function of Temperature | 96 |
| 6.11 | Real-Space STM Images of AP Adsorbed on Pt(111) at 280 K | 97 |
| 6.12 | IRAS and STM Study on AP Adsorbed on H/Pt(111) at 200 K | 100 |
| 6.13 | Statistics and STM Images of AP Dimers on H/Pt(111) at 190 K | 101 |
| 6.14 | IRAS and STM Study on AP Adsorbed on H/Pt(111) at 240 K | 102 |
| 6.15 | Proposed Hydrogenation Mechanism of Acetophenone | 103 |

Acronyms

- AC - Allyl cyanide
- AC/Pd(111) – Pd(111) functionalized with allyl cyanide
- AP – Acetophenone
- AP/Pd(111) – Pd(111) functionalized with acetophenone
- B3LYP – B3LYP (Becke, 3 parameter, Lee-Yang-Parr) DFT functional
- BET – BET (Brunauer, Emmett and Teller) isotherm
- DFT – Density Functional Theory
- DLa-TGS – Deuterated L-alanine TriGlycerine Sulfate detector
- DOS – Density of States
- EI – Electron Ionization
- EP – Ethyl pyruvate
- FT – Fourier Transformation
- FTIR – Fourier Transform Infrared Spectroscopy
- GCA – Glass Capillary Array
- H,D/Pd(111) – Hydrogen/deuterium-covered Pd(111)
- H,D/Pt(111) – Hydrogen/deuterium-covered Pt(111)
- HREELS – High Resolution Electron Energy Loss Spectroscopy
- IR – Infrared
- IRAS – Infrared Reflection Absorption Spectroscopy
- MB – Molecular Beam
- MCT – Mercury-Cadmium-Telluride (HgCdTe) Detector
- MIR – Mid-infrared
- MP – 2-Methyl-2-pentenal
- MP/Pd(111) – Pd(111) functionalized with 2-methyl-2-pentenal
- MSSR – Metal Surface Selection Rule
- OPD – Optical Path Difference
- QMS – Quadrupole Mass Spectrometry
- R-NEA – R-Naphthylethylamine
- STM – Scanning Tunneling Microscopy
- TFAP – 2,2,2-Trifluoroacetophenone
- TPD – Temperature Programmed Desorption
- UHV – Ultra-high Vacuum ($< 10^{-8}$ mbar)
- ZPD – Zero Path Difference

1 List of Publications

1. *Mechanisms Acting in Ligand-Directed Heterogeneous Catalysis: Electronic, Geometric and Enol-Induced Effects*
Carsten Schröder, Ann-Katrin Baumann, Marvin C. Schmidt, Jan Smyczek, Philipp A. Haugg, Ole-Christian Graap and Svetlana Schaueremann, *J. Phys. Chem. C* **2022**, 126, 4907–4920.
2. *Disordered two-dimensional self-organization of ethyl pyruvate molecules on the Pt(111) surface*
Christopher Witt, Marvin C. Schmidt, **Carsten Schröder**, Svetlana Schaueremann and Bernd Hartke, *J. Phys. Chem. C* **2021**, 125, 26167–26179.
3. *Competing Reaction Pathways in Heterogeneously Catalysed Hydrogenation of Allyl Cyanide: The Chemical Nature of Surface Species*
Carsten Schröder, Philipp A. Haugg, Ann-Katrin Baumann, Marvin C. Schmidt, Jan Smyczek and Svetlana Schaueremann, *Chem. Eur. J.* **2021**, 27, 17240–17254.
4. *Formation and Real Space Distribution of Acetophenone Dimers on H-containing Pt(111)*
Marvin Schmidt, Smadar Attia, **Carsten Schröder**, Ann-Katrin Baumann and Svetlana Schaueremann, *J. Phys. Chem. C* **2021**, 125, 19311–19324.
5. *Understanding Ligand-Directed Heterogeneous Catalysis: When the Dynamically Changing Nature of the Ligand Layer Controls the Hydrogenation Selectivity*
Carsten Schröder, Marvin C. Schmidt, Philipp A. Haugg, Ann-Katrin Baumann, Jan Smyczek and Svetlana Schaueremann, *Angew. Chem. Int. Ed.* **2021**, 60, 16349–16354.
6. *Tuning the Strength of Molecular Bonds in Oxygenates via Surface-Assisted Intermolecular Interactions: Atomistic Insights*
Carsten Schröder, Marvin C. Schmidt, Christopher Witt, Smadar Attia, Jann Weber, Ann-Katrin Baumann, Bernd Hartke and Svetlana Schaueremann, *J. Phys. Chem. C* **2020**, 124, 28159–28168.
7. *Temperature-Dependent Formation of Acetophenone Oligomers Accompanied by Keto-Enol Tautomerism: Real Space Distribution*
Marvin C. Schmidt, Smadar Attia, **Carsten Schröder**, Ann-Katrin Baumann, Svetlana Schaueremann, *J. Phys. Chem. C* **2020**, 124, 14262–14271.
8. *Adsorption geometry and self-assembling of chiral modifier (R)-(+)-1-(1-naphthylethylamine) on Pt(111)*
Smadar Attia, Evan J. Spadafora, Marvin C. Schmidt, **Carsten Schröder**, Ann-Katrin Baumann and Svetlana Schaueremann, *Phys. Chem. Chem. Phys.* **2020**, 22, 15696–15706.

9. *Keto–Enol Tautomerization as a First Step in Hydrogenation of Carbonyl Compounds*
Smadar Attia, Marvin C. Schmidt, **Carsten Schröder**, Jann Weber, Ann-Katrin Baumann, Swetlana Schauermaun, *J. Phys. Chem. C* **2019**, 123, 29271–29277.
10. *Formation and Stabilization Mechanisms of Enols on Pt through Multiple Hydrogen Bonding*
Smadar Attia, Marvin C. Schmidt, **Carsten Schröder**, Swetlana Schauermaun, *ACS Catal.* **2019**, 9, 6882–6889.
11. *Surface-Driven Keto–Enol Tautomerization: Atomistic Insights into Enol Formation and Stabilization Mechanisms*
Smadar Attia, Marvin-Christopher Schmidt, **Carsten Schröder**, Pascal Pessier, Swetlana Schauermaun, *Angew. Chem. Int. Ed.* **2018**, 57, 16659–16664.

Conference contributions

Presentations

1. *Ligand-Induced Heterogeneous Catalysis: Selective Hydrogenation of Acrolein on Ligand-Modified Pd(111)*, keynote lecture at virtual Bunsentagung Regensburg, 2021.
2. *Ligand-induced Heterogeneous Catalysis: an atomistic view*, GDCH Weihnachtskolloquium Kiel, 2020.
3. *Enantioselective reactions on chirally-modified Pt(111) surfaces*, Workshop presentation at Jahrestreffen Deutscher Katalytiker, Weimar, 2018.

Posters

1. *Enantioselective Hydrogenation of Ethyl Pyruvate on Chirally-Modified Pt(111) Surfaces*, Future Perspectives in Catalysis Workshop, Bremerhaven, 2019.
2. *Adsorption Study of Ethyl Pyruvate on Pt(111)*, Jahrestreffen Deutscher Katalytiker, Weimar, 2019.
3. *Enantioselective Reaction of Acetophenone on R-NEA-Modified Pt(111) Surfaces*, JCF Frühjahrssymposium, Konstanz, 2018.
4. *Keto-Enol Tautomerization of Acetophenone on Pt(111)*, Jahrestreffen Deutscher Katalytiker, Weimar, 2018.
5. *Enantioselective Catalysis on Chirally Modified Pt(111) Surfaces*, Life Science Nord, Kiel, 2017.

2 Introduction

In these days, heterogeneous catalysis is the basis for modern chemical industry. A vast majority of over 90 % of chemical products have at least one catalytic step in the production.^[1] The application for catalysts is not limited to manufacturing processes but is also used in environmental technologies, such as exhaust gas treatment in automobiles.^[2] Over the past decades, the demand for alternative energy sources and storage has increased tremendously in order to enable the transition from fossil fuels to renewable energies.^[3]

The classification of catalysis is usually according to the state of aggregation of the catalyst and the reactants: i) either both consist of the same physical state, e.g. liquid, then it is denoted as homogeneous catalysis or ii) catalyst and reactants have a different physical state, e.g. solid catalyst and liquid or gaseous reactants, then it is named heterogeneous catalysis. The fraction of heterogeneously catalyzed processes exceeds the homogeneously catalyzed processes by almost a factor of 10. Heterogeneous catalysis has several major advantages over homogeneous catalysis: i) simple separation of reactants, products and catalysts, ii) wide range of operating conditions in terms of temperature and pressure, iii) simple and effective realization in continuous flow processes.^[4-7]

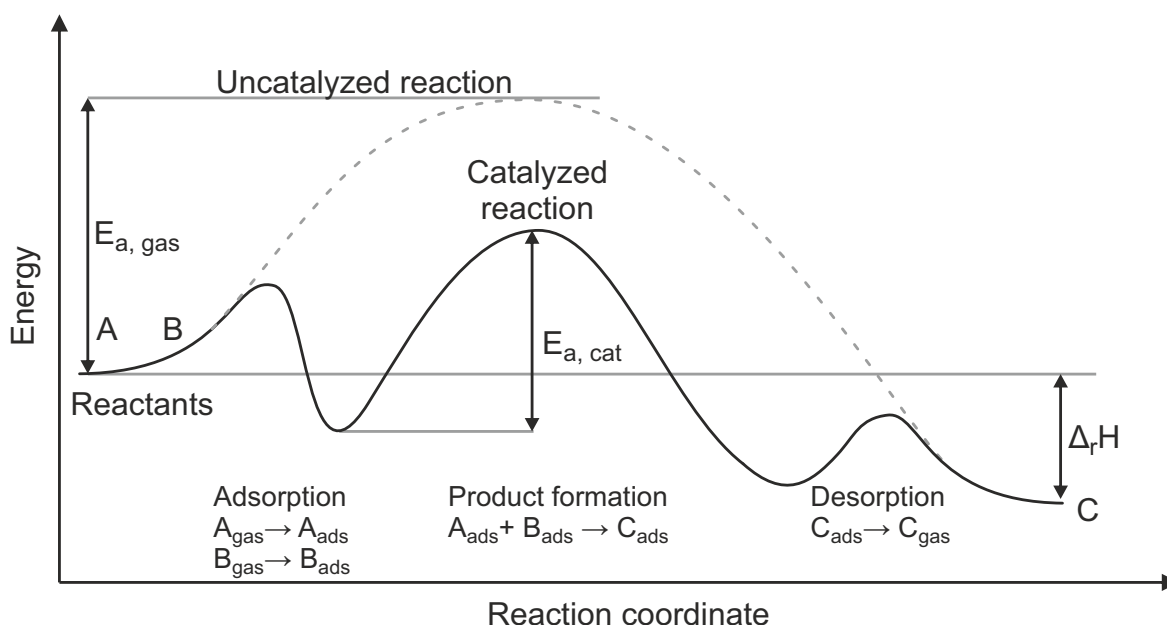


Figure 2.1: Energy diagram of a heterogeneously catalyzed bimolecular reaction $A + B \rightarrow C$. The activation barrier (E_a) of the catalyzed reaction (black line) is significantly lower than the uncatalyzed reaction (dashed line) in the gas phase. Adapted from Ref.[5,6,8].

The major benefit of an efficient catalyst is that it promotes a specific desired reaction path. Hence, the activation barrier may be lower compared to the uncatalyzed reaction and the reaction becomes kinetically more favorable. Because of the lower activation barrier, the

reaction rate increases compared to the uncatalyzed reaction but the change in enthalpy still equals the uncatalyzed reaction. Thus, catalysts can only change the kinetics of a chemical reaction while the thermodynamics and equilibrium constant remain the same. A catalyst accelerates both the product formation $A + B \rightarrow C$ as well as the reverse process of product decomposition $C \rightarrow A + B$ to the same extent.^[8] Figure 2.1 illustrates the main steps of a heterogeneously catalyzed bimolecular reaction of two gaseous species (black line) and, for comparison, the uncatalyzed reaction in the gas phase (dashed line). The adsorbed reactants (A_{ads} , B_{ads}) form the product C_{ads} on the surface which desorbs in a subsequent step into the gas phase. The overall reaction rate over a catalytic surface depends on several factors: while the activity of a catalyst increases with decreasing activation energy, the bonding strength of both the reactants and products on the surface still may change it in different directions.^[9] A weak bonding of the reactants on the surface results in low surface concentrations of the reactants and hence a low conversion into the product. However, a strong bonding of either reactants or the product on the surface results in the accumulation of surface species and a self-poisoning of the catalyst with reduced activity.

The interdisciplinary research in the field of heterogeneous catalysis is crucial for the development of new industrial processes. That involves, among others, scientists who discover new reactive materials, engineers who address the limitations of the heat and mass transport as well as business economists who design the entire process profitable. While some performance data, e.g. catalyst lifetime, can be obtained directly from commercial catalysts, the investigation of the underlying atomistic-level mechanisms of heterogeneously catalyzed reactions cannot be performed in industrial plants.^[6]

There are basically two different approaches for the research of advanced catalytic materials that are illustrated in Figure 2.2: i) trial-and-error method, in which structural parameters of a catalyst are systematically changed and ii) understanding the fundamental processes at the interfaces. The former is a well-established method for the synthesis of e.g. zeolites where high throughput reactors allow the fast screening and characterization of new materials.^[10,11] The latter is a rational approach in which the structure–reactivity relationships are investigated with the aid of rigorous surface-sensitive tools.

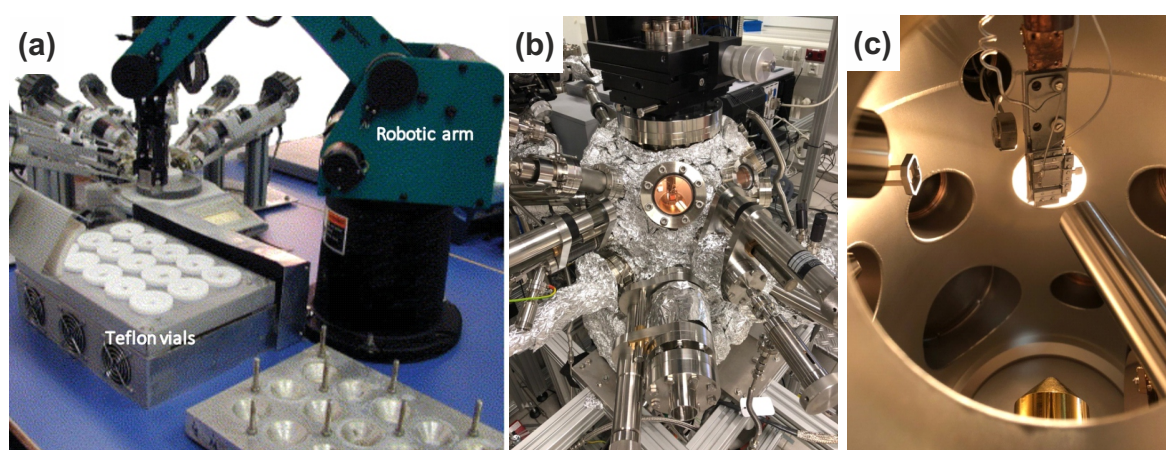


Figure 2.2: Two different scientific approaches in catalysis research: (a) automated high throughput robotic system (Figure reprinted with permission from Ref.[12]), (b) ultra-high vacuum (UHV) apparatus with surface-sensitive methods and (c) a Pd(111) single crystal inside of an UHV chamber which was used in this work.

Obtaining a microscopic-level understanding on the kinetics and dynamics on the catalytic surfaces is the main research field of surface science, which has been established and improved with various spectroscopic and microscopic tools in the last decades.^[5,13,14]

A major drawback in the research of real powdered materials is the structural and compositional complexity that hinders a detailed and direct investigation of the principles on the catalytic surface at atomistic scale. An illustration of the composition of an industrial catalyst is presented in Figure 2.3.

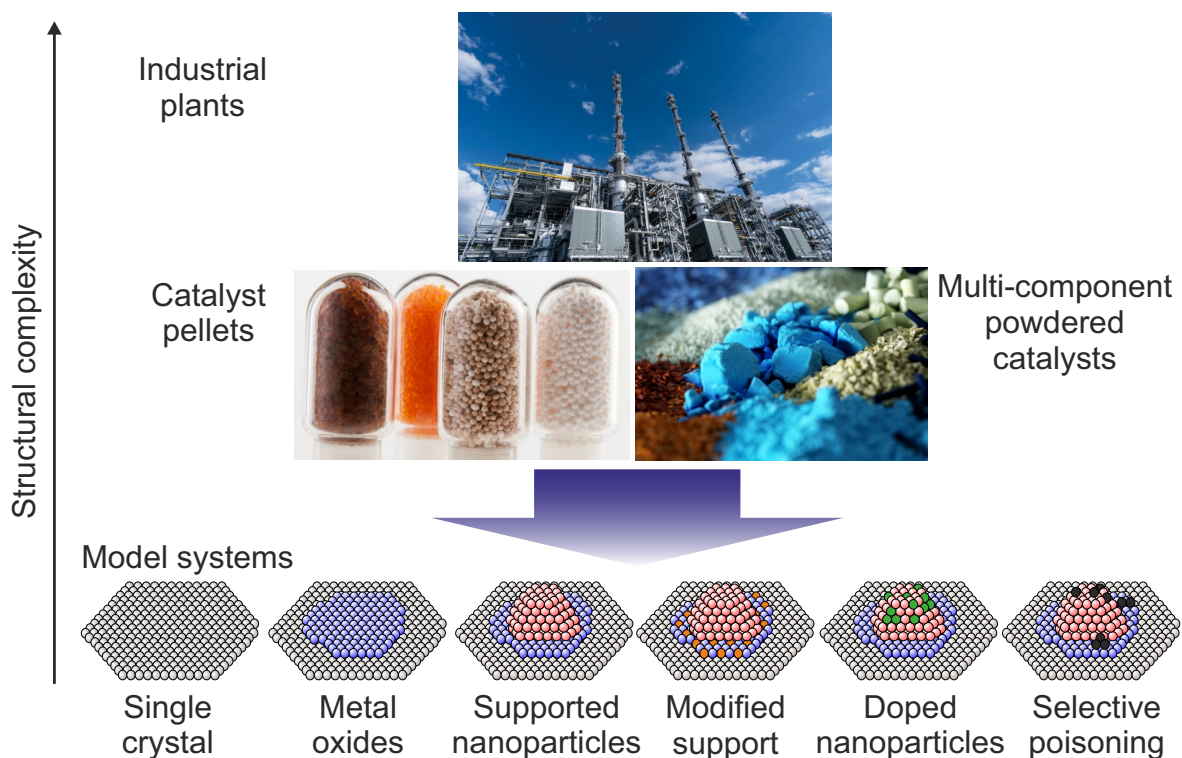


Figure 2.3: Catalysis at industrial scale and the model catalyst approach to address specific properties of real catalysts at well-defined model surfaces. Any modification of the support or doping of the surface can be achieved under reproducible conditions. Adapted from Ref.[15–17] and reprinted with permission from BASF SE^[18].

The reactor inside of an industrial plant is usually filled with pellets that contain the catalyst. The term catalyst often refers to several different components, e.g. support material and catalytic active material, that have different functions and which may be present in multiple phases.^[19] While both the pellets and the usually porous support are necessary to control the mass and heat flow through the reactor, the desired chemical reaction is performed over the catalytic active surface. This surface may contain supported nanoparticles, e.g. oxide-supported metal nanoparticles, in which either the support, the nanoparticles or both, the support and the nanoparticle, can selectively be modified by incorporation of specific chemical elements that change the electronic structure. The variation on the supporting material or active surface are usually based on empirical observations in which additions were made to improve the performance or correct deficits of a catalyst.^[6]

One of the key issues in catalysis is the dynamic change of the real catalytic surfaces under operative conditions. A catalytic material can be prepared under well-defined conditions but

its properties, such as structure, morphology or composition, may change drastically upon transfer to industrial process conditions. A well-known phenomenon of such a dramatic change of the surface structure during the course of a chemical reaction is the sintering of particles that can be described by the models of Ostwald ripening^[20] and particle migration.^[21] The thermal deactivation of a nanoparticle-based catalyst due to the formation of larger particles is an important process that results in the loss of the active metal surface area. Besides changes in morphology, the catalytic material can also be chemically altered by reducing the oxide supports, oxidizing reactive metal sites or decomposition of reactant molecules. Thus, the dynamic change of the real catalytic surfaces under operative conditions is one of the most important issues in catalysis that affects the performance of catalysts. These are just a few examples that directly affect the lifetime of a catalyst, which is one of the most critical parameters for industrial catalysts, along with selectivity, cost and integrability into economic processes.^[22]

To achieve an atomistic-level understanding of the catalytic processes in terms of specific reaction mechanisms, interaction of the reactants with the surface, identification of the chemical nature of the intermediates and lateral interactions of coadsorbed surface species, the model catalyst approach was developed.^[15–17,23–25] This approach on simplified model systems under well-defined and reproducible conditions allows the finding of a direct correlation between a microscopic picture and catalytic properties. Figure 2.3 visualizes the model catalyst approach as well as how a great variety of issues from real catalysis can be addressed and investigated on simplified model systems. Studies can be performed on simple single crystals or structurally more complex supported nanoparticles. Both, the support and surface of the nanoparticles can be selectively functionalized or poisoned to create a tailor-made and well-defined catalytic surface.

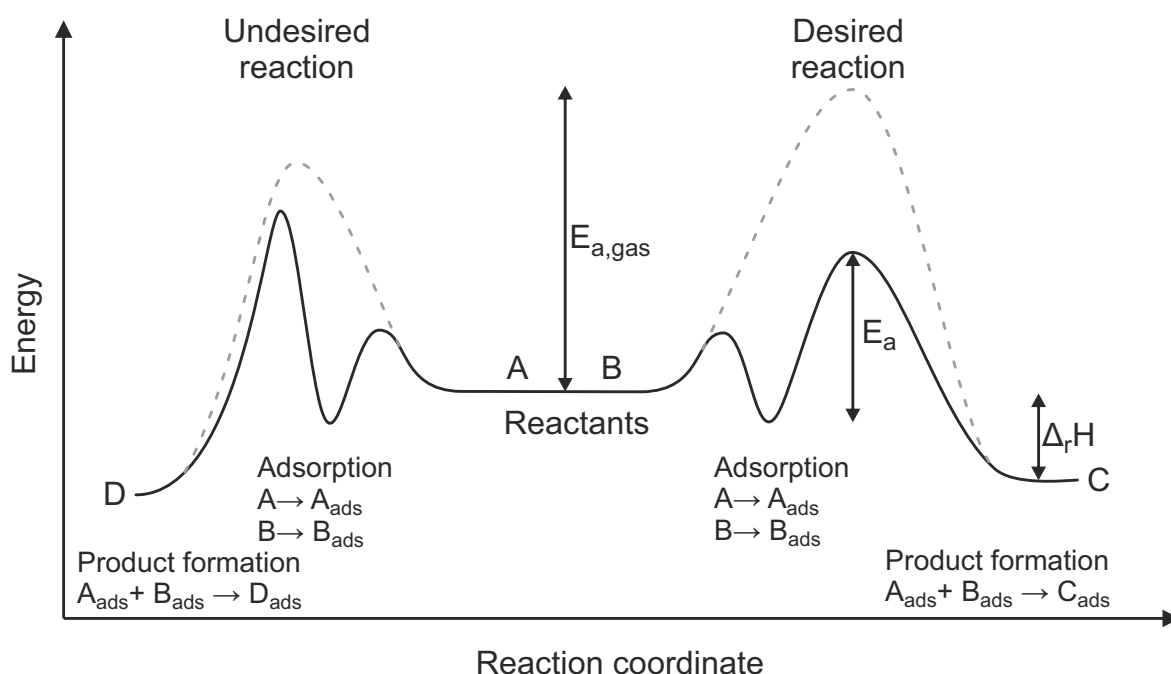


Figure 2.4: Activation energies and selectivity of multi-pathway reactions $A + B \rightarrow C$ (desired product) and $A + B \rightarrow D$ (undesired product). Illustrated is the influence of a catalyst (solid line) on the activation barrier (E_a) of the uncatalyzed reaction (dashed line).^[5]

One of the key challenges in heterogeneous catalysis is imparting selectivity to a multi-pathway reaction with different feasible products. Slight differences in the activation barriers often result in kinetic control over a chemical reaction – regardless of the thermodynamic stability of the possible products. A strategy to overcome this issue is the development of selective catalysts that promote the outcome of chemical reactions toward the desired products. Various examples from biocatalysis and photochemical reactions already show that catalysts are not only able to accelerate chemical reactions but also selectively produce a target molecule.^[26,27]

The concept of a selective catalyst influencing the activation barrier and thus the outcome of a multi-pathway reaction from an undesired product ($A \rightarrow D$) to a desired product ($A \rightarrow C$) can easily be transferred to heterogeneous catalysis (Fig. 2.4). In this case, the uncatalyzed reaction of $A + B \rightarrow D$ (dashed line) is related to the kinetically preferred reaction that also yields the thermodynamically more stable product. The utilization of a suitable heterogeneous catalyst can promote the reaction $A + B \rightarrow C$ by lowering the activation barrier of this reaction path and thus change the outcome of the chemical reaction toward the desired product C. However, it remains a challenging task to design a selective catalytic material.

A recent approach in catalysis has been to combine the advantages of heterogeneous and homogeneous catalysis by employing adsorbed ligands to promote the selectivity of a multi-pathway surface reaction toward a desired product.^[28–33] The resulting hybrid materials thus provide lateral interactions between the adsorbed ligands and the reactants, which is typical phenomenon in homogeneous catalysis, as well as interactions with the metal surface which is a typical property of heterogeneous catalysis.

One type of multi-pathway reactions with particular importance to industrial application is the partial hydrogenation of unsaturated ketones and aldehydes to unsaturated alcohols. This is a very challenging task for heterogeneous catalysis since almost every commercially employed efficient hydrogenation catalyst selectively yields the thermodynamically more stable saturated aldehyde as the hydrogenation product.^[32–35] Another complicating factor in the hydrogenation reactions of these classes of molecules is the very stable C=O double bond, which is difficult to activate as compared to the more reactive C=C bond.^[36–38] Therefore, from both the thermodynamic as well as kinetic points of view, the selective hydrogenation of unsaturated ketones and aldehydes to unsaturated alcohols is particularly difficult.

A strategy to overcome this deficit is the rational-based functionalization of the catalytically active metal surface with organic adsorbates that are capable of establishing lateral interactions with the desired reaction intermediates and thus also promote the formation of the unsaturated alcohol. This has been investigated for the α,β -unsaturated cinnamaldehyde on different surfaces.^[32,33] In particular, Kahsar et al.^[32] reported the chemoselective hydrogenation of cinnamaldehyde toward cinnamyl alcohol over Pt/Al₂O₃ functionalized with thiolate self-assembled monolayers. A similar observation was reported by Wu et al.^[33] for a CoPt₃ surface which was functionalized with the primary amine oleylamine as a ligand.

To understand the fundamental processes of the adsorption and reactivity of α,β -unsaturated aldehydes on commonly used hydrogenation catalysts, our group previously performed a detailed mechanistic study on the smallest α,β -unsaturated aldehyde acrolein adsorbed on different Pd model surfaces in the UHV.^[39–42] In particular, both the hydrogenation over Pd(111) nanoparticles, which consists mainly of Pd(111) facets and a smaller amount of

The apparatus comprises infrared reflection absorption spectroscopy (IRAS), scanning tunneling microscopy (STM), low energy electron diffraction (LEED) and molecular beam techniques (MB). The evolution of products in the gas phase was monitored by an attached quadrupole mass spectrometer (QMS). This unique combination of techniques (Fig. 2.6) allows the in-situ investigation of surface processes and reactions under well-defined and reproducible conditions to obtain a mechanistic picture at atomistic scale.

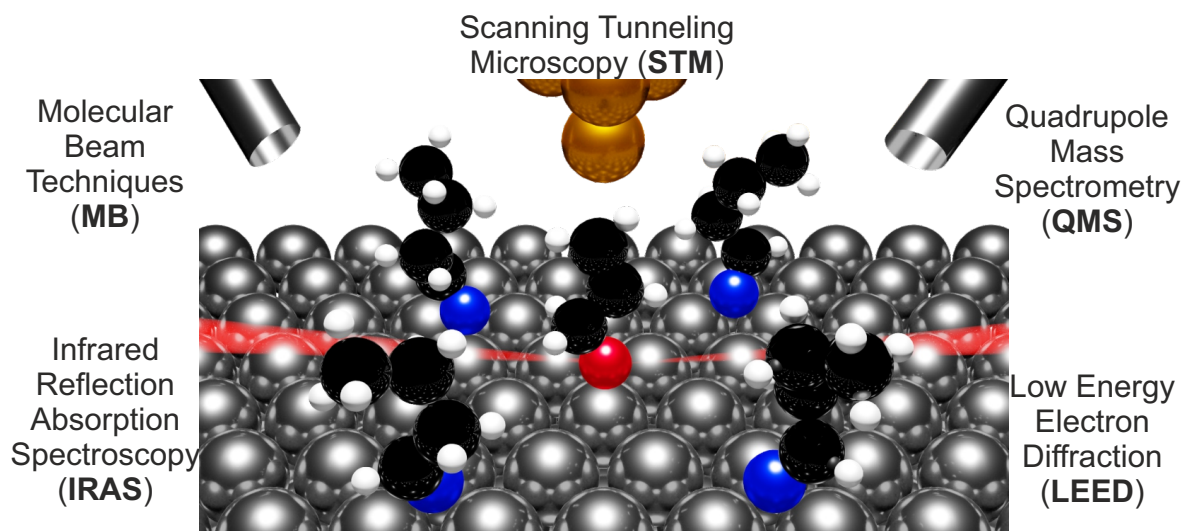


Figure 2.6: Visualization of the experimental techniques employed in this study: adsorbed molecules, dosed via molecular beams onto the surface, are investigated by means of infrared reflection absorption spectroscopy (IRAS) and scanning tunneling microscopy (STM).

In the second project of this study, we performed detailed investigations of surface–adsorbate and adsorbate–adsorbate interactions with respect to the hydrogenation reaction of prochiral α -methyl ketones. For hydrogenation reactions performed over metal surfaces, no selectivity toward one of the two feasible enantiomers is reported, as metal surfaces are achiral and two enantiomeric products are formed in equal quantities.

However, chirality is a very important aspect for chemical industry and the ability to selectively produce a specific enantiomer is of particular interest for the production of pharmaceuticals, flavors and agrochemicals. There are numerous examples in which two enantiomers may have different properties. For instance, the enantiomers of the terpenoid carvone of which (4S)-(+)-carvone smells like caraway and is the main constituent of dill seed oils while (4R)-(-)-carvone has a mint-like odor and is the main constituent of spearmint.^[46]

The importance of enantioselective hydrogenation reactions obtained with homogeneous catalysts was acknowledged by the Nobel Prize for Knowles^[47], Noyori^[48] and Sharpless^[49] in 2001. Starting in the mid 1950s by Akabori et al.^[50], great effort in many studies has been made to investigate enantioselective reactions in heterogeneous catalysis to combine the huge potential of heterogeneous catalysis with an economically and environmentally profitable chemical reaction process. However, homogeneous catalysis still contributes the main part to the industrial application of asymmetric hydrogenation reactions.^[51]

For the hydrogenation of C=O double bond containing prochiral molecules, several different systems for ketones were found to yield a high amount of selectivity over naturally-occurring as well as synthetic chirally-modified metal surfaces.^[52–56]

One of the first studies in that field was performed by Orito et al.^[56] on the α -ketoester methyl pyruvate (MePy) over chirally-modified Pt(111). The authors reported a high yield of (+)-methyl lactate over Pt/C which was chirally-modified with cinchonidine prior to the reaction. Figure 2.7 shows the reaction published in their first work.^[56]

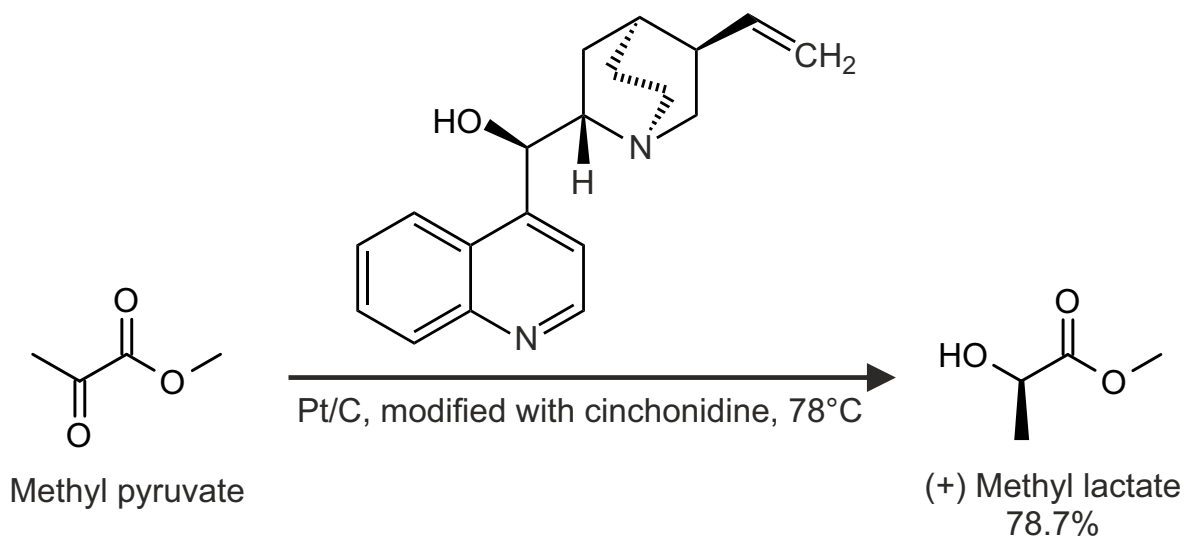


Figure 2.7: Reaction scheme for the originally reported Orito reaction. Methyl pyruvate was hydrogenated over cinchonidine-modified Pt/C.^[56]

As reported in later studies by various authors, which are summarized in the review by Mallat et al.^[52], the selective hydrogenation over modified Pt(111) is not limited to methyl pyruvate as a reactant or cinchonidine as a modifier, but can be applied on various combinations of different modifiers and so called activated ketones. The term activated ketone in organic chemistry refers to as a ketone that has an electron-withdrawing substituent in α -position and for a few examples even in β -position.^[52] Thus, this selective type of chemical reaction over chirally-modified surfaces is named after Yoshio Orito.

The fundamental processes of the lateral interactions between different, both natural or artificial chiral modifiers and prochiral molecules were topic of several surface science studies over the last decades.^[53,57–82] In this type of reaction, the reactant undergoes a direct interaction with the chiral modifier, forming a chiral 1:1 docking complex on the surface. In this complex, the reactant has a specific orientation toward the underlying metal surface, so it can only be hydrogenated from one side.^[69–71] For instance, Mahapatra et al.^[79] investigated the coadsorption of methyl pyruvate (MePy) and an artificial chiral modifier R-1-(1-naphthyl)ethylamine (R-NEA) and suggested the enol form of MePy, resulting from the keto–enol tautomerization of the ketone group, to form the docking complex with R-NEA. The hydrogenation of the enol form of α -methyl ketones, that are stabilized by the chiral modifier, thus provides a plausible explanation for the enhanced catalytic performance in the Orito reaction.

The keto–enol tautomerization as a first step for the hydrogenation reaction of carbonyl compounds was recently suggested in theoretical studies as an alternative low–barrier mechanism that has significantly lower activation barriers than the direct hydrogenation of the ketone.^[83–86] However, the enol tautomer of a ketone is in general thermodynamically less stable than the ketone and thus needs to be stabilized either via a chelated ring-like keto–enol tautomer or via the formation of oligomers.^[86–92] The experimental confirmation of

this mechanism as well as the fundamental understanding of the elementary steps in the hydrogenation of α -methyl ketones are not fully investigated. Despite the recent progress in the field of enantioselective heterogeneous catalysis, the deep atomistic-level understanding of adsorbate–adsorbate interactions has only been investigated and understood for a few reactive systems. Because of both, the numerous possibilities to build molecular complexes that consist of two or more adsorbates as well as the challenging task of the experimental identification of lateral interactions of single adsorbates, the mechanisms involved in the hydrogenation of simple α -methyl ketones are poorly understood.

In this project, we studied the adsorption geometry of two different types of α -methyl ketones as well as the chemical transformation of both over pristine Pt(111) and Pt(111) pretreated with hydrogen. In particular, ethyl pyruvate (EP), an α -keto ester, and acetophenone (AP), a methyl phenyl ketone, were investigated under a broad range of temperature and different surface conditions. This combination of α -methyl ketones was selected as prototypes for a possible intramolecular stabilization of an enol form via a chelated ring-like enol tautomer, in the case of EP, and for the intermolecular stabilization of the enol form as in the case of AP. The different mechanisms in the stabilization of the enol form may therefore most likely be the reason for the Orito reaction to perform better with ketones that are capable of establishing an intramolecular stabilization of the enol form.

A key aspect with particular importance for obtaining an atomistic understanding of the hydrogenation mechanism of ketones has been addressed in the both parts of this project. First, the effect of an electron-withdrawing substituent, i.e. the α -ester group, on the lateral interactions of the adsorbed molecules on pristine Pt(111) and Pt(111) pretreated with surface hydrogen has been studied. In the second part of the project, we studied the adsorption geometry, dynamic transformation and lateral interactions of acetophenone over both pristine Pt(111) and Pt(111) pretreated with surface hydrogen. The detailed investigation of the structural and chemical properties of both molecules adsorbed on Pt(111) provides a deeper understanding of the fundamental processes in the hydrogenation reaction of α -methyl ketones in terms of stabilization of reaction intermediates.

The present thesis is divided into the following chapters: At first, Chapter 3 provides an introduction into the processes at the gas–solid interface and the basic kinetic adsorption models. The experimental methods employed in this study are briefly described in Chapter 4. In Chapter 5, the concept and results from the systematical study on the partial hydrogenation of acrolein over three different functionalized Pd(111) surfaces, i.e. i) 2-methyl-2-pentenal, ii) allyl cyanide and iii) acetophenone, as well as the characterization of the ligand molecules are elaborated. In Chapter 6, the experimental results of the combined spectroscopic and microscopic adsorption studies on two different ketones i) ethyl pyruvate and ii) acetophenone on pristine and hydrogen-covered Pt(111) are presented. Both projects were investigated theoretically in collaboration with the Hartke group (CAU Kiel, Germany) for ethyl pyruvate and the Liu group (Nanjing University, China) for acetophenone adsorbed on Pt(111) and Pd(111). In Chapter 7 the results of both projects investigated in this work are summarized and future trends, related to lateral interactions for selective heterogeneous catalysts are illustrated. The reprints of the publications, that build the basis for this cumulative thesis, are presented in Chapter 8.

3 Theoretical Background

Heterogeneous catalysis is a process that starts with the adsorption of reactants on the surface of the catalyst. In this thesis, the focus is on the interactions of gaseous molecules with solid surfaces and the processes on this interface are described in detail. Recently, several comprehensive reviews had been published on interactions at the solid–solid interface that can be found in the work of Meiwes-Broer^[93], at the solid–liquid interface in the work of Zaera^[94], Uhlmann et al.^[95] as well as Neto et al.^[96] and at the liquid–gas interface in the work of Nathanson^[97] and Oron et al.^[98]

3.1 Scattering

The fraction of atoms or molecules, which do not irreversibly remain on the surface, are scattered from the surface. The direct scattering process can be divided into i) direct elastic scattering, in which the molecule preserves its impact momentum and energy upon reflection back into the gas phase, and ii) direct inelastic scattering, in which both the vibrational and rotational state of the molecule may change.^[99,100]

Figure 3.1 visualizes the process on an inert surface as a simple model of elastic and inelastic scattering.

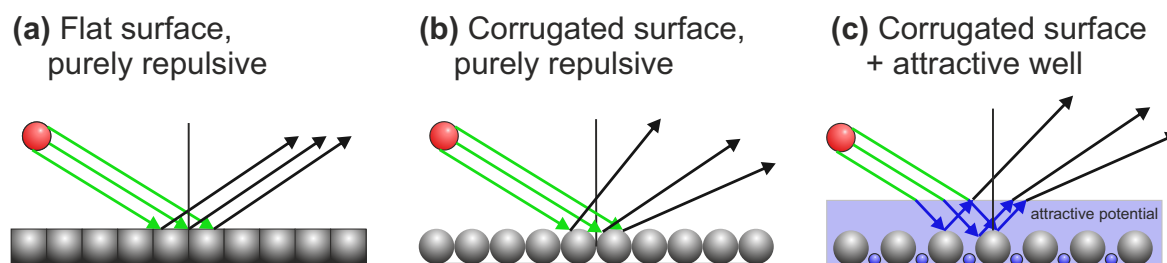


Figure 3.1: Scattering processes for a molecule (red) on (a) a purely repulsive flat surface, (b) corrugated, purely repulsive surface and (c) corrugated surface with an attractive well potential (blue). Adapted with permission from Ref.[100].

Assuming the metal surface to be perfectly flat (Fig. 3.1a), the momentum along the surface is conserved and thus the angle of incidence approximately equals the scattering angle. As a result, the angular distribution ($\Delta\theta$) of the scattered particles is very narrow. This is an appropriate assumption in case of large mass differences between the surface and the scattered atoms or molecules, for helium scattering on a metal surface as an example.^[100] When the mass difference between the scattered molecule, e.g. CO, N₂ or O₂, and the metal surface atoms is similar, a transfer of perpendicular momentum from the molecule to the surface or vice versa is possible, resulting in a heating or cooling of the surface. Depending on the involved states, the scattering process can thus be divided into i) vibrationally, ii) rotationally or iii) both vibrationally and rotationally inelastic scattering.

The morphology of the surface has a decisive influence on the scattering process. Assuming the surface not to be perfectly flat but corrugated (Fig. 3.1b), the momentum parallel to the surface is not conserved. The scattered molecules thus have an angular distribution which has a broader width with increasing energy of the particle.

Taking into account that attractive forces between the surface and the molecule may be involved in the interaction, the model becomes more complicated (Fig. 3.1c). Upon contact with the surface, a physisorbed or chemisorbed state may appear in which exchange of thermal energy is possible. In this trapping process, the perpendicular component of the momentum is fully transferred from the molecule to the surface. When the thermal energy of the surface is higher than the desorption energy, the molecule overcomes the chemisorbed state and desorbs again. This process is often named trapped-desorption which results in a $\cos(\theta)$ angular dependence of the scattered particles.^[99–102]

3.2 Physisorption and Chemisorption

When a particle (A) impinges from the gas phase (gas) on a surface and remains on a site of a surface (o), it is adsorbed (ad) on the surface (Eq. 3.1).



The process is usually divided into two different attractive forces: physisorption and chemisorption. The physisorbed molecule is hardly perturbed on a surface upon adsorption and the bonding mechanism can be related to dispersive interactions. The correlated electron fluctuation sets up a dipole in the adsorbed molecule, which induces an image dipole in the polarizable solid.^[103] Dispersive interactions are long-range attractive forces that are relatively weak and in the range of less than $30 \text{ kJ}\cdot\text{mol}^{-1}$.^[5,8]

These attractive forces are limited by the Coulomb repulsion. When an atom approaches the surface, the electrons start to interact strongly with the electrons of the surface resulting in strong repulsive forces at very short distance. A simple model of the potential function ($u(r)$) which combines the short range repulsive Coulomb forces ($u_{\text{repulsive}}(r)$) and the long-range attractive dispersive interactions ($u_{\text{attractive}}(r)$),

$$u(r) = u_{\text{attractive}}(r) + u_{\text{repulsive}}(r), \quad (3.2)$$

is the Lennard-Jones potential,

$$u(r) = \epsilon \frac{n}{n-m} \left(\frac{n}{m} \right)^{(m/(n-m))} \left[\left(\frac{\sigma}{r} \right)^n - \left(\frac{\sigma}{r} \right)^m \right], \quad (3.3)$$

where ϵ describes the potential well depth, σ the width of the potential at $u(r) = 0$ and r is the internuclear distance. Usually a specific form of the Lennard-Jones(12,6) potential (Eq. 3.4) is used. The value of the exponent $m = 6$ represents the assumption that the attractive forces are only based on induced dipoles and values of n were found empirically, ranging from 9 to 12.^[99]

$$u(r) = 4\epsilon \left[\left(\frac{\sigma}{r} \right)^{12} - \left(\frac{\sigma}{r} \right)^6 \right] \quad (3.4)$$

Figure 3.2 visualizes the Lennard-Jones(12,6) potential.

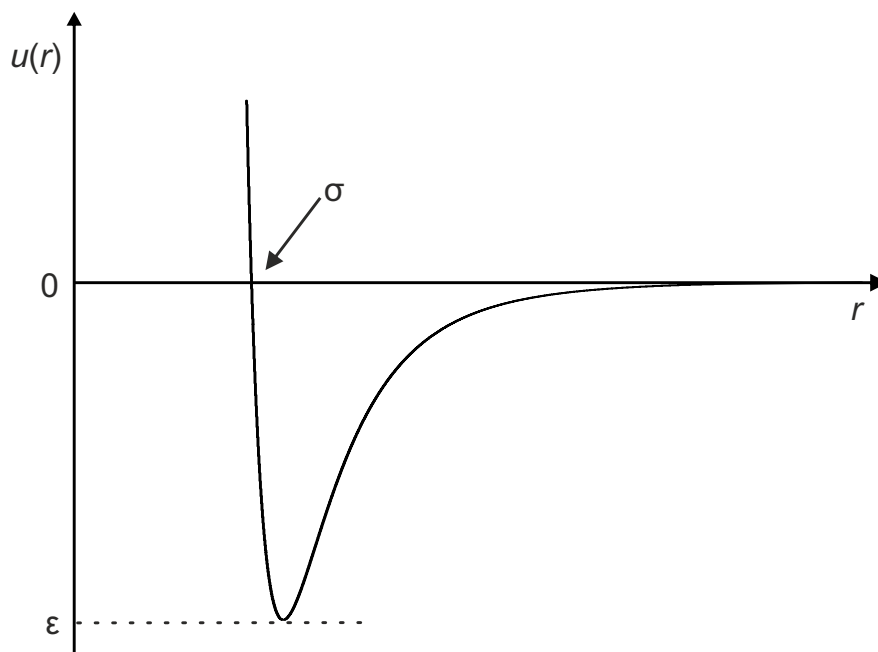


Figure 3.2: Visualization of the Lennard-Jones(12,6) potential (u) as a function of the distance (r) from the surface. ϵ is the potential well depth and σ the potential well width. Adapted from Ref.[104].

Physisorption potentials usually have their energy minimum several angstroms outside the surface and a depth of $3\text{--}30\text{ kJ}\cdot\text{mol}^{-1}$. Thus, physisorption is often a low temperature adsorption process, since molecules have a mean kinetic energy of $3.5\text{ kJ}\cdot\text{mol}^{-1}$ at room temperature and can easily overcome the potential well barrier.^[8,103]

These dispersive interactions are not limited to molecule–surface interface but also occur between adsorbed molecules on the surface or intermolecular interactions in condensed matter where the correlated fluctuating charge in neighboring molecules induces an attractive force.^[103] Therefore, the infrared signatures of physisorbed molecules are similar to unperturbed molecules in the gas phase.

When a surface strongly interacts with an adsorbed molecule, the adsorption geometry and electronic structure of a molecule is strongly perturbed, forming new covalent or ionic bonds between the surface and the adsorbed molecule. In contrast to physisorption, chemisorbed molecules and atoms are closer and stronger bonded to the surface.

In case of simple molecules, like hydrogen adsorbed on transition metals, this may lead to a dissociative adsorption forming a new chemical bond with the surface atoms. The interactions between adsorbate and metal surface have a decisive influence on whether the chemisorption of a molecule is direct or dissociative.

Hammer et al.^[105] studied the adsorption of CO on various surfaces in an extended theoretical study. They reported the change from molecular to dissociative adsorption of 4d transition metals with decreasing atomic number. The authors explained this trend with the upshift of the energy of the d states with respect to the Fermi level of the metal atoms involved in the bonding with the adsorbate. Brodén et al.^[106] came to the same conclusion in an experimental study on the chemisorption of CO on different transition metals using synchrotron radiation.

In case of chemisorption of C=C bonds containing small molecules, e.g. ethylene, the binding state has two limiting types of interactions between complete ($sp^2 \rightarrow sp^3$) rehybridization, resulting in a strong di- σ arrangement and a weaker binding π mode in which the double bond character is preserved.^[107] The reality of adsorbed olefins show seamless transition between both types of adsorption depending on the nature of the substrate or the conditions.^[108] Description of the process of physis- or chemisorption via a single Lennard-Jones potential, which is only dependent on the distance from the surface, has two major disadvantages. The attractive potential is monotonically decreasing while the molecule approaches the surface until the equilibrium position is reached. This does not reflect the experimental data obtained for e.g. dissociative adsorption of hydrogen on Cu(110), where Campbell et al.^[109] reported an activation energy of $(14.3 \pm 1.4) \text{ kcal}\cdot\text{mol}^{-1}$. Furthermore, this model excludes different adsorption sites with differing adsorption energies.

Figure 3.3 schematically shows four different cases of chemisorption: (a) direct, (b) precursor-mediated, (c) unactivated dissociative and (d) activated dissociative chemisorption.

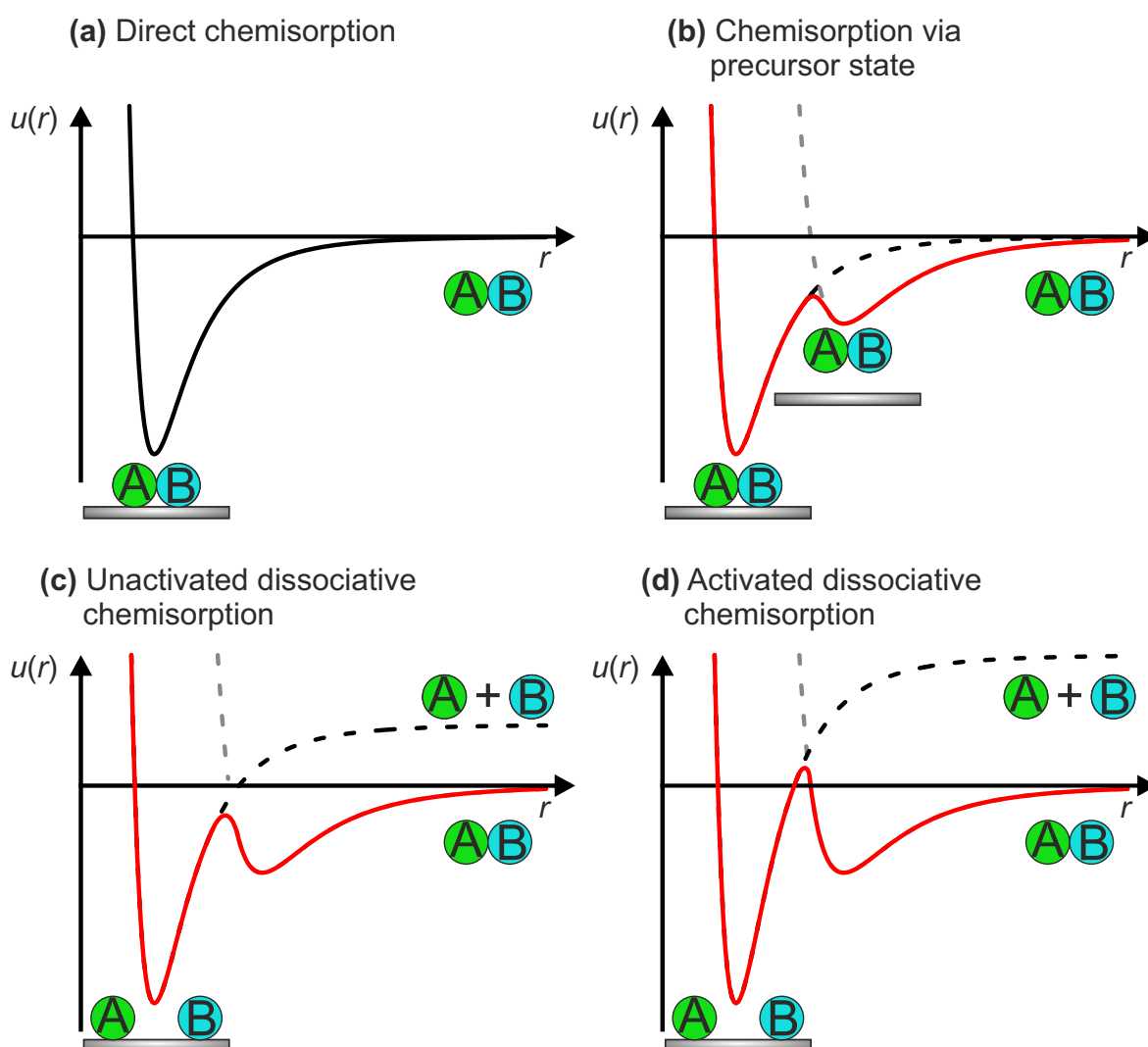


Figure 3.3: 1D potential energy curves along the r axis for four different cases of chemisorption of a diatomic molecule on a solid surface. In (a) direct chemisorption, (b) precursor-mediated chemisorption, (c) unactivated and (d) activated dissociative precursor-mediated chemisorption. Reproduced with permission from Ref.[110].

The direct chemisorption (Fig. 3.3a) equals the previously mentioned Lennard-Jones potential. If there are several different adsorption sites available on the surface, each of them can be described with its own potential curve. Those potential wells may cross each other resulting in a precursor-mediated chemisorption with respect to the lowest lying state (Fig. 3.3b). A typical example for precursor-mediated chemisorption is the crossing of physisorption with chemisorption in which molecules first adsorb weakly upon impingement on surfaces. This is commonly called “intrinsic precursor state” for occurrence above the free surface or “extrinsic precursor state” for occurrence above islands of already adsorbed particles on the surface.^[99,110]

Experimentally, this precursor-mediated adsorption was identified by, e.g. Redulic et al.^[111] for nitrogen adsorbed on W(100) in a broad range of temperature. The authors showed that the sticking probability of N_2 initially decreases with both increasing kinetic energy and surface temperature. The latter is a general trend since the sticking coefficient is higher on cold surfaces but the kinetic energy has no such trend.

The sticking probability in relation to kinetic energy of the adsorbed species is dependent on the adsorption path. While the sticking probability of the nitrogen on W(100) on the precursor-mediated adsorption path initially decreases with higher kinetic energy, it increases once a second activated adsorption path is accessible. The decrease of the sticking probability with higher kinetic energy is explained by the need of energy dissipation of the particle in the precursor state. While the particle equilibrates in the precursor state, both the desorption as well as transition into a lower lying chemisorbed state are two competing processes with different energy barriers. The probability to overcome the desorption energy barrier is higher with increasing kinetic energy. The precursor-mediated chemisorption model can also be applied to dissociative adsorption (Fig. 3.3c-d). The dissociation process becomes activated once the energy barrier is above the potential well of the weaker bond precursor state. Otherwise it becomes an unactivated precursor-mediated dissociative chemisorption.

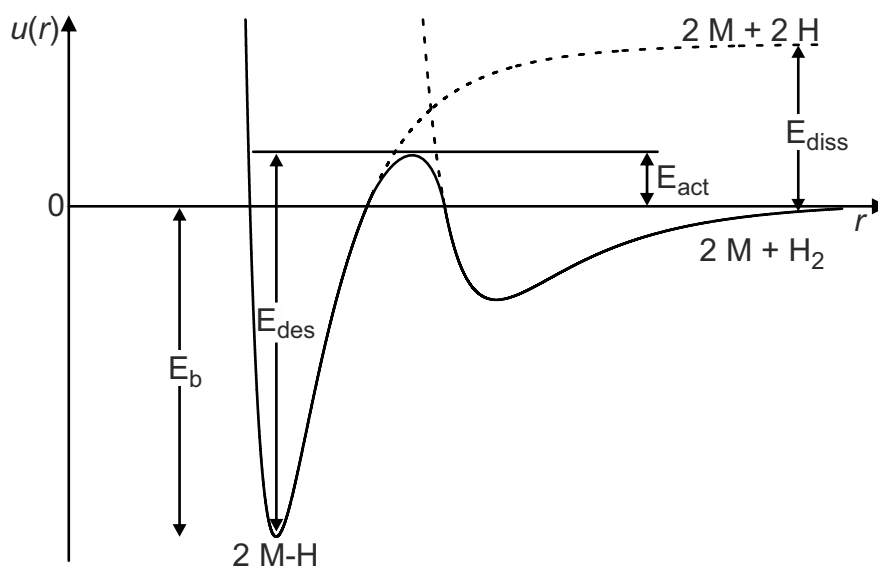


Figure 3.4: Potential curves as a function of the distance (r) between the Cu(110) metal surface (M) and the hydrogen atom (H) and molecule (H_2) of activated dissociative chemisorbed hydrogen via a physisorbed precursor state. The corresponding energies are binding energy (E_b), desorption energy (E_{des}), activation energy (E_{act}) and dissociation energy (E_{diss}). Adapted from Ref.[103].

The activated dissociative chemisorption of hydrogen on Cu(110) via a physisorbed precursor state according to Campbell et al.^[109] is shown in Figure 3.4. The figure shows a simplified model of the potential wells dependent on the distance between the surface and the adsorbed particle of chemisorbed and physisorbed hydrogen on a Cu(110) surface (M) including an energy barrier for the dissociation. The corresponding energies are binding energy (E_b), desorption energy (E_{des}), activation energy (E_{act}) and dissociation energy (E_{diss}).

A detailed description and experimental detection of precursor states in adsorption can also be found in a review about kinetic measurements on solid surfaces using molecular beams by Francisco Zaera.^[110]

3.3 Hydrogen Adsorption on Pd and Pt

The dissociative chemisorption (Eq. 3.5) of hydrogen on a metal surface (\circ) plays an important role in hydrogenation reactions.



In contrast to Cu(110), the dissociation of hydrogen on Pd surfaces has no activation barrier and thus already occurs at very low temperature.^[112] Mitsui et al.^[113] showed in a low temperature scanning tunneling microscopy (STM) study on H_2 adsorbed on a Pd(111) surface that hydrogen can dissociate already at 37 K. Chemisorbed surface hydrogen is able to diffuse into the metal bulk. This is an activated process and was reported to occur below 130 K on Pd(110) single crystals.^[112,114]

This results in two different forms of hydrogen with different binding energy (E_{bind}): i) strongly bonded surface hydrogen with E_{bind} about 0.5 eV/H atom and ii) weakly bonded subsurface hydrogen with E_{bind} ranging between 0.3 eV/H atom for low hydrogen uptakes and 0.1 eV/H atom for higher hydrogen uptakes.^[112,115] A more detailed description of chemisorbed subsurface hydrogen and the experimental technique resonant nuclear reaction analysis to investigate hydrogen concentration as a function of material depth can be found in the publications of Markus Wilde.^[116,117]

In early hydrogen temperature programmed desorption (TPD) studies on Pt(111), a similar observation of two energetically different hydrogen species was also observed: a weakly bound β_1 - and a strongly bound β_2 -species.^[112] A different TPD study by Greenlief et al.^[118] proposed the involvement of subsurface adsorption sites for the adsorption of hydrogen on Pt(111). This general opinion is nowadays outdated, since several other studies could prove that the previously assigned different surface species were related to both stepped or defected surfaces.^[119–123]

There are numerous publications in surface science by many different authors reporting both experimental and theoretical results about the adsorption of hydrogen on various surfaces. The works of Klaus Christmann provide an extended overview on the adsorption of hydrogen over various metal surfaces.^[99,112]

3.4 Adsorption and Sticking

As described in the previous section, when a particle (A) impinges on a surface area (A_{surface}), it can either be scattered back directly into the gas phase (A_{gas}) or be adsorbed on the surface (A_{ad}). The change of the number of adsorbed particles per area and time equals the adsorption rate (r_{ad}) (Eq. 3.6).

$$r_{\text{ad}} = \frac{\partial A_{\text{ad}}}{A_{\text{surface}} \partial t} = \frac{\partial \theta}{\partial t} \quad (3.6)$$

The coverage (θ) is the ratio of adsorbed molecules in relation to the number of surface atoms (Eq. 3.7).

$$\theta = \frac{\text{number of adsorbed particles}}{\text{number of surface atoms}} \quad (3.7)$$

Initially, all molecules usually stick on a non-repulsive pristine surface unless the surface temperature is too high. This can be explained by the transition into a strong chemisorbed state. With increasing coverage, the reactivity of the surface decreases and therefore the adsorption rate correspondingly. According to the simplified Langmuir adsorption model^[124], each adsorption site can adsorb a single particle. When a particle impinges on an occupied site, it is scattered back from the surface whereas a vacant adsorption (\circ) site results in the adsorption. In case of atomic associative adsorption, the kinetic model^[99] is



with the rates of adsorption (r_{ad}) and desorption (r_{des})

$$r_{\text{ad}} = k_{\text{ad}} \cdot A_{\text{gas}} \cdot \circ = k_{\text{ad}} p_A (1 - \theta), \quad (3.9)$$

$$r_{\text{des}} = k_{\text{des}} \cdot A_{\text{ad}} = k_{\text{des}} \theta. \quad (3.10)$$

This can be rewritten in equilibrium $r_{\text{ad}} = r_{\text{des}}$ as

$$\frac{\theta}{1 - \theta} = \frac{k_{\text{ad}}}{k_{\text{des}}} \cdot p_A. \quad (3.11)$$

Using the equilibrium constant K_A and the activation energies for adsorption (E'_{ad}) and desorption (E'_{des})

$$K_A = \frac{k_{\text{ad}}}{k_{\text{des}}} = \frac{k_{\text{ad},0}}{k_{\text{des},0}} \cdot \exp\left(\frac{-(E'_{\text{ad}} - E'_{\text{des}})}{k_B T}\right), \quad (3.12)$$

where $E_{\text{ad}} = E'_{\text{ad}} - E'_{\text{des}}$ and E'_{ad} is zero for atomic and associative adsorption, this results in

$$\frac{\theta}{1 - \theta} = \frac{k_{\text{ad},0}}{k_{\text{des},0}} \cdot p_A \cdot \exp\left(\frac{E_{\text{ad}}}{k_B T}\right). \quad (3.13)$$

The ratio of adsorbed and scattered molecules is the sticking coefficient (S , Eq. 3.14) which describes the probability for a particle to stick on the surface.^[99]

$$S = \frac{A_{\text{ad}}}{A_{\text{gas}}} \quad (3.14)$$

The value of the sticking coefficient is between 0 and 1 and is assumed to be 1 at low temperature as well as low coverage. The coverage-dependent sticking probability ($S_L(\theta)$) according to the Langmuir model is therefore

$$S_L(\theta) = S_0 (1 - \theta)^n = S_0 \left(1 + \frac{\theta}{1 - \theta}\right)^{-n}, \quad (3.15)$$

where S_0 is the initial sticking coefficient, which corresponds to the sticking coefficient on a pristine surface, and n is the reaction order.

The Langmuir adsorption isotherm has been modified several times to extend its application to a wider range of adsorption models. Fowler and Guggenheim^[125] introduced an energy term which reflects the intermolecular interactions between adsorbed molecules. The adsorption energy is dependent on the lateral interaction and thus the Langmuir equation (Eq. 3.13) becomes

$$\frac{\theta}{1 - \theta} = \frac{k_{\text{ad},0}}{k_{\text{des},0}} \cdot p_A \cdot \exp\left(\frac{(E_{\text{ad}} + z w \theta)}{k_B T}\right), \quad (3.16)$$

where z is the number of neighbor sites and w the lateral interaction energy.

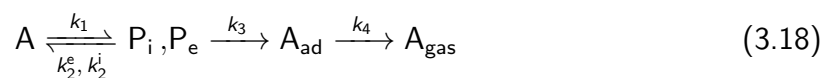
The equal treatment of all adsorption sites is one of the most striking deficits of the Langmuir model. Initially, the particles occupy the energetically lowest lying sites upon adsorption on the surface. With increasing coverage, particles also adsorb on energetically different lying sites. Temkin^[126] and Freundlich^[127] suggested a model which reflects the heterogeneity of the surface in which they propose the adsorption energy being dependent on the surface coverage. The former assumes a linear decrease of the adsorption energy with increasing coverage, the latter an exponential decrease of the adsorption energy. In case of the linear decrease of the adsorption energy, the Langmuir equation (Eq. 3.13) becomes

$$\frac{\theta}{1 - \theta} = \frac{k_{\text{ad},0}}{k_{\text{des},0}} \cdot p_A \cdot \exp\left(\frac{(E_{\text{ad}} \cdot (1 - \theta))}{k_B T}\right), \quad (3.17)$$

where the adsorption energy decreases linear with the coverage.

These models may be sufficient for direct adsorption, but are insufficient for the previously discussed more complex precursor-mediated adsorption model.

Kisliuk^[128] expanded the model of Langmuir including parameters for the precursor state (Eq. 3.18). This kinetic model is visualized in Figure 3.5. A gaseous species (A) can chemisorb on a surface via two different precursor states, intrinsic and extrinsic. The intrinsic precursor (P_i) is a weakly bond state above the free surface and an extrinsic precursor (P_e) is a weakly bond state above a specific area of the surface where adsorbed particles are already present.



The corresponding adsorption rates for this model are

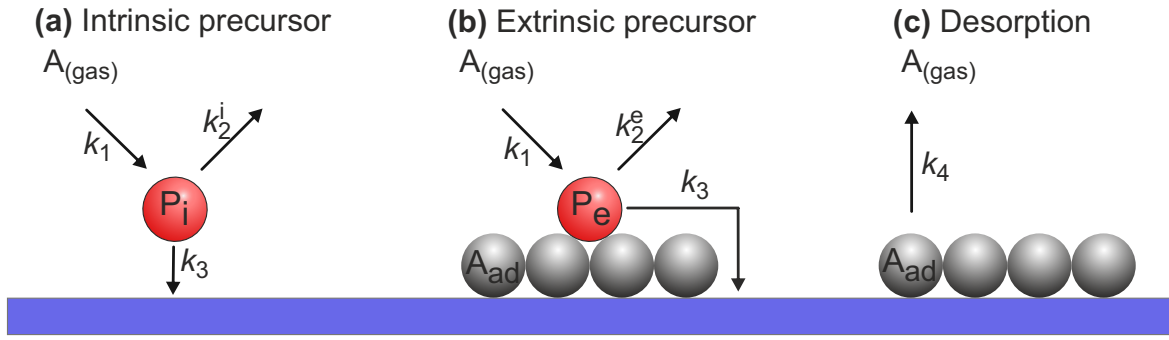


Figure 3.5: Kisluk adsorption model for the precursor-mediated adsorption. A gaseous species (A) adsorbs on a surface via an intrinsic precursor (P_i) or extrinsic precursor (P_e). Adapted from Ref.[99].

$$r_{ad} = r_1 - r_2 - r_4, \quad (3.19)$$

where r_1 is the adsorption into the precursor states P_i (intrinsic) or P_e (extrinsic), r_2 the desorption rate of the precursors and r_4 the desorption rate of the chemisorbed particle. Assuming a very low precursor concentration on the surface, the stationary principle results in

$$\frac{\partial P_{i,e}}{\partial t} \approx 0 \rightarrow r_3 = r_1 - r_2 \quad (3.20)$$

for the reaction rate of the precursor. That simplifies (Eq. 3.19) to (Eq. 3.21) where the adsorption rate is only dependent on the reaction rate of the precursor and the desorption rate of the chemisorbed species. For low coverage ($\theta < 0.95$)^[99], the desorption rate of chemisorbed particles is significantly lower compared to the reaction rate of the precursor ($r_3 \gg r_4$).

$$r_{ad} = r_3 - r_4 \approx r_3 = r_1 - r_2 \quad (3.21)$$

The reaction rates r_1 , r_2 and r_3 can be expressed as

$$r_1 = S_p \cdot A_{\text{impact}} \cdot F, \quad (3.22)$$

$$r_2 = r_2^i + r_2^e = N_p [k_2^i (1 - \theta) + k_2^e \theta], \quad (3.23)$$

$$r_3 = k_3 N_p (1 - \theta), \quad (3.24)$$

with S_p sticking coefficient of the precursor, N_p the number of precursors, A_{impact} area of impact, F impact rate of gaseous particles and θ surface coverage. The sticking coefficient S is

$$S = \frac{r_{ad}}{A_{\text{impact}} \cdot F}. \quad (3.25)$$

Equations 3.20-3.25 can be summarized to

$$r_{ad} = \frac{k_3 \cdot S_p \cdot A_{\text{impact}} \cdot F (1 - \theta)}{[k_2^i (1 - \theta) + k_2^e \theta] + k_3 (1 - \theta)}, \quad (3.26)$$

$$S = \frac{k_3 S_p (1 - \theta)}{k_2^i + k_3 - \theta(k_2^i - k_2^e + k_3)}. \quad (3.27)$$

Dividing (Eq. 3.27) by $S_0 = \frac{k_3}{k_2^i + k_3}$, which equals the sticking coefficient for $\theta = 0$, results in an expression for the sticking coefficient that is normalized to the initial sticking coefficient

$$\frac{S}{S_0} = \frac{S_p (1 - \theta)}{1 - \theta + \frac{k_2^e}{k_3 + k_2^i} \theta}, \quad (3.28)$$

which can be rewritten as (Eq. 3.30) using the precursor state parameter (K_p) (Eq. 3.29).

$$K_p = \frac{k_2^e}{k_3 + k_2^i} \quad (3.29)$$

$$\frac{S}{S_0} = \frac{S_p}{1 + K_p \frac{\theta}{1 - \theta}} = S_p \left(1 + K_p \frac{\theta}{1 - \theta} \right)^{-1} \quad (3.30)$$

Figure 3.6 shows the graph of sticking coefficient depending on the surface coverage according to Equation 3.30 at different values of K_p .

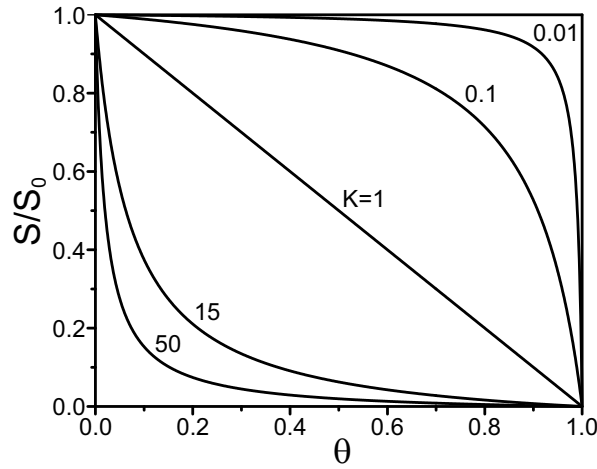


Figure 3.6: Coverage-dependent sticking coefficient normalized on the initial sticking coefficient (S/S_0) for the precursor-mediated adsorption at different values of the precursor state parameter K_p . The sticking coefficient of the precursor $S_p = 1$. Adapted from Ref.[128].

The precursor state parameter is $K_p = 1$ for a Langmuir-type of adsorption and a molecule becomes sticky on a surface when $K_p \ll 1$. This applies for either a low desorption rate for an extrinsic precursor or a high desorption rate of an intrinsic precursor.

There are many examples for non-Langmuirian behavior in adsorption on surfaces caused by precursor states. Just to mention a few, there are Hirsimäki et al.^[129], showing an increasing sticking probability compared to the Langmuirian adsorption for the adsorption of CO on Pd(110) and NO on Pd(320), and Youngs et al.^[130], for formic acid adsorbed on Cu(110).

Besides the coverage, the temperature has a significant influence on the sticking probability on surfaces. The temperature- and coverage-dependent sticking coefficient ($S(T, \theta)$)^[103] of a molecule with the mass (m) is expressed by

$$S(T, \theta) = \frac{\sqrt{2\pi mk_B T} \partial\theta}{p \partial t}, \quad (3.31)$$

with Boltzmann constant k_B . Experimentally, the sticking coefficients can be determined by measuring the coverage (θ) as a function of dosage using a combination of molecular beam techniques and either surface-sensitive spectroscopy or mass spectrometry.^[100] On the one hand, sticking coefficients are important for the determination of the absolute coverages in spectroscopic studies; on the other hand, a good estimation of the exposure to coverage relation can be achieved by the determination of the exposure limit when no more molecules chemisorb on the surface. This can clearly be identified in infrared studies when the molecules retain the spectroscopic signatures of the gas phase species where no chemisorption potential of the underlying surface perturbs the molecule.

The previously described models are suitable for the adsorption of particles up to a full monolayer. At either high pressure or very low temperature, the particles may also adsorb in layers more distant from the surface. In case of low temperature, thermal energy is not sufficient to overcome the energy barrier for physisorption. A commonly used method for multilayer adsorption is the BET isotherm, named after Brunauer, Emmett and Teller.^[131] Their model is based on the assumption of a Langmuirian behavior without any interaction between particles in the first layer and every adsorbed particle in the adjacent layers being an allowed adsorption site for particles of the next higher layer. The BET isotherm using an inert gas, e.g. N_2 , Ar or Kr, is nowadays a well-established method for the determination of surface areas of porous materials.^[132]

3.5 Desorption

If all of the molecules impinging on a surface were either adsorbed or scattered, heterogeneous catalysis would not have such wide range application. Therefore desorption (des), which is the reverse process of adsorption, is of great importance as it critically determines the steady-state concentration of the reactants on the surface. During desorption, a surface-bonded species desorbs from the surface, leaving a free surface area.



This process is favored once the energy of the particle is higher than the binding energy so that the activation barrier of the attractive potential well can be overcome.

$$k_{des} = A_{des} \cdot \exp\left(-\frac{E_{des}}{k_B T}\right) \quad (3.33)$$

The most common way to bring energy into a system is heating the surface. Desorption energies can be measured by the temperature-dependent desorption rate (Eq. 3.34). This equation is often called Polanyi-Wigner equation where the order (n) of desorption reaction and the coverage (θ) needs to be considered.^[133]

$$r_{\text{des}}(T, \theta) = A_{\text{des}} \cdot \theta(T)^n \cdot \exp\left(-\frac{E_{\text{des}}}{k_{\text{B}} T}\right) \quad (3.34)$$

Examples for different desorption orders are i) 0th order: Ag desorption on Ru(001)^[134], ii) 1st order: CO desorption on Pt(112)^[135] and iii) 2nd order: N₂ desorption on Rh(100)^[136]. Desorption is an important process being applied in the temperature programmed desorption (TPD), a widely used technique to determine the desorption temperature, desorption order and energy. After adsorbing molecules on a cold surface (T_0), the sample is heated with a constant heating rate (β) up to several hundred Kelvin. The temperature becomes therefore a time-dependent parameter.

$$T(t) = T_0 + \beta \cdot t \quad (3.35)$$

The time-dependent desorption rate, which can directly be measured with mass spectrometry, can be expressed as

$$r_{\text{des}}(t, \theta) = A_{\text{des}} \cdot \theta(T)^n \cdot \exp\left(-\frac{E_{\text{des}}}{k_{\text{B}} (T_0 + \beta \cdot t)}\right). \quad (3.36)$$

Recently, several comprehensive reviews had been published on TPD methods and their application that can be found in the work of David King^[137], a microkinetic simulation of TPD spectra in the work of Wang et al.^[138] and a more theoretical analysis of first-order kinetics TPD data treatment in the work of Patrick Barrie.^[139]

3.6 Diffusion

In Section 3.2 the chemisorbed molecule is illustrated as a particle being “trapped” at the bottom of a potential well along the surface normal coordinate. The molecule may only leave this potential well when the energy is high enough to overcome the desorption barrier. This is true when the desorption from the surface is considered but neglects the three dimensionality of the surface. There are different adsorption sites on surfaces, at which the molecular species might have different adsorption energy. The energy barrier between two local energy minima is usually significantly lower than the desorption energy. Being chemisorbed on the surface does not necessarily mean being immobile on the surface.^[140] The residence time (τ) of an adsorbed particle at an adsorption site (i) with an activation barrier (E_{diff} , diffusion energy) and pre-exponential factor (A_{diff}) is expressed by

$$\tau_i = A_{\text{diff}} \cdot \exp\left(\frac{E_{\text{diff}}}{k_{\text{B}} T}\right). \quad (3.37)$$

The diffusion energy barrier is usually 10–20 % of the adsorption energy allowing molecules to move between different sites before having sufficient thermal energy to leave the chemisorption potential. The mobility and residence time at a specific adsorption site is dependent on the thermal energy. A high energy barrier $E_{\text{diff}} \gtrsim 10k_{\text{B}} T$ means immobile particles whereas a low energy barrier of $E_{\text{diff}} \lesssim k_{\text{B}} T$ corresponds to unhindered diffusion across the surface.^[99]

3.7 Lateral Interactions

The previously mentioned adsorption and desorption models are based on the assumption of non-interacting atoms or molecules on the surface. This ideal model usually collapses on highly covered surfaces where lateral interactions of neighboring molecules become important.

Upon adsorption on a surface, there are two different types of bonding that prevent the molecule from immediate desorption: the molecule may interact with the surface (surface–adsorbate interaction) or with other adsorbed molecules (adsorbate–adsorbate interaction). Lateral interactions can either be attractive or repulsive. The former is the driving force for molecules that are mobile on the surface to form adsorbate oligomers. There are many publications in surface science in which the authors show that attractive lateral interactions of adsorbed molecules result in the formation of self-assembled structures on surfaces, hence this is not a rare phenomenon. In addition, attempts are also being made to build chemically customized interfaces via attractive lateral interactions of adsorbed molecules. Some of the latest scientific results on how 2D self-assembled molecular networks can be employed to customize interfaces are summarized in the review by Verstraete et al.^[141]

Repulsive lateral interactions may result in a weakening of the surface–adsorbate bonding. On transition metals, a weakening of the bonding of the adsorbate with the surface, as the coverage of adsorbed molecules increases, may be related to a smaller overlap of the individual molecular orbitals of the molecules with the underlying d-orbitals of the metal surface or be related to a change in the π electron donation/back donation interaction.^[105] The difference in adsorption energy of a species (*i*) due to lateral interactions with a neighboring species (*n*) can be expressed as

$$E_{\text{ad}}^i = E_0^i - \sum_j n_j w_{i,j}, \quad (3.38)$$

where E_0^i equals the adsorption energy of non-interacting molecules, (*j*) the number of neighbors and $w_{i,j}$ the interaction energy. Attractive lateral interactions result in negative values of w and repulsive forces in positive values of w .^[8] Lateral interaction energies can significantly influence the adsorption behavior on surfaces. There are several studies in which the authors propose examples that show repulsive lateral interactions.

Just to mention a few, van Bavel et al.^[142] measured the repulsion energies between nitrogen and CO on Rh(100) using temperature programmed desorption. They reported coadsorbed nitrogen reduces the desorption temperature of CO from 500 K on pristine Rh(100) to 240 K on nitrogen coadsorbed Rh(100). They calculated the reduction of adsorption energy of CO on pristine Rh(100) from 135 kJ·mol⁻¹ to 59 kJ·mol⁻¹ when each CO molecule is surrounded by four nitrogen atoms. Thus the interaction energy $\omega_{\text{CO-N}}$ is 19 kJ·mol⁻¹ per neighbor.

Fernandez-Torrente et al.^[143] investigated the adsorption of tetrathiafulvalene (C₆H₄S₄, TTF) on Au(111) in a combined STM and DFT study. The authors showed that the charge transfer from the molecule to the gold surface results in the spontaneous formation of a superlattice of charged monomers due to a long-range repulsive potential.

Not only the adsorption energies but also activation barriers of competing chemical reactions may be influenced by lateral interactions. Surfaces and their reactivity may be significantly altered by adsorbing molecules prior to the reaction. The adsorbate–adsorbate interaction is the principle of ligand-directed catalysis as adsorbate-functionalized surfaces have different geometric or electronic characteristics compared to pristine surfaces.^[144]

3.8 Reaction Mechanisms at Gas–Solid Interfaces

The interaction of atoms or molecules with a surface and the models that describe the processes at the interface have been presented in the previous sections. The microscopic-level understanding of the elementary processes occurring on the catalytic surfaces, such as details of e.g. the reaction mechanisms, kinetics and the adsorbate–surface bonding, are crucial for achieving a rational-based design of new catalysts for industrial applications.

The fundamental model of a bimolecular surface reaction of A and B (Eq. 3.39) can be expressed in two different ways: i) both reactants are adsorbed on the surface prior to the reaction or ii) one reactant is adsorbed on the surface and reacts with a gaseous species.



The first is called Langmuir-Hinshelwood mechanism which was proposed by Irving Langmuir in 1922^[145] and further developed by Cyril Hinshelwood in 1926.^[146] A typical example for a Langmuir-Hinshelwood reaction mechanism is the CO oxidation on Pt(111).^[147] This reaction involves the dissociative adsorption of O₂, the chemisorption of CO, diffusion of both adsorbed species on the surface and the formation with subsequent desorption of CO₂. The processes involved in the Langmuir-Hinshelwood mechanism are presented in Equations 3.40-3.43.

Adsorption of A on a vacant surface site (○)



Adsorption of B on a vacant surface site (○)



Diffusion of A and B on the surface with formation of product (P)



Desorption of P, leaving vacant surface sites



The second reaction mechanism is called the Eley-Rideal mechanism which was proposed for the isotopic exchange of hydrogen and deuterium on a tungsten surface published in 1938.^[148] An additional example for this mechanism was proposed by Jenkins et al.^[149] for the catalytic hydrogenation of ethylene on a nickel catalyst. However, reactions involving the Eley-Rideal mechanism are extremely rare and there are only a few dynamic studies for which this mechanism was proven.^[8] The processes involved in the Eley-Rideal mechanism are presented in Equations 3.44-3.46.

Adsorption of A on a vacant surface site (○)



Reaction of A_{ad} with B_g forming P_{ad}



Desorption of P, leaving a vacant surface site



Both the Langmuir-Hinshelwood and the Eley-Rideal mechanism exclude the occurrence of physisorbed reactants. Harris and Kasemo^[150] suggested an intermediate process in which one adsorbed reactant is chemisorbed and the other being trapped in a hot precursor state. Chemisorption of A on a vacant surface site (\circ)



Physisorption of B in a precursor state (pre)



Reaction of A_{ad} with B_{pre} forming P_{ad}



Desorption of P, leaving a vacant surface site



Figure 3.7 visualizes the Langmuir-Hinshelwood (a), Eley-Rideal (b) and Harris-Kasemo model (c) for reaction mechanism in heterogeneous catalysis.

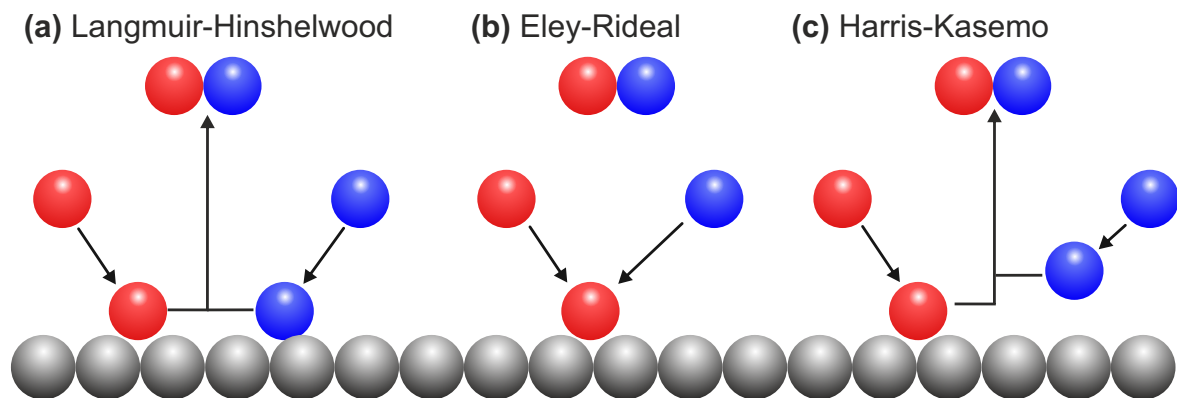


Figure 3.7: Reaction mechanisms in heterogeneous catalysis: (a) Langmuir-Hinshelwood model of both chemisorbed species forming the product, (b) Eley-Rideal model where only one reactant is chemisorbed on the surface, reacting with a molecule in the gas phase and (c) the Harris-Kasemo model of a precursor reacting with a chemisorbed particle.

4 Experimental Techniques

The brief introduction into the processes and kinetics at the gas–solid interface, provided in the previous Chapter 3, shows that a precise control over the reactants under well-defined conditions is essential for an atomistic study in heterogeneous catalysis. Both the experimental approach and technical realization of how molecules can be investigated on surfaces will be presented in the following chapter.

4.1 Molecular Beam Techniques

The microscopic investigation of surface kinetics and dynamics depends on two points, a well-defined as well as a reproducible flux of molecules. This controlled flux of spatially directed and collision-free molecules is denoted as a molecular beam (MB). The typical generation of such a controlled flux of molecules is achieved by the expansion of a gaseous species from a high-pressure reservoir into the vacuum. Once a directed flux of molecules is formed, this beam can further be temporally or physically modified. The former can be achieved via implementation of a mechanical chopper or shutter which allows a specific temporal modulation with a tunable rotation velocity or opening frequency. In the latter case, e.g. a laser is crossed onto the formed molecular beam which allows a photoexcitation creating atomic or molecular radicals.^[151]

For this work, the application of molecular beams was essential to investigate the hydrogenation behavior of hydrocarbons under well-defined and reproducible reaction conditions. There are several more applications of molecular beams in physical chemistry and surface science which are described in detail in the book on atomic and molecular beam methods by Scoles^[151] or the reviews on molecular beam methods applied in surface science by Zare^[110] as well as Libuda and Freund.^[23] In the following part, the physical principle of the two different ways to create molecular beams via i) a supersonic expansion and via ii) an effusive beam source are briefly described.

In fluid dynamics, the dynamic of the system is characterized by the dimensionless Knudsen number (K_n), which describes the ratio of the mean free path of the particle (λ) and the diameter (d) of the tube.

$$K_n = \frac{\lambda}{d} = \frac{k_B T}{\sqrt{2}\pi(2r)^2 p \cdot d} \quad (4.1)$$

with the Boltzmann constant (k_B), the temperature of the gas (T), hard sphere radius of the gaseous particle (r) and the total pressure (p). The Knudsen number ranges from small values $K_n \ll 1$ where the flux is dominated by intermolecular collisions and $K_n \geq 1$ where the flux of molecules is almost collision-free.^[152] For the operation of molecular beams, collision-free conditions are required.

4.1.1 Supersonic Molecular Beams (SMB)

One way to create a constant flux of molecules is the supersonic expansion of a gaseous species from a high pressure reservoir into an evacuated vessel. These supersonic molecular beams operate at low Knudsen numbers in the stagnation stage. The schematic drawing of the supersonic molecular beam used in this work, including its typical pressure in the different stages and the required pump size, is shown in Figure 4.1.

A compressed gas ($p > 1$ bar) is being expanded into the vacuum (stage 1) by passing through a nozzle. This nozzle controls the flux of molecules and can also be operated in a pulsed mode. The expanded gaseous molecules pass a skimmer, which is placed in front of the nozzle, and two different apertures in stages 2 and 3 before entering into the main measurement chamber. In stage 2, the beam can on top be modulated by e.g. a mechanical chopper.

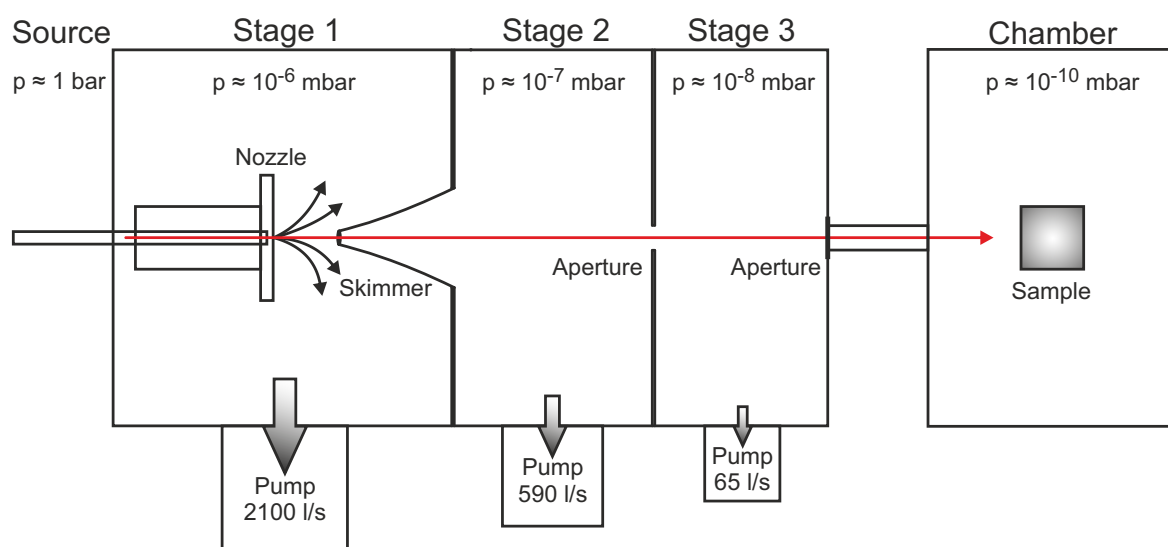


Figure 4.1: Drawing of a supersonic molecular beam (red). The gaseous molecules expand through the nozzle into the evacuated vessel. The skimmer and apertures subsequently form the molecular beam. The typical pressure range and pumping speed specifically applied in our experimental setup is indicated at each stage. Adapted from Ref.[151].

Inside the gas reservoir, high pressure and correspondingly low Knudsen numbers causes frequent intermolecular collisions. Figure 4.2 shows a schematic visualization of the continuum free-jet expansion which corresponds to a permanently opened nozzle. The supersonic expansion is an isentropic process in which the inner energy of a gaseous species is converted into kinetic energy in direction of the expanded mass flow.^[153] As a consequence upon expansion, both the vibrational and rotational states of the molecules as well as the radial velocity distribution are cooled down. Numerous collisions of the gaseous species in the early stage of the expansion and thus an equilibrium of the individual velocities are the reasons for a narrow velocity distribution in the direction of the mass flow.

The pressure difference between the gas reservoir (stagnation stage) and the evacuated stages accelerates the gaseous particles.^[153] This is expressed by the Mach number (M) which equals the ratio of the flow velocity with respect to the speed of sound. There are different zones arising from the supersonic expansion of which only the zone along the direction of flow will be described briefly.

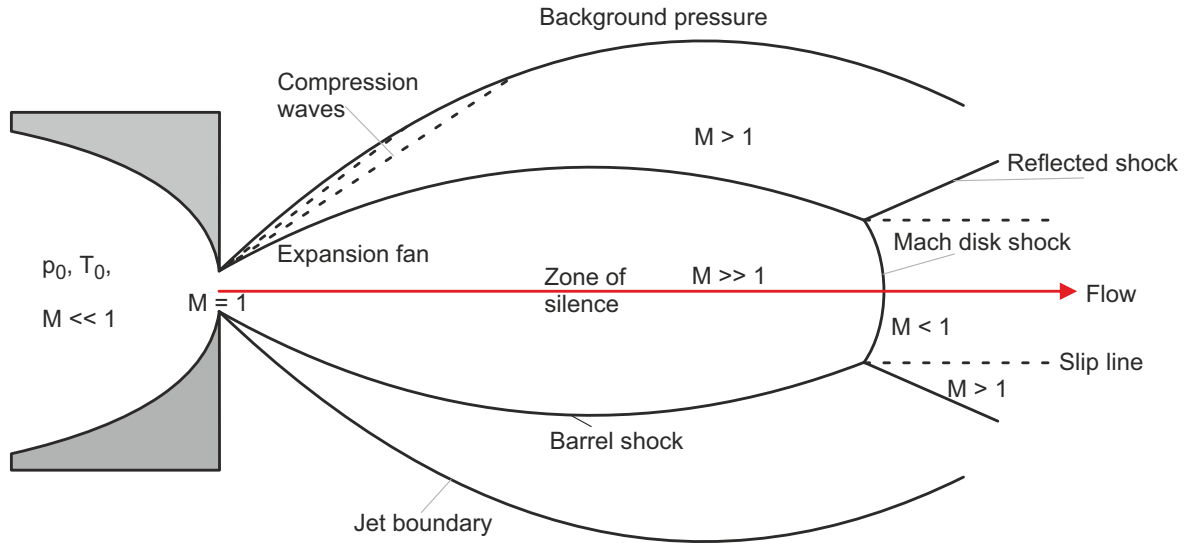


Figure 4.2: Schematic visualization of a continuum free-jet expansion with their corresponding zones and Mach numbers (M). The resulting flux of molecules is indicated as a red arrow. Adapted from Ref.[151].

The zone of isentropic expansion between the nozzle exit and the so called Mach disk is the zone of silence where $M \gg 1$. A typical length of this zone is usually several centimeters long, depending on the nozzle diameter, the ratio of the pressure in the stagnation stage and the background pressure. The skimmer is placed into the zone of silence selecting only the gaseous molecules that have the narrow radial velocity distribution, i.e. molecules with a small velocity component perpendicular to the expansion direction, for forming the molecular beam. This is also referred to as geometric cooling.^[154]

Behind the Mach disk, the velocity of the molecules becomes subsonic. The resulting velocity distribution of the molecules in a supersonic expansion is presented in (Eq. 4.2).

$$N(v) \propto v^3 \cdot \exp\left(-\frac{M(v - v_{\parallel})^2}{2k_B T_{\text{trans}}}\right) \quad (4.2)$$

with

$$v_{\parallel} \approx \sqrt{\frac{2k_B T_0}{\langle M \rangle} \left(\frac{\gamma}{\gamma - 1}\right)}, \quad \gamma = \frac{C_p}{C_v} \quad (4.3)$$

and the parallel particle velocity (v_{\parallel}), flow velocity (v), the Boltzmann constant (k_B), molar Mass (M), average molecular mass ($\langle M \rangle$), heat capacities ($C_{p/v}$), initial temperature in the stagnation stage (T_0) and the translational temperature (T_{trans}). Typical translational temperatures are $T_{\text{trans}} \leq 1$ K.^[152] Apart from the translational cooling, vibrational and rotational cooling also occurs. Spectroscopic studies on molecules expanded in free-jet expansions showed typical rotational temperature of $T_{\text{rot}} = 10$ K and vibrational temperature $T_{\text{vib}} \approx 100$ K.^[155] This allows, for instance, the investigation of usually unstable van der Waals clusters in the gas phase.^[156] Another major advantage of supersonic molecular beams, compared to any other source of molecular fluxes, is the well-controllable energy distribution, which render them the preferential source in scattering and adsorption experiments.^[110]

4.1.2 Effusive Molecular Beams (EB)

The second method to create molecular beams is the effusive molecular beam technique which operates at very high Knudsen numbers. Thus, effusive molecular beam sources have a negligible number of intermolecular collisions after exiting the source. The schematic drawing of the general setup is presented in Figure 4.3.

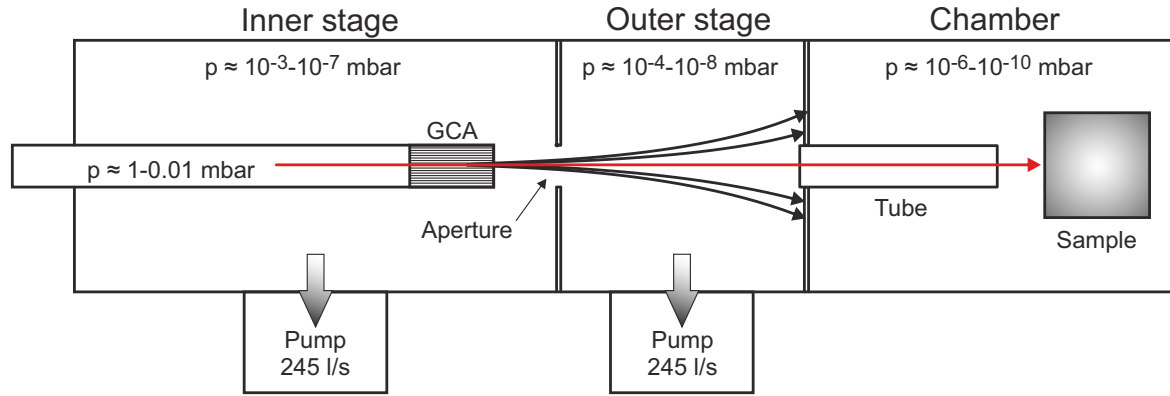


Figure 4.3: Visualization of an effusive molecular beam. The gaseous particles pass through the glass capillary array (GCA) into the inner and outer pumping stage, creating a collision-free flux of molecules (molecular beam). Adapted from Ref.[151].

The molecular beam consists of two differentially pumped stages. The gas source passes through a multi-array channel tube (glass capillary array, GCA), which consists of very narrow tubes of several μm diameter directing the molecules along the direction indicated with the red arrow. Only particles with a narrow velocity distribution are able to pass the GCA and following apertures. The resulting velocity distribution ($N(v)$) is expressed by

$$N(v) \propto v^3 \cdot \exp\left(-\frac{Mv^2}{2k_B T_0}\right), \quad (4.4)$$

with the flow velocity (v), the Boltzmann constant (k_B), molar Mass (M) and the temperature in the stagnation stage (T_0). Since the total number of molecules passing the GCA is dependent on the transmission probability (W) of the molecules that pass through the GCA, the intensity of the velocity distribution has to be multiplied by a peaking factor (κ). The peaking factor is proportional to the ratio (β) of the diameter ($2r$) of the GCA and its length (L).

$$\beta = \frac{2r}{L} \quad (4.5)$$

According to Clausing^[157], the values for the transmission probability are

$$W(\beta \rightarrow \infty) = 1 \quad \text{and} \quad W(\beta \rightarrow 0) = \frac{4\beta}{3}. \quad (4.6)$$

The former represents a short tube with a large diameter and the latter represents many long tubes with a small diameter, which is the case for the description of GCA. The peaking factor (κ) of effusive molecular beams operating at small values of β is therefore

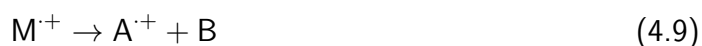
$$\kappa = \frac{1}{W} = \frac{4\beta}{3} = \frac{8r}{3L}. \quad (4.7)$$

Because of both, the lower operating pressure and lower pumping flux compared to supersonic molecular beams, effusive beams are very efficient ways to produce stable fluxes of molecules with a very low consumption of molecules. On the other hand, stable fluxes in effusive beams are at some point limited to the vapor pressure of the substances. While in supersonic molecular beams stable fluxes can be formed even with molecules having a very low vapor pressure, using a seed gas as a carrier, this is not the case with effusive beams as the GCA usually renders it impossible for the molecules to pass. For specific application in surface science, e.g. determination of the sticking coefficients, the use of molecular beams are obligatory. Although sticking coefficients can in general be measured via both effusive and supersonic molecular beams, the variation of the energy of the impinging molecules and thus the energy-dependence can only be realized by using supersonic expansion molecular beams. Additional information on effusive and supersonic molecular beams are available in various surface science publications.^[23,110,151]

Apart from the well-controlled transport of the molecules to the reaction chamber, a suitable detection of the reactants and products formed during the course of the reaction is needed to investigate the kinetics of a chemical reaction.

4.2 Quadrupole Mass Spectrometry (QMS)

Mass spectrometry is a widely used method in vacuum systems to detect reactants in the gas phase. The basic principle of mass spectrometry consists of three parts: i) the generation of ions from the chemical compound under investigation, ii) subsequent separation of the generated ions by their mass-to-charge ratio (m/z) and finally, iii) the detection of the ions.^[158] There are several different methods to generate ions of chemical compounds which are more or less destructive. The former mentioned are related to hard ionization techniques since they cause the ions to fragment intensely and the latter are usually indicated as soft ionization techniques which usually result in larger and only slightly fragmented ions. One of the most common methods is the electron ionization (EI) which is hard ionization technique. In the EI, electrons (e^-) emitted by a filament are accelerated by an electric field onto the target molecules. The electrons have a kinetic energy of approximately 70 eV which is sufficient to either ionize the molecule (M, Eq. 4.8) or force molecules to further decompose into its characteristic fragments (A, B, Eq. 4.9).



In the next step, the ions need to be separated by a mass analyzer according to their m/z ratio. One of the simplest mass analyzers is the quadrupole which is schematically drawn in Figure 4.4. The quadrupole consists of four cylindrical shaped rods with each comprising a direct current (DC, U) and an alternating current (AC, V) component. The ions entering the quadrupole along the z -axis are influenced by an attractive force by the rod having the opposite charge of the ion. Since the charge of the rods are altered periodically, the ions start to oscillate along x - and y -axis due to changing repulsive and attractive forces.

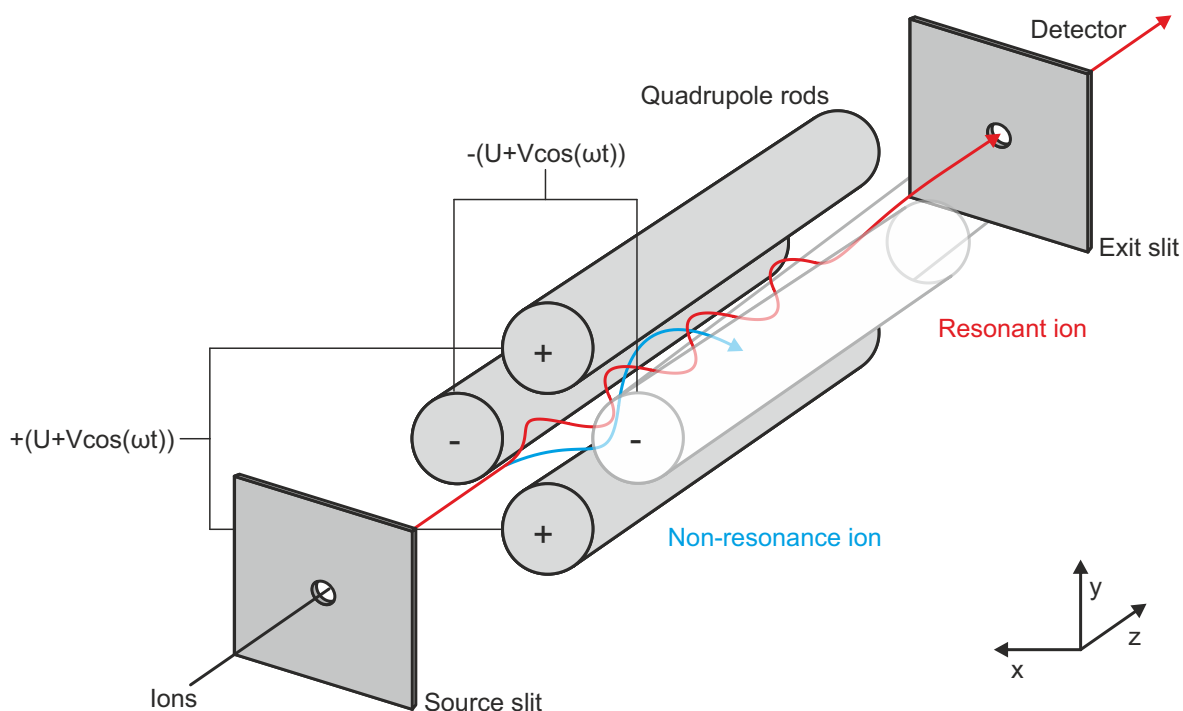


Figure 4.4: Visualization of the QMS principle. The ions may have a stable trajectory (red) through the quadrupole analyzer or collide with the quadrupole rods (blue). The desired m/z ratio can be selected by applying a specific AC voltage. Adapted from Ref.[99,158].

The equations of motion in x and y direction are

$$\frac{\partial^2 x}{\partial \tau^2} + (a_x + 2q_x \cos(2\tau))x = 0, \quad (4.10)$$

$$\frac{\partial^2 y}{\partial \tau^2} + (a_y + 2q_y \cos(2\tau))y = 0, \quad (4.11)$$

with the parameters

$$a_x = -a_y = \frac{4eU}{m_i r_0^2 \omega^2}, \quad q_x = -q_y = \frac{2eV}{m_i r_0^2 \omega^2}, \quad \tau = \frac{\omega t}{2}, \quad (4.12)$$

and the mass of the fragment (m_i), the DC voltage (U), the AC voltage (V) with its frequency (ω) and the distance between two rods ($2r_0$). Therefore, only a specific m/z ratio can have a stable trajectory through the quadrupole rods (Fig. 4.4, red trajectory) while other ions collide with the rods and lose its charge (Fig. 4.4, blue trajectory). The separated ions are afterwards detected by a secondary electron multiplier (SEM).

In addition to the detection of the species in the gas phase, several surface-sensitive techniques were applied in the works presented in this thesis to detect adsorbed molecules on the surface.

4.3 Scanning Tunneling Microscopy (STM)

The STM measurements were conducted in a complementary apparatus by a different person, so that the principle of the STM technique will be described here only briefly.

STM is a surface-sensitive technique which provides a direct real-space image of a conductive surface by moving a tiny metal tip in close proximity across a surface area without being in direct contact with the surface. The basic physical principle of STM is the quantum chemical effect of tunneling electrons through a potential barrier between the surface and the metal tip. The image itself is obtained by recording the electrical tunnel current (I) as a function of the position on the surface. The tunnel current ($I(z)$, Eq. 4.13) is dependent on several parameters which are explained below.

$$I(z) \propto V_b \cdot \rho(0, E_F) \cdot \exp\left(-\frac{2 \cdot d \sqrt{2m\phi}}{\hbar}\right) \quad (4.13)$$

The work function (ϕ) is the minimum energy to release an electron from the bulk into the vacuum, which is usually in the range of a few eV. The bias voltage (V_b) which is the voltage applied on the metal tip to allow electrons to tunnel into the surface or vice versa. The density of states (DOS, $\rho(z, E)$) for an electron with the wave function (ψ_n) is presented in Equation 4.14. This is often referred to as the local density of states (LDOS, $\rho(0, E_F)$) at the Fermi energy (E_F). The Fermi level is the upper limit of occupied states in a metal.^[99] The LDOS is the number of electrons per unit and its volume, at a specific point in space at a given energy.^[159]

$$\rho(z, E) = \frac{1}{\epsilon} \sum_{\epsilon_n = E - \epsilon}^E |\psi_n(z)|^2 \quad (4.14)$$

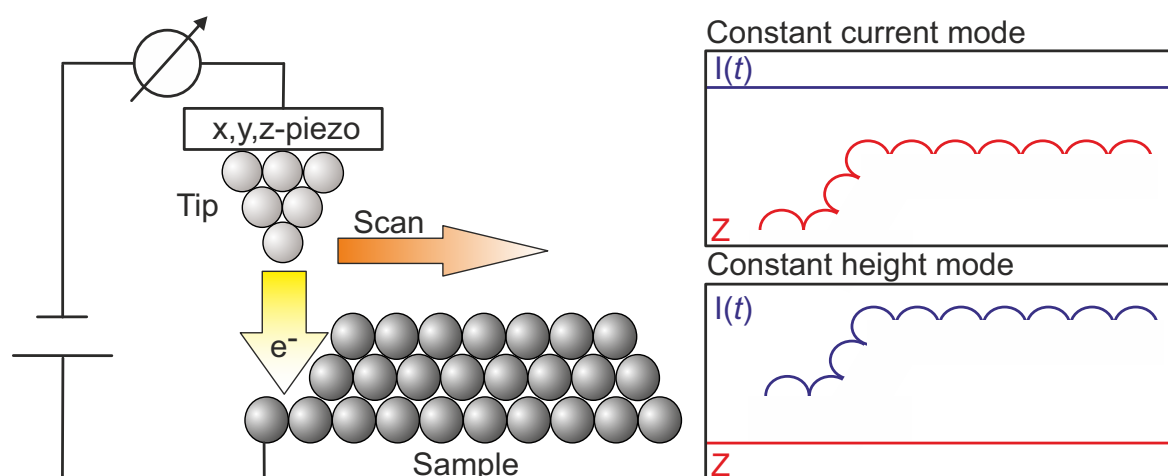


Figure 4.5: Visualization of the STM principle in general. The metal tip is attached to a movable piezoelectric x, y, z - translator. The different measuring modes are illustrated as: constant current and constant height mode. Adapted from Ref.[99,103,159].

Lastly, the tunneling current is dependent on the gap distance (d) between the sample and the tip. The resulting STM image is therefore a convolution of the topographic and electronic structure of the molecule adsorbed on a surface.

A simplified schematic visualization of the STM setup is shown in Figure 4.5. The metal tip, e.g. made out of tungsten, is attached to a piezoelectric element which allows the movement along the x -, y - and z -axis. The tunnel current is measured while the tip scans across the sample surface. There are two different measuring modes: i) constant current mode, where the sample tip follows the topology of the surface and ii) the constant height mode, where the tunneling current varies with the topology of the surface. A detailed theoretical and experimental description of STM can be found in the book by Chen.^[159]

STM is a technique that provides a microscopic picture of a possible self-organization of molecules on surfaces or the morphology of a catalyst. However, this technique is not able to create an image of the chemical bond with the surface. Infrared spectroscopy of adsorbed molecules, which is described below, is one of the methods required for this.

4.4 Infrared Spectroscopy

Experiments on the interaction of electromagnetic radiation with matter show that only discrete portions of energy can be absorbed by a molecule. The energy of the photon has to be equal to the difference of neighboring energy states to excite a molecule from a lower level E_1 to a higher level E_2 .

$$\Delta E = E_2 - E_1 = h \cdot \nu \quad (4.15)$$

Upon absorption, the energy is temporarily conserved in the molecule, forming an excited state. In the simplest case, this excited state becomes deactivated after emitting a photon of the same energy. Depending on the energy of the electromagnetic radiation, different levels in the molecular system can be excited. The total energy (E_{total} , Eq. 4.16) of a molecule is therefore the sum of all molecular levels (electronic (E_{el}), vibrational (E_{vib}) and rotational (E_{rot})) as well as the translational energy (E_{trans}).

$$E_{\text{total}} = E_{\text{trans}} + E_{\text{el}} + E_{\text{vib}} + E_{\text{rot}} \quad (4.16)$$

Using electromagnetic radiation in the ultraviolet and visible light allows the spectroscopy on electronic states of a molecule. Both the rotational and infrared spectroscopy are powerful techniques to investigate the structure of molecules which require less-energetic radiation in the infrared light or below. In particular, infrared spectroscopy is a suitable method for the characterization of adsorbed molecules on surfaces.^[160]

A classical model for the description of molecular vibrations is the harmonic oscillator

$$V = \frac{1}{2}kx^2, \quad (4.17)$$

where the potential energy is dependent on the force constant (k) and the elongation coordinate (x). Applied on molecular vibrations, the vibrational term ($G(v)$) thus becomes

$$G(v) = \frac{1}{2\pi c} \sqrt{\frac{k}{\mu}} \left(v + \frac{1}{2} \right), \quad (4.18)$$

where k is the force constant, μ the reduced mass and v the vibrational level. The selection rule for vibrational transitions is $\Delta v = \pm 1$. The descriptions of vibrations as a harmonic

oscillator disregards the possibility of dissociation. An improved description of molecular vibrations is the anharmonic oscillator (Eq. 4.19), which can be expressed as a power series in $\left(v + \frac{1}{2}\right)$,

$$G(v) = \frac{1}{2\pi c} \sqrt{\frac{k}{\mu}} \left(\left(v + \frac{1}{2}\right) - x_e \left(v + \frac{1}{2}\right)^2 + y_e \left(v + \frac{1}{2}\right)^3 - \dots \right), \quad (4.19)$$

with the anharmonicity constants (x_e , y_e) showing the deviation from the harmonic oscillator.^[99]

The intensity of a transition from a state ψ_1 to a state ψ_2 , resulting from the absorption of electromagnetic radiation, can in general be described as Equation 4.20.^[161]

$$I \propto \int \psi_1 \boldsymbol{\mu} \psi_2 d\tau, \quad (4.20)$$

where $\boldsymbol{\mu}$ is the transition dipole moment operator. The transition dipole moment operator usually has the form

$$\boldsymbol{\mu} = \sum_i q_i x_i + \sum_i q_i y_i + \sum_i q_i z_i, \quad (4.21)$$

where q is the charge of the particle (i) and x, y, z are the Cartesian coordinates.

The state function (ψ) can be separated into an electronic (e) and a nuclear (n) compound using the Born-Oppenheimer separation (BO, Eq. 4.22)^[162] in which the nuclear compound is dependent on the nuclear coordinates (\vec{R}) and the electronic compound is dependent on both, the nuclear and electronic (\vec{r}) coordinates.

$$\psi(\vec{r}, \vec{R}) = \psi_e(\vec{r}, \vec{R}) \cdot \psi_n(\vec{R}) \quad (4.22)$$

According to Cotton^[163], a transition by infrared radiation is allowed if one or more integrals of

$$I \propto \int \psi_1 x \psi_2 d\tau, \quad I \propto \int \psi_1 y \psi_2 d\tau \quad \text{or} \quad I \propto \int \psi_1 z \psi_2 d\tau \quad (4.23)$$

will be $\neq 0$, where x, y, z refers to the orientation of the oscillating electric vector of radiation relative to the Cartesian system, which is fixed in the molecule. This can be expressed as the variation of the dipole moment, which originates from two particle charges $\pm\delta q$, separated by the internuclear distance $R = R_e + d$

$$\boldsymbol{\mu} = R\delta q = R_e\delta q + d\delta q = \boldsymbol{\mu}_0 + d\delta q \quad (4.24)$$

with d the displacement from the equilibrium distance and $\boldsymbol{\mu}_0$ the dipole moment operator for equilibrated internuclear distance for the nuclei. For the transition from ψ_1 to ψ_2 thus follows

$$\langle \psi_1 | \boldsymbol{\mu} | \psi_2 \rangle = \boldsymbol{\mu}_0 \langle \psi_1 | \psi_2 \rangle + \delta q \langle \psi_1 | d | \psi_2 \rangle, \quad (4.25)$$

where the transition dipole moment equals the non-equilibrium part in Equation 4.26 and the former part containing $\boldsymbol{\mu}_0$ is zero. The variation of the distance between two charges equals the change in the dipole moment, resulting in

$$\langle \psi_1 | \boldsymbol{\mu} | \psi_2 \rangle = \delta q \langle \psi_1 | d | \psi_2 \rangle = \left(\frac{\partial \boldsymbol{\mu}}{\partial d} \right) \langle \psi_1 | d | \psi_2 \rangle \neq 0 \quad (4.26)$$

for the transition dipole moment. So a vibration is IR active when the dipole moment varies with displacement of d which is the selection rule for infrared spectroscopy.^[164]

4.4.1 Detectors in Infrared Spectroscopy

Detectors in the infrared spectroscopy convert the IR radiation into an electrical signal. There are two common types of detectors: i) liquid nitrogen cooled semiconductors, e.g. HgCdTe (mercury-cadmium-telluride, MCT), which convert absorbed photons into an electrical signal and ii) pyroelectric detectors, e.g. DLa-TGS (Deuterated L-alanine TriGlycerine Sulfate), which convert the spontaneous variation in polarization as a function of temperature into an electrical signal.^[160,165]

The experimental setup comprises two of these detectors – their characteristics being briefly presented. The DLa-TGS detector is less sensitive compared to the MCT detector, since the change in capacitance with temperature in the DLa-TGS detector is less sensitive to small intensity changes than the direct photon absorption in the MCT detector. On the other hand, DLa-TGS detectors can be operated at room temperature and have no cooling nor stabilization time as required for liquid nitrogen cooled semiconductors.

The MCT detector has its best sensitivity in the spectral region between 800 and 2500 cm^{-1} which renders the detector preferentially being used in studies on molecules involving carbon and atoms of the V-VII group. Above 3000 cm^{-1} , the sensitivity is approximately half of the maximum which is around 1800 cm^{-1} . For studies on hydrocarbons the InSb (indium antimonide) detector is preferentially applied having a significantly higher sensitivity in the region related to the stretching vibrations of C–H bonds.

4.4.2 Fourier Transform Infrared Spectroscopy (FTIR)

The implementation of the Fourier transformation (FT) into infrared spectroscopy induced IR spectroscopy to become a widely used analytic method. Before, the infrared spectroscopy was performed by slow scanning instruments containing gratings as the dispersive element. The wavelength was selected by changing the incidence angle. In FTIR spectrometers, the entire spectral range of the mid-infrared (MIR, 400–4000 cm^{-1} in this study) is measured simultaneously, granting a significant reduction in acquisition time. The general setup of the FTIR spectrometer (Bruker Vertex 80v) is shown in Figure 4.6. The broad band MIR spectrum, emitted by a globar (silicon carbide, SiC), is focused by a parabolic mirror and passes through the aperture (APT, 1.2x6 mm slit). The parabolic mirror collimates and reflects the IR beam into the interferometer consisting of a beam splitter (BMS, KBr) which splits the IR beam into two parts where the first half is reflected onto a fixed mirror and the second half is reflected onto a movable mirror. Depending on the path difference, constructive interference of different wavelengths can occur. The wavelength is determined by a helium neon laser (He Ne) which allows a spectral resolution $\leq 0.2 \text{ cm}^{-1}$. The IR beams reflected from both, the fixed and the movable mirrors, are subsequently collated, reflected and focused by different plane and parabolic mirrors onto the sample in the UHV chamber after passing a p-polarizing filter (P). The IR beam is then detected by an external liquid

nitrogen cooled MCT detector. The Bruker Vertex 80v comprises also a DLa-TGS detector inside the sample compartment, which was only used for testing the intensity of the MIR source.

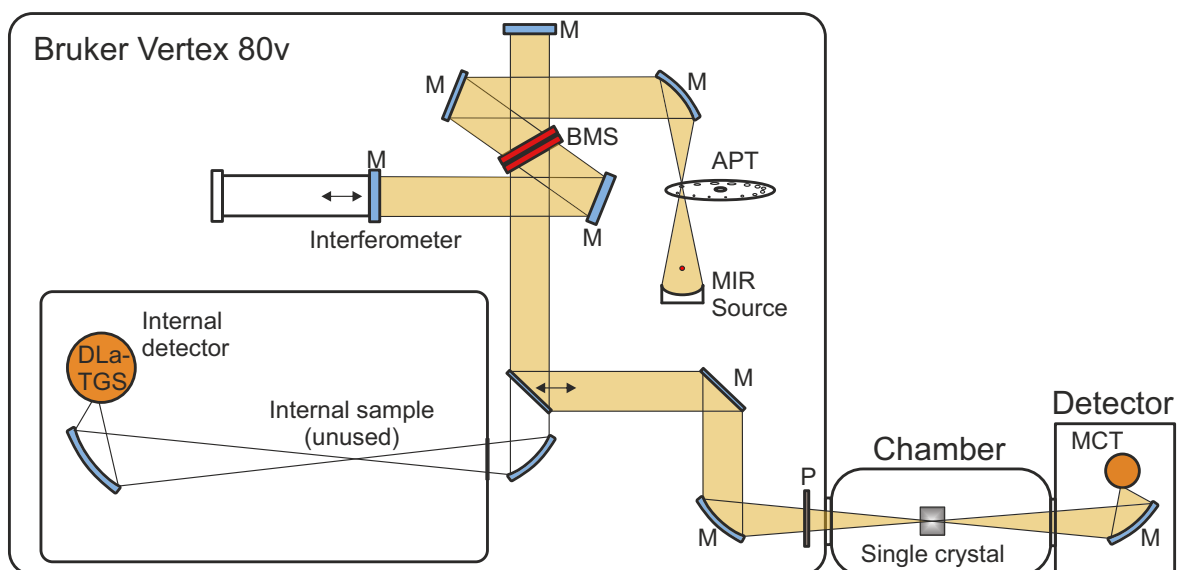


Figure 4.6: Illustrated beam path of the Bruker Vertex 80v. The IR beam is emitted by a globar, the beam profile was selected by different apertures (APT). The spectral information was obtained using a Michelson-type interferometer. The (p-pol) IR beam was focused onto the sample crystal inside the UHV chamber and detected by a liquid nitrogen cooled MCT detector. See text for details.

The typical detector signal, dependent on the optical path difference (OPD, δ) of the interferometer mirror, is shown in Figure 4.7. At $\delta = 0$ (zero path difference, ZPD), all the wavelengths are in phase and a constructive interference resulting in a strong signal at the detector (centerburst). The intensity at the detector decreases with increasing δ in both directions from the ZPD because of the wavelengths being out of phase and are unable to interfere constructively. In this case, the light returns to the source instead of traveling toward the detector. The intensity of the light beam with λ_0 at the detector ($I(\delta)$) as a function of optical path difference is expressed by

$$I(\delta) = \frac{1}{2} \cdot I(\lambda_0) \cdot \left(1 + \cos \left(2\pi \frac{\delta}{\lambda_0} \right) \right) = \frac{1}{2} \cdot I(\lambda_0) + \frac{1}{2} \cdot I(\lambda_0) \cdot \cos \left(2\pi \frac{\delta}{\lambda_0} \right), \quad (4.27)$$

where only the modulated component ($I(\delta)$) is important in spectroscopic measurements (Eq. 4.28).

$$I(\delta) = \frac{1}{2} \cdot I(\lambda_0) \cdot \cos \left(2\pi \frac{\delta}{\lambda_0} \right) = \frac{1}{2} \cdot I(\tilde{\nu}_0) \cdot \cos (2\pi \tilde{\nu}_0 \delta) \quad (4.28)$$

The amplitude of the signal at the detector ($S(\delta)$) is dependent on various effects, as there are detector response, beam splitter efficiency and amplifier characteristics which are summarized as a instrumental parameter ($B(\lambda_0)$, Eq. 4.29).^[160]

$$S(\delta) = B(\lambda_0) \cdot \tilde{\nu}_0 \cdot \cos (2\pi \tilde{\nu}_0 \delta) \quad (4.29)$$

The mathematical operation which transforms the experimentally obtained interferogram (Fig. 4.7a) into a single beam spectrum (Fig. 4.7b) is the Fourier transformation which is represented by the integral

$$S(\delta) = \int_{-\infty}^{+\infty} B(\tilde{\nu}) \cdot \cos(2\pi\tilde{\nu}\delta) d\tilde{\nu}. \quad (4.30)$$

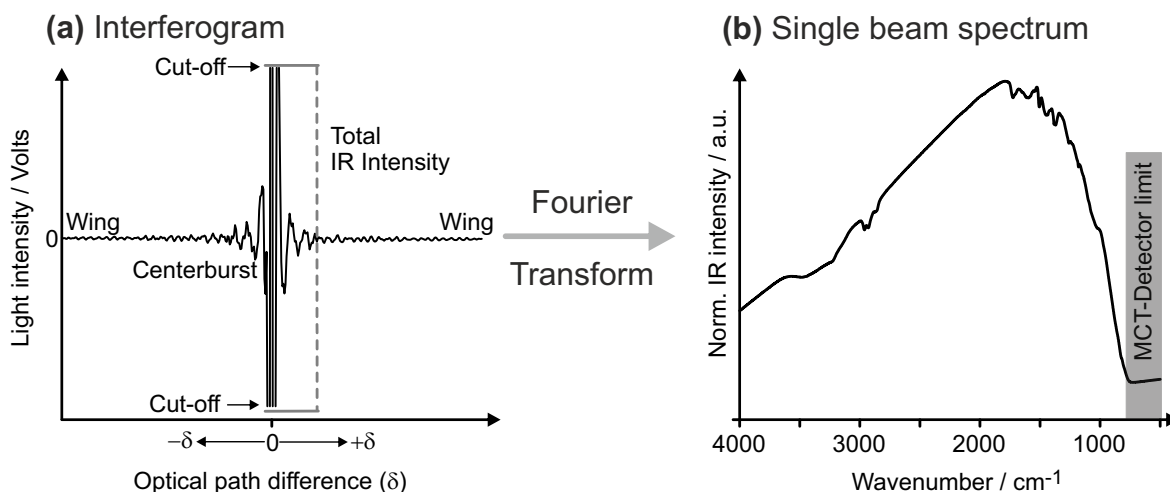


Figure 4.7: (a) Typical experimentally obtained double-sided interferogram of the light intensity, i.e. the detector voltage ($U(\delta)$), as a function of the optical path difference (δ) in the interferometer. At $\delta = 0$, both beams have the same beam path length. (b) Fourier transformation of an interferogram resulting in a single beam IR spectrum. Below $\tilde{\nu} = 750 \text{ cm}^{-1}$, the MCT detector has reached its detection limit.

The major reason for FTIR spectrometers being applied in a wide range of applications are their advantages over single channel dispersive spectrometers:

- Connes' advantage: the wavenumber precision is very high due to the very accurate determination of the position of the movable mirror via the He Ne laser.
- Fellgett's advantage: simultaneous detection of all wavenumbers result in a reduction of the intensity fluctuation at the detector and therefore an improved signal-to-noise-ratio.
- Jacquinot's advantage^[166]: the optical throughput (Θ) of spectrometers with a dispersive element (grating) is dependent on the focal length (f) of the collimating mirror, the effective area of the grating (A_G) and the grating constant (a) of the grating. Both optical elements are absent in a FTIR spectrometer. The optical throughput in a FTIR spectrometer is dependent on the effective area of the interferometer mirrors. According to Griffiths^[160], achieved improvements are in the order of

$$\frac{\Theta_I}{\Theta_G} = \frac{2\pi \cdot A_M \cdot \Delta\tilde{\nu}}{\frac{\tilde{\nu}_{\max}}{h \cdot A_G \cdot \Delta\tilde{\nu}} \cdot f \cdot a \cdot \tilde{\nu}^2} \geq 100. \quad (4.31)$$

In addition, dispersive spectrometers have less optical throughput with increasing spectral resolution, while the optical throughput is independent of the spectral resolution (interferometer length) in FTIR spectrometers. The combination of all three advantages mentioned above allows FTIR spectrometers to be up to 1000 times more sensitive than grating spectrometers.^[160]

4.4.3 Infrared Reflection Absorption Spectroscopy (IRAS)

The geometry of adsorbed molecules on catalytic surfaces consisting of transition metals is a key question that is addressed in various mechanistic studies. An important tool for determining this geometry on metal interfaces is the selection rule for adsorbed molecules, which is presented below. Figure 4.8a shows two limiting cases of adsorbed molecules on a metal surface: a flat-oriented and a perpendicular-oriented molecule with respect to the surface normal. In both cases, the adsorbed molecule induces an image dipole moment below the surface with opposite charge distribution. In case of a dipole moment parallel to the surface, the image dipole is also parallel to the surface.

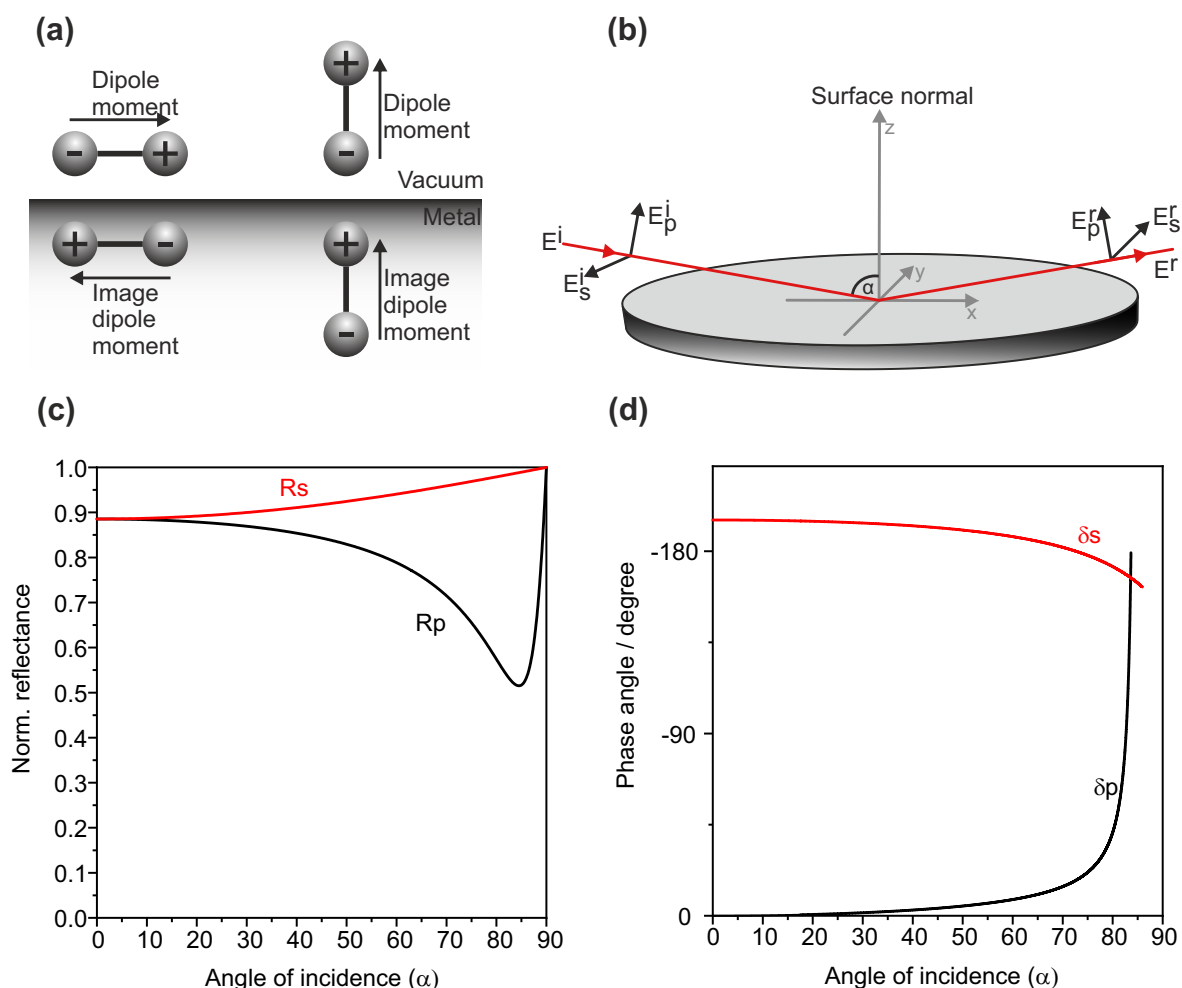


Figure 4.8: Visualization of the phenomena of: (a) metal surface selection rule, (b) the physical basics for an IRAS setup, (c) reflectance and (d) phase change for s- and p-polarized light as a function of the angle of incidence (α). Adapted from Ref.[99,167,168].

The result is a cancellation of the effective dipole moment. In the case of a dipole moment perpendicular to the surface, the resulting image dipole has the same orientation, resulting in a constructive reinforcement of both dipole moment vectors. This results in the metal surface selection rule (MSSR) which explains why only vibrations with a transition dipole moment non-parallel to the surface are visible in IRAS on metal surfaces.^[168] The vibrations with a dipole moment perpendicular to the surface can only be excited by p-polarized light, so that the IRAS experiments are performed with p-polarized (Bruker F351) MIR light to improve the signal-to-noise ratio. Additionally to the interaction of IR light with molecules adsorbed on metal surfaces being restricted to the p-polarized component of the light, Greenler^[169], Francis and Ellison^[170] showed that the resulting electrical field vector of the reflected beam, the phase change (δ) and reflectance (R) depends on the angle of incidence (α). This can be explained by the complex index of refraction (\tilde{n} , Eq. 4.32) which is valid for metals in a broad spectral range of IR light^[171] and the Fresnel equations (Eq. 4.33-4.35).

$$\tilde{n} = n + ik, \quad (4.32)$$

$$R_p = \frac{(n - \sec(\alpha))^2 + k^2}{(n + \sec(\alpha))^2 + k^2}, \quad (4.33)$$

$$R_s = \frac{(n - \cos(\alpha))^2 + k^2}{(n + \cos(\alpha))^2 + k^2}, \quad (4.34)$$

$$\tan(\delta_p - \delta_s) = \frac{2k \tan(\alpha) \sin(\alpha)}{\tan^2(\alpha) - (n^2 + k^2)}, \quad (4.35)$$

where α is the angle of incidence and p, s polarization components.

Figure 4.8b shows a schematic drawing of a typical experimental setup of IRAS on a metal surface. The angle of incidence (α) is usually chosen to be between 82° and 88° ^[172] and the (unpolarized) incident light has p and s components which change phase upon reflection. The quintessence of the Fresnel equations is visualized in Figure 4.8c-d for the parameters of Pd (0.66 eV, $n = 3.34$ and $k = 9.89$) obtained from the work of Johnson and Christy.^[171] While the reflectance and phase change of s-polarized light is almost independent on the angle of incidence, both change significantly for p-polarized light. At $82^\circ \leq \alpha \leq 88^\circ$ both the reflectance and phase change are optimal for most of the metals to provide a good sensitivity. A detailed description on the solution of the Fresnel equation for reflection on metal surfaces can be found in the Handbook of Optics.^[167] The combination of high reflectivity, phase change and the selection rule for s-polarized light renders IRAS an excellent method to study the adsorption geometry of molecules on metal catalysts.

4.5 UHV IRAS/Molecular Beam Setup

A schematic drawing of the functional parts of the experimental setup is provided in Figure 4.9. The UHV IRAS/molecular beam setup comprises the unique combination of spectroscopic and molecular beam techniques for the in-situ investigation of surface reactions in heterogeneous catalysis under well-defined and reproducible conditions.

The main part of the setup consists of two effusive molecular beams and a third source for dosing a well-defined flux of molecules onto a sample plate which is centered in a ultra-high vacuum (UHV) chamber. The third source can either be a supersonic molecular beam or a gas doser. The molecular beams are aligned onto the sample surface. A quadrupole mass spectrometer is used in two respects, first one to detect the evolution of products in the gas phase as well as to check the purity of the reactants. All three molecular beams and the IR beam are crossed at the same point. The IR beam is used to characterize adsorbed species spectroscopically. The setup allows an in-situ IR-measurement of adsorbed species and the simultaneous detection of reactants and formed products in the gas phase by the mass spectrometer.

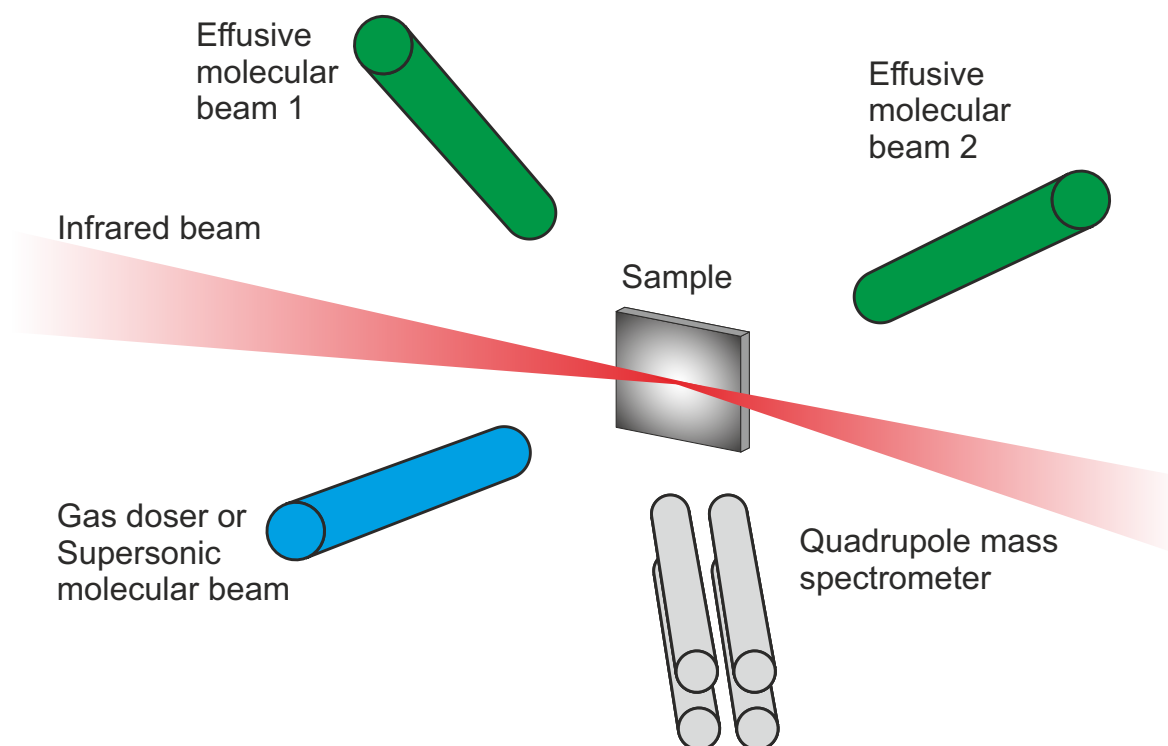
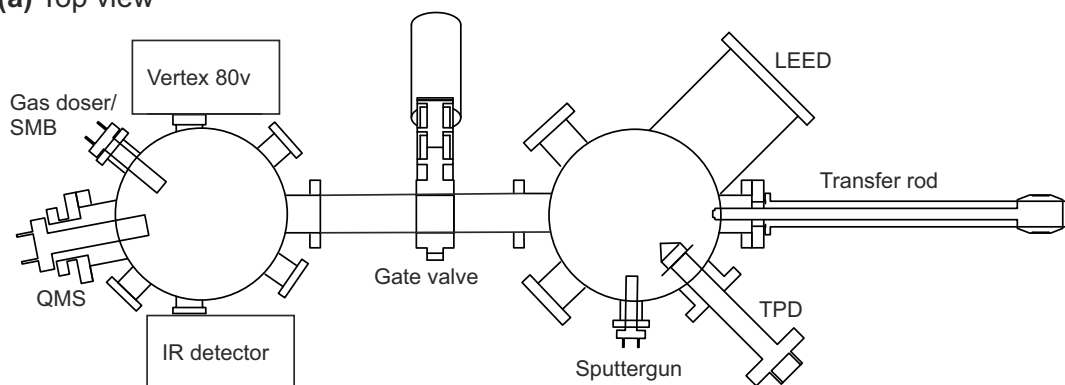


Figure 4.9: Schematic illustration of the functional parts of the experimental setup. Two effusive molecular beams, a gas doser or supersonic molecular beam and the IR beam are crossed at the same point on the sample plate.

In the following section the experimental setup of the apparatus used in this work will be briefly described. Further information on the setup, technical details and alignment procedures are summarized in the review^[173] and thesis^[174] by Attia. The technical drawing of the experimental setup is provided in Figure 4.10. The apparatus consists of two independent vacuum chambers. The first is used for preparation of the sample plate and the second for the kinetic and spectroscopic measurements. The sample (MaTeck GmbH) can be transferred between both chambers without breaking the vacuum. The preparation chamber comprises standard tools for sample preparation: a sample holder which allows temperature selection and precise control between 100 and 1300 K, a sputter gun (SPECS, IQE 11/35), a gas doser for oxidation, two metal evaporators (Omicron, EFM3-EVC 300), a quartz microbalance (tectra, QMB-im-mod), LEED/AES (SPECS, ErLEED 150 4-grids) and a QMS (Hiden, Hal/3F 301 PIC system type 553201) for temperature-controlled desorption (TPD-QMS). The main chamber comprises two effusive molecular beams (glass capillary

array GCA, Collimated Holes, Inc., holes size $50\ \mu\text{m}$, holes density $2 \cdot 10^6$ holes/ cm^2 , 1 mm thickness), a supersonic molecular beam (orifice diameter: $100\ \mu\text{m}$, Parker, General Valves Series 9) or a gas doser (VAT, 59024-GE01), an infrared spectrometer (angle of incidence: 83° , Bruker, Vertex 80v) and a QMS (Hiden, Hal/3F 301 PIC system type 553201). The UHV is generated by a combination of turbomolecular pumps supported by rotary vane pumps with subsequently heating the chamber for 48 h at $100\text{--}120^\circ\text{C}$.

(a) Top view



(b) Side view

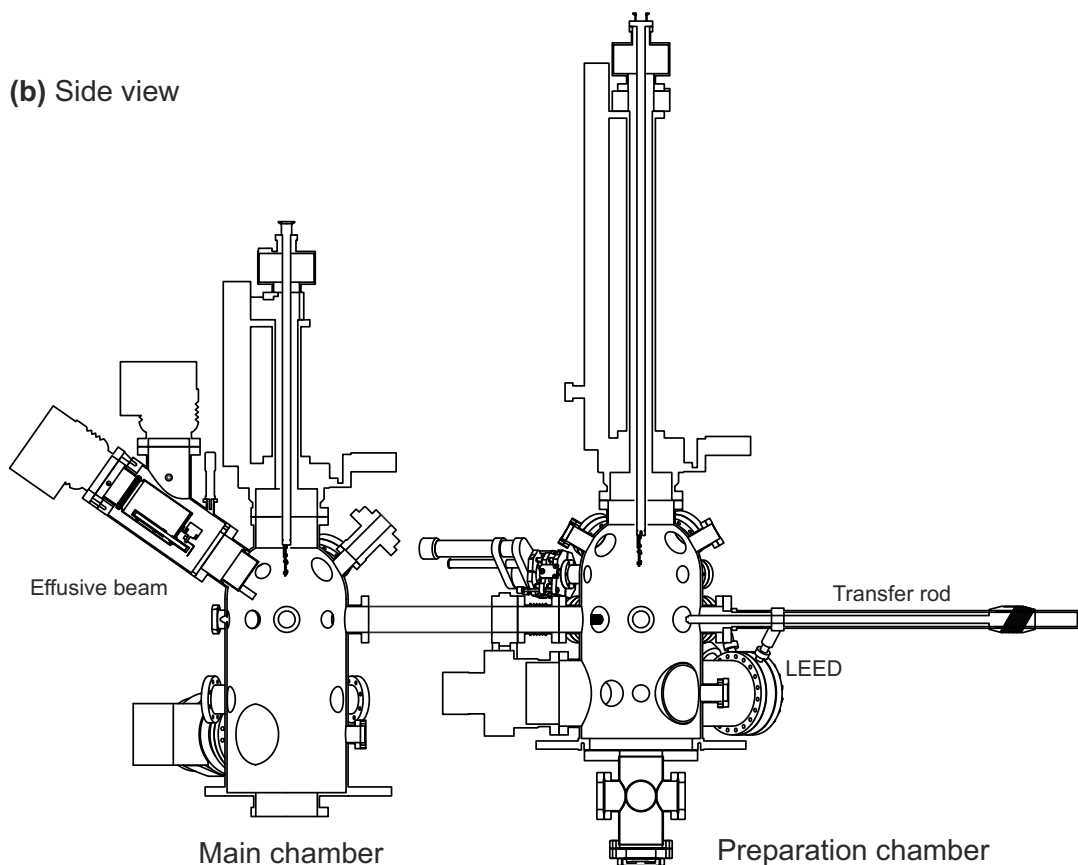


Figure 4.10: Technical drawing of the experimental setup employed in this study: (a) the top view onto the plane in which the sample plate is crossed with both effusive beams, the third source and the IR beam and (b) the side view into both chamber centers.

5 Selective Partial Hydrogenation of Acrolein over Functionalized Pd(111)

This chapter provides a summary of the published studies in

Angewandte Chemie from Ref.[175]. (Full text in Section 8.1.)

Carsten Schröder, Marvin C. Schmidt, Philipp A. Haugg, Ann-Katrin Baumann, Jan Smyczek and Swetlana Schaueremann, *Angew. Chem. Int. Ed.* **2021**, 60, 16349–16354.,

Chemistry - A European Journal from Ref.[176]. (Full text in Section 8.2.)

Carsten Schröder, Philipp A. Haugg, Ann-Katrin Baumann, Marvin C. Schmidt, Jan Smyczek and Swetlana Schaueremann, *Chem. Eur. J.* **2021**, 27, 17240–17254.

and

The Journal of Physical Chemistry C from Ref.[177]. (Full text in Section 8.3.)

Carsten Schröder, Ann-Katrin Baumann, Marvin C. Schmidt, Jan Smyczek, Philipp A. Haugg, Ole-Christian Graap and Swetlana Schaueremann, *J. Phys. Chem. C* **2022**, 126, 4907–4920.

Improving the selectivity of chemical reactions has gained great importance in modern chemistry and is one of the most challenging topics in catalysis research. Chemical processes often include non-selective catalytic steps which are economically inefficient and produce waste. The undesired byproducts need to be separated from the target product in subsequent separation and purification steps to yield the chemical in the purity and quality which is needed for further application. This increases the demand for selective catalysts to provide a more economical and sustainable use of resources.

Various examples of chemical reactions including both high selectivity and activity are well-known from biocatalyzed reactions.^[178] In the recent years, the application of enzymatic reactions in the production of pharmaceuticals has gained high interest. Especially for simple types of reactions, e.g. hydrolysis, the use of enzymes enables feasible reaction paths without using protecting groups.^[179] A major drawback of enzymatic reactions is the design of new catalysts: the tremendous 3D structural complexity hinders the rational development of new catalytic reactions. A strategy to overcome this inherent problem is i) the identification of the active site, ii) transfer to simpler chemical environment and iii) investigation by means of theoretical and experimental techniques.^[180] The investigation and design of new enzyme-derived catalysts are illustrated in Figure 5.1 for the nitrogenase enzyme 1M1Y (Fig. 5.1a) as an example, which was characterized by Schmid et al.^[181]

This enzyme allows diazotrophic microorganisms to convert nitrogen as N_2 into building blocks for nucleic acids and proteins.^[182] After the identification of the active site (FeMo cofactor, Fig. 5.1b), less complex models can be applied to investigate the nature of the activity and selectivity by means of both theoretical and experimental techniques (Fig. 5.1c).

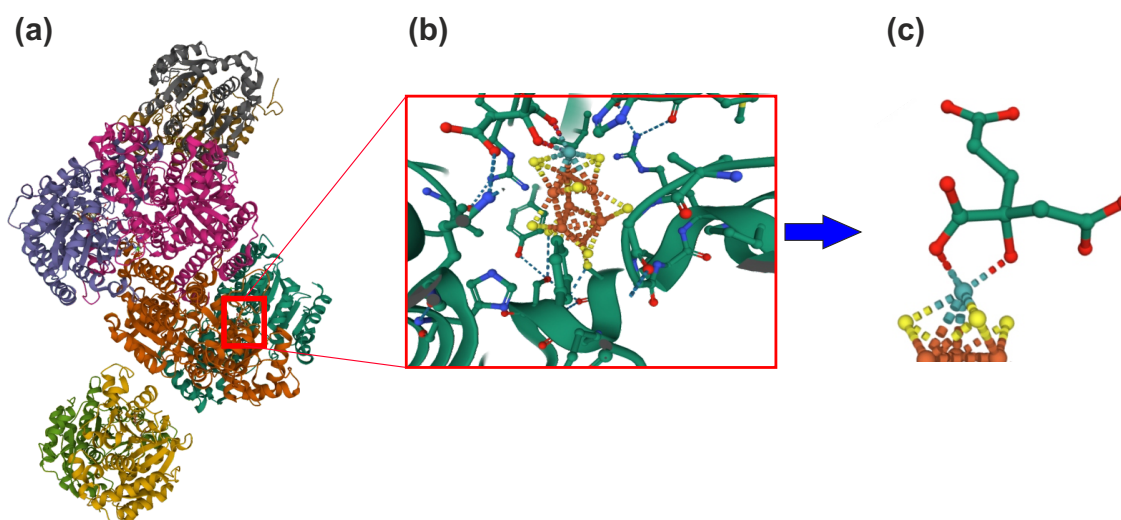


Figure 5.1: Illustration of the adaptation of enzyme-derived model catalysts (PDB ID 1M1Y). (a) After characterizing the enzyme and (b) identifying the active site, (c) a model system can be obtained and investigated by means of both theoretical and experimental techniques.^[181,183]

The detailed mechanistic studies can therefore be performed on simplified model systems that only contain the atoms involved in the desired chemical reactions. This also allows, for instance, the improvement and optimization of specific chemical reactions to develop new and better performing types of catalysts for industrial purpose. There are some examples where highly reactive sites were successfully implemented in homogeneous catalysis.^[47,184] Specifically, the selectivity in the epoxidation for styrene derivatives as well as non-conjugated terminal alkenes was promoted by the modification of active iron atom with porphyrin ligands.

A similar strategy for the rational design of new selective catalysts in heterogeneous catalysis is currently in development.^[29–31] The selectivity of surface reactions is difficult to control as it is conditional on the differences in the height of the activation barrier of parallel reaction pathways. Applying subtle changes to the electronic structure or morphology of the surface may impart selectivity toward the desired target product but can also influence the activity of the catalysts. Tuning catalytic surfaces to both a high activity and selectivity is the main goal of the research in catalysis.

The partial hydrogenation reaction of polyunsaturated hydrocarbons is a typical example of a multi-pathway reaction in which different products are kinetically accessible. For industrial application, the selective partial hydrogenation of α,β -unsaturated ketones and aldehydes is of broad interest. However, the hydrogenation at the $C=C$ bond yields the thermodynamically more stable saturated aldehyde and therefore, a selective hydrogenation toward the desired unsaturated alcohol can only be performed over catalysts that significantly lower the activation barriers of the corresponding reaction paths. The activation barriers of heterogeneously catalyzed chemical reactions are dependent on numerous parameters, e.g. electronic, geometric or structural properties of both the reactant and the surface.

Augustine^[185] investigated the hydrogenation reaction of different α,β -unsaturated aldehydes over Ir/C catalyst in ethanol. In this study, the author systematically changed the geometric structure of the reactant and analyzed the yield of both feasible partial hydrogenation products, the unsaturated alcohol and the saturated aldehyde, as a function of increasing number of substituents adjacent to the ethylenic double bond. The author reported that the selectivity toward the formation of the unsaturated alcohol decreases with less steric hindrance of the substituents (Fig. 5.2). Thus, the selective hydrogenation of acrolein at the C=O entity is one of the most challenging tasks due to the absence of any major steric hindrance to the hydrogenation of the C=C bond.^[45]

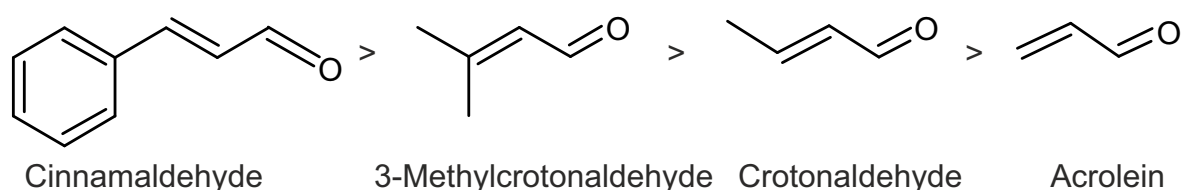


Figure 5.2: Study on the selectivity of the hydrogenation reaction of substituted α,β -unsaturated aldehydes toward the formation of the unsaturated alcohol over Ir/C according to Augustine.^[185]

However, acrolein is an α,β -unsaturated aldehyde with particular importance because of the relevance of its partial hydrogenated product, the unsaturated alcohol allyl alcohol (2-propenol), for industrial application, e.g. the synthesis of glycerol, allyl esters and epoxidation. The reaction scheme of the three possible products obtained from the first hydrogenation step is presented in Figure 5.3.

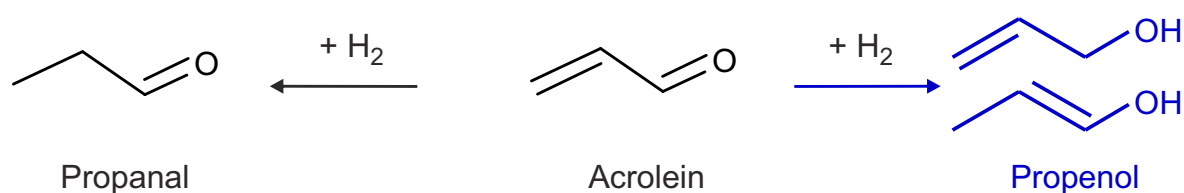


Figure 5.3: Feasible products of the partial hydrogenation of acrolein over Pd(111).

Among the three hydrogenation products, 1-propenol, 2-propenol and propanal, the latter is the thermodynamically most stable species in the gas phase.^[186] In an experimental study by František Tureček^[187], the heats of formation of both 1-propenol and propanal were determined by employing mass spectrometry. The author reported that 1-propenol, which is the enol tautomer of propanal, is by 17–22 $\text{kJ}\cdot\text{mol}^{-1}$ less stable than the saturated aldehyde. These experimental observations are further supported by results of a theoretical investigation by Bellarosa et al.^[188], in which the authors reported a difference in energy between both tautomers of about 38 $\text{kJ}\cdot\text{mol}^{-1}$ as well as an activation barrier for this tautomerization reaction of about 56 $\text{kJ}\cdot\text{mol}^{-1}$ in water as a solvent.

Propanal is by 35 $\text{kJ}\cdot\text{mol}^{-1}$ more stable than isomeric species 2-propenol (allyl alcohol) and thus, from both kinetic and thermodynamic points of view, the partial hydrogenation of the more reactive C=C bond is favored, providing propanal as a product and the formation of 1-propenol is usually not observed. This is in good agreement with the results obtained from the hydrogenation of acrolein over conventional supported catalysts based on monometallic Pd, Pt or Ni that only yield the saturated aldehyde instead of the unsaturated alcohol.^[35,189]

One idea to overcome the problem of minor selectivity toward the unsaturated alcohol is the application of less active but more selective hydrogenation catalysts or bimetallic surfaces. Nørskov et al.^[190,191] investigated the electronic factors that determine the catalytic reactivity of metal surfaces in a theoretical DFT (Density Functional Theory) approach. According to their model, the trends in catalytic reactivity of transition metals can directly be correlated with the hybridization energy between the bonding and anti-bonding adsorbate states and the d-band of the metal. The d-band was further analyzed in theoretical studies by İnođlu et al.^[192] and Li et al.^[193]. Both authors reported that the width of the d-band decreases with increasing group number. The correlation between the width of the d-band of transition metals and the selectivity in the hydrogenation of α,β -unsaturated aldehydes toward the unsaturated alcohols was proposed.^[45,194]

In a systematic study performed by Ryndin et al.^[194], both the selectivity and activity of the partial hydrogenation reaction of the multi-functional oxopromegestone (17 α -methyl-17 β -(1,2-dioxopropyl)-estra-4,9-dien-3-one, Fig 5.4) molecule over different metal surfaces were investigated. The author showed that the order of chemoselectivity (Os > Ir > Pt = Pd > Rh) toward the hydrogenation of the terminal ketone group was almost inverse to the order of the activity (Pd > Rh > Pt > Ir > Os).

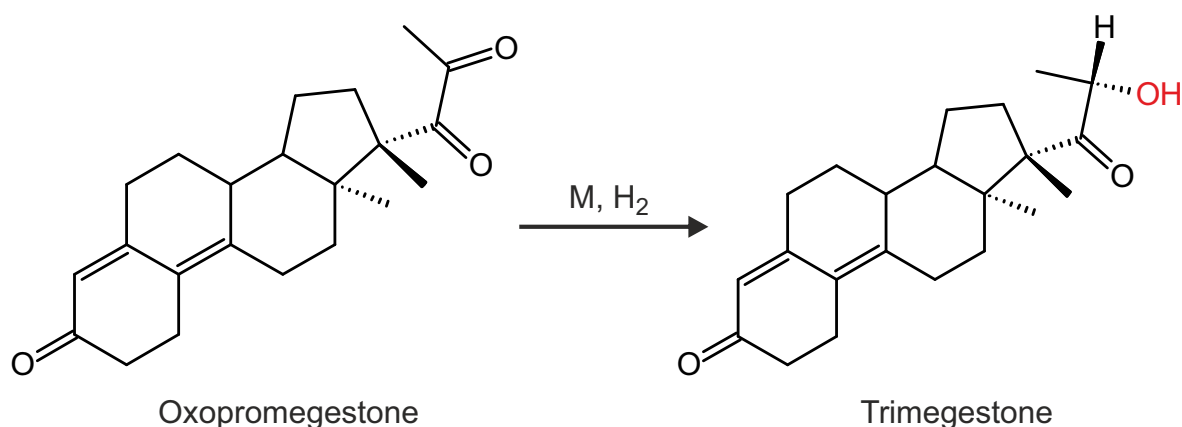


Figure 5.4: Chemoselectivity of the hydrogenation reaction of the multi-functional molecule oxopromegestone over different transition metals (M) investigated by Ryndin et al.^[194].

Rylander^[195] reported a similar observation in the experimental hydrogenation study of cinnamaldehyde, crotonaldehyde and acrolein over Os/C in isopropanol in which the conversion rate of the unsaturated alcohol was relatively high (95 % cinnamyl alcohol, 90 % crotyl alcohol and 73 % allyl alcohol). Mäki-Arvela suggested that the increasing width of the d-band (Pd < Pt < Ir \approx Os) and thus repulsive interaction between the metal surface and the molecule hinders the chemisorption of the C=C bond.^[45] However, pristine Os is not an active hydrogenation catalyst and despite the high selectivity not attractive for industrial application.

A general attempt to combine the advantages of both, active and selective catalytic materials, is the formation of bimetallic surfaces, in which one highly selective metal is paired with a highly active metal.^[196] The degree of the filling of the d-band can be altered by varying the composition of the alloy and thus the catalytic activity can be controlled. This is a very promising approach but it has one severe weak point when transferring it into real catalysis. After dispersing the bimetallic alloy onto a carrier, the resulting catalyst rather

consists of bimetallic clusters than a bimetallic alloy. The component with the lower heat of sublimation usually accumulates on the surface rendering the composition of the active surface difficult to control.

In several studies, the authors focused on the investigation of the partial hydrogenation reaction of acrolein toward propenol over different bimetallic surfaces.^[35,36,39,41,197] Marinelli et al.^[36] investigated the activity and selectivity in the hydrogenation of acrolein over different bimetallic Pt-containing surfaces. Compared to pristine Pt, the selectivity toward the unsaturated alcohol could be enhanced from 1.6 % (Pt) to 27.5 % after adding Sn as a promoter to the Pt. A similar trend was shown in the study by Claus et al.^[35] who reported an increase of selectivity toward propenol formation from 34 % (Au/ZnO) to 63 % (Au-In/ZnO) after adding indium to the gold nanoparticles. The opposite trend of decreasing selectivity was reported by Muir et al.^[197] in a temperature-programmed reaction spectroscopy study on Ag(111) and Pd/Ag(111). While on pristine Ag(111), the authors obtained a maximum value of 19 % selectivity toward propenol, adding Pd to the metal surface reduced this dramatically to 3 % for (0.9 %)Pd/Ag(111).

A novel strategy is to combine the advantages of heterogeneous and homogeneous catalysis by employing adsorbed ligands on a metal surface to promote the selectivity of a multi-pathway surface reaction toward a desired product.^[29–33] Over these hybrid materials, the reactants can interact with the underlying metal surface, which is typical for heterogeneous catalysis, and on top, the surface adsorbates may additionally establish lateral interactions with the reactants, which is a typical property of homogeneous catalysts. A chemical reaction thus may have improved selectivity toward a desired product as compared to the pristine metal surface. In Figure 5.5, the cartoon of the general concept of ligand-directed catalysis is illustrated.

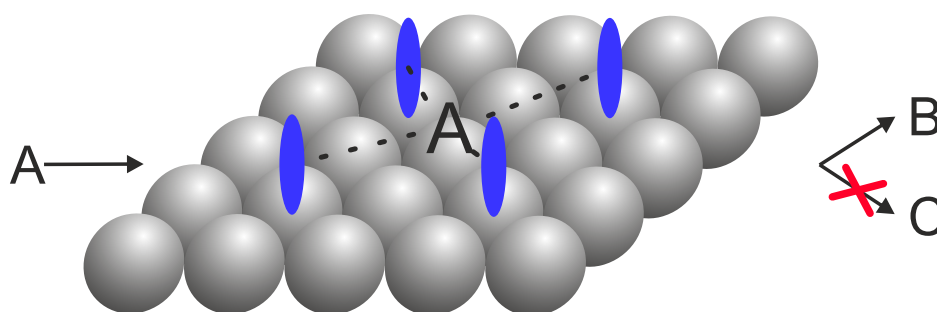


Figure 5.5: Concept of ligand-directed heterogeneous catalysis: Adsorbed ligands (blue) on the surface prior to the reaction of A to B. Lateral interactions (dashed line) between the A and the ligands promote the formation of the desired product B of a multi-pathway reaction.

A heterogeneously catalyzed reaction of the type



usually yields both the products B and C. Adsorbing a specific adsorbate on the surface prior to the reaction promotes the formation of the desired species B by, for instance, lowering the activation barrier of the corresponding reaction path, and equation 5.1 becomes



A few model studies on ligand-directed chemoselective catalysis were published in the recent years.^[32,33,198–203] Chen et al.^[198] reported the chemoselective partial hydrogenation of nitrobenzene toward N-hydroxylanilines over platinum nanowires functionalized with ethylenediamine. Tsunoyama et al.^[200] demonstrated the electron-donating effect of adsorbed poly(N-vinyl-2-pyrrolidone) (PVP) to the small gold clusters (d less than 1.5 nm) rendering the PVP-Au more active for the aerobic oxidation of alcohol than the same nanoparticles being stabilized by a larger ligand (poly(allylamine), PAA). The PVP ligand was also used as a capping for Au/SiO₂ nanoparticles in liquid phase by Huang and co-workers^[199] who showed the enhancement in selectivity of the partial oxidation of benzyl alcohol to benzaldehyde from 43 % to close to 100 %.

The chemoselective hydrogenation of different α,β -unsaturated aldehydes was shown in recent studies by Kahsar et al.^[32] over Pt/Al₂O₃, functionalized with thiolate self-assembled monolayers, by Wu et al.^[33] over primary amine functionalized Pt₃Co and by Cano et al.^[202,203] over secondary phosphine oxides (SPOs) functionalized gold nanoparticles. The Au-SPO system in combination with acrolein was also investigated by Almora-Barrios et al.^[201] in a theoretical study. The authors identified a cooperative effect at the interface of the Au-SPO nanoparticle that enables the heterolytic cleavage of the hydrogen molecule with its kinetically favorable concerted addition to the carbonyl group of acrolein.

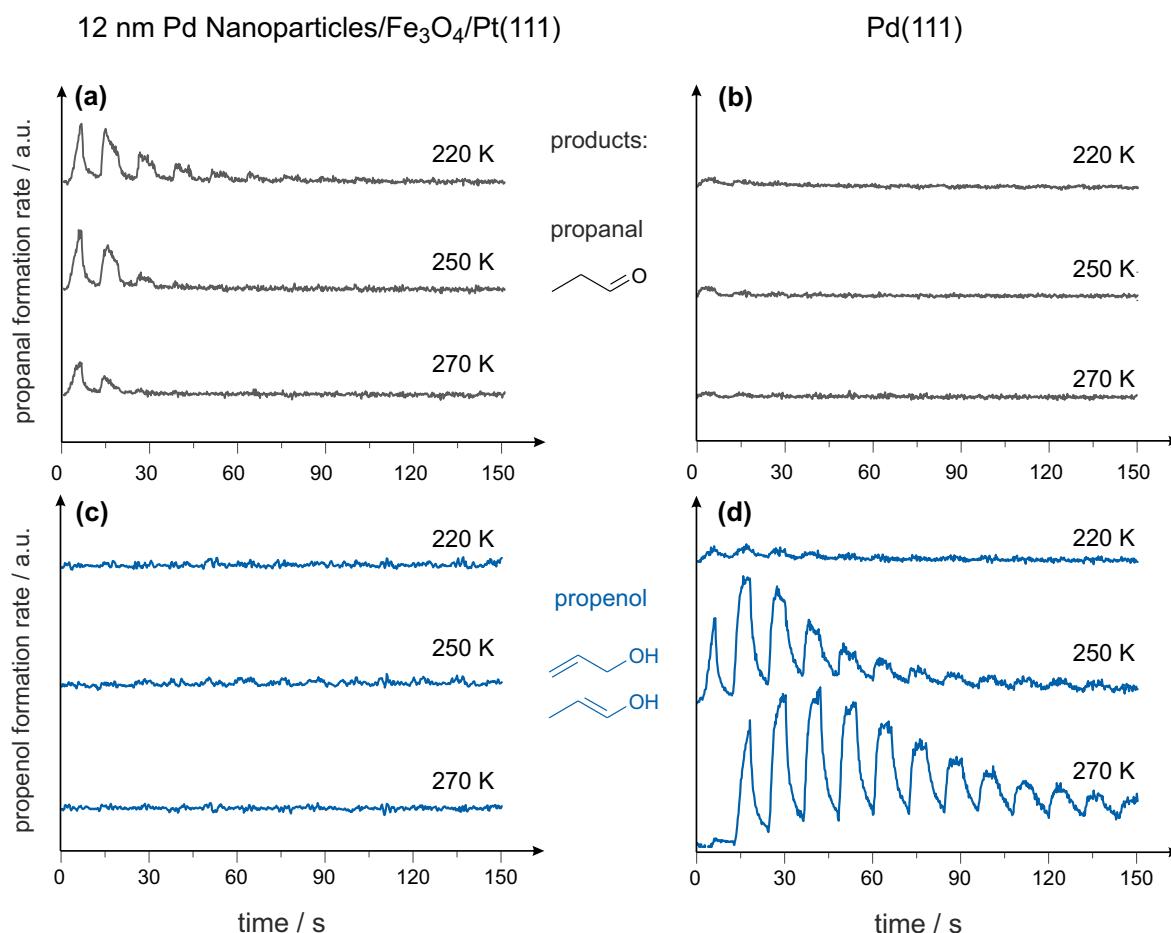


Figure 5.6: Results from the previous kinetic study on acrolein hydrogenation over 12 nm Pd nanoparticles (a and c) and Pd(111) single crystal (b and d). The formation rates of the products propanal (a-b) and propenol (c-d) are shown for both experiments at indicated temperatures. Reprinted with permission from the Journal of the American Chemical Society from Ref.[39].

Our group previously investigated the hydrogenation reaction of acrolein on 12 nm Pd nanoparticles and Pd(111) single crystals as an extended Pd surface. [39,41,42] In Figure 5.6, the main results from the kinetic study are presented. In the experiments on Pd nanoparticles, it could be confirmed what was already known from real catalysis on powdered material: it is not possible to hydrogenate acrolein at the C=O entity while keeping the C=C bond intact. The catalyst consisting of 12 nm Pd nanoparticles was 100 % selective toward the formation of the undesired aldehyde propanal. However, the experiments under the same conditions performed on a Pd(111) single crystal surface revealed a completely different outcome: acrolein was selectively hydrogenated toward propenol.

A detailed spectroscopic investigation of the chemical composition of the active surface revealed the different temporal evolution of adsorbed species during the course of the reaction. In Figure 5.7, the results of the combined kinetic and spectroscopic study on a Pd(111) surface being exposed to a continuous flux of H₂ and acrolein molecules at 270 K are summarized, as they build the basis for the studies conducted in this work. The kinetic curves related to the formation rates of propenol (blue) and propanal (black) in the gas phase (Fig. 5.7a) show that the reaction is 100 % selective toward the formation of propenol, although it is important to note that the surface is not immediately turning over acrolein to propenol.

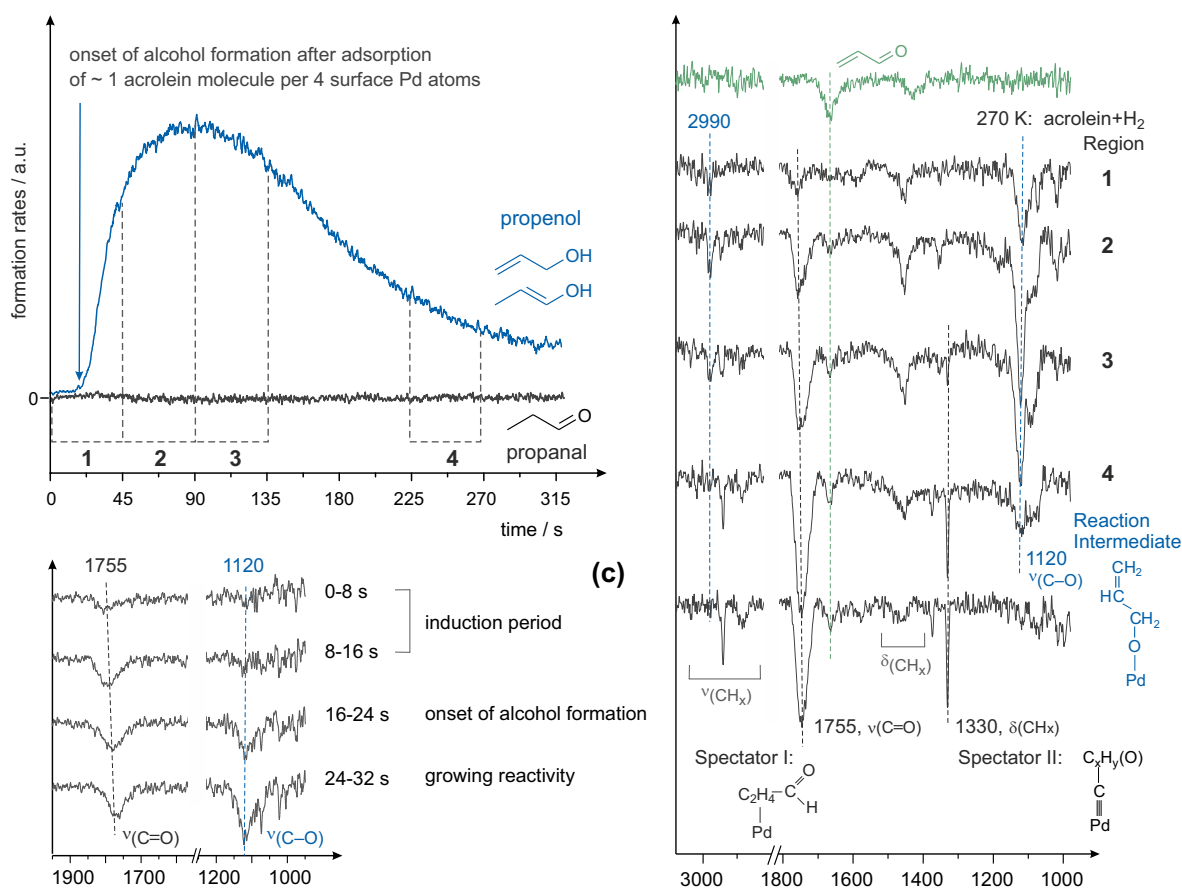


Figure 5.7: Results from the combined kinetic and spectroscopic study on acrolein hydrogenation over Pd(111): (a) formation rates of propenol (blue) and propanal (black) over Pd(111) at 270 K, (b) IRAS spectra obtained during the time regions indicated in (a). (c) IR spectra obtained during the early stage of the reaction. Reprinted with permission from the Journal of the American Chemical Society from Ref.[39].

In the IR spectra obtained during the course of the reaction (Fig. 5.7b), the evolution of several vibrational bands at different stages of the reaction can be identified. The surface species with particular importance to the hydrogenation reaction of acrolein over Pd(111) are presented in Figure 5.8.

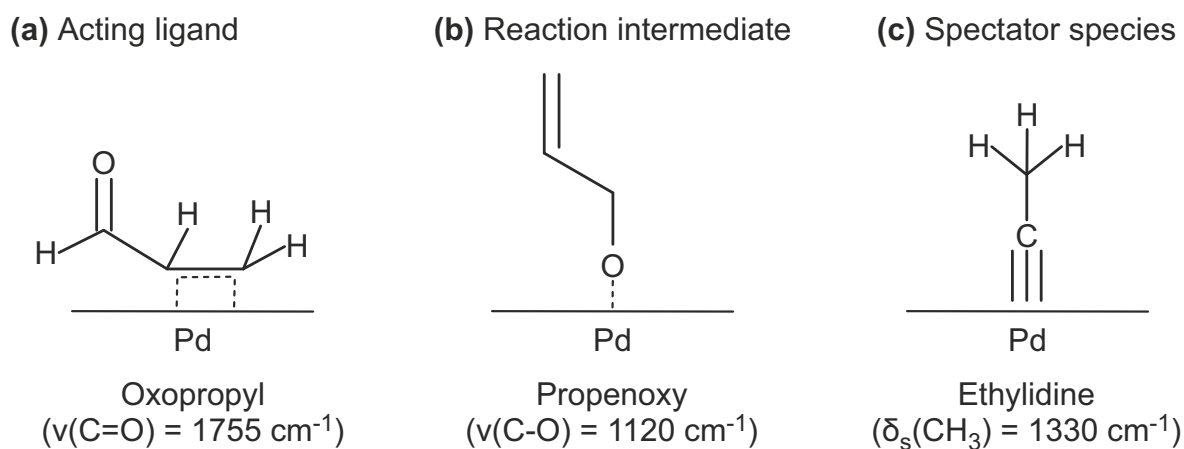


Figure 5.8: Visualization of the proposed acting surface species in the hydrogenation reaction of acrolein over initially pristine Pd(111): the oxopropyl ligand imparts selectivity toward the formation of the propenoxy intermediate and the ethylidene species deactivates the catalyst. [39,41,42,204]

The band with its characteristic vibration located at 1755 cm^{-1} was assigned to the stretching vibration ($\nu(\text{C}=\text{O})$) of an oxopropyl ligand species (Fig. 5.8a), 1120 cm^{-1} to the stretching vibration ($\nu(\text{C}-\text{O})$) of the reaction intermediate (Fig. 5.8b) and 1330 cm^{-1} to the deformation vibration ($\delta_s(\text{Pd}\equiv\text{C}-\text{CH}_3)$) of an ethylidene spectator species (Fig. 5.8c). This assignment based on i) the spectroscopic signatures in the IR spectrum and the correlation of the temporal evolution of ii) adsorbates on the surface (Fig. 5.7c) as well as iii) the formation of propenol in the gas phase (Fig. 5.7a).

Thus, the hydrogenation reaction of acrolein over initially pristine Pd(111) could be divided into three different stages: i) the induction period, in which the acrolein molecules form the active oxopropyl ligand layer, ii) the period of growing formation rate of propenol, in which the propenoxy reaction intermediate could be detected spectroscopically and iii) the deactivation of the catalyst, in which the ethylidene species poisons the catalyst.

Based on the experimental data on the hydrogenation reaction of acrolein obtained in this combined spectroscopic and kinetic study, it was concluded, that the acrolein molecules form a densely packed oxopropyl layer in the early stage of the reaction, which renders the surface nearly 100 % selective toward the formation of the propenoxy reaction intermediate and thus also toward the unsaturated alcohol as a product. Derived therefrom, it was hypothesized that the spontaneous formation of a reactive ligand layer by acrolein molecules is the decisive prerequisite for rendering the initial pristine surface selective toward the formation of the desired product.

This conclusion sets up the starting point for the present study: a detailed investigation of both, the geometric and electronic structure of the reactive ligand layer, that is required to promote selectivity in the hydrogenation reaction of acrolein over Pd(111). Obtaining a full atomistic-level understanding of the related surface phenomena allows the design of a tailor-made functionalized surface with desired catalytic properties.

Two key parameters, i.e. the lateral interactions between the adsorbed ligands and reactants as well as the induction period, have a decisive effect on the chemical reaction. The former is required as in experiments performed over both, the initially pristine Pd(111) surface and the supported Pd nanoparticles, no formation of the desired product propenol was reported. Propenol was formed only over the Pd(111) surface covered with the densely packed oxopropyl ligand layer, which is formed on initially pristine Pd(111) during the induction period by acrolein molecules. Thus, the reduction of the induction period is an important kinetic parameter, which indicates that the surface has already been rendered selective toward the formation of propenol.

The potential influence of lateral interactions on the hydrogenation reaction of acrolein in terms of coverage of adsorbed species on the surface was also addressed by a theoretical DFT study by Tuokko et al.^[186] The authors showed for acrolein and the partial hydrogenated reaction intermediates adsorbed on Pd(111) and Pt(111) at different coverage, that geometric effects influence the potential energy surfaces and hence the chemoselectivity. In the same study, the authors also suggested larger space requirements for reactions at the C=O entity of acrolein than at the C=C tail. Thus, the selectivity toward propenol formation is more favorable at low coverages of adsorbed species, while the hydrogenation of the C=C bond toward propanal is kinetically favored at high coverages of reactants.

Both the experimental and theoretical studies provided some starting ideas about the role of the ligand layer in terms of promoting the chemoselective hydrogenation of the C=O entity in α,β -unsaturated aldehydes and ketones. However, the atomistic-level understanding of the related surface phenomena are still missing. In particular, it is not well-understood what type of ligand-directed effects, i.e. the pure geometric and/or electronic effects, play a role in rendering the catalytic surface highly selective toward hydrogenation of the C=O bond. To obtain deeper insights into these aspects of ligand-assisted catalysis, a systematic study on the chemoselective partial hydrogenation of acrolein to propenol is presented.

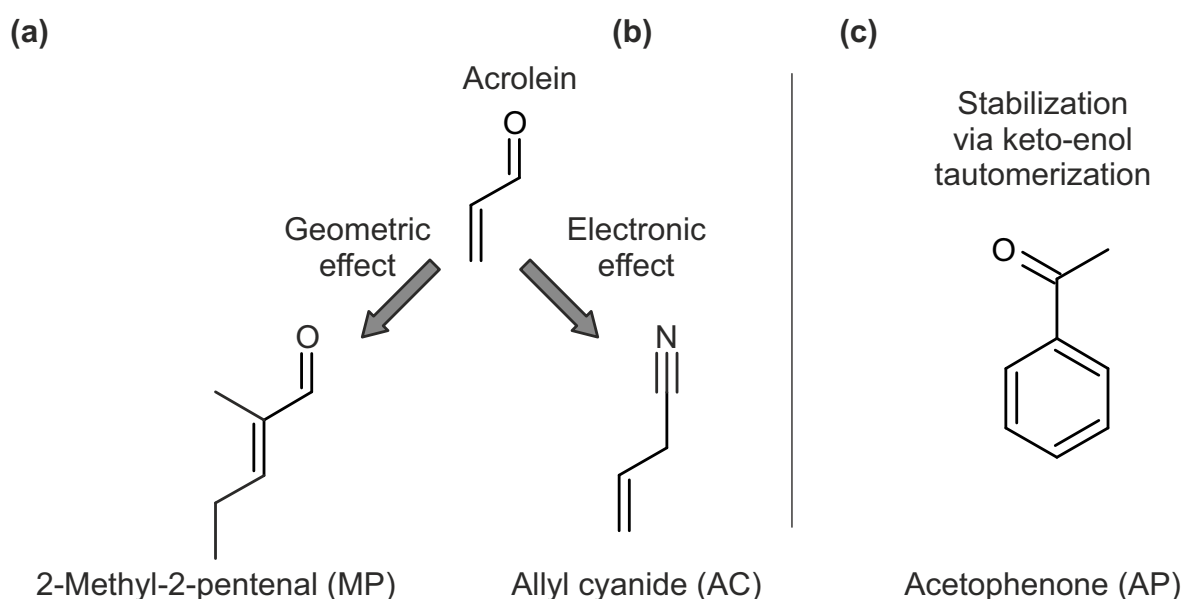


Figure 5.9: Model systems to investigate geometric and electronic effects as well as a potential stabilization of reaction intermediates via keto-enol tautomerization of surface complexes.

Three different prototypes of ligands were utilized for the functionalization of the Pd(111) surface: 2-methyl-2-pentenal (MP, Fig. 5.9a), allyl cyanide (AC, Fig. 5.9b) and acetophenone (AP, Fig. 5.9c). The combination of these ligands allows an investigation of the mechanistic details of the related surface processes in presence of i) a ligand structurally similar to previously identified oxopropyl ligand, but possessing a larger aliphatic tail (MP), in order to address the geometric effects, ii) surface adsorbates possessing a functional group with high electron density (AC) to address the electronic effects, and iii) an adsorbate capable of undergoing keto–enol tautomerization followed by 1:1 lateral interactions with coadsorbed reactants or intermediates (AP).

We employ a unique combination of surface-sensitive operando spectroscopy (infrared reflection absorption spectroscopy, IRAS) with multi-molecular beam techniques, scanning tunneling microscopy (STM) and mass spectrometry, that allows the investigation of reaction kinetics under well-defined isothermal conditions and simultaneously monitor the evolution of the desired reaction intermediates on the surface as well as the formation of products in the gas phase. Additionally, real-space information on the ligand layer were obtained by STM and the chemical composition of the ligand layer as well as its dynamic transformations under operational conditions were monitored by IRAS.

In this project, we focused on several key questions related to ligand–acrolein and ligand–surface interaction. After confirming the hypothesis of a reactive ligand layer promoting chemoselectivity, several questions remained:

- Are there artificial ligands promoting chemoselectivity toward propenol formation?
- Which type of chemical structure is required to impart selectivity to a metal surface?
- Is the promotion of selectivity related to geometric and/or electronic effects?
- How does a ligand interact with the metal surface?
- How does a ligand affect the activity and selectivity of the reaction?
- How does the ligand layer self-assemble on the surface?
- How stable are ligand overlayers under reaction conditions?

In this chapter, the main results from the combined reactivity and adsorption studies of acrolein hydrogenation over different functionalized surfaces are presented. In particular, the influence of three effects of the ligand, i.e. geometric, electronic and the capability to undergo a keto–enol tautomerization of a neighboring molecule followed by 1:1 intermolecular interactions, are pointed out on the example of i) 2-methyl-2-pentenal-, ii) allyl cyanide-, and iii) acetophenone-functionalized Pd(111). Important general considerations for the experimental planning, choice of ligands and the design of the measurements, are discussed at the beginning.

5.1 Experimental Design

Investigating the influence of a specific new parameter on a chemical system requires a deep understanding of the reference system. This can be illustrated by an example from homogeneous catalysis as described hereafter.

In organic synthesis, the choice of the right solvent may also have a key influence on the kinetics of the reactions. Chase et al.^[205] reported in their recent study a strong correlation of the reaction rate with the solvents basicity in the photo-induced isomerization reaction of propenal to propanal using $\text{Fe}(\text{CO})_4$ as a catalyst.^[206] The authors showed that solvents with high basicity were able to coordinate with the unsaturated $\text{Fe}(\text{CO})_4$ and thus most likely prevent the ethylene group of propenal from binding to the metal atom. In this case, the effect of a new parameter on the kinetics of the reaction, i.e. different ligand at the iron atom, needs to be analyzed with respect to the entire parameters of the reaction.

Although heterogeneous catalysis is a solvent-free way to promote lower-energetic reaction paths for chemical reactions, the situation is not simpler. Especially for hydrogenation reactions, the conditions under which the reactions are performed, can be decisive. For obvious reasons, the reaction temperature and the stoichiometric composition of the reactants are important for the hydrogenation reaction of acrolein over Pd(111). Moreover, there were additional parameters that needed to be optimized to allow a systematic investigation of the effect of different ligands on the partial hydrogenation of acrolein over Pd(111).

In the following section, the conditions of the reaction are evaluated with respect to the experimental methods used in this study to obtain a clear kinetic, spectroscopic and microscopic picture of the investigated system. At first, a detailed analysis of the IR spectra obtained during the hydrogenation reaction of acrolein over pristine Pd(111) at 250 K will be presented.

5.1.1 Analysis of the IR Spectra of Acrolein under Reactive Conditions

This section reflects a brief summary of the results that are presented in

The Journal of Physical Chemistry C from Ref.[177]. (Full text in Section 8.3.)

Carsten Schröder, Ann-Katrin Baumann, Marvin C. Schmidt, Jan Smyczek, Philipp A. Haugg, Ole-Christian Graap and Swetlana Schauermaun, *J. Phys. Chem. C* **2022**, 126, 4907–4920.

and

Angewandte Chemie from Ref.[175]. (Full text in Section 8.1.)

Carsten Schröder, Marvin C. Schmidt, Philipp A. Haugg, Ann-Katrin Baumann, Jan Smyczek and Swetlana Schauermaun, *Angew. Chem. Int. Ed.* **2021**, 60, 16349–16354.

In the study by Dostert et al.^[39], the authors presented a spectroscopic analysis of the reactive species during the hydrogenation of acrolein. Based on the time-resolved IRAS spectra shown in Figure 5.7, three different surface species were identified: i) oxopropyl ligand species, ii) propenoxy reaction intermediate and iii) ethylidene species. (*cf. Fig 5.8.*)

The oxopropyl ligand species originates from acrolein in which the former C=C bond establishes a strong attractive interaction with the underlying Pd(111) surface (cf. Fig 5.8a). The ligand is formed on the surface prior to the surface is turning over acrolein to propenol, as it is formed during the induction period, and remains on the surface even when the formation of propenol decreases again. This surface species is identified by its characteristic vibration at 1755 cm^{-1} , which is in the typical range for the C=O stretching vibration $\nu(\text{C}=\text{O})$ of saturated aldehydes.^[40,207–209]

The ethylidene species (cf. Fig 5.8c) is a well-known thermal decomposition product that arises from unsaturated olefins, e.g. ethylene, over transition metals.^[204] The ethylidene spectator species is continuously formed on the surface during the entire course of the reaction and thus has the highest concentration when the Pd(111) surface is exposed to acrolein for a long time. This species has no positive effect on the catalyst in terms of promoting selectivity or reducing the induction period and is most likely only blocking surface sites, resulting in the decrease of reactivity of the metal surface. Its spectroscopic signature is the symmetric deformation vibration $\delta_s(\text{CH}_3)$ of the CH_3 group at 1330 cm^{-1} . (*Full discussion and detailed analysis in Ref.[175] and Section 8.1.*)

A careful look at the IR spectrum 3 shown in Figure 5.7b reveals the presence of an additional shoulder red-shifted to the reaction intermediate at approximately 1097 cm^{-1} . This vibrational band has not been discussed in detail in the previous investigation of the reaction at 270 K. The band lies in the typical vibrational range for the stretching vibration of C–O single bonds, in which the oxygen atom is attached to the Pd(111) surface, as it was demonstrated for dissociated esters^[73,75] and alcohols^[210–213] adsorbed on transition metals. An additional red-shift of a vibrational band, that is related to a stretching vibration of a C–O single or C=O double bond, was previously observed in systems where hydrogen bonding between the oxygen atom and acidic hydrogen atoms of neighboring molecules were established, as a strong H-bonding of an O atom usually weakens the C–O or C=O bond.^[214–217]

However, a similar temporal behavior as the propenoxy reaction intermediate (cf. Fig 5.8b) can be identified. This led to the important question whether this band belongs to the same reaction intermediate or it can be assigned to a different intermediate species. It cannot be unambiguously deduced from the spectra provided in Figure 5.7 and thus, a detailed spectroscopic analysis of the hydrogenation reaction of acrolein on pristine Pd(111) at 250 K was performed in this work.

In Figure 5.10, the results from the spectroscopic study on a pulsed acrolein exposure onto hydrogen-covered Pd(111) at 250 K are presented. Initially, the vibrational band at 1097 cm^{-1} grows and almost saturates in intensity before the band at 1120 cm^{-1} appears. At higher exposure of acrolein (spectrum 4 and 5), the intensity of the band located at 1120 cm^{-1} exceeds the intensity of the band at 1097 cm^{-1} . The different growth in intensity of the bands suggests that it is rather unlikely that those bands correspond to the same surface species. Both vibrational bands are located in the typical range of $\nu(\text{C}-\text{O})$ vibrations and thus, we propose that they correspond to individual surface species in different chemical environments. We assign the reaction intermediate with the higher frequency R_2 (1120 cm^{-1}) to a free-standing propenoxy species while R_1 (1097 cm^{-1}) can most likely be related to an intermediate that is stabilized by an intermolecular hydrogen bonding and the vibration is thus red-shifted compared to the one of R_2 . (*cf. Ref.[177] as well as Sections 5.2 and 8.3.*)

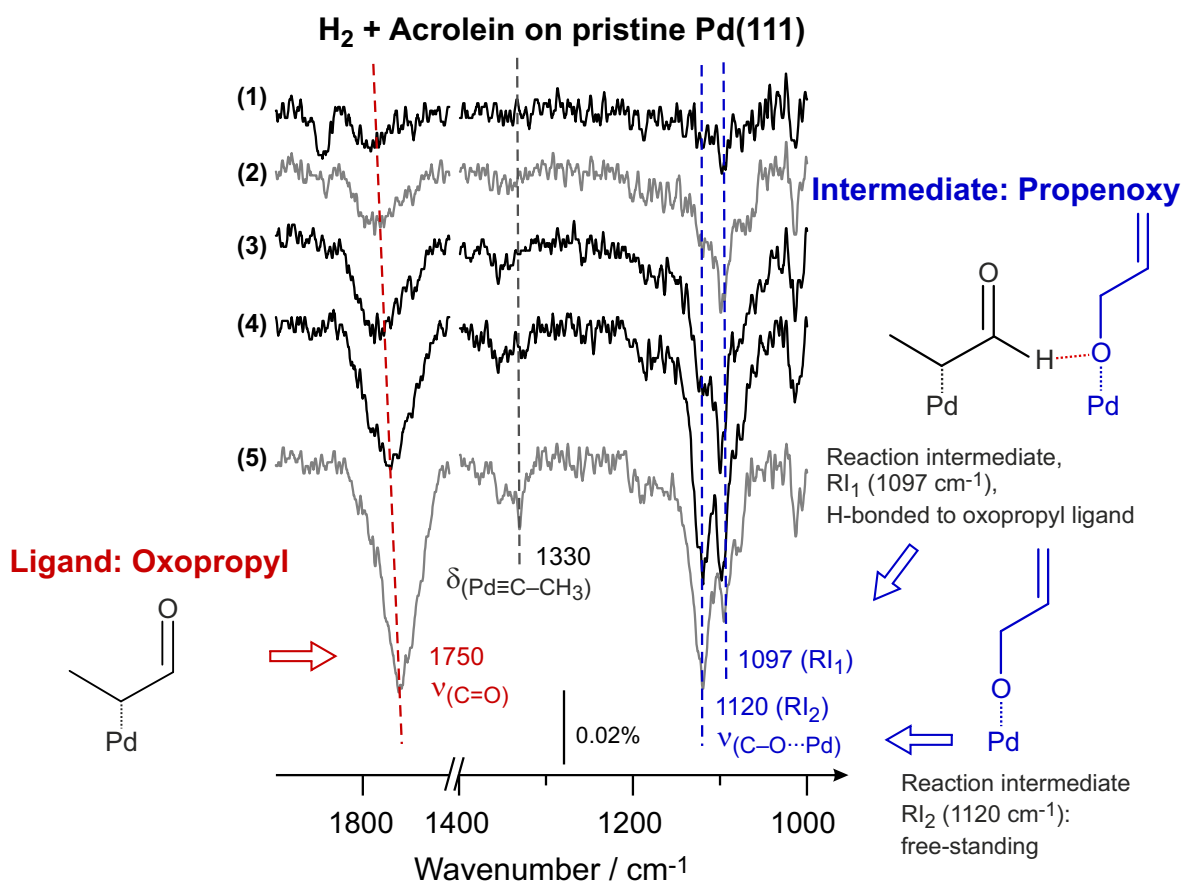


Figure 5.10: IRAS spectra of acrolein dosed on H/Pd(111) at 250 K. The sample was exposed to continuous flux of hydrogen of $7.7 \cdot 10^{14}$ molecules·cm⁻²·s⁻¹ for 10 min prior the exposure to acrolein. Acrolein was dosed at a flux of $2.4 \cdot 10^{12}$ molecules·cm⁻²·s⁻¹; total exposures for the IR spectra: 20 s (1), 40 s (2), 60 s (3), 120 s (4), 600 s (5).

Having assigned all vibrational bands of acrolein under reactive conditions at 250 K, we will point out the effect of tunable parameters, i.e. temperature and fluxes of the reactants, on the reaction kinetics in the following sections.

5.1.2 Parameters that Affect the Hydrogenation of Acrolein over Pd(111): Reaction Temperature

Dostert et al.^[39] reported that acrolein reacts to propenol over Pd(111) in the range between 220 K and 290 K. Above 290 K, acrolein decomposes on the surface to CO. The authors performed a detailed study at 270 K where they reported a fairly high conversion rate as well as detectable intermediates on the surface. For lower reaction temperature, the formation rate of propenol in the gas phase decreases. That has a direct influence on the quality of the kinetic data: the lower the formation rate, the lower the signal-to-noise ratio of the kinetic data.

However, the reaction temperature chosen in this study was set to 250 K because of the following reasons. First, different types of ligands were planned to be investigated which do not necessarily have a similar desorption behavior like acrolein. As discussed in Sections 3.5

and 3.6, both the desorption and diffusion rate increase at elevated temperature. Related to the desorption rate, both the in-situ spectroscopic characterization of reaction intermediates and the real-space microscopic identification of the reactive ligand layer on the catalyst is usually less difficult at lower temperature. The diffusion is especially important in STM experiments. Secondly, the influence of ligands on the induction period was one key factor to be investigated in this study. The higher the temperature, the less distinct would be the effect with respect to the temporal resolution of the experiment, which is in the range of a few seconds. Lastly, the formation rate of propenol in the gas phase at 250 K was sufficiently high enough to obtain a clear picture of the kinetics of the reaction.

5.1.3 Parameters that Affect the Hydrogenation of Acrolein over Pd(111): Flux Rates of the Reactants Acrolein and Hydrogen

This section reflects a brief summary of the results that are presented in

*The Journal of Physical Chemistry C from Ref.[177]. (Full text in Section 8.3.)
Carsten Schröder, Ann-Katrin Baumann, Marvin C. Schmidt, Jan Smyczek, Philipp A. Haugg, Ole-Christian Graap and Swetlana Schauer mann, J. Phys. Chem. C **2022**, 126, 4907–4920.*

In this section, the influence of the acrolein and hydrogen fluxes on the propenol formation rates as well as the optimization of both fluxes with respect to experimental parameters is described.

For the efficiency of hydrogenation reactions, the quantitative relationship between the reactants is crucial. A general phenomenon in surface-mediated chemical reactions is competitive adsorption of the reactants. The reaction mechanisms in heterogeneous catalysis at the gas–solid interface (cf. Section 3.8 and Figure 3.7) usually involve the adsorption of both reactants that form the product on the surface in subsequent steps.

Therefore, it is highly desired to maintain a suitable high steady-state concentration of both adsorbed reactants species on the surface. When the hydrogen concentration is too low, the conversion rate could be too low or partial hydrogenated species could be formed. When the hydrogen concentration is too high with respect to the other reactant, competitive adsorption may hinder the reactant from being hydrogenated. For the investigation of the kinetics of a reaction, the variation of the fluxes of the reactants in a broad range is highly desired. From a technical point of view with respect to the experimental setup employed in this study, the signal-to-noise ratio and thus the quality of the data increases with higher flux rate.

In molecular beam apparatuses, however, flux rates cannot be increased infinitely to meet both criteria equally. As mentioned in Section 4.1, an effusive source can only generate a stable flux of molecules when collision-free conditions are present inside of the GCA. With increasing inlet pressure at the inner stage of the beam, the effective flux reaches a maximum and does not increase further linearly (cf. Ref. [173]). Thus, the parameter space was limited by the flux generated for hydrogen molecules of $8.5 \cdot 10^{14}$ molecules·cm⁻²s⁻¹.

All hydrogenation experiments in this work were performed with a hydrogen flux of $7.7\text{--}8.5\cdot 10^{14}$ molecules $\cdot\text{cm}^{-2}\cdot\text{s}^{-1}$. Since the flux rate of hydrogen was set to a fixed value, the flux rate of acrolein had to be adjusted to meet the following criteria: i) the signal-to-noise ratio of the kinetic data had to be high enough to obtain a clear picture of the influence of an artificial ligand on the reaction; ii) the flux rate must not be too high to have a partial turnover of acrolein, leaving non-reactive acrolein molecules on the surface; iii) the flux rate must not be too low to have a duration of a single experiment of a few hours.

In Figure 5.11a, the results of different hydrogen to acrolein ratios at different fluxes of acrolein and in (b) a close-up on the induction period are presented.

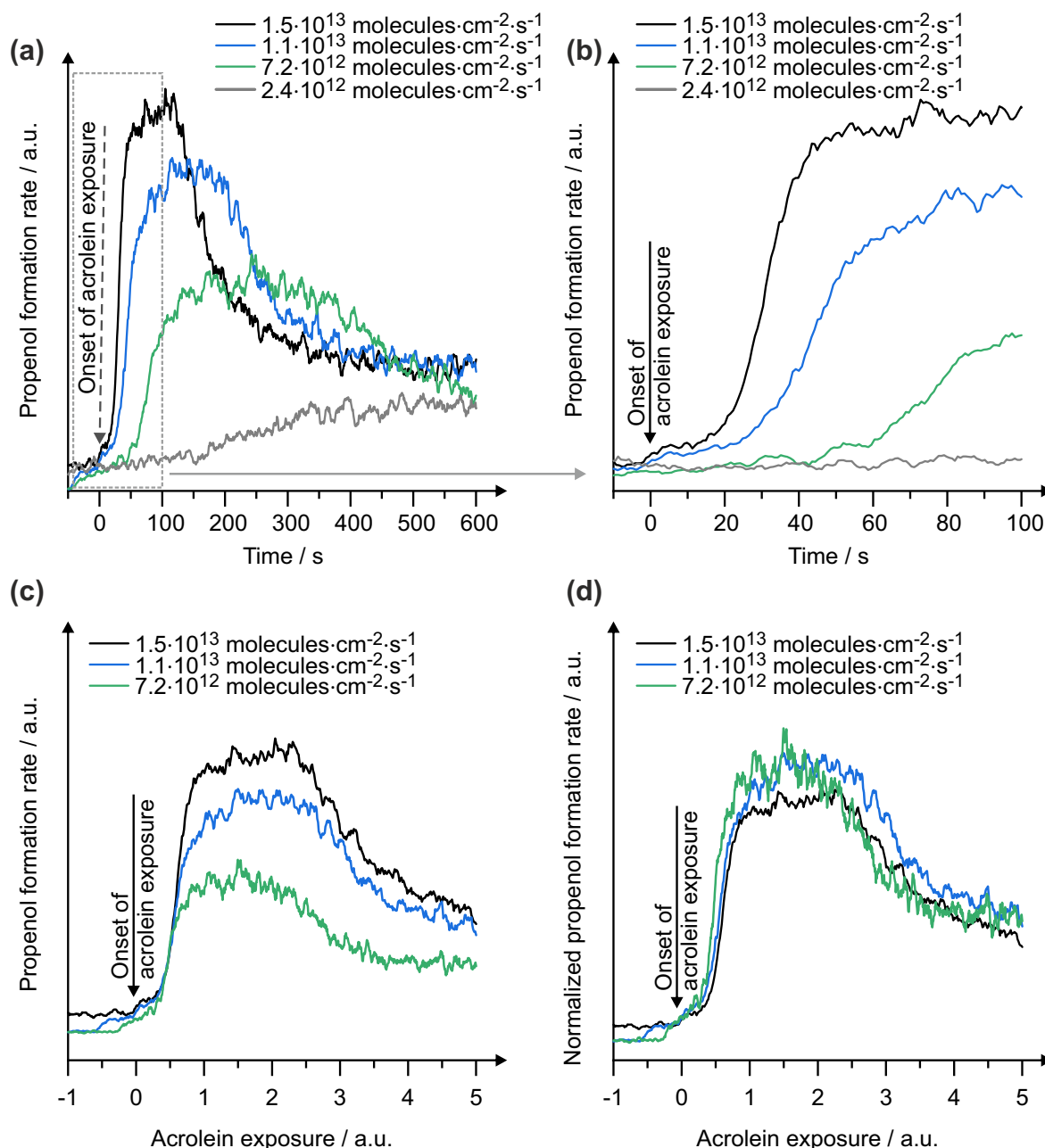


Figure 5.11: Propenol formation rate in the gas phase as a function of acrolein flux at 250 K. Pd(111) was exposed to a continuous flux of hydrogen ($7.7\cdot 10^{14}$ molecules $\cdot\text{cm}^{-2}\cdot\text{s}^{-1}$) and different continuous exposures of acrolein ($2.4\text{--}15\cdot 10^{12}$ molecules $\cdot\text{cm}^{-2}\cdot\text{s}^{-1}$). See text for details.

A very low flux of acrolein ($2.4 \cdot 10^{12}$ molecules \cdot cm $^{-2}$ s $^{-1}$) results in a slow rise in the formation rate of acrolein where the identification of a clear onset point is hard to determine. Thus, this acrolein flux was not used for kinetic investigations, however, it was suitable for spectroscopic studies. A too high flux of acrolein results in a very short induction period that complicates a quantitative interpretation with respect to the reduction or elongation of the induction period. This high flux also results in adsorbed, but partly non-reacting acrolein molecules. These could be identified spectroscopically via the stretching vibration of the carbonyl group ($\nu(\text{C}=\text{O})$ band at 1660 cm $^{-1}$) which is the spectroscopic signature of molecular adsorbed acrolein. (*Data not shown, cf. Ref.[40] for details.*)

Figure 5.11c shows the same kinetic curves as in (a) of the same figure, with time axis scaled with the acrolein flux. The duration of the induction period is directly proportional to the acrolein flux and thus, the change of flux does not change the kinetics of the reaction on the surface. Additional scaling of the propenol formation rate axis with the acrolein flux yields the normalized kinetic curves presented in in Figure 5.11d. The maximum value of the formation rate is also proportional to the acrolein flux. (*cf. Ref.[177] and Section 8.3.*)

As a summary of all these considerations and observations, for all experiments conducted in this work, the hydrogen flux was set to $7.7\text{--}8.5 \cdot 10^{14}$ molecules \cdot cm $^{-2}$ s $^{-1}$ and acrolein fluxes were set to $2.4\text{--}11 \cdot 10^{12}$ molecules \cdot cm $^{-2}$ s $^{-1}$.

5.1.4 Parameters that Affect the Hydrogenation of Acrolein over Pd(111): Hydrogen Pretreatment of the Catalyst

In this section, the effect of the pretreatment of the Pd(111) surface with hydrogen on the propenol formation rate, the induction period and the catalytic performance is elaborated.

As addressed in the previous section, a low hydrogen to acrolein ratio results in a partial molecular adsorption of acrolein molecules which do not react with hydrogen to form any reactive intermediates. Thus, acrolein molecules can most likely inhibit the adsorption of hydrogen in a competitive adsorption process if it is adsorbed as an intact molecule. Based on this, it can be deduced, that the presence of hydrogen on the surface prior to the exposure to acrolein is essential for the kinetics of the reaction.

In Figure 5.12, the formation rates of propenol over initially pristine Pd(111) as a function of hydrogen exposure, ranging from very low to high exposure of hydrogen onto the surface, are presented. The Pd(111) surface was pretreated with i) a single pulse (30 s pulse duration, green curve) of hydrogen as well as a continuous hydrogen exposure for ii) a short (30 s, blue curve) and iii) a long (10 min, black curve) time prior to the exposure of acrolein to the surface at 250 K. The kinetic curve obtained after a the single pulse (Fig 5.12, green curve) of hydrogen shows a very long induction period of approximately 35 s and a low maximum formation rate. The latter can easily be explained by the consumption of hydrogen atoms from the surface by acrolein molecules. The former may indicate that the pretreatment time of the catalyst may have an influence on the induction period. To further clarify this aspect, two additional experiments were conducted with continuous exposure of hydrogen at different pretreatment times.

Interestingly, the induction period for both experiments is shorter compared to the single pulse exposure to hydrogen, but the difference between 10 min (induction period 25 s) and 30 s (induction period 28 s) pretreatment time is rather small albeit present.

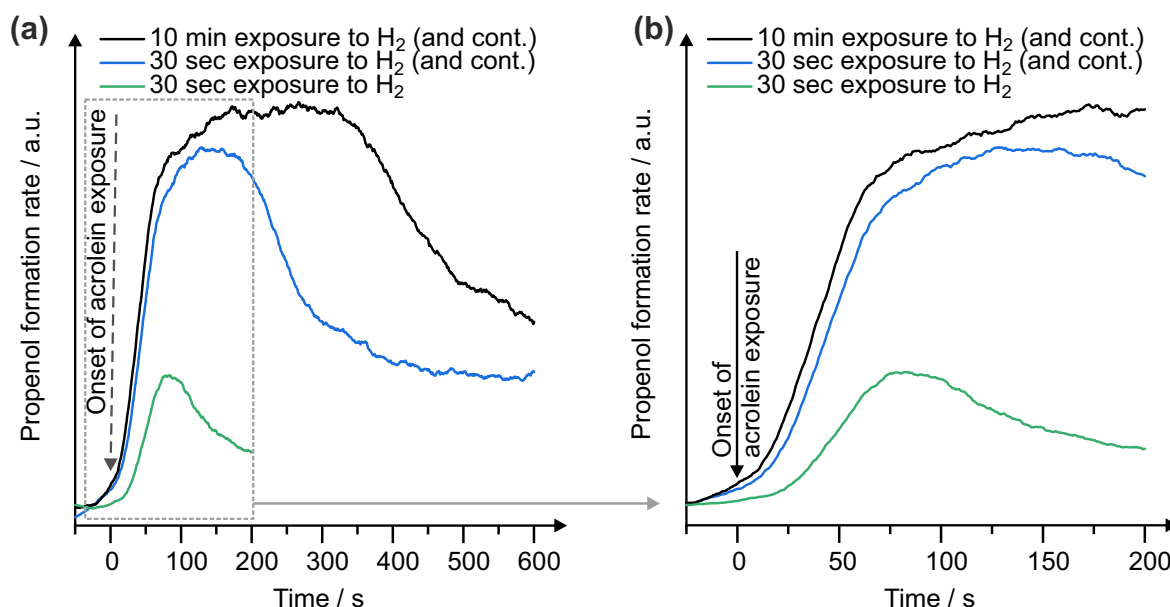


Figure 5.12: (a) Formation rates of propenol in the gas phase over Pd(111) as a function of hydrogen pretreatment time shown for a continuous experiment of 600 s at 250 K and (b) close-up of the induction period. Pd(111) was exposed to a flux of hydrogen ($8.5 \cdot 10^{14}$ molecules·cm⁻²·s⁻¹) for the indicated time and continuously to acrolein ($1.1 \cdot 10^{13}$ molecules·cm⁻²·s⁻¹) hereinafter. The induction periods are: 35 s (green), 28 s (blue) and 25 s (black).

In consideration of the fact that there are drastic differences in the duration of the induction period as a function of pretreatment time, it can be speculated that some hydrogen, which is not regular surface hydrogen, may be formed on the surface upon long exposure, e.g. hydrogen adsorbed below the uppermost layer of the Pd(111) surface, that may have a stronger binding energy. However, at this particular reaction temperature, no subsurface hydrogen should be present in this system.^[112,117]

It is important to point out is that the absolute turnover rate of the catalyst depends on the hydrogen pretreatment time. The catalyst is turning over more acrolein molecules to propenol when the surface is conditioned with hydrogen for a longer duration. As a consequence of these observations, the Pd(111) catalyst surfaces used in the presented studies were exposed to a continuous flux of hydrogen for 10 minutes prior to the onset of the acrolein exposure and then further continuously exposed to hydrogen.

The next crucial consideration for the investigation of ligand-directed catalysis is the choice of the chemical structure that most-likely promotes chemoselectivity which will be presented in the next section.

5.1.5 Parameters that Affect the Hydrogenation of Acrolein over Pd(111): Artificial Ligand Layer

In this section, important considerations for the choice of the prototypes of the ligands for the investigation of geometric, electronic and keto–enol tautomerization effects on ligand-directed catalysis as well as the design of the measurements are presented.

The model of the chemoselective ligand-directed hydrogenation of acrolein over initially pristine Pd(111) is based on the hypothesis of a reactive ligand layer. This ligand layer, consisting of oxopropyl surface species, is formed by acrolein molecules in the early stage of the reaction. Based on the spectroscopic data, the ligands most likely adsorb via the former C=C bond onto the metal surface.^[39] This is illustrated in Figure 5.13 with the oxopropyl ligand in black and the propenoxy reaction intermediate in blue.

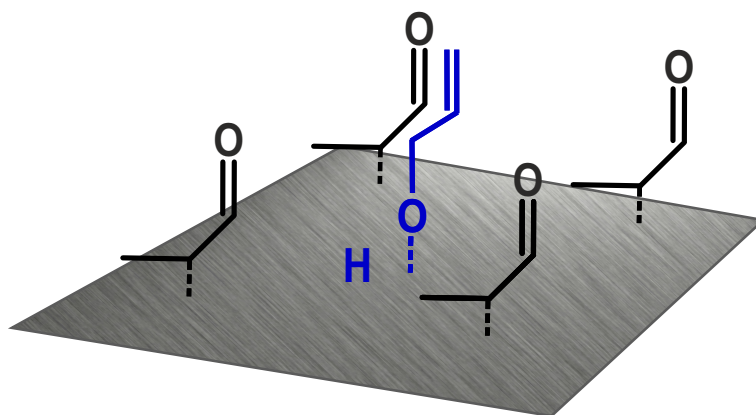


Figure 5.13: Hypothesized model of a ligand layer consisting of oxopropyl surface species (black) promoting selectivity of the Pd(111) surface toward the formation of the propenoxy reaction intermediate (blue) on the surface and, correspondingly, propenol in the gas phase.

An important property of organic adsorbates for ligand-directed catalysis is their stability under operating conditions. Unwanted side reactions, e.g. decomposition or the formation of hydrogenated species, may result in the self-poisoning and thus deactivation of the catalyst. The stability of the oxopropyl ligand under hydrogen was previously shown in the experimental study by Dostert et al.^[39]

The major focus of this study was the investigation of the electronic and geometric effects of the adsorbed ligands as well as their role in the partial hydrogenation of acrolein over Pd(111). Thus, our first approach was to slightly alter the chemical structure of the acrolein molecule by i) adding additional aliphatic side groups to the acrolein backbone and ii) replacing the C=O group by a C≡N group. The chemical structures of both acrolein-derived ligand molecules, detailed investigated in this work, are drawn in Figure 5.14a-b.

2-Methyl-2-Pentenal (MP)

The adsorption and thermal chemistry of both acrolein and its C₄-homolog (crotonaldehyde) were investigated in a combined IRAS and TPD study by de Jesús et al.^[218] The authors showed crotonaldehyde being less reactive compared to acrolein.

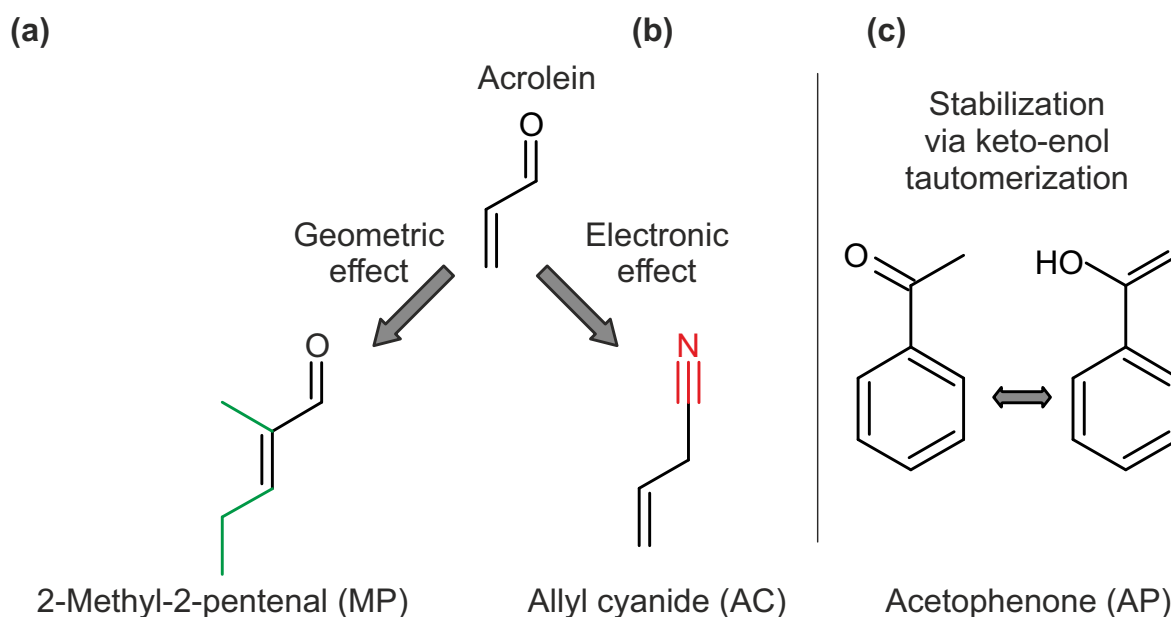


Figure 5.14: Model systems derived from acrolein: (a) 2-methyl-2-pentenal and (b) allyl cyanide as well as acetophenone that is capable of undergoing keto–enol tautomerization, followed by 1:1 lateral interaction.

For the study on the influence of the geometric effects of the ligand on the hydrogenation reaction of acrolein, 2-methyl-2-pentenal (MP) was selected, as it equals the chemical structure of acrolein with additional alkyl side groups. A potentially stable ligand possessing the same functional groups but a longer alkyl chain thus reflects the following two assumptions as compared to acrolein: i) less reactivity toward formation of the unsaturated C_6 -alcohol and ii) similar oxoalkyl ligand species formed on the surface. The former assumption can be supported by the previously mentioned trend of lower reactivity with increasing steric hindrance of the alkyl chain that was reported in the study by de Jesús et al.^[218] as well as the observations from experiments performed in this study, since none of the hydrogenation attempts on MP over Pd(111) at 250 K resulted in the desorption of either the saturated aldehyde (2-methyl-2-pentanal) nor saturated or unsaturated alcohol (2-methyl-2-pentanol) into the gas phase (*data not shown*). The latter will be discussed in the next Section 5.2.

Allyl Cyanide (AC)

Nitriles are molecules possessing a functional group with high electron density ($C\equiv N$) that are well-suited prototypes for studying the electronic effects of electron-rich coadsorbed molecules. In many different surface science studies by various authors, the investigation of the adsorption behavior of nitriles and isocyanides over different pristine metal surfaces had been addressed.^[219–231]

However, the adsorption of unsaturated nitriles was investigated in none of them and thus remains poorly understood. For saturated nitriles and isocyanides, two different adsorption configurations ($\eta_1(N)$ or $\eta_2(N,C)$) are suggested for acetonitrile (MeCN)^[222,228], methyl isocyanide (MeNC)^[224,229], HCN^[230], HCNH^[232] and azomethane^[231] adsorbed on Pt(111), MeCN and MeNC on Pd(111)^[224], MeCN on TiO₂-supported Au^[227], MeNC on Rh(111)^[223] and HCNH on Ru(001)^[226]. (See Ref.[176] and Section 8.2 for full discussion.)

Both discussed adsorption geometries are shown in Figure 5.15. In the $\eta_1(\text{N})$ configuration (Fig. 5.15a), only the nitrogen and surface metal atoms are involved in the interaction. The C atom of the nitrile group is pointing away from the surface, having no direct contact to the underlying metal. In the $\eta_2(\text{N,C})$ configuration (Fig. 5.15b), both the C and N atoms of the nitrile group are interacting with the metal surface, resulting in a close to parallel orientation of the adsorption geometry with respect to the surface plane, depending on the steric hindrance of the alkyl chain R. Allyl cyanide (Fig. 5.15c) with its two functional groups, the $\text{C}\equiv\text{N}$ and $\text{C}=\text{C}$ group, has various possibilities to interact with the metal surface. The nitrile group may adopt a η_1 or η_2 configuration while the interaction of the $\text{C}=\text{C}$ bond can range from a weakly-bound π type to a strong perturbed di- σ type of bonding.

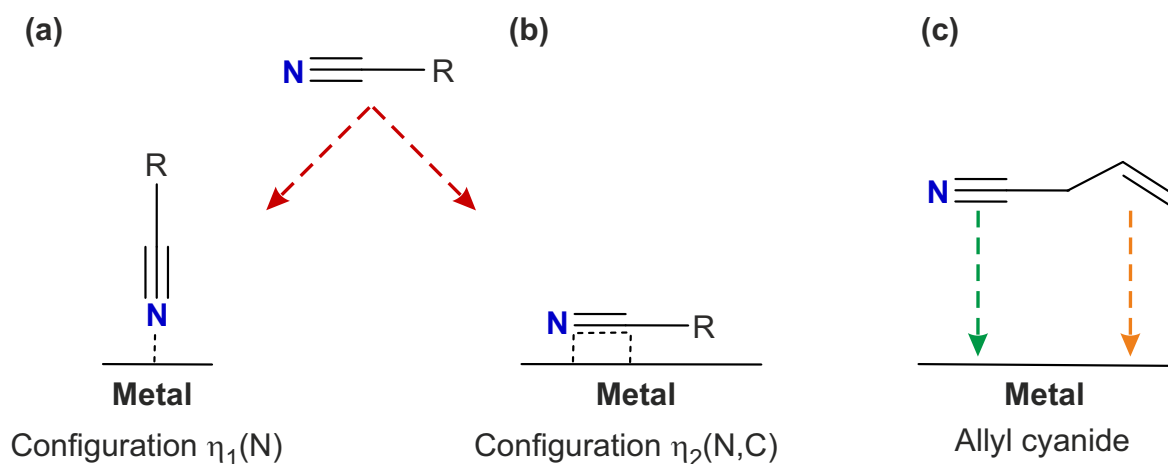


Figure 5.15: Proposed adsorption geometry for nitriles adsorbed on metal surfaces. ^[219–231]

The adsorption and reaction mechanisms of nitriles in the presence of hydrogen on transition metals are insufficiently researched. Vogt et al. ^[233] investigated the reaction of acetonitrile and hydrogen on Al_2O_3 -supported Pt in a combined in-situ infrared and DFT study. The authors reported an imine intermediate and amine reaction product performing their studies at 313 K. The reduction of nitriles to amines is a well-known reaction which can be performed at relatively mild conditions at 60–80 °C. ^[234] The reactivity of unsaturated nitriles over Pd(111) in the presence of hydrogen at low temperatures (approximately 250 K) has not been investigated so far.

The unsaturated C_4 -nitrile (allyl cyanide) became preferred over the homologous C_3 -nitrile (2-propennitrile) as well as C_5 -nitrile (2-pentennitrile) because of two considerations. First, the conjugated π system of 2-propennitrile may result in an undesirable perfectly flat-oriented geometry upon adsorption on the Pd(111) surface, which may hinder the adsorption of acrolein and is on top, according to the metal surface selection rule (MSSR) ^[168], difficult to detect by IRAS, as the IR spectra only contain the out-of-plane vibrations of the olefinic hydrogen atoms. Secondly, the 2-pentennitrile molecule would address both geometric and electronic effects at the same time. Because of both reasons, allyl cyanide with the methylene group ($-\text{CH}_2-$) adjacent to the $\text{C}\equiv\text{N}$ group was selected as a ligand, despite the facts of various possibilities to interact with the surface as well as the formation of hydrogenation products as unwanted side reactions which both will be addressed in Section 5.3.

Acetophenone (AP)

The third ligand examined for suitability to promote chemoselectivity was acetophenone (AP). In our recent studies on acetophenone adsorbed on Pt(111)^[215,235–239], we revealed several interesting phenomena of self-assembly and keto–enol tautomerization. Depending on the reaction conditions, there are acetophenone monomers or oligomers present on the surface. The type of lateral interactions between acetophenone molecules is also sensitive to the surrounding hydrogen concentration. Therefore, acetophenone was a promising molecule for a tunable ligand capable of undergoing keto–enol tautomerization followed by 1:1 lateral interactions with coadsorbed ligands or reaction intermediates.

The stability of a molecule under reactive conditions is one of the key properties for a ligand to promote a catalytic reaction. Furthermore, the capability of the metal surface to remain a highly active and effective hydrogenation catalyst must be preserved. For instance, it is well-known that CO is a very effective and persistent catalyst poison for metals of the platinum group. In a DFT study by Lischa et al.^[240] on hydrogen adsorption on CO-precovered Pd(210), the authors reported an inhibition of hydrogen adsorption in the presence of CO at the surface. To avoid a potentially irreversible self-poisoning of the catalytic surface due to decomposition reactions of the ligand molecules on the pristine and thus highly reactive metal surface, the catalyst was saturated with hydrogen prior to the reaction.

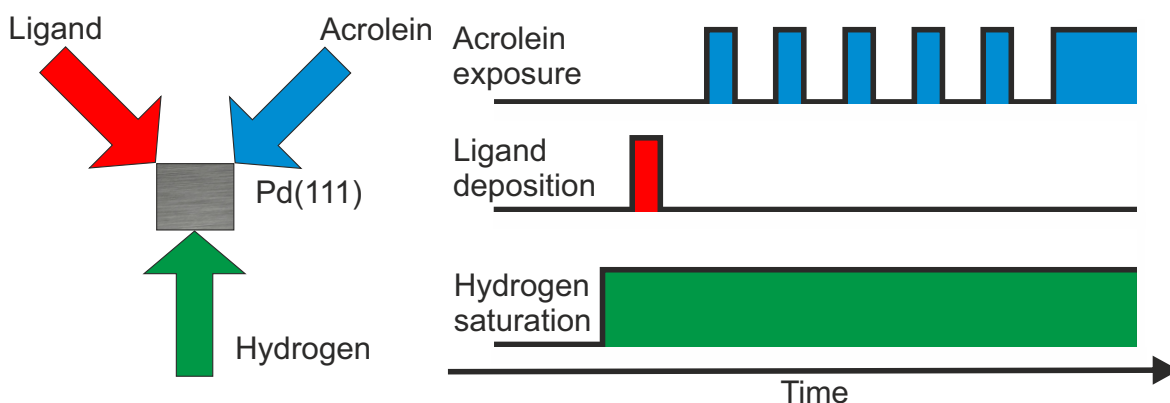


Figure 5.16: Design of the experiments to investigate ligand-directed catalysis for the selective partial hydrogenation of acrolein.

As a result of all these considerations, the surface was prepared in-situ both under isothermal conditions and in the presence of hydrogen. The molecules were dosed via three individual inlet sources: two effusive molecular beams and a gas doser. This separation of the reactants provides a prevention of two points, mutual contamination and undesirable reactions outside the reaction chamber. The experimental design is illustrated in Figure 5.16. Prior to the reaction of the organic molecules, the surface was saturated with hydrogen and further exposed to a continuous flux of hydrogen throughout the entire reaction. This ensures that no decomposition reaction of organic molecules emerge on the highly reactive, pristine metal surface that would not occur in the presence of hydrogen. As a next step, the ligand was dosed onto the surface in a desired amount. The ligand-functionalized surface was thereafter exposed to acrolein molecules in a defined pulsed sequence or continuous mode. The formation of products in the gas phase was continuously monitored by employing

the QMS. This design of the measurements thus allowed to create a tunable and tailor-made surface with a desired amount of adsorbed ligands. Bringing together unsaturated molecules in combination with hydrogen and a good hydrogenation catalyst at sufficiently high temperature always enables chemical reactions. Thus, the possible dynamic change of the ligand at the catalyst upon exposure to hydrogen also had to be considered. This will be addressed in the following sections that contain the characterization of the ligands in broad range of temperature on pristine and hydrogen-covered Pd(111).

5.2 Hydrogenation of Acrolein over 2-Methyl-2-Pentenal-Functionalized Pd(111)

This section reflects a brief summary of the results that are presented in

The Journal of Physical Chemistry C from Ref.[177]. (Full text in Section 8.3.)

Carsten Schröder, Ann-Katrin Baumann, Marvin C. Schmidt, Jan Smyczek, Philipp A. Haugg, Ole-Christian Graap and Swetlana Schauer mann, *J. Phys. Chem. C* **2022**, 126, 4907–4920.

In this section, the influence of geometric effects of an artificial ligand, that has a larger steric hindrance as compared to acrolein, on the hydrogenation reaction of acrolein is presented by the example of 2-methyl-2-pentenal (MP).

The experiments over Pd(111), which is functionalized with 2-methyl-2-pentenal (MP), were conducted in two respects: i) in order to confirm the proposed ligand layer and ii) to address the geometric effects of an artificial ligand, that has a similar geometric structure as the oxopropyl ligand, on the hydrogenation reaction of acrolein over Pd(111). Since 2-methyl-2-pentenal (MP) does not have any additional functional groups that can interact directly with the surface, the adsorption geometry was assumed to be most likely similar to the previously suggested oxopropyl species. (*cf. Section 5.1.1*)

In Figure 5.17a, the kinetic curves of the formation rates of propenol in the gas phase for the hydrogenation reaction of acrolein over MP-functionalized Pd(111) at 250 K are presented for two different exposures of MP (0.3 L and 0.8 L) as well as on initially pristine Pd(111) for reference. Most interestingly, the induction period is strongly reduced with increasing MP exposure. On initially pristine Pd(111), the formation of the reactive ligand layer during the induction period is the decisive step for rendering the surface chemoselective toward the formation of propenol. It is important to emphasize that the reduction or even the complete disappearance of this induction period shows that a reactive ligand layer has already been formed on the surface prior to the exposure of acrolein molecules.

The kinetic curves of the formation rates of both propenol and propanal, presented in Figure 5.17b, highlight that the reactive MP-functionalized surface also remains selective toward the formation of propenol. The conversion rate is approximately 33 % during the period of largest conversion and approximately 8 % in the later stages of the reaction. This demonstrates that the functionalization of Pd(111) with MP results in a highly selective and active catalyst for the partial hydrogenation of acrolein toward the unsaturated alcohol.

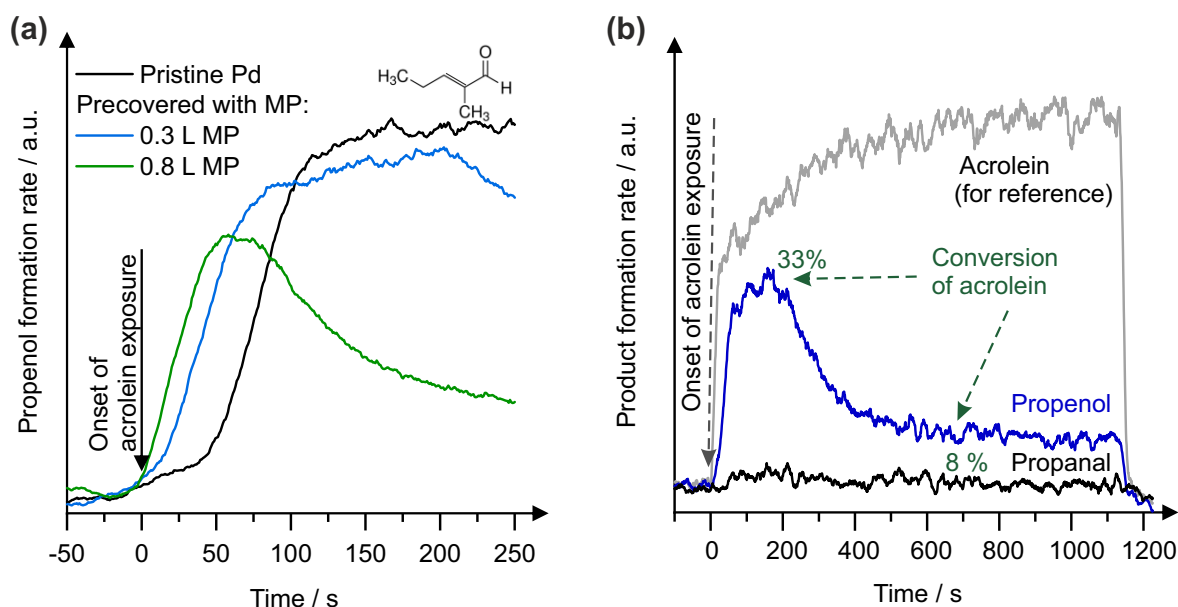


Figure 5.17: Results of the kinetic study on acrolein hydrogenation over MP-functionalized Pd(111) for two different MP coverages (0.3 and 0.8 L). (a) Formation rate of propenol in the gas phase over MP-functionalized Pd(111) and pristine Pd(111) for reference; (b) conversion rate and selectivity of the MP-functionalized (0.3 L) Pd(111) toward propenol.

As a next step, we identify the surface species that promote chemoselectivity using infrared spectroscopy. Figure 5.18 summarizes the results of acrolein hydrogenation over two different surfaces: (a) pristine Pd(111) and (b) MP-functionalized Pd(111). (*Detailed description in Ref.[177] as well as Section 8.3.*)

Each catalyst was conditioned with hydrogen for 10 min prior to the exposure to the identical sequence of acrolein pulses (Fig. 5.18c-d). The MP-functionalized surface instantly produces propenol while on pristine Pd(111), there is a pronounced induction period. The results from this pulsed sequence are in good agreement with the experiments conducted over the same Pd(111), both initially pristine as well as MP-functionalized, surfaces but in a continuous manner.

On initially pristine Pd(111), there are two individual bands at 1120 and 1097 cm^{-1} that appear with a different temporal evolution. Both bands may most likely be related to the same type of reaction intermediate R_2 (1120 cm^{-1}) and R_1 (1097 cm^{-1}) on different adsorption sites. A plausible explanation for the red-shift of the vibration in R_1 , as compared to R_2 , is the stabilization of the reaction intermediate via an intermolecular hydrogen bonding. The band at 1097 cm^{-1} appears prior to the band at 1120 cm^{-1} which has not been reported before. (*cf. Ref.[177] as well as Sections 5.1.1 and 8.3.*)

On the Pd(111) surface functionalized with MP, two bands evolve during the course of the reaction. The first band can be related to the same intermediate R_2 as observed on pristine Pd(111) while the second band is located at 1088 cm^{-1} , which is by additional 9 cm^{-1} more red-shifted than the band related to the intermediate R_1 on pristine Pd(111). The temporal evolution of this band on the surface is similar to the one assigned as R_1 at 1097 cm^{-1} for pristine Pd(111). To clarify whether this band originates from the ligand MP itself, the dynamic transformation of the MP ligand from non-reactive to reactive conditions was investigated. The results are shown in Figure 5.18b (spectrum 1b) for the

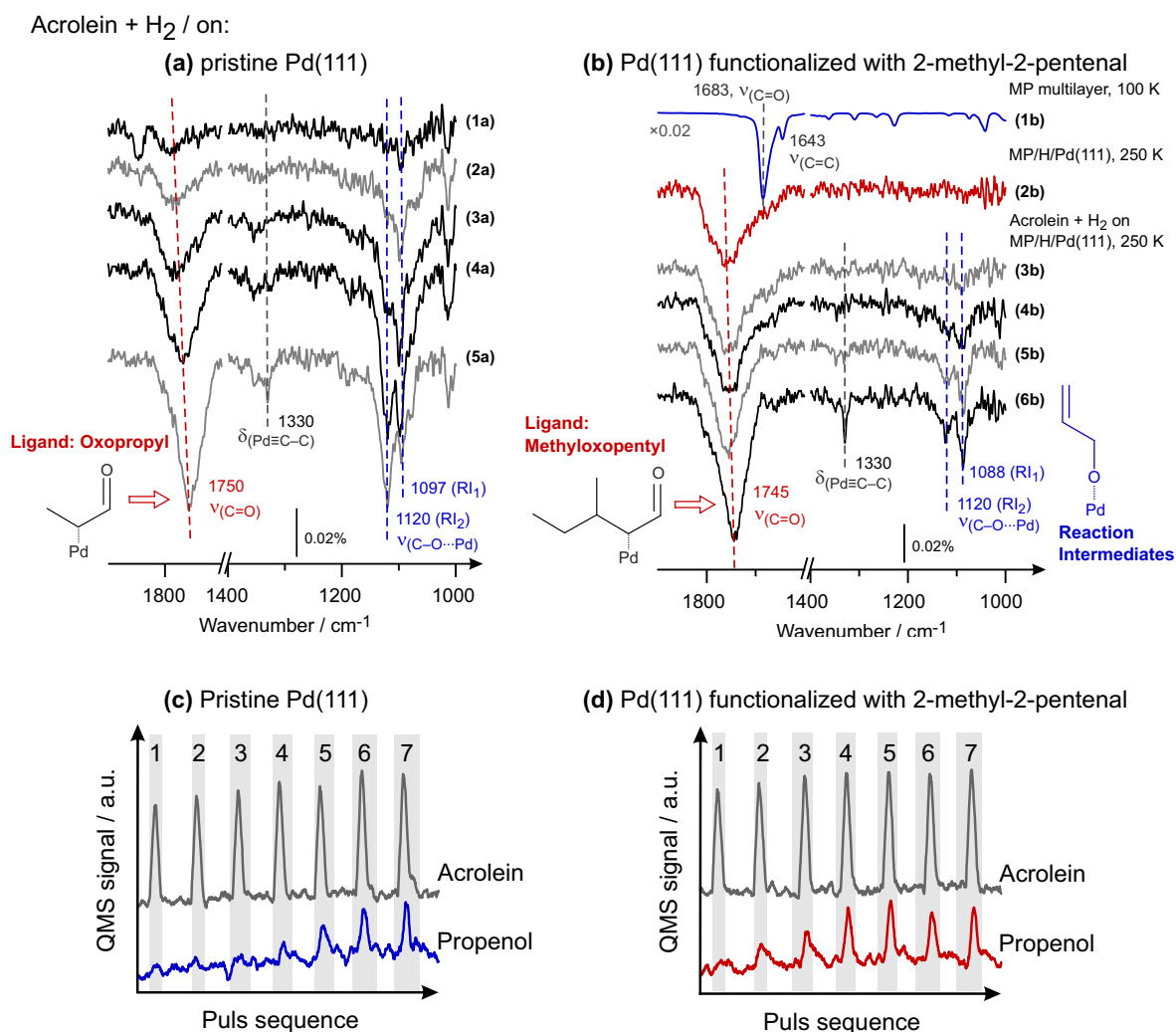


Figure 5.18: Combined spectroscopic and kinetic investigation of acrolein hydrogenation over (a, c) pristine and (b, d) MP-functionalized Pd(111) at 250 K. Both surfaces were exposed to a continuous flux of hydrogen throughout the entire reaction ($7.7 \cdot 10^{14}$ molecules \cdot cm⁻²s⁻¹) and acrolein was exposed to the surface in a pulsed sequence shown in (c) and (d). The spectrum 1b is the multilayer spectrum of 47 L MP at 100 K on pristine Pd(111), 2b: 0.58 L MP under reactive conditions (H₂, 250 K) and 1a-5a and 3b-6b different exposures of acrolein at a flux of $2.4 \cdot 10^{12}$ molecules \cdot cm⁻²s⁻¹. Exposure times were: 20 s (1a, 3b), 40 s (2a, 4b), 60 s (3a), 100 s (5b), 120 s (4a), 500 s (6b), 600 s (5a).

unperturbed multilayer spectra at 100 K and for operational conditions at 250 K in the presence of hydrogen (Fig. 5.18b, spectrum 2b). It is important to point out that there are no vibrational bands between 1050 and 1150 cm⁻¹ present in either the unperturbed MP molecule or in the MP spectrum for the catalyst at operational conditions. This part of the spectrum contains no vibrational bands in both cases. Thus, the band located at 1088 cm⁻¹ can be most likely related to the same reaction intermediate R₁ as on pristine Pd(111), which has a stronger red-shift due to a different chemical surrounding. The intensity of the band related to the intermediate R₂ is much lower compared to pristine Pd(111). While on pristine Pd(111), the band related to the intermediate R₂ is much more intense than the one of R₁, this changes on MP-functionalized Pd(111) where the band related to R₂ is less intense than the one of R₁.

The study on MP-functionalized Pd(111) demonstrated that Pd(111) can be functionalized with an artificial ligand, which is structurally similar to acrolein, that renders the surface selective toward propenol formation. MP forms a structurally similar surface species which promote the formation of the same types of the reaction intermediates (RI_1 and RI_2) as previously reported for acrolein.

However, the distribution as well as the temporal evolution of both surface species strongly differ from the case of methyl-oxopentyl ligand. The species RI_1 appears first and saturates at approximately the same quantity as on the oxopropyl-covered surface, but the reaction intermediate RI_2 appearing in the following remains only minor surface species.

Derived from the combination of the observation on both, initially pristine and ligand-functionalized, Pd(111) surfaces let us to propose the following scenario that is summarized in Figure 5.19.

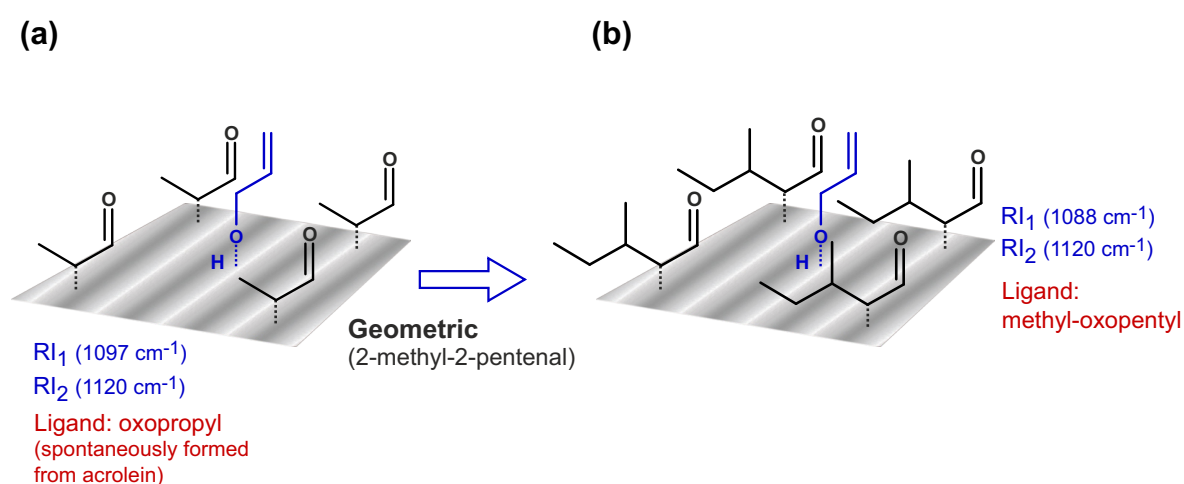


Figure 5.19: Illustration of the geometric effect of the MP ligand, with respect to the hydrogenation of acrolein, in comparison with initially pristine Pd(111) surface.

The reaction intermediate RI_1 appears first and establishes an hydrogen bonding to the neighboring ligand species (either oxopropyl or methyl-oxopentyl) forming 1:1 complexes. After nearly all ligand species become involved into these complexes, the other type of the reaction intermediate RI_2 is formed, that has not established intermolecular hydrogen bonding and thus remains free-standing.

The amounts of the free-standing reaction intermediate RI_2 , that can be formed on the surface, is dependent on the available surface space. The more spacious methyl-oxopentyl ligands cover a larger area on the surface, as compared to the smaller oxopropyl ligand, reducing the available surface area for the free-standing reaction intermediate RI_2 .

Only this scenario can explain i) the saturation of the RI_1 at similar coverages, ii) frequency shift of RI_1 and iii) the formation of different quantities of RI_2 . (cf. Ref.[177] and Section 8.3 for detailed discussion.)

As a next step, the influence of electronic effects of the ligand onto the hydrogenation reaction of acrolein is addressed by the detailed investigation of the reaction over allyl cyanide-functionalized Pd(111).

5.3 Hydrogenation of Acrolein over Allyl Cyanide-Functionalized Pd(111)

This section reflects a brief summary of the results that are presented in

Angewandte Chemie from Ref.[175]. (Full text in Section 8.1.)

Carsten Schröder, Marvin C. Schmidt, Philipp A. Haugg, Ann-Katrin Baumann, Jan Smyczek and Swetlana Schauermaun, *Angew. Chem. Int. Ed.* **2021**, *60*, 16349–16354.

and

Chemistry - A European Journal from Ref.[176]. (Full text in Section 8.2.)

Carsten Schröder, Philipp A. Haugg, Ann-Katrin Baumann, Marvin C. Schmidt, Jan Smyczek and Swetlana Schauermaun, *Chem. Eur. J.* **2021**, *27*, 17240–17254.

In this section, the influence of the electronic effect of an artificial ligand, that exhibits an electron-rich nitrile group, on the hydrogenation reaction of acrolein as well as the characterization of the ligand species under non-operating and operating conditions are presented by the example of allyl cyanide (AC).

To investigate the potential influence of an electronic effect of an electron-rich nitrile entity at the coadsorbed ligand molecule on the hydrogenation of acrolein, a kinetic study on the reaction of acrolein with hydrogen under isothermal conditions over AC-functionalized Pd(111) catalysts at different coverages of allyl cyanide was performed. In Figure 5.20a, the kinetic curves related to the propenol formation rates over three functionalized Pd(111) surfaces at different exposures of allyl cyanide (0.3 L, 0.8 L and 2.1 L) as well as on initially pristine Pd(111) for reference are presented.

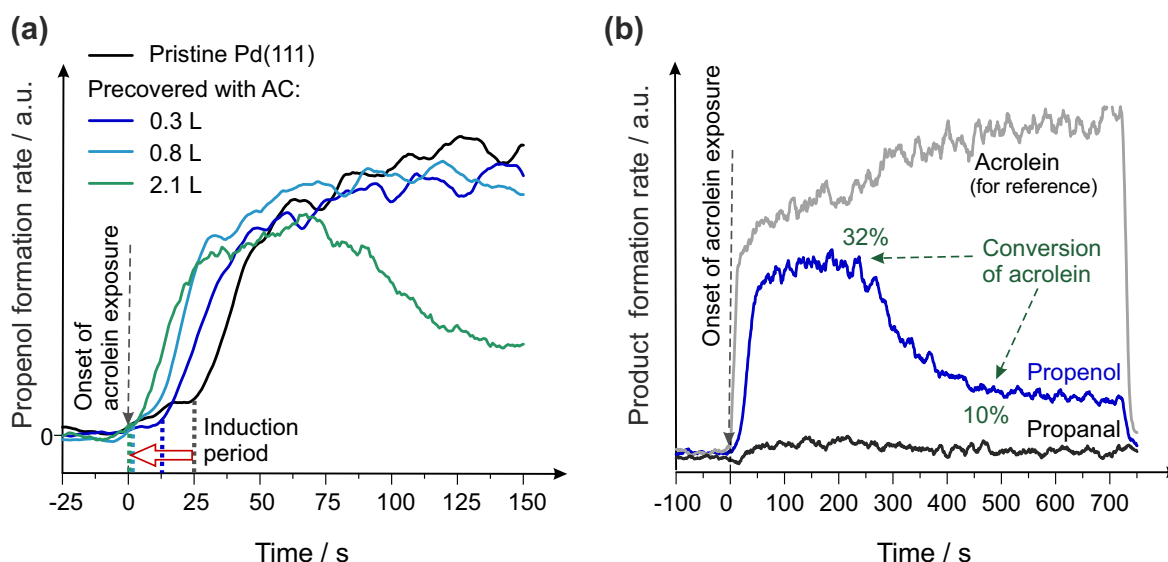


Figure 5.20: Results of the kinetic study on acrolein hydrogenation over different Pd(111) surfaces at 250 K. (a) Formation rates of propenol over initially pristine and AC-functionalized Pd(111). (b) Formation rates of propenol and propanal over Pd(111) functionalized with 0.8 L AC. (Full experimental details, see Section 8.1 and Ref.[175].)

At the time indicated as zero, the second effusive beam was opened to expose the surface to a continuous flux of acrolein. The experiments performed over the surface functionalized with allyl cyanide clearly show that the induction period could be significantly reduced and even completely removed by functionalizing the catalyst with AC, rendering the catalyst immediately reactive toward the formation of propenol.

Increasing the activity of a catalyst toward the desired product is one major achievement in catalyst research, however, the key factor remains the selectivity toward propenol. Figure 5.20b shows the kinetic curves related to the formation rates of both feasible products, the desired propenol and the undesired propanal, as well as acrolein for reference. The functionalized surface is close to 100 % selective toward propenol formation at fairly high conversion rate of about 32 % at maximum turnover rate and approximately 10 % in the region of low reactivity. The results of this kinetic study clearly demonstrate that the catalyst can be activated by an artificial non-aldehyde ligand and the formation of propenol is not dependent on the spontaneous formation of an oxoalkyl ligand layer.

As a next step, we probed the composition of the catalytic surface under reactive conditions employing infrared spectroscopy. Figure 5.21 shows the results of the combined kinetic and spectroscopic study. The time slots (1–5) indicated in the kinetic curves related to the formation rate of propenol (Fig. 5.21a) equal the time in which the IR spectra were obtained after the same acrolein pulse (Fig. 5.21b). On the AC-functionalized Pd(111), there are different surface species which can be identified by their characteristic IR signatures. Briefly, there are N-butylimine species ($\nu(\text{C}=\text{N}\cdots\text{Pd})$ at $1746\text{--}1755\text{ cm}^{-1}$) and amines species ($\delta(\text{NH}_2)$ at 1582 cm^{-1}), which exact nature and formation will be discussed in detail later. The former species is formed via the partial hydrogenation of AC at the $\text{C}=\text{C}$ and $\text{C}\equiv\text{N}$ bonds, resulting in the surface-bonded species containing an electron-rich imine group ($\text{C}=\text{N}\cdots\text{Pd}$). The amine species is formed via an alternative reaction pathway in which both, the $\text{C}=\text{C}$ and $\text{C}\equiv\text{N}$ bonds, are fully hydrogenated.

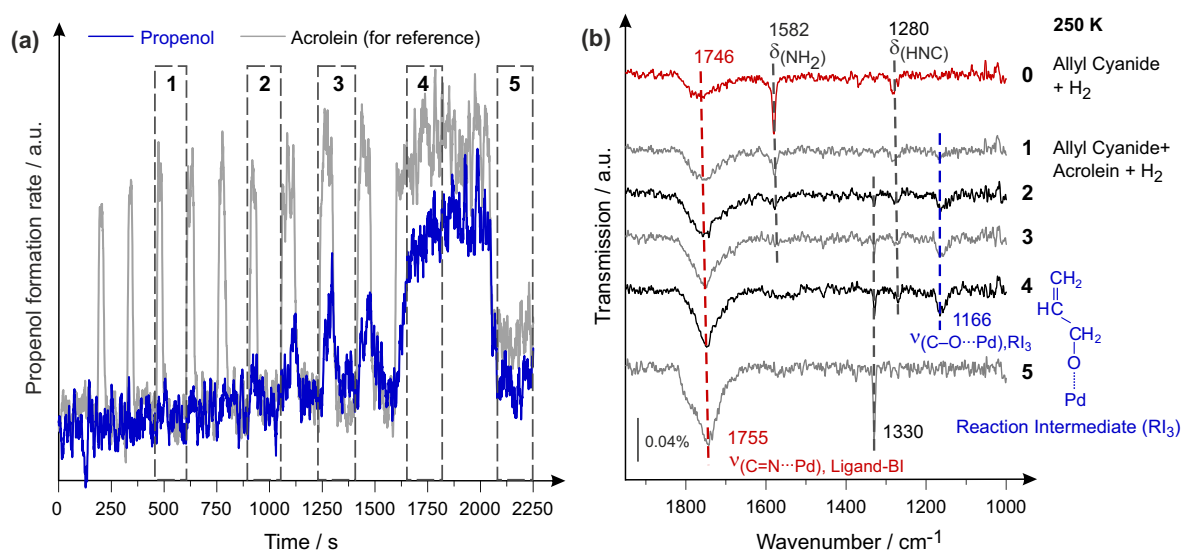


Figure 5.21: Hydrogenation of acrolein over Pd(111) precovered with 1.0 L allyl cyanide at 250 K. (a) Propenol formation rate measured in a pulsed experiment. (b) IR spectra of 1.0 L AC prior the beginning of the reaction (spectrum 0) and IR spectra obtained on the same surface after the beginning of the reaction. The spectra 1–5 were obtained during the time slots indicated in (a) as 1–5. (Full experimental details, see Section 8.1 and Chapter II of SI in Ref.[175].)

In spectra 1–5 of Figure 5.21b, the IR spectra of the same functionalized surface as in spectrum 0, that is exposed to a pulsed sequence of acrolein, are presented. It is important to point out that the evolution of propenol in the gas phase can again be correlated with the appearance of a vibrational band on the surface, located at 1166 cm^{-1} . This band appears in the range that is typical for the stretching vibration of C–O bonds ($\nu(\text{C–O})$) and the related surface species is thus denoted as the reaction intermediate RI_3 . In contrast to both oxoalkyl-functionalized Pd(111) surfaces, there are not two individual IR bands for reaction intermediates. (*cf. Ref.[175] and Section 8.1 for detailed discussion.*)

However, the vibrational frequency of RI_3 (1166 cm^{-1}) is strongly blue-shifted by 69 and 46 cm^{-1} compared to both reaction intermediates RI_1 and RI_2 that are observed on the initially pristine Pd(111) surface that is rendered active by the oxopropyl ligand layer. (*cf. Sections 8.3 and 5.1.1.*) These large frequency shifts with respect to the reaction intermediates RI_1 and RI_2 may be related to a strong perturbation of the electronic structure of the reaction intermediate RI_3 resulting from the interaction with the ligand layer consisting of N-butylimine species. There are two possible scenarios for the strengthening of the C–O bond that is most likely the reason for the observed significant blue-shift of the related vibrational band. (*See Refs.[175] and [177] as well as Sections 8.3 and 8.1 for details.*)

First, the filling of the d-band of the underlying metal surface may be strongly altered on the N-butylimine containing surface. As a consequence, the degree of the donation and backdonation of electron density between the metal and the molecular orbitals of the reaction intermediate may change. Both the depletion of electron density from the anti-bonding molecular orbitals of the reaction intermediate into the d-orbitals of the Pd as well as the donation of electron density from the d-orbitals of the metal surface into bonding molecular orbitals of RI_3 result in a strengthening of the C–O bond. This will be denoted as surface-mediated, as this mechanism involves the electronic states of the surface. The other scenario is related to the direct lateral interactions between the adsorbed N-butylimine species and the reaction intermediate RI_3 , in which electron density from the imine group is donated into a bonding molecular orbital associated with the C–O entity of RI_3 .

Derived from the experimental observations, the illustrated scenario in Figure 5.22 summarizes the electronic effect of the AC ligand on the hydrogenation reaction of acrolein.

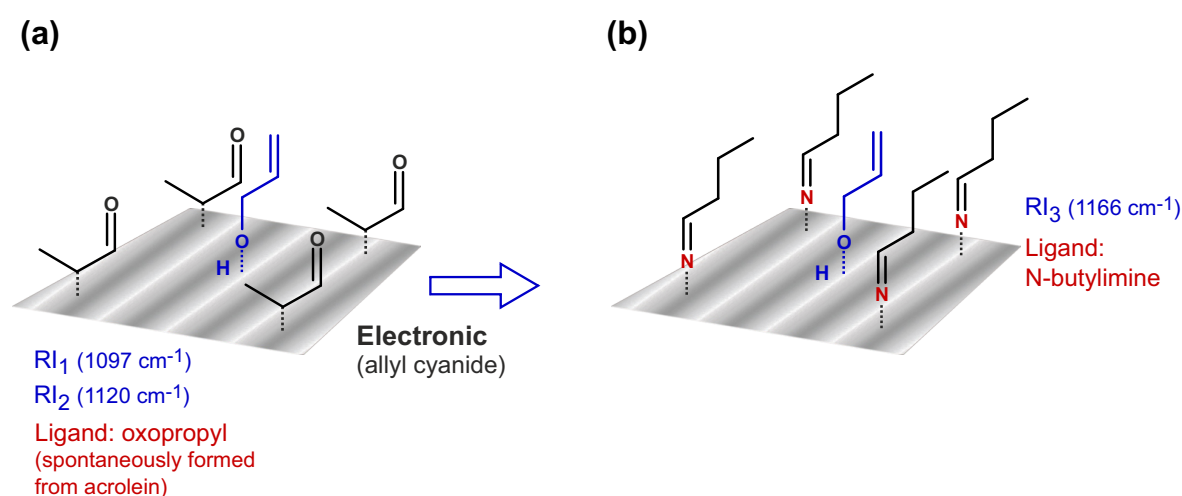


Figure 5.22: Illustration of the electronic effect of the AC ligand with respect to the hydrogenation reaction of acrolein in comparison to the initially pristine Pd(111) surface.

On the surface functionalized with the allyl cyanide, the desired propenoxy reaction intermediate RI_3 is formed. In contrast to the initially pristine Pd(111) surface, only one reaction intermediate is observed that also has a strong blue-shift as compared to both RI_1 and RI_2 . The electron-rich imine group thus most likely interacts directly with the reaction intermediate or changes the electronic structure of the underlying metal surface, resulting in either a direct or surface-mediated electronic ligand effect.

To get more atomistic-level insights into the chemical and geometric structure of the active ligand layer that forms and dynamically changes under the reaction conditions, a combined microscopic and spectroscopic study was performed on AC adsorbed on pristine and hydrogen-precovered Pd(111) in a broad range of temperature. Figure 5.23 shows the results from the STM experiments under non-reactive (Fig. 5.23a-c) and reactive (Fig. 5.23d) conditions. Under non-reactive conditions, allyl cyanide forms a well-ordered 2D layer that consists of individual molecules having brighter (head) and darker (tail) protrusions. Each molecule has a two-point interaction with neighboring molecules which is realized via a two head and one tail and vice versa interaction.

The geometric parameters obtained from the microscopic study are presented in Figure 5.23b. The 2D layer consists of two parallel rows R_1 and R_2 which are inclined with respect to the axis R_3 by $69 \pm 1^\circ$. The intermolecular distance with respect to the underlying metal ($d_{Pd-Pd} = 2.75 \text{ \AA}$) between two AC heads along R_3 is $d_1 \approx 3 d_{Pd-Pd}$ and along R_1 and R_2 is $d_2 \approx 5 d_{Pd-Pd}$. Bringing the surface from non-reactive to reactive conditions (Fig. 5.23d) changes the pattern of the ligand layer dramatically. The species formed in the STM have a more roundish footprint and the intermolecular distance along both b_1 and b_2 axes are approximately $3 d_{Pd-Pd}$. Both axes are inclined by $\omega = 53 \pm 2^\circ$ resulting in a hexagonal structure. (Full discussion in Section 8.1 and Ref.[175].)

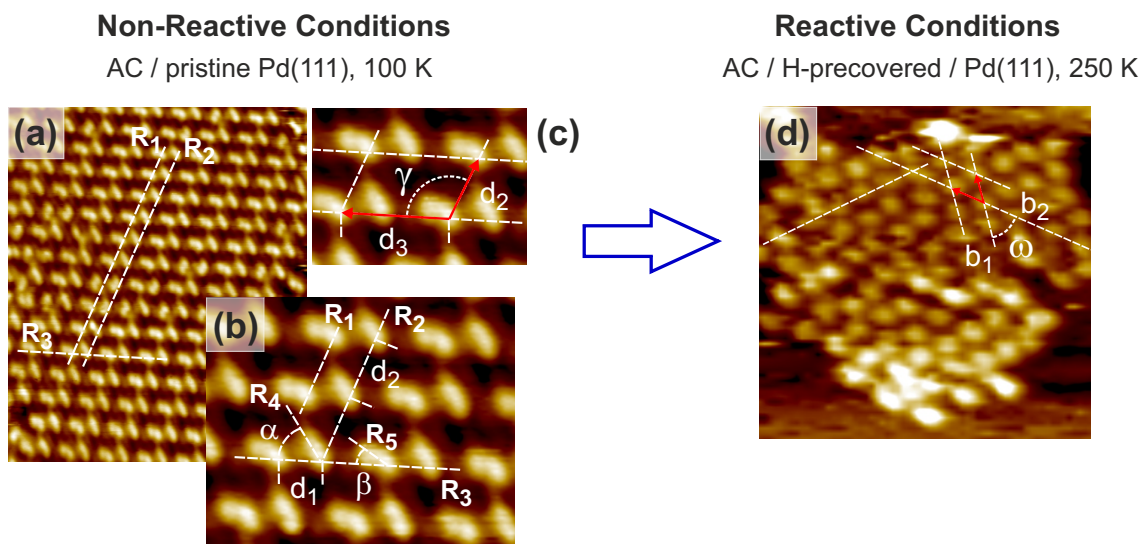


Figure 5.23: STM images of AC: (a) pristine Pd(111) at 230 K ($15.9 \times 19.1 \text{ nm}^2$), (b) close-up image from (a) ($5.8 \times 4.6 \text{ nm}^2$) with indication of the three main rows in the 2D layer, (c) close-up image on the unit cell of the AC layer and (d) AC on hydrogen-precovered Pd(111) at 250 K ($10.6 \times 10.8 \text{ nm}^2$). Reprinted with permission from Ref.[175], Angewandte Chemie International Edition. Copyright 2021 John Wiley and Sons.

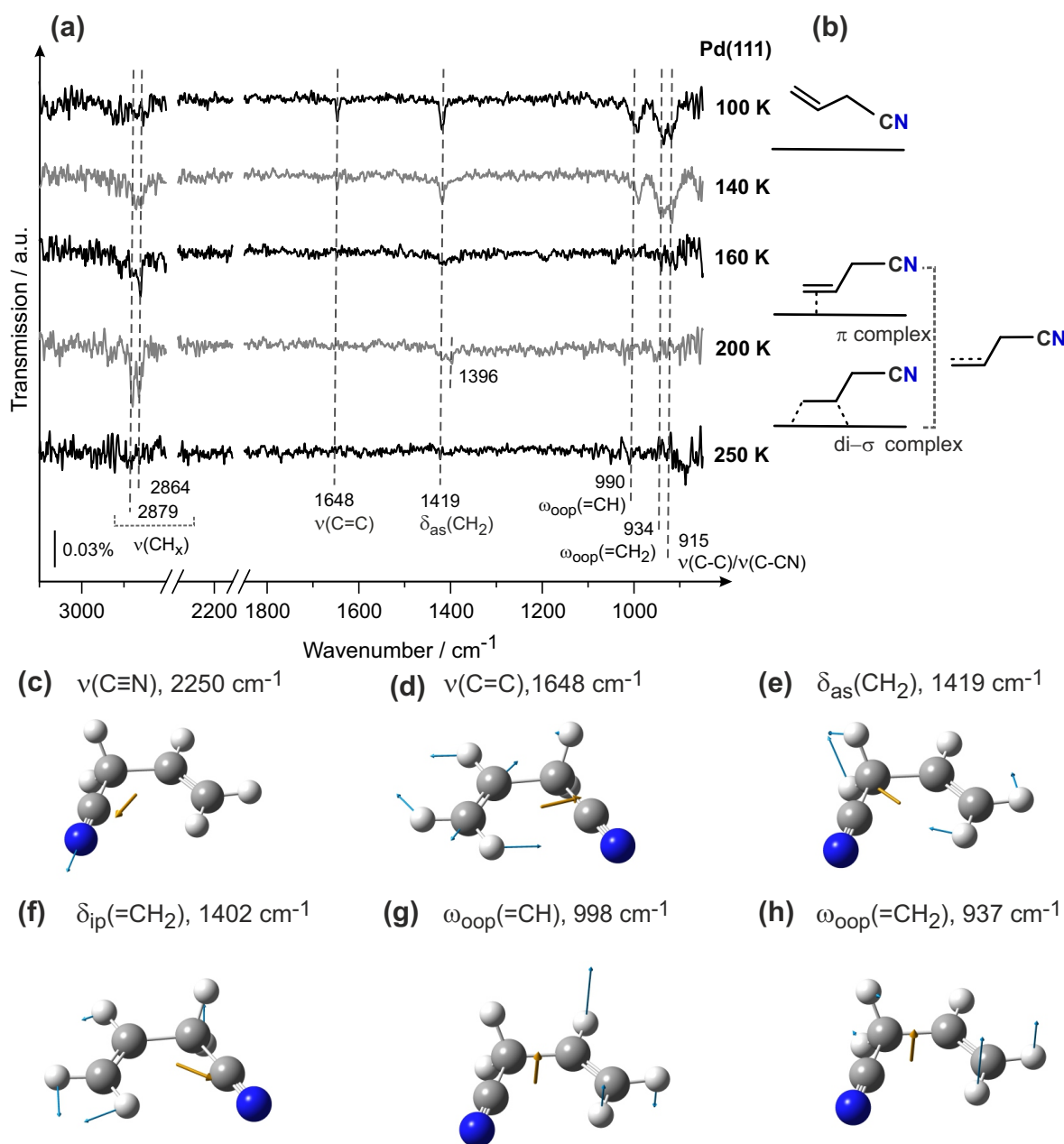


Figure 5.24: IRAS adsorption study on AC on pristine Pd(111). (a) IR spectra of AC obtained on Pd(111) at submonolayer coverage in the temperature range 100 – 250 K. AC was dosed at a flux of $7.2 \cdot 10^{12}$ molecules \cdot cm $^{-2}$ \cdot s $^{-1}$; the total AC exposure amounts to $4.3 \cdot 10^{14}$ molecules \cdot cm $^{-2}$; (b) suggested adsorption geometries based on spectroscopic data; (c-h) visualization of the vibrational modes related to the characteristic vibrational bands of a single AC molecule in the gas phase obtained from a DFT calculation using Gaussian 16^[241] and GaussView 6.1.^[242] (Full description in Ref.[176].)

The microscopic picture obtained from STM experiments shows that allyl cyanide forms a well-ordered 2D ligand layer under both reactive as well as non-reactive conditions. However, the structure of the self-assembled molecule layers exhibit strongly different patterns in terms of structure and periodicity. To fully understand and correlate the microscopic picture with the spectroscopic data of the chemical transformation leading to the active catalytic surface, we performed an IRAS study under the same reactive and non-reactive conditions.

Figure 5.24a shows the results of the IRAS study of allyl cyanide adsorbed at submonolayer coverage on pristine Pd(111) at indicated temperatures. The most prominent vibrational bands in the IR spectra are labeled with their frequencies and the visualization of the corresponding vibrational mode is shown in Figure 5.24c-h. As a result of the spectral shifts of the vibrational bands and according to the metal surface selection rule, the following adsorption model can be deduced that is summarized in Figure 5.24b. The absence of any vibrational band in the region of the nitrile stretching vibration ($\nu(\text{C}\equiv\text{N})$, Fig. 5.24c) in the IR spectra obtained between 100 – 250 K indicates that this part of the molecule adopts a nearly parallel orientation with respect to the metal surface.

Below 160 K, the spectroscopic signature of the C=C bond, i.e. $\nu(\text{C}=\text{C})$ (Fig. 5.24d), $\omega_{\text{oop}}(\text{=CH}_2)$ (Fig. 5.24h) and $\omega_{\text{oop}}(\text{=CH})$ (Fig. 5.24g), can be detected that has no spectral shift compared to the value of the unperturbed molecule in the multilayer. We propose that this part of the molecules is tilted away from the surface. Once the temperature increases, any vibrational bands related to an olefin group are absent. The vanishing of all vibrational bands related to the olefin group can originate either from the formation of a π complex in which the intact C=C bond is orientated nearly parallel to the surface or due to the formation of a di- σ complex, in which each C atom forms a covalent bond to the underlying Pd atom. Above 200 K, the vibrational band related to the former methylene ($-\text{CH}_2-$) group disappears which most likely indicates the abstraction of an H atom at the related part of the molecule. This observation is in good agreement with the microscopic picture of AC at the same temperature, in which the formation of long-range ordered structures are shown, rather than the decomposition of the molecules. (Full discussion in Ref.[176] and Section 8.2.)

Having characterized the ligand spectroscopically under non-reactive conditions, we put the focus on the investigation of the chemical transformation of allyl cyanide to a catalytic active species.

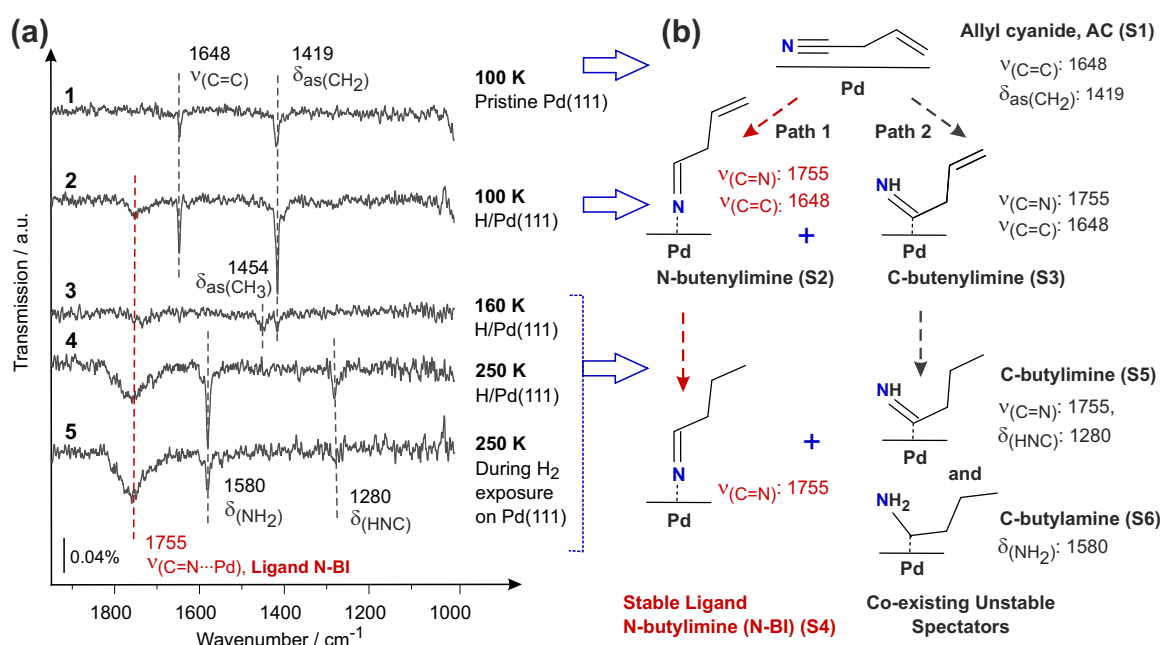


Figure 5.25: Chemical transformation of allyl cyanide over Pd(111) in the presence of hydrogen. (a) IR spectra obtained for AC adsorbed on Pd(111) at indicated temperature and (b) the proposed adsorption model based on the spectroscopic data. (Full discussion in Ref.[176] and Section 8.2.)

In the next study, a detailed investigation on the dynamic transformation of the catalytic surface under reactive conditions was performed. In Figure 5.25a, the IR spectra of AC in the presence of hydrogen are presented. On pristine Pd(111) at 100 K (Fig. 5.25a, spectrum 1), there are two major bands present which can be assigned to the $\nu(\text{C}=\text{C})$ and $\delta(\text{CH}_2)$ vibration. The presence of these two bands in combination with the absence of the $\nu(\text{C}\equiv\text{N})$ vibration indicates flat-oriented AC molecules, with the nitrile group being parallel to the surface while the $\text{C}=\text{C}$ bond is inclined with respect to the surface plane. Upon exposure of hydrogen to the surface, a new vibrational band at 1755 cm^{-1} appears which is not present on pristine Pd(111) at temperatures between 100 and 250 K. This band can be assigned to the $\nu(\text{C}=\text{N}\cdots\text{Pd})$ vibration of a surface-bound imine group.

Heating the catalyst to operational conditions, a step-wise hydrogenation of first the $\text{C}=\text{C}$ group and then the formerly $\text{C}\equiv\text{N}$ group can be observed. Based on the spectroscopic data, two different reaction pathways can be proposed that result in the C-butylamine species (S6) and the N-butylimine ligand (S4). The former species (S6) is considered to be unstable because of two reasons: Figure 5.25a, spectrum 5 shows the resulting IRAS spectra of an AC layer that is annealed in the presence of hydrogen at 250 K. The intensity of the vibrational band at 1580 cm^{-1} decreases with time. The second reason can be deduced from the experiment presented in Figure 5.26a, which shows the kinetic curve related to the formation rate of propenol in the gas phase over AC-functionalized Pd(111) at 250 K. Additionally, the integrals of the vibrational bands related to two surface species, i.e. amine (1580 cm^{-1}) and the ethylidene 1330 cm^{-1} , that are formed during the course of the reaction, are added to the same part of the figure. (Full discussion in Ref.[176] and Section 8.2.)

Prior to the catalyst is turning over acrolein toward propenol, the remaining S6 spectator species desorb from the catalyst. The latter species (S4) is present both during annealing of the catalyst in hydrogen atmosphere and during the course of the reaction when the catalyst is turning over acrolein. The amine species is thus denoted as an unstable spectator species.

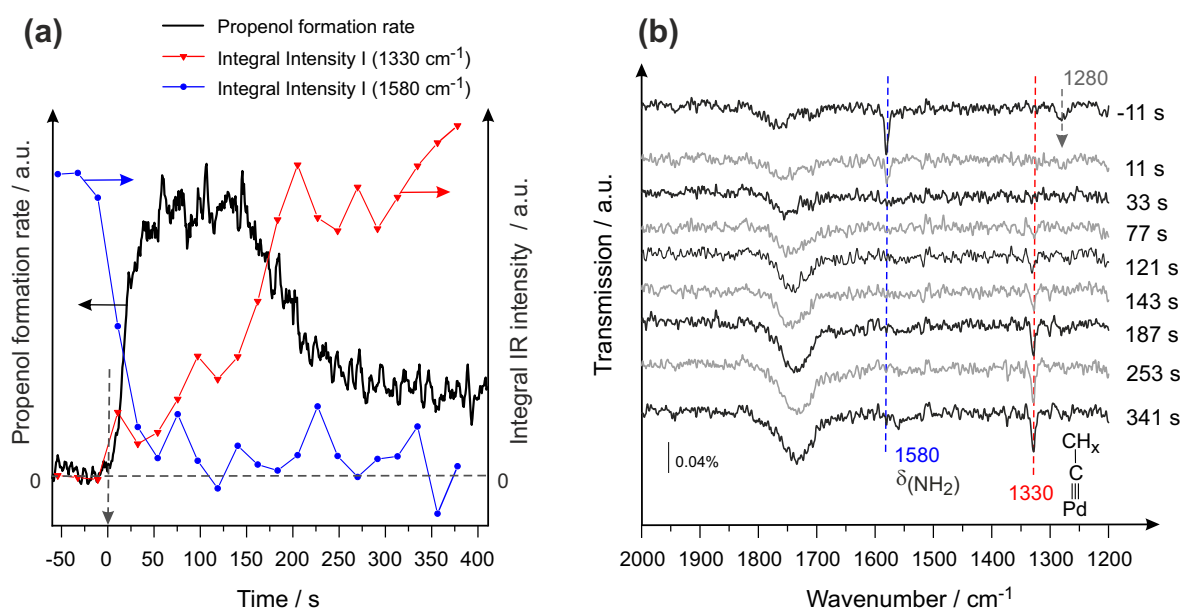


Figure 5.26: Detailed spectroscopic and kinetic analysis of the temporal evolution of two species on the surface and the propenol formation rate in the gas phase. The amine surface species vanish prior to the catalyst producing propenol and the ethylidene species is constantly formed on the surface and results in the deactivation of the catalyst. (Full discussion in Ref.[175].)

Furthermore, the temporal evolution of the integral related to the band of the ethylidene-like surface species can directly be correlated with the deactivation of the catalyst. The curves in Figure 5.26a show that this surface species grows continuously upon exposure of acrolein to the surface. It can be deduced that the decomposition reaction of acrolein to ethylidene, as it was reported on pristine Pd(111), cannot be inhibited by functionalizing the surface with allyl cyanide.

The study on AC-functionalized Pd(111) demonstrated that the electronic structure of the coadsorbed ligand has a dramatic effect on the hydrogenation reaction of acrolein. In contrast to both oxoalkyl ligand species, i.e. oxopropyl and methyl-oxopentyl, only one reaction intermediate R_1 was observed in the presence of allyl cyanide ligands on the surface. The vibrational band related to this intermediate was significantly blue-shifted by 69 and 46 cm^{-1} as compared to the initially pristine Pd(111) surface. The analysis of the chemical and structural properties of allyl cyanide adsorbed on Pd(111) revealed that AC forms a layer consisting of reactive ligand molecules that is capable of promoting the selectivity toward propenol formation. As it was presented in the results of the microscopic study, AC adsorbates form ordered layers in the temperature range between 100 and 250 K on pristine Pd(111) as well as on Pd(111) that is covered with coadsorbed surface hydrogen. However, the presence of hydrogen causes the dynamic transformation of the chemical nature of the ligand and thus both layers exhibit a strongly different pattern. The results from the detailed spectroscopic investigation show that AC molecules undergo a chemical transformation as the catalytic surface dynamically changes from non-reactive to reactive conditions. Several surface species, i.e. amines and imines, are formed via independent reaction paths. The latter species, N-butylimine, form a ligand layer that is capable of promoting selectivity toward propenol formation in the partial hydrogenation of acrolein.

These experimental observations are summarized in Figure 5.27. One of the most striking conclusions we could draw from this combined study was that allyl cyanide molecules do not form a reactive ligand layer on pristine Pd(111), but only on Pd(111) surface covered with hydrogen at sufficiently high temperature.

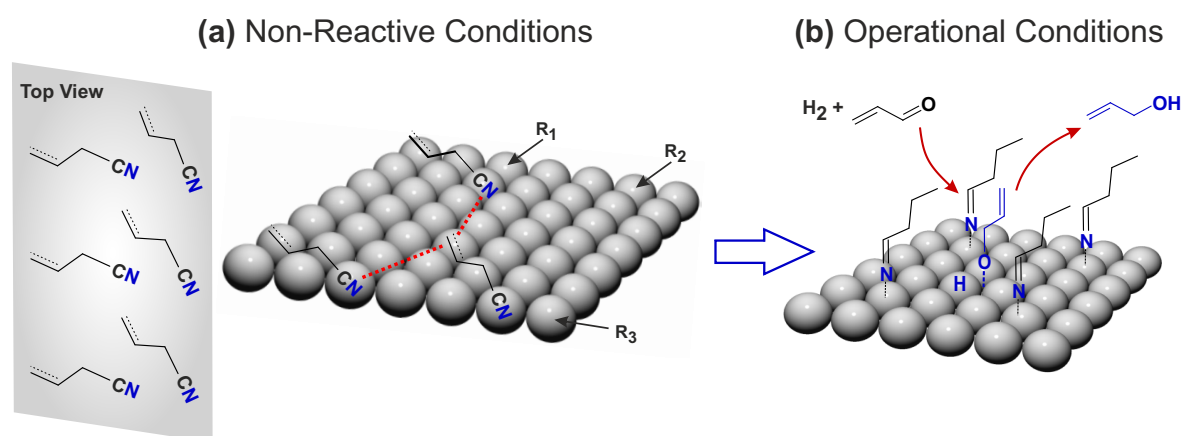


Figure 5.27: Dynamic transformation of allyl cyanide over Pd(111) from non-reactive to reactive conditions in the presence of hydrogen. Adapted from Ref.[175].

5.4 Hydrogenation of Acrolein over Acetophenone-Functionalized Pd(111)

This section reflects a brief summary of the results that are presented in

The Journal of Physical Chemistry C from Ref.[177]. (Full text in Section 8.3.)

Carsten Schröder, Ann-Katrin Baumann, Marvin C. Schmidt, Jan Smyczek, Philipp A. Haugg, Ole-Christian Graap and Svetlana Schauermaun, *J. Phys. Chem. C* **2022**, 126, 4907–4920.

In this section, the influence of a ligand, that is capable of undergoing a keto–enol tautomerization followed by 1:1 lateral interactions with adsorbed reactants and intermediates, on the hydrogenation reaction of acrolein is presented by the example of acetophenone (AP).

The adsorption geometry and dynamic transformation of acetophenone on pristine and H-containing Pt(111) was previously investigated by our group.^[215,235–239] The observation with particular importance to this project is, briefly summarized, that acetophenone is capable of undergoing a keto–enol tautomerization upon adsorption on Pt(111) above 136 K that results in the formation of ketone–enol dimers, in which the enol form of one acetophenone molecule is being stabilized by a neighboring AP molecule in the keto form. The capability to undergo a keto–enol tautomerization followed by 1:1 lateral interactions with coadsorbed reactants, thus potentially also with the propenoxy reaction intermediate, was the main aspect investigated in this study.

The results from the kinetic study on AP-functionalized Pd(111) are shown in Figure 5.28 for two different AP exposures and pristine Pd(111) for reference. Interestingly, low exposure (0.12 L) of acetophenone results in the elongation of the induction period whereas a higher exposure (0.78 L) renders the catalytic surface immediately active.

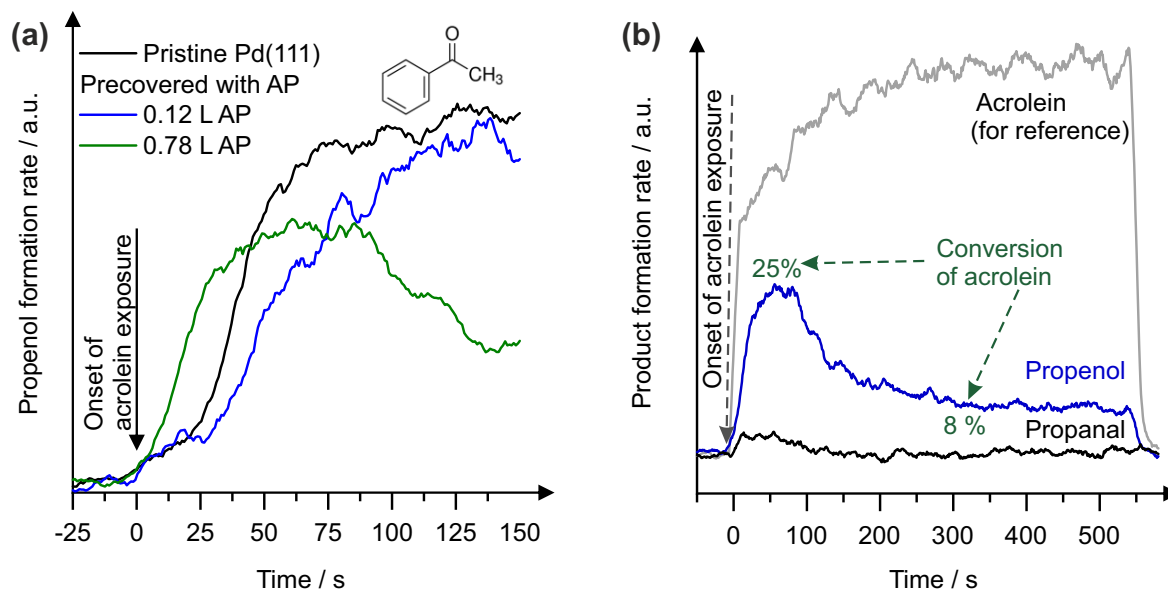


Figure 5.28: Results of the kinetic study on acrolein hydrogenation over AP-functionalized Pd(111) at 250 K. (a) Kinetic curves of the formation rates of propenol related to two different exposures of AP (0.12 and 0.78 L) and pristine Pd(111) for reference; (b) conversion rate and selectivity of the AP-functionalized (0.78 L) Pd(111) toward propenol.

The comparison of the kinetic curves for the propenol formation rate over AP-functionalized Pd(111) and pristine Pd(111) reveals that the maximum turnover rate for the low exposure of AP is similar to that on pristine Pd(111), albeit there is a pronounced delay in the onset. However, the high exposure of AP results in a decrease of both, the induction period and maximum turnover rate of the catalyst. The selectivity and conversion rate (Fig 5.28b) toward propenol are rather high, although lower compared to an AC- or MP-functionalized catalyst. Since the activity of the catalyst dramatically changes with the coverage of acetophenone, a detailed analysis of the reactivity with respect to the AP coverage was performed as a first step.

Figure 5.29 presents the results of the kinetic curves related to the formation rate of propenol over AP-functionalized Pd(111) with exposures of AP between 0.12 L and 1.10 L at 250 K. For low exposure of AP (0.12 L and 0.18 L), the induction period prolongates. For a medium exposure of 0.30 L, the induction period is similar to the one of pristine Pd(111) whereas for high exposure, this period is reduced. Once the induction period is being reduced compared to initially pristine Pd(111), the maximum turnover rate of the catalyst is lower than on pristine Pd(111).

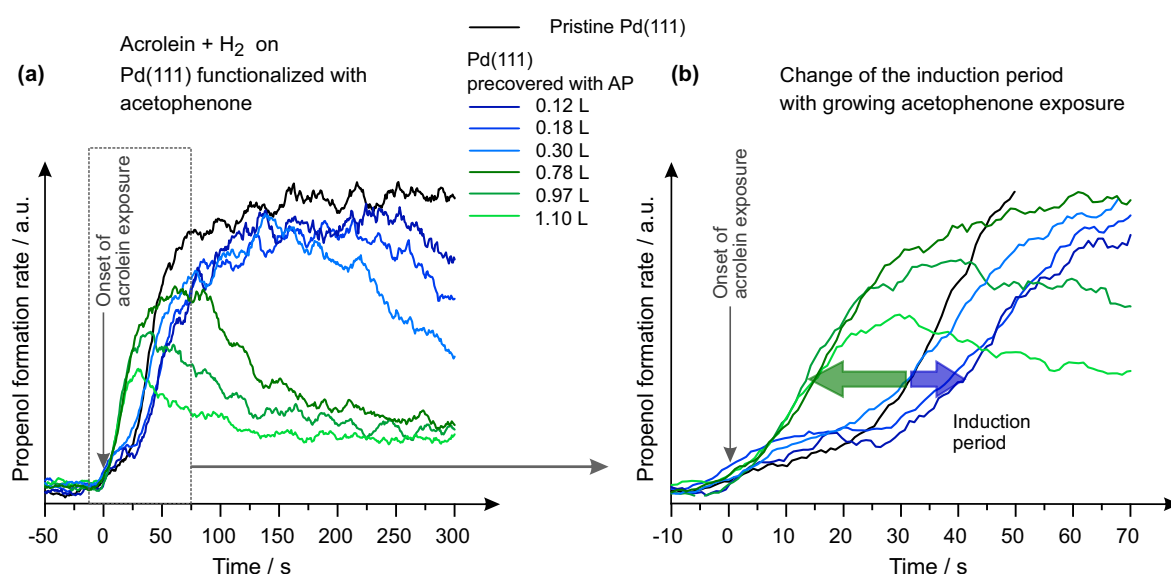


Figure 5.29: Results of the kinetic study on acrolein hydrogenation over AP-functionalized Pd(111) for different AP exposures between 0.12 L and 1.10 L at 250 K. (a) Formation rate of propenol for a time frame of 300 s of the reaction and (b) close-up on the induction period.

As a next step, we probed the composition of the catalytic surface under operational conditions employing infrared spectroscopy. Two aspects especially needed to be addressed: i) which effect promotes the reduction of the induction period and ii) how does the adsorption state of AP molecules on the surface change from low to high coverage inducing a change of the induction period.

The results of the spectroscopic data for the functionalized surfaces exposed to 0.12 L and 1.10 L AP from this study are presented in Figure 5.30. The IR spectra were obtained during the reaction of acrolein over AP-functionalized Pd(111) at different stages, including the induction period, time of maximum turnover rate as well as the late stages of low propenol formation rate. The IR spectrum of the unperturbed multilayer of acetophenone molecules at 100 K is shown in Figure 5.30a (spectrum 1).

This spectrum serves as a reference for the characteristic vibrational bands of acetophenone molecules that are not directly interacting with the Pd surface. A detailed assignment of the characteristic vibrational bands of acetophenone can be found in the works of Gambi et al.^[243], Chen et al.^[244] and Attia et al.^[215] Briefly, the most prominent bands are $\nu(\text{C}=\text{O})$ at 1686 cm^{-1} , $\delta(\text{CH}_3)$ at 1361 cm^{-1} and $\nu_{\text{ip}}(\text{C}-\text{C}_{\text{ring-acetyl}})$ at 1275 cm^{-1} .

The IR spectra 1a-5a were obtained for low coverage of AP (0.12 L) under reactive conditions, i.e. hydrogen precovered Pd(111) at 250 K. Spectrum 1a is related to pure AP adsorbed on Pd(111) and spectra 2a-5a were recorded upon acrolein exposure onto the same surface as in 1a. The absence of all characteristic bands related to the AP multilayer spectrum most likely indicates, according to the metal surface selection rule (MSSR), that AP molecules are oriented flat with respect to the surface, i.e. both the axis of the $\text{C}=\text{O}$ group as well as the phenyl ring lie parallel with respect to the surface plane.

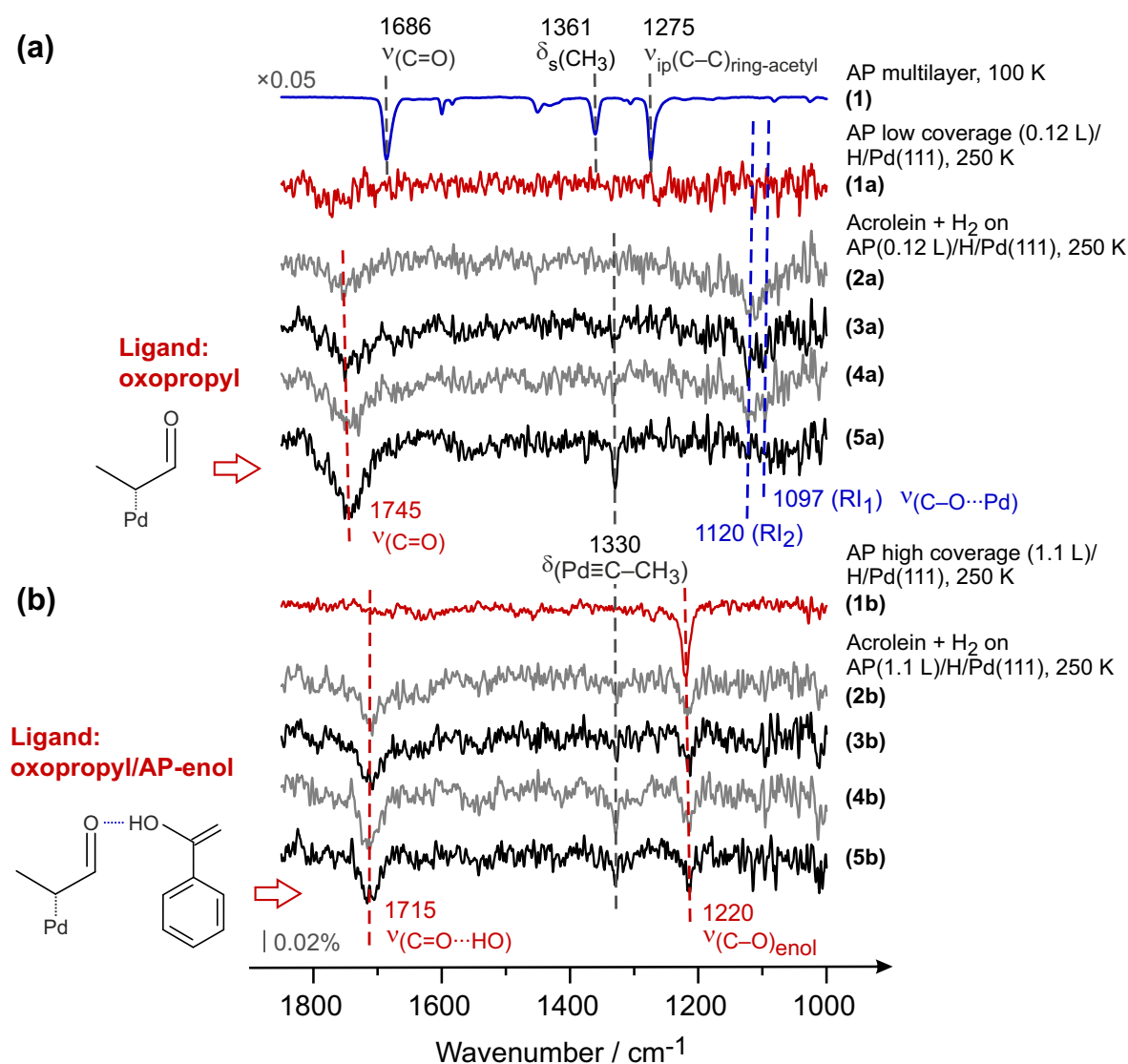


Figure 5.30: Spectroscopic study on acrolein over AP-functionalized Pd(111) at 250 K for two different AP exposures: (a) 0.12 L and (b) 1.1 L. The spectra of unperturbed AP multilayer at 100 K is shown in (a) spectrum 1 and high coverage exposure of AP adsorbed on H/Pd(111) at 250 K in (b) spectrum 1b. Spectra 1a–5a and 2b–5b were obtained during the course of the reaction of acrolein over the same surfaces related to spectra 1a and 1b.

Upon exposure of acrolein to the surface, the evolution of the surface species closely resembles that one observed on the initially pristine Pd(111) surface. A pronounced vibrational band at 1745 cm^{-1} evolves, that was previously assigned to the stretching vibration of the C=O bond of the oxopropyl ligand, which is spontaneously formed by acrolein molecules. There are also two vibrational bands with small intensity present at 1097 and 1120 cm^{-1} , that are related to the propenoxy reaction intermediates RI_1 and RI_2 . (See Ref.[177] as well as Section 8.3 for full text and complete discussion.)

Overall, these observations suggest that on the surface functionalized with small amounts of AP, the same surface species, i.e. ligand and reaction intermediates, are formed as on the initially pristine surface, just at smaller concentrations and with a larger time delay. This observation is in good agreement with the elongation of the induction period and the combination of both might be related to the same fact that randomly distributed coadsorbed AP species possibly hinder the formation of the ordered oxopropyl ligand layer.

After adsorbing large amounts of AP onto Pd(111) at 250 K in the presence of hydrogen, the spectrum of pure AP looks different (spectrum 1b). There is a new vibrational band at 1220 cm^{-1} that is not present in the multilayer spectra of AP at 100 K or under reactive conditions at 250 K. In our investigations on the adsorption of AP on Pt(111), we assigned this band as the $\nu(\text{C}-\text{O})$ stretching vibration of the enol form of acetophenone.^[235–238] (See Ref.[177] as well as Section 8.3 for full text and complete discussion.)

Upon exposure of acrolein to the surface functionalized with a high amount of acetophenone, this enol band of AP remains on the surface. There are no vibrational bands in the range that is typical for the reaction intermediates. Interestingly, a new vibrational band at 1715 cm^{-1} evolves that is not present in the spectra of i) AP multilayer at 100 K, ii) AP on H/Pd(111) at 250 K, iii) acrolein on H/Pd(111) or iv) acrolein on H/Pd(111) functionalized with low coverage of AP. However, the frequency is in the typical range of the stretching vibrations of C=O bonds, in which the C=O group is not conjugated to a C=C group. Moreover, the frequency is red-shifted by 30 cm^{-1} as compared to both Pd(111) precovered with low amounts of AP as well as initially pristine Pd(111). This is a typical value of a red-shift for carbonyl compounds where the ketone group is being stabilized by an intermolecular hydrogen bond of a neighboring hydroxyl group.^[214,245–248] Since this prominent frequency shift of the carbonyl group was observed to occur only in the presence of the enol form of AP, it can be quite safely concluded that it results from hydrogen bonding between the carbonyl group of the oxopropyl species and the H atom of the OH group belonging to the enol form of AP.

Derived from the experimental observations, the illustrated scenario in Figure 5.31 summarizes the effect of the keto–enol tautomerization of acetophenone on the hydrogenation reaction of acrolein. While low concentrations of acetophenone only hinder the formation of the oxopropyl ligand layer, that are spontaneously formed by acrolein molecules, high concentrations of AP have a positive effect. As a consequence for this hindrance, the induction period is elongated and less surface species are formed as compared to initially pristine Pd(111). We propose, that the reduction on the induction period for high coverage of AP thus results from the lateral interaction between the enol form of AP and the oxopropyl surface species formed by acrolein itself. The newly formed oxopropyl/enol-AP complex serves as a complex ligand in the hydrogenation of acrolein as indicated by the strong reduction of the induction period in propenol formation rate.

These effects might arise either via the direct interaction of the reaction intermediate with the coadsorbed imines or be mediated by the surface, i.e. the degree of donation / backdonation of the electron density between the underlying Pd and the reaction intermediate might be strongly changed in the presence of the electron-rich imine species. The N-butylimine layer also results in the pronounced shortening of the induction period as compared to the one on initially pristine Pd(111), pointing to the fact that the functionalized surface provides the correct environment for a fast formation of the desired reaction intermediate.

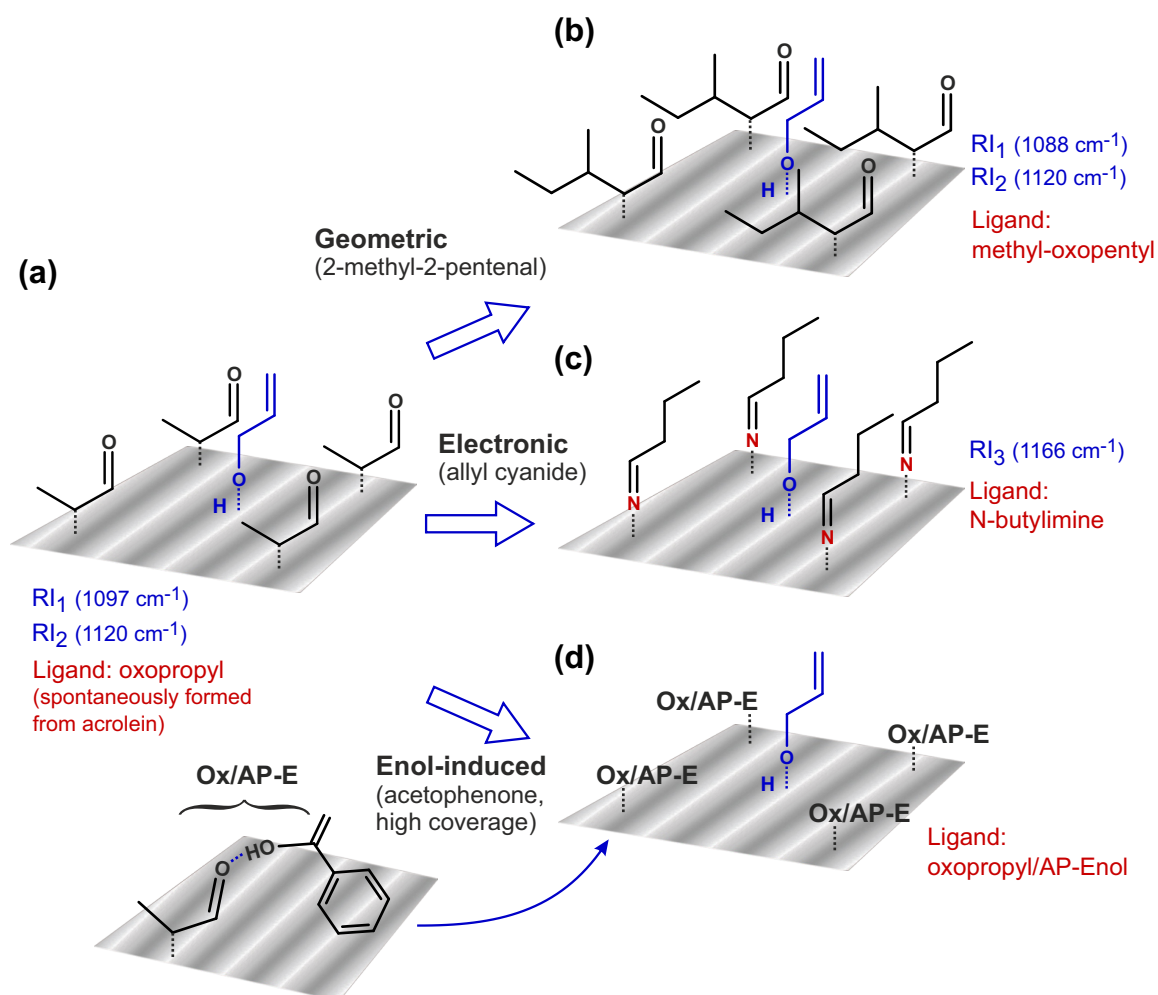


Figure 5.32: Summary of the proposed lateral interactions promoting chemoselectivity. For each investigated model system, the suggested active species are (a) oxopropyl-, (b) methyl-oxopentyl-, (c) N-butylimine- and (d) enol-stabilized oxopropyl-ligand.

The comparison of the two structurally similar ligand layers, methyl-oxopentyl (Fig. 5.32b, formed from 2-methyl-2-pentenal) and oxopropyl (Fig. 5.32a, formed from acrolein) species, allows us to deduce the role of the geometric effects in the formation of the propenoxy reaction intermediate. First, two different types of the reaction intermediates, i.e. RI₁ and RI₂, were identified, which are separated by 23 cm⁻¹. The reaction intermediate RI₁ (lower frequency) appears first at low acrolein exposures and saturates at similar amounts on both surfaces. The second reaction intermediate (RI₂) evolves at higher acrolein exposures on both surfaces but its final surface concentration strongly differs on both functionalized sur-

faces: it is low on the surface covered with a spacious methyl-oxopentyl species (MP), while it is considerably more abundant on the surface functionalized with a less spacious oxopropyl ligand. The observed behavior arises most likely from the fact that the RI_1 undergoes H-bonding with the coadsorbed ligand, which leads to the pronounced red-shift of the vibrational band related to the C–O bond in RI_1 . As soon as nearly all ligands become involved into 1:1 complexes with the reaction intermediate RI_1 , the evolution of RI_2 starts. RI_2 is most likely a free-standing adsorbate and can be formed in larger amounts on the surface precovered with the smaller ligand (oxopropyl species) and in smaller amounts on the surface covered with a spacious methyl-oxopentyl ligand.

Finally, functionalization of Pd(111) with acetophenone (Fig. 5.32d) results in two types of reactive behavior: at low acetophenone coverages, the presence of the ligand elongates the induction period and does not exhibit any significant effect on the reaction intermediates. In contrast, at high acetophenone coverages, the enol form of acetophenone is formed, which builds a 1:1 complex with the oxopropyl species spontaneously formed by acrolein molecules. The presence of these oxopropyl/enol-AP complexes strongly reduces the induction period suggesting that this surface provides a beneficial ligand environment for formation of propenol.

6 Lateral Interactions of Prochiral Adsorbates on Simple Crystalline Pt(111) Surfaces

This chapter provides a summary of the published studies in

The Journal of Physical Chemistry C from Ref.[249]. (Full text in Section 8.4.)
Carsten Schröder, Marvin C. Schmidt, Christopher Witt, Smadar Attia, Jann Weber, Ann-Katrin Baumann, Bernd Hartke and Swetlana Schaueremann, *J. Phys. Chem. C* **2020**, 124, 51, 28159–28168.,

The Journal of Physical Chemistry C from Ref.[250]. (Full text in Section 8.5.)
Christopher Witt, Marvin C. Schmidt, **Carsten Schröder**, Swetlana Schaueremann and Bernd Hartke, *J. Phys. Chem. C* **2021**, 125, 47, 26167–26179.,

Angewandte Chemie from Ref.[236]. (Full text in Section 8.6.)
Smadar Attia, Marvin-Christopher Schmidt, **Carsten Schröder**, Pascal Pessier, Swetlana Schaueremann, *Angew. Chem. Int. Ed.* **2018**, 57, 16659–16664.,

ACS Catalysis from Ref.[237]. (Full text in Section 8.7.)
Smadar Attia, Marvin C. Schmidt, **Carsten Schröder**, Swetlana Schaueremann, *ACS Catal.* **2019**, 9, 8, 6882–6889.,

The Journal of Physical Chemistry C from Ref.[238]. (Full text in Section 8.8.)
Smadar Attia, Marvin C. Schmidt, **Carsten Schröder**, Jann Weber, Ann-Katrin Baumann, Swetlana Schaueremann, *J. Phys. Chem. C* **2019**, 123, 48, 29271–29277.,

The Journal of Physical Chemistry C from Ref.[235]. (Full text in Section 8.9.)
Marvin C. Schmidt, Smadar Attia, **Carsten Schröder**, Ann-Katrin Baumann, Swetlana Schaueremann, *J. Phys. Chem. C* **2020**, 124, 26, 14262–14271.

and

The Journal of Physical Chemistry C from Ref.[239]. (Full text in Section 8.10.)
Marvin Schmidt, Smadar Attia, **Carsten Schröder**, Ann-Katrin Baumann and Swetlana Schaueremann, *J. Phys. Chem. C* **2021**, 125, 35, 19311–19324.

The hydrogenation of carbonyl compounds is of particular importance for the synthesis of agrochemicals and pharmaceuticals as the transformation of a C=O bond into a C–O single bond usually creates a new chiral center. As a result, two different enantiomers are accessible that may have dramatic different chemical properties.^[251] However, one of the major challenges in the hydrogenation of carbonyl groups remains the activation of the stable C=O bond, which is usually realized by employing a suitable catalyst.

For instance, the chiral molecule (R)-1,2-pentanediol, which is a key intermediate for the production of various fungicides at industrial scale, is obtained by the hydrogenation of the prochiral 1-hydroxypentan-2-one by employing homogeneous catalysis.^[252,253]

The infamous thalidomide story is one of the most well-known and documented cases that demonstrate the dramatic effects of different enantiomers to the human body which underlines the importance of pure enantiomers in pharmaceutical industry.^[254,255] Administered to pregnant women as a sleeping pill in the early 1960s, soon dramatic effects on the newborn babies were monitored that could be traced back to different enantiomers of thalidomide. While the (R)-enantiomer was found out to have a sedating effect, the (S)-enantiomer was found out to be toxic to reproduction. The need for pure enantiomers is not limited to pharmaceutical application or synthesis of agrochemicals, but is also needed for materials with specific optical properties. The traditional approach for the synthesis of pure enantiomers is the separation of a racemic pool.^[256] A more elegant and economically as well as an environmentally more profitable way is the enantioselective catalysis where only one enantiomer with a high enantioselective excess (*ee*, Eq. 6.1) can be built out of a prochiral precursor molecule.

$$ee(\%) = 100 \cdot \frac{([R] - [S])}{([R] + [S])}, \quad (6.1)$$

with the concentration of two different enantiomers [R] and [S].

In the last century, great effort has been made to perform enantioselective chemical reactions at a large scale. An early strategy to overcome the deficit of achirality of metal surfaces was to deposit an active catalytic material onto a chiral support to impart chirality. However, none of the tested substrates quartz^[257], synthetic chiral polymers^[258–260] or cellulose^[261] were reported to have a good performance with respect to the promotion of enantioselectivity toward one enantiomer.

Yoshio Orito performed experiments applying the opposite approach and reported in 1979 that the prochiral molecule methyl pyruvate (MePy) can be selectively hydrogenated toward (+)-methyl lactate after functionalizing a Pt surface with cinchonidine as a chiral modifier (Fig. 6.1).^[56] In contrast to the hydrogenation reactions performed over functionalized Pt(111), no selectivity toward an enantiomer is reported on pristine Pt(111), as low-index facets, e.g. (111), (110) and (100), of metal surfaces are in general achiral.^[52]

However, a novel idea in enantioselective catalysis is to employ naturally chiral metal surfaces in which the intrinsic chirality arises from surface defects, i.e. step and kink atoms, of high-index metal facets, e.g. Cu(643) or Pt(531).^[262,263] In recent experimental^[264–267] and theoretical^[268–270] surface science studies, it was proven that either the difference in adsorption energies or the extend of the uptake of the formed enantiomers result in the promotion toward one enantiomer, although the available area for enantiospecific adsorption is not large.^[271]

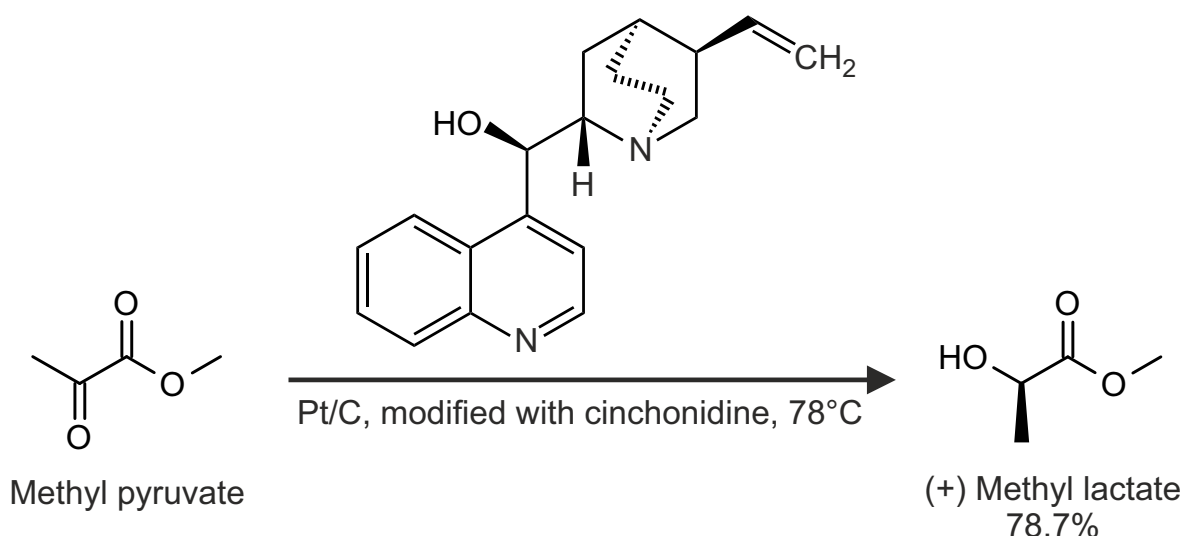


Figure 6.1: Reaction scheme for the originally reported Orito reaction. Methyl pyruvate was hydrogenated over cinchonidine-functionalized Pt/C. The catalyst was preheated in hydrogen atmosphere at 200–400 °C prior to functionalization with cinchonidine.^[56]

Further studies in the last decades showed that the enantioselective reaction is not limited to the combination of cinchonidine and α -ketoesters, in which an ester group is adjacent to the ketone group (Fig. 6.2a). A more general classification for suitable substrates is the presence of an electron-withdrawing substituent in α -position and for a few examples even in β -position.^[52] The enantioselective hydrogenation of these types of ketones is thus named after Yoshio Orito. There are several different classes of naturally-occurring chiral modifiers, e.g. cinchona alkaloids and derivatives (Fig. 6.2c), as well as synthetic modifiers, e.g. R-naphthylethylamine (R-NEA, Fig. 6.2d) that consist of a naphthalene frame with a nitrogen or oxygen substituted ethyl or propyl side chain, which can impart strong stereochemical control in hydrogenation reactions over noble metal catalysts, like Pt, Rh or Ir.^[57]

A wide range of systems of α -ketoacids, α -ketoamides, α -diketones and α -ketoacetals hydrogenated with a large enantioselective excess over different chirally-functionalized surfaces are known and are summarized in the review by Mallat et al.^[52]

The investigation of the fundamental processes and atomistic details leading to the enantioselectivity was topic of various different surface science studies on different metal surfaces. Just to mention a few, the adsorption of some natural^[53,58,59,61,82] and synthetic^[57,60–63,76,81] chiral modifiers, prochiral ketones^[62,64–69,71–78] as well as the coadsorption of both natural^[53,59,61,66,79] or synthetic^[57,61,64,66,69–71,77,80,81] modifier with a prochiral molecule were studied on different metal surfaces.

The most simple type of α -ketoester, methyl pyruvate, was investigated in atomistic-level studies on pristine or chirally-functionalized Pt(111)^[64,65] and Pd(111)^[68,75,79] surfaces by several groups. On pristine Pd(111), the enol form of MePy, which results from the keto–enol tautomerization of the carbonyl group, was suggested by Garvey et al.^[68] to be involved in the reaction mechanism. The same enol form of MePy was also proposed by Mahapatra et al.^[79] to be the active species in the 1:1 chiral docking complex between MePy and NEA. In this complex, the reactant has a specific orientation toward the underlying metal surface, so it can only be hydrogenated from one side, resulting in the selective hydrogenation toward one enantiomer.^[69–71]

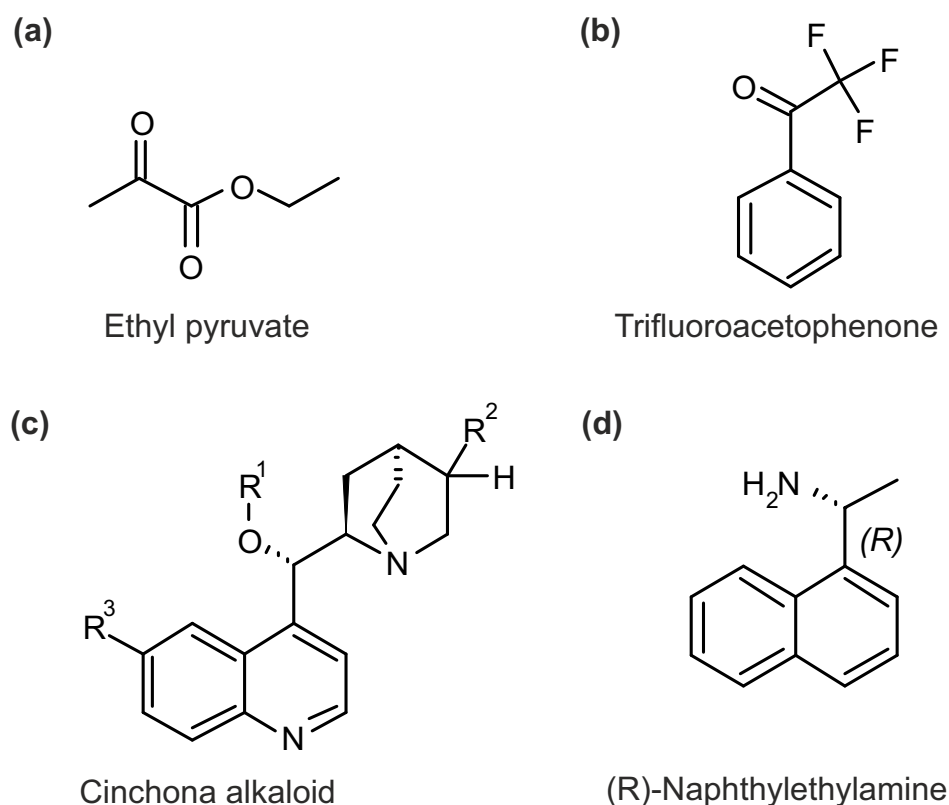


Figure 6.2: Chemical structure of: prochiral ketones (a) α -ketoester (EP) and (b) trifluoroacetophenone (TFAP) and chiral modifiers: (c) naturally-occurring cinchona alkaloids and (d) synthetic (R)-naphthylethylamine (R-NEA). Adapted from Ref.[54].

Interestingly, the Orito reaction was reported to yield a higher excess of an enantiomer for ketones with an electron-withdrawing CF_3 group in α -position, as compared to their α -methyl ketone counterparts, although the CF_3 group may prevent a feasible keto–enol tautomerization. For instance, in a hydrogenation study over cinchonidine-functionalized Pt, the authors showed that the enantioselective excess changes dramatically from 92 % (trifluoroacetophenone, TFAP, Fig. 6.2b)^[54] to 20 % (acetophenone).^[272]

In a different study on TFAP, the authors reported to yield a high selectivity toward the formation of the (R)-alcohol upon hydrogenation over cinchona alkaloid-functionalized Pt/ Al_2O_3 .^[54] The TFAP/NEA system had been investigated in surface science studies in the group of McBreen.^[63,66,70,80] Goubert et al.^[70] showed in a combined STM and DFT study of TFAP and NEA on Pt(111) that both molecules form a similar 1:1 docking complex which was previously reported for α -ketoesters and R-NEA, that was shown to consist of the enol form of MePy and R-NEA.

Rasmussen et al.^[83] performed a theoretical investigation on the hydrogenation reaction of TFAP on Pt(111), showing that the ketone group is being remotely activated by the chemisorbed phenyl ring. This chemisorbed phenyl ring enables the migration of the $\text{C}=\text{C}$ bond toward the ketone group, forming an enol species that is being hydrogenated in a subsequent step. The hydrogenation of the enol form of the prochiral molecule, that forms a chiral complex on the surface, thus provides a plausible explanation for the enhanced catalytic performance in the Orito reaction. However, the enol tautomer of a ketone is in general thermodynamically less stable than the ketone form and thus needs to be stabilized either via a chelated ring-like keto–enol tautomer or via the formation of oligomers.^[86–92]

The activation barriers for the hydrogenation of ketones in the enol form were predicted to be significantly lower than the direct hydrogenation route as shown by recent theoretical studies.^[83,85] According to the DFT calculations by De Vrieze et al.^[85], the activation barrier of the enol hydrogenation pathway of acetol over copper is favored by about 30 kJ·mol⁻¹ as compared to the direct hydrogenation of the ketone. The experimental confirmation of this reaction path as well as the fundamental understanding of the elementary steps in the hydrogenation of prochiral α -methyl ketones are not fully investigated.

Despite the numerous amount of studies on this topic, there is no distinct adsorption model of α -ketoesters as well as α -methyl ketones on Pt(111) and thus the fundamental-level understanding of adsorbate–adsorbate interactions is still poorly understood. Because of both, the challenging task of the experimental identification of lateral interactions of single adsorbates as well as the numerous possibilities to build molecular complexes that consist of two or more adsorbates, the mechanisms involved in the hydrogenation of simple α -methyl ketones are by far not fully understood. In this project, we studied the adsorption geometry and lateral interactions of two different types of α -methyl ketones as well as the chemical transformation of both over pristine Pt(111) and Pt(111) pretreated with hydrogen.

In particular, ethyl pyruvate (EP), an α -keto ester, and acetophenone (AP), a methyl phenyl ketone, were investigated under a broad range of temperature and different surface conditions. This combination of α -methyl ketones was selected as a prototype for a possible intramolecular stabilization of an enol form via a chelated ring-like enol tautomer, in case of EP, and for the intermolecular stabilization of the enol form as in case of AP. The different mechanisms in the stabilization of the enol form may therefore most likely be the reason for the Orito reaction to perform better with ketones that are capable of establishing an intramolecular stabilization of the enol form.

A key aspect with particular importance for obtaining an atomistic understanding of the hydrogenation mechanism of ketones has been addressed in the both parts of this project. First, the effect of electron-withdrawing substituent, i.e. the α -ester group, on the adsorption geometry of a molecule as well as on the lateral interactions between adsorbed molecules on pristine Pt(111) and Pt(111) pretreated with surface hydrogen has been studied. In the second part of the project, we investigated the adsorption, chemical transformation and lateral interaction of acetophenone over both pristine Pt(111) and Pt(111) pretreated with surface hydrogen.

The detailed analysis of the adsorption geometry and lateral interactions of both molecules over Pt(111) provides a deeper understanding on the fundamental processes of the hydrogenation reaction of α -methyl ketones in terms of stabilization of intermediates. In this chapter, the main results from the adsorption studies on pristine and hydrogen precovered Pt(111) surfaces of two different ketones i) ethyl pyruvate and ii) acetophenone in a broad range of temperature and coverage are presented. Additionally, the results of theoretical calculations are reported that were conducted in collaboration with the Hartke group (CAU Kiel).

6.1 Adsorption Geometry and Lateral Interaction of Ethyl Pyruvate on Pt(111)

This section reflects a brief summary of the results that are presented in

The Journal of Physical Chemistry C from Ref.[249]. (Full text in Section 8.4.)

Carsten Schröder, Marvin C. Schmidt, Christopher Witt, Smadar Attia, Jann Weber, Ann-Katrin Baumann, Bernd Hartke and Svetlana Schauermaun, *J. Phys. Chem. C* **2020**, 124, 51, 28159–28168.,

and

The Journal of Physical Chemistry C from Ref.[250]. (Full text in Section 8.5.)

Christopher Witt, Marvin C. Schmidt, **Carsten Schröder**, Svetlana Schauermaun and Bernd Hartke, *J. Phys. Chem. C* **2021**, 125, 47, 26167–26179.

One of the key issues in hydrogenation reactions of unsaturated hydrocarbons is the influence of coadsorbed hydrogen on the adsorption state, geometry and lateral interactions of molecules adsorbed on metal surfaces. The adsorption of unsaturated hydrocarbons on metal surfaces has been discussed in literature for a long time. There are two limiting cases of a strong di- σ and a weaker π bonding where the initial C=C bond remains almost unperturbed.^[107,273–275] Studies on the hydrogenation reaction of ethylene on Pt(111) indicate that the adsorption state in the presence of coadsorbed hydrogen can be described as a π -bonded state.^[108,276,277] The adsorption of ketones on metal surfaces enables a third type of interaction that involves the lone electron pair of the oxygen atom.^[278]

There is an ongoing debate about the chemical nature of the surface species of α -ketoesters adsorbed on various transition metals that are summarized in Figure 6.3.

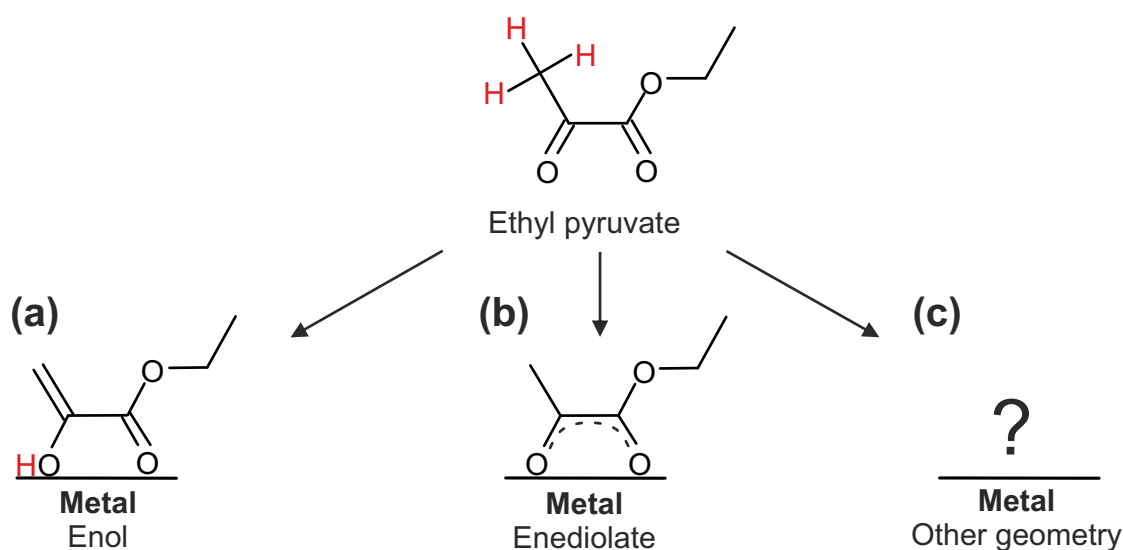


Figure 6.3: Proposed structures of α -ketoesters adsorbed on transition metal surfaces.^[64,65,73–75]

For methyl pyruvate adsorbed on both Ni(111)^[73,74] and Pt(111)^[64,65] at low temperature, the enediolate species (Fig. 6.3b) was proposed, while a more parallel orientation of the adsorption geometry with respect to the metal surface was reported on Pd(111)^[75]. Further, a keto–enol tautomerization (Fig. 6.3a) was observed on Pt(111) at elevated temperature.^[65] However, none of these studies addressed the lateral interactions of structurally more complex α -ketoesters which we report in this study on ethyl pyruvate (EP). We employed a combination of surface-sensitive techniques, including infrared reflection absorption spectroscopy (IRAS), molecular beams and scanning tunneling microscopy (STM), capable of providing both spectroscopic information about the chemical nature of adsorbed surface species and microscopic information about their distribution in real space, to address the details of mutual lateral interactions of EP adsorbed on Pt(111) surfaces. In order to obtain insights into the adsorption geometry, we performed an adsorption study with ¹²C-EP and ¹³C-EP on both pristine and H-covered Pt(111) under well-defined conditions in the UHV. Figure 6.4 presents the results from the IRAS study of ¹²C-EP (spectra 2 and 4) and ¹³C-EP (spectra 3 and 5) at submonolayer and multilayer coverage adsorbed on pristine Pt(111) at 100 K. The most intense bands of the ketone and ester groups are assigned by the comparison of the multilayer IR spectra to the calculated IR spectrum of a single molecule in the gas phase using DFT/B3LYP.

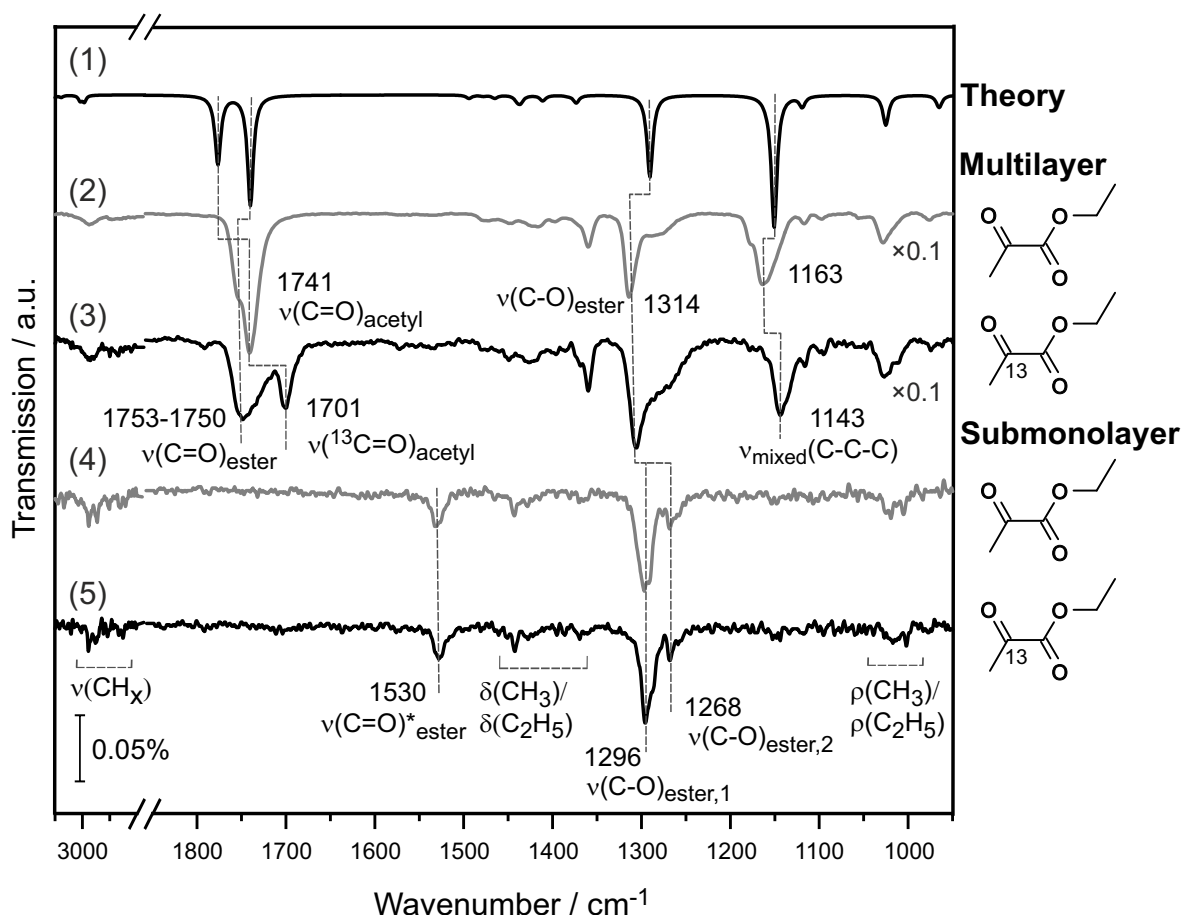


Figure 6.4: (1) Calculated gas phase IR spectrum of EP using DFT (B3LYP/aug-cc-pvqz with gd3 correction term). IR spectra of EP adsorbed on Pt(111) at 100 K: (2) ¹²C-EP and (3) ¹³C-EP multilayer (exposure: (2) $2.9 \cdot 10^{15}$ and (3) $1.1 \cdot 10^{15}$ molecules·cm⁻²); (4) ¹²C-EP and (5) ¹³C-EP at submonolayer coverage ($7.2 \cdot 10^{13}$ molecules·cm⁻²). Adapted from Ref.[249].

Briefly, the most important vibrational bands in the multilayer spectrum are the stretching vibrations of the ester carbonyl group $\nu(\text{C}=\text{O}_{\text{ester}})$ at 1753–1750 cm^{-1} , keto group $\nu(\text{C}=\text{O}_{\text{acetyl}})$ at 1741 cm^{-1} and the mixed vibration at 1314 cm^{-1} that includes mostly the stretching vibration of the C–O single bond ($-(\text{C}=\text{O})\text{C}-\text{OC}_2\text{H}_5$) in the ester group ($\nu(\text{C}-\text{O}_{\text{ester}})$). (A detailed assignment of all vibrational bands of EP are summarized in the SI of Ref.[249] and Section 8.4.)

The most important observation is the appearance of a vibrational band at submonolayer coverage at 1530 cm^{-1} , which has no spectral shift upon isotopic labeling of the ketone carbon atom with ^{13}C . This observation strongly suggests that this vibrational band is neither related to the C=C stretching vibration ($\nu(\text{C}=\text{C})$) of enols formed by surface-induced keto–enol tautomerization nor related to a surface enediolate (cf. Fig. 6.3b), where both carbonyl atoms are perpendicular to the surface.

Therefore, we assigned this vibration to the isotopically unlabeled ester carbonyl atom which must be strongly shifted from its unperturbed vibrational frequency in the gas phase ($\nu(\text{C}=\text{O})_{\text{ester, gas}} = 1750 \text{ cm}^{-1}$). This shift most likely results from a strong rehybridization of the molecular orbitals of EP with the d-orbitals of underlying Pt atom(s). The ketone group on the other hand is most likely oriented parallel to the surface and therefore absent in the IRAS spectra.

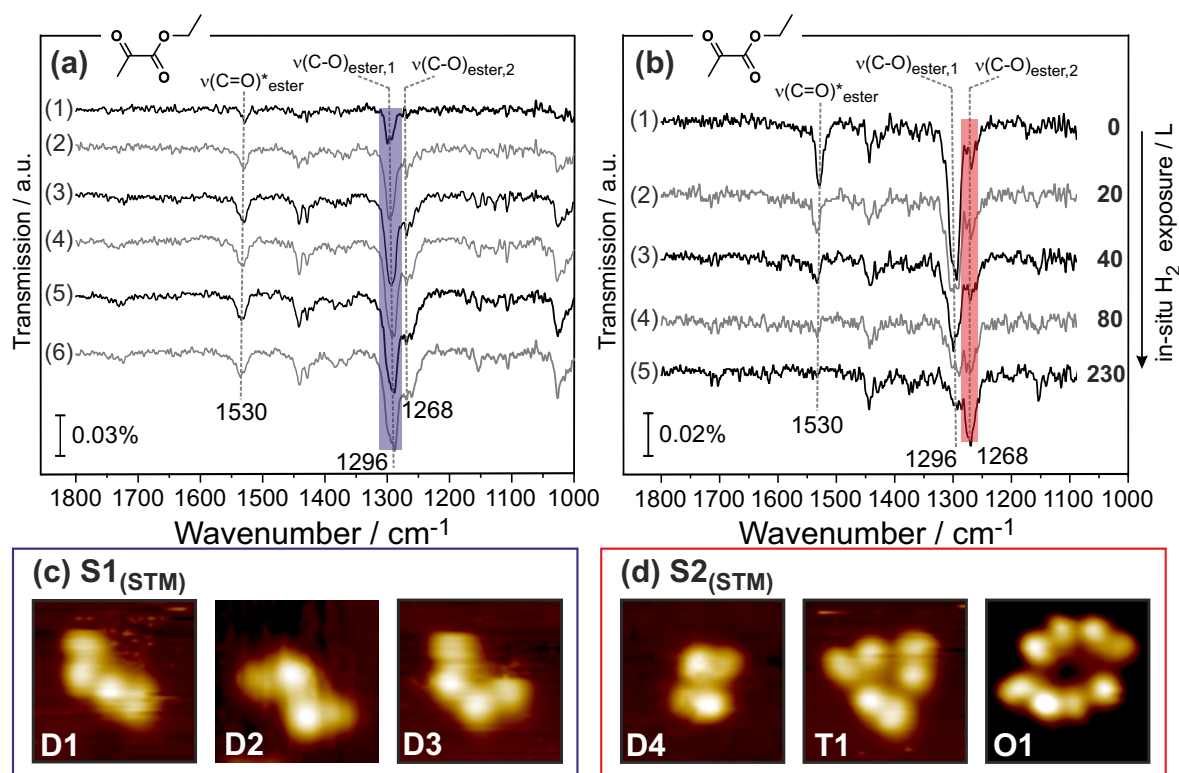


Figure 6.5: IRAS spectra of EP adsorbed on Pt(111) at 100 K. EP exposures in (a): (1) $1.4 \cdot 10^{13}$, (2) $4.3 \cdot 10^{13}$, (3) $7.2 \cdot 10^{13}$, (4) $1.0 \cdot 10^{14}$, (5) $1.1 \cdot 10^{14}$, (6) $1.3 \cdot 10^{14}$ molecules· cm^{-2} and (b) during in-situ H_2 exposure at a constant coverage of EP. The initial coverage of EP (spectrum 1) amounts to $7.2 \cdot 10^{13}$ molecules· cm^{-2} . The spectra 2–5 were acquired after H_2 exposures indicated on the right side of (b). (c) Close-up STM images of different oligomers with in $\text{S1}_{(\text{STM})}$ (dimers D1, D2 and D3) and (d) $\text{S2}_{(\text{STM})}$ (dimer D4, trimer T1 and tetramer O1) species. The dimer D4 was observed only on H-covered Pt(111) surface. (Full experimental details in Ref.[249].)

The second observation we obtained from the spectroscopic data was two different types of intermolecular interactions, based on the spectral shift of the $\nu(\text{C}-\text{O})_{\text{ester}}$ vibration. Both bands at 1296 and 1268 cm^{-1} can be assigned to the same vibration in a different chemical environment. To further address the chemical nature of the adsorbed species, two additional experiments at 100 K were performed in which IR spectra were recorded at different coverage of EP on pristine Pt(111) (Fig. 6.5a) as well as on Pt(111) that was continuously exposed to a flux of hydrogen at constant EP coverage (Fig. 6.5b).

Both the vibrations at 1530 and 1296 cm^{-1} are observed on pristine Pt(111) at lowest coverage, while the band at 1268 cm^{-1} is initially absent and only grows in intensity at higher coverages. It should be emphasized that the intensity distribution between the vibrational bands at 1268 and 1296 cm^{-1} is clearly changing with increasing coverage and the species related to the band at 1268 cm^{-1} is either not present at the lowest coverage or is present at a negligibly small concentration. (*Full discussion in Ref.[249] and Section 8.4*)

This distribution dramatically changes when the surface is exposed to hydrogen. While initially on pristine Pt(111) (Fig. 6.5b, (1)), the combination of both bands at 1530 and 1296 cm^{-1} are the most prominent bands in the IR spectra, the band located at 1268 cm^{-1} becomes dominant under H-containing conditions. We concluded from the combination of these two experiments that there exist at least two different species on the surface. The first species, denoted as $\text{S1}_{(\text{IRAS})}$, exhibiting a combination of two characteristic vibrational bands at 1530 and 1296 cm^{-1} , while the second species, denoted as $\text{S2}_{(\text{IRAS})}$, exhibiting a prominent band at 1268 cm^{-1} . Their relative abundance is dependent on both, coverage and the presence of hydrogen on the surface. The species $\text{S1}_{(\text{IRAS})}$ appears already at low coverage on pristine Pt(111), while $\text{S2}_{(\text{IRAS})}$ evolves at both high coverage and coadsorbed hydrogen. However, the species $\text{S1}_{(\text{IRAS})}$ can convert into the species $\text{S2}_{(\text{IRAS})}$ in the presence of hydrogen. (*Full discussion in Ref.[249] and Section 8.4.*)

We performed STM experiments under the same conditions on pristine and H-covered Pt(111) to clarify whether the spectroscopic observations of a different chemical environment can be supported by a microscopic picture. Briefly, the majority of all adsorbed species are agglomerated in assemblies of two, three or four individual molecules. The close-up images of these structures measured with submolecular resolution are displayed in Figure 6.5c-d. The species formed on the surface consist of a combination of elongated protrusions exhibiting a brighter spot and a darker area. All molecular assemblies can be divided into two classes, denoted as $\text{S1}_{(\text{STM})}$ and $\text{S2}_{(\text{STM})}$. In the former class of surface species, the intermolecular interaction is between two bright protrusions (Fig 6.5c, D1–D3) whereas in the latter class of surface species the interaction between the bright and the dark protrusions is present (Fig 6.5d, D4, T1, O1). (*Full discussion in Ref.[249] and Section 8.4.*)

In collaboration with the Hartke group (CAU Kiel), we performed a theoretical modeling of the adsorption geometry of an EP monomer species on Pt(111) as well as the corresponding STM images at the DFT level to identify the parts of the molecules that exhibit the bright and dark protrusions. According to this modeling of the STM images, the position of the bright protrusion is related to the acetyl group of ethyl pyruvate whereas the dark protrusion is related to the ester group. (*Full text and related discussions in Ref.[249] and Ref.[250] as well as Section 8.4 and Section 8.5.*)

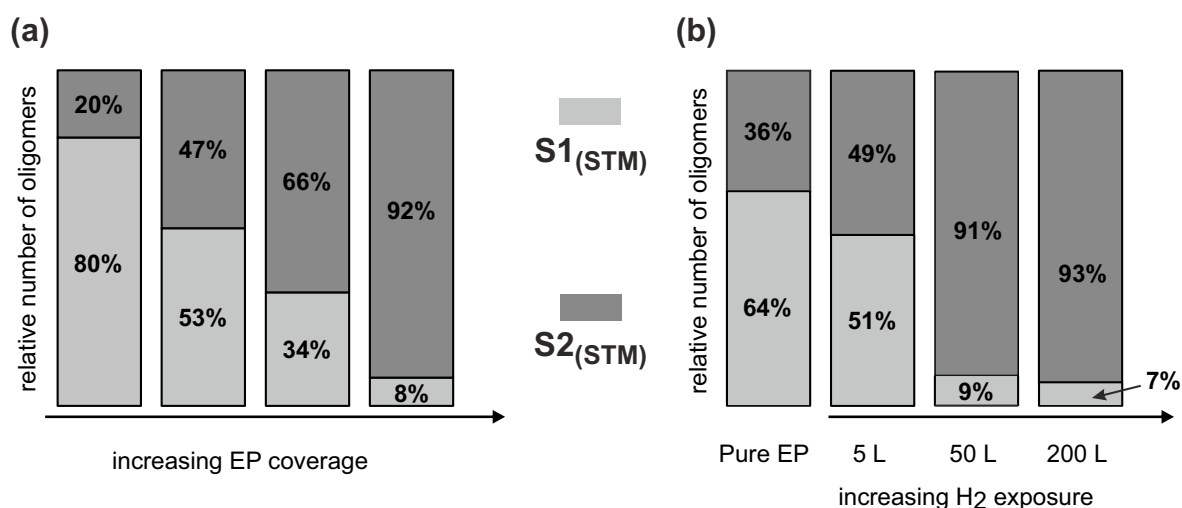


Figure 6.6: Relative abundance of the two types of surface species $S1_{(STM)}$ and $S2_{(STM)}$ for two different cases: (a) as a function of EP coverage and (b) as a function of hydrogen exposure. Adapted from Ref.[249]. (Full description and related STM data in Ref.[249], Fig. 4–5.)

Based on the statistical evaluation of the surface species detected by STM as a function of EP coverage (Fig 6.6a) as well as a function of hydrogen exposure (Fig 6.6b), a strong correlation between the evolution of the surface assemblies detected by STM and the vibrational bands in the IR spectra can be established: $S1_{(IRAS)}/S1_{(STM)}$ as well as $S2_{(IRAS)}/S2_{(STM)}$.

In Figure 6.7, the results from the experimental and theoretical studies are summarized. In the IRAS, the combination of several vibrational bands was detected that can be related to individual surface species. In the STM experiments, two classes of lateral interactions were shown. Both observations let us propose that individual surface species were formed that are sensitive to specific surface conditions. While the $S1_{(IRAS)}/S1_{(STM)}$ species, is the most abundant species at low coverage, the $S2_{(IRAS)}/S2_{(STM)}$ species is present at both high coverage as well as in the presence of hydrogen.

The first species, denoted as $S1_{(IRAS)}$, exhibiting a combination of two characteristic vibrational bands at 1530 and 1296 cm^{-1} , while the second species, denoted as $S2_{(IRAS)}$, exhibiting a prominent band at 1268 cm^{-1} . The microscopic picture obtained by STM revealed, that the species $S1_{(IRAS)}$ can be correlated with a specific intermolecular interaction in which two EP molecules interact via their bright protrusion. The second species $S2_{(IRAS)}$ can be correlated with an intermolecular interaction in which one EP molecule interacts with its dark protrusion with a bright protrusion of a neighboring EP molecule. According to the DFT modeling, the bright protrusion can be related to the ketone group and thus, we propose the following adsorption model which is consistent with all experimental observations made in this study. (Full text and related discussions in Ref.[249] and Ref.[250] as well as Section 8.4 and Section 8.5.)

Figure 6.7a-b shows a proposed configuration of the dimer species D1, D3 (Fig. 6.7a) and D2 (Fig. 6.7b), in which the interaction is established between two acetyl groups of EP, which are predicted to appear as a bright protrusion in the STM images (species $S1_{(IRAS)}/S1_{(STM)}$). Here, a hydrogen atom of the methyl group establishes hydrogen bonding with the acetyl-carbonyl group of the second EP molecule.

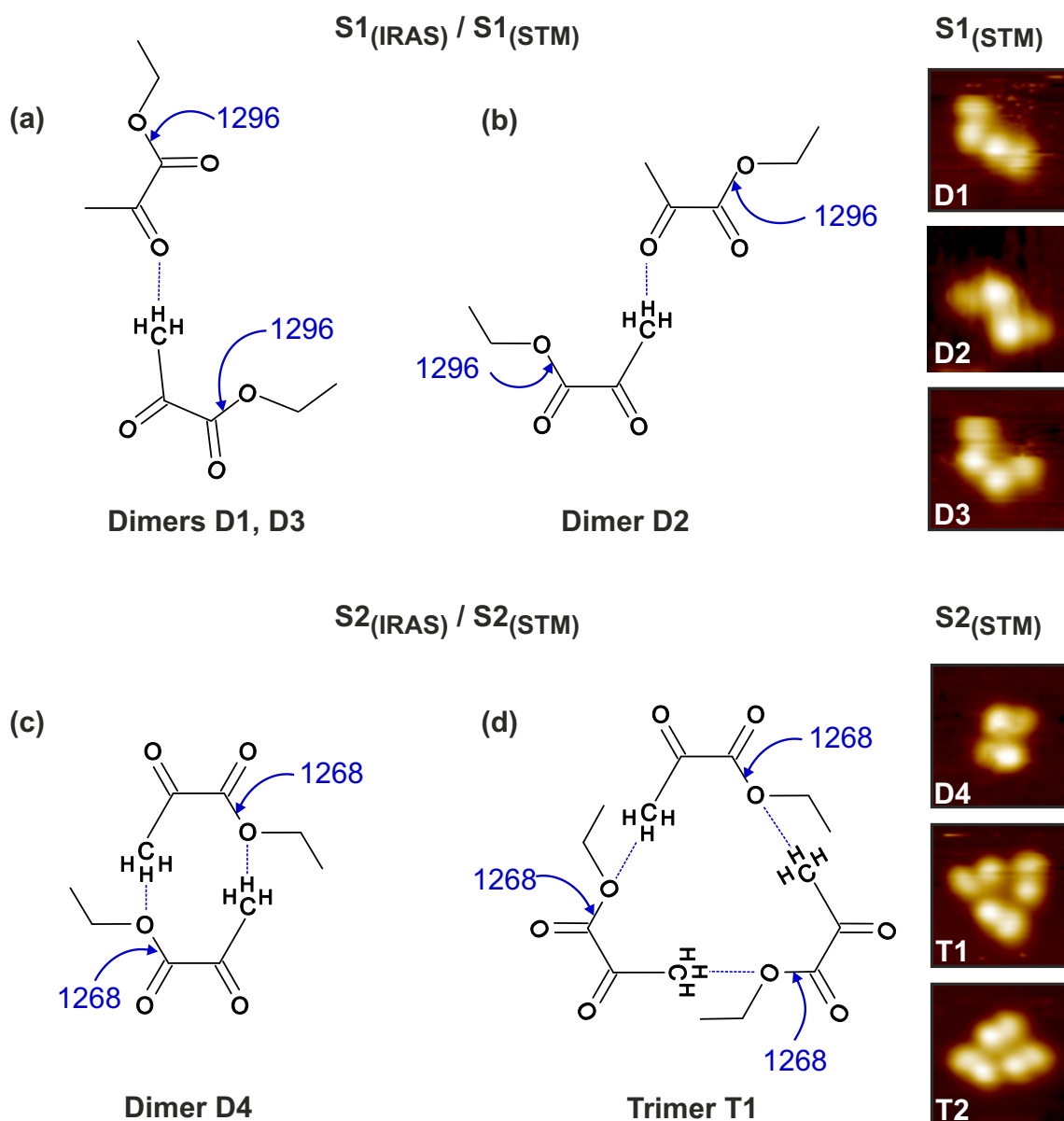


Figure 6.7: Suggested models for different types of EP oligomers and their corresponding close-up STM images: (a) and (b) dimer assemblies formed between two acetyl groups related to the species S1_(IRAS)/S1_(STM); (c) selected dimer and (d) trimer assemblies formed between the acetyl and ester groups related to the species S2_(IRAS)/S2_(STM). The dimer D4 was observed only on H-covered Pt(111) surface. Reproduced with permission from JPC C from Ref.[249].

In this configuration, the ester C–O bond is not directly involved in lateral interactions, which is consistent with the spectroscopic observation that the vibrational frequency at 1296 cm⁻¹ is only slightly red-shifted as compared to the multilayer value of 1314 cm⁻¹. The number of the frequencies of the $\nu(\text{C}-\text{O})_{\text{ester}}$ vibrational bands are highlighted in the models with blue color. Both acetyl-carbonyl groups of the dimer are most likely oriented close to parallel with respect to the underlying metal surface, since the corresponding vibrational bands are not seen in the IR spectra. The only other observed prominent band at 1530 cm⁻¹ is most likely related to the ester-carbonyl group of ethyl pyruvate.

The second type of interaction is based on establishing a connection between the brighter and the darker protrusions of the surface species and is exemplified for selected oligomer structures D4 (Fig. 6.7c). In this type of species ($S2_{(IRAS)}/S2_{(STM)}$), the ester group of one molecule is involved into hydrogen bonding with the methyl group of the neighboring species. As a result, the stretching vibration of the ester group $\nu(C-O_{\text{ester}})$ is strongly red-shifted to 1268 cm^{-1} which is observed by IRAS. The absence of all vibrational bands in the range that is typical for the stretching vibration of C=O groups is an indication that all carbonyl groups are oriented nearly parallel to the surface.

The Hartke group (CAU Kiel) theoretically analyzed ethyl pyruvate adsorbed both, as a single molecule and clusters, on Pt(111) employing a force field (FF) method that is optimized for geometry, frequency and non-covalent interactions (GFN).^[279] (Detailed discussion in Ref.[250] and full text in Section 8.5.)

The computational standard for molecules adsorbed on (metal) surfaces is nowadays DFT calculations which requires a lot of computational capacity. An approach to reduce the computational costs significantly, lower level semiempirical methods, e.g. GFN-1^[280] and GFN-2^[281], and force field methods, e.g. GFN-FF^[279], are an alternative to provide good results for both adsorption geometries and IR spectra of adsorbed molecules. One aspect that is in good agreement with the experimentally obtained data is presented in Figure 6.8.

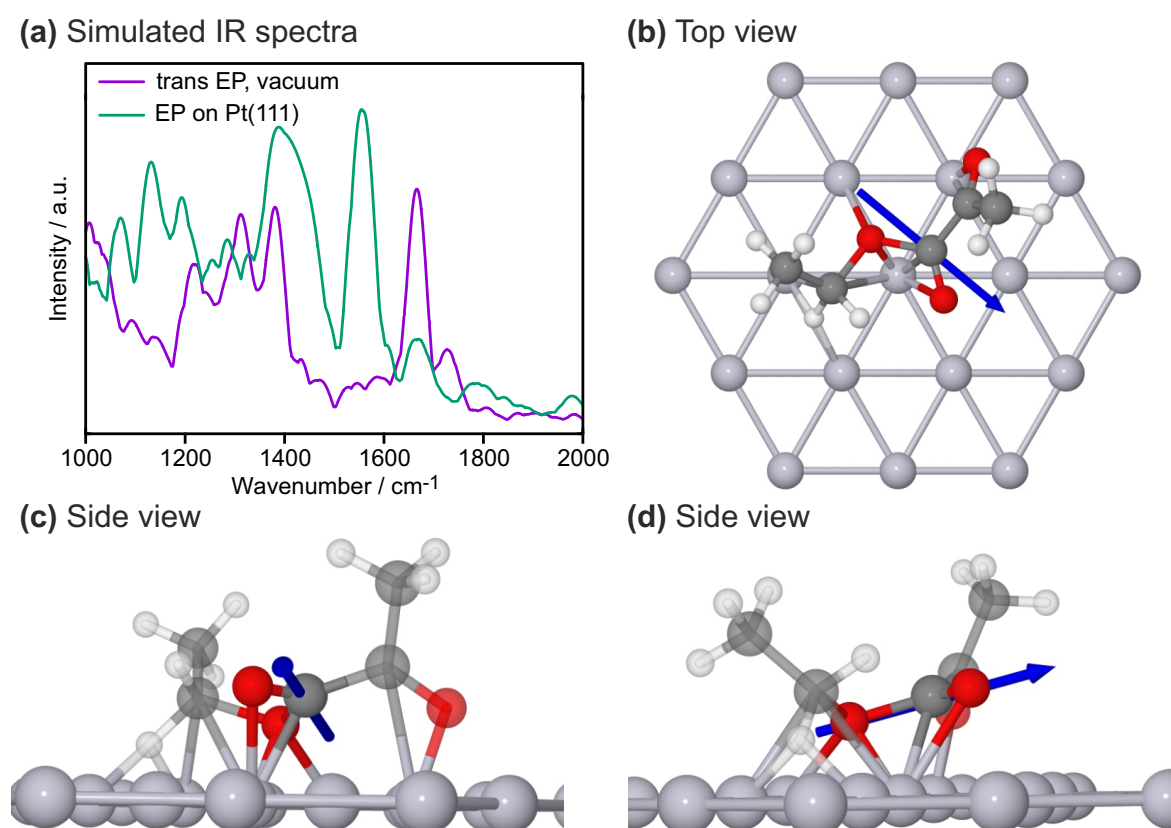


Figure 6.8: (a) Simulated IR spectrum of ethyl pyruvate adsorbed on Pt(111) and (c-d) the visualization of the vibrational mode related to the band at 1560 cm^{-1} . Adapted from Ref.[250].

The simulated IR spectra of a single EP molecule in the gas phase as well as EP adsorbed on Pt(111) are shown in Figure 6.8a. A similar shift of the stretching vibration of the ester carbonyl group $\nu(\text{C}=\text{O}_{\text{ester}})$, as observed in the IRAS data, was obtained. The simulated value of 1560 cm^{-1} is close to the experimentally observed frequency at 1530 cm^{-1} . Figure 6.8b-d provides the visualization of the displacement vector (blue) of the atoms involved in the vibration of interest, located at 1560 cm^{-1} in the calculated spectrum, from three different views. According to the results of the calculation, the experimentally observed IR band at 1530 cm^{-1} can indeed be assigned to the ester carbonyl group. However, a more accurate description of the calculated vibrational mode itself is rather a displacement of the C-atom in the Pt–O–C–O–Pt bond than a true $\nu(\text{C}=\text{O})_{\text{ester}}$ vibration.

In this study, we investigated the details of mutual lateral interactions in ethyl pyruvate oligomers adsorbed on a well-defined Pt(111) surface employing a combination of IRAS, STM, molecular beam techniques as well as theoretical modeling at the DFT level. We pointed out that the proposed enediolate geometry as well as the keto–enol tautomerization of ethyl pyruvate are unlikely models to describe the adsorption state of EP on Pt(111) at low temperature. The IRAS data strongly suggest an upright-standing ester carbonyl group and close to parallel orientation of the ketone carbonyl group with respect to the surface plane. The microscopic study showed a large variety of different oligomers formed on the surface without long-range ordering.

Based on the combination of spectroscopic and microscopic observations, all species can be attributed to two large classes of oligomers exhibiting different types of intermolecular binding. The first class, denoted as $S1_{(\text{IRAS})}/S1_{(\text{STM})}$, exhibits a nearly unperturbed $\nu(\text{C}=\text{O})$ and a strongly perturbed $\nu(\text{C}=\text{O}_{\text{ester}})$ vibration. The intermolecular interaction in these species is realized via H-bonding between two acetyl groups, in which an oxygen atom of the carbonyl group is bonded to a hydrogen atom of the methyl group of a neighboring molecule. In the STM images, these species appear as dimers, in which the individual molecules are connected to each other via their bright protrusions. DFT modeling of the STM images performed for EP monomer species confirms that the position of the bright protrusion is related to the acetyl group of EP.

The second class of species $S2_{(\text{IRAS})}/S2_{(\text{STM})}$ exhibits a characteristic vibrational band related to a strongly red-shifted C–O stretching vibration of the ester group. The shift is proposed to arise from a second type of intermolecular interaction involving hydrogen bonding between the oxygen atom of the C–O_{ester} group and the methyl group of a neighboring EP molecule that significantly weakens of the C–O bond. In the STM images, the corresponding surface species show an interaction between the bright and the dark protrusions of the neighboring molecules.

The relative abundance of the species formed on the surface is strongly dependent on the chemical surrounding and are sensitive to surface hydrogen. While the $S1_{(\text{IRAS})}/S1_{(\text{STM})}$ species are predominantly present on pristine Pt(111) at low coverage, the $S2_{(\text{IRAS})}/S2_{(\text{STM})}$ species are only present at high coverage and in the presence of surface hydrogen.

In the next study, we investigated the adsorption geometry and lateral interactions of an α -methyl ketone, acetophenone, over Pt(111) in a broad range of temperatures and surface coverages.

6.2 Adsorption Study of Acetophenone on Pristine Pt(111)

This section reflects a brief summary of the results that are presented in

Angewandte Chemie from Ref.[236]. (Full text in Section 8.6.)

*Smadar Attia, Marvin-Christopher Schmidt, **Carsten Schröder**, Pascal Pessier, Swetlana Schauermaun, *Angew. Chem. Int. Ed.* **2018**, 57, 16659–16664.,*

ACS Catalysis from Ref.[237]. (Full text in Section 8.7.)

*Smadar Attia, Marvin C. Schmidt, **Carsten Schröder**, Swetlana Schauermaun, *ACS Catal.* **2019**, 9, 8, 6882–6889.,*

and

The Journal of Physical Chemistry C from Ref.[235]. (Full text in Section 8.9.)

*Marvin C. Schmidt, Smadar Attia, **Carsten Schröder**, Ann-Katrin Baumann, Swetlana Schauermaun, *J. Phys. Chem. C* **2020**, 124, 26, 14262–14271.*

The hydrogenation of carbonyl compounds is an important class of chemical reactions with particular relevance for industrial application. There are numerous examples for heterogeneously catalyzed reactions, e.g. hydrogenation of unsaturated aldehydes^[45] or enantioselective hydrogenation of prochiral ketones^[54,252,253], in which a generally very stable C=O bond is chemically transformed into a C–O bond. However, one of the major challenges in the hydrogenation of carbonyl groups remains the activation of the C=O bond.

In several recent theoretical studies, the keto–enol tautomerization as a first step in the hydrogenation reaction of carbonyl compounds was suggested as an alternative low–barrier mechanism that has significantly lower activation barriers than the direct insertion of hydrogen atoms into the C=O entity of the ketone.^[83–86] The enol tautomer is in general thermodynamically less stable than the corresponding ketone itself and thus needs to be stabilized either via a chelated ring-like keto–enol tautomer or via the formation of oligomers.^[86–92] The intramolecular stabilization of enols in compounds comprising multiple carbonyl groups is well-understood, whereas the intermolecular stabilization of enols via lateral interactions with neighboring molecules is poorly investigated.

In a combined scanning tunneling microscopy (STM) and high-resolution electron energy loss spectrometry (HREELS) study by Demers-Carpentier et al.^[72] on prochiral ketones adsorbed on Pt(111), the authors reported for acetophenone the formation of surface agglomerates containing three acetophenone molecules, after heating the sample surface to 300 K. Based on the spectroscopic data obtained in the same study, the authors proposed that these oligomers comprise exclusively the enol species of acetophenone.

The atomistic-level understanding of the mechanisms and energetics of lateral interactions that result in the formation of the proposed enol-containing oligomers is, however, not fully understood. To address the details of the transformation of acetophenone toward the

enol tautomer and specifically the stabilization of the unstable enol form, we employed a unique combination of surface-sensitive techniques including infrared reflection absorption spectroscopy (IRAS), STM and molecular beam techniques to identify the chemical nature of the formed surface species and to obtain the real space information on their distribution over the surface as well as on the lateral interactions between the individual molecules.

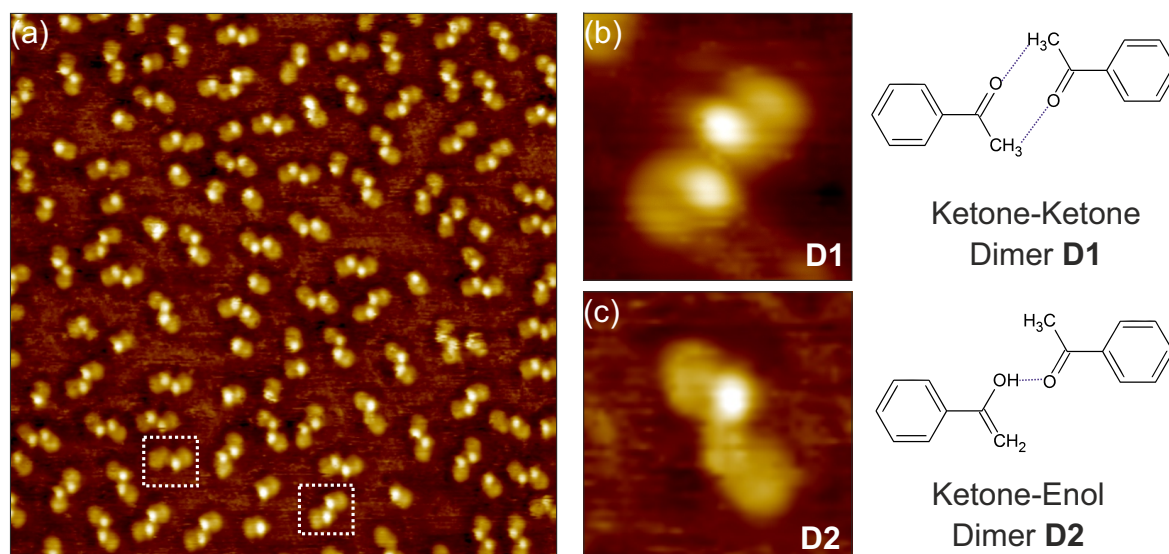


Figure 6.9: (a) $15 \times 15 \text{ nm}^2$ STM image of acetophenone adsorbed on pristine Pt(111) at 200 K. Scanning temperature was 115 K after deposition. Close-up STM images of (b) the symmetric D1 dimer and (c) the anti-symmetric D2 dimer. (*Experimental details in Refs.[236,237].*)

The STM images obtained of acetophenone at 200 K (Fig 6.9) revealed the presence of two different types of dimer species that represent the majority (82 %) of all molecules on the surface. The remaining fraction (18 %) of molecules are monomers which are imaged as a protrusion enclosing a brighter and a darker area. The larger fraction among the dimer species (84 % of the dimer species, D1, Fig 6.9a) consists of two identical protrusions with a bright spot at one end, in which both acetophenone molecules are interacting via the brighter protrusion. The less abundant dimer species (16 % of the dimer species, D2, Fig 6.9b) is imaged as an anti-symmetric protrusion. In this type of dimer, one molecule is imaged as a bright and dark spot whereas the second molecule is imaged as an elongated structure without a bright protrusion. The lateral interactions between the two molecules in this dimer can be attributed to the bright spot of one molecule interacting with the dark protrusion of the second molecule. (*Full discussion in Ref.[236] and Ref.[235] as well as Section 8.6 and Section 8.9.*)

As a next step, we investigated the chemical nature of the surface species that are formed by acetophenone molecules in a broad range of temperature employing infrared spectroscopy. The infrared spectra of the unperturbed acetophenone molecule in the gas phase, which serves as a reference, was previously characterized by Gambi et al.^[243], Chen et al.^[244] as well as Attia et al.^[215].

Briefly, the most prominent bands are related to the C=O stretching vibration ($\nu(\text{C}=\text{O})$) at 1686 cm^{-1} , the deformation vibration of the methyl group ($\delta(\text{CH}_3)$) at 1361 cm^{-1} and the stretching vibration of the C–C bond between the phenyl ring and the acetyl group ($\nu_{\text{ip}}(\text{C}-\text{C}_{\text{ring-acetyl}})$) at 1275 cm^{-1} .

In Figure 6.10, the results of the infrared spectra recorded on acetophenone adsorbed on Pt(111) at indicated temperatures (115–280 K) are presented. (Full discussion in Ref.[236] and Ref.[237] as well as Section 8.6 and Section 8.7.)

The adsorption of acetophenone on Pt(111) at 115 K results in an unperturbed ketone form of AP which is characterized by the $\nu(\text{C}=\text{O})$ vibration that is located at the same frequency (1683 cm^{-1}) as in the multilayer spectra.^[215] With increasing temperature, additional vibrational bands evolve that are not present in the infrared spectrum related to the unperturbed molecule. In particular, above 136 K, there are vibrational bands at 1203 as well as 1634 cm^{-1} and above 280 K a third vibrational band at 1663 cm^{-1} appears.

It is important to emphasize that there is a strong correlation between the appearance of the bands at 1203 and 1663 cm^{-1} . Both vibrational bands are evolving above 136 K and are present in the infrared spectra recorded in a broad range of temperature. According to the frequency shifts of the bands in the infrared spectra obtained in the experiments performed with isotopically labeled acetophenone, in which the carbon atom of the carbonyl group was isotopically labeled ($^{13}\text{C}=\text{O}$), we assigned the band at 1203 cm^{-1} to the stretching vibration of the C–O bond ($\nu(\text{C}-\text{O})$) of the enol tautomer of acetophenone that is formed on the metal surface. (Full discussion and related data in Ref.[236] and Section 8.6.)

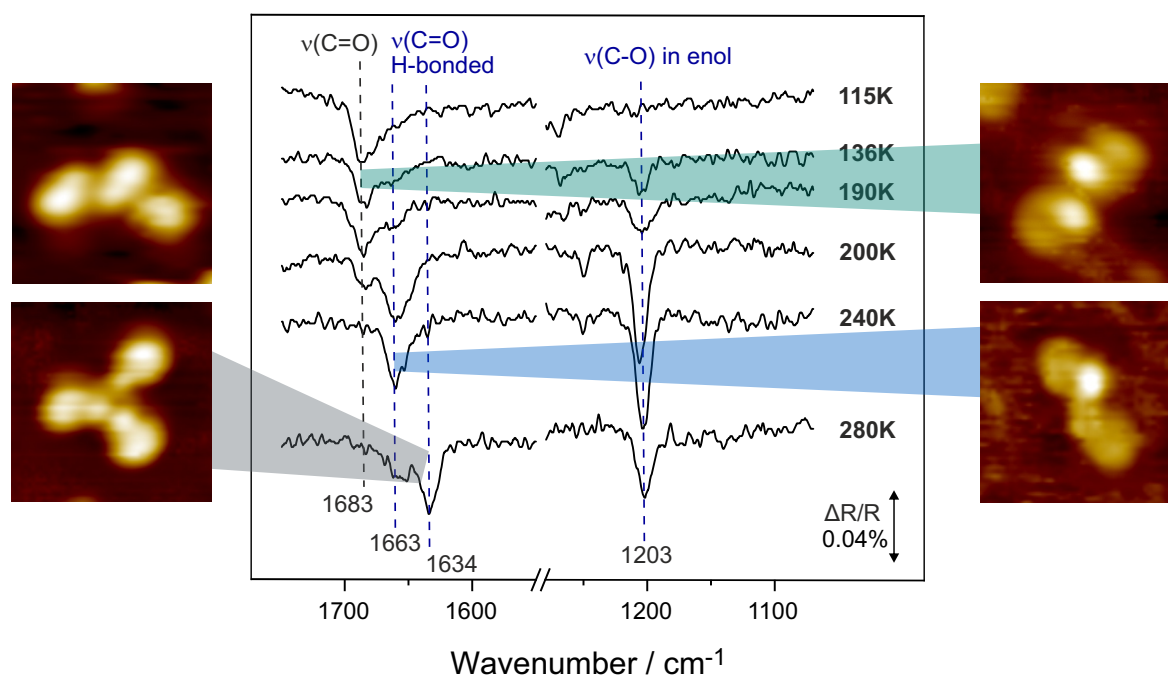


Figure 6.10: IRAS spectra of acetophenone at submonolayer coverage adsorbed on Pt(111) at indicated temperatures and surface species imaged by STM. (Experimental details in Ref.[237].)

The microscopic picture obtained by STM under the same conditions revealed the presence of acetophenone monomers on the surface, in which the molecule is imaged as a protrusion that encloses each a brighter and a darker area, as well as the formation of two types of dimers. The first type of dimer, D1, consists of two identical protrusions that enclose each a brighter and a darker area, similar as compared to the acetophenone monomer, and thus we assumed that the lateral interactions between the molecules in this dimer do not result in a large shift in the vibrational frequencies.

However, the second type of dimer, D2, consists of a combination of different protrusions in which one part encloses a darker and a brighter area whereas the second part consist of a dark area. The resulting dimer is therefore asymmetric. Based on both the microscopic and spectroscopic observations, we concluded that the dimer species D2 consists of two acetophenone molecules, in which one molecule is present in the enol form and the second remains in the ketone form. Therefore, we assigned the vibrational band at 1663 cm^{-1} , which always appears in combination with the vibrational band at 1203 cm^{-1} , to the stretching vibration of the C=O bond in the ketone of the D2 dimer. The band related to the stretching vibration of the carbonyl group is red-shifted by 20 cm^{-1} which is in a typical range of frequency shifts for ketones that establish a hydrogen bonding toward an acidic hydrogen atom, i.e. in this case the H atom of the enol.^[214] We therefore concluded that the enol form of acetophenone is formed on the Pt(111) surface but can only exist while being stabilized by surrounding ketones. Above 280 K, an additional vibrational band evolves at 1634 cm^{-1} . To clarify whether this additional red-shift of a band is related to the formation of new types of oligomers on the surface, we performed a STM study at this temperature. The microscopic picture of acetophenone adsorbed on Pt(111) at 285 K is presented in Figure 6.11a and the close-up images of the AP oligomers in Fig. 6.11b-e. (Full discussion in Ref.[236] and Ref.[237] as well as Section 8.6 and Section 8.7.)

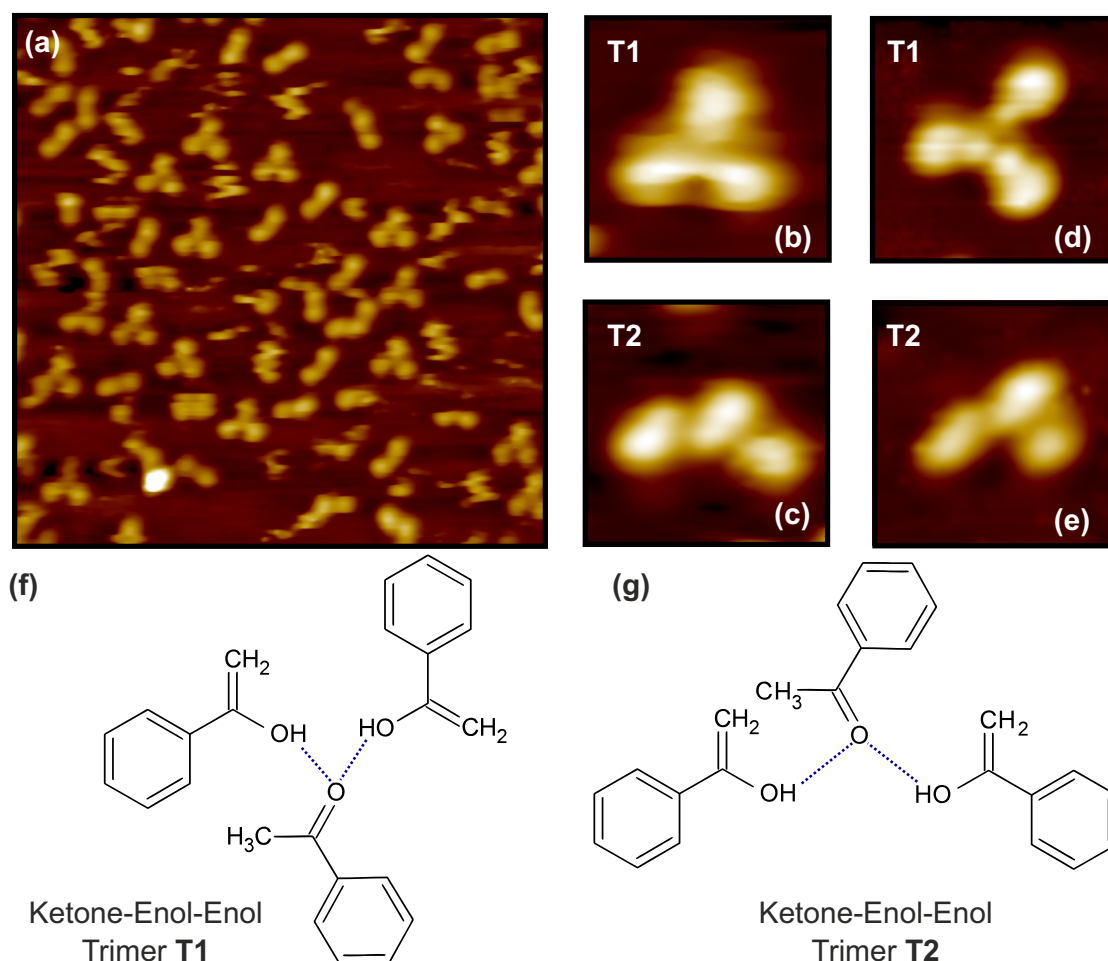


Figure 6.11: (a) STM images of AP adsorbed on pristine Pt(111) (exposure 285 K, scanning temperature 285 K, $15 \times 15\text{ nm}^2$), (b-e) close-up images and (f-g) proposed structures of the trimers (exposure at 285 K, scanning temperature 115 K). (Experimental details in Ref.[237].)

There are two different types of trimers observed at this temperature: a more roundish self-assembly of three AP molecules (trimer T1) and a more linear (trimer T2). The correlation of the formation of trimers on the surface and the appearance of an additional vibrational band, that is more red-shifted than the band related to the C=O stretching vibration in the ketone–enol dimer, let us assign this vibrational band to the C=O group of an acetophenone ketone that is connected to two AP molecules in the enol form via hydrogen bonding. The vibrational band is red-shifted by 49 cm^{-1} as compared to the same frequency of the unperturbed molecule in the gas phase. This red-shift is about twice as much as in the ketone–enol dimer, where the interaction of the H atom of the enol entity with the oxygen atom of the C=O bond in the ketone results in a shift of 20 cm^{-1} .

Based on the strong temperature dependence that is observed for the formation of different types of dimers and trimers of acetophenone on Pt(111), we concluded that the kinetic effects exhibit a key role in the process. The formation of ketone–ketone dimers at low temperature indicate that the acetophenone molecules have sufficient kinetic energy to overcome the diffusion barrier. As evidenced by the spectra obtained from IRAS, the first kinetic barrier for the keto–enol tautomerization can be overcome above approximately 136 K. The activation barrier to form a second enol form, resulting in a ketone–enol–enol trimer, however, is significantly higher as compared to the formation of the first enol and is thus observed at around 280 K. This is most likely an indication for the mechanism being a concerted process within a complex of molecules (dimers or trimers) rather than the tautomerization of an individual acetophenone monomer adsorbed on the surface. If the latter case was true, the rate-limiting step of the overall process would be keto–enol tautomerization of the monomer with a formation of dimer or trimer in a second step, that most likely has a lower activation barrier. As a consequence of this scenario, the activation barriers for the formation of both ketone–enol dimers and ketone–enol–enol trimers would exhibit a similar activation barrier, which strongly contradicts the experimental observation. (*Full discussion in Ref.[236] and Ref.[237] as well as Section 8.6 and Section 8.7.*)

In the study on acetophenone adsorbed on pristine Pt(111), we could show with two complementary methods that the molecule undergoes a keto–enol tautomerization. The enol form of acetophenone on Pt(111) needs to be stabilized via a neighboring ketone form of acetophenone. This stabilization results in the formation of different oligomers, dimers or trimers, depending on the adsorption temperature. The spectroscopic study of acetophenone on pristine Pt(111) revealed the presence of several surface species appearing at different temperatures: i) a low temperature species where acetophenone remains almost unperturbed in the ketone form, ii) a ketone–enol complex which is most dominant around 240 K and iii) a ketone–enol–enol complex above 280 K.

As a next step, we investigated the influence of coadsorbed hydrogen on i) the adsorption geometry, ii) the strength of intermolecular interaction and iii) the hydrogenation reaction of acetophenone.

6.3 Adsorption Study of Acetophenone on Hydrogen-covered Pt(111)

This section reflects a brief summary of the results that are presented in

Angewandte Chemie from Ref.[236]. (Full text in Section 8.6.)

*Smadar Attia, Marvin-Christopher Schmidt, **Carsten Schröder**, Pascal Pessier, Svetlana Schauer mann, *Angew. Chem. Int. Ed.* **2018**, 57, 16659–16664.,*

ACS Catalysis from Ref.[237]. (Full text in Section 8.7.)

*Smadar Attia, Marvin C. Schmidt, **Carsten Schröder**, Svetlana Schauer mann, *ACS Catal.* **2019**, 9, 8, 6882–6889.,*

and

The Journal of Physical Chemistry C from Ref.[239]. (Full text in Section 8.10.)

*Marvin Schmidt, Smadar Attia, **Carsten Schröder**, Ann-Katrin Baumann and Svetlana Schauer mann, *J. Phys. Chem. C* **2021**, 125, 35, 19311–19324.*

To further understand the chemical transformation of acetophenone in the presence of hydrogen, we performed a combined IRAS and STM adsorption study of acetophenone on hydrogen precovered Pt(111). It is important to note that the adsorption of hydrogen on surfaces does not always result in one adsorption state equally distributed over the entire surface. Not only different adsorption sites on the surface but also sites in the subsurface or the bulk itself may absorb hydrogen, depending on the condition of the catalyst.

In early TPD studies on the desorption behavior of hydrogen on Pt(111), two different species of chemisorbed hydrogen were suggested: a weakly bound β_1 - and a strongly bound β_2 -species.^[112] The former β_1 -species desorbs above 225 K while the latter β_2 -species is present up to approximately 325 K. These experiments are summarized in the review by Christmann.^[112] This interpretation of those two desorption peaks in the TPD spectra has been discussed intensively over the last decades.^[119–123,282] In more recent studies on the hydrogen desorption behavior on different Pt surfaces, the double (β_1, β_2)-peak structure was shown to be an artifact which is most likely related to surface defects, e.g. steps.^[119–121] Poelsema et al.^[119] showed in TPD studies hydrogen on defect-free Pt(111) with a step density of $\approx 0.1\%$ that a single desorption peak results from a Pt(111) surface. This assignment of a single desorption peak TPD spectra was also confirmed by Jo^[121] on flat Pt(111). The author also showed in the study that the same Pt(111) surface yielded a multi-peak desorption spectra after being intentionally defected via argon sputtering. The experiments on stepped Pt(533) and Pt(553) surfaces by van der Niet et al.^[122] and Gee et al.^[123] further supported that both stepped and defected surfaces result in multi-peak desorption TPD spectra. An investigation of the isosteric heat of adsorption by Poelsema et al.^[119] revealed a linear decrease from about 75 to 50 kJ·mol⁻¹ with increasing coverage ($0 < \Theta < 1$) of surface hydrogen. This results in strong repulsive lateral interactions with an energy of about 5 kJ·mol⁻¹ per neighboring hydrogen atom. The authors suggested a hydrogen capture into a molecular precursor state to explain these observed phenomena.

A more accurate explanation of the obtained experimental results can thus be related to a different coverage of surface hydrogen. However, our first interpretation of the experimental results based on the outdated hypothesis of β_1 - and β_2 -H-species. To clarify whether the adsorption state or coverage of the coadsorbed hydrogen influences the adsorption geometry and lateral interactions of acetophenone, we performed combined microscopic and spectroscopic studies at 200 K and 240 K.

The results of the microscopic study at 200 K are presented in Figure 6.12b-d. Most interestingly, the STM images show that the majority of acetophenone molecules adsorb as monomers (79 %) and only a negligible amount of dimers (21 %) are formed on the surface. This is a dramatic change as compared to the STM data obtained for the adsorption of AP on pristine Pt(111), in which the majority of acetophenone molecules form dimers (82 %) and only a small fraction of monomers (18 %) are present on the surface. (Full discussion of the STM data in Ref.[239] and [237] as well as Sections 8.10 and 8.7.)

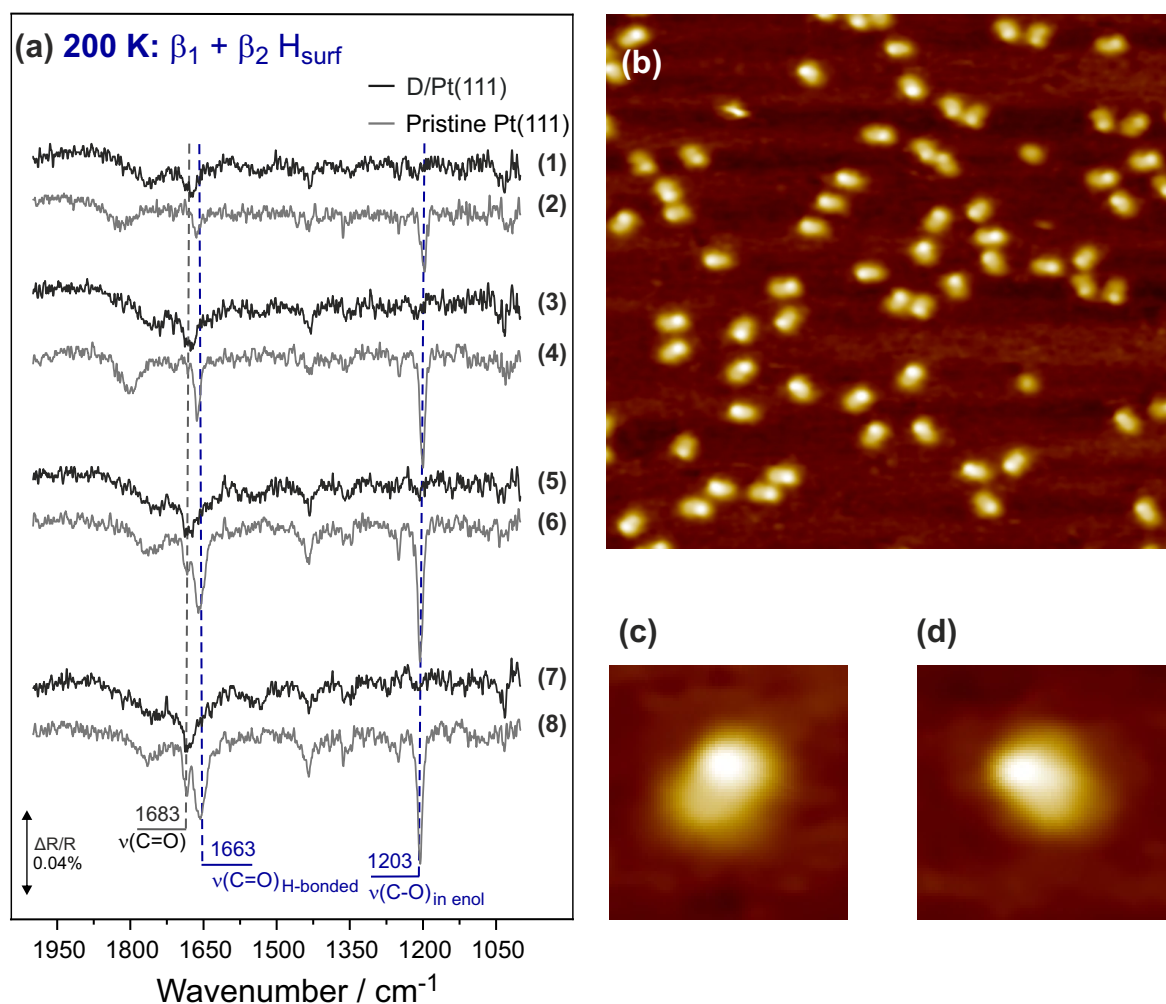


Figure 6.12: (a) IRAS spectra of acetophenone on pristine Pt(111) (grey) and D/Pt(111) (black) at 200 K. Acetophenone exposures: (1) 3.1, (2) 1.7, (3) 5.8, (4) 2.1, (5) 20, (6) 6.5, (7) 39, (8) $12 \cdot 10^{14}$ molecules \cdot cm $^{-2}$. (b) 23×23 nm 2 STM image of acetophenone adsorbed on H/Pt(111) (Exposure at: 150 K (H $_2$), 190 K (acetophenone), acquisition temperature 115 K), (c-d) close-up images of acetophenone monomers. (Experimental details in Ref.[238].)

The spectroscopic data from the adsorption study of AP on D/Pt(111) and pristine Pt(111) for reference at 200 K are shown in Figure 6.12 for different exposures of acetophenone. Most interesting to point out here is that the combination of both vibrational bands located at 1663 and 1203 cm^{-1} , that was related to the spectroscopic signature of the ketone–enol dimer formed on pristine Pt(111) at 200 K, is absent. We therefore concluded that the presence of hydrogen at 200 K prevents the formation of ketone–enol dimers. The only important vibrational band, that is visible in the IR spectra recorded for acetophenone adsorbed on hydrogen covered Pt(111) at 200 K, is located at 1683 cm^{-1} which was previously assigned as the unperturbed stretching vibration of the C=O group in acetophenone and thus related to the ketone form of AP as monomers or in ketone–ketone dimers. (Full discussion of the IRAS data in Ref.[237] as well as Section 8.7.)

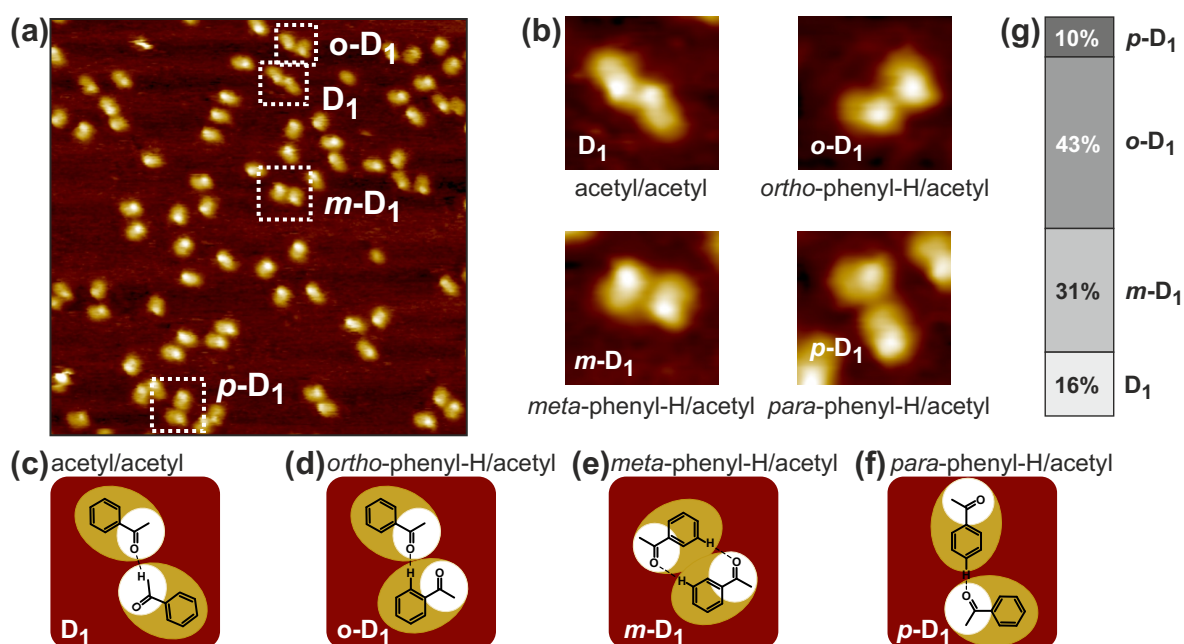


Figure 6.13: (a) STM image of AP adsorbed on the H precovered ($\Theta \approx 0.95$ ML) Pt(111) surface (exposure at 190 K, acquisition temperature of 120 K, $19 \times 19 \text{ nm}^2$); (b) Close-up images of the species present on the surface; (c-f) proposed structures of dimer species shown in (b) and (g) statistical distribution of different dimer species. (Full experimental details in Ref.[239].)

A detailed analysis of the dimers formed in the presence of surface hydrogen reveal the formation of a new type of dimers that are not observed on pristine Pt(111). Figure 6.13 shows the STM data of AP being exposed to H/Pt(111) at 190 K. In addition to the dimers formed on pristine Pt(111), where both acetyl groups of AP are involved in the lateral interactions, the newly formed dimers interact with the phenyl hydrogen atoms and the acetyl group (Fig 6.13b). The additional three dimers correspond to the lateral interactions between the acetyl group and the *ortho*- (*o*-D₁, Fig 6.13d), *meta*- (*m*-D₁, Fig 6.13e) or *para*-hydrogen (*p*-D₁, Fig 6.13f) of the phenyl ring. This type of interaction was previously suggested for TFAP on pristine Pt(111) by McBreen and coworkers.^[66,283–285] Both, the higher amount of *ortho*- and *meta*-H-atoms as well as the high acidity of the *ortho*-hydrogen, are most likely responsible for the distribution of the relative abundance of the phenyl-H/acetyl dimers: *o*-D₁ dimer (43 %), *m*-D₁ (31 %) and *p*-D₁ (10 %) (Fig 6.13g). (Full discussion of the STM data in Ref.[239] as well as Section 8.10.)

As the next step, we investigated the adsorption of acetophenone on hydrogen precovered Pt(111) at 240 K. Figure 6.14 shows the results of acetophenone adsorbed on D/Pt(111) at 240 K and on pristine Pt(111) for reference. The images obtained from STM clearly show the presence of dimers on the surface that represent the absolute majority of all surface species. The protrusions of the dimer species are different as compared to the dimers observed on pristine Pt(111) at the same temperature. The IR spectra for the same system also contain the typical combination of two vibrational bands, one related to the enol vibration at 1203 cm^{-1} and the other vibration at 1663 cm^{-1} related to the C=O stretching vibration of the ketone form of AP in the ketone–enol dimer. Interestingly, there is an additional vibrational band at 1036 cm^{-1} which does not appear on i) pristine Pt(111), ii) in the unperturbed multilayer spectra of AP or iii) at elevated temperature on pristine Pt(111). This vibration was only observed in the presence of hydrogen on the surface. Based on the spectral position in the IR spectra, we assigned this band to a $\nu(\text{C}-\text{O})$ vibration. There is a significant shift of 150 cm^{-1} toward lower wavenumbers compared to the $\nu(\text{C}-\text{O})$ vibration in the ketone–enol dimer which implies that the chemical environment of the C–O group dramatically changes compared to the enol form. This frequency was also not reported in the HREELS spectra of the hydrogenated form of AP, 1-phenylethanol, that was investigated by Demers-Carpentier et al.^[72]

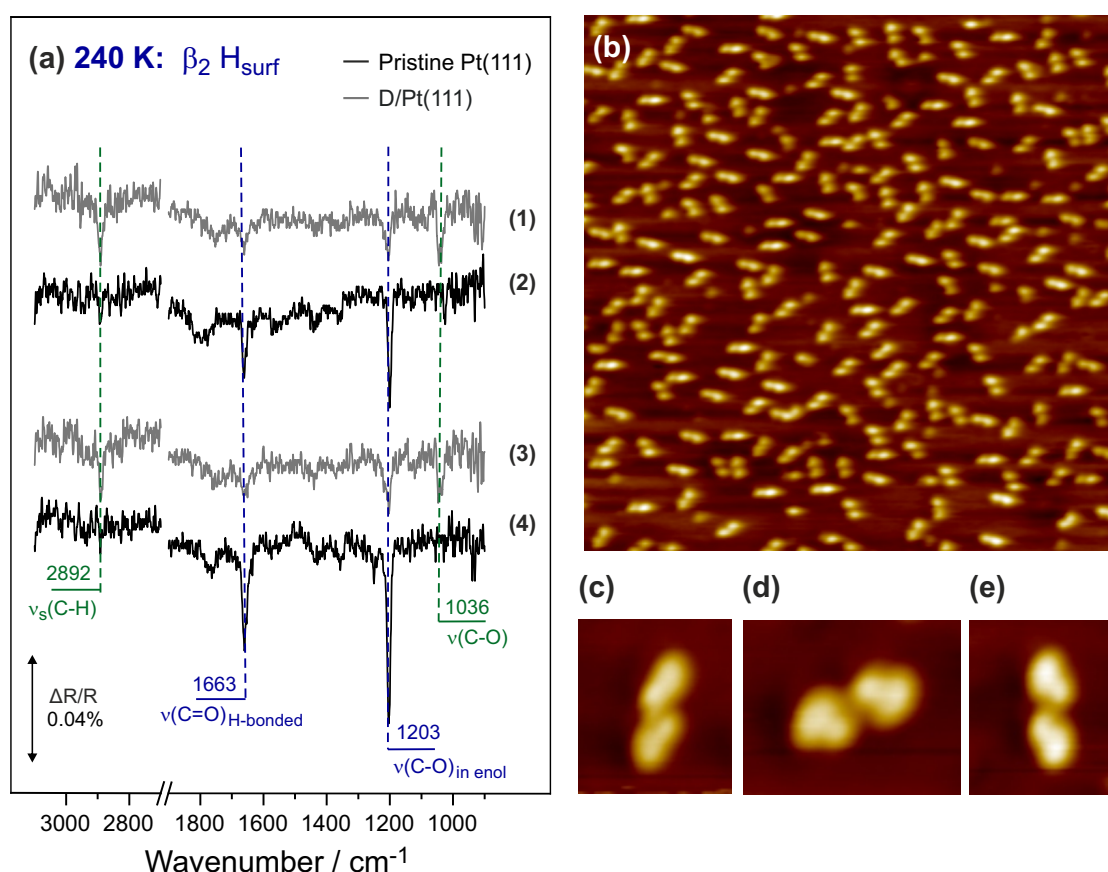


Figure 6.14: (a) IRAS spectra of AP adsorbed on pristine (black) and D/Pt(111) (grey) at 240 K. AP exposures: (1) 4.0 , (2) 2.7 , (3) 5.4 , (4) $4.0 \cdot 10^{14}$ molecules· cm^{-2} . (b) $30 \times 30\text{ nm}^2$ STM image of AP adsorbed on H/Pt(111) (H_2 exposure at 150 K followed by heating to 240 K and AP exposure at 240 K; acquisition temperature 115 K). (c-e) Close-up STM images of the species obtained at this experiment. (Full experimental details in Ref.[238].)

In combination with the vibration, related to the newly formed C–O single bond, a second vibrational band at 2892 cm^{-1} evolves that has a similar frequency as the vibrational band related to the C–H stretching vibration of the methyl group in 1-phenylethanol (2886 cm^{-1}). (Full discussion in Ref.[237] as well as Section 8.7.)

Based on the spectroscopic data, we assigned this vibrational band to a C–O stretching vibration related to a partially hydrogenated ketone–enol dimer in which one additional hydrogen is inserted into the C=C bond of the enol group. We propose the model presented in Figure 6.15 as a possible scenario for the mechanism of the H-insertion into the ketone–enol dimer. There are two carbon atoms in the C=C bond of the enol in which the hydrogen can possibly be inserted, that are denoted as carbon atoms C(1) and C(2) in Figure 6.15. Therefore, two different pathways can be discussed: i) C(1) is connected to the underlying Pt surface and the hydrogen is inserted into the =CH₂ group (forming species A) and ii) the opposite case in which C(2) is attached to the Pt surface and the hydrogen binds with the C(1) atom (forming species B).

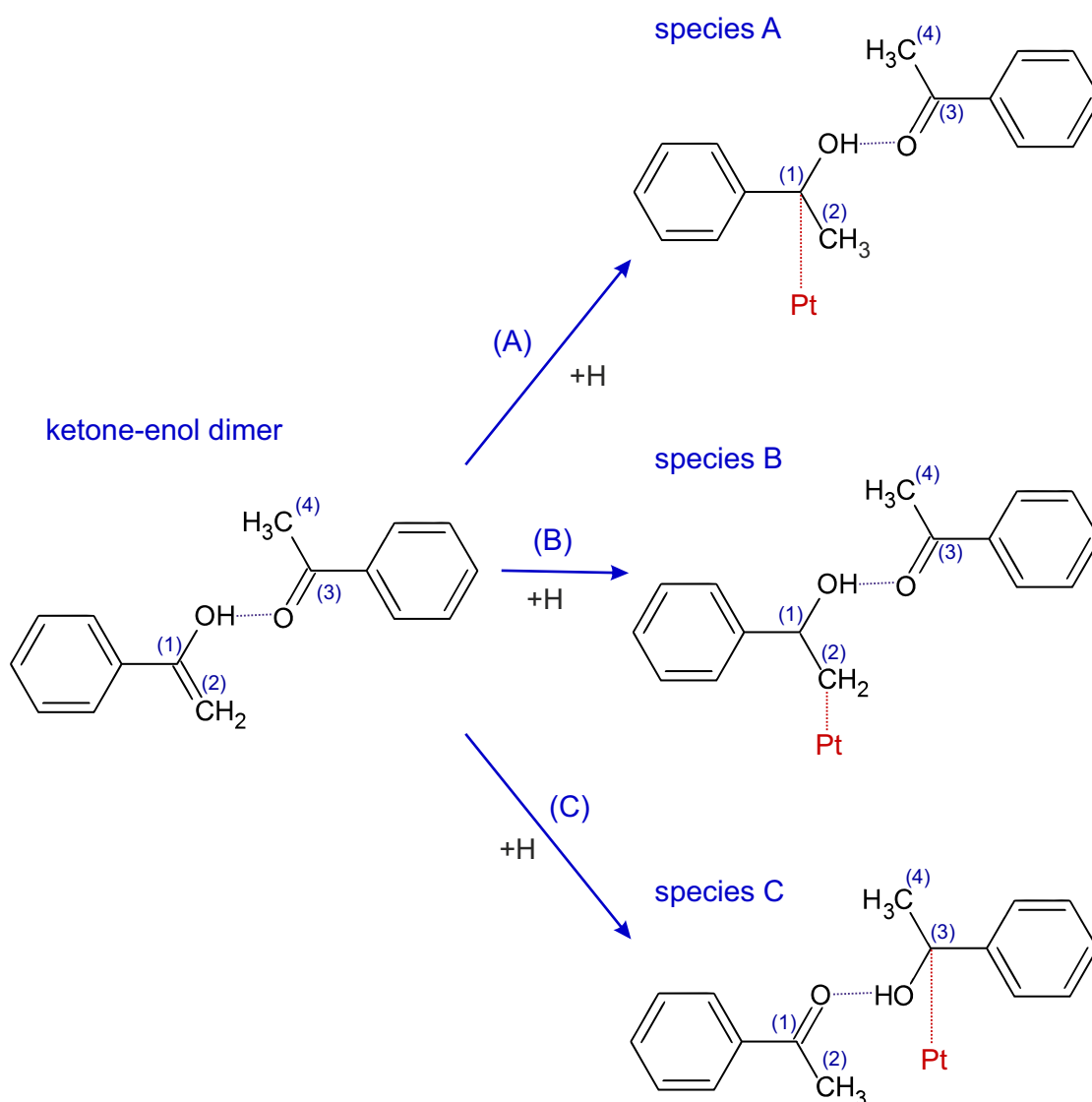


Figure 6.15: Proposed reaction mechanism of the hydrogenation of ketone-enol dimer of acetophenone. Reproduced from Ref.[238].

Both, species A and B, exhibit a similar spectroscopic signature that contains the stretching vibration of the C–O bond, however, the formation of species A is most likely in better agreement with the strong red-shift by 150 cm^{-1} of the related vibration as compared to the $\nu(\text{C–O})$ vibration in the ketone–enol dimer.

In case of species A, in which the C(1) atom establishes a bonding with the underlying Pt surface, the resulting reduced mass of the (Pt)C–O entity should strongly increase and thus, a significant red-shift of the related stretching vibration of the C–O bond is expected that should exceed the shift of the same group in case of species B. A third plausible scenario is the insertion of a hydrogen atom into the ketone at the oxygen atom of the ketone group. In this case, the chemical nature of the keto group changes as the oxygen atom of the former carbonyl group is not available for intermolecular hydrogen bonding and as a consequence, the dimers should fall apart. Assuming the molecule in the enol form of the original dimer can possibly transfer back to its ketone form to reestablish the intermolecular hydrogen bonding (pathway C), however, results in the identical species A.

Based on the experimental data, it cannot be unambiguously deduced if the hydrogen atom is inserted into the C=C or C=O bond. A plausible scenario is the former case as theoretical calculation predicted this pathway to be the one with the lower activation barrier as compared to the direct hydrogenation of the C=O bond.^[83–86] The red-shift of the stretching vibration related to the carbonyl group indicates that the intermolecular hydrogen bonding with the acidic hydrogen of the enol group weakens the C=O bond significantly and with this potentially also lowers the activation barrier for the direct insertion of the hydrogen. Both scenarios are in agreement with the spectroscopically observed reaction intermediate. However, it is important to point out that the formation of dimers on the surface, which forms partly hydrogenated acetophenone, appears to be the crucial first step in the hydrogenation of acetophenone. The mechanism can be most likely described as the stabilization of the C=C bond of the enol, that can be hydrogenated via a lower activation barrier pathway, or weakening of the C=O bond due to the acidic hydrogen of the enol.

In summary, we conclude that the normally unstable enol form of acetophenone is stabilized by acetophenone ketones on the surface via hydrogen bonding. The formation of enols can be prevented at high surface coverage of hydrogen (200 K, $\Theta \approx 0.95\text{ ML}$). This observation suggests that high concentration of surface hydrogen either prevents the formation of the enol species or forces the disaggregation of the ketone–enol dimers. At lower hydrogen coverage (260–240 K, $\Theta \approx 0.5\text{--}0.57\text{ ML}$), enols can be formed again, creating ketone–enol dimers on the surface. Additionally, a new type of dimer is observed in the presence of hydrogen at 240 K that is not formed on pristine Pt(111) at the same temperature. By means of an additional spectroscopic study, we identified a partially hydrogenated acetophenone species that is most likely attached to the second acetophenone molecule via hydrogen bonding. This observation suggests that dimers are preserved during the hydrogenation process and the formation of dimers appears to be crucial for the first hydrogenation step in this reaction.

Recently, we started a collaboration with the group of Wei Liu (Nanjing University of Science and Technology) to further support the experimental results on acetophenone over Pt(111) and H/Pt(111) with DFT calculations.

7 Conclusions

The aim of the present work was to investigate the fundamental processes of heterogeneous catalysis at the gas–solid interface under well-defined and reproducible conditions using the model catalyst approach. In particular, we focused on studying the influence of surface–adsorbate as well as adsorbate–adsorbate interactions on the hydrogenation of reactants containing C=O double bonds over Pt(111) and Pd(111) metal surfaces. Understanding important aspects of the coadsorbates, for instance, the influence on the adsorption geometry of the reactants, the role of intermolecular interactions, stabilization of the reaction intermediates as well as their potential to promote the selectivity of the overall chemical reaction were the main points of this investigation.

An unique combination of surface-sensitive spectroscopic (infrared reflection absorption spectroscopy, IRAS) and microscopic (scanning tunneling microscopy, STM) tools as well as molecular beam techniques was employed to investigate the surface reactions under operational conditions. In particular, we investigated the influence of lateral interactions on chemical reactions in heterogeneous catalysis by the example of i) artificial ligands which promote chemoselectivity, ii) lateral interactions weakening specific chemical bonds in a molecule and iii) stabilization of usually unstable enols via intermolecular interactions.

Partial Hydrogenation of Acrolein over Functionalized Pd(111) In this study, we provided for the first time a comprehensive atomistic-level description of ligand-directed heterogeneous catalysis for the chemoselective partial hydrogenation of the α,β -unsaturated aldehyde acrolein. Moreover, we investigated systematically the influence of geometric and electronic effects of ligand molecules as well as the stabilization of adsorbates via keto–enol tautomerization. It was shown that the functionalization of the Pd(111) with i) allyl cyanide, ii) 2-methyl-2-pentenal and iii) acetophenone results in the instantaneous and selective formation of the desired unsaturated alcohol (propenol) which is thermodynamically less stable as compared to the saturated aldehyde (propanal). The spectroscopic investigation revealed that the chemical structure of the ligand dramatically influences the electronic structure of the reaction intermediates formed on the surface. Thus, on the surface functionalized with allyl cyanide, the vibrational band related to the desired propenoxy reaction intermediate is strongly blue-shifted as compared to the pristine Pd(111) surface. The more spacious methyloxopentyl ligand results, however, in a strong change in the distribution of the abundance of the same reaction intermediates that are also observed on pristine Pd(111). This ligand is thus most likely occupying some of the active surface sites. The effect of the interaction of acetophenone with acrolein is strongly dependent on the AP coverage. While low coverage of AP hinders the hydrogenation of acrolein, high coverage of AP promotes the formation of the reactive ligand layer by acrolein molecules that can be most likely related to the intermolecular interaction of the oxopropyl ligand and the enol form of AP that results from the keto–enol tautomerization of acetophenone. The microscopic picture of the coadsorbed ligands show the formation of ligand layers that dynamically transforms their patterns upon bringing the catalyst to operational conditions.

Intermolecular Interactions of Ethyl Pyruvate Adsorbed on Pt(111) In this combined experimental and theoretical study, we investigated the adsorption and lateral interactions of ethyl pyruvate on Pt(111) and hydrogen precovered Pt(111) surfaces. EP molecules were shown to form a variety of different types of dimers, trimers and tetramers upon adsorption on Pt(111). Based on the correlation of both microscopic and spectroscopic data as well as according to DFT modeling, these surface species can be attributed to two large classes of oligomers that exhibit different types of intermolecular binding. The first class of species show lateral interactions that can most likely be related to the methyl group of one molecule and the ketone group of the neighboring molecule. In the second class of species, the interactions between the ester-O and the neighboring methyl group, that result in a strong weakening of the corresponding ester-O bond, fits best to the experimental data as well as the theoretical modeling. The lateral interactions are sensitive to surrounding hydrogen and can be transformed from one species to the other via in-situ hydrogen adsorption.

Keto–Enol Tautomerization as the First Step in the Hydrogenation of Carbonyl Compounds In this study, we investigated the surface-driven keto–enol tautomerization of the α -methyl ketone acetophenone. It was found out that the enol form of acetophenone is not formed from a monomer but exists only in combination with a neighboring ketone molecule forming different types of ketone–enol oligomers. According to the experimental observations, there are a ketone–enol dimers that most likely exhibit a strong hydrogen bonding between the –OH group of the enol and the C=O entity of the ketone, which points to a significant perturbation of the electronic structure. It was also shown that at elevated temperature, the evolution of ketone–enol–enol trimers are observed. The hydrogenation process occurs in these ketone–enol dimers that results in the formation of partly hydrogenated acetophenone species attached via hydrogen bonding to the second acetophenone molecule.

In summary, for all the systems studied, we observed strong effects of lateral interactions between coadsorbed molecules that significantly affect the chemical processes occurring at the catalytic surfaces, i.e. a reactive ligand layer promoting chemoselectivity toward a desired product, formation of ketone–enol dimers as the first step of the hydrogenation reaction of acetophenone and a strong weakening of the ester bond due to intermolecular interactions in the case of ethyl pyruvate. The results of these studies provide deep atomistic-level insights in the mechanisms of surface processes mediated by coadsorbed ligand molecules. We could show that one of the most important aspects in heterogeneous catalysis, i.e. controlling the activation barriers of competing chemical reactions, can be addressed by ligand-directed catalysis. Moreover, the experimental results presented in this work provide a starting idea of how lateral interactions can be employed as useful tools for rational design of new catalytic materials with tailor-made catalytic properties.

8 Reprints of Publications

8.1 Understanding Ligand-Directed Heterogeneous Catalysis: When the Dynamically Changing Nature of the Ligand Layer Controls the Hydrogenation Selectivity

Publication Data and Reprint

Reference: Carsten Schröder, Marvin C. Schmidt, Philipp A. Haugg, Ann-Katrin Baumann, Jan Smyczek and Svetlana Schauermann

DOI: 10.1002/anie.202103960

Submitted: 19.03.2021

Accepted: 19.05.2021

Contribution: Development of the experimental approach, all IRAS measurements, experimental planning (IR and STM), complete IR and kinetic data analysis, development of the adsorption models, preparation of the manuscript, DFT gas phase calculations.

Copyright: Reprinted with permission from *Angewandte Chemie International Edition* from Ref.[175]. Copyright 2021 John Wiley and Sons.



Heterogeneous Catalysis Hot Paper

How to cite: *Angew. Chem. Int. Ed.* **2021**, *60*, 16349–16354

International Edition: doi.org/10.1002/anie.202103960

German Edition: doi.org/10.1002/ange.202103960

Understanding Ligand-Directed Heterogeneous Catalysis: When the Dynamically Changing Nature of the Ligand Layer Controls the Hydrogenation Selectivity

Carsten Schröder, Marvin C. Schmidt, Philipp A. Haugg, Ann-Katrin Baumann, Jan Smyczek, and Swetlana Schauerermann*

Abstract: We present a mechanistic study on the formation and dynamic changes of a ligand-based heterogeneous Pd catalyst for chemoselective hydrogenation of α,β -unsaturated aldehyde acrolein. Deposition of allyl cyanide as a precursor of a ligand layer renders Pd highly active and close to 100% selective toward propenol formation by promoting acrolein adsorption in a desired configuration via the C=O end. Employing a combination of real-space microscopic and *in-operando* spectroscopic surface-sensitive techniques, we show that an ordered active ligand layer is formed under operational conditions, consisting of stable *N*-butylimine species. In a competing process, unstable amine species evolve on the surface, which desorb in the course of the reaction. Obtained atomistic-level insights into the formation and dynamic evolution of the active ligand layer under operational conditions provide important input required for controlling chemoselectivity by purposeful surface functionalization.

One of the major challenges in heterogeneous catalysis is a precise control over the selectivity of a catalytic process, which depends on subtle differences in the energy barriers of competing reaction pathways. A promising strategy to tackle this problem is to introduce a specific selective interaction between a reactant and an active site, which governs the chemical transformations in the desired direction. This idea has been successfully realized in enantioselective heterogeneous catalysis via functionalization of metal surfaces with ligand-like adsorbates—chiral modifiers—with many of these systems being nowadays well-understood at the mechanistic level.^[1] Recently, a new type of ligand-directed heterogeneous catalysis—chemoselective catalysis—gained more attention as new highly chemoselective powdered catalysts were developed for partial hydrogenation of multi-unsaturated

oxygenates or semi-hydrogenation of alkynes.^[2] These developments demonstrate a great potential of this emerging technology to controllably tune the surface structure and the lateral reactant-ligand interactions in order to provide the tailor-made environment for the desired reaction steps.

Despite the impressive progress in this field demonstrated on powdered materials, the mechanistic details of the underlying ligand-directed surface processes remain only poorly understood for the most systems. Recently, we reported a mechanistic study on selective hydrogenation of an α,β -unsaturated aldehyde acrolein over Pd(111), in which the C=O bond was hydrogenated with 100% selectivity to produce the target product propenol.^[3] This chemistry occurs, however, not on pristine Pd(111), but on the surface densely packed with oxopropyl ligands, which are spontaneously formed on the early stages of partial acrolein hydrogenation. Although this mechanistic study provided some starting ideas about the microscopic origin of the ligand-related effects, an in-depth atomistic understanding of the active ligand layer is largely missing. Specifically, the elementary steps leading to formation of an active ligand layer, its chemical composition and the possible dynamic changes under the reaction conditions needs to be understood, in order to approach rational design of this new promising class of materials with tailor-made catalytic properties.

Here, we report the proof-of-principal mechanistic study on purposeful formation of a catalytically highly efficient ligand layer based on model Pd(111) catalyst functionalized with allyl cyanide (AC) for selective hydrogenation of acrolein. By combination of *in operando* infrared reflection absorption spectroscopy (IRAS), scanning tunnelling microscopy (STM) and molecular beam techniques, formation and dynamic changes of the ligand layer under reaction conditions were investigated at the atomistic level. While AC forms a self-assembled 2D layer under non-reactive conditions, in which the flat lying molecules largely preserve their chemical nature, strong changes occur under the reactive conditions both in terms of the chemical nature and the spatial distribution of the ligand species. Specifically, AC transforms to *N*-butylimine species resulting from partial hydrogenation of the original ligand, which are adsorbed in a more upright configuration and form a more densely packed layer, adopting the hexagonal symmetry of the underlying metal. On this active layer, acrolein nearly instantaneously forms the desired propenoxy reaction intermediate followed by evolution of the target product propenol. The dynamic changes of the ligand layer induced by the reaction conditions were identified as

[*] C. Schröder, M. C. Schmidt, P. A. Haugg, A.-K. Baumann, J. Smyczek, Prof. Dr. S. Schauerermann
Institute of Physical Chemistry, Christian-Albrechts-University Kiel
Max-Eyth-Str. 2, 24118 Kiel (Germany)
E-mail: schauerermann@pctc.uni-kiel.de

Supporting information and the ORCID identification number(s) for the author(s) of this article can be found under:
<https://doi.org/10.1002/anie.202103960>.

© 2021 The Authors. *Angewandte Chemie International Edition* published by Wiley-VCH GmbH. This is an open access article under the terms of the Creative Commons Attribution Non-Commercial NoDerivs License, which permits use and distribution in any medium, provided the original work is properly cited, the use is non-commercial and no modifications or adaptations are made.

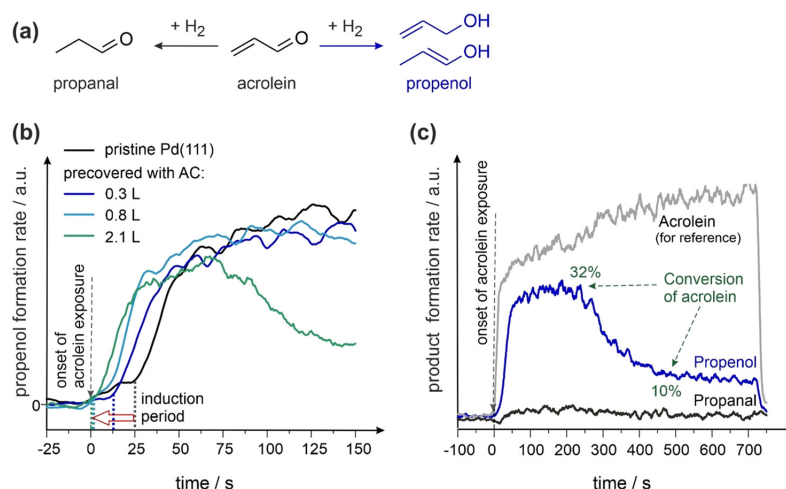


Figure 1. a) Competing reaction pathways for acrolein hydrogenation (b) Formation rates of propenol on pristine and AC-precovered Pd(111) at 250 K; (c) formation rates of propenol and propenal on Pd(111) precovered with 0.8 L AC at 250 K.

a crucial process rendering the surface highly active and selective in partial hydrogenation of acrolein at the C=O bond. Obtained insights provide a deep atomistic level understanding of the most important working principles of ligand-directed heterogeneous catalysis.

Selective partial hydrogenation of acrolein, leading to formation of propenol as a target and propenal as a non-desired product (Figure 1a), was investigated on Pd(111) surface functionalized with AC. The catalytic activity was probed by molecular beams combined with quadrupole mass spectrometry (QMS) under isothermal conditions in an apparatus described elsewhere.^[4] Figure 1b shows the time evolution of the propenol formation rate in the gas phase for pristine and AC-precovered Pd(111) at different AC coverages. In each experiment, the surface was first exposed continuously to a H₂ beam, at a time indicated as zero the second molecular beam was opened to dose acrolein (for details see Supporting Information, SI; in the following, the simultaneous exposure to H₂ and acrolein at the reaction temperature will be denoted as “reaction conditions” for the reactivity measurements). On pristine Pd(111), a prolonged induction period is observed before the onset of propenol evolution. Previously, we have shown that during the induction period an oxopropyl ligand layer is formed as a result of a single H insertion into the C=C bond of adsorbed acrolein, which turns the surface close to 100% selective toward C=O bond hydrogenation.^[3,5] On Pd(111) functionalized with AC prior the reaction, the induction period becomes either strongly reduced at intermediate AC coverages or even completely vanishes at coverages close to a monolayer. For all functionalized surfaces propenol is formed with the estimated selectivity in the range 95–100%, which will be denoted in the following as “close to 100%”, and fairly high conversion (up to 32%) as exemplarily shown in Figure 1c. These observations demonstrate that surface functionalization with AC

renders it highly selective and can be used for rational design of ligand-containing catalysts without relying on spontaneous formation of the oxopropyl ligand layer.

To get more insights into the formation of the active ligand layer and the reaction intermediate, a combination of *in operando* IRAS and kinetic studies via molecular beams was performed in a broad reaction parameter range. Figure 2a shows the propenol formation rate over AC-functionalized Pd(111) at 250 K upon pulsing of acrolein onto the surface continuously exposed to H₂. During the indicated periods of time (1–5), IR spectra were obtained on this surface, shown in Figure 2b as spectra 1–5. The spectrum 0

corresponds to the same surface prior to exposure to acrolein. On this non-reactive surface, two most important peaks are observed at 1746 and 1582 cm⁻¹, which are not present in non-perturbed AC and are related to a partly hydrogenated derivatives of AC. The band at 1746 cm⁻¹ was previously described as a (C=N...Pd) stretching vibration for structurally similar acetonitrile and methyl isocyanide.^[6] The band at 1582 cm⁻¹ is typical of δ(NH₂) deformation vibration in simple amines.^[7] While the exact nature and formation of these species will be discussed the detail later, it is important to point out that AC does not retain its original chemical structure in presence of H₂ and transforms to two new species with spectroscopic signatures characteristic of imines and amines. Upon dosing of acrolein (spectra 1–4), a new band at 1166 cm⁻¹ appears nearly instantaneously on AC-functionalized Pd(111), which presence strongly correlates with the evolution of propenol in the gas phase, and vanishes when the acrolein beam is interrupted (spectrum 5). Following the assignment made in our previous study on pristine Pd(111), we attribute this band to a C-O vibration in a direct reaction intermediate (RI) propenoxy-species CH₂=CH-CH-O...Pd, in which the C-O entity is attached to Pd through the O atom (for details see SI, Chapter IV). Importantly, on the AC-covered surface, this band shifts by 46 cm⁻¹ pointing to a strong lateral interaction between the RI and the ligand layer.

Another striking observation is that the evolution of two prominent AC-related surface species is not directly correlated with the reactant supply or evolution of the target product propenol: the imine species containing a C=N...Pd bond (1746–1755 cm⁻¹) remain constantly present on the surface irrespectively of the reactant supply, while the species containing a -NH₂ group slowly disappear in the course of the reaction. Additionally, a band at 1330 cm⁻¹ evolves, which results from partial decomposition of acrolein to ethylidene-

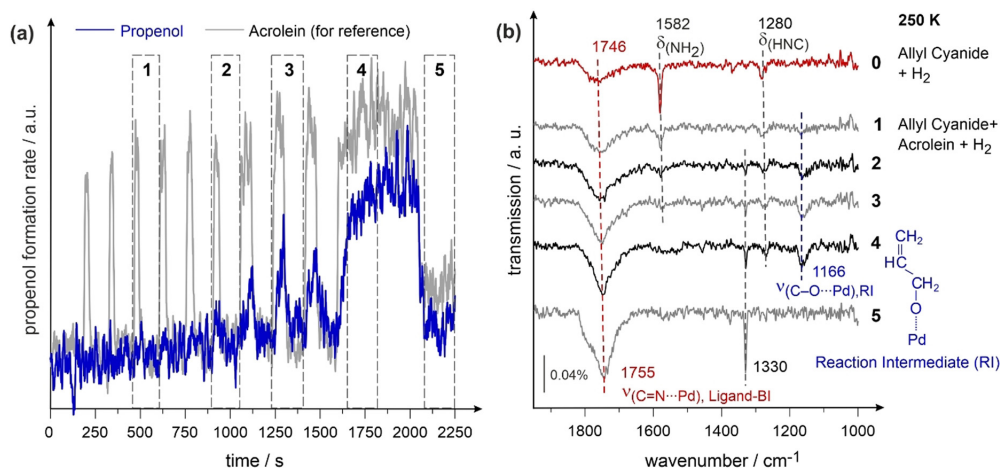


Figure 2. a) Formation rate of propenol on Pd(111) precovered with 1.0 L AC at 250 K measured in a pulsed experiment; b) IR spectra of 1.0 L AC prior to the beginning of the reaction (spectrum 0) and IR spectra obtained on the same surface after the beginning of the reaction. The spectra 1–5 were obtained during the time slots indicated in (a) as 1–5; full details can be found in Chapter II in SI.

like species.^[8] The evolution of these species is responsible for reactivity decrease after the initial period of high propenol formation rate (more details on reactivity decrease in Chapter VIII in SI).

These datasets provide a clear indication that formation of the direct RI propenoxy ($\text{CH}_2=\text{CH}-\text{CH}-\text{O}\cdots\text{Pd}$) species and the target product propenol is strongly affected by the ligand formed under the reaction conditions on the AC-functionalized surface.

To get more atomistic level insights into the chemical and geometric structure of the active ligand layer forming and dynamically changing under the reaction conditions, a combined microscopic and spectroscopic study was performed on AC adsorbed on pristine and H-containing Pd(111) in a broad temperature range. Figure 3 shows the STM images obtained

under non-reactive (Figure 3a–c) vs. reactive conditions (Figure 3d). Note that the term “reaction conditions” for STM measurements is related to AC adsorbed on Pd(111) in presence of H_2 at the specific reaction temperature. In both cases, AC adsorbates form ordered layers on these surfaces, exhibiting, however, strongly different patterns. To the best of our knowledge, this is the first experimental proof of the formation of an active ligand layer obtained by real space microscopy (Figure 3d), which exhibits a high degree of ordering and by this provides a specific confinement, allowing for a desired adsorption configuration of the reactant. In our previous studies on acrolein hydrogenation, formation of an ordered oxopropyl ligand layer was hypothesized,^[3a] but was not yet proven experimentally. Complementarily, the chemical nature of the adsorbed species was investigated by IRAS on both types of surfaces (Figure 4).

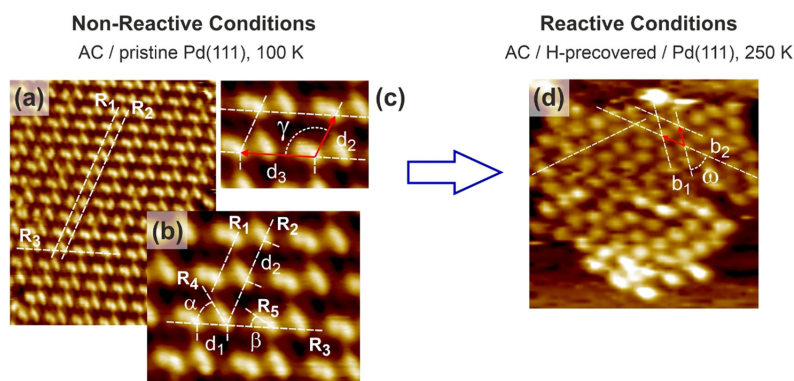


Figure 3. a) STM image of allyl cyanide on pristine Pd(111) at 230 K ($15.9 \times 19.1 \text{ nm}^2$); b) close-up image ($5.8 \times 4.6 \text{ nm}^2$) from (a) indicating three main rows in the 2D self-organized AC layer; c) close-up image showing the unit cell of the 2D AC layer; d) STM image of allyl cyanide on H-precovered Pd(111) at 250 K ($10.6 \times 10.8 \text{ nm}^2$). Full experimental details can be found in Chapter II in SI.

Under non-reactive conditions, AC forms a 2D self-assembled layer (Figure 3a–c), which consists of individual entities, each showing a brighter (head) and darker (tail) protrusions. Generally, each adsorbate in this layer exhibits a 2-point interaction, which is realized via interaction of each head with two tails and each tail with two heads. Figure 3b shows this structure in more detail: there are two parallel rows R_1 and R_2 of adsorbates, which are inclined with respect to the axis R_3 by $69 \pm 1^\circ$. The distance between the heads in the row R_3 $d_1 = 8.3 \pm 0.2 \text{ \AA}$,

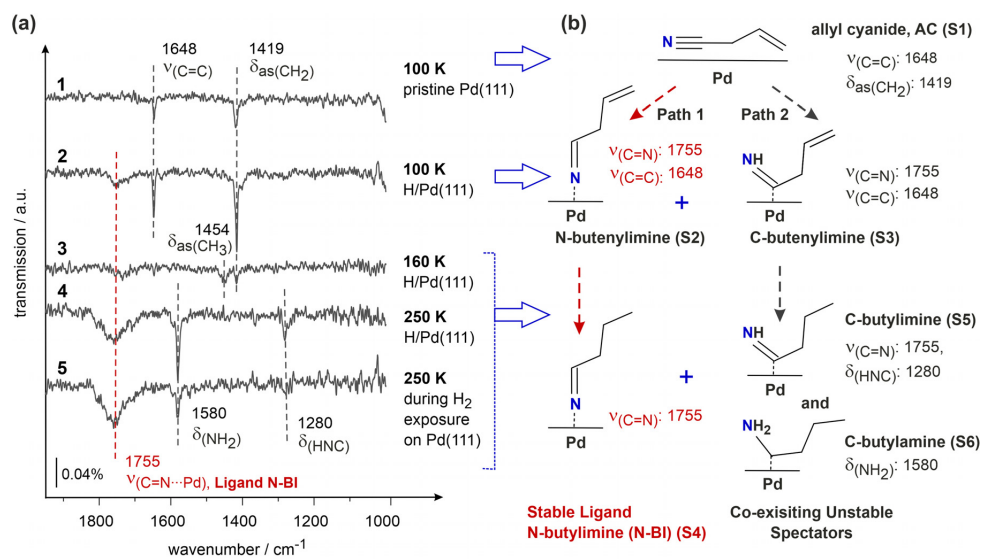


Figure 4. a) IR spectra of AC adsorbed on Pd(111) at indicated temperatures. The spectrum 1 is obtained on pristine and the spectra 2–4 on H-precovered Pd(111). Spectrum 5 is recorded during continuous H₂ exposure under the reaction conditions (full details can be found in Chapter II in SI); b) Reaction Scheme showing chemical transformations of AC according to two competing reaction pathways as deduced from (a).

which corresponds to $(3.0 \pm 0.1) \times d_{\text{Pd-Pd}}$ with $d_{\text{Pd-Pd}}$ being the spacing between two Pd atoms (2.75 Å). The distance d_2 between two heads along the rows R_1 and R_2 amounts to $(4.8 \pm 0.1) \times d_{\text{Pd-Pd}}$. The main axis R_4 of the molecules lying in the row R_1 is inclined with respect to the axis R_3 by $\alpha = 61 \pm 1^\circ$, while the main axis R_5 of the molecules constituting the row R_2 is tilted by the angle $\beta = 37 \pm 1^\circ$ with respect to R_3 . Figure 3c shows the unit cell of the AC 2D self-organized layer with the lattice parameters $d_2 = (4.8 \pm 0.1) \times d_{\text{Pd-Pd}}$; $d_3 = (7.6 \pm 0.1) \times d_{\text{Pd-Pd}}$ and $\gamma = 106 \pm 1^\circ$.

The IR spectra related to non-reactive conditions are shown in Figure 4a (spectrum 1, 100 K) and in Figure SI_2 in SI (100–250 K). At 100 K, only two major vibrational bands are observed: at 1648 ($\nu(\text{C}=\text{C})$) and 1419 cm^{-1} ($\delta(\text{CH}_2)$), while the normally intense band related to the CN-group (2250 cm^{-1}) is not seen.^[9] The latter observation originates most likely from the nearly parallel orientation of the CN-group with respect to the metal plane making it invisible for IRAS due to the metal surface selection rule (MSSR).^[10] At elevated temperatures, the intensity of both bands (1648 and 1419 cm^{-1}) strongly decrease most probably due to the changes in the adsorption configuration making the entire molecule oriented nearly flat with respect to the metal plane (for additional discussion see SI, Chapter V), which is consistent with the elongated form of the adsorbates imaged by STM. Combined microscopic and spectroscopic information result in the atomistic model of this ligand layer under non-reactive conditions shown in Figure 5a. The adsorbates are separated by $5 \times d_{\text{Pd-Pd}}$ along the row R_3 , while the distance between R_1 and R_2 corresponds to the separation by $3 \times d_{\text{Pd-Pd}}$. The angles between the molecular axes with respect to R_3 (α and β) amount to $\approx 37^\circ$ and 61° , respectively. The mutual

intermolecular interactions between the adsorbates are most likely based on H-bonding between the N-atom of each molecule and the H atoms of the terminal CH₂ group of two neighboring adsorbates (visualized by red dotted lines). It should be noted that while the exact position of the CN groups cannot be derived unambiguously from the STM data, it is likely that the electron rich CN group is related to the brighter part of the molecule, that is, the head-position.

Upon transition to the reactive conditions, the 2D self-assembled ligand layer undergoes dramatic changes both in terms of the geometric structure and the chemical nature of the adsorbates. Here, an ordered layer of the hexagonal symmetry is formed (Figure 3d) with the adsorbates exhibiting a nearly round footprint in STM. The spacing between the adsorbates along the axes shown in Figure 3d is $b_1 = (2.7 \pm 0.3) \times d_{\text{Pd-Pd}}$ and $b_2 = (3.1 \pm 0.1) \times d_{\text{Pd-Pd}}$ (red vectors b_1 and b_2 show the unit cell of this layer; $\omega = 53 \pm 2^\circ$). This transition is also accompanied by substantial changes in the chemical composition of the originally deposited AC ligand. Figure 4a shows the IR spectra obtained on H-precovered Pd(111) surface at successively increasing temperatures (spectra 2 and 3), which finally reaches the state of the catalyst under operational conditions (spectra 4 and 5). At 100 K, AC adsorbed on H-covered surface still retains two peaks typical of molecularly adsorbed AC: 1648 ($\nu(\text{C}=\text{C})$) and 1419 ($\delta(\text{CH}_2)$) cm^{-1} .^[9] Importantly, a new peak at 1755 cm^{-1} appears, which is present neither in multilayer nor in the gas phase AC.^[9] Previously, this vibration was observed for structurally similar molecules acetonitrile and methyl isocyanide upon adsorption on Pd(111)^[6b] and was attributed to imine species, in which the band at 1755 cm^{-1} is related to the stretching vibration of the (C=N) bond in the (C=N---Pd) fragment. This

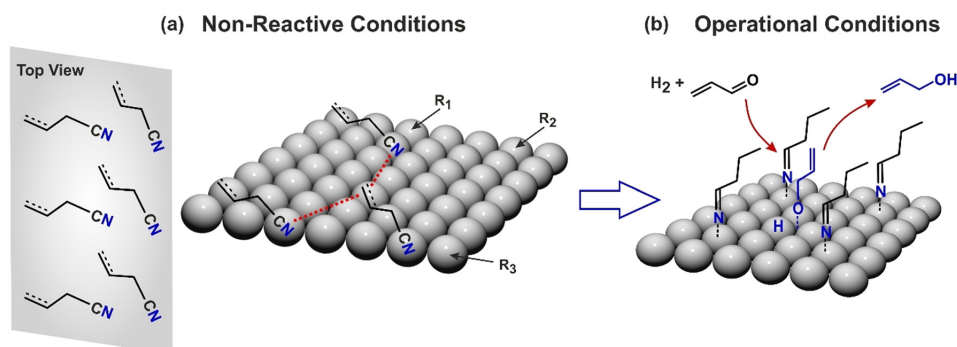


Figure 5. Model of adsorbed AC-derived species under a) non-reactive and b) operational conditions in presence of H_2 and acrolein. For additional discussion on the AC structure in (a), see SI, Chapter V.

observation suggests partial reduction of the $C\equiv N$ triple to the $C=N$ double bond accompanied by formation of the species strongly bound to Pd. Generally, two possible configurations of these species are possible: bound either through the N or the C atom, which are shown in the scheme of the Figure 4b and indicated as N- and C-butylimine (S2 and S3, respectively).

At 160 K, the further hydrogenation step occurs giving rise to (i) disappearance of the peaks at 1648 ($\nu(C=C)$) and 1419 ($\delta(CH_2)$) cm^{-1} and (ii) appearance of a new peak at 1454 cm^{-1} corresponding to the CH_3 deformation vibration ($\delta(CH_3)$).^[11] The combination of these observations suggest that the $C=C$ bond becomes hydrogenated in this temperature range and a new terminal $-CH_3$ group appears.

At 250 K (spectra 4 and 5), further hydrogenation steps occur mainly resulting in (i) significant growth of the peak at 1755 cm^{-1} ($-C=N\cdots Pd$) and (ii) appearance of two new peaks at 1580 and 1280 cm^{-1} , which are characteristic of $-NH_2$ and HNC deformation vibrations, respectively.^[12] Simultaneous appearance of these bands means that both imine and amine species are formed and co-exist in this temperature range. It also suggests that at least two reaction pathways run in parallel to transfer the originally deposited AC to co-existing imine and amine surface species.

Figure 4b displays a model for the proposed AC reaction pathways, which is consistent with all spectroscopic observations. For all species, the characteristic bands employed for assignment are given next to the proposed structure. At 100 K, AC deposited on pristine Pd(111) exhibits an adsorption geometry with the CN group oriented nearly parallel to the surface, while the $C=C$ group is inclined and hence visible in IRAS (species S1). When H is co-adsorbed at 100 K, a fraction of these species is capable of forming the imine group ($-C=N\cdots Pd$, 1755 cm^{-1}). The formed butenylimine species can be bound to the surface either via the N-end (N-butylimine, S2 species) or via the C-atom (C-butylimine, S3 species) and undergo further partial hydrogenation steps. In the first pathway, the N-butylimine species (S2) is hydrogenated at the $C=C$ bond producing the N-butylimine (S4) species in the temperature range 160–250 K. In the second pathway, the C-butylimine (S3) species are also

hydrogenated at the $C=C$ bond forming C-butylimine species (S5). However, hydrogenation does not stop at this stage and in the fraction of S5 species, the imine group is hydrogenated to amine forming C-butylamine species (S6). The species S5 and S6 co-exist on the surface and evolve in a very similar way: they appear in the same temperature range and both disappear in a correlated way upon prolonged H_2 exposure in the course of the reaction as can be deduced from the comparison of the spectra 4 and 5 in Figure 4b. Note that the characteristic vibrations used to identify the species S5 and S6 ($\delta(HNC)$ at 1280 and $\delta(NH_2)$ at 1580 cm^{-1}) cannot originate from the same surface species. On the other hand, the nearly identical evolution of these species upon temperature variation and prolonged exposure to H_2 suggest that the species S5 and S6 are strongly correlated, most likely as a precursor (S5) and the product (S6). Thus, the combination of all spectroscopic data suggest that the originally adsorbed AC species S1 becomes partly hydrogenated under the reaction conditions along two competing reaction pathways: the first one leads to formation of the N-butylimine (S4) species, while the second results in the formation of the mixture of C-butylimine (S5) and C-butylamine (S6) species.

It is important to emphasize that one type of species—N-butylimine (S4)—remains present on the catalytic surface under the reaction conditions and serves as an active ligand layer. The other two species—C-butylimine (S5) and C-butylamine (S6)—quickly disappear after prolonged H_2 exposure (see Figure 4b, spectra 4 and 5; Figure 2, spectra 0–5), most likely as a result of successive hydrogenation of the $C=N$ bond of C-butylimine (S5) to C-butylamine (S6) followed by H insertion into the $C\cdots Pd$ bond to produce molecular butylamine that is able to desorb (for additional discussion on the stability of S5 and S6 species see SI, Chapter X; the stability of the S4 species is additionally discussed in SI, Chapter III). This observation suggests that species building an active ligand layer under the reaction conditions are the stable N-butylimine (S4) species, while the mixture of the unstable species C-butylimine (S5) and C-butylamine (S6) are the spectators disappearing in the course of the reaction without affecting the catalytic efficiency.

Figure 5 b shows the model of the geometric orientation of the active N-butylimine (S4) species based on the STM data: all ligand molecules are separated by approx. $3 \times d_{\text{Pd-Pd}}$, meaning that each third Pd atom along the main axis is covered by the ligand. The clearly visible band at 1755 cm^{-1} characteristic of the imine species suggests a rather upright adsorption geometry, which is also reflected in this model.

Summarizing, we provide for the first time a comprehensive atomistic level description of a ligand-based heterogeneous catalyst for chemoselective hydrogenation of α,β -unsaturated aldehyde acrolein. Deposition of allyl cyanide as a precursor of an active ligand layer renders the catalyst highly active and close to 100% selective toward propenol formation and eliminates the induction period observed on pristine surfaces. Formation and dynamic evolution of the active ligand layer under the reaction conditions were investigated by combination of *in operando* spectroscopic and microscopic surface sensitive techniques. On pristine Pd and under non-reactive conditions, AC forms a self-assembled 2D layer with the species oriented close to parallel to the surface and exhibiting a two-point interaction between the -CN and the CH_x groups of neighboring molecules. Upon transferring to the reaction conditions, both the chemical nature of the adsorbates and the geometric configuration of the ligand layer drastically change. In two competing reaction pathways, both stable N-butylimine active ligand species and unstable spectator species are formed. These latter species comprising C-butylamine and C-butylimine desorb in the course of the reaction after prolonged H_2 exposure. The stable N-butylimine species forms an ordered ligand layer acting under the reaction conditions, in which every third Pd atom is covered by N-butylimine adsorbate. With this we provide for the first time a direct microscopic proof that ordered layers of active ligand species are formed, which govern the interaction of acrolein with the catalyst by lateral interactions and by this render the surface highly chemoselective.

Obtained atomistic-level insights highlight the exceptional importance of controlling the chemical and geometrical structure of dynamically changing active ligand layer under operational conditions. Related effects are expected to play a key role for chemoselective hydrogenation of all types of multi-unsaturated hydrocarbons over ligand-functionalized catalysts including practically relevant powdered materials.

Acknowledgements

This work has been supported by the German Science Foundation (DFG, Grant SCHA 1477/6-1). Open access funding enabled and organized by Projekt DEAL.

Conflict of interest

The authors declare no conflict of interest.

Keywords: chemoselective hydrogenation · functionalized surfaces · heterogeneous catalysis · infrared spectroscopy · scanning tunnelling microscopy

- [1] a) F. Meemken, A. Baiker, *Chem. Rev.* **2017**, *117*, 11522; b) A. J. Gellman, W. T. Tysoe, F. Zaera, *Catal. Lett.* **2015**, *145*, 220.
- [2] a) S. G. Kwon, et al., *Nano Lett.* **2012**, *12*, 5382; b) S. T. Marshall, J. W. Medlin, *Surf. Sci. Rep.* **2011**, *66*, 173; c) S. T. Marshall, et al., *Nat. Mater.* **2010**, *9*, 853; d) P. Sonström, M. Baumer, *Phys. Chem. Chem. Phys.* **2011**, *13*, 19270.
- [3] a) K.-H. Dostert, et al., *J. Am. Chem. Soc.* **2015**, *137*, 13496; b) K.-H. Dostert, et al., *ACS Catal.* **2017**, *7*, 5523; c) S. Schauer- mann, *J. Phys. Chem. Lett.* **2018**, *9*, 5555.
- [4] S. Attia, E. J. Spadafora, J. Hartmann, H.-J. Freund, S. Schauer- mann, *Rev. Sci. Instrum.* **2019**, *90*, 053903.
- [5] C. P. O'Brien, K.-H. Dostert, S. Schauer- mann, H.-J. Freund, *Chem. Eur. J.* **2016**, *22*, 15856.
- [6] a) S. Katano, et al., *J. Phys. Chem. B* **2006**, *110*, 20344; b) K. Murphy, S. Azad, D. W. Bennett, W. T. Tysoe, *Surf. Sci.* **2000**, *467*, 1.
- [7] a) D. Jentz, H. Celio, P. Mills, M. Trenary, *Surf. Sci.* **1995**, *341*, 1; b) W. Erley, J. C. Hemminger, *Surf. Sci.* **1994**, *316*, L1025.
- [8] F. Zaera, *Langmuir* **1996**, *12*, 88.
- [9] J. R. Durig, G. A. Guirgis, A. S. Drew, *J. Raman Spectrosc.* **1994**, *25*, 907.
- [10] F. M. Hoffmann, *Surf. Sci. Rep.* **1983**, *3*, 107.
- [11] D. C. McKean, et al., *Spectrochim. Acta Part A* **1985**, *41*, 435.
- [12] L. Vogt, E. Schulte, S. Collins, P. Quaino, *Top. Catal.* **2019**, *62*, 1076.

Manuscript received: March 19, 2021
Revised manuscript received: May 3, 2021
Accepted manuscript online: May 19, 2021
Version of record online: June 18, 2021

8.2 Competing Reaction Pathways in Heterogeneously Catalyzed Hydrogenation of Allyl Cyanide: The Chemical Nature of Surface Species

Publication Data and Reprint

Reference: Carsten Schröder, Philipp A. Haugg, Ann-Katrin Baumann, Marvin C. Schmidt, Jan Smyczek and Swetlana Schauermann

DOI: 10.1002/chem.202103238

Submitted: 07.09.2021

Accepted: 04.10.2021

Contribution: Development of the experimental approach, planning/supervision of IRAS measurements, supervision of Philipp Haugg's bachelor thesis, complete experimental planning and data analysis, development of the adsorption models, preparation of the manuscript, DFT gas phase calculations.

Copyright: Reprinted with permission from Chemistry - A European Journal from Ref.[176]. Copyright 2021 John Wiley and Sons.

Special
Issue

Competing Reaction Pathways in Heterogeneously Catalyzed Hydrogenation of Allyl Cyanide: The Chemical Nature of Surface Species

Carsten Schröder,^[a] Philipp A. Haugg,^[a] Ann-Katrin Baumann,^[a] Marvin C. Schmidt,^[a] Jan Smyczek,^[a] and Swetlana Schauer^{*,[a]}

Abstract: We present a mechanistic study on the formation of an active ligand layer over Pd(111), turning the catalytic surface highly active and selective in partial hydrogenation of an α,β -unsaturated aldehyde acrolein. Specifically, we investigate the chemical composition of a ligand layer consisting of allyl cyanide deposited on Pd(111) and its dynamic changes under the hydrogenation conditions. On pristine surface, allyl cyanide largely retains its chemical structure and forms a layer of molecular species with the CN bond oriented nearly parallel to the underlying metal. In the presence of hydrogen, the chemical composition of allyl cyanide strongly changes. At 100 K, allyl cyanide transforms to unsaturated

imine species, containing the C=C and C=N double bonds. At increasing temperatures, these species undergo two competing reaction pathways. First, the C=C bond become hydrogenated and the stable N-butylimine species are produced. In the competing pathway, the unsaturated imine reacts with hydrogen to fully hydrogenate the imine group and produce butylamine. The latter species are unstable under the hydrogenation reaction conditions and desorb from the surface, while the N-butylimine adsorbates formed in the first reaction pathway remain adsorbed and act as an active ligand layer in selective hydrogenation of acrolein.

Introduction

Controlling selectivity in chemical transformations of multi-unsaturated hydrocarbons is one of the most important challenges in modern heterogeneous catalysis. Specifically for the competing reaction pathways exhibiting only small differences in the activation barriers, the distribution of the products might be very broad and is difficult to control by using typical single-metal heterogeneous catalysts. Thus, a catalytic surface showing high activity for the desired reaction route might also greatly accelerate the unwanted reaction paths. A strategy to overcome this problem is to introduce a specific selective interaction between a reactant and a catalytically active site, which can govern the chemical transformations only into the desired direction. Such highly specific reactant/active site interactions are ubiquitous in enzymes^[2] and have been successfully implemented into homogeneous catalysts through

for example modification of an active metal site with specific organic ligands.^[3]

Currently, a similar approach is being developed for heterogeneously catalyzed reactions by combining two functionalities inherent to heterogeneous and homogeneous catalysis: high activity of a catalytic metal surface and a specific interaction between the reactant and the active site, directing the chemical transformations towards the desired reaction route.^[4] One of the most successful strategies within this approach is the functionalization of a catalytic surface with ligand-like adsorbates, for example organic adsorbates or covalently bonded functional groups, allowing for a selective promotion of the desired reaction pathway. Recently, such surface modification has gathered significant interest for the development of "ligand-directed" heterogeneous catalysis for a variety of reactions,^[4b,e,5] in which the pre-adsorbed surface ligands induce specific adsorbate-adsorbate interactions with the reactant and by this turn the catalytic surface highly chemoselective. Thus, the deposition of n-alkanethiol onto Pd nanoparticles was reported to dramatically enhance the catalytic selectivity in 1-epoxy-3-butene selective hydrogenation on the olefinic bond from 10 to 94%.^[4a] Kunz et al.^[5b] reported that the modification of Pt nanoparticles with proline results both in strong increase of chemoselectivity in hydrogenation of acetophenone to phenylethanol and considerable raise of the conversion to almost 100%. Binghui et al.^[6] demonstrated that the presence of surface oleyamine array on PtCo nanocrystals leads to >90% selectivity towards C=O bond hydrogenation in α,β -unsaturated aldehydes containing both C=C and C=O double bonds. Recently, Medlin et al.^[5f] demonstrated in a

[a] C. Schröder, P. A. Haugg, A.-K. Baumann, M. C. Schmidt, J. Smyczek, Prof. Dr. S. Schauer
Institute of Physical Chemistry
Christian-Albrechts-University Kiel
Max-Eyth-Str. 2, 24118 Kiel (Germany)
E-mail: schauer@pctc.uni-kiel.de

Part of a Special Issue on Contemporary Challenges in Catalysis.

© 2021 The Authors. Chemistry - A European Journal published by Wiley-VCH GmbH. This is an open access article under the terms of the Creative Commons Attribution Non-Commercial NoDerivs License, which permits use and distribution in any medium, provided the original work is properly cited, the use is non-commercial and no modifications or adaptations are made.

number of studies that “surface crowding” with thiolate-based self-assembled monolayers and other organic surface modifiers can be used to control the orientation of various multi-unsaturated reactants and considerably improve the selectivity towards the desired reaction pathway. Glorius et al.^[7] reported significantly enhanced selectivity and activity in selective hydrogenation of acetophenone, trans-stilbene and phenylacetylene over Pd/Al₂O₃ and Ru/Al₂O₃ catalysts functionalized with N-heterocyclic carbens.

In our recent mechanistic studies^[8] on chemoselective hydrogenation of an α,β -unsaturated aldehyde acrolein to unsaturated alcohol propenol over model Pd catalysts, we have shown that surface functionalization with ligands turns the catalyst highly active and nearly 100% selective toward the target product unsaturated alcohol. Specifically, it was shown that Pd(111) functionalized with allyl cyanide (AC) prior the reaction becomes highly active and selective toward the formation of the desired product propenol. In that study, we found indications that the chemical nature of the originally deposited AC dynamically changes under the reactive conditions – in presence of hydrogen and at elevated temperatures – allowing formation of a specific ligand layer, which enables acrolein adsorption in the desired adsorption geometry – via the O-end – and by this promotes its selective hydrogenation. The surface ligand species were identified as N-butylimine species, which remain stable under the reaction conditions applied for acrolein hydrogenation.^[8]

While some aspects of the chemical transformation of AC on Pd(111) under the reaction conditions were addressed in the latter study, the full atomistic-level details of adsorption and reactivity behavior of AC under hydrogenation reaction conditions resulting in formation of an active ligand layer remain unknown. Specifically, AC is able to transform not only to N-butylimine species but also undergo alternative reaction pathways resulting in formation of the different partly hydrogenated surface species (e.g. amines). These competing processes might crucially affect the final composition of the surface turning over and by this decisively determine the overall efficiency of the catalyst. It appears feasible to control the surface composition of the ligand layer by tuning the pre-treatment and reaction parameter such, that mainly the desired ligand species would be produced and the competing reaction pathways of AC would be minimized. However, the control over the chemical composition requires detailed knowledge of the competing surface processes and how they specifically depend on the experimentally controllable parameters such as reaction temperature, AC coverage and hydrogen flux. This detailed information on these dependencies is not available at the moment. The main goal of this study is to obtain detailed atomistic-level understanding of the competing reaction pathways of AC under hydrogenation conditions resulting in formation of either the desired ligand layer (N-butylimine species) or the undesired side products of partial or full AC hydrogenation. Specifically, the effects of the experimentally controllable parameters, such as reaction temperature, presence of hydrogen and AC coverage, on the competing surface processes need to be explored, which will allow to prepare

tailor-made active ligand layers with the desired catalytic properties.

Previously adsorption behavior of structurally similar molecules – simple nitriles and isocyanides – was addressed by a variety of surface sensitive spectroscopies on pristine transition metal surfaces.^[9] Specifically, two possible adsorption configurations – $\eta_1(\text{N})$ or $\eta_2(\text{N,C})$ – were proposed for acetonitrile,^[9d,j] methyl isocyanide,^[9g,k] azomethane,^[9l] HCNH^[10] and HCN^[9m] adsorbed on Pt(111), methyl isocyanide and acetonitrile^[9f] on Pd(111), acetonitrile on TiO₂-supported Au,^[9i] methyl isocyanide on Rh(111)^[9e] and HCNH on Ru(001).^[9n] In the $\eta_1(\text{N})$ configuration, the N atom directly interacts with the underlying metal, while the nearest C atom is attached only to N. In the $\eta_2(\text{N,C})$ configuration, both N and the nearest C establish bonds to the underlying metal surface. Adsorption and reactivity behavior of these compounds on H-containing transition metal surfaces and/or under hydrogenation reaction conditions at elevated temperatures was not yet investigated in surface science studies to the best of our knowledge.

To obtain a deeper microscopic understanding of the processes resulting in the formation of the active ligand layer, we performed a comprehensive spectroscopic study on adsorption and reactivity behavior of AC on pristine and H-containing Pd(111) surface. A combination of infrared reflection absorption spectroscopy (IRAS) and molecular beam techniques was employed in this study in a broad range of temperature and coverage conditions. Specifically we show, that on the pristine Pd(111) surface at 100 K AC adopts an adsorption configuration with the CN-entity oriented nearly parallel to the surface, while the C=C bond is tilted with respect to the surface plane. With increasing temperature, the spectroscopic observations suggest a strong rehybridization of the C=C bond resulting in formation of either π - or di- σ bonded adsorbates on pristine Pd(111). The presence of co-adsorbed H dramatically changes both the chemical structure and the adsorption configuration of originally adsorbed AC. Already at the lowest investigated temperature (100 K), molecular AC transfers to butylimine species, in which a C=N entity is formed exhibiting a characteristic vibrational band at 1755 cm⁻¹. At elevated temperatures, the imine adsorbates can undergo two competing reaction pathways: (i) one resulting in hydrogenation of the C=C bond and leading to formation of strongly bound saturated imine adsorbates (N-butylimine species); (ii) the other resulting in a stepwise hydrogenation of the C=C and the C=N bonds and formation of the saturated amine species, which can desorb as molecular butylamine. The saturated N-butylimine species formed in the first reaction pathway was found to be stable under the reaction condition and form an active ligand layer governing chemoselective acrolein hydrogenation. The amine species formed in the second pathway are unstable and readily desorb in presence of hydrogen. Obtained results provide important atomistic-level details on chemical transformations of AC under the hydrogenation reaction conditions, which play a key role in formation of active ligand layers in ligand-directed heterogeneous catalysis.

Experimental Section

All experiments were performed in an ultrahigh vacuum (UHV) apparatus combining molecular beam techniques, IRAS and quadrupole mass spectrometry (QMS). The apparatus is equipped with a dedicated preparation chamber, which is separated from the experimental chamber by an UHV gate valve. After preparation, the sample can be transferred from the preparation to the experimental chamber without breaking the vacuum. Both chambers are operating at a base pressure $< 2.0 \cdot 10^{-10}$ mbar. Full details on the apparatus design can be found elsewhere.^[11]

The Pd(111) single crystal (10×10 mm, MaTeck GmbH) was cleaned prior to use in the preparation chamber by repeated cycles of Ar^+ ion bombardment at room temperature, followed by annealing at 1100 K and subsequent oxidation in $1 \cdot 10^{-6}$ mbar O_2 at 700–750 K. The last step contains the rapid flash of the sample to 900 K. Shortly before each experiment the sample was flashed to 600–800 K before cooling to the required temperature to remove CO adsorbates. The long range order and cleanliness of the Pd(111) single-crystal were checked by Low Energy Electron Diffraction (LEED), Auger Electron Spectroscopy (AES) and additionally by IRAS of adsorbed CO to probe the abundance of adsorption sites. Allyl cyanide (Sigma-Aldrich, 98%) was purified with multiple pump-freeze-thaw cycles before each experiment. Hydrogen (Linde HiQ 6.0) was used without any further purification.

Two doubly differentially pumped effusive molecular beams were used for dosing the molecules onto the surface. Typical flux rates were $8.5 \cdot 10^{14}$ molecules $\cdot \text{cm}^{-2} \cdot \text{s}^{-1}$ for H_2 and $7.2 \cdot 10^{12}$ molecules $\cdot \text{cm}^{-2} \cdot \text{s}^{-1}$ for allyl cyanide. The IRAS data were obtained using a vacuum Fourier transform infrared (FTIR) spectrometer (Bruker Vertex 80v) with a spectral resolution of 2 cm^{-1} combined with a mid-infrared (MIR) polarizer and using p-polarized IR light. The spectrometer was equipped with a narrow band Mercury-Cadmium-Telluride (MCT) detector.

The deposition of molecules as well as the evolution of reaction products was monitored by a quadrupole mass spectrometer (QMS) (Hidden HAL 301/3F). A detailed description of the setup can be found elsewhere.^[11]

The vibrational spectra were calculated at the B3LYP level with the aug-cc-pvqz basis set of a single molecule in the gas phase using the Gaussian16 software.^[12] The computed frequencies were used to assign the specific vibrational modes to the experimentally measured vibrational frequencies of the unperturbed molecules adsorbed in the multilayer coverage regime.

Results and Discussion

Adsorption of AC was investigated on well-defined Pd(111) surface under UHV conditions in the temperature range 100–250 K by combination of IRAS and molecular beam techniques. The surface coverage was varied in a broad range – from submonolayer to multilayer coverages. The spectra obtained for AC multilayers at 100 K were used as a reference for molecular species, which are not perturbed by the direct interaction with the underlying metal surface. The assignment of the experimentally observed vibrational band was performed by comparison of these spectra with the known gas phase spectra^[13] and theoretical calculations performed in this study.

Assignment of vibrational bands in allyl cyanide

Figure 1 shows multilayer IR spectra of AC obtained at 100 K during increasing exposure (1–4) and a theoretical spectrum (5) resulting from harmonic B3LYP/aug-cc-pvqz gas phase calculation using the Gaussian16 software.^[12] At this temperature, a simultaneous continuous growth of all vibrational bands was observed, which is characteristic for the formation of multilayers. The calculated IR spectrum was corrected by a factor of 0.965, scaled on the $\nu(\text{C}=\text{C})$ vibrational band at 1648 cm^{-1} , which can be clearly identified in the experimentally measured multilayer spectra. A detailed assignment of all vibrational bands, based on the harmonic B3LYP gas phase frequency calculation, is summarized in Table 1. The last column of this table also shows the references to the previously published reports that were used for additional verification of the assignment made in this study.

There is a good agreement in spectral position as well as simulated intensities of the calculated spectra compared to the experimental data, which provides a sufficient level of accuracy for comparison of theoretically computed and experimentally measured spectra. In the region of the C–H stretch vibrations, the IR bands are observed at $3093 (\nu_{\text{as}}(\text{=CH}_2))$, $3032 (\nu(\text{=CH}))$ and $2990 (\nu_{\text{s}}(\text{=CH}_2)) \text{ cm}^{-1}$, which can be assigned to the asymmetric and symmetric =C–H stretching modes containing the olefinic C atom. The C–H stretching vibrations related to the aliphatic $-\text{CH}_2-$ entity exhibit lower vibrational frequencies: at $2940 (\nu_{\text{as}}(\text{CH}_2))$ and $2918 (\nu_{\text{s}}(\text{CH}_2)) \text{ cm}^{-1}$. The nitrile stretching vibration $\nu(\text{C}\equiv\text{N})$ is observed at 2250 cm^{-1} with a small shoulder at 2265 cm^{-1} , which can be related to intermolecular interactions of AC in the multilayer ice as previously shown in experimental spectroscopic^[13b] and theoretical studies.^[13a] Specifically, it was reported that the nitrile stretching vibration $\nu(\text{C}\equiv\text{N})$ is highly sensitive to the chemical surrounding. Thus, the IR experiments of Getahun et al.^[14] on nitrile containing amino acids in water and tetrahydrofuran (THF) solvent show a frequency blue-shift of up to 10 cm^{-1} when THF was replaced by water. A similar trend was reported by Lindquist et al.^[15] in a theoretical study on acetonitrile/water and acetonitrile/THF clusters. The very sharp band at 1648 cm^{-1} can be assigned to the $\nu(\text{C}=\text{C})$ stretching vibration. The assignment of the stretching vibrations $\nu(\text{CH}_2)$, $\nu(\text{C}\equiv\text{N})$ and $\nu(\text{C}=\text{C})$ are in good agreement with previously reported assignment performed in the studies on gaseous, liquid and solid AC by Durig^[13a] and Verma.^[13b]

The intense band at 1419 cm^{-1} is related to the asymmetric deformation vibration $\delta_{\text{as}}(\text{CH}_2)$ of the methylene group. A small shoulder visible at 1402 cm^{-1} can be assigned to the in plane deformation vibration $\delta_{\text{ip}}(\text{=CH}_2)$ of the terminal vinyl group. The vibrational band at 1325 cm^{-1} is typical for the symmetric deformation vibration $\delta_{\text{s}}(\text{CH}_2)$ of the methylene group. The band at 1296 cm^{-1} is assigned according to the calculations to the in-plane bending vibration $\delta_{\text{ip}}(\text{=CH})$ of the C–H bond with carbon being involved in the olefinic group. Previously, the bands at similar frequencies 1287 and 1294 cm^{-1} were reported by Verma et al.^[13b] for solid AC adsorbed on CsBr plate at 90 K

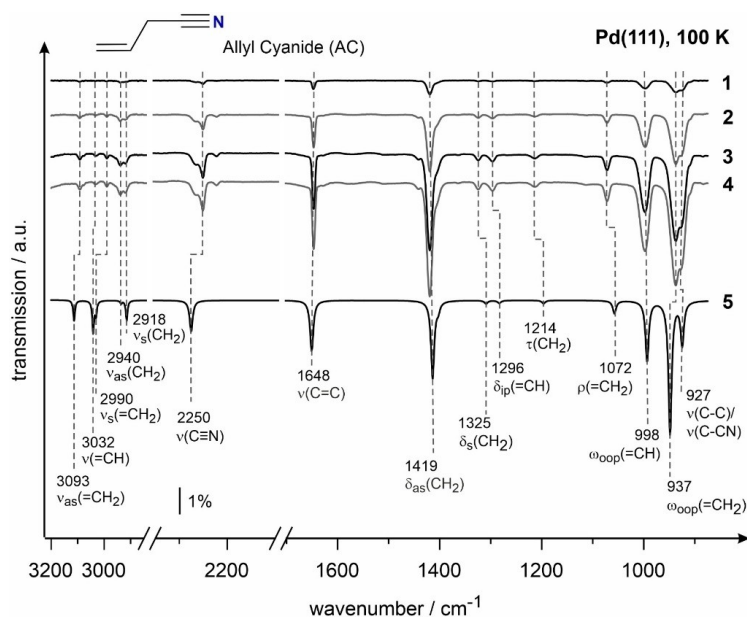


Figure 1. IR spectra of allyl cyanide (AC) obtained at 100 K on Pd(111) in the multilayer coverage range. AC was dosed at a flux of $1.0 \cdot 10^{14}$ molecules \cdot cm $^{-2}$ \cdot s $^{-1}$. Allyl cyanide exposures: (1) $6.0 \cdot 10^{15}$, (2) $3.0 \cdot 10^{16}$, (3) $4.2 \cdot 10^{16}$, (4) $5.4 \cdot 10^{16}$ molecules \cdot cm $^{-2}$. The spectrum (5) results from theoretical calculation by using B3LYP-aug-pvqz gas phase calculation of allyl cyanide with a correction factor of $f=0.965$.

Table 1. Assignments of vibrational modes of allyl cyanide and its partly hydrogenated derivatives. ν : stretching, δ : deformation, τ : twisting, ρ : rocking, ω : wagging, γ : scissoring vibrations.

| Frequency [cm $^{-1}$] | Multilayer (100 K) | Sub monolayer (140 K) | Sub monolayer (H $_2$, 250 K) | Theoretically calculated spectrum (B3LYP / aug-cc-pvqz, $f=0.965$) | Assignment | Ref. |
|-------------------------|--------------------|-----------------------|--------------------------------|---|-----------------------|----------------|
| 3093 | | | | 3113 | $\nu_{as}(=CH_2)$ | [13] |
| 3032 | | | | 3040 | $\nu(=CH)$ | [13a] |
| 2990 | | | | 3030 | $\nu_s(=CH_2)$ | [13a] |
| 2940 | | | | 2935 | $\nu_{as}(=CH_2)$ | [13a] |
| 2918 | | | | 2914 | $\nu_s(=CH_2)$ | [13b] |
| | 2879 | | | | $\nu_{as}(=CH_2)$ | [18] |
| | 2864 | | | | $\nu_s(=CH_2)$ | [18] |
| 2250 | | | | 2275 | $\nu(C\equiv N)$ | [13] |
| | | 1755 | | | $\nu(C=N)$ | [9d,f,k, 22] |
| 1648 | 1648 | | | 1650 | $\nu(C=C)$ | [13] |
| | | 1608, 1580 | | | $\delta(NH_2)$ | [9 h,m, 24,25] |
| 1419 | 1419 | | | 1413 | $\delta_{as}(CH_2)$ | [13] |
| 1402 | | | | 1402 | $\delta_{ip}(=CH_2)$ | [13b] |
| 1325 | | | | 1308 | $\delta_s(CH_2)$ | [13] |
| 1296 | | | | 1282 | $\delta_{ip}(=CH)$ | [13a] |
| | | 1275 | | | $\delta(HNC)$ | [9 l, 10, 20] |
| 1214 | | | | 1196 | $\tau(CH_2)$ | [13a] |
| 1072 | | | | 1057 | $\rho(=CH_2)$ | [13a] |
| 998 | 990 | | | 993 | $\omega_{oop}(=CH)$ | [13b] |
| 937 | 934 | | | 948 | $\omega_{oop}(=CH_2)$ | [13a] |
| 927 | 915 | | | 924 | $\nu(C-C)/\nu(C-CN)$ | [13] |

and at 1285 cm $^{-1}$ for liquid AC. Durig assigned the band at 1300 cm $^{-1}$ measured in gaseous and at 1288 cm $^{-1}$ in solid AC to the same $\delta_{ip}(=CH)$ vibrational mode.^[13a] This slight difference between 1296 cm $^{-1}$ observed in our study and 1288 cm $^{-1}$

reported for solid AC by Durig may be related to intermolecular interactions in the multilayer AC ice.

The weak band at 1214 cm $^{-1}$ is related to the twisting vibration $\tau(CH_2)$ of the methylene group. The vibrational band

at 1072 cm^{-1} can be assigned to the rocking vibration of the vinyl group $\rho(=\text{CH}_2)$ according to our calculations. Previously, Durig et al.^[13a] reported the band at 1066 cm^{-1} in the gas phase, 1070 cm^{-1} in the liquid phase and 1075 cm^{-1} in solid AC and assigned them to the same rocking vibration of the vinyl group $\rho(=\text{CH}_2)$. On the other hand, Verma et al.^[13b] assigned a band at 1070 cm^{-1} measured for liquid AC to a combination vibration of a valence and torsion vibration of the $\text{C}-\text{C}\equiv\text{N}$ entity. The very intense bands at 998 cm^{-1} ($\omega_{\text{oop}}(=\text{CH})$) and 937 cm^{-1} ($\omega_{\text{oop}}(=\text{CH}_2)$) are assigned to the out-of-plane wagging vibrations of the vinyl hydrogens. Both assignments are in a good agreement with the assignment of Durig et al.,^[13a] while Verma assigned the vibration at 936 cm^{-1} in liquid AC and 947 cm^{-1} in solid AC to the stretching mode of the $\text{C}-\text{C}\equiv\text{N}$ entity ($\nu(\text{C}-\text{C}\equiv\text{N})$). The same author assigned the vibration at 906 cm^{-1} in liquid AC to out-of-plane wagging mode of the vinyl hydrogen.^[13b] Based on our calculations, the vibration at 927 cm^{-1} can be assigned to a mixed mode of the $\nu(\text{C}-\text{C}\equiv\text{N})$ and $\nu(\text{C}-\text{C})$ stretching vibrations, which rather agrees with the assignment suggested by Durig.^[13a]

Generally, the previous assignments of the vibrational bands of AC performed by Durig and Verma can be confirmed with just a few exceptions related to the low-frequency range, in which contradictory assignments were suggested by these two groups. A detailed visualization of the most prominent and for further discussion most important vibrational bands are shown in Figure 2. The blue arrows show the displacement vector of the individual atoms involved in each vibrational mode, while the gold arrow displays the resulting dynamic dipole moment. The arrow related to the resulting dynamic dipole moment is arbitrarily placed in the center of mass of AC. In the following, the orientation of the dynamic dipole moments with respect to the metal surface plane will be discussed for the selected vibrations. On metal surfaces, only those vibrational modes are visible in IR spectra, whose dynamic dipole moment has a non-zero projection onto the surface normal as a consequence of the metal surface selection rule (MSSR).^[16] Consequently, the

absence of certain IR vibrational peaks indicates that the related bonds are oriented nearly parallel to the surface and therefore not visible. It should be also kept in mind that the geometrical structure of adsorbed species might significantly differ from the alone-standing unperturbed molecules shown in Figure 2.

IR spectra of allyl cyanide adsorbed on Pd(111) at 100 K: coverage dependence

Having identified the vibrational modes in the multilayer, we studied adsorption of AC as a function of coverage to obtain detailed understanding of the chemical nature and the adsorption geometry of molecular species closely interacting with Pd surface. Figure 3 shows the IR spectra recorded on pristine Pd(111) at 100 K after successive exposure to AC in the range $7.2 \cdot 10^{13}$ to $4.3 \cdot 10^{15}$ molecules $\cdot \text{cm}^{-2}$. Importantly, the highest AC coverage corresponds to a few monolayers, which allows us to directly follow the evolution of the individual vibrational bands starting from sub-monolayer to multilayer coverage. This approach ensures a univocal assignment of the vibrational bands detected at submonolayer coverages by direct comparison with the bands observed for multilayers, whose assignment was discussed in the previous section (Figure 1).

At the lowest coverage (Figure 3 spectra 1 and 2), only one vibrational band at 1419 cm^{-1} is visible in the spectra, which is related to the asymmetric deformation vibration of the methylene group $\delta_{\text{as}}(\text{CH}_2)$. This observation indicates that AC adopts a flat lying adsorption geometry with both the nitrile and vinyl group being oriented parallel to the surface. The presence of the vibrational band at 1419 cm^{-1} further indicates that the original geometric structure of AC becomes strongly perturbed upon adsorption on the metal surface. The dynamic dipole moment of the $\delta_{\text{as}}(\text{CH}_2)$ vibration lies in the same plane as the dynamic dipole moments of the $\text{C}\equiv\text{N}$ and $\text{C}=\text{C}$ stretching

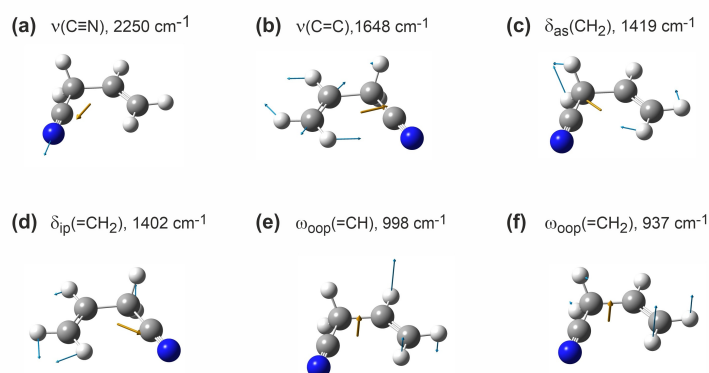


Figure 2. Visualization of selected vibrational modes of allyl cyanide in the gas phase using GaussView 6.1.^[1] Blue arrows indicate the displacement vector of the individual atoms involved in the vibrational mode, gold arrows show the resulting dynamic dipole moment vector of the corresponding mode.

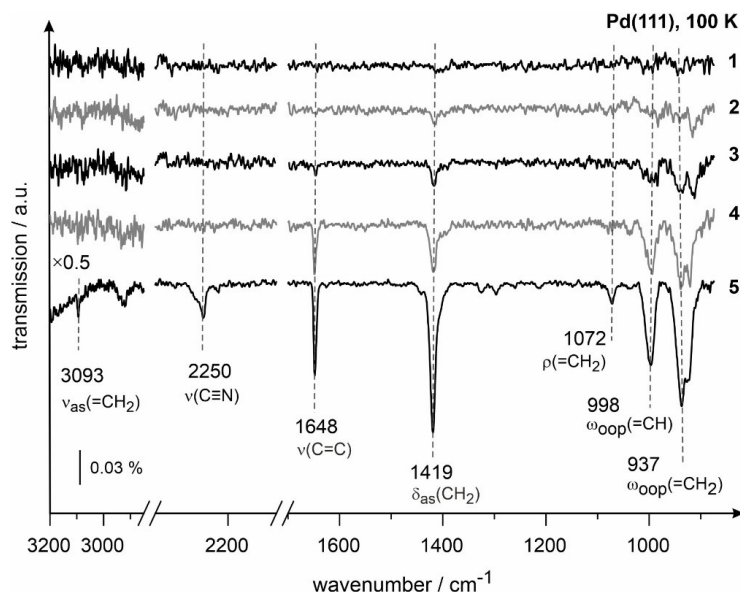


Figure 3. IR spectra of AC obtained at 100 K on Pd(111) in sub- and multilayer coverage range. AC was dosed at a flux of $7.2 \cdot 10^{12}$ molecules \cdot cm $^{-2} \cdot$ s $^{-1}$. AC exposures: in (1) $7.2 \cdot 10^{13}$, (2) $2.9 \cdot 10^{14}$, (3) $3.6 \cdot 10^{14}$, (4) $7.2 \cdot 10^{14}$, (5) $4.3 \cdot 10^{15}$ molecules \cdot cm $^{-2}$.

vibrations for the gaseous AC (Figure 2). The fact, that the latter two vibrations are not seen in the infrared spectra suggests that the related bands are oriented nearly parallel to the surface and not visible due to MSSR. If the geometrical structure of AC would be retained upon adsorption, also the band at 1419 cm^{-1} ($\delta_{\text{as}}(\text{CH}_2)$) would be invisible due to the same effect. Since this band is observed in the adsorbed AC, the related dynamic dipole moment must be inclined with respect to the plane containing the C=C and C≡N bonds (see Figure 2). Most likely, this means that the H atoms of the $-\text{CH}_2$ -group become lifted above the surface, so that the resulting dynamic dipole moment of $\delta_{\text{as}}(\text{CH}_2)$ vibration is inclined with respect to the C=C/C≡N plane and the plane of the metal surface. With increasing AC coverage, the band at 1419 cm^{-1} grows in intensity and a band at 1648 cm^{-1} appears in spectrum 3, which is related to the C=C stretching vibration $\nu(\text{C}=\text{C})$. Simultaneously, the bands at 998 cm^{-1} ($\omega_{\text{oop}}(\text{=CH})$) and 937 cm^{-1} ($\omega_{\text{oop}}(\text{=CH}_2)$) related to wagging vibrations of the vinyl group evolve. The spectrum 5 obtained at the highest exposure $4.3 \cdot 10^{15}$ molecules \cdot cm $^{-2}$ contains three additional bands at 3093 cm^{-1} ($\nu_{\text{as}}(\text{=CH}_2)$), 2250 cm^{-1} ($\nu(\text{C}\equiv\text{N})$) and 1072 cm^{-1} ($\rho(\text{=CH}_2)$). Taking into account the density of surface Pd atoms on Pd(111), which amounts to $1.5 \cdot 10^{15}$ atoms \cdot cm $^{-2}$, and assuming that the sticking coefficient of AC is close to unity at 100 K, it might be concluded that the transition from the (sub-)monolayer to multilayer coverage occurs approximately between the spectra 2 and 4. In our previous STM studies,^[8] adsorption of AC was investigated on a pristine Pd(111) surface in a broad range of temperature conditions. Based on the adsorption model developed for pristine Pd(111), the space demand for a single AC molecule was estimated to be

approximately 8.5 Pd atoms. Assuming this space requirement, we estimate the saturation coverage of AC laying in the range $1.6 \cdot 10^{14}$ – $1.8 \cdot 10^{14}$ molecules \cdot cm $^{-2}$, which roughly correspond to the spectra 1 and 2 in Figure 3. In this case, it might be concluded that when adsorbed below the monolayer coverage, most of AC surface species are lying flat on the surface with the C=C and C≡N bonds being oriented close to parallel to the underlying metal and therefore invisible in IRAS due to MSSR.^[16] Upon transition to the second and the further layers, the newly incoming molecules adopt a random orientation with respect to the surface, so that first the C=C and then the C≡N bonds become visible.

At sub-monolayer coverages (spectra 1–2), the absence of both vibrational bands related to out-of-plane wagging vibrations of the vinyl hydrogens ($\omega_{\text{oop}}(\text{=CH})$ and $\omega_{\text{oop}}(\text{=CH}_2)$) at 998 and 937 cm^{-1} may indicate that the vinyl group undergoes strong rehybridization losing the π -bond character. There are two limiting types of interactions usually discussed in the literature:^[17] a strong di- σ -interaction resulting in a rehybridization of both carbon atoms and a weaker π -bonded type of interaction. If the C=C bond would be preserved and participate in a π -type bonding, either the out-of-plane wagging ($\omega_{\text{oop}}(\text{=CH})$ at 988 and $\omega_{\text{oop}}(\text{=CH}_2)$ at 937 cm^{-1}) or in-plane deformation ($\delta_{\text{ip}}(\text{=CH}_2)$ at 1402 cm^{-1}) vibrations of the olefinic hydrogen atoms would be expected to be visible in the infrared spectra, which is not the case. On the other hand in case of a di- σ -bonding, one could expect the appearance of new or spectrally shifted vibrational bands in the region of CH stretching or CH deformation vibrations, which was either not observed here. Based on the available experimental data, it seems not to be

possible to distinguish between these two conceivable bonding types. At increasing coverages (spectra 3–5), all bands related to the C=C bond – 1648, 998 and 937 cm^{-1} – become visible in the spectra, pointing to a lesser extent of the olefin bond perturbation in the high coverage regime. A similar coverage-dependent change of the adsorption configuration from a di- σ bonding at low coverages to a π -complex at higher coverages have been reported by Lee et al.^[18] in an IRAS adsorption study of C4-olefins on Pt(111) at 80 K.

Previously, adsorption behavior of simplest types of nitriles and isocyanides, such as HCN, acetonitrile and methyl isocyanide, was investigated in surface science studies on a variety of metals.^[9a,c-g,i-k,m,19] Koerdtsch et al. investigated the adsorption behavior of HCN on Pd(111) in a combined high resolution energy loss spectroscopy (HREELS) performed in an off-specular mode and temperature programmed desorption (TPD) study.^[9a] The authors proposed a di- σ bonded $\eta_2(\text{C},\text{N})$ adsorption configuration for the C=N bond, in which the formed nitrile groups show an imine character as concluded based on the observed strong frequency shift from 0.259 meV (2089 cm^{-1}) to 0.191 meV (1540 cm^{-1}). The NEXAFS study by the same authors confirmed this conclusion by showing that the C–N axis is oriented parallel to the surface.^[9b] In a more recent IRAS study on acetonitrile and methyl isocyanide adsorbed on Pd(111) at 80 K, Murphy et al. reported a close to parallel orientation of the isocyanide group at low coverages and a more upright $\eta_1(\text{C})$ -configuration in the higher coverage regime.^[9f] In this study, a prominent shift of the nitrile stretching vibration from 2249 to 1755 cm^{-1} was observed for acetonitrile, which was explained by a strong weakening of the nitrile group due to interaction with the underlying Pd. This considerable shift was interpreted as a consequence of a strong rehybridization of the related orbitals and formation of a $\eta_2(\text{C},\text{N})$ adsorption configuration of the original nitrile groups, in which the original triple C=N bond rather turns to double C=N imine bond. In a combined EELS and TPD study by Avery et al.^[9g] on adsorption of methyl isocyanide on Pt(111), two types surface species were suggested: (i) a terminally bonded species observed at low coverage with a characteristic vibrational band at 2265–2240 cm^{-1} and (ii) an imine-like species observed at higher coverages, exhibiting a vibrational band in the range 1600–1770 cm^{-1} . In the same group, the adsorption of acetonitrile was investigated on Pt(111) by a combination EELS, X-ray photoelectron spectroscopy (XPS) and TPD,^[9d] in which an $\eta_2(\text{C},\text{N})$ -configuration was deduced for acetonitrile, showing the characteristic vibrational band at 1615 cm^{-1} in the typical imine region ($\nu(\text{C}=\text{N})$). A similar imine-related vibrational band at 1660 cm^{-1} was also observed in an IR study by Szilágyi et al.^[9c] on acetonitrile and methyl isocyanide adsorption on Pt(111)/SiO₂. In a combined EELS, Auger electron spectroscopy (AES) and TPD study by Semancik et al.^[9e] on adsorption of methyl isocyanide on Rh(111), two different adsorption species were reported: (i) a low-coverage species, exhibiting a vibrational band at 1710 cm^{-1} , which were assigned to a bridged-bonded geometry, and (ii) a second type of species related to the high coverage range, showing a vibrational band at 2170 cm^{-1} and interpreted as on-top bonded species. Friend et al.^[19] inves-

tigated acetonitrile and methyl isocyanide on Ni(111) surfaces at 100 K by HREELS and TPD and reported vibrational bands for acetonitrile at 1680–1700 cm^{-1} (low coverage) and 2240 cm^{-1} (high coverages). For methyl isocyanide, these features appear at 1760 cm^{-1} at low coverage and at 2160 cm^{-1} at high coverage. In both cases, the strongly red-shifted vibrational band was assigned as an $\eta_2(\text{C},\text{N})$ -configuration with both the C and N atom of the nitrile and isocyanide group being bonded to the surface.^[19] The adsorption geometry of nitriles was hypothesized to play a crucial role in hydrogenation of nitrile compounds. A combined theoretical and FTIR study on acetonitrile hydrogenation to ethyl amine on Pt nanoparticles supported on Al₂O₃ by Vogt et al.^[20] proposed $\eta_2(\text{C},\text{N})$ adsorption configuration for chemisorbed nitriles and identified an imine species as the key reaction intermediate.

Thus, formation of two possible surface species was hypothesized in previous experimental reports on structurally similar molecules containing a nitrile or an isocyanide group. For the most of investigated surfaces,^[9a,c-g,i-k,m,19] the adsorption configuration of the CN entity – either in nitrile or isocyanide compounds – was discussed to be oriented nearly parallel to the metal surface. Most of the authors hypothesized a $\eta_2(\text{C},\text{N})$ adsorption configuration with both C and N atoms establishing σ bonds with the underlying metal. At increasing coverage, a more upright adsorption configuration was reported for the most investigated systems. These general observations are in a good agreement with the adsorption behavior of AC deduced from the IR spectra shown in Figure 3. It should be noted, however, that on the pristine Pd(111) surface no vibrational peaks in the range 1600–1750 cm^{-1} were observed in our work, which were interpreted in the earlier studies as imine –C=N species formed due to the strong interaction with the underlying metal and/or donation of the electron density from the metal to the C=N bond. In the following, we will demonstrate and discuss formation of imine-like species on H-precovered Pd(111).

Adsorption of allyl cyanide on Pd(111) in the temperature range 100–250 K

As a next step, adsorption of allyl cyanide was investigated on pristine Pd(111) in the temperature range from 100 to 250 K at sub-monolayer coverages. For each temperature, the surface was exposed to 4.3 10^{14} molecules $\cdot \text{cm}^{-2}$ allyl cyanide. Note that the identical exposure does not result in the same surface coverages at different surface temperatures as the sticking coefficients may vary as a function of temperature.

Figure 4 shows the IR spectra obtained for this experimental series. At 100 K, intense vibrational bands at 1648 ($\nu(\text{C}=\text{C})$), 1419 ($\delta_{\text{as}}(\text{CH}_2)$), 990 ($\omega_{\text{oop}}(\text{=CH})$), 934 ($\omega_{\text{oop}}(\text{=CH}_2)$), 915 ($\nu(\text{C}-\text{C})/\nu(\text{C}-\text{CN})$) cm^{-1} are visible at this particular exposure, while neither noticeable bands in the $\nu(\text{CH}_2)$ nor in $\nu(\text{C}=\text{N})$ regions could be observed, most likely due to MSSR. The combination of these observations suggests that the nitrile group of AC is

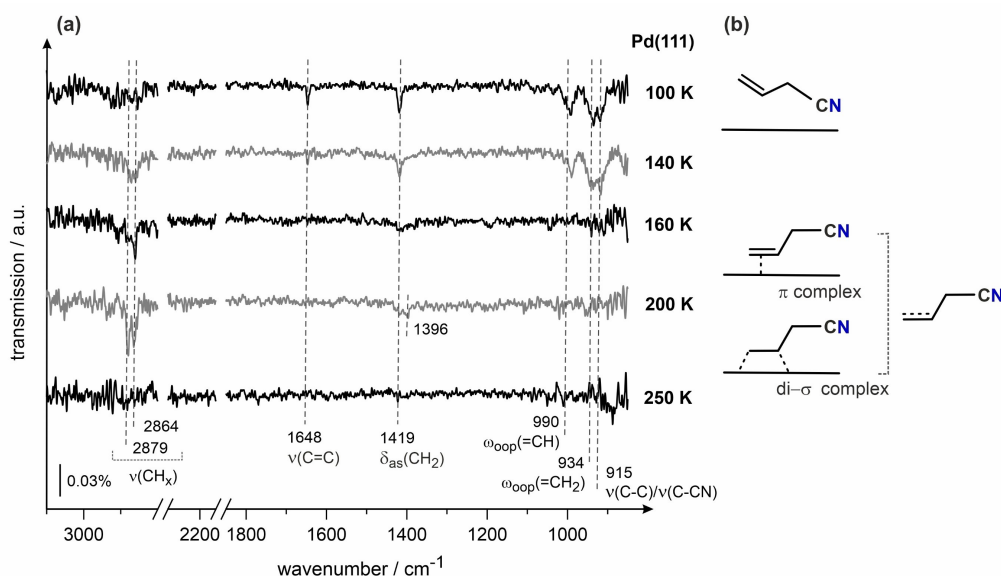


Figure 4. IR spectra of AC obtained on Pd(111) at submonolayer coverages in the temperature range 100–250 K. AC was dosed at a flux of $7.2 \cdot 10^{12}$ molecules \cdot cm $^{-2} \cdot$ s $^{-1}$; the total AC exposure amounts to $4.3 \cdot 10^{14}$ molecules \cdot cm $^{-2}$. Acquisition temperatures are indicated next to the spectra.

oriented nearly parallel to the surface, while the C=C bond is tilted with respect to the surface plane.

Only minor changes occur until 140 K: the band at 1648 cm $^{-1}$ ($\nu(\text{C}=\text{C})$) loses some intensity compared to the out-of-plane modes of the vinyl H-atoms ($\omega_{\text{oop}}(\text{=CH})$ and $\omega_{\text{oop}}(\text{=CH}_2)$), which are related to the same functional group of the molecule. That observation indicates that the C=C bond is still present in the molecular species but the orientation of the vinyl group becomes more parallel with respect to the surface than at 100 K resulting in higher relative intensity of the out-of-plane modes. Importantly, two vibrational bands appear at 2879 and 2864 cm $^{-1}$, which is a typical range for C–H stretching vibrations in alkanes.^[18] Note that the vibrational bands at these frequencies do not appear in the multilayer and therefore cannot be related simply to the $-\text{CH}_2-$ groups of the originally deposited AC. With increasing temperature (160–200 K), these new vibrational bands grow in intensity, while the bands associated with the vinyl group at 1648 ($\nu(\text{C}=\text{C})$), 990 ($\omega_{\text{oop}}(\text{=CH})$) and 934 ($\omega_{\text{oop}}(\text{=CH}_2)$) vanish. The absence of both in-plane ($\nu(\text{C}=\text{C})$) and out-of-plane vibrations related to the vinyl group most likely indicates that the C=C bond is either strongly rehybridized or does not exist anymore under these temperature conditions. Also the original $-\text{CH}_2-$ group is affected by temperature-induced structural changes since the band at 1419 cm $^{-1}$ ($\delta_{\text{as}}(\text{CH}_2)$) strongly decreases in intensity and a small new band at 1396 cm $^{-1}$ evolves, which is most likely related to a similar C–H deformation vibration of the CH_x entity formed in the modified AC surface species.

Based on these spectroscopic observations, it is impossible to undoubtedly deduce the chemical composition of AC-related

species formed in the temperature range 140–200 K on pristine Pd(111). Vanishing of the C=C bond can originate either (i) from formation of the π -complex with the intact C=C bond being nearly parallel oriented to the metal surface or (ii) due to formation of a di- σ complex, in which each C atom forms a covalent bond to the underlying Pd atom, so that the C=C bond does not exist anymore. There is an ongoing debate on this issue in the literature for different types of olefins, which is – to the best of our knowledge – not finally resolved.^[17] Specifically, similar evolution of C=C-related spectroscopic signatures was reported by Lee et al.^[18] for adsorption of simple olefins – butenes – on Pt(111) and assigned to the formation of a di- σ -bonded surface intermediate. On the other hand, notable changes of the spectral region related to the CH_x deformation vibrations (bands at 1419 and 1396 cm $^{-1}$) suggest that also the methylene group of original AC is strongly affected in the high temperature range. Similar behavior was previously reported for a close type of nitrile compounds – alkoxybenzonnitriles, in which strong changes of the CH_x deformation vibrational bands were detected and linked to self-assembling of these species graphene.^[21] In our previously published work, we reported that also AC self assembles in the 2D layers in the high temperature region and deduced the precise atomistic model of these adsorption layers (for more details, see^[8]). In view of this fact, it is likely that also the changes of the vibrational bands at 1419 and 1396 cm $^{-1}$ observed in this study are associated with the self-assembling process, in which strong intermolecular interactions keeping the molecular species together might be responsible for the observed behavior.

Above 250 K, no IR vibrational can be detected on the surface, even though that according to the STM data, the surface is almost completely covered by AC.^[8] Vanishing of all vibrational bands occurs most likely due to the nearly flat orientation of all main bands parallel to the surface plane, making them not detectable by IRAS due to MSSR.^[16] Potentially, also some hydrogen atoms of AC can be stripped off at elevated temperatures, however, their desorption from Pd cannot be observed experimentally in this temperature range since the barrier for desorption of surface-adsorbed H can be overcome only above 300 K. It should be noted that the ability of the AC-derivatives to efficiently diffuse at elevated temperatures, which is proven by formation of the long-range ordered structures (2D self-assembled layers), allow us to exclude a high degree of dissociation rather safely in these adsorbates. Indeed, if H would be stripped off the molecules in substantial amounts, it should form surface species strongly bound to Pd, which are most likely not capable to efficiently diffuse and strongly rearrange to form large areas of self-assembled 2D layers that are observed experimentally.

Figure 4b shows the proposed configuration of the AC species adsorbed on pristine Pd(111) in the temperature range 100–250 K. At the lowest temperatures, the nitrile group is oriented nearly parallel to the metal surface, while the C=C bond is inclined. The latter conclusion is based on the simultaneous observation of the stretching vibration of the C=C bond as well as wagging out-of-plane vibrations related to the vinyl group. In the range 140–160 K, a transition to new surface species occurs, in which the C=C bond seems to be highly

rehybridized, forming most likely either di- σ or π -bonded complexes, in which all main bonds are oriented flat with respect to the surface. As reflection of these considerations, we replace the C=C double bond via the dotted line between two C atoms. Above 250 K no spectroscopic signatures of adsorbed species were detected by IRAS, while in STM AC coverages close to a monolayer were detected. These observations suggest a flat-lying adsorption configuration of all main bonds in AC-derivatives formed at this temperature.

Adsorption of allyl cyanide on H-precovered Pd(111) in the temperature range 100–250 K

To further understand the chemical transformation of AC in presence of co-adsorbed H and the state of the ligand layer under the reaction conditions – at elevated temperatures and under continuous H₂ exposure – adsorption of AC on the H-containing Pd(111) was investigated in the same temperature range as described in the previous section. Figure 5 shows the IR spectra obtained on H-containing Pd(111) surface at successively increasing temperatures.

In the temperature range 100–140 K, AC adsorbed on H-precovered surface still retains a number of peaks typical of molecularly adsorbed AC: 1648 ($\nu(\text{C}=\text{C})$), 1419 ($\delta_{\text{as}}(\text{CH}_2)$), 990 ($\omega_{\text{oop}}(\text{=CH})$), 934 ($\omega_{\text{oop}}(\text{=CH}_2)$) and 915 cm^{-1} ($\nu(\text{C}-\text{C})/\nu(\text{C}-\text{CN})$).^[13a] Importantly, a new vibrational band at 1755 cm^{-1} appears on H-precovered Pd(111), which is present neither in

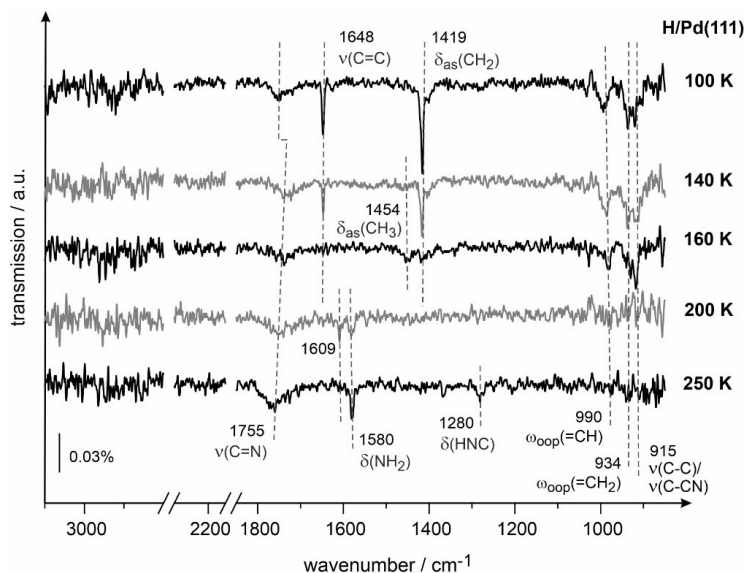


Figure 5. IR spectra of AC obtained on H-containing Pd(111) at submonolayer coverages in the temperature range 100–250 K. AC and H₂ were continuously dosed via independent molecular beams at fluxes $7.2 \cdot 10^{12}$ molecules $\cdot \text{cm}^{-2} \cdot \text{s}^{-1}$ and $8.5 \cdot 10^{14}$ molecules $\cdot \text{cm}^{-2} \cdot \text{s}^{-1}$, respectively. Prior to the deposition of AC, H₂ was continuously dosed for 10 min onto the surface. The total AC exposure is $4.3 \cdot 10^{14}$ molecules $\cdot \text{cm}^{-2}$. Surface temperatures are indicated next to the spectra.

multilayer nor in the gas phase AC.^[13a] As discussed above, the bands appearing in the vibrational range 1600–1770 cm^{-1} after adsorption of structurally similar nitriles and isocyanides were previously attributed to the imine $\text{C}=\text{N}$ species both in experimental^[9a,d,f,22] and theoretical^[9k] studies. Following this assignment, we attribute the new band at 1755 cm^{-1} to the imine-like species, in which the original $\text{C}\equiv\text{N}$ triple bond is partially reduced to a $\text{C}=\text{N}$ double bond. It should be noted that the vibrational band is located at a similar frequency on Pd(111) precovered with D instead of H. Figure 6 shows a series of the related IR spectra obtained at 250 K on the D-precovered surface at different AC coverages, in which the evolution of the

band at 1755 cm^{-1} can be observed, which has the same frequency as measured on the H-covered surface. This observation suggests that the frequency of the newly formed imine ($\text{C}=\text{N}$) group is not strongly affected by the nature of hydrogen isotope (H vs. D) inserted into the $\text{C}\equiv\text{N}$ bond to form imine species.

Generally, two possible types of imine species evolving on H-precovered surface at 100–140 K are possible, which can be formed in two competing reaction pathways as shown in Figure 7. The species formed in the pathway 1 are bound through the N atom to Pd, producing the $\text{C}=\text{N}\cdots\text{Pd}$ entity, which will be denoted later as N-butenylimine species (or

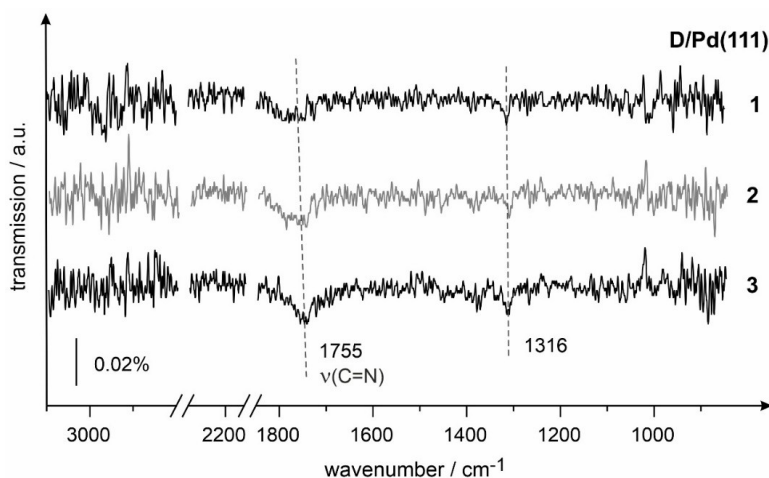


Figure 6. IR spectra of AC obtained at 250 K on D-containing Pd(111). AC and D_2 were continuously dosed via independent molecular beams at fluxes $7.2 \cdot 10^{12}$ molecules $\cdot \text{cm}^{-2} \cdot \text{s}^{-1}$ and $8.5 \cdot 10^{14}$ molecules $\cdot \text{cm}^{-2} \cdot \text{s}^{-1}$, respectively. Prior to the AC exposure, the surface was exposed to D_2 for 10 min. The total AC exposures are: (1) $2.2 \cdot 10^{14}$, (2) $4.3 \cdot 10^{14}$, (3) $1.1 \cdot 10^{15}$ molecules $\cdot \text{cm}^{-2}$.

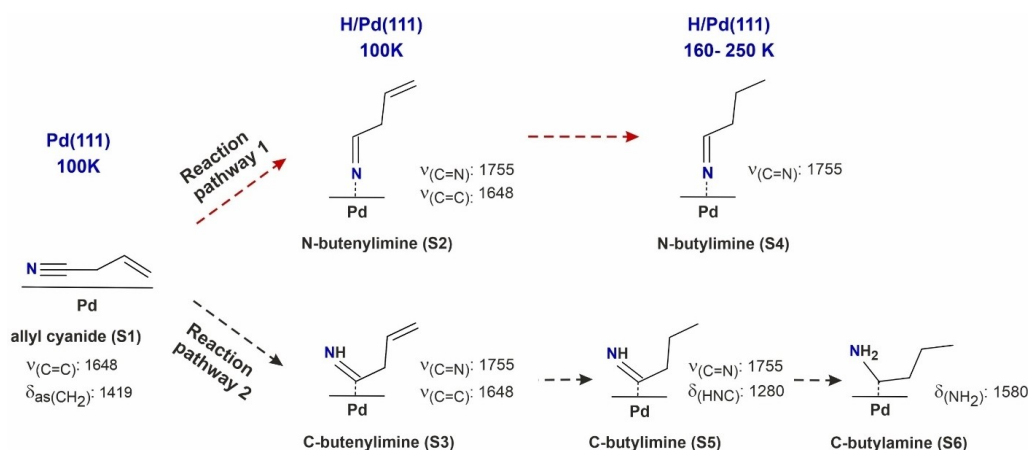


Figure 7. Proposed adsorbate structures and chemical transformation of AC on pristine and H-containing Pd(111). Reaction pathways 1 and 2 show the proposed partial hydrogenation steps in different temperature ranges. The frequencies of the vibrational bands used for assignment of the individual surface species are indicated next to the corresponding structures.

species S2). In the alternative reaction pathway 2, the species S3 is formed, which is connected to Pd via the C atom and will be denoted as C-butenylimine species. The geometric configuration of AC adsorbed on pristine Pd(111) at 100 K (as discussed above) is also shown in Figure 7 and denoted as species S1. It is important to note, that the spectroscopic signature of both proposed imine species S2 and S3 is the same and comprises two characteristic vibrations: the band at 1755 cm^{-1} related to the imine fragment $\text{C}=\text{N}$ and the band at 1648 cm^{-1} assigned to the $\text{C}=\text{C}$ stretching vibration ($\nu(\text{C}=\text{C})$). The latter band clearly indicates that the $\text{C}=\text{C}$ double bond is preserved in the species formed at 100–140 K at H-precured Pd(111) surface.

At 160 K (Figure 5), the peaks at 1648 cm^{-1} ($\nu(\text{C}=\text{C})$) and 1419 cm^{-1} ($\delta_{\text{as}}(\text{CH}_2)$) disappear, while a new peak at 1454 cm^{-1} corresponding to the CH_3 deformation vibration ($\delta_{\text{as}}(\text{CH}_3)$) evolves. The combination of these observations might suggest that the $\text{C}=\text{C}$ bond becomes hydrogenated in this temperature range and a new terminal $-\text{CH}_3$ group appears. It should be noted, however, that the bands at 990 cm^{-1} ($\omega_{\text{oop}}(\text{C}=\text{CH})$) and 934 cm^{-1} ($\omega_{\text{oop}}(\text{C}=\text{CH}_2)$) are still visible in the spectra, even though they are strongly reduced in the intensity as compared to the low temperature regime. Most likely, a stepwise transition from the unsaturated butenylimine species ($\text{CH}_2=\text{CH}-\text{CH}_2-\text{CN}$) to saturated butylimine species ($\text{CH}_3-\text{CH}_2-\text{CH}_2-\text{CN}$) occurs in this temperature range and a combination of these both surface species temporarily exists on the surface. This hypothesis would explain the coexistence of the new band at 1454 cm^{-1} related to the terminal CH_3 group, which can originate only from hydrogenation of the $\text{C}=\text{C}$ bond on one hand, and the bands at 990 cm^{-1} ($\omega_{\text{oop}}(\text{C}=\text{CH})$) and 934 cm^{-1} ($\omega_{\text{oop}}(\text{C}=\text{CH}_2)$) suggesting that some surface species still preserve their $\text{C}=\text{C}$ bond, on the other hand. At the temperatures above 160 K, all vibrations related to $\text{C}=\text{C}$ double bond ($\nu(\text{C}=\text{C})$, $\omega_{\text{oop}}(\text{C}=\text{CH})$ and $\omega_{\text{oop}}(\text{C}=\text{CH}_2)$) completely vanish, suggesting that in the higher temperature range this transition is completed and all olefinic groups become fully hydrogenated (see spectra above 160 K in Figure 5). It should be emphasized that the conclusion on the hydrogenation of the $\text{C}=\text{C}$ bond above 160 K is based on the combination of two observations: vanishing of the $\text{C}=\text{C}$ stretching vibration ($\nu(\text{C}=\text{C})$) and disappearance of the bands related to the $\text{C}-\text{H}$ out-of-plane wagging vibrations ($\omega_{\text{oop}}(\text{C}=\text{CH})$ and $\omega_{\text{oop}}(\text{C}=\text{CH}_2)$). As the dynamic dipole moments of these vibrational modes lie not in the same plane, their simultaneous disappearance cannot be related to the metal surface selection rule and therefore arises most likely from the hydrogenation of the $\text{C}=\text{C}$ bond. This observation is in an agreement with earlier hydrogenation studies on simple olefins adsorbed on Pd(110) and Pd(111), where the onset of $\text{C}=\text{C}$ bond hydrogenation was reported to occur around 160 K^[23]

At 200 K (Figure 5), additional new bands appear at 1609 cm^{-1} and 1580 cm^{-1} . Both bands lie in the vibrational region typical for deformation vibration of amino groups $\delta(\text{NH}_x)$. In previous studies, formation of vibrational bands in the range $1560\text{--}1616\text{ cm}^{-1}$ upon adsorption of simple amines at different transition metal surfaces was reported.^[9,10,24] Interestingly, both bands appear first at 200 K at comparable intensities. However,

the band at 1609 cm^{-1} decreases in intensity at 250 K, while the band at 1580 cm^{-1} simultaneously grows (Figure 5), suggesting that these bands may be correlated as an intermediate (species related the band at 1609 cm^{-1}) and the final product (species related the band at 1580 cm^{-1}). Another observation pointing to the same hypothesis was made in a series of experiments shown in Figure 8. Here, the surface was continuously exposed to H_2 , and to AC at different exposures (from $7.2 \cdot 10^{13}$ to $7.2 \cdot 10^{14}$ molecules $\cdot\text{cm}^{-2}$). At the lowest exposures (spectra 2–3), the band at 1609 cm^{-1} dominates the spectrum, while the band at 1580 cm^{-1} is hardly seen. With increasing exposure, the band at 1609 cm^{-1} decreases in intensity and finally vanishes, while the band at 1580 cm^{-1} concomitantly grows and the eventually becomes the dominant band in the spectrum 5. This correlated behavior, which was observed as a function of both temperature (Figure 5) and the exposure (Figure 8), suggests that the species related to the band at 1609 cm^{-1} might be the surface precursor, which completely transforms into surface amines ($-\text{NH}_2$) exhibiting the band at 1580 cm^{-1} ($\delta(\text{NH}_2)$). The exact chemical nature of the species related to the band at 1609 cm^{-1} is unclear yet. It should be a structurally similar species, containing an amino group, which can be for example adsorbed at a different adsorption sites or having a different local environment (e.g. different intermolecular interactions) than the species related the band at 1580 cm^{-1} . As a possible scenario, it can be hypothesized that the band at 1580 cm^{-1} can be related to the amine species, which are involved in intermolecular interactions with neighboring molecules and are formed at higher coverages, while the band at 1609 cm^{-1} can be rather associated with alone-standing amines present in the low coverage range. This hypothesis is in good agreement with the previous studies on intermolecular interactions of amines, in which the amine group was shown to be involved into hydrogen bonding with foreign molecules. Thus, for aniline/dimethyl sulfoxide (DMSO) complex the deformation vibration $\delta(\text{NH}_2)$ was observed to blue shift by 12 cm^{-1} per intermolecular hydrogen bond with a neighboring DMSO molecule.^[25] Additionally, IR studies on intermolecular interactions of aniline in liquid phase revealed a blue-shift of $20\text{--}30\text{ cm}^{-1}$ for the NH_2 deformation vibration $\delta(\text{NH}_2)$ when aniline forms adducts with other aniline molecules.^[26]

At 250 K, the spectra (Figure 5) show intense vibrational bands at 1755 cm^{-1} ($\nu(\text{C}=\text{N})$), 1580 cm^{-1} ($\delta(\text{NH}_2)$) and 1280 cm^{-1} . The latter band is new and was assigned in the previous theoretical study to the deformation vibration of the imine fragment $\text{H}-\text{N}=\text{C}-$ in the hydrogenation of acetonitrile, which was calculated as one of the products in nitrile hydrogenation.^[20] Following this assignment, we will denote this vibration as $\delta(\text{HNC})$. It is important to emphasize that the calculated vibration at 1280 cm^{-1} is related to the fragment, in which a $\text{N}=\text{C}$ exist and a H atom is attached to N. This fragment should be discriminated from the N-butenylimine species S2 shown in Figure 5, in which N is attached to Pd but not to a H atom.

Simultaneous appearance of the bands at 1755 , 1580 and 1280 cm^{-1} means that both imine and amine species are formed and co-exist in this temperature range. It also suggests that at least two reaction pathways run in parallel to transfer

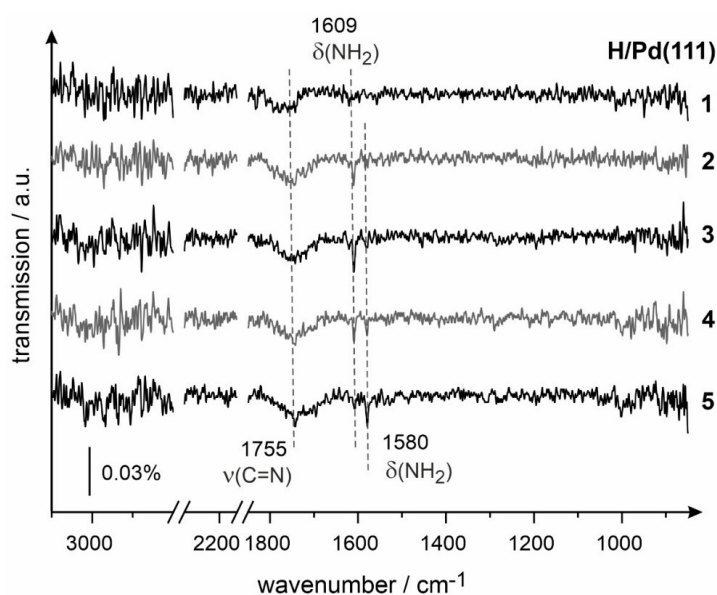


Figure 8. IR spectra of AC obtained on H-containing Pd(111) at 200 K. AC and H₂ were dosed via independent molecular beams at fluxes $7.2 \cdot 10^{12}$ molecules \cdot cm⁻² \cdot s⁻¹ and $8.5 \cdot 10^{14}$ molecules \cdot cm⁻² \cdot s⁻¹, respectively. AC exposures are: (1) $7.2 \cdot 10^{13}$, (2) $2.9 \cdot 10^{14}$, (3) $3.6 \cdot 10^{14}$, (4) $4.3 \cdot 10^{14}$, (5) $7.2 \cdot 10^{14}$ molecules \cdot cm⁻².

the originally deposited AC to co-existing imine and amine surface species.

It is also important to emphasize that the bands at 1580 ($\delta(\text{NH}_2)$) and 1280 ($\delta(\text{HNC})$) cm⁻¹ show a strongly correlated evolution upon prolonged H₂ exposure at a constant temperature. Figure 9 displays a series of IR spectra obtained at 250 K and a continuous exposure of H₂ during different times. At the lowest H₂ exposure (spectrum 1–2), both bands at 1580 and 1280 cm⁻¹ are clearly visible. While the exposure increases (spectra 5–6), a strong simultaneous intensity decrease of both bands is observed, which occurs in a correlated way. The possible reasons of this behavior will be discussed in the following.

Figure 7 shows the proposed model for the competing reaction pathways in successive AC hydrogenation, which is consistent with all spectroscopic observations. For all proposed species, the most important vibrational bands employed for assignment are displayed next to the proposed structure.

At 100 K, AC adsorbed on pristine Pd(111) exhibits an adsorption configuration with the C=C bond is inclined with respect to the surface plane (and therefore visible in IRAS), while the CN group is oriented nearly parallel to the surface (species S1). Upon adsorption of AC on H-precovered surface at 100 K, a fraction of the surface species forms the imine group (C=N) giving rise to a characteristic vibrational band at 1755 cm⁻¹. The formed butenylimine species still contain the C=C double bond (band at 1648 cm⁻¹) and can be principally bound to Pd either via the N atom (N-butenylimine, S2 species) or via the C atom (C-butenylimine, S3 species). Both types of

butenylimine species can undergo further hydrogenation steps, which can be divided into two competing reaction pathways resulting in formation of saturated N-butenylimine (pathway 1) and C-butenylimine species (pathway 2). In the first pathway, the N-butenylimine species (S2) is hydrogenated at the C=C bond producing the N-butenylimine (S4) species in the temperature range 160–250 K. This process is accompanied by stepwise disappearance of all vibrational signatures characteristic for C=C bonds (bands at 1648, 990 and 934 cm⁻¹). In the second pathway, the C-butenylimine (S3) species become also hydrogenated at the C=C bond in the same temperature range forming C-butenylimine species (S5), which exhibits a combination of characteristic bands at 1755 (C=N) and 1280 (HNC) cm⁻¹. In contrast to the first reaction pathway, further hydrogenation steps occur at the imine group of S5 species: the imine group becomes hydrogenated to amine forming C-butenylimine species (S6), showing a typical deformation vibration of the amino groups at 1580 cm⁻¹ ($\delta(\text{NH}_2)$). It is important to emphasize that the species S5 and S6 co-exist on the surface and evolve in a correlated fashion: they appear in the same temperature range and both disappear in a correlated way upon prolonged H₂ exposure in the course of the reaction (Figure 9). Note that the characteristic vibrational bands used to assign the species S5 and S6 ($\delta(\text{HNC})$ at 1280 and $\delta(\text{NH}_2)$ at 1580 cm⁻¹, correspondingly) cannot originate from the same surface species. On the other hand, the nearly simultaneous evolution of these species with increasing temperature and simultaneous disappearance upon prolonged exposure to H₂ suggest that the species S5 and S6 are strongly correlated, most likely as a precursor (S5) and

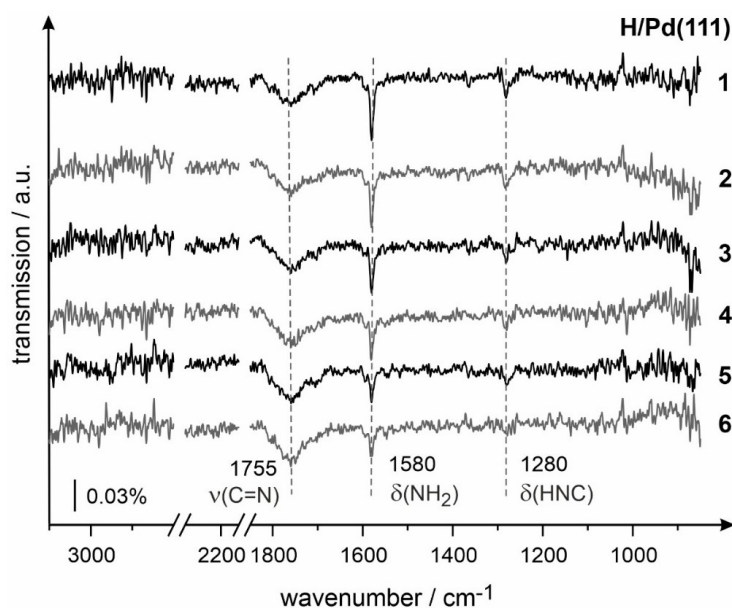


Figure 9. IR spectra of AC obtained at H-containing Pd(111) at 250 K. AC and H₂ were dosed via independent molecular beams at fluxes $7.2 \cdot 10^{12}$ molecules \cdot cm⁻² \cdot s⁻¹ and $8.5 \cdot 10^{14}$ molecules \cdot cm⁻² \cdot s⁻¹, respectively. AC exposure is 1.0 L, H₂ beam was continuously running. Spectra 1–6 correspond to different H₂ exposure times: (1) 0, (2) 135, (3) 270, (4) 405, (5) 540, (6) 675 sec.

the product (S6). These considerations are reflected in the proposed reaction mechanism for the reaction pathway 2, showing that the species C-butylimine species (S5) is the direct precursor to the C-butylamine species (S6).

Summarizing, the combination of all spectroscopic data allows us to conclude that the originally adsorbed AC species S1 undergo successive hydrogenation steps along two competing reaction pathways: in the first pathway, the N-butylimine (S4) species are formed, while the second pathway leads to the formation of the mixture of C-butylimine (S5) and C-butylamine (S6) species. It is important to note that under the hydrogenation reaction conditions (prolonged H₂ exposure, temperatures around 250 K), only one type of species – N-butylimine (S4) – remains present on the catalytic surface, while the other two species – C-butylimine (S5) and C-butylamine (S6) – readily disappear from the surface after prolonged H₂ exposure (see Figure 9). Most likely, the surface species S5 and S6 become fully hydrogenated to molecular butylamine, which is able to desorb. This observation suggests that the active ligand layer, acting in the reaction of chemoselective hydrogenation of acrolein over AC-functionalized Pd(111) catalyst, consists of the stable N-butylimine (S4) species formed in the first pathway. In contrast, the mixture of the unstable C-butylimine (S5) and C-butylamine (S6) species are the spectator species, which readily disappear in the early stages of the reaction.

It should be also noted that the existence of two reaction pathways most likely originates from different adsorption configurations of butylimine species S2 and S3. While

attached to Pd through the N-atom, the N-butylimine (S2) species remain protected from further hydrogenation of the imine part of the molecule. In case of C-butylimine (S3) adsorbates, the non-bonded N-atom can be further attacked by hydrogen and become hydrogenated to amine as observed for the second reaction pathway.

Formation of the stable ligand layer consisting of S4 species turns Pd(111) surface highly active and nearly 100% selective for acrolein hydrogenation.

The different surface species formed as a result of partial AC hydrogenation should be verified in the future theoretical studies to obtain deeper insights in the competing reaction pathways of AC leading to formation of a highly active ligand layer. The structures of all AC-related surface species deduced from the above discussed spectroscopic information provide important starting structures for the future computational studies.

Conclusions

Adsorption of allyl cyanide on pristine and H-containing Pd(111) was investigated by a combination of IRAS, molecular beam techniques and theoretical calculations at B3LYP level.

On pristine Pd(111) surface allyl cyanide adsorbs in the configuration, in which the nitrile groups are oriented parallel to the surface plane, while the C=C bond is tilted. With increasing temperature, the spectroscopic observations suggest

that strong rehybridization of the C=C bond occurs, which might result in formation of π - or di- σ -bonded surface species on the olefinic part of the molecule.

In presence of hydrogen, allyl cyanide undergoes dramatic changes in both the chemical structure of the adsorbed species and their adsorption configuration. At 100 K, allyl cyanide converts to unsaturated imine species – butenylimine – exhibiting characteristic vibrational bands at 1755 cm^{-1} related to the $\text{C}=\text{N}$ fragment and at 1648 cm^{-1} corresponding to the C=C bond. At increasing temperatures, these species can undergo two competing reaction pathways, including stepwise partial hydrogenation at different functional groups. In the first pathway, the C=C bond becomes hydrogenated in the temperature range 160–200 K to produce saturated imine – N-butylimine species – which remain stable under the reaction conditions up to at least 250 K. We hypothesized that these species are strongly bound to Pd via the N-atom as ($\text{C}=\text{N}\cdots\text{Pd}$), which protects the imine group from further hydrogenation. In the competing reaction pathway, the butenylimine species are fully hydrogenated to butyl amine, which desorbs from the surface as molecular species after prolonged hydrogen exposure. In this pathway, both C=C and C=N groups become hydrogenated in the temperature range 160–200 K (for C=C bond) and 200–250 K (for C=N bond). Based on all spectroscopic observations, we propose a mechanistic model explaining the evolution of stable saturated butylimine species resulting from the first reaction pathway and the unstable butylamine adsorbates formed in the second reaction pathway. According to this model, the originally adsorbed allyl cyanide can form butenylimine species in two different configurations: bound via the N- vs. C-atom of the original nitrile group. While attached to Pd through the N-atom, the butenylimine species remain protected from further hydrogenation of the imine part of the molecule. In the opposite case of bonding through the C-atom, the non-bonded N-atom can be further attacked by hydrogen and become hydrogenated to amine as observed for the second reaction pathway. Under the reaction conditions relevant for chemoselective hydrogenation of acrolein (250 K, high hydrogen flux), only the strongly bound N-butylimine species remain on the surface and act as a ligand layer, while the butylamine species desorb.

Obtained microscopic-level insights into the chemical structure of adsorbates formed on AC-functionalized Pd surface and their dynamic changes under the reaction conditions provide important information for purposeful modification of metal catalysts by functionalization with ligand layers to achieve better catalytic performance.

Acknowledgements

This work has been supported by the German Science Foundation (DFG, Grant SCHA 1477/6-1, INST 257/543-1 FUGG). Open Access funding enabled and organized by Projekt DEAL.

Conflict of Interest

The authors declare no conflict of interest.

Keywords: allyl cyanide · infrared spectroscopy · ligand-directed catalysis · reaction mechanisms · reactive intermediates

- [1] R. Dennington, T. A. Keith, J. M. Millam, *GaussView, Version 6.1*, Semichem Inc., Shawnee Mission, KS, 2016.
- [2] T. H. Rod, J. K. Nørskov, *Surf. Sci.* **2002**, *500*, 678–698.
- [3] a) J. P. Collman, Z. Wang, A. Straumanis, M. Quelquejeu, E. Rose, *J. Am. Chem. Soc.* **1999**, *121*, 460–461; b) M. S. Taylor, E. N. Jacobsen, *Angew. Chem. Int. Ed.* **2006**, *45*, 1520–1543.
- [4] a) S. T. Marshall, M. O'Brien, B. Oetter, A. Corpuz, R. M. Richards, D. K. Schwartz, J. W. Medlin, *Nat. Mater.* **2010**, *9*, 853–858; b) F. Meemken, A. Baiker, *Chem. Rev.* **2017**, *117*, 11522–11569; c) A. J. Gellman, W. T. Tysoe, F. Zaera, *Catal. Lett.* **2015**, *145*, 220–232; d) P. Gallezot, D. Richard, *Catal. Rev. Sci. Eng.* **1998**, *40*, 81–126; e) S. T. Marshall, J. W. Medlin, *Surf. Sci. Rep.* **2011**, *66*, 173–184.
- [5] a) P. Sonstrom, M. Baumer, *Phys. Chem. Chem. Phys.* **2011**, *13*, 19270–19284; b) I. Schrader, S. Neumann, A. Sulce, F. Schmidt, V. Azov, S. Kunz, *ACS Catal.* **2017**, *7*, 3979–3987; c) S. Kunz, *Top. Catal.* **2016**, *59*, 1671–1685; d) L. Rodríguez-García, K. Hungerbühler, A. Baiker, F. Meemken, *ACS Catal.* **2017**, *7*, 3799–3809; e) C.-H. Lien, J. W. Medlin, *J. Catal.* **2016**, *339*, 38–46; f) S. H. Pang, J. W. Medlin, *J. Phys. Chem. Lett.* **2015**, *6*, 1348–1356; g) G. J. Hutchings, F. King, I. P. Okoye, M. B. Padley, C. H. Rochester, *J. Catal.* **1994**, *148*, 453–463; h) M. E. Chiu, G. Kyriakou, F. J. Williams, D. J. Watson, M. S. Tikhov, R. M. Lambert, *Chem. Commun.* **2006**, 1283–1285; i) R. A. Sheldon, H. van Bekkum, in *Fine Chemicals through Heterogeneous Catalysis*, Wiley-VCH Verlag GmbH, **2007**, pp. 351–471; j) S. Attia, M. C. Schmidt, C. Schröder, S. Schaueremann, *ACS Catal.* **2019**, *9*, 6882–6889; k) S. Attia, M. C. Schmidt, C. Schröder, J. Weber, A.-K. Baumann, S. Schaueremann, *J. Phys. Chem. C* **2019**, *123*, 29271–29277; l) S. Attia, E. J. Spadafora, J. Hartmann, H.-J. Freund, S. Schaueremann, *Rev. Sci. Instrum.* **2019**, *90*, 053903; m) S. Attia, E. J. Spadafora, M. C. Schmidt, C. Schröder, A.-K. Baumann, S. Schaueremann, *Phys. Chem. Chem. Phys.* **2020**, *22*, 15696–15706; n) M. C. Schmidt, S. Attia, C. Schröder, A.-K. Baumann, P. Pessier, S. Schaueremann, *J. Phys. Chem. C* **2020**, *124*, 14262–14271; o) K.-H. Dostert, C. P. O'Brien, F. Ivars-Barceló, S. Schaueremann, H.-J. Freund, *J. Am. Chem. Soc.* **2015**, *137*, 13496–13502; p) C. P. O'Brien, K.-H. Dostert, S. Schaueremann, H.-J. Freund, *Chem. Eur. J.* **2016**, *22*, 15856–15863; q) K.-H. Dostert, C. P. O'Brien, F. Mirabella, F. Ivars-Barceló, S. Attia, E. Spadafora, S. Schaueremann, H.-J. Freund, *ACS Catal.* **2017**, *7*, 5523–5533; r) S. Attia, M.-C. Schmidt, C. Schröder, P. Pessier, S. Schaueremann, *Angew. Chem. Int. Ed.* **2018**, *57*, 16659–16664.
- [6] W. Binghui, H. Huaqi, Y. Jing, Z. Nanfeng, F. Gang, *Angew. Chem. Int. Ed.* **2012**, *51*, 3440–3443.
- [7] a) J. B. Ernst, S. Muratsugu, F. Wang, M. Tada, F. Glorius, *J. Am. Chem. Soc.* **2016**, *138*, 10718–10721; b) J. B. Ernst, C. Schwermann, G.-i. Yokota, M. Tada, S. Muratsugu, N. L. Doltsinis, F. Glorius, *J. Am. Chem. Soc.* **2017**, *139*, 9144–9147.
- [8] C. Schröder, M. C. Schmidt, P. A. Haug, A.-K. Baumann, J. Smyczek, S. Schaueremann, *Angew. Chem. Int. Ed.* **2021**, *60*, 16349–16354.
- [9] a) M. E. Kordes, W. Stenzel, H. Conrad, *Surf. Sci.* **1988**, *205*, 100–116; b) M. E. Kordes, T. Lindner, J. Somers, W. Stenzel, H. Conrad, A. M. Bradshaw, G. P. Williams, *Spectr. Acta A Mol. Spec.* **1987**, *43*, 1561–1566; c) T. Szilágyi, *Appl. Surf. Sci.* **1988**, *35*, 19–26; d) B. A. Sexton, N. R. Avery, *Surf. Sci.* **1983**, *129*, 21–36; e) S. Semancik, G. L. Haller, J. T. Yates, *J. Chem. Phys.* **1983**, *78*, 6970–6981; f) K. Murphy, S. Azad, D. W. Bennett, W. T. Tysoe, *Surf. Sci.* **2000**, *467*, 1–9; g) N. R. Avery, T. W. Matheson, *Surf. Sci.* **1984**, *143*, 110–124; h) Y. Ren, D. Esan, I. Waluyo, J. D. Krooswyk, M. Trenary, *J. Phys. Chem. C* **2017**, *121*, 9424–9432; i) J. Raskó, J. Kiss, *Catal. Lett.* **2006**, *109*, 71–76; j) E. C. Ou, P. A. Young, P. R. Norton, *Surf. Sci.* **1992**, *277*, 123–131; k) S. Katano, E. Herceg, M. Trenary, Y. Kim, M. Kawai, *J. Phys. Chem. B* **2006**, *110*, 20344–20349; l) D. Jentz, M. Trenary, X. D. Peng, P. Stair, *Surf. Sci.* **1995**, *341*, 282–294; m) D. Jentz, H. Celio, P. Mills, M. Trenary, *Surf. Sci.* **1995**, *341*, 1–8.
- [10] W. Erley, J. C. Hemminger, *Surf. Sci.* **1994**, *316*, L1025–L1030.
- [11] S. Attia, E. J. Spadafora, J. Hartmann, H. J. Freund, S. Schaueremann, *Rev. Sci. Instrum.* **2019**, *90*, 053903.
- [12] M. J. Frisch, et al., *Gaussian 16 Rev. C.01*, Wallingford, CT, 2016.

- [13] a) J. R. Durig, G. A. Guirgis, A. S. Drew, *J. Raman Spectrosc.* **1994**, *25*, 907–921; b) A. L. Verma, *J. Molec. Spect.* **1971**, *39*, 247–254.
- [14] Z. Getahun, C. Y. Huang, T. Wang, B. De Leon, W. F. DeGrado, F. Gai, *J. Am. Chem. Soc.* **2003**, *125*, 405–411.
- [15] B. A. Lindquist, S. A. Corcelli, *J. Phys. Chem. B* **2008**, *112*, 6301–6303.
- [16] F. Hoffmann, *Surf. Sci. Rep.* **1983**, *3*, 107–192.
- [17] F. Zaera, *ACS Catal.* **2017**, *7*, 4947–4967.
- [18] I. Lee, F. Zaera, *J. Phys. Chem. C* **2007**, *111*, 10062–10072.
- [19] C. M. Friend, E. L. Muetterties, *J. Gland, J. Phys. Chem.* **1981**, *85*, 3256–3262.
- [20] L. Vogt, E. Schulte, S. Collins, P. Quaino, *Top. Catal.* **2019**, *62*, 1076–1085.
- [21] H. D. Castillo, J. M. Espinosa-Duran, J. R. Dobscha, D. C. Ashley, S. Debnath, B. E. Hirsch, S. R. Schrecke, M. H. Baik, P. J. Ortoleva, K. Raghavachari, A. H. Flood, S. L. Tait, *Chem. Commun.* **2018**, *54*, 10076–10079.
- [22] R. D. Adams, D. A. Katahira, L. W. Yang, *Organometallics* **1982**, *1*, 231–235.
- [23] a) S. Ohno, M. Wilde, K. Mukai, J. Yoshinobu, K. Fukutani, *J. Phys. Chem. C* **2016**, *120*, 11481–11489; b) A. Doyle, *J. Catal.* **2004**, *223*, 444–453.
- [24] D. F. Johnson, Y. Wang, J. E. Parmeter, M. M. Hills, W. H. Weinberg, *J. Am. Chem. Soc.* **1992**, *114*, 4279–4290.
- [25] C. Greve, E. T. Nibbering, H. Fidder, *J. Phys. Chem. B* **2013**, *117*, 15843–15855.
- [26] H. Wolff, W. Hagedorn, *J. Phys. Chem.* **1980**, *84*, 2335–2337.

Manuscript received: September 7, 2021
Accepted manuscript online: October 5, 2021
Version of record online: October 27, 2021

8.3 Mechanisms Acting in Ligand-Directed Heterogeneous Catalysis: Electronic, Geometric and Enol-Induced Effects

Submission Data

Reference: Carsten Schröder, Ann-Katrin Baumann, Marvin C. Schmidt, Jan Smyczek, Philipp A. Haugg, Ole-Christian Graap and Swetlana Schauerermann

DOI: 10.1021/acs.jpcc.2c00987

Submitted: 03.12.2021

Accepted: 24.02.2022

Contribution: Development of the experimental approach, planning/supervision/performance of IRAS measurements, supervision of Philipp Haugg's, Jan Smyczek's and Ole Graap's bachelor theses, complete experimental planning and data analysis, development of the adsorption models, preparation of the manuscript, DFT gas phase calculations.

Copyright: Reprinted with permission from JPC C from Ref.[177]. Copyright 2022 American Chemical Society.

Mechanisms Acting in Ligand-Directed Heterogeneous Catalysis: Electronic, Geometric, and Enol-Induced Effects

Published as part of *The Journal of Physical Chemistry virtual special issue "Cynthia Friend Festschrift"*.

Carsten Schröder, Ann-Katrin Baumann, Marvin C. Schmidt, Jan Smyczek, Philipp A. Haugg, Ole-Christian Graap, and Swetlana Schauermaⁿ*



Cite This: *J. Phys. Chem. C* 2022, 126, 4907–4920



Read Online

ACCESS |



Metrics & More

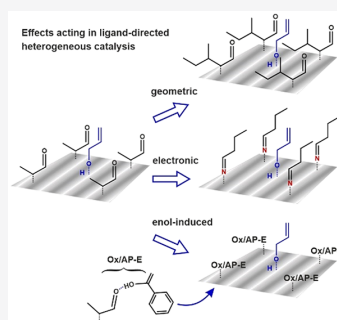


Article Recommendations



Supporting Information

ABSTRACT: We present a mechanistic study on the role of the ligand layer in promoting chemoselective hydrogenation of an α,β -unsaturated aldehyde acrolein toward propanol over functionalized heterogeneous catalysts. By creating a ligand-containing overlayer on Pd(111) via deposition of different types of organic adsorbates, we address the electronic and the geometric effects as well as the effects induced by formation of enol-containing ligand complexes, which play a crucial role in rendering the catalytic surface highly selective toward the hydrogenation of the C=O bond. Toward this goal, we apply a rigorous surface science approach by measuring the isothermal reaction kinetics via multiple molecular beam techniques and by simultaneous monitoring the evolution of the reaction intermediates via *operando* infrared reflection absorption spectroscopy (IRAS). Additionally, the chemical composition of the ligand layer and its dynamic changes under the operational conditions are addressed by IRAS. Specifically, three types of ligand precursors were employed to functionalize the Pd(111) surface: allyl cyanide, 2-methyl-2-pentenal, and acetophenone. We show that principally different fundamental effects—geometric, electronic as well as the effects related to more complex lateral interactions with keto–enol complexes—are acting in catalysis on different types of ligand-functionalized surfaces. It was demonstrated that, by changing the functional groups and the chain length of the ligand, it becomes possible to efficiently tune the interaction of acrolein with the ligand-modified surface to produce the desired reaction intermediate—propenoxy species—and finally the target product propanol. The outcome of this study provides deep atomistic-level insights in surface processes underlying ligand-directed heterogeneous catalysis and offers a prospect of rational design of new catalytic materials with tailor-made catalytic properties.



INTRODUCTION

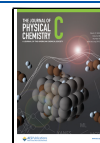
Production of numerous industrially important unsaturated hydrocarbons often relies on heterogeneously catalyzed hydrogenation of their multiunsaturated precursors. In these types of reactions, high chemoselectivity of the overall process is of a pivotal importance as it allows economical production of the target product without expensive separation steps from the undesired components. One of the most challenging tasks here is to improve the chemoselectivity of the multipathway reactions, in which either the undesired products are thermodynamically more stable than the target product or activation barriers to the unwanted components are lower. Indeed, in many cases, the adjustment of the surface structure of the catalytically active material, such as, e.g., changing the particle size, addition of foreign atoms, etc., may result in the acceleration of all reaction pathways including the unwanted reactions, so that the overall selectivity remains poor. One of the important developments of the recent years in the rational design of new catalysts introduces a promising approach based on functionalized interfaces, which are capable of controllable

tuning of the interaction of the reactants with the catalyst. In the scope of this approach, the reactant interacts not only with the underlying metal but also with the coadsorbed organic ligands, exhibiting lateral interactions with the reactants.^{1–7} On these catalytic surfaces functionalized with organic ligands, two independent parameters—the interaction with the underlying catalytically active metal and the lateral interactions with the coadsorbed ligands—can be independently tuned, which should allow selective formation of only one desired reaction intermediate resulting in the preferential formation of the desired reaction product. This approach was recently successfully applied for a broad range of catalytic processes on a variety of functionalized surfaces, such as, e.g., the

Received: February 10, 2022

Revised: February 24, 2022

Published: March 4, 2022



ACS Publications

© 2022 American Chemical Society

4907

<https://doi.org/10.1021/acs.jpcc.2c00987>
J. Phys. Chem. C 2022, 126, 4907–4920

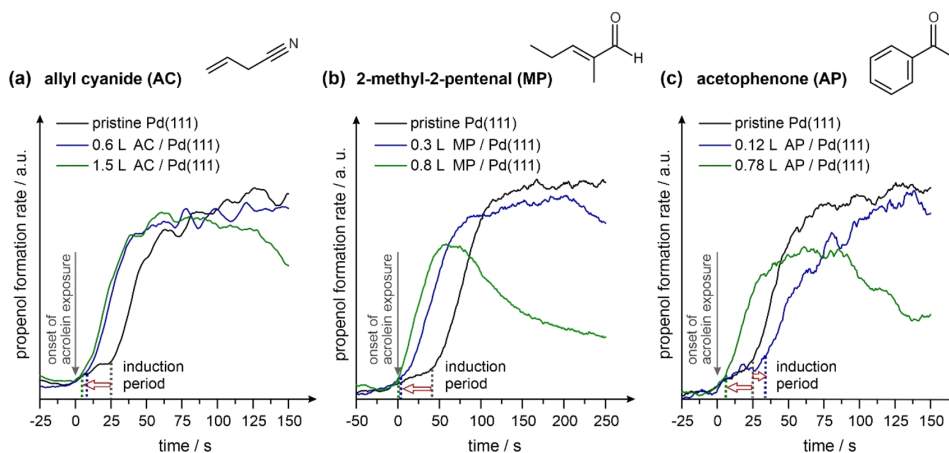


Figure 1. Propenol formation rates on pristine and ligand-modified Pd(111) at different exposures of (a) allyl cyanide (AC), (b) 2-methyl-2-pentenal (MP), and (c) acetophenone (AP) at 250 K (full experimental details in Supporting Information). The exposures in langmuir of all three ligands are indicated next to the kinetic curves. The estimated saturation surface coverages of the ligands deduced from a combination of spectroscopic, kinetic, and scanning tunneling microscopy (STM) results amount to approximately 0.25 monolayer (ML) for AC, 0.25 ML for MP, and 0.2 ML for AP ligands as references to the number of surface Pd atoms.

following: selective hydrogenation of acetophenone, *trans*-stilbene, and phenylacetylene over Pd and Rh nanoparticles functionalized with N-heterocyclic carbenes;^{1,2} selective hydrogenation on the olefinic bond in 1-epoxy-3-butene on *n*-alkanethiol precovered Pd nanoparticles;³ nearly 100% chemoselective hydrogenation of acetophenone to phenylethanol on Pt nanoparticles functionalized with proline;⁴ above 90% chemoselective hydrogenation of the C=O bond in α,β -unsaturated aldehydes in the presence of surface oleylamine array on Pt₃Co nanocrystals;⁵ control of the orientation of various multiunsaturated reactants and considerable improvement of the selectivity in studies on thiolate-based self-assembled monolayers and other organic surface modifiers.⁶ Earlier, a similar approach was utilized to promote enantioselective reactions on heterogeneous catalysts functionalized with chiral organic ligand layers or with individually adsorbed chiral modifier-molecules.⁷

Despite the recent developments in this field, the atomistic-level understanding of the highly selective catalytic systems based on ligand-functionalized surfaces remains rather limited. Thus, in the catalytic literature on ligand-functionalized powdered materials, different possible atomistic origins of the enhanced chemoselectivity were put forward, comprising mostly geometric and/or electronic effects.^{1–13} The geometric effects are usually discussed in terms of the modification of the geometric structure of the surface by adsorbed ligands, such as, e.g., building of ligand ensembles being able to specifically interact with a reactant, molecular recognition leading to formation of 1:1 modifier–reactant complexes, or surface restructuring.¹¹ The electronic effects are commonly explained by the ligand-induced changes in the distribution of the electron density near the surface.^{8,11–13} This type of surface modification can result from, e.g., dipole–dipole coupling producing electrostatic forces on the surface that alter the way the nearby adsorbates bind or via electron donation or withdrawal from the surface by a ligand, especially when the ligand is significantly more electropositive or electronegative than the metal. Also, a competition for the d-electrons of an underlying metal between different adsorbates—the ligands

and the reactants—can be related to the electronic effects, which might affect the binding strength and the adsorption geometry of the reactants on the ligand-functionalized surfaces.^{12,14,15} Although these hypotheses provide some useful starting ideas about the possible microscopic origins of the ligand-related effects, their experimental verification is still lacking, mainly due to a vast complexity of the real powdered catalysts and a strong heterogeneity of the different adsorption sites on these materials.

In our recent studies, employing a rigorous surface science approach, we addressed the mechanistic aspects of ligand-induced heterogeneous catalysis.^{16–19} Specifically, selective hydrogenation of acrolein—the simplest α,β -unsaturated aldehyde—to the desired product unsaturated alcohol (propenol) over ligand-functionalized surfaces was investigated. For this system, we provided first microscopic-level insights into the mechanisms acting in ligand-directed catalysis. It was shown that a densely packed ligand layer can be formed on Pd(111) under the operational conditions, which promotes the adsorption of acrolein in the desired adsorption configuration—via the C=O double bond—thus enabling hydrogenation of this bond to form propenol with close to 100% selectivity. Two different types of ligand surface species were identified in these studies—oxopropyl^{18,19} and *N*-butylimine^{16,17} surface species—which are formed and dynamically change under the operational condition. In contrast to the ligand-functionalized surfaces, the other entity—the C=C double bond—tends to be predominantly hydrogenated on the pristine Pd(111) surface.^{18,19}

These studies provided some starting ideas about the role of the ligand layer in promoting the selective hydrogenation of C=O bond in α,β -unsaturated aldehydes and ketones. However, the full atomistic-level understanding of the related surface phenomena is still missing. Specifically, it is not well understood what type of ligand-induced effects—the pure geometric and/or electronic effects—play a role in rendering the catalytic surface highly selective toward hydrogenation of the C=O bond. To obtain deeper insights into these aspects of ligand-assisted catalysis, we performed a systematic study on

chemoselective hydrogenation of acrolein to propenol, in which three different types of ligands were utilized for surface functionalization of Pd(111): allyl cyanide (AC), 2-methyl-2-pentenal (MP), and acetophenone (AP). The combination of these ligands allowed us to study the mechanistic details of the related surface processes (i) in the presence of surface adsorbates possessing a functional group with high electron density (AC) to address *the electronic effects*, (ii) in the presence of a ligand structurally similar to already known oxopropyl ligand, but possessing a larger aliphatic tail (MP) in order to address *the geometric effects*, and (iii) in the presence of an adsorbate capable of undergoing keto–enol tautomerization followed by 1:1 lateral interactions and with coadsorbed reactant (AP). We employ a unique combination of surface sensitive *operando* spectroscopy (infrared reflection absorption spectroscopy, IRAS) with multimolecular beam techniques, which allows one to study the reaction kinetics under well-defined isothermal conditions and simultaneously monitor the evolution of the desired reaction intermediate on the surface. Additionally, the chemical composition of the ligand layer and its dynamic changes under the operational conditions were monitored by IRAS. Specifically, we show that principally different effects—geometric and electronic as well as the effects related to more complex interactions with keto–enol complexes—are acting in catalysis on different types of ligand-functionalized surfaces. We demonstrate that by changing the functional groups of the ligand and the chain length, it becomes possible to effectively tune the interaction of acrolein and the desired reaction intermediate—propenoxy species ($\text{CH}_2=\text{CH}-\text{CH}-\text{O}\cdots\text{Pd}$)—with the ligand-modified surface. The results of this study provide deep atomistic-level insights in surface processes underlying ligand-directed heterogeneous catalysis and offer important tools for rational design of new catalytic materials.

RESULTS AND DISCUSSION

Acrolein conversion to the target product propenol was investigated on four different catalytic surfaces: pristine Pd(111) and Pd(111) functionalized with three different ligands—allyl cyanide (AC), 2-methyl-2-pentenal (MP), and acetophenone (AP). Full experimental details are given in the [Supporting Information](#). [Figure 1](#) shows the formation rates of the target product propenol measured on three surfaces functionalized with (i) allyl cyanide ([Figure 1a](#)), (ii) 2-methyl-2-pentenal ([Figure 1b](#)), and (iii) acetophenone ([Figure 1c](#)). All functionalized surfaces were pretreated with H_2 at the reaction temperature for an extended period of time as described in the [Supporting Information](#), followed by the ligand deposition and further H_2 treatment to allow for possible chemical transformations of the ligand layer under the reaction conditions. In the kinetic measurements, each surface—either pristine or functionalized with the ligand—was continuously exposed to H_2 at the reaction temperature (prior the reaction) via an effusive molecular beam; at the time moment indicated as zero, the acrolein beam was opened. Formation rates of both feasible partial hydrogenated products propenol (target molecule) and propanal (undesired, not shown) were monitored in the gas phase by quadrupole mass spectrometry (QMS), while the evolution of different adsorbate species formed on the surface turning over was followed by *operando* IRAS. Each graph shown in [Figure 1](#) contains also the kinetic curve measured on pristine Pd(111) under identical conditions plotted as a reference, while the colored lines are related to the kinetic

curves obtained on functionalized surfaces for different ligand coverages. It can be clearly seen that kinetic behavior of this reaction is strongly affected by the presence of the ligand layer. Thus, the propenol formation rate measured on pristine Pd(111) ([Figure 1a](#)) exhibits a clear induction period (the time between zero and the onset of propenol formation rate) of about 25 s. The origin of this behavior was addressed in our previous studies.^{16,18–20} Briefly, acrolein adsorbs on the pristine surface during this time and forms a densely packed ligand layer consisting of oxopropyl species, which occupy approximately every second Pd atom (corresponding to the surface coverage of approximately 0,4 oxopropyl species per surface Pd atom^{18,19}). The oxopropyl species are formed from acrolein via an addition of one H atom to the C=C double bond.²⁰ After a complete oxopropyl layer is formed, acrolein starts adsorbing in the desired adsorption geometry—via the C=O end—and forms the target reaction intermediate propenoxy species ($\text{CH}_2=\text{CH}-\text{CH}-\text{O}\cdots\text{Pd}$) via an addition of an H atom to the C=O bond, which can be further hydrogenated to propenol.^{19,20} Thus, the induction period observed on pristine Pd(111) is related to the prolonged formation of the oxopropyl ligand layer, rendering the surface active toward acrolein hydrogenation to propenol.¹⁹ It should be emphasized that the reaction of selective acrolein hydrogenation to propenol occurs not on the pristine Pd(111) surface, but on the surface already covered by a densely packed layer of oxopropyl ligand species (absolute coverage 0,4 oxopropyl adsorbates per surface Pd atom), which is completely formed by the end of the induction period. For this reason the term “initially pristine” Pd(111) is related to the surface covered by an oxopropyl ligand layer.

Once the surface was pretreated with allyl cyanide at different coverages (blue and green lines in [Figure 1a](#)), the induction period is nearly eliminated, and almost instantaneous formation of propenol is observed.¹⁶ The absolute formation rates of propenol reach the similar level as on pristine Pd(111); however, at higher AC coverage, the propenol formation rate starts declining earlier than that on the initially pristine Pd(111). The reason for the reactivity decline was discussed in our previous studies and was referred to acrolein decomposition producing ethylidene(-like) species.^{18,19} A very similar scenario can be also observed in case of Pd(111) functionalized with 2-methyl-2-pentenal (MP, [Figure 1b](#)). Also here, the induction period is nearly eliminated when the surface was pretreated with MP prior the reaction, suggesting that the functionalized surface immediately offers the environment, which is capable of promoting the formation of the desired reaction intermediate propenoxy species and the target product propenol. In contrast, the effect of acetophenone (AP) as a ligand appears more complex ([Figure 1c](#)): at lower AP coverages, a significant increase of the induction period is observed (from 25 to 33 s), while at the higher AP ligand coverages, the induction period drastically decreases as compared to that for the pristine surface. Note that in neither case was formation of the undesired product propanal detected. Also note that the acrolein flux used in the experiments shown in [Figure 1b](#) was chosen to be about a factor of 2 lower than the acrolein flux related to [Figure 1](#), parts a and c. In this case ([Figure 1b](#)), the induction period on pristine Pd(111) amounts to about 50 s, which is twice longer than the induction period of approximately 25 s measured on the same pristine surface with the higher acrolein flux (see the black traces in the [Figure 1](#), parts a and c). This effect is related

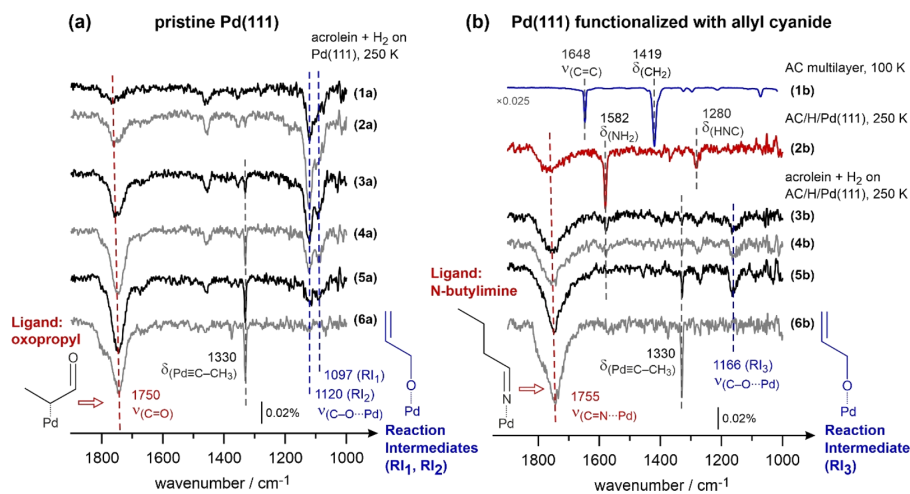


Figure 2. IR spectra obtained during acrolein hydrogenation on (a) pristine Pd(111) and (b) Pd(111) functionalized with AC at the reaction temperature 250 K (AC coverage 0.25 ML). The acrolein exposure times: 110 s (1a) to 1100 s (6a); 120 s (3b) to 1030 s (6b). The spectra 1b and 2b were recorded for pure AC under nonreactive conditions at 100 K and under the reactive conditions (in the presence of H₂ but prior to acrolein exposure, 250 K, AC exposure 1.0 L), correspondingly (full information on exposure times and fluxes in Chapter 3 in the Supporting Information).

not to the irreproducibility of the measurement but merely to the fact that the oxopropyl ligand, which is formed on the initially pristine Pd(111) surface during the induction period, is built up at a factor of 2 slower rate when acrolein is dosed at a factor of 2 lower flux. More detailed discussion on the dependency of the reactivity curves on acrolein flux can be found in Chapter 4 in the Supporting Information.

These observations suggest that strongly different mechanisms may act in rendering the surface highly selective toward acrolein hydrogenation. To explore the atomistic-level details of the underlying surface processes and the effects related to the chemical structure of the ligand layer under the reaction conditions, we performed *operando* IRAS studies on the surfaces turning over, allowing us to monitor the time evolution of different adsorbate species.

Figure 2 shows the comparison of the surface composition under the reaction conditions monitored as a function of the reaction time for two different surfaces—pristine Pd(111) (Figure 2a) and Pd(111) functionalized with AC (Figure 2b). On initially pristine Pd(111), three major surface species can be identified in the course of the reaction: the oxopropyl ligand species (1750 cm⁻¹, ν(C=O)); this species results from attachment of a single H atom to the C=C double bond of acrolein), the propenoxy reaction intermediate (the bands at 1120 and 1097 cm⁻¹, ν(C-O)); the species results from attachment of a single H atom to the C=O of acrolein), and ethylidene species resulting from decomposition of acrolein (the band at 1330 cm⁻¹, δ(Pd≡C-CH₃)).¹⁹ The proposed structures for each species are shown next to the corresponding bands in Figure 2a. It is important to note that these three species were shown to evolve at different stages of the reaction: the oxopropyl ligand species appears at the early stages of acrolein exposure—in the induction period of the reaction—and forms a densely packed overlayer on Pd(111), in which approximately every second Pd atom is covered by the ligand. The time-resolved IR spectra clearly showing this effects are discussed in the previous study.¹⁹ Importantly, the evolution of the oxopropyl ligand is not correlated to the evolution of propenol in the gas phase: even when the propenol formation

rate decreases to zero, the oxopropyl ligand remains adsorbed on the surface indicating that this cannot be the direct reaction intermediate.¹⁸ In contrast—the propenoxy species (bands at 1120 and 1097 cm⁻¹) show a very clear correlation with the evolution of propenol in the gas phase—the intensity of these bands grows and later declines, showing a strong correlation with the formation rate of propenol in the gas phase.^{18,19} Based on this very strong correlation (for more details see ref 19), we assign the propenoxy species to the direct reaction intermediate, which can be transferred to propenol via an insertion of a single H atom into the O···Pd bond. It is important to emphasize that by performing *operando* IR measurements with higher time resolution, it was possible to prove that the reaction intermediate appears not on the clean Pd(111) surface but on the surface containing a densely packed layer of the oxopropyl species.¹⁹ This observation suggests that the overlayer of ligand species critically affects the interaction of acrolein with the functionalized metal surface and promotes formation of the desired reaction intermediate. The third surface species identified on this surface is ethylidene species²¹ (1330 cm⁻¹, δ(Pd≡C-CH₃)), which is formed as a result of acrolein decomposition and poisons the catalytic surface leading to reactivity decline. The latter effect is observed for all investigated ligand-functionalized systems and will not be further discussed separately for each of them.

Based on this correlation, two vibrational bands—at 1097 and 1120 cm⁻¹—can be related to the propenoxy reaction intermediate. Both bands lie in the typical vibrational range of a C-O single bond with O attached to Pd as it was demonstrated for a broad range of dissociated alcohols^{22–25} and esters^{26,27} adsorbed on transition metals. In the following, these species will be indicated as RI₁ (band at 1097 cm⁻¹) and RI₂ (band at 1120 cm⁻¹) species. Note that both bands show strong correlation with the formation rate of propenol in the gas phase. The reason for the appearance two different types of the propenoxy reaction intermediate is not quite clear though it can be potentially related (i) to the different adsorption sites on Pd (111)—on-top vs bridge vs hollow sites—or (ii) to the possible lateral interactions with the neighboring surface

species, e.g., oxopropyl ligand species. Indeed, it is well-known that the lateral interaction, e.g., hydrogen bonding between an O atom of one molecule and an acidic H atom of the other molecule, might result in a strong frequency shift of the band related to the involved atoms. Such effects were previously described for a broad range of hydrocarbon compounds, both in the gas phase and adsorbed on surfaces.^{28,29} As strong H-bonding of an O atom with the neighboring molecules usually weakens the C–O bond containing this O, a red shift of this band can be expected.³⁰ In the scope of this model, the band at 1097 cm^{-1} would be related to a H-bonded reaction intermediate RI_1 , while the less perturbed band at 1120 cm^{-1} (RI_2) would rather correspond to the free-standing species. Figure 3a shows the proposed model of such a

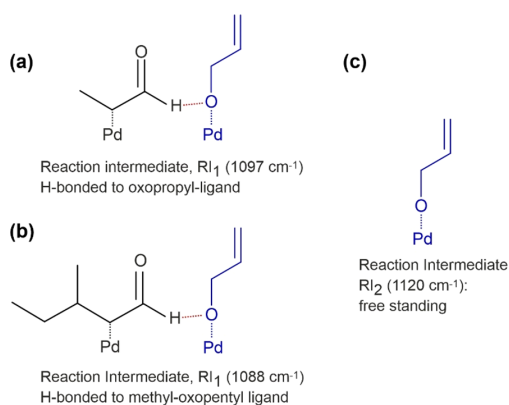


Figure 3. Proposed structures of the reaction intermediates RI_1 and RI_2 . In the scope of the suggested model, RI_1 is capable of building a complex with the coadsorbed ligand, either oxopropyl (a) or methyl-oxopentyl (b) species, while RI_2 is a free-standing adsorbate (c).

complex between an oxopropyl ligand and the O atom of the propenoxy reaction intermediate RI_1 . Note that significant frequency shifts are expected only if an acidic H atom is involved,^{30,31} so that the most likely candidate for such an oxopropyl–propenoxy complex might involve the H atom of the aldehyde group.

In the following, we will specifically focus on the appearance of the bands related to the reaction intermediate—their frequencies and the relative intensities—as a function of the chemical composition of the catalytic surface functionalized with different types of ligands.

The first example of this surface composition on the functionalized catalyst is shown in Figure 2b for the case of allyl cyanide. Spectrum 1b is related to the multilayer of AC adsorbed on pristine Pd(111) at 100 K in absence of hydrogen, which serves as a reference for a largely unperturbed form of AC. Two major peaks can be identified in this spectrum, which are related to the C=C stretching vibration ($\nu(\text{C}=\text{C})$) at 1648 cm^{-1} and C–H deformation vibration ($\delta(\text{CH}_2)$) at 1419 cm^{-1} . Note that the band related to the other prominent C≡N vibration lies outside the shown range, but can be seen in the full range spectrum in the Supporting Information (Figure S1). Spectrum 2b shows the composition of the surface, which was pretreated with AC and H_2 at the reaction temperature 250 K. It can be clearly seen that the chemical nature of the adsorbed species drastically changes under these conditions.

Previously we have shown^{16,17} that the main surface species formed are *N*-butylimine species, resulting from partial hydrogenation of AC at the C=C and C≡N bonds, with the C=C bond being hydrogenated to C–C bond and the C≡N bond forming imine species (C=N...Pd bond, $\nu(\text{C}=\text{N})$, appearing at 1755 cm^{-1} in spectrum 2b). There is also a second AC derivative—the amine species (the characteristic band $\delta(\text{NH}_2)$ at 1582 cm^{-1}) resulting from the alternative reaction pathway of AC hydrogenation. Importantly, only the *N*-butylimine species remain stable in the course of the reaction—when the AC-functionalized surface is exposed to acrolein and H_2 simultaneously at 250 K—while the amine-related species disappear already at the early stages of the reaction, desorbing from the surface as fully hydrogenated butylamine.¹⁶ This conclusion can be deduced from the series of spectra 2b–4b shown in Figure 2b, which were obtained during acrolein and H_2 exposure: while the band at 1755 cm^{-1} (stable *N*-butylimine ligand) remains present and intense during the entire course of the reaction, the amine-related species ($\delta(\text{NH}_2)$, 1582 cm^{-1}) quickly disappear. Additionally, the chemical transformations of originally deposited AC under the reaction conditions were found to be accompanied by strong changes of the spacial distribution of adsorbed AC species and formation of a densely packed *N*-butylimine ligand layer. More details on the microscopic structure of the formed ligand layer resolved by STM can be found elsewhere.¹⁶ The most interesting observation was done, however, for the reaction intermediate (RI_3), which appears in approximately the same range typical for C–O single bond stretching vibration and whose time evolution is also strongly correlated with the formation rate of propenol detected in the gas phase. However, its vibrational frequency (1166 cm^{-1}) is strongly blue-shifted with respect to the reaction intermediates RI_1 and RI_2 observed on the surface covered with oxopropyl ligand layer (see Figure 2a). This exceptionally large frequency shift (by 69 and 46 cm^{-1}) with respect to the reaction intermediates RI_1 and RI_2 suggests a strong perturbation of the electronic structure of the reaction intermediate RI_3 by the interaction with ligand layer consisting of *N*-butylimine species containing an electron-rich imine group. Indeed, the blue shift suggests the strengthening of the C–O bond in the reaction intermediate, which can potentially arise from two possible reasons. First, the degree of donation and backdonation of the electron density between the molecular orbitals of the reaction intermediate and the metal might be strongly altered on the *N*-butylimine containing surface. Indeed, previous theoretical calculations on acrolein interaction with Pd(111)³² showed that a strong rehybridization of the molecular orbitals of acrolein and the d-orbitals of Pd occurs, resulting in a substantial depletion of the electron density mostly on the (former) HOMO–1 orbital of acrolein and gaining the electron density on the (former) LUMO orbital. In the same study, it was also demonstrated that the electron density redistribution between acrolein and the underlying metal might be strongly affected by coadsorbates, such as, e.g., H. In the case of Pd(111) functionalized with *N*-butylimine, similar effects can be expected to play a role—the presence of the electron-rich imine group might affect the availability of d-electrons and change the degree of donation/backdonation between the molecular orbitals of RI_3 and the d-orbitals of Pd, so that the C–O bond in the reaction intermediate becomes strengthened and the corresponding frequency shifts to higher

values. In the following, we will refer to this mechanism as to “surface mediated”.

The other possible scenario might be related to the direct intermolecular interaction between coadsorbed *N*-butylimine species and the reaction intermediate RI_3 , e.g., donation of the electron density from the electron-rich imine group to the molecular orbital associated with the C–O entity. In order to result in the experimentally observed blue frequency shift, i.e., strengthening of the C–O bond, the corresponding molecular orbital of RI_3 must be bonding. The exact origin of the C–O bond strengthening on *N*-butylimine containing Pd(111) should be addressed in the upcoming theoretical calculations.

Even though the exact reason for the strong frequency shift in RI_3 cannot be unambiguously deduced from the available experimental data set, it can be rather confidently concluded that these exceptionally large shifts are rather related to the electronic effects, i.e., to the (direct or surface mediated) interaction between the electron-rich imine groups and the molecular orbitals related to the C–O entity, and it cannot be explained merely by crowding and/or dipole coupling effects. Indeed, the ligand densities are comparable in both reactive systems, so that about similar distributions of ligand-adsorbates and the associated dipoles are expected on these two surfaces. In this case, no strong differences in the frequencies (RI_1 , RI_2 vs RI_3) can be expected merely due to the crowding and/or dipole coupling effects. In contrast, different electronic coupling between the adsorbates—either in a direct way or through the Pd surface as described above—might potentially result in significant shifts of the band positions.

To further investigate the possible role of the electronic vs geometric effects, we studied hydrogenation of acrolein and evolution of the surface species on Pd(111) functionalized with 2-methyl-2-pentenal, which is structurally very similar to acrolein itself and was expected to build the ligand layer similar to oxopropyl ligand species. Figure 4 shows the comparison of

the propenol formation rate measured on the initially pristine Pd(111) and the same catalyst precovered with 2-methyl-2-pentenal under otherwise identical reaction conditions. Both kinetic experiments were carried out in a pulsed manner: the surface was first continuously exposed to H_2 and at the time moment zero acrolein was dosed for 20 s pulses with a flux of 2.4×10^{12} molecules·cm⁻²·s⁻¹, while the time between pulses amounted to 110 s. It can be easily seen that the onset of propenol formation rate in the gas phase occurs significantly earlier on the surface functionalized with 2-methyl-2-pentenal: the measurable reaction rate can be seen already in the second pulse, while on the initially pristine Pd(111), approximately the same formation rate of propenol was reached in the fifth pulse. Similar to the case of *N*-butylimine ligand described above, this observation suggests that preadsorbed ligand turns the surface active and chemoselective and enables nearly instantaneous formation of the desired propenoxy reaction intermediate.¹⁶ To obtain more atomistic-level insights into the composition of the surface turning over, an *operando* IRAS study was simultaneously performed during the pulsed kinetic experiments shown in Figure 4. Figure 5 shows the comparison of the surface composition under the reaction conditions obtained on pristine Pd(111) (Figure 5a) and Pd(111) precovered with 2-methyl-2-pentenal (Figure 5b). Note that the reactant fluxes were deliberately chosen to be low, so that the evolution of two possible reaction intermediates RI_1 and RI_2 , previously observed on pristine Pd(111), could be measured in the time-resolved way. Specifically, Figure 5a shows a series of IR spectra obtained during the acrolein pulses displayed in Figure 4a. From this data set, it can be clearly seen that the peak at 1097 cm⁻¹ related to the reaction intermediate RI_1 , appears first and dominates the spectrum at low acrolein exposures (spectra 1a–2a). However, with increasing total amount of deposited acrolein, the band at 1120 cm⁻¹ related to the reaction intermediate RI_2 starts to grow (spectrum 4a), and finally its intensity prevails over the intensity of RI_1 species (spectrum 5a). This noncorrelated time evolution of these vibrational peaks additionally confirms our initial hypothesis that the bands at 1120 and 1097 cm⁻¹ are related to two independent reaction intermediates.

Figure 5b shows the IR spectra obtained on Pd(111) precovered with 2-methyl-2-pentenal. The uppermost spectrum was measured for a multilayer of 2-methyl-2-pentenal serving as a reference for the unperturbed state of MP, in which the absolute majority of the molecular species are not in the direct contact with the metal surface. The most prominent peak in this spectrum is the band at 1683 cm⁻¹ related to the $\nu(C=O)$ stretching vibration,^{33,34} which is conjugated to the C=C double bond of MP. The shoulder at 1643 cm⁻¹ is attributed to the stretching vibration $\nu(C=C)$.^{33,34} Spectrum 2b shows 2-methyl-2-pentenal adsorbed on Pd(111) in the presence of hydrogen and at 250 K, which corresponds to the reaction temperature used in the kinetic studies shown in Figure 4b. It can be clearly seen that the chemical structure of the ligand undergoes strong changes under the reaction conditions: the band at 1683 cm⁻¹ and the shoulder at 1643 cm⁻¹ disappear, while an intense band at 1745 cm⁻¹ is formed. This chemical changes are most likely related to partial hydrogenation of 2-methyl-2-pentenal: one H atom becomes incorporated into the C=C double bond producing the methyloxopentyl ligand, whose proposed structure is shown close to the band at 1745 cm⁻¹. In this surface species, the C=O double bond is preserved but is not conjugated to the C=C

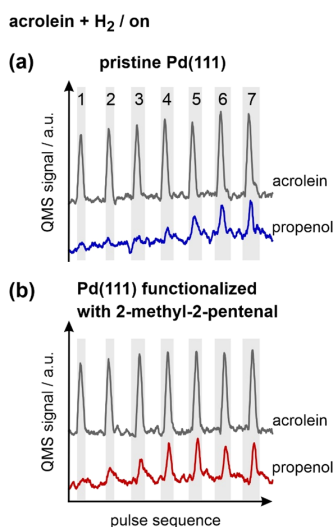


Figure 4. Propenol formation rates of propenol on (a) pristine Pd(111) and (b) Pd(111) functionalized with MP obtained at 250 K under continuous H_2 exposure and acrolein dosed as a sequence of pulses. For each surface, the evolution of acrolein in the UHV chamber is plotted as a reference (full description in Supporting Information).

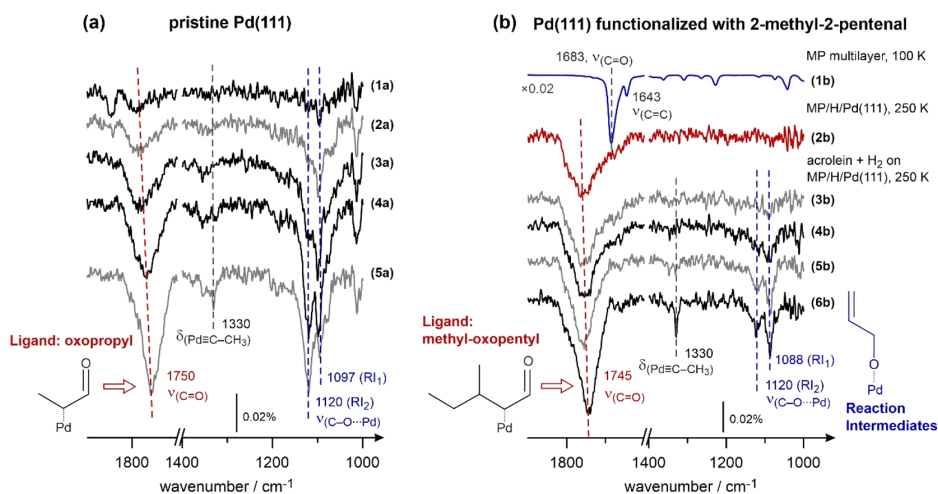


Figure 5. IR spectra obtained during acrolein hydrogenation on (a) pristine Pd(111) and (b) Pd(111) functionalized with MP at the reaction temperature 250 K. The spectra 1b and 2b were recorded for pure MP under nonreactive conditions at 100 K and under the reactive conditions (in the presence of H₂ but prior to acrolein exposure, 250 K), correspondingly (full description in the [Supporting Information](#)).

double bond, so that the frequency of the carbonyl group shifts by approximately 60 cm⁻¹ to 1745 cm⁻¹. Previously, nearly identical frequencies in the similar range were detected for a range of carbonyl compounds with the nonconjugated carbonyl groups.^{33,35–37} A very similar half-hydrogenation of the C=C bond was previously observed in our studies on acrolein in the same temperature range, producing oxopropyl surface species,^{18–20} whose chemical structure is shown in [Figure 5a](#) close to the band at 1750 cm⁻¹. Similar vibrational frequencies of the major visible bands (1750 cm⁻¹ for the oxopropyl species and 1745 cm⁻¹ for the methyloxopentyl species) arise from the very similar chemical structures of these ligands. Indeed, the local configuration of the C=O group in the ligand remains the same for both species: they contain a nonconjugated C=O double bond with the β-C atom being attached to Pd, while the only difference is related to the length of the aliphatic tail.

The similar chemical nature of both ligands—oxopropyl and methyloxopentyl—results in formation of very similar reaction intermediates exhibiting vibrational bands at 1120 cm⁻¹ (RI₂) and 1088 cm⁻¹ (RI₁). Note that the latter frequency slightly differs from the frequency of the RI₁ observed on the oxopropyl-covered surface (1097 cm⁻¹).^{18–20} However, as these bands are still very close in frequencies and exhibit a similar temporal evolution, which will be discussed later, we will denote both species as RI₁. The appearance of two bands related to the reaction intermediate on this surface, which are very similar to the RI observed on the surface covered with oxopropyl ligand, additionally confirms our hypothesis discussed above for the case of *N*-butylimine ligand: the electronic structure of the ligand might strongly affect the strength of the C–O bond in the reaction intermediates: (i) it becomes stronger when the electronically rich CN group is introduced into the ligand, and (ii) it remains unchanged when only the length of the aliphatic tail is changed but electronic properties of the functional group—the unconjugated C=O group—remain preserved, as in the case of oxopropyl vs methyloxopentyl species.

The more spacious methyloxopentyl ligand results, however, in a strong change in the distribution of the RI₁ vs RI₂ species.

While on both surfaces the formation of the reaction intermediate begins with the RI₁ species, the final distribution of the reaction intermediates RI₁ vs RI₂ is drastically different. On the oxopropyl-covered surface ([Figure 5a](#)), the species RI₂ start to significantly grow in spectrum 3a (after the band at 1097 cm⁻¹ reaches the saturation) so that the species RI₂ eventually dominates the spectrum (spectra 4a and 5a). In contrast, on the surface precovered with methyloxopentyl ([Figure 5b](#)), the species RI₂ grow somewhat in intensity with increasing acrolein exposure (also after the band at 1088 cm⁻¹ reaches the saturation); however, the intensity of RI₂ always remains minor. Interestingly, the integral intensities of the bands related to the species RI₁, which were reached after saturation, are approximately similar on both surfaces ([Figure S3](#) in [Supporting Information](#)). Even though the IR spectra do not provide accurate quantitative information, the amounts of the RI₁ species produced on both surfaces seem to be comparable. In contrast, the oxopropyl-covered surface appears to be able to additionally accommodate large amounts of RI₂ species after the surface was saturated with RI₁ adsorbates, so that the RI₂ species finally prevail. In contrast, on the surface covered with more spacious methyloxopentyl species, the RI₂ species can still be formed after the saturation coverage of RI₁ was reached, but the absolute amount of RI₂ remains, however, very small (see [Figure S3](#) and the related discussion in [Supporting Information](#)).

These observations suggest that comparable and finite amounts of RI₁ reaction intermediates can be built on both surfaces. In contrast, the surface covered with the smaller ligand (oxopropyl) can additionally accommodate large quantities of the second reaction intermediate RI₂, while on the surface covered with the more spacious ligand (methyloxopentyl) substantially smaller amounts of RI₂ can be formed. One of the possible scenarios for this type of behavior is consistent with our previously described hypothesis that the species RI₁ and RI₂ are related to the reaction intermediate bound via an H bonding to the aldehyde-H of the ligand surface species (RI₁) and to a free-standing reaction intermediate (RI₂), correspondingly. The schematic illustrations of the H-bonding between the reaction intermediate RI₁

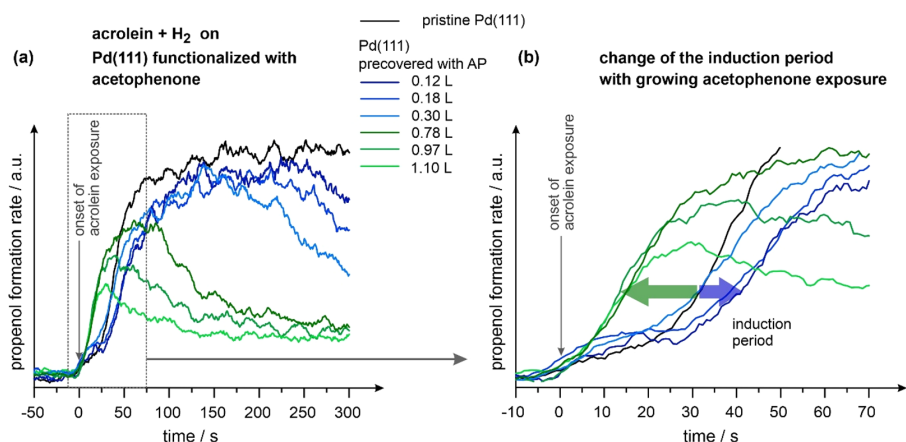


Figure 6. (a) Propenol formation rates on Pd(111) functionalized with AP at different exposures measured at 250 K. The black trace was obtained on pristine Pd(111) under otherwise identical reaction conditions (full description in Supporting Information). (b) Inset showing the changes of the induction period as a function of AP exposure.

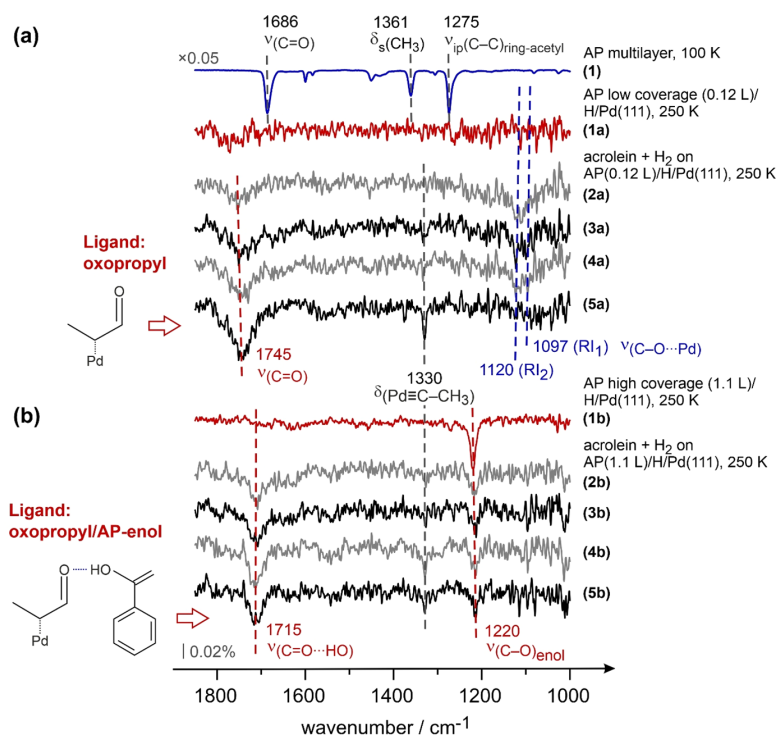


Figure 7. IR spectra obtained during acrolein hydrogenation at 250 K on Pd(111) functionalized with AP for two different AP exposures: (a) 0.12 L and (b) 1.1 L. Spectrum 1 corresponds to pure AP adsorbed as multilayer under nonreactive conditions at 100 K. Spectra 1a and 1b were recorded for pure AP adsorbed on Pd(111) under the reactive conditions (in the presence of H₂ but prior to acrolein exposure, 250 K) for low (0.12 L) and high (1.1 L) AP coverages, correspondingly (full description in the Supporting Information).

and both, the oxopropyl and methyloxopentyl species, are shown in Figure 3. Indeed, establishing of H bonding between the RI₁ and the aldehyde-H of the ligand results in formation of 1:1 complexes, which absolute amount is limited by the number of ligand adsorbates on the surface. This hypothesis might explain why the RI₁ species are formed at about comparable amounts on both surfaces since the absolute amounts of the ligand adsorbates in the densely packed ligand

layers are comparable. In contrast, the free-standing species RI₂ form at higher acrolein exposures after the intensity of the bands related to RI₁ saturates. This might occur via formation of RI₂ at the empty spaces between the 1:1 ligand/RI₁ complexes. On the surface covered with the smaller ligand (oxopropyl), more space is potentially available, so that larger amounts of RI₂ species can be formed, which corresponds to the experimental observation. On the surface covered with

more spacious ligand (methyloxopentyl), less empty space is most likely available, resulting in a minor formation of the free-standing RI_2 . In our view, this is the only hypothesis that explains two experimentally observed facts: (1) the saturation of the reaction intermediate RI_1 at comparable coverages on both types of surfaces and (2) drastically different amounts of the additionally formed reaction intermediate RI_2 , whose abundance is anticorrelated with the size of the aliphatic tail. In the scope of this model, the slight differences in the frequencies of the reaction intermediate RI_1 might be related to their slightly different chemical bonding to the ligands (oxopropyl vs methyloxopentyl). For the proposed free-standing RI_2 , the frequencies (1120 cm^{-1}) coincide on both surfaces suggesting that they are not affected by the coadsorbed ligand.

To further explore the possible effects of strong lateral interactions between the coadsorbed ligands and the reaction intermediates, the reactivity of acrolein hydrogenation was investigated on the surface precovered with acetophenone, which was shown in our previous studies to be capable of undergoing strong intermolecular interactions.^{29,38–42} Figures 6 and 7 show the kinetic data of propenol formation and the related IR spectra obtained under operational conditions, correspondingly. In these experiments, the surface was covered with different amounts of acetophenone, which can be tentatively divided into low (exposure: 0.12–0.30 L) and high (exposure: 0.78–1.10 L) AP coverages. Depending on the AP coverage range, strongly different kinetic behavior and formation of surface species was observed. Figure 6a shows the formation rate of the target product propenol on Pd(111) covered with low (blue lines) and high (green lines) AP coverages. The black line is related to propenol formation rate on the initially pristine Pd(111), i.e., covered with spontaneously formed oxopropyl species. It can be clearly seen that the induction period is strongly affected by the AP coverage, as shown in Figure 6b, displaying the induction period on a shorter time scale. While functionalization of Pd(111) with small AP coverage results in the significant elongation of the induction period (from approximately 20 s on the pristine surface to 35 s on Pd(111) exposed to 0.12 L of AP), the induction period drastically shortens (below 5 s) on the surface exposed to more than 0.78 L of AP. In this latter case, the structure of the formed ligand layer obviously allows for nearly instantaneous formation of the desired propenoxy reaction intermediate leading to a quick evolution of propenol in the gas phase. It is important to note that the presence of AP on the metal surface exhibits a pronounced nonlinear behavior on the reactivity: at small coverage it strongly inhibits the target reaction, while it greatly promotes it at high coverages. This observation suggests a complex interplay of the ligand layer and acrolein coadsorbed on the surface, which must critically depend on AP coverage.

To investigate the mechanistic details on the underlying surface processes, *operando* IR spectroscopic studies were carried out on the functionalized Pd(111) surfaces turning over. Figure 7a shows the composition of the surface under the reaction conditions for low AP coverage (exposure: 0.12 L), while the Figure 7b displays the IR spectra obtained on the surface exposed to 1.1 L of AP. The uppermost spectrum (1) was obtained for an AP multilayer at 100 K and shows the most important spectroscopic signatures of acetophenone, which is not in direct contact with the underlying metal surface and should serve as a reference for an unperturbed AP

molecule. The detailed assignment of the AP vibrational bands was performed in the previous studies.^{29,43,44} Briefly, the major band at 1686 cm^{-1} is related to the stretching vibration of the C=O bond, the band at 1361 cm^{-1} to the symmetric deformation vibration of the methyl group ($\delta_s(\text{CH}_3)$), and the prominent band at 1275 cm^{-1} mostly to the in-plane skeletal deformation of the ring, which involves also at part the acetyl group.

Spectra 1a–5a were collected for low AP exposure (0.12 L) under the reaction conditions, i.e., at 250 K and in the presence of hydrogen. Spectrum 1a is related to pure AP adsorbed at 250 K on H/Pd(111) surface, while spectra 2a–5a were collected on this AP-functionalized Pd(111) upon continuous exposure to H_2 and acrolein. Importantly, the spectrum of AP on H/Pd(111) surface at 250 K (spectrum 1a) strongly differs from the multilayer spectrum of AP collected at 100 K: nearly no bands can be seen for this low AP coverage. This observation is most likely related to the fact that AP molecules are oriented flat with respect to the surface, i.e., both the phenyl ring and the axis of the C=O vibration lie parallel with respect to the surface plane. As a consequence, these vibrations cannot be seen due to the metal surface selection rule (MSSR) allowing only the vibrations with a nonzero perpendicular component of the dynamic dipole moment.⁴⁵ Once H_2 and acrolein are dosed on this surface, the evolution of the surface species closely resembles that one observed on the initially pristine Pd(111) surface (see Figure 2a and 5a): (i) the prominent vibrational band at 1745 cm^{-1} appears, which was previously assigned to the C=O bond of oxopropyl surface ligands, that spontaneously forms due to partial hydrogenation of acrolein itself, followed by (ii) the evolution of the (very minor) vibrational bands at 1097 and 1120 cm^{-1} related to the propenoxy reaction intermediates RI_1 and RI_2 discussed above. The intensities of these both bands remain, however, significantly smaller than that on the initially clean Pd(111). Overall, it seems that on the surface functionalized with small amounts of AP, the same surface species are formed as on the initially pristine surface, just at smaller concentrations and with a larger time delay. These observations suggest that the ligand layer acting in this surface process is most likely the oxopropyl layer—the same ligand layer as formed on the pristine Pd(111) surface. We did not find any spectroscopic evidence that small amounts of coadsorbed AP species play any positive role in this catalytic process. In contrast, the presence of small amounts of AP results in the elongation of the induction period as compared to pristine Pd(111) surface, i.e., the slower formation of the active oxopropyl ligand layer and the desired reaction intermediates. The elongation of the induction period might be related to the fact that randomly distributed coadsorbed AP species possibly hinder the formation of the ordered oxopropyl ligand layer, which is required for the formation of the desired propenoxy intermediate.

In contrast, when AP was predeposited in large amounts (exposure: 1.1 L) the reaction was pronouncedly promoted as compared to the pristine Pd(111) surface. Spectrum 1b (Figure 7b) shows the composition of the H-precovered Pd(111) surface at 250 K, which was functionalized with AP at high coverage. The major vibrational band visible in this spectrum is at 1220 cm^{-1} , which is typical for a stretching vibration of a C–O single bond. In our previous studies,^{39,40,46} this band was identified as the C–O single bond formed in the enol form of acetophenone, which occurs in a broad

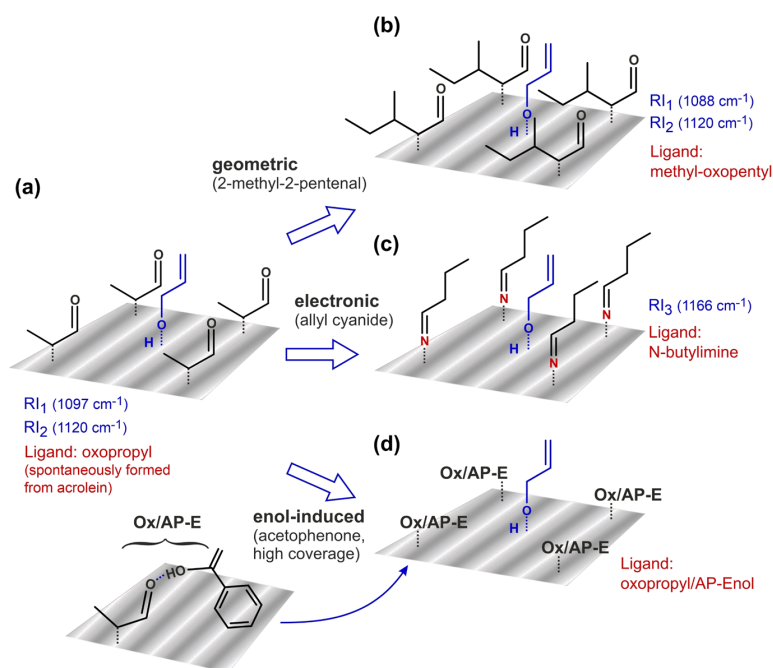


Figure 8. Proposed ligand structures formed on the surface under the reaction conditions: (a) oxopropyl spontaneously formed from acrolein on pristine Pd(111), (b) methyl-oxopentyl on Pd(111) modified with MP, (c) *N*-butylimine formed on AC-modified Pd(111), and (d) oxopropyl/AP-enol complexes formed on Pd(111) functionalized with AP at high AP exposure. Next to each surface, the characteristic frequencies of the reaction intermediates are indicated.

temperature range above approximately 140 K. Spectra 2b–5b were obtained under continuous H₂ and acrolein exposure on the surface functionalized with AP at high coverage. Under these conditions, a new band at 1715 cm⁻¹ is formed, with the frequency being still typical for the range of the stretching C=O vibration, which is not conjugated to the C=C double bond. Obviously, also on this surface, formation of oxopropyl species occurs, which is the result of a single H addition of the C=C double bond of acrolein. However, the frequency of this band is pronouncedly red-shifted by 30 cm⁻¹ as compared to two other surfaces—initially pristine Pd(111) and Pd(111) containing low coverage of AP—both showing formation of oxopropyl ligands. Such strong red shift is indicative of the strong lateral interaction between the carbonyl group of oxopropyl and a neighboring molecule, most likely due to hydrogen bonding. The comparable frequency shifts were described both for the adsorbed surface species on transition metals^{38–40} as well as in solutions and in chelating complexes.^{47–55} Since this prominent frequency shift of the carbonyl group was observed to occur only in the presence of the enol form of AP, it can be quite safely concluded that it results from hydrogen bonding between the carbonyl group of the oxopropyl species and the H atom of the OH group belonging to the enol form of AP. Also note that a pronounced frequency shift of C=O group is expected for H bonding involving acidic H,⁵⁶ such as, e.g., the one in the OH group of enol, while H bonding to nonacidic H (e.g., of the CH₃-group of AP in ketone form) usually does not lead to a notable shift.^{55,56} The proposed structure of the resulting oxopropyl/AP-enol complex is shown next to the band at 1715 cm⁻¹, in which the band at 1220 cm⁻¹ is related to the C–O single bond in AP-enol, while the band at 1715 cm⁻¹ is the stretching

vibration ($\nu(\text{C}=\text{O})$) of the carbonyl group in oxopropyl species. The combination of these bands remains stable in the course of the reaction, suggesting that this complex might act as a ligand turning the surface chemoselective. It should be noted, however, that no vibrational bands related to the reaction intermediates were observed at any notable intensity on this particular surface, even though relatively large amounts of propenol were desorbed into the gas phase. This might be most likely due to the low surface concentration of the reaction intermediate, which quickly converts into the final product and desorbs. Another possible reason for missing vibrational signatures of the reaction intermediate might be related to its specific adsorption configuration on the oxopropyl/AP-enol containing surface, in which the C–O bond might be oriented close to parallel to the underlying metal and therefore be not visible due to the MSSR.⁴⁵ This reason is, however, less likely as it implies highly strained adsorption configuration of the reaction intermediated.

Figure 8 summarizes the different types of ligands formed under the reaction conditions and their effects on the propenoxy reaction intermediates. On the initially pristine Pd(111) surface (Figure 8a), oxopropyl ligand species are formed spontaneously as a result of partial acrolein hydrogenation at the C=C bond. In our previous studies^{18–20} it was shown that they form a closely packed ligand layer, which promotes formation of the desired propenoxy reaction intermediate. Two types of the reaction intermediates (RI₁ and RI₂) can be distinguished on this surface with RI₁ appearing first and saturating at lower acrolein exposures. In the following, the second reaction intermediate RI₂ appears and finally becomes the dominant RI species.

The ligand structurally similar to acrolein—2-methyl-2-pentenal—forms the methyloxopentyl surface species shown in Figure 8b, which are structurally similar to oxopropyl. The same types of the reaction intermediates (RI_1 and RI_2) are formed on this surface, however, their distribution strongly differs from the case of oxopropyl ligand: the species RI_1 appears first and saturates at approximately the same quantity as on the oxopropyl-covered surface, but the reaction intermediate RI_2 appearing in the following remains only minor surface species. This is in contrast to the case of oxopropyl ligand layer, at which RI_2 was found to be built at amounts exceeding RI_1 . The combination of the observation on two ligand-modified surfaces lets us to propose the following scenario: the reaction intermediate RI_1 appears first and forms an H bond to the neighboring ligand species (either oxopropyl or methyloxopentyl) building 1:1 complexes. After nearly all ligand species become involved into these complexes, the other type of the reaction intermediate RI_2 is formed, which is most likely not involved into hydrogen bonding and remains free-standing. Depending on the available surface space, different amounts of RI_2 can be formed: larger concentrations on the surface covered with relatively small oxopropyl ligand and smaller concentrations on the surface functionalized with structurally similar but more spacious ligand methyloxopentyl. Only this scenario can explain both the saturation of the RI_1 at similar coverages on both surfaces and formation of pronouncedly different quantities of RI_2 . The discussed observation might be related to the geometric effects imposed by the ligand layer since structurally and electronically similar ligand species result in the formation of the same types of reaction intermediates, which differ only in the intensity distribution in the IR spectra.

On the surface functionalized with the allyl cyanide containing an electron-rich functional group, electronic effects of the ligand layer on the reaction intermediate could be clearly deduced (Figure 8c). Under the reaction conditions, allyl cyanide converts to *N*-butylimine species, serving as an active ligand layer in acrolein hydrogenation. The propenoxy reaction intermediate (RI_3) formed on this surface exhibit a strongly blue-shifted (by more than 40 cm^{-1} as compared to RI_1 and RI_2) vibrational band related to the C–O single bond, suggesting its considerable strengthening. This effect might arise either from the direct interaction between the reaction intermediate and the electron-rich imine group of the ligand, or can be related to a “surface-mediated” process, in which donation of the *d*-electrons from the metal to the reaction intermediate and backdonation of the electron density form the molecular orbitals of the reaction intermediate to the metal are strongly affected by the presence of the coadsorbed ligand possessing an electron-rich functional group.

The third investigated case of acetophenone, serving as a ligand at high acetophenone coverage, represent the complex case, which we denote as “enol-induced” effect (Figure 8d). In this case, the enol form of acetophenone formed under the reaction conditions exhibits a strong lateral interaction with the oxopropyl ligand that is spontaneously formed in a partial hydrogenation of acrolein at the C=C bond. Most likely, the OH group of enol-AP establishes H bonding with the carbonyl group of the oxopropyl species, leading to a strong red-shift of the latter vibrational band. The newly formed oxopropyl/enol-AP complex serves as a complex ligand in hydrogenation of acrolein as indicated by the strong reduction of the induction period in propenol formation rate. It should be also noted that

all three functionalized surface show high catalytic performance both in terms of selectivity and absolute acrolein conversion rate. More detailed discussion on this issue can be found in Chapter 6 of Supporting Information.

CONCLUSIONS

In summary, Pd(111) functionalized with three different organic ligands—allyl cyanide, 2-methyl-2-pentenal, and acetophenone—was investigated with respect to its catalytic activity in the reaction of acrolein hydrogenation. The organic ligand layers formed upon surface functionalization under the reaction conditions turn the surface highly active and close to 100% chemoselective with respect to the target product propenol and promote formation of the desired propenoxy surface reaction intermediate.

To address the mechanistic details of the underlying surface process, we employed a combination of surface sensitive *operando* IRAS with multimolecular beam techniques, allowing to study the reaction kinetics under well-defined isothermal conditions and simultaneously monitor the evolution of the desired reaction intermediate on the surface. By employing the combination of three types of ligands, we addressed different aspects of ligand/reactant interaction: *electronic* and *geometric* effects as well as the effect arising from the *strong lateral interactions* with ligands capable of forming 1:1 carbonyl/enol complexes.

Specifically, electronic effects were observed on the surface containing *N*-butylimine species formed under the reaction conditions after deposition of allyl cyanide. The presence of the electronically rich imine group results in a strong frequency shift of the C–O single bond in the propenoxy reaction intermediate by more than 40 cm^{-1} , indicating that this bond is considerably strengthened on this surface. These effects might arise either via the direct interaction of the reaction intermediate with the coadsorbed imines or be mediated by the surface, i.e., the degree of donation/backdonation of the electron density between the underlying Pd and the reaction intermediate might be strongly changed in the presence of the electron-rich imine species. The *N*-butyl imine layer also results in the pronounced shortening of the induction period (as compared to the pristine Pd(111)), pointing to the fact that the functionalized surface provide the correct environment for a fast formation of the desired reaction intermediate.

Comparison of the two structurally similar ligand layers—methyloxopentyl (formed from 2-methyl-2-pentenal) and oxopropyl (formed from acrolein) species—allows us to deduce the role of the geometric effects in the formation of the propenoxy reaction intermediate. First, two different types of the reaction intermediates— RI_1 and RI_2 —were identified, which are separated by 23 cm^{-1} . The reaction intermediate RI_1 (lower frequency) appears first at low acrolein exposures and saturates at similar amounts on both surfaces. The second reaction intermediate (RI_2) evolves at higher acrolein exposure on both surfaces, but its final surface concentration strongly differs on both functionalized surfaces: it is low on the surface covered with a spacious methyloxopentyl species, while it is considerably higher on the surface functionalized with a less spacious oxopropyl ligand. The observed behavior arises most likely from the fact that the RI_1 undergoes H bonding with the coadsorbed ligand, which leads to the pronounced red-shift of the C–O bond in RI_1 . As soon as nearly all ligands become involved into 1:1 complexes with reaction intermediate RI_1 , the RI_2 starts evolving. RI_2 is most likely a free-standing

adsorbate and can be formed in larger amounts on the surface precovered with the smaller ligand (oxopropyl species) and in smaller amounts on the surface covered with a spacious methyloxopentyl ligand.

Finally, functionalization of Pd(111) with acetophenone results in two types of reactive behavior: at low acetophenone coverages, the presence of the ligand elongates the induction period and does not exhibit any significant effect on the reaction intermediates. In contrast, at high acetophenone coverages, the enol form of acetophenone is formed, which builds a 1:1 complex with the oxopropyl species spontaneously formed in acrolein partial hydrogenation. The presence of these oxopropyl/enol-AP complexes strongly reduces the induction period, suggesting that this surface provides a beneficial ligand environment for formation of propenol.

The results of this study provide deep atomistic level insights in the mechanisms of ligand-directed heterogeneous catalysis and the different effects that can be employed as useful tools for rational design of new catalytic materials with tailor-made catalytic properties.

■ ASSOCIATED CONTENT

Supporting Information

The Supporting Information is available free of charge at <https://pubs.acs.org/doi/10.1021/acs.jpcc.2c00987>.

Experimental section; full range IR spectrum of allyl cyanide; full experimental details for Figures 1,2, and 4–7; effect of acrolein flux on the length of the induction period and the propenol formation rate on Pd(111); time evolution of the reaction intermediates; and evaluation of selectivities and total conversion of acrolein (PDF)

■ AUTHOR INFORMATION

Corresponding Author

Swetlana Schauermaann – Institute of Physical Chemistry, Christian-Albrechts-University Kiel, 24118 Kiel, Germany; orcid.org/0000-0002-9390-2024; Email: schauermaann@pctc.uni-kiel.de

Authors

Carsten Schröder – Institute of Physical Chemistry, Christian-Albrechts-University Kiel, 24118 Kiel, Germany
Ann-Katrin Baumann – Institute of Physical Chemistry, Christian-Albrechts-University Kiel, 24118 Kiel, Germany
Marvin C. Schmidt – Institute of Physical Chemistry, Christian-Albrechts-University Kiel, 24118 Kiel, Germany
Jan Smyczek – Institute of Physical Chemistry, Christian-Albrechts-University Kiel, 24118 Kiel, Germany
Philipp A. Haugg – Institute of Physical Chemistry, Christian-Albrechts-University Kiel, 24118 Kiel, Germany
Ole-Christian Graap – Institute of Physical Chemistry, Christian-Albrechts-University Kiel, 24118 Kiel, Germany

Complete contact information is available at: <https://pubs.acs.org/doi/10.1021/acs.jpcc.2c00987>

Notes

The authors declare no competing financial interest.

■ ACKNOWLEDGMENTS

This work has been supported by the German Science Foundation (DFG, Grant SCHA 1477/6-1, and DFG, Grant INST 257/543-1 FUGG).

■ REFERENCES

- (1) Ernst, J. B.; Muratsugu, S.; Wang, F.; Tada, M.; Glorius, F. Tunable Heterogeneous Catalysis: N-Heterocyclic Carbenes as Ligands for Supported Heterogeneous Ru/K-Al₂O₃ Catalysts To Tune Reactivity and Selectivity. *J. Am. Chem. Soc.* **2016**, *138*, 10718–10721.
- (2) Ernst, J. B.; Schwermann, C.; Yokota, G.-i.; Tada, M.; Muratsugu, S.; Doltsinis, N. L.; Glorius, F. Molecular Adsorbates Switch on Heterogeneous Catalysis: Induction of Reactivity by N-Heterocyclic Carbenes. *J. Am. Chem. Soc.* **2017**, *139*, 9144–9147.
- (3) Marshall, S. T.; O'Brien, M.; Oetter, B.; Corpuz, A.; Richards, R. M.; Schwartz, D. K.; Medlin, J. W. Controlled selectivity for palladium catalysts using self-assembled monolayers. *Nat. Mater.* **2010**, *9*, 853–858.
- (4) Schrader, I.; Neumann, S.; Šulce, A.; Schmidt, F.; Azov, V.; Kunz, S. Asymmetric Heterogeneous Catalysis: Transfer of Molecular Principles to Nanoparticles by Ligand Functionalization. *ACS Catal.* **2017**, *7*, 3979–3987.
- (5) Wu, B.; Huang, H.; Yang, J.; Zheng, N.; Fu, G. Selective Hydrogenation of α,β -Unsaturated Aldehydes Catalyzed by Amine-Capped Platinum-Cobalt Nanocrystals. *Angew. Chem., Int. Ed.* **2012**, *51*, 3440–3443.
- (6) Pang, S. H.; Medlin, J. W. Controlling Catalytic Selectivity via Adsorbate Orientation on the Surface: From Furfural Deoxygenation to Reactions of Epoxides. *J. Phys. Chem. Lett.* **2015**, *6*, 1348–1356.
- (7) Meemken, F.; Baiker, A. Recent Progress in Heterogeneous Asymmetric Hydrogenation of C=O and C=C Bonds on Supported Noble Metal Catalysts. *Chem. Rev.* **2017**, *117*, 11522–11569.
- (8) Hammer, B.; Nørskov, J. K. Theoretical surface science and catalysis - Calculations and concepts. *Adv. Catal.* **2000**, *45*, 71–129.
- (9) Kuchkina, N. V.; et al. Hydrophobic Periphery Tail of Polyphenylenepyridyl Dendrons Control Nanoparticle Formation and Catalytic Properties. *Chem. Mater.* **2014**, *26*, 5654–5663.
- (10) Lu, L.; Zou, S.; Fang, B. The Critical Impacts of Ligands on Heterogeneous Nanocatalysis: A Review. *ACS Catal.* **2021**, *11*, 6020–6058.
- (11) Chen, K.; Wu, H.; Hua, Q.; Chang, S.; Huang, W. Enhancing catalytic selectivity of supported metal nanoparticles with capping ligands. *Phys. Chem. Chem. Phys.* **2013**, *15*, 2273–7.
- (12) Almora-Barrios, N.; Cano, I.; van Leeuwen, P. W. N. M.; López, N. Concerted Chemoselective Hydrogenation of Acrolein on Secondary Phosphine Oxide Decorated Gold Nanoparticles. *ACS Catal.* **2017**, *7*, 3949–3954.
- (13) Tsunoyama, H.; Ichikuni, N.; Sakurai, H.; Tsukuda, T. Effect of electronic structures of Au clusters stabilized by poly(N-vinyl-2-pyrrolidone) on aerobic oxidation catalysis. *J. Am. Chem. Soc.* **2009**, *131*, 7086–93.
- (14) Cano, I.; Chapman, A. M.; Urakawa, A.; van Leeuwen, P. W. Air-stable gold nanoparticles ligated by secondary phosphine oxides for the chemoselective hydrogenation of aldehydes: crucial role of the ligand. *J. Am. Chem. Soc.* **2014**, *136* (6), 2520–8.
- (15) Cano, I.; Chapman, A. M.; Urakawa, A.; van Leeuwen, P. W. Air-stable gold nanoparticles ligated by secondary phosphine oxides for the chemoselective hydrogenation of aldehydes: crucial role of the ligand. *J. Am. Chem. Soc.* **2014**, *136*, 2520–8.
- (16) Schröder, C.; Schmidt, M. C.; Haugg, P. A.; Baumann, A. K.; Smyczek, J.; Schauermaann, S. Understanding Ligand-Directed Heterogeneous Catalysis: When the Dynamically Changing Nature of the Ligand Layer Controls the Hydrogenation Selectivity. *Angew. Chem., Int. Ed.* **2021**, *60*, 16349–16354.
- (17) Schröder, C.; Haugg, P. A.; Baumann, A. K.; Schmidt, M. C.; Smyczek, J.; Schauermaann, S. Competing Reaction Pathways in Heterogeneously Catalyzed Hydrogenation of Allyl Cyanide: The

Chemical Nature of Surface Species. *Chem. Eur. J.* **2021**, *27*, 17240–17254.

(18) Dostert, K. H.; O'Brien, C. P.; Mirabella, F.; Ivars-Barceló, F.; Attia, S.; Spadafora, E.; Schauerermann, S.; Freund, H. J. Selective Partial Hydrogenation of Acrolein on Pd: A Mechanistic Study. *ACS Catal.* **2017**, *7* (8), 5523–5533.

(19) Dostert, K. H.; O'Brien, C. P.; Ivars-Barceló, F.; Schauerermann, S.; Freund, H. J. Spectators Control Selectivity in Surface Chemistry: Acrolein Partial Hydrogenation Over Pd. *J. Am. Chem. Soc.* **2015**, *137*, 13496–502.

(20) O'Brien, C. P.; Dostert, K. H.; Schauerermann, S.; Freund, H. J. Selective Hydrogenation of Acrolein Over Pd Model Catalysts: Temperature and Particle-Size Effects. *Chem. Eur. J.* **2016**, *22*, 15856–15863.

(21) Zaera, F. On the Mechanism for the Hydrogenation of Olefins on Transition-Metal Surfaces: The Chemistry of Ethylene on Pt(111). *Langmuir* **1996**, *12*, 88–94.

(22) Stacchiola, D.; Burkholder, L.; Tysøe, W. T. Enantioselective chemisorption on a chirally modified surface in ultrahigh vacuum: adsorption of propylene oxide on 2-butoxide-covered palladium(111). *J. Am. Chem. Soc.* **2002**, *124*, 8984–9.

(23) Lee, I.; Zaera, F. Enantioselectivity of adsorption sites created by chiral 2-butanol adsorbed on Pt(111) single-crystal surfaces. *J. Phys. Chem. B* **2005**, *109*, 12920–6.

(24) Skoplyak, O.; Barteau, M. A.; Chen, J. G. Ethanol and ethylene glycol on Ni/Pt(111) bimetallic surfaces: A DFT and HREELS study. *Surf. Sci.* **2008**, *602*, 3578–3587.

(25) Davis, J. L.; Barteau, M. A. Spectroscopic identification of alkoxide, aldehyde, and acyl intermediates in alcohol decomposition on Pd(111). *Surf. Sci.* **1990**, *235*, 235–248.

(26) Castonguay, M.; Roy, J. R.; Rochefort, A.; McBreen, P. H. Orientation and Conformation of Methyl Pyruvate on Ni(111). *J. Am. Chem. Soc.* **2000**, *122*, 518–524.

(27) Burkholder, L.; Tysøe, W. T. Structure and Reaction Pathways of Methyl Pyruvate on Pd(111). *J. Phys. Chem. C* **2009**, *113*, 15298–15306.

(28) Madsen, F.; Terpager, I.; Olskær, K.; Spanget-Larsen, J. Ultraviolet-visible and infrared linear dichroism spectroscopy of 1,8-dihydroxy-9,10-anthraquinone aligned in stretched polyethylene. *Chem. Phys.* **1992**, *165*, 351–360.

(29) Attia, S.; Schauerermann, S. Coverage-Dependent Adsorption Geometry of Acetophenone on Pt(111). *J. Phys. Chem. C* **2020**, *124*, 557–566.

(30) Max, J. J.; Chapados, C. Infrared spectroscopy of acetone-methanol liquid mixtures: hydrogen bond network. *J. Chem. Phys.* **2005**, *122*, 014504.

(31) Max, J. J.; Chapados, C. Infrared spectroscopy of methanol-hexane liquid mixtures. II. The strength of hydrogen bonding. *J. Chem. Phys.* **2009**, *130*, 124513.

(32) Liu, W.; Jiang, Y.; Dostert, K. H.; O'Brien, C. P.; Riedel, W.; Savara, A.; Schauerermann, S.; Tkatchenko, A. Catalysis beyond frontier molecular orbitals: Selectivity in partial hydrogenation of multi-unsaturated hydrocarbons on metal catalysts. *Sci. Adv.* **2017**, *3*, e1700939.

(33) Dostert, K. H.; O'Brien, C. P.; Mirabella, F.; Ivars-Barceló, F.; Schauerermann, S. Adsorption of acrolein, propanal, and allyl alcohol on Pd(111): a combined infrared reflection-absorption spectroscopy and temperature programmed desorption study. *Phys. Chem. Chem. Phys.* **2016**, *18*, 13960–73.

(34) Murillo, L. E.; Chen, J. G. A comparative study of the adsorption and hydrogenation of acrolein on Pt(111), Ni(111) film and Pt–Ni–Pt(111) bimetallic surfaces. *Surf. Sci.* **2008**, *602*, 919–931.

(35) Davis, J. L.; Barteau, M. A. The influence of temperature and surface composition upon the coordination of acetone to the Pd(111) surface. *Surf. Sci.* **1989**, *208*, 383–403.

(36) Davis, J. L.; Barteau, M. A. Polymerization and decarbonylation reactions of aldehydes on the Pd(111) surface. *J. Am. Chem. Soc.* **1989**, *111*, 1782–1792.

(37) Esan, D. A.; Trenary, M. Surface chemistry of propanal, 2-propenol, and 1-propanol on Ru(001). *Phys. Chem. Chem. Phys.* **2017**, *19*, 10870–10877.

(38) Attia, S.; Schmidt, M. C.; Schröder, C.; Pessier, P.; Schauerermann, S. Surface-Driven Keto-Enol Tautomerization: Atomistic Insights into Enol Formation and Stabilization Mechanisms. *Angew. Chem., Int. Ed.* **2018**, *57*, 16659–16664.

(39) Attia, S.; Schmidt, M. C.; Schröder, C.; Schauerermann, S. Formation and Stabilization Mechanisms of Enols on Pt through Multiple Hydrogen Bonding. *ACS Catal.* **2019**, *9*, 6882–6889.

(40) Attia, S.; Schmidt, M. C.; Schröder, C.; Weber, J.; Baumann, A. K.; Schauerermann, S. Keto-Enol Tautomerization as a First Step in Hydrogenation of Carbonyl Compounds. *J. Phys. Chem. C* **2019**, *123*, 29271–29277.

(41) Schmidt, M. C.; Attia, S.; Schröder, C.; Baumann, A. K.; Schauerermann, S. Formation and Real-Space Distribution of Acetophenone Dimers on H-containing Pt(111). *J. Phys. Chem. C* **2021**, *125*, 19311–19324.

(42) Schmidt, M. C.; Attia, S.; Schröder, C.; Baumann, A. K.; Pessier, P.; Schauerermann, S. Temperature-Dependent Formation of Acetophenone Oligomers Accompanied by Keto-Enol Tautomerism: Real Space Distribution. *J. Phys. Chem. C* **2020**, *124*, 14262–14271.

(43) Gambi, A.; Giorgianni, S.; Passerini, A.; Visinoni, R.; Gheretti, S. Infrared studies of acetophenone and its deuterated derivatives. *Spectrochim. Acta, Part A* **1980**, *36*, 871–878.

(44) Chen, M.; Maeda, N.; Baiker, A.; Huang, J. Molecular Insight into Pt-Catalyzed Chemoselective Hydrogenation of an Aromatic Ketone by In Situ Modulation–Excitation IR Spectroscopy. *ACS Catal.* **2012**, *2*, 2007–2013.

(45) Hoffmann, F. Infrared reflection-absorption spectroscopy of adsorbed molecules. *Surf. Sci. Rep.* **1983**, *3*, 107–192.

(46) Attia, S.; Schmidt, M. C.; Schröder, C.; Pessier, P.; Schauerermann, S. Surface-Driven Keto–Enol Tautomerization: Atomistic Insights into Enol Formation and Stabilization Mechanisms. *Angew. Chem., Int. Ed.* **2018**, *57*, 16659–16664.

(47) Dunbar, R. C.; Moore, D. T.; Oomens, J. IR-spectroscopic characterization of acetophenone complexes with Fe⁺, Co⁺, and Ni⁺ using free-electron-laser IRMPD. *J. Phys. Chem. A* **2006**, *110*, 8316–26.

(48) Velasquez, J.; Pillai, E. D.; Carnegie, P. D.; Duncan, M. A. IR spectroscopy of M+(Acetone) complexes (M = Mg, Al, Ca): cation-carbonyl binding interactions. *J. Phys. Chem. A* **2006**, *110*, 2325–30.

(49) Garvey, M.; Bai, Y.; Boscoboinik, J. A.; Burkholder, L.; Sorensen, T. E.; Tysøe, W. T. Identifying Molecular Species on Surfaces by Scanning Tunneling Microscopy: Methyl Pyruvate on Pd(111). *J. Phys. Chem. C* **2013**, *117*, 4505–4514.

(50) Humblot, V.; Bingham, C. J. A.; Le Roux, D.; Mateo Marti, E.; McNutt, A.; Nunney, T. S.; Ortega Lorenzo, M.; Roberts, A. J.; Williams, J.; Surman, M.; Raval, R. Synchrotron far-infrared RAIRS studies of complex molecules on Cu(110). *Surf. Sci.* **2003**, *537*, 253–264.

(51) Jones, T. E.; Baddeley, C. J. Investigating the mechanism of chiral surface reactions: the interaction of methylacetoacetate with (S)-glutamic Acid modified Ni{111}. *Langmuir* **2006**, *22*, 148–52.

(52) Jones, T. E.; Baddeley, C. J. Influence of Modification Conditions on the Interaction of Methylacetoacetate with (R,R)-Tartaric Acid-Modified Ni{111}. *J. Phys. Chem. C* **2007**, *111*, 17558–17563.

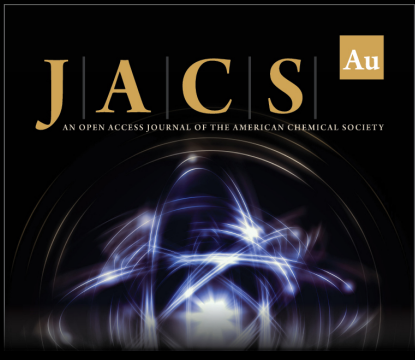
(53) Ontaneda, J.; Nicklin, R. E. J.; Cornish, A.; Roldan, A.; Grau-Crespo, R.; Held, G. Adsorption of Methyl Acetoacetate at Ni{111}: Experiment and Theory. *J. Phys. Chem. C* **2016**, *120*, 27490–27499.

(54) Skliar, D. B.; Gelmi, C.; Ogunnaik, T.; Willis, B. G. Interaction of 2,2,6,6-tetramethyl-3,5-heptanedione with the Si(100)-2 × 1 surface: Scanning tunneling microscopy and density functional theory study. *Surf. Sci.* **2007**, *601*, 2887–2895.

(55) Thijs, R.; Zeegers-Huyskens, T. Infrared and Raman studies of hydrogen bonded complexes involving acetone, acetophenone and benzophenone—I. Thermodynamic constants and frequency shifts of


the νOH and $\nu\text{C}=\text{O}$ stretching vibrations. *Spectrochim. Acta, Part A* **1984**, *40*, 307–313.


(56) Meemken, F.; Baiker, A.; Schenker, S.; Hungerbuhler, K. Chiral modification of platinum by co-adsorbed cinchonidine and trifluoroacetic acid: origin of enhanced stereocontrol in the hydrogenation of trifluoroacetophenone. *Chem. Eur. J.* **2014**, *20*, 1298–309.



JACS Au
AN OPEN ACCESS JOURNAL OF THE AMERICAN CHEMICAL SOCIETY

Editor-in-Chief
Prof. Christopher W. Jones
Georgia Institute of Technology, USA

Open for Submissions 

pubs.acs.org/jacsau  ACS Publications
Most Trusted. Most Cited. Most Read.

4920

<https://doi.org/10.1021/acs.jpcc.2c00987>
J. Phys. Chem. C **2022**, *126*, 4907–4920

8.4 Tuning the Strength of Molecular Bonds in Oxygenates via Surface-Assisted Intermolecular Interactions: Atomistic Insights

Publication Data and Reprint

Reference: Carsten Schröder, Marvin C. Schmidt, Christopher Witt, Smadar Attia, Jann Weber, Ann-Katrin Baumann, Bernd Hartke, and Svetlana Schauer mann

DOI: 10.1021/acs.jpcc.0c09659

Submitted: 26.10.2020

Accepted: 07.12.2020

Contribution: Performance of all IRAS measurements, supervision of Jan Webers's bachelor thesis, complete experimental planning of IR and STM experiments and IR data analysis, development of the adsorption models, preparation of the manuscript, cooperation with the Hartke group initiated and managed.

Copyright: Reprinted with permission from JPC C from Ref.[249]. Copyright 2020 American Chemical Society.

Tuning the Strength of Molecular Bonds in Oxygenates via Surface-Assisted Intermolecular Interactions: Atomistic Insights

Carsten Schröder, Marvin C. Schmidt, Christopher Witt, Smadar Attia, Jann Weber, Ann-Katrin Baumann, Bernd Hartke, and Swetlana Schauerma^{*}Cite This: *J. Phys. Chem. C* 2020, 124, 28159–28168

Read Online

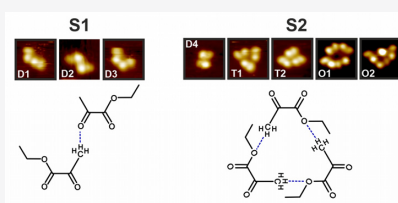
ACCESS |

Metrics & More

Article Recommendations

Supporting Information

ABSTRACT: Lateral interactions between coadsorbed hydrocarbon species play an important role in their chemical transformations on catalytic metal surfaces. In this report, we present a mechanistic study on mutual lateral interactions of the α -ketoester ethyl pyruvate adsorbed on a well-defined Pt(111) surface, resulting in a strong weakening of ester bonds. By employing a combination of surface-sensitive spectroscopic and microscopic techniques as well as theoretical calculations, we address the atomistic-level structure of surface assemblies containing several ethyl pyruvate species. We report formation of different types of surface oligomers comprising topologically different dimer, trimer, and tetramer species. Based on a combination of spectroscopic and microscopic observations, all species can be attributed to two large classes of oligomers exhibiting different types of intermolecular bonding. In the first class of species, the intermolecular interaction is realized via H-bonding between two acetyl groups of ethyl pyruvate, that is, a carbonyl and a methyl group of the neighboring molecules, while in the second type of species the bonding interaction involves the ester-O of one molecule and the acetyl group of a neighboring adsorbate. For the latter type of species, a strong IR frequency shift of the ester C–O vibration was observed pointing to a significant weakening of the related ester bonds, which might exert a strong impact on the chemical transformations involving this group. We demonstrate that the particular type of intermolecular interaction in ethyl pyruvate assemblies can be effectively tuned by controlling the adsorption parameters, such as surface coverage and the presence of coadsorbed hydrogen. Obtained results provide important insights into the details of lateral interactions of complex multifunctional molecules adsorbed on catalytically relevant surfaces. We show that the parameter space in a catalytic process involving ester compounds can be purposefully varied to tune the strength of the ester bond toward improving the catalytic performance.



INTRODUCTION

Lateral interactions between molecular species adsorbed on a metal surface might play a crucial role in controlling activity and selectivity of heterogeneously catalyzed multipathway reactions. Particularly for reactions involving hydrocarbons, the selectivity often depends on subtle differences in the activation barriers of individual reaction routes,¹ which are determined not only by the bonding of the reactants to the underlying catalyst but also by their intermolecular interactions with the surrounding adsorbates. The latter type of interactions can greatly modify the overall energy landscape and by this strongly alter the selectivity toward the desired reaction. There are two types of new emerging fields in heterogeneous catalysis based on this phenomenon—enantioselective^{2,3} and ligand-assisted^{4,5} heterogeneous catalysis—that strongly rely on intermolecular interactions between coadsorbed reactants and the modifier molecules. The latter species are employed for surface functionalization rendering the catalyst highly active and selective toward the desired reaction path. Recently, an atomistic-level understanding of such complex functionalized catalysts was achieved in studies combining surface-sensitive spectroscopies and microscopy with the theoretical approach

for a number of enantio- and chemoselective catalytic systems,^{2,3,5–17} allowing to develop first rational ideas for optimizing lateral interactions in this type of reaction.

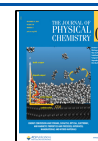
Despite this recent progress in the field, the deep fundamental-level understanding of adsorbate–adsorbate interactions is available only for a very limited number of reactive systems because of their vast complexity and numerous possibilities to build molecular complexes comprising two or more adsorbates. Experimental identification of adsorbed surface species and a microscopic-level understanding of the mutual lateral interactions between single adsorbates still remain a highly challenging task.

One of the most important reactive systems in the field of enantioselective heterogeneous catalysis involves α -ketoesters, which can be efficiently hydrogenated over chirally modified

Received: October 26, 2020

Revised: December 3, 2020

Published: December 15, 2020



ACS Publications

© 2020 American Chemical Society

28159

<https://dx.doi.org/10.1021/acs.jpcc.0c09659>
J. Phys. Chem. C 2020, 124, 28159–28168

surface to corresponding chiral lactates. Several groups reported atomistic-level studies on surface chemistry of the simplest α -ketoester methyl pyruvate (MP), over either pristine or chirally modified Pd(111)^{18–20} and Pt(111)^{21,22} metal surfaces. On pristine Pd(111), formation of enol species as a result of keto–enol tautomerization of the carbonyl group of MP was proposed.¹⁸ The same enol form of MP was also suggested to be the active species in the 1:1 chiral docking complexes between MP and the chiral modifier (1-naphthyl)-ethylamine (NEA).¹⁹ On Pt(111), formation of enediolate species was put forward,²² in which both carbonyl groups directly interact with two underlying Pt atoms. These and some other studies²³ provided first valuable ideas about the interaction of α -ketoesters with transition metal surfaces. However, a number of important questions still remain unresolved. Specifically, there is no general agreement on the chemical nature of the adsorbed surface species and on the possibility of keto–enol tautomerization vs enediolate formation upon adsorption on transition metal surfaces. Also, the interaction of structurally more complex α -ketoesters and the details of their lateral interaction with coadsorbed molecular species remain largely unexplored.

To address the details of mutual lateral interactions in structurally more complex α -ketoesters, we performed a mechanistic study of ethyl pyruvate (EP) adsorbed on a well-defined Pt(111) surface, both pristine and H-containing. We employed a unique combination of experimental techniques²⁴ including molecular beams, infrared reflection–absorption spectroscopy (IRAS), and scanning tunneling microscopy (STM), capable of providing both spectroscopic information about the chemical nature of adsorbed surface species and microscopic information about their distribution in real space. Complementarily, theoretical modeling of the adsorption structure of EP monomer and modeling of the STM images were performed at the density functional theory (DFT) level to understand the details of lateral interactions between neighboring surface species. Specifically, we show that EP forms a large number of oligomers including different types of dimer, trimer, and tetramer species, the relative abundance of which strongly depends on the adsorption parameters such as surface coverage and the presence of hydrogen. Based on a combination of spectroscopic and microscopic observations, all species can be attributed to two large classes of oligomers exhibiting different types of intermolecular bonding. In the first class of species the intermolecular interaction involves two acetyl groups of neighboring EP species, while in the second type of species the bonding interaction is realized via H-bonding between the ester-O of one molecule and the acetyl group of a neighboring EP species. This latter type of interaction significantly weakens the ester bond as suggested by a strong frequency shift of the related C–O ester vibration, which might potentially exert a strong impact on the chemical transformations involving the ester group. The intermolecular interaction in ethyl pyruvate assemblies can be effectively tuned by changing the adsorption parameters, such as surface coverage and the presence of coadsorbed hydrogen, providing by this an experimentally accessible tool to affect the strength of the ester bond by changing the nature and the concentration of coadsorbed species. Additionally, by performing spectroscopic investigation with isotopically labeled (¹³C)EP, we addressed the previously proposed adsorption models put forward for α -ketoester MP with transition metal surfaces. The spectroscopic observations obtained in our study suggest

that both previously discussed models suggesting enol or enediolate formation are not valid for a structurally more complex α -ketoester EP.

The obtained results provide important benchmarks for theoretical modeling of mutual lateral interactions in complex molecular assemblies formed on transition metal surfaces. Currently, theoretical modeling of mutual lateral interaction in large assemblies of ethyl pyruvate is being performed by global structure optimization employing a combination of semi-empirical and force-field approaches.

METHODS

All experiments were performed in two independent ultrahigh-vacuum (UHV) apparatuses—UHV-IRAS/molecular beam and UHV-STM apparatus—each equipped with a dedicated preparation chamber. After the preparation the samples were transferred *in situ* in the main part of each apparatus.

Sample Preparation. The Pt(111) single crystal (MaTeck GmbH) was cleaned prior to use in a dedicated preparation chamber (base pressure $< 2 \times 10^{-10}$ mbar) by repeated cycles of Ar⁺ ion bombardment at room temperature, followed by annealing at 1200 K and subsequent oxidation in 1×10^{-7} mbar of O₂ at 650–750 K to remove residual carbon. The last step contains the rapid flash of the sample to 1000 K. Shortly before each experiment the sample was flashed to 600–800 K before cooling to the required temperature to remove CO adsorbates. The long-range order and cleanliness of the Pt(111) single-crystal were checked by low-energy electron diffraction (LEED), Auger electron spectroscopy (AES), and additionally IRAS of adsorbed CO to probe the abundance of adsorption sites.

Ethyl pyruvate (Sigma-Aldrich, purity >97%) and ¹³C-ethyl pyruvate (Sigma-Aldrich, 99% ¹³C, purity 98%) were purified prior to each experiment by repeated freeze–pump–thaw cycles.

IRAS/Molecular Beam Experiments. The IRAS/molecular beam experiments were performed in a specially designed UHV apparatus (base pressure $> 2 \times 10^{-10}$ mbar). The apparatus contains two effusive doubly differentially pumped multichannel array sources operated at room temperature. Further details on the apparatus can be found elsewhere.²⁵ Ethyl pyruvate and hydrogen were independently dosed via two molecular beams at typical fluxes of 7.2×10^{12} and 5×10^{14} molecules s⁻¹ cm⁻², respectively.

IRAS data have been acquired by using a vacuum Fourier transform infrared (FT-IR) spectrometer (Bruker Vertex 80v) with a spectral resolution of 2 cm⁻¹, a mid-infrared (MIR) polarizer, and using p-polarized IR light. The spectrometer is equipped with a narrow-band mercury cadmium telluride (MCT) detector. All IRAS spectra were acquired at the same surface temperature that was used for ethyl pyruvate deposition (100 K). An automated quadrupole mass spectrometer (QMS) system (Hiden, HAL 301/3F) was employed for continuous monitoring of the partial pressures of gaseous species.

STM Experiments. The STM measurements were performed in an UHV (base pressure $< 1 \times 10^{-10}$ mbar) apparatus by employing a variable temperature (90–300 K) Aarhus 150 SPM (SPECS). All measurements were performed in a constant current mode, and the bias voltage *U*_T was applied to the sample. The etched W-Tip was commercially produced by SPECS and *in situ* sharpened by repeated cycles of 1.25 keV Ar⁺ bombardment with 5×10^{-6} mbar back-

pressure for 5 min. The sharpness of the W-Tip was validated on the pristine Pt(111) surface. The quality of the sample was additionally verified by acquiring STM images prior to the deposition. EP was dosed through an individual gas doser onto the Pt(111) surface kept at the desired deposition temperature and then transferred to the STM chamber for measurements. For the hydrogen deposition, the measurement chamber was backfilled with hydrogen through an individual gas doser with 1×10^{-6} mbar during the STM experiment.

DFT Calculations. DFT calculations of the adsorption geometry of EP monomer adsorbed on Pt(111) were performed by using a Quantum ESPRESSO26-27 with the PBE28 functional and projector-augmented-wave pseudopotential Pt.pbe-n-kjpaw_psl.1.0.0.UPF from ref 29, and the analogue pseudopotentials for the other elements have been used. The kinetic energy cutoff for the wave functions was set to 50 Ry, and a $2 \times 2 \times 2$ k -point grid was used to sample the Brillouin zone. These values have been arrived at by sampling different values for a platinum slab until the energy was converged to within 10^{-4} Ry. To separate the images in the z -direction, a 90 Å vacuum was used. The energy convergence cutoff for the optimization itself was set to 10^{-6} Ry. For the STM calculation, the Tersoff–Hamann³⁰ approach was used. The sample bias was 120 meV, and the isovalue was set to 0.5×10^{-6} .

Vibrational frequencies of an isolated EP molecule were calculated within the harmonic approximation at the B3LYP level with the aug-cc-pvqz basis set and gd3 correction of single molecules in the gas phase using the Gaussian16 software.³¹

RESULTS AND DISCUSSION

Experimentally, interaction of EP with the Pt(111) surface was investigated by a combination of molecular beam techniques, IRAS and STM in two independent ultrahigh-vacuum apparatuses.²⁴ Figure 1 shows the IR spectrum theoretically calculated at the DFT level for the gas phase (spectrum 1) and experimentally measured spectra of EP adsorbed on Pt(111) at 100 K (spectra 2–5). The assignment of the vibrational bands

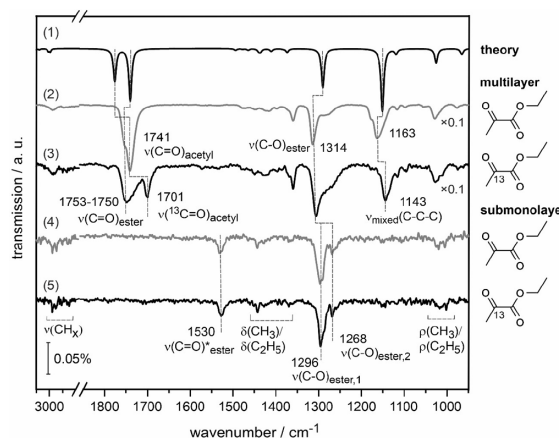


Figure 1. (1) Calculated gas phase spectrum of EP using DFT. IR spectra of EP adsorbed on Pt(111) at 100 K: (2, 3) EP and ^{13}C -EP multilayer (total exposure 2.9×10^{15} and 1.1×10^{15} molecules cm^{-2}); (4, 5) EP and ^{13}C -EP at submonolayer coverage (7.2×10^{13} molecules cm^{-2}).

was performed based on the comparison of the theoretical spectrum with the experimental spectra (2, regular EP) and spectra (3, ^{13}C -labeled EP) obtained for multilayer coverages. The spectra of EP multilayers, in which the absolute majority of the molecules is not in immediate contact with the underlying metal, serve as a reference for the nearly unperturbed molecular state of EP. In the isotopically labeled component, the carbon atom involved in the carbonyl group of the acetyl entity ($\text{CH}_3(\text{C}=\text{O})-$) was labeled with ^{13}C (see Figure 1). In the further discussion, we will denote this carbonyl group as the acetyl–carbonyl group, while the carbonyl group involved into the ester entity ($-(\text{C}=\text{O})\text{C}-\text{O}-\text{C}_2\text{H}_5$) of EP will be denoted as ester–carbonyl. Table S1 of the Supporting Information summarizes the experimentally observed and theoretically computed vibrational bands.

The most important vibrational bands in the multilayer spectrum comprise the $\text{C}=\text{O}$ stretching vibration at 1741 cm^{-1} (1701 cm^{-1} for the ^{13}C -isotope) in the acetyl–carbonyl group ($\nu(\text{C}=\text{O})_{\text{acetyl}}$),²⁰ the $\text{C}=\text{O}$ stretching vibration at 1749 – 1753 cm^{-1} in ester–carbonyl ($\nu(\text{C}=\text{O})_{\text{ester}}$),^{20,25} and the mixed vibration at 1314 cm^{-1} including mostly the stretching mode of the $\text{C}-\text{O}$ single bond ($-(\text{C}=\text{O})\text{C}-\text{O}-\text{C}_2\text{H}_5$) in the ester group ($\nu(\text{C}-\text{O})_{\text{ester}}$).^{20,26} Further visible vibrations are related to the deformation vibrations of the $-\text{CH}_2-$ and $-\text{CH}_3$ groups in the range 1360 – 1476 cm^{-1} ($\delta(\text{CH}_x)$), a mixed mode at 1162 cm^{-1} ($\nu_{\text{mixed}}(\text{C}-\text{C}-\text{C})$) mostly involving the stretching vibration of all skeletal carbons, and the stretching vibration of the CH_x groups ($\nu(\text{CH}_x)$) lying around 3000 cm^{-1} . Upon isotopic labeling of the acetyl–carbonyl group by ^{13}C , the vibrational band ($\nu(\text{C}=\text{O})_{\text{acetyl}}$) shifts from 1741 to 1701 cm^{-1} . The shift by 40 cm^{-1} is in an excellent agreement with the previously reported values of 30 – 40 cm^{-1} for simple carbonyl compounds, for example, acetophenone.^{9,10} As expected, the other major vibrational bands related to the ester group ($\nu(\text{C}=\text{O})_{\text{ester}}$ and $\nu(\text{C}-\text{O})_{\text{ester}}$) do not experience any major shifts upon isotopic labeling of the acetyl–carbonyl group. The band at 1162 cm^{-1} assigned to the mixed mode vibration $\nu_{\text{mixed}}(\text{C}-\text{C}-\text{C})$ shifts by 19 cm^{-1} . The displacement vectors related to this vibrational band $\nu_{\text{mixed}}(\text{C}-\text{C}-\text{C})$ are shown in the Supporting Information (Figure S1), demonstrating that the labeled ^{13}C atom is strongly involved in this vibrational mode.

Adsorption of EP at submonolayer coverages was investigated at the same temperature both with regular and ^{13}C -labeled species. Spectra 4 and 5 in Figure 1 are related to the coverage close to saturation for the regular and ^{13}C -labeled EP, respectively. In this coverage range, the intensity distribution of the most important vibrational peaks drastically changes: while both bands at 1753 and 1741 cm^{-1} completely vanish, the band $\nu(\text{C}-\text{O})_{\text{ester}}$ remains very pronounced and shifts from 1314 to 1296 cm^{-1} . Additionally, two new bands at 1268 and 1530 cm^{-1} evolve; their positions are not affected by isotopic labeling of the acetyl–carbonyl group.

Vanishing of the bands involving both carbonyl groups might be potentially related to two microscopic reasons: (i) the orientation of the $\text{C}=\text{O}$ bonds can be nearly parallel to the underlying metal and the related vibrations becomes invisible because of the metal surface selection rule;²⁷ (ii) the $\text{C}=\text{O}$ bond is considerably perturbed due to strong interaction with the underlying metal and/or coadsorbed species and the related vibrational band significantly shifts. The red-shift of the $\nu(\text{C}-\text{O})_{\text{ester}}$ vibration (from the gas phase value 1314 cm^{-1} to 1296 cm^{-1}) lies in the range typical for adsorption of gaseous

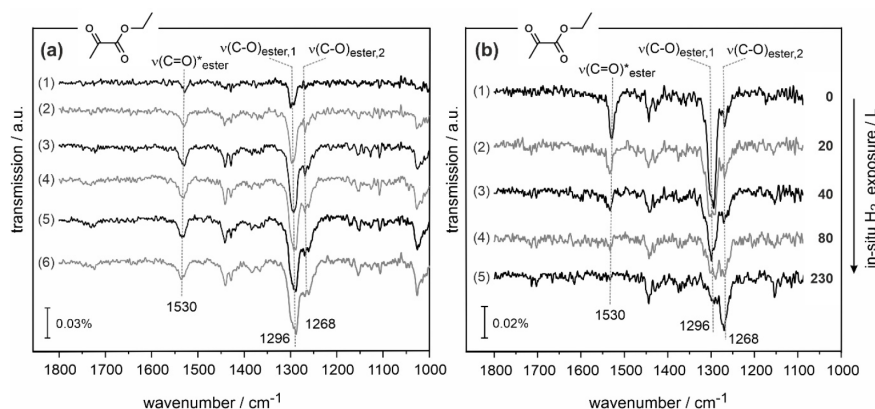


Figure 2. IRAS spectra of EP adsorbed on Pt(111) at 100 K. The spectra were obtained for (a) increasing EP exposure and (b) during *in situ* H₂ exposure at a constant coverage of EP (full details are given in the [Supporting Information](#)).

hydrocarbon species on metal surfaces^{28–30} and can be explained by possible rehybridization of the related molecular orbitals upon interaction with the underlying metal as well as by the wall effect.²⁷ The band at 1268 cm⁻¹ lies close to the band $\nu(\text{C}-\text{O})_{\text{ester}}$ 1296 cm⁻¹ and can be assigned to the same vibrational mode, which is red-shifted from the less perturbed state (1296 cm⁻¹) due to, for example, H-bonding. Previously, pronounced red-shifts due to H-bonding between an O atom and a H atom of two neighboring molecules were reported for a number of different hydrocarbon compounds,^{31,32} for example, adsorbed acetophenone forming dimer species on Pt(111).^{9,11} In the following, we will distinguish between two $\nu(\text{C}-\text{O})_{\text{ester}}$ vibrational bands and will denote the band at 1296 cm⁻¹ as $\nu(\text{C}-\text{O})_{\text{ester},1}$ and the band at 1268 cm⁻¹ as $\nu(\text{C}-\text{O})_{\text{ester},2}$.

The band at 1530 cm⁻¹ is present neither in the multilayer nor in the gas phase spectra of EP and therefore must arise from a strong interaction of the adsorbed EP species with Pt. Importantly, this vibrational band does not shift upon isotopic labeling of the acetyl-carbonyl group, indicating that the C atom of the acetyl-carbonyl is not involved into the appearance of this new band. The exact assignment of the band at 1530 cm⁻¹ is rather ambiguous. In the previous studies on structurally more simple MP adsorbed on Pt(111) by McBreen et al., a band at a similar frequency (1543 cm⁻¹) was assigned to $\nu(\text{C}-\text{O})$ or the mixed $\nu(\text{C}-\text{O}) + \nu(\text{C}-\text{C})$ mode of an enediolate species,²² in which both carbonyl groups establish two bonds to underlying two Pt atoms forming a structural fragment Pt...O...C...C...O...Pt. In the latter studies from the same group performed at higher temperatures (300 K), a band in a similar frequency range was observed at 1594 cm⁻¹ on Pt(111), which was interpreted as a $\nu(\text{C}=\text{C})$ mixed mode of enol species formed after keto-enol tautomerization of the acetyl groups of MP.²¹ The group of Tysøe investigated MP adsorption on Pd(111), where formation of a weak band in the same frequency range (1558 cm⁻¹) was observed.²⁰ In this report, the band was assigned to a C=C bond formed in the enol or enolate form of MP, implying that keto-enol tautomerization of the acetyl group of MP must have occurred. The hypothesis of enol or enolate formation was supported by a study from the same group, combining STM and theoretical modeling of MP species adsorbed on Pd(111).¹⁸ On the basis of the comparison of the experimentally measured STM line

profiles across the adsorbates and theoretically modeled profiles for ketone and enol forms of MP, the authors concluded that only the enol form of the adsorbed species can explain the experimental observations.

It should be emphasized that both models recently proposed in the literature—formation of enol or enediolate species—are in strong disagreement with our experimental observations obtained by IR spectroscopy. If the band at 1530 cm⁻¹ observed in our study would originate either from the C=C bond (as suggested by the enol model) or from enediolate species, it must shift upon ¹³C isotopic labeling of acetyl-carbonyl since this ¹³C atom would be directly involved in the corresponding C=C bond of the enol species or the Pt...O...C...C...O...Pt fragment of enediolate. No isotopic shift of the band at 1530 cm⁻¹ was observed in our IR spectra, so it can be quite safely concluded that the labeled ¹³C atom is not involved in the related vibration. The only remaining possibility to assign this band is the hypothesis that this vibration originates from the ester-carbonyl, which must be strongly shifted from its unperturbed value due to pronounced mixing of its molecular orbitals with the d-orbitals of underlying Pt atom(s). Such a scenario for interaction of carbonyl compounds with transition metals is in agreement with the adsorption model of acetone previously suggested by Ibach et al. Investigating acetone adsorption on Pt(111) by a combination of IRAS and off-specular high-resolution electron energy loss spectroscopy (HREELS), the authors observed formation of vibrational peaks in the range 1520–1585 cm⁻¹ (IRAS) and 1550 cm⁻¹ (HREELS), which were assigned to a side-on $\eta_2(\text{CO})$ adsorption configuration of acetone,³³ in which the carbonyl group forms a fragment Pt...C...O...Pt, in either the π or di- σ configuration. This conclusion was additionally corroborated by the earlier studies on decomposition of isopropanol, producing the $\eta_2(\text{CO})$ configuration in the same frequency range (1584 cm⁻¹).³⁴ The band at 1530 cm⁻¹ observed in our study can be thus most likely related to the $\eta_2(\text{CO})$ configuration, that is, to the fragment Pt...C...O...Pt formed for the ester-carbonyl group. In the studies by the Tysøe and McBreen groups, the bands in the frequency range 1540–1590 cm⁻¹ were rather assigned to the C=C bond of enols, enolates, or enediolates. While this might be true for MP, in the case of EP adsorption on Pt(111) the assignment of the band at 1530 cm⁻¹ to the C=C bond (formed in the

original acetyl–carbonyl group) can be excluded as in the opposite case an isotopic shift must be observed for the labeled component.

Summarizing the observations obtained in this coverage range, the absence of the C=O vibrational band related to acetyl–carbonyl arises from the nearly parallel the orientation of this band with respect to the metal surface.²⁷ In contrast, the C=O vibration of the ester–carbonyl is most likely visible but significantly red-shifted due to strong rehybridization of the related molecular orbital with the d-orbitals of underlying Pt leading to formation of $\eta_2(\text{CO})$ adsorption configuration. The earlier suggested models based on formation of enol, enolate, or enediolate species involving the original acetyl–carbonyl groups are inconsistent with the obtained IR spectra for isotopically labeled EP.

To further address the chemical nature of the adsorbed species and the origin of the band at 1530 cm^{-1} , the IR spectra were recorded at different EP coverages on pristine Pt(111) (Figure 2a) and on the same surface continuously exposed to H_2 at a constant EP coverage (Figure 2b). On pristine Pt(111), a combination of bands at 1530 and 1296 cm^{-1} is observed at the lowest coverage, while the band at 1268 cm^{-1} is missing. With increasing coverage, both bands at 1530 and 1296 cm^{-1} simultaneously grow in intensity (spectrum 2) and eventually saturate (spectra 3 and 4). The vibrational band $\nu(\text{C}-\text{O})_{\text{ester},2}$ at 1268 cm^{-1} appears at higher coverages (spectra 2 and 3) and grows in intensity when the EP coverage increases. It should be emphasized that the intensity distribution between the peaks at 1268 and 1296 cm^{-1} is clearly changing with increasing coverage. While at the lowest coverage the peak at 1268 cm^{-1} is not seen and the peak at 1296 cm^{-1} has a noticeable intensity, this difference becomes less pronounced at the highest coverage, at which the intensity of the band at 1268 cm^{-1} is just about factor of 2 lower than that of the band at 1296 cm^{-1} . This observation suggest that the species related to the band at 1268 cm^{-1} is either not present at the lowest coverage or is present at a negligibly small concentration. Interestingly, if the EP-containing surface is continuously exposed to H_2 , the intensity distribution of these bands drastically changes: while the bands at 1530 and 1296 cm^{-1} gradually and simultaneously disappear, the band at 1268 cm^{-1} grows in intensity and becomes the dominant vibrational peak after prolonged H_2 exposure (Figure 2b).

The observed evolution of the vibrational bands suggests that at least two distinct types of surface species exist on Pt(111): (i) the species $\text{S1}_{(\text{IRAS})}$, exhibiting a combination of two characteristic peaks at 1530 and 1296 cm^{-1} , and (ii) the species $\text{S2}_{(\text{IRAS})}$, showing a prominent vibrational band at 1268 cm^{-1} . The relative abundance of these species strongly depends on the coverage conditions and the presence of coadsorbed H: (i) species $\text{S1}_{(\text{IRAS})}$ appears already at the lowest coverage on pristine Pt(111) surface, while the species $\text{S2}_{(\text{IRAS})}$ starts evolving with growing coverage of EP; (ii) the species $\text{S1}_{(\text{IRAS})}$ almost completely converts into the species $\text{S2}_{(\text{IRAS})}$ after prolonged H_2 exposure. It should be noted that quantitative information about the relative population of both types of EP species cannot be unambiguously deduced from the IR spectra. First, because of the metal surface selection rule,²⁷ the IR intensity depends on the projection of the dynamic dipole moment on the surface normal. With this, if a given bond is only slightly inclined with respect to the metal surface, the related vibrational band is seen as a low-intensity vibration. Additionally, dipole coupling effects, such

as for example intensity transfer to high-frequency bands,^{27,35} might result in diminishing the IR intensity of the low-frequency vibration. Despite these complications, it can be quite safely concluded that surface species with two distinctly different spectroscopic signatures can be distinguished on Pt(111), which exhibit different dependencies on the coverage condition and the presence of coadsorbed H.

The appearance of two distinct vibrational bands related to C–O vibration in the ester group suggests that this group can be involved in different type of interactions with the underlying metal and/or with the coadsorbed species. The adsorption configuration of these species was investigated by STM under temperature conditions nearly identical with those of the IRAS experiments (118 and 100 K , respectively). Figure 3a displays

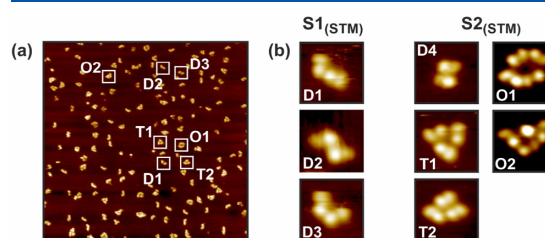


Figure 3. (a) STM image of EP adsorbed on pristine Pt(111) at 118 K ($52.2 \times 52.2\text{ nm}^2$, full details in the Supporting Information). (b) Close-up images of different oligomers divided in $\text{S1}_{(\text{STM})}$ (dimers D1, D2, and D3) and $\text{S2}_{(\text{STM})}$ (dimer D4, trimers T1 and T2, tetramers O1 and O2) species. The dimer D4 was observed only on H-covered Pt(111) surface.

an image obtained on pristine Pt(111) showing the overview of different surface assemblies. Interestingly, nearly all adsorbed species are agglomerated in assemblies of two, three, or four individual molecules. The close-up images of these structures measured with submolecular resolution are displayed in Figure 3b. Generally, all assemblies consist of a combination of elongated protrusions exhibiting a brighter spot and a darker area. Specifically, four types of dimers (D1–D4), two types of trimers (T1, T2), and two types of tetramers (O1, O2) were identified in our studies. Note that dimer D4 evolves only on H-covered surface and is not present on pristine Pt(111). Figure 4a–c shows the full data set of STM images obtained as a function of coverage on pristine Pt(111), which changes in the range $(1.8\text{--}70.7) \times 10^{12}$ molecules/ cm^2 as well as the statistical evaluation of the abundance of different types of oligomers. The STM images obtained on Pt(111) precovered with EP during continuous H_2 exposure and the statistical evaluation of the oligomer distribution obtained during this treatment are displayed in Figure 5a,b.

To find a correlation between the structure of the molecular assemblies as observed by STM and the type of intermolecular bonding in these assemblies deduced from IR spectra, we analyzed the structure of the assemblies with respect to the intermolecular intensity distribution. All molecular assemblies can be divided into two classes: (i) species $\text{S1}_{(\text{STM})}$ —the species interacting exclusively via the bright spots (D1–D3) and (ii) species $\text{S2}_{(\text{STM})}$ —the species interacting via the bright spot and a darker protrusion either exclusively (D4, T1, O1) or at least at part (T2, O2). For the latter species (T2, O2), the interaction between the bright and the dark protrusions is present as well as the interaction between two bright spots.

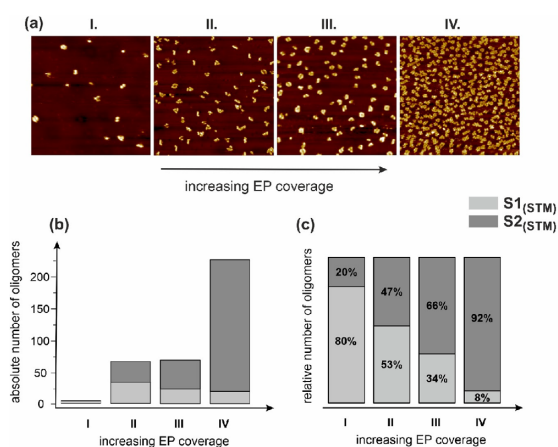


Figure 4. (a) STM images ($37.3 \times 37.3 \text{ nm}^2$) of EP adsorbed on pristine Pt(111) at different coverages at 100 K (full details in the Supporting Information). (b) Absolute number and (c) relative abundance of two types of surface species $S1_{(STM)}$ and $S2_{(STM)}$ shown for different EP surface coverages.

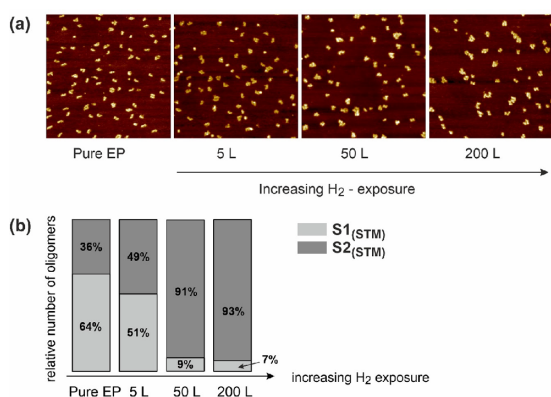


Figure 5. (a) STM images ($32.9 \times 32.9 \text{ nm}^2$) of EP adsorbed on Pt(111) obtained after different H_2 exposures indicated on the horizontal axis (full details in the Supporting Information). (b) Relative abundance of two types of surface species $S1_{(STM)}$ and $S2_{(STM)}$ shown for different H_2 exposures.

Figures 4b,c and 5b show the relative abundance of the species $S1_{(STM)}$ and $S2_{(STM)}$ as a function of increasing coverage (Figure 4b,c) and increasing H_2 exposure (Figure 5b). There is a clear trend observed in these plots on pristine Pt: the species $S1_{(STM)}$ prevails at low coverages, while at higher coverages the concentration of $S2_{(STM)}$ starts growing and this species eventually dominates. Note that the absolute amount of species $S1_{(STM)}$ in Figure 4b rather quickly levels off and remains almost constant up to the highest coverage (IV), while the abundance of species $S2_{(STM)}$ grows almost by 2 orders of magnitude between the lowest and the highest coverages (I and IV). For a series of the experiments involving H_2 exposure, the initial coverage distribution is chosen such that the relative population of surface oligomers on pristine Pt(111) surface amounts to 64% for the species $S1_{(STM)}$ (Figure 5a,b). During a continuous H_2 exposure, nearly full conversion of the species $S1_{(STM)}$ to $S2_{(STM)}$ is observed, while the overall concentration

of adsorbed EP molecules does not notably change during H_2 treatment.

A strong correlation between the evolution of the surface assemblies detected by STM and the vibrational bands in the IR spectra can be established. The combination of two peaks appearing first on the pristine Pt(111) surface (1530 and 1296 cm^{-1} , species $S1_{(IRAS)}$) can be clearly correlated to the evolution of the species $S1_{(STM)}$, while the band at 1268 cm^{-1} (species $S2_{(IRAS)}$), evolving at higher coverages, correlates with the appearance of the species $S2_{(STM)}$. The evolution of the surface species on the H-containing surface is also in very good agreement with this assignment: while on the pristine surface the bands at 1530 and 1296 cm^{-1} are clearly visible in IR spectra and a large fraction of the microscopically observed assemblies are $S1_{(STM)}$ species, prolonged H_2 exposure results in nearly full conversion of the assemblies to $S2_{(STM)}$ species accompanied by the full conversion of the bands at 1530 and 1296 cm^{-1} ($S1_{(IRAS)}$) to the band 1268 cm^{-1} ($S2_{(IRAS)}$). With this, both investigated adsorption systems suggest a clear correlation between the spectroscopically detected species $S1_{(IRAS)}$ and microscopically observed assemblies $S1_{(STM)}$. Similarly, the appearance of the species $S2_{(IRAS)}$ correlates with the evolution of the surface assemblies $S2_{(STM)}$. On the basis of these correlations, it can be concluded that the lateral interaction typical for the species $S1_{(STM)}$ occurring via two bright spots leads to the vibrational signature comprising a combination of the bands 1530 and 1296 cm^{-1} , while the interaction via the bright spot and the dark protrusion results in the evolution of the vibrational band at 1268 cm^{-1} .

Based purely on intensity distribution in the STM data, it is not possible to assign a specific fragment of the EP molecule—the ester—or the acetyl—part of EP—to a bright or a dark protrusion seen in the STM images. In the previous studies on MP adsorbed on Pd(111), assignment of the STM intensity distribution was performed based on theoretical modeling of STM images.¹⁸ Specifically, adsorption of the original MP molecule was found to result in a homogeneous intensity distribution, while the pattern comprising a bright and a dark protrusion was predicted for the enol form of MP, in which the acetyl-carbonyl group undergoes keto-enol tautomerization. In this enol species, the bright part of adsorbed MP was assigned to the ester part of the molecule. This assignment cannot be, however, transfer to EP adsorbed on Pt(111), as we can safely exclude formation of enol species involving the original acetyl-carbonyl group of EP on this surface.

It is important to note that the intensity distribution in the individual molecules constituting all oligomer species is very similar. Figure 6 shows three selected oligomers—dimer, trimer, and tetramer species (Figure 6a)—and the corresponding line profiles measured along the main axes connecting the bright and the dark protrusions (Figure 6b). All line profiles exhibit two maxima with typical distances between them indicated in Figure 6b. Each value was obtained from the statistical evaluation of line scans measured for 10–15 oligomers with the same structure. It can be seen that the intensity distribution and the distances between the intensity peaks in each individual molecule are very similar for all oligomers, suggesting that the chemical nature of the monomer species does not drastically alter due to lateral intermolecular interactions in the particular oligomer species. To address the intensity distribution in these individual EP molecules, we performed theoretical modeling of EP adsorption geometry in monomer species adsorbed on Pt(111) and the corresponding

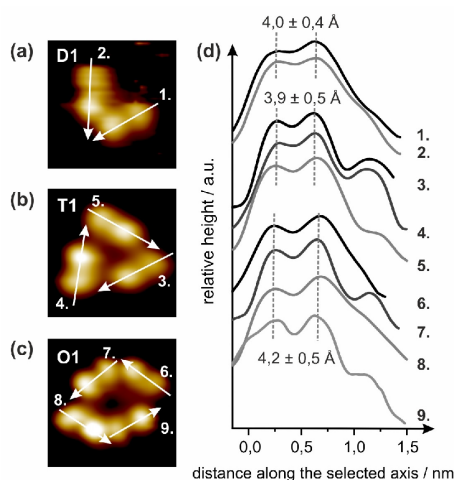


Figure 6. (a–c) Close-up images of selected oligomer species: dimer D1, trimer T1, and oligomer O1. (d) Line profiles measured along the axes 1–9 indicated at the close-up images.

STM image at the DFT level. The structural calculations were performed with the PBE functional and projector-augmented wave pseudopotentials; the STM images were simulated with the Tersoff–Hamann approach (for more details see the [Methods](#) section). [Figure 7](#) shows the calculated structure of

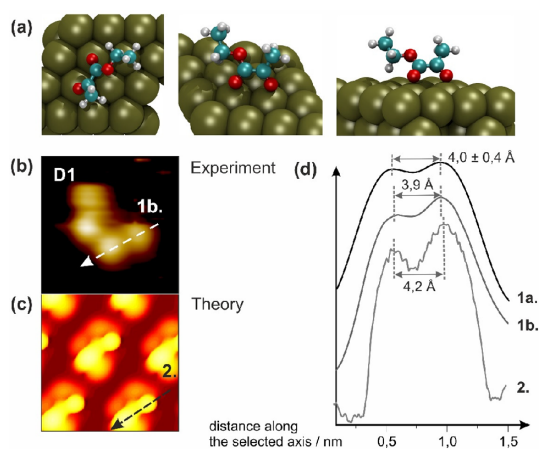


Figure 7. (a) Adsorption geometry of EP monomer calculated at the DFT level. (b, c) Experimental and theoretically calculated STM images. (d) STM line profiles along the axes shown in (b) and (c): (1a) is an average of 14 line profiles in individual EP monomers agglomerated in dimers D1 as shown in (b); (1b) is measured for a single EP monomer along the axis 1b; (2) is derived from the computed STM image shown in (c).

the EP monomer ([Figure 7a](#)) together with the experimental ([Figure 7b](#)) and modeled STM image ([Figure 7c](#)). [Figure 7d](#) displays the line profile derived from the experimental (lines 1a and 1b) and modeled (line 2) STM images along the main axis. Note that line 1b is related to the experimental STM image shown in [Figure 7b](#), while line 1a is an average from 14 experimental line scans measured for D1 species. In the

computed configuration both carbonyl groups are inclined and point down toward two Pt atoms, while the $(\text{C}_2\text{H}_5)\text{C}-\text{O}$ group is lifted above the surface. It should be noted that the adsorption configuration of EP agglomerated in oligomers might differ from the one calculated for a monomer species. Currently, we perform detailed theoretical calculations at DFT, semiempirical, and force field levels to describe the intermolecular interactions in the whole variety of oligomer species, which will be the subject of upcoming reports. In this study, we mostly focus on the intensity distribution in the monomer species to draw conclusions on the position of brighter vs darker spots seen by STM in the individual molecule. For the computed adsorption configuration of the monomer, the modeled STM image exhibits an inhomogeneous intensity distribution with the higher intensity positioned at the acetyl part and the lower intensity relating to the ester part of EP. If this intensity distribution remains the same in the individual EP molecules involved in oligomers, the following conclusion can be made on the two observed types of lateral interactions. First, in the STM species $\text{S1}_{(\text{STM})}$ exhibiting interaction between two bright spots, a H of the methyl group of one monomer is bonded to the acetyl-carbonyl of the other monomer. In this case, the ester groups are not directly involved in H-bonding between two monomers, which is consistent with the spectroscopic observation that the C–O bond of the ester group remains nearly unperturbed and the corresponding vibrational band has only a minor frequency shift with respect to the multilayer value (19 cm^{-1}). Second, in the STM species $\text{S2}_{(\text{STM})}$ showing the interaction between the bright and the dark protrusions, a methyl group of one monomer must be H-bonded to one of the O atoms of the ester group. Taking into account the fact that the frequency of the C–O single bond (1268 cm^{-1}) is strongly red-shifted in this type of species (by 47 cm^{-1} as compared to the multilayer value), it can be quite safely concluded that the ester-O is involved in H-bonding with the H atom of the methyl group. This hypothesis is in excellent agreement with earlier IR studies reported for a large variety of O-containing hydrocarbon compounds in the liquid phase, in which the effects of H-bonding on vibrational frequencies of CO bonds were investigated.^{31,32} Generally, the CO bonds show frequency shifts of $10\text{--}40\text{ cm}^{-1}$ from their unperturbed value upon establishing a H bond with a foreign molecule. Also in our earlier studies on adsorption of acetophenone on Pt(111), frequency shifts of $20\text{--}50\text{ cm}^{-1}$ were found for C=O vibration involved in H-bonding with one or two neighboring molecules.^{9,11} The frequency shift of 28 cm^{-1} observed in this study (as compared to the value of nearly unperturbed species $\text{S1}_{(\text{IRAS})}$ 1296 cm^{-1}) is in good quantitative agreement with the earlier reported typical range of a few tens of wavenumbers.

On the basis of these considerations, we propose adsorption configurations for different types of surface species shown in [Figure 8](#), which are consistent with all experimental observations made in this study. [Figure 8](#) shows a proposed configuration of the dimer species D1 and D3 ([Figure 8a](#)) and D2 ([Figure 8b](#)), in which the interaction is established between two acetyl groups of EP, which are predicted to appear as a bright protrusion in STM images (species $\text{S1}_{(\text{IRAS})}/\text{S1}_{(\text{STM})}$). Here, a H atom of the methyl group establishes H-bonding with the acetyl-carbonyl group of the second EP molecule. In this configuration, the ester C–O bond is not directly involved in intermolecular interaction, which is consistent with the spectroscopic observation that its vibrational frequency (1296

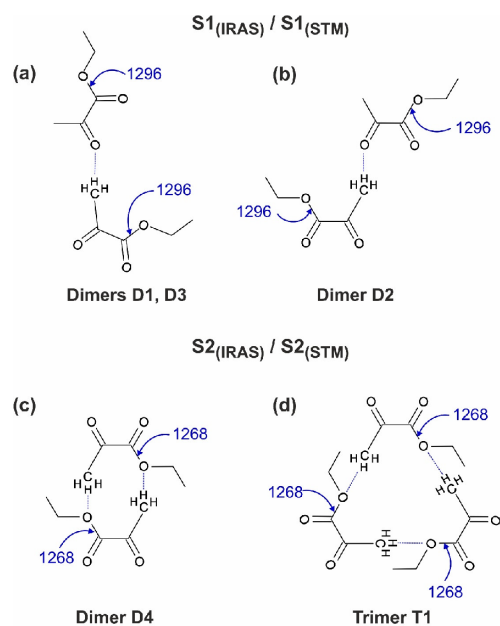


Figure 8. Proposed models for different types of EP oligomers: (a, b) the dimer assemblies formed between two acetyl groups related to the species $S1_{(IRAS)}/S1_{(STM)}$; (c, d) selected dimer and trimer assemblies formed between the acetyl and ester groups related to the species $S2_{(IRAS)}/S2_{(STM)}$.

cm^{-1}) is only slightly shifted as compared to the multilayer value (1314 cm^{-1}). The frequencies of the $\nu(\text{C}-\text{O})_{\text{ester}}$ vibrational bands are highlighted in the models with blue color. Both acetyl–carbonyl groups of the dimer are most likely oriented close to parallel to the underlying metal surface, since the corresponding vibrational bands are not seen in the spectra. The only other observed prominent band at 1530 cm^{-1} is most likely related to one or both ester–carbonyl(s) of EP. As discussed above, the strong red-shift of this band can arise from substantial rehybridization of the related molecular orbital with the d-electrons of Pt and might be indicative of a $\eta_2(\text{CO})$ configuration suggested in earlier studies for acetone adsorption. The experimentally observed configurations of the dimers D1 and D3 differ slightly with respect to the relative orientation of the individual molecules (see Figure 3b), which is most likely dictated by the underlying metal support. The stabilities of D1, D2, and D3 dimers on Pt(111) seem to be similar as these species are observed simultaneously.

The second type of interaction based on establishing a connection between the brighter and the darker protrusions of the surface species is exemplified for selected oligomer structures D4 and T1 (Figure 8c,d). In this type of species ($S2_{(IRAS)}/S2_{(STM)}$), the ester group of one molecule is involved into H-bonding with the methyl group of the neighboring species. This interaction results in a strong red-shift of the $\nu(\text{C}-\text{O})_{\text{ester}}$ vibration to 1268 cm^{-1} observed spectroscopically. Because no other vibrational bands in the range of carbonyl groups could be observed for this species, it can be concluded that all $\text{C}=\text{O}$ groups are oriented nearly parallel to the surface for this type of adsorption configuration. It should be noted that the species T2 and O2 exhibit not only the interaction between the bright and the dark protrusions but

also the interaction between the bright and the bright protrusions. In this case, one molecule with be involved on one side into the acetyl–carbonyl/acetyl–methyl interaction, the same as in species $S1_{(IRAS)}$, and on the other side, the ester-O will be involved in the interaction with the methyl group of the acetyl entity of the neighboring species, the same as in species $S2_{(IRAS)}$.

It should be emphasized that the strong red-shift of the $\nu(\text{C}-\text{O})_{\text{ester}}$ vibration observed for the second type of surface species $S2_{(IRAS)}/S2_{(STM)}$ implies that this bond is significantly weakened by the lateral interaction with the neighboring molecules as compared to the less perturbed $S1_{(IRAS)}/S1_{(STM)}$ state. This observation suggests that the chemical transformations involving this notably weakened ester bond might be significantly facilitated in the second type of complex. This phenomenon opens a prospect of rational control of the catalytic transformations involving ester groups by tuning the parameter space of a catalytic reaction, such as the concentration of surface adsorbates and the presence of coadsorbed H to create the second type of EP assembly with strongly weakened ester bonds.

Exposure of the EP-precovered surface to H_2 results in a complete switching of the intermolecular interaction from type $S1_{(IRAS)}/S1_{(STM)}$ to type $S2_{(IRAS)}/S2_{(STM)}$. In terms of the model discussed above, this means that H-bonding involving an acetyl–carbonyl group disappears, and the other type of bonding involving the ester-O atom evolves. This hypothesis is in an excellent agreement with our earlier studies on a the simple carbonyl compound acetophenone adsorbed on the Pt(111) surface.^{9,12} While acetophenone was observed to form two types of dimers involving a carbonyl group on pristine Pt(111), exposure to H_2 below 240 K resulted in rupture of all H bonds and falling apart of all dimer species. This phenomenon originates most likely from a high propensity of carbonyl groups to build a quasi-H-bonding to H atoms adsorbed on the metal. In this case, the bonding of the carbonyl groups to surface-adsorbed H seems to produce a more stable surface species than acetophenone dimers connected via H-bonding between the carbonyl and the methyl group of the neighboring molecules. In the case of EP, a similar behavior is observed—in the presence of surface-adsorbed H the bonding involving a carbonyl group disappears. However, a different type of H-bonding involving the ester-O is possible in EP, which cannot be realized in a simple carbonyl acetophenone. As a result, a new type of intermolecular interaction prevails on H-covered surfaces, producing the $S2_{(IRAS)}/S2_{(STM)}$ species binding via the ester-O atom.

CONCLUSIONS

Summarizing, in this study the details of mutual lateral interactions in ethyl pyruvate oligomers adsorbed on well-defined Pt(111) surface were addressed by a combination of IRAS, STM, molecular beam techniques, and theoretical modeling at the DFT level. It was shown that EP forms a large number of different oligomer species including different types of dimers, trimers, and tetramers. Based on a combination of spectroscopic and microscopic observations, all species can be attributed to two large classes of oligomers exhibiting different types of intermolecular binding. The first class of species— $S1_{(IRAS)}/S1_{(STM)}$ —comprising three topologically different types of dimers, shows two characteristic vibrational bands, related to nearly unperturbed C–O

stretching vibration of the ester group and most likely strongly perturbed ester–carbonyl vibration. Intermolecular interaction in these species is realized via H-bonding between two acetyl groups, in which an O atom of the carbonyl group is bonded to a H atom of the methyl group of a neighboring molecule. In STM images, this species appears as dimers connected to each other via two bright protrusions. DFT modeling of the STM images performed for EP monomer species confirms that the position of the bright protrusion is related to the acetyl group of EP. The second class of species— $S2_{(IRAS)}/S2_{(STM)}$ —comprising a dimer and four different types of trimers and tetramers, exhibits a characteristic vibrational band related to a strongly red-shifted C–O stretching vibration of an ester group $\nu(\text{CO})_{\text{ester},2}$. The shift is proposed to arise from a second type of intermolecular interaction involving H-bonding between the ester-O and the methyl group of neighboring EP. In STM images, the corresponding surface species show an interaction between the bright and the dark protrusions of the neighboring molecules. The latter type of interaction significantly weakens the ester bond as evidenced by a strong frequency shift, which might exert a considerable impact on the chemical transformations involving the ester group.

The abundance of both types of surface species depends on surface coverage of EP and on the presence of coadsorbed H. On the pristine surface, the species $S1_{(IRAS)}/S1_{(STM)}$ prevail at low coverages, while the species $S2_{(IRAS)}/S2_{(STM)}$ dominate in the high coverage regime. In the presence of H, the species $S1_{(IRAS)}/S1_{(STM)}$ become fully converted into the species $S2_{(IRAS)}/S2_{(STM)}$, suggesting that the binding via acetyl groups converts to binding via the acetyl–ester entities on H-containing surfaces. With this, the type of intermolecular interaction in ethyl pyruvate assemblies can be effectively tuned by changing the adsorption parameters, such as surface coverage and the presence of coadsorbed hydrogen, providing by this an experimentally accessible way to affect the strength of the ester bond by changing the nature and concentration of coadsorbed species.

The obtained results provide important insights into the details of lateral interactions of complex multifunctional molecules adsorbed on catalytically relevant surfaces. We show that the parameter space in a catalytic process involving ester compounds can be purposefully varied to tune the strength of the ester bond toward improving the catalytic performance.

■ ASSOCIATED CONTENT

SI Supporting Information

The Supporting Information is available free of charge at <https://pubs.acs.org/doi/10.1021/acs.jpcc.0c09659>.

Assignment of vibrational modes of ethyl pyruvate (Table S1); full figure caption for Figures 2–5 (PDF)

■ AUTHOR INFORMATION

Corresponding Author

Swetlana Schauer mann – Institut für Physikalische Chemie, Christian-Albrechts-Universität zu Kiel, 24118 Kiel, Germany; orcid.org/0000-0002-9390-2024; Email: schauer mann@pctc.uni-kiel.de

Authors

Carsten Schröder – Institut für Physikalische Chemie, Christian-Albrechts-Universität zu Kiel, 24118 Kiel, Germany

Marvin C. Schmidt – Institut für Physikalische Chemie, Christian-Albrechts-Universität zu Kiel, 24118 Kiel, Germany

Christopher Witt – Institut für Physikalische Chemie, Christian-Albrechts-Universität zu Kiel, 24118 Kiel, Germany

Smadar Attia – Institut für Physikalische Chemie, Christian-Albrechts-Universität zu Kiel, 24118 Kiel, Germany

Jann Weber – Institut für Physikalische Chemie, Christian-Albrechts-Universität zu Kiel, 24118 Kiel, Germany

Ann-Katrin Baumann – Institut für Physikalische Chemie, Christian-Albrechts-Universität zu Kiel, 24118 Kiel, Germany

Bernd Hartke – Institut für Physikalische Chemie, Christian-Albrechts-Universität zu Kiel, 24118 Kiel, Germany;

orcid.org/0000-0001-8480-0862

Complete contact information is available at:

<https://pubs.acs.org/doi/10.1021/acs.jpcc.0c09659>

Notes

The authors declare no competing financial interest.

■ ACKNOWLEDGMENTS

Financial support by the German Science Foundations (DFG, Grants SCHA 1477/3-1 and HA 2498/16-2) is gratefully acknowledged.

■ REFERENCES

- (1) Somorjai, G. A. *Introduction to Surface Chemistry and Catalysis*, 2nd ed.; John Wiley & Sons: New York, 2010.
- (2) Meemken, F.; Baiker, A. Recent Progress in Heterogeneous Asymmetric Hydrogenation of C=O and C=C Bonds on Supported Noble Metal Catalysts. *Chem. Rev.* **2017**, *117*, 11522–11569.
- (3) Gellman, A. J.; Tysoe, W. T.; Zaera, F. Surface Chemistry for Enantioselective Catalysis. *Catal. Lett.* **2015**, *145*, 220–232.
- (4) Marshall, S. T.; O'Brien, M.; Oetter, B.; Corpuz, A.; Richards, R. M.; Schwartz, D. K.; Medlin, J. W. Controlled Selectivity for Palladium Catalysts Using Self-Assembled Monolayers. *Nat. Mater.* **2010**, *9*, 853–858.
- (5) Marshall, S. T.; Medlin, J. W. Surface-Level Mechanistic Studies of Adsorbate–Adsorbate Interactions in Heterogeneous Catalysis by Metals. *Surf. Sci. Rep.* **2011**, *66*, 173–184.
- (6) Tysoe, W. *Molecular-Level Design of Heterogeneous Chiral Catalysts*, 2018; DOI: [10.2172/1160339](https://doi.org/10.2172/1160339).
- (7) Ernst, J. B.; Schwermann, C.; Yokota, G.-i.; Tada, M.; Muratsugu, S.; Doltsinis, N. L.; Glorius, F. Molecular Adsorbates Switch on Heterogeneous Catalysis: Induction of Reactivity by N-Heterocyclic Carbenes. *J. Am. Chem. Soc.* **2017**, *139*, 9144–9147.
- (8) Dostert, K.-H.; O'Brien, C. P.; Ivars-Barceló, F.; Schauer mann, S.; Freund, H.-J. Spectators Control Selectivity in Surface Chemistry: Acrolein Partial Hydrogenation over Pd. *J. Am. Chem. Soc.* **2015**, *137*, 13496–13502.
- (9) Attia, S.; Schmidt, M.-C.; Schröder, C.; Pessier, P.; Schauer mann, S. Surface-Driven Keto–Enol Tautomerization: Atomistic Insights into Enol Formation and Stabilization Mechanisms. *Angew. Chem., Int. Ed.* **2018**, *57*, 16659–16664.
- (10) Attia, S.; Schauer mann, S. Coverage-Dependent Adsorption Geometry of Acetophenone on Pt(111). *J. Phys. Chem. C* **2020**, *124*, 557–566.

- (11) Attia, S.; Schmidt, M. C.; Schröder, C.; Schauer mann, S. Formation and Stabilization Mechanisms of Enols on Pt through Multiple Hydrogen Bonding. *ACS Catal.* **2019**, *9*, 6882–6889.
- (12) Attia, S.; Schmidt, M. C.; Schröder, C.; Weber, J.; Baumann, A.-K.; Schauer mann, S. Keto–Enol Tautomerization as a First Step in Hydrogenation of Carbonyl Compounds. *J. Phys. Chem. C* **2019**, *123*, 29271–29277.
- (13) Attia, S.; Spadafora, E. J.; Schmidt, M. C.; Schröder, C.; Baumann, A.-K.; Schauer mann, S. Adsorption Geometry and Self-Assembling of Chiral Modifier (R)-(+)-1-(1-Naphthylethylamine) on Pt(111). *Phys. Chem. Chem. Phys.* **2020**, *22*, 15696–15706.
- (14) Schmidt, M. C.; Attia, S.; Schröder, C.; Baumann, A.-K.; Pessier, P.; Schauer mann, S. Temperature-Dependent Formation of Acetophenone Oligomers Accompanied by Keto–Enol Tautomerism: Real Space Distribution. *J. Phys. Chem. C* **2020**, *124*, 14262–14271.
- (15) Dostert, K.-H.; O'Brien, C. P.; Mirabella, F.; Ivars-Barceló, F.; Attia, S.; Spadafora, E.; Schauer mann, S.; Freund, H.-J. Selective Partial Hydrogenation of Acrolein on Pd: A Mechanistic Study. *ACS Catal.* **2017**, *7*, 5523–5533.
- (16) Schauer mann, S.; Freund, H.-J. Model Approach in Heterogeneous Catalysis: Kinetics and Thermodynamics of Surface Reactions. *Acc. Chem. Res.* **2015**, *48*, 2775–2782.
- (17) Liu, W.; Savara, A.; Ren, X.; Ludwig, W.; Dostert, K.-H.; Schauer mann, S.; Tkatchenko, A.; Freund, H.-J.; Scheffler, M. Toward Low-Temperature Dehydrogenation Catalysis: Isophorone Adsorbed on Pd(111). *J. Phys. Chem. Lett.* **2012**, *3*, 582–586.
- (18) Garvey, M.; Bai, Y.; Boscoboinik, J. A.; Burkholder, L.; Sorensen, T. E.; Tysoe, W. T. Identifying Molecular Species on Surfaces by Scanning Tunneling Microscopy: Methyl Pyruvate on Pd(111). *J. Phys. Chem. C* **2013**, *117*, 4505–4514.
- (19) Mahapatra, M.; Burkholder, L.; Garvey, M.; Bai, Y.; Saldin, D. K.; Tysoe, W. T. Enhanced Hydrogenation Activity and Diastereomeric Interactions of Methyl Pyruvate Co-Adsorbed with R-1-(1-Naphthyl)Ethylamine on Pd(111). *Nat. Commun.* **2016**, *7*, 12380.
- (20) Burkholder, L.; Tysoe, W. T. Structure and Reaction Pathways of Methyl Pyruvate on Pd(111). *J. Phys. Chem. C* **2009**, *113*, 15298–15306.
- (21) Lavoie, S.; Laliberté, M.-A.; Mahieu, G.; Demers-Carpentier, V.; McBreen, P. Keto-Enol Driven Assembly of Methyl Pyruvate on Pt(111). *J. Am. Chem. Soc.* **2007**, *129*, 11668–11669.
- (22) Lavoie, S.; Laliberté, M. A.; McBreen, P. H. Adsorption States and Modifier–Substrate Interactions on Pt(111) Relevant to the Enantioselective Hydrogenation of Alkyl Pyruvates in the Orito Reaction. *J. Am. Chem. Soc.* **2003**, *125*, 15756–15757.
- (23) Bürgi, T.; Atamny, F.; Knop-Gericke, A.; Hävecker, M.; Schedel-Niedrig, T.; Schlögl, R.; Baiker, A. Adsorption Mode of Ethyl Pyruvate on Platinum: An in Situ Xanes Study. *Catal. Lett.* **2000**, *66*, 109–112.
- (24) Attia, S.; Spadafora, E. J.; Hartmann, J.; Freund, H.-J.; Schauer mann, S. Molecular Beam/Infrared Reflection-Absorption Spectroscopy Apparatus for Probing Heterogeneously Catalyzed Reactions on Functionalized and Nanostructured Model Surfaces. *Rev. Sci. Instrum.* **2019**, *90*, 053903.
- (25) Demers-Carpentier, V.; Rasmussen, A. M. H.; Goubert, G.; Ferrighi, L.; Dong, Y.; Lemay, J.-C.; Masini, F.; Zeng, Y.; Hammer, B.; McBreen, P. H. Stereodirection of an A-Ketoester at Sub-Molecular Sites on Chirally Modified Pt(111): Heterogeneous Asymmetric Catalysis. *J. Am. Chem. Soc.* **2013**, *135*, 9999–10002.
- (26) Castonguay, M.; Roy, J. R.; Rochefort, A.; McBreen, P. H. Orientation and Conformation of Methyl Pyruvate on Ni(111). *J. Am. Chem. Soc.* **2000**, *122*, 518–524.
- (27) Hoffmann, F. M. Infrared Reflection-Absorption Spectroscopy of Adsorbed Molecules. *Surf. Sci. Rep.* **1983**, *3*, 107–192.
- (28) Dostert, K.-H.; O'Brien, C. P.; Liu, W.; Riedel, W.; Savara, A.; Tkatchenko, A.; Schauer mann, S.; Freund, H.-J. Adsorption of Isophorone and Trimethyl-Cyclohexanone on Pd(111): A Combination of Infrared Reflection Absorption Spectroscopy and Density Functional Theory Studies. *Surf. Sci.* **2016**, *650*, 149–160.
- (29) Zaera, F. An Organometallic Guide to the Chemistry of Hydrocarbon Moieties on Transition Metal Surfaces. *Chem. Rev.* **1995**, *95*, 2651–2693.
- (30) Ma, Z.; Zaera, F. Organic Chemistry on Solid Surfaces. *Surf. Sci. Rep.* **2006**, *61*, 229–281.
- (31) Fried, S. D.; Bagchi, S.; Boxer, S. G. Measuring Electrostatic Fields in Both Hydrogen-Bonding and Non-Hydrogen-Bonding Environments Using Carbonyl Vibrational Probes. *J. Am. Chem. Soc.* **2013**, *135*, 11181–11192.
- (32) Nolasco, M. M.; Ribeiro-Claro, P. J. A.; Paulo, J. A. C-H...O Hydrogen Bonds in Cyclohexenone Reveal the Spectroscopic Behavior of C_{sp3}-H and C_{sp2}-H Donors. *ChemPhysChem* **2005**, *6*, 496–502.
- (33) Vannice, M. A.; Erley, W.; Ibach, H. A Rairs and HREELS Study of Acetone on Pt(111). *Surf. Sci.* **1991**, *254*, 1–11.
- (34) Vannice, M. A.; Erley, W.; Ibach, H. A Rairs and Hreels Study of Isopropyl Alcohol on Pt(111). *Surf. Sci.* **1991**, *254*, 12–20.
- (35) Hollins, P. The Influence of Surface Defects on the Infrared Spectra of Adsorbed Species. *Surf. Sci. Rep.* **1992**, *16*, 51–94.

8.5 Disordered Two-Dimensional Self-Organization of Ethyl Pyruvate Molecules on the Pt(111) Surface

Publication Data and Reprint

Reference: Christopher Witt, Marvin-Christopher Schmidt, Carsten Schröder, Swetlana Schauer mann and Bernd Hartke

DOI: 10.1021/acs.jpcc.1c07058

Submitted: 09.08.2021

Accepted: 05.11.2021

Contribution: IR measurements, scientific discussion, interpretation of IR data, preparation of the IR part of the manuscript

Copyright: Reprinted with permission from JPC C from Ref.[250]. Copyright 2021 American Chemical Society.

Disordered Two-Dimensional Self-Organization of Ethyl Pyruvate Molecules on the Pt(111) Surface

Christopher Witt, Marvin-Christopher Schmidt, Carsten Schröder, Swetlana Schaueremann, and Bernd Hartke*

Cite This: *J. Phys. Chem. C* 2021, 125, 26167–26179

Read Online

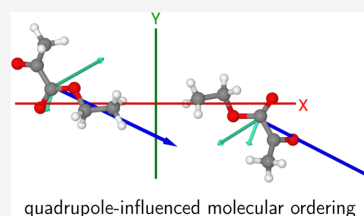
ACCESS |

Metrics & More

Article Recommendations

Supporting Information

ABSTRACT: Ethyl pyruvate on a pristine Pt(111) surface in submonolayer coverage neither forms regular superstructures nor a completely random distribution. Instead, a random, widely scattered pattern of a few typical ethyl pyruvate oligomers is found. With global structure optimization of ethyl pyruvate clusters on Pt(111) and without prescribing any adsorption locations or configurations, we can simulate this behavior qualitatively. From an in-depth analysis of our simulation results, we propose that (1) a mix of a large number of possible adsorption configurations leads to disorder, (2) repulsion from molecular charges and dipoles leads to typically large distances between ethyl pyruvate molecules and oligomers, and (3) residual attractive quadrupole interactions lead to remnants of order, in particular to the experimentally observed ethyl pyruvate oligomers with short intraoligomer distances and with typical relative molecular orientations. Additionally, we propose that an experimentally observed, characteristic infrared absorption band for ethyl pyruvate on Pt(111) arises from the surface-perpendicular component of an ester carbonyl vibration directly bound to surface Pt atoms.



INTRODUCTION

Molecules on surfaces are key players in heterogeneous catalysis¹ and on-surface synthesis.^{2–4} One obvious reason is the influence of the surface on each single adsorbed molecule, steric or electronic or by strong local electric fields,⁵ leading to intramolecular changes, as for example, in surface-driven keto-enol tautomerization.⁶ However, intermolecular interactions between several surface-adsorbed molecules are also clearly important, as demonstrated by ligand-directed heterogeneous catalysis.^{7,8}

Hence, molecular interaction and self-assembly on (metal) surfaces^{9–11} is not only a research field on its own, ranging from investigations of interaction modes^{12,13} to two-dimensional crystal engineering¹⁴ but also an important ingredient for on-surface synthesis and heterogeneous catalysis. There, it is vital to fully understand the intricate interplay between molecule–molecule and molecule–surface interactions, to be able to advance from trial-and-error to systematic, rational design.

Likewise, in the ecosystem of computational methods in catalysis,^{15–17} molecular interaction and self-assembly on surfaces is also a key area. In contrast to the same situation in vacuo, however, there are substantial additional challenges. For molecules of nontrivial size, finding the preferred adsorption site(s) and conformations of just one molecule already requires an expensive conformational search, as shown, e.g., for a single camphor molecule on Au(111).¹⁸ Theoretical studies of many adsorbate molecules quickly drown in the deluge of possibilities that arises from combining all of the intra- and intermolecular arrangements and conformations with all of the different

positions and orientations relative to the underlying surface. Therefore, many studies apply simplifications at this juncture. For example, they perform Monte Carlo simulations on predefined monomer adsorption grids^{19–21} or employ machine-learning on coarse-grained models assembled from single-molecule adsorption data.^{22,23}

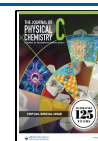
However, since a few decades, nondeterministic global optimization techniques^{24–29} have been developed and applied to such vast search spaces, with considerable success. Tools like evolutionary algorithms (EA) are well established in chemistry, for example, for global cluster structure optimization in vacuo,³⁰ in solvents^{31,32} and on surfaces,^{33,34} and also for different aims like abstract point charges for catalysis by optimized external electric fields.^{35,36}

EAs have also been applied to simplified models of molecular interaction on surfaces, for example, to study complex, charged molecules under electrochemical conditions, by system-specific, simple force fields,³⁷ or to optimize graph representations for NO on Pt₂Sn(111) and for propyne on a PdIn(021) step surface.³⁸ However, as we^{33,34} and others³⁹ have shown, it is also possible and useful to apply EA methods to such systems

Received: August 9, 2021

Revised: November 5, 2021

Published: November 18, 2021



directly, without strong a priori model assumptions on intermolecular interactions.

Here we are presenting results of such an approach to ethyl pyruvate (EP) on the Pt(111) surface. This is one family of the broader class of α -ketoesters on transition-metal surfaces, which was extensively investigated in previous studies, employing rigorous surface-science approaches.^{40–48} α -Ketoesters belong to the most important prochiral precursors for enantiopure lactates, which are produced in a heterogeneously catalyzed way over chirally modified transition-metal surfaces.⁴⁹ Several groups reported atomistic-level studies on the surface chemistry of the simplest α -ketoesters methyl pyruvate or ethyl pyruvate, either over pristine or chirally modified Pd(111)^{40–42} and Pt(111)^{43,46,47} metal surfaces. On pristine Pd(111),⁴⁰ methyl pyruvate was proposed to undergo keto-enol tautomerization on the carbonyl group to the enol form of the adsorbate. In the study from the same group, the enol isomer of methyl pyruvate was also discussed to be the active species in 1:1 chiral complexes between the chiral modifier (1-naphthyl)ethylamine (NEA) and methyl pyruvate.⁴¹ In contrast to these adsorbate structures derived for Pd(111), McBreen et al.⁴⁶ proposed the formation of enediolate species formed from methyl pyruvate on the pristine Pt(111) surface. In this adsorption configuration, both carbonyl groups directly interact with two underlying Pt atoms. A more recent study from the same group⁴³ provided indications that the enol form of methyl pyruvate can be formed on Pt(111); however, only at elevated temperatures. Adsorption of ethyl pyruvate on Pt(111) was reported by Bürgi et al.,⁴⁷ who suggested a tilted adsorption configuration, binding via the O-atom lone pair of the ketone group in the full coverage range under low-temperature conditions (150 K). It was also concluded that the alternative adsorption configuration (via π - or di- σ -bonding) is rather unlikely. In contrast, a further report on EP adsorption on Pt(111) proposed two coexisting adsorption configurations, which were identified in the presence of hydrogen by X-ray absorption near-edge spectroscopy (XANES).⁴⁴ Along with the already proposed configuration bonded to Pt via the O-atom lone pair of the ketone group, coexisting π -bonded ethyl pyruvate was identified in this study. Additionally, the authors suggested that EP bonded via the O-atom lone pair serves as a precursor state to the final π -bonded species that are relevant for building the transition state complex during hydrogenation.⁴⁴ In our own recent studies on adsorption of EP on Pt(111) performed with a combination of infrared reflection-absorption spectroscopy (IRAS) and scanning tunneling microscopy (STM) in the low-temperature regime,⁵⁰ we were able to safely exclude the formation of the enol and enediolate species proposed in the earlier studies for methyl pyruvate on Pt(111).⁴⁶

In the temperature range close to 300 K, several reports suggest possible polymerization of α -ketoesters.^{45,48} Thus, in the absence of coadsorbed hydrogen, methyl pyruvate was found to polymerize on Pt(111) at 300 K, yielding polymer chains, partly dendritic, and of average length equivalent to ~ 9 monomer units, which results in irreversible deactivation of the Pt catalyst.⁴⁵ The observed strongly tilted C=O bond suggests that the polymer is bound to the surface predominantly via the oxygen lone pairs. Based on a combination of near-edge X-ray absorption fine structure (NEXAFS), STM, and temperature-programmed reaction (TPR) spectroscopy, the authors suggested that polymerization occurs by hydrogen elimination from the monomer followed by an aldol condensation involving the elimination of methanol. Additionally, coadsorbed hydrogen

was shown to completely suppress this process, as only monomer units were found by STM under these conditions.^{45,48}

Given this context of other works on similar systems and the initially sketched considerations regarding intermolecular interactions on surfaces, EP was chosen in this study for two major reasons. From the practical perspective, EP is an important prochiral precursor for heterogeneously catalyzed production of the enantiopure compound ethyl lactate, which can be formed with high enantioselective excess⁴⁹ on transition metals functionalized with chiral modifiers. To understand this type of reaction at the atomistic level, it is crucial to address the mutual intermolecular interactions of ethyl pyruvate molecules on metal surfaces. From the fundamental point of view, many-body intermolecular interactions of adsorbates on metals are highly interesting, as they play an important role in affecting the energy barriers for a large range of surface-mediated processes, such as diffusion, adsorption, bond activation, chemical transformations in heterogeneously catalyzed reactions. To investigate these types of phenomena, it is crucial to identify the factors determining the interaction strength and the ordering of molecular adsorbates on surfaces. Ethyl pyruvate combines a number of the most relevant structural features in governing intermolecular interactions, such as the presence of two nonequivalent carbonyl groups, one of them being an ester group and each of them being capable of forming hydrogen bonds with the neighboring adsorbates, a less symmetric charge distribution than methyl pyruvate, and the presence of spatially separated dipole and quadrupole moments across the molecule, which can potentially contribute to intermolecular interactions. Particularly this latter feature was already recognized to play an important role in intermolecular interactions of various molecules in the gas phase and in bulk phases^{51,52} but was not broadly addressed in studies on molecular species adsorbed on surfaces so far. Last but not least, EP combines rigid molecular parts (e.g., the COO ester group) with floppy degrees of freedom (e.g., the C–C bond between the two carbonyl C-atoms), enabling an interesting interplay between intramolecular distortions and intermolecular interactions. The combination of these structural and electronic parameters is highly interesting, and our comparisons of experiment and theory make it possible to test them, deducing the factors playing the most important roles in the ordering of these molecular species on metal surfaces.

In a previous report on EP@Pt(111),⁵⁰ we focused on the experimental perspective and on infrared (IR) spectra. In the present contribution, we focus on theoretical modeling of EP molecules on Pt(111) and its relations to experimental STM images.

These experimental STM images show no tendency of EP molecules to form regular superstructures at submonolayer coverages. However, the EP arrangement is also not completely random. Instead, oligomers of two, three, or four EP molecules are found, irregularly scattered over the Pt(111) surface, with interoligomer distances being much larger than the intraoligomer ones and with a few typical intraoligomer EP arrangements.

This strong disorder with some interspersed remnants of order does not seem to lend itself to any obvious explanations. Nevertheless, with global structure optimization techniques applied to the system EP@Pt(111), we can theoretically reproduce these experimental findings at least qualitatively, and we can rationalize this behavior with simple explanations based on our calculations.

METHODS

Theoretical Approaches. Global Structure Optimization.

To arrive at low-energy structures of $(\text{EP})_n@Pt(111)$, we have used global structure optimization by evolutionary algorithms, as implemented in the OGOLEM program,^{53–55} which contains the global optimization expertise accumulated in the Hartke group since 1992. OGOLEM was originally designed for clusters in vacuo but was later extended to clusters in liquids³¹ and recently to clusters on surfaces.^{33,34} All EA techniques, including crossover and mutation operators, are the same as used in those previous on-surface applications.^{33,34}

The typical system behavior during global optimization is also very similar. The optimizations start from randomly generated, compact but noncolliding clusters of a prescribed number of EP molecules directly above the surface. To model this surface, a slab of six Pt layers, prearranged as a (111) single-crystal surface, is supplied and remains rigid during all global and local optimization steps. In the Supporting Information, we supply evidence that this number of layers can be considered converged and that the assumption of a fully rigid Pt(111) surface is reasonable. EP molecules are input as gas-phase trans or cis minima (with respect to the carbon–carbon bond between the two carbonyl groups), but during the global optimization, the internal structures of all EP molecules are free to change completely during the local optimizations that follow each successful global optimization step. In particular, no adsorption locations or conformations are prescribed at any point, nor any EP–EP distances or relative orientations. Nevertheless, a characteristically structured submonolayer of adsorbed EP molecules quickly forms in every case, with all EP molecules in direct contact with the Pt(111) surface. If the EP number density is too high for the given surface area, one or several EP molecules remain without surface contact, van-der-Waals bound to other surface-attached EP molecules. We have discarded these cases as likely not relevant for the experimental situation. This finding also indicates already that tight EP packings are not easy to achieve.

As usual in nondeterministic global search, there is no strict “convergence” criterion. To ensure arriving at sufficiently reproducible, low-energy results, we have done repeated EA runs for each number n of the $(\text{EP})_n@Pt(111)$ system ($n = 1, 2, \dots, 12$), with a number of global optimization steps in each run that is large enough to have proceeded beyond the typical, initial, exponential fall-off in best-so-far energies. For the larger cases $n \geq 8$, these were 20 000–60 000 global steps in each EA run (corresponding to at least the same number of local optimizations). The final structures from these runs were not exactly the same but invariably shared the same characteristics (reported below) and had total energies within 0.7% of each other. For the smaller cases like $n = 1, 2, 3$, a total of 1 000 000 steps has been used in each run.

Note that we have no periodicity in our calculations, not even along the surface-parallel xy -plane. Instead, our surface slabs were large enough (between $40 \text{ \AA} \times 40 \text{ \AA}$ and $60 \text{ \AA} \times 60 \text{ \AA}$ in xy) to accommodate the chosen number n of EP molecules, plus sufficient empty space to the slab borders, to avoid artifacts there. As clearly shown in our previous study of triazatriangulene (TATA) on Au(111),³⁴ adsorbed molecules with a tendency toward regular superstructures will indeed form ordered 2D-structures easily and reproducibly in such a setting. Hence, missing order in our simulations cannot be ascribed to missing xy -periodicity.

Intermolecular Interactions. DFT is the standard computational approach for molecules on (metal) surfaces. Basic difficulties, however, are well known. Treating clusters of several surface-adsorbed molecules in this manner and in quasi-isolation of one cluster from the other becomes computationally challenging or even impossible since this implies big periodic supercells in 2D or, in conjunction with the requirement to include several surface layers, big periodic supercells in 3D. Hence, with such an approach, it is impossible to treat systems of several molecules on a surface, even with supercomputer resources.⁵⁶ Furthermore, while DFT overcomes some of the fundamental deficiencies of HF in the description of solids, organic–inorganic interfaces pose a long list of further challenges,⁵⁷ and additionally, the strong correlation remains an unsolved problem for DFT in surface-science settings,⁵⁸ irrespective of the functional chosen.

Stepping down to lower levels of theory, modern semiempirical methods are an attractive alternative, in particular, Grimme’s GFN-xTB⁵⁹ that offers high-quality parameters for the whole relevant part of the periodic table ($Z \leq 86$). Sadly, for metallic surfaces, the self-consistent charge cycles in these methods fail to converge. This does work, however, for the force-field cousin of these methods, GFN-FF.⁶⁰ While organic molecules on transition-metal surfaces were not the intended design aim of GFN-FF, transition-metal complexes with organic ligands were contained in the GFN-FF training and validation sets, with good results. For example, GFN-FF-optimized structures of huge metal–organic framework compounds of a few thousand atoms, containing many Pd-, V-, Fe-, or Co-atoms, show heavy-atom root-mean-square deviations (RMSD) of only 0.43–1.22 Å compared to the experiment.⁶⁰ For the TMG145 benchmark set of transition-metal complexes, mean absolute deviations (MAD) of only 9.7 pm and 8.4° were reported,⁶⁰ for bond distances and bond angles, respectively, relative to high-end DFT calculations and essentially on par with semiempirical GFN2-xTB results. For supramolecular noncovalent interaction energies in the S30L benchmark, GFN-FF achieved a MAD of 4.15 kcal/mol compared to DLPNO-CCSD(T)/CBS reference data, “outperforming most of the semiempirical methods and on par with some dispersion-corrected DFT methods”.⁶⁰ The results reported below indicate reasonable performance of GFN-FF for EP@Pt(111) at least at a qualitative level. Of course, the strength of this choice is that it allows us to globally optimize $(\text{EP})_n@Pt(111)$ for nontrivial values of n and with several 10 000 global and local optimization steps at the GFN-FF level, without any simplifying assumptions and within a few wall-clock days on high-end desktop workstations with moderate parallelization of a few dozen threads.

Infrared Spectra. Infrared (IR) spectra were calculated from MD trajectories of EP oligomers on Pt(111) at the GFN-FF level, followed by Fourier transformation of the dipole moment autocorrelation.^{61–63} For this purpose, we employed a version of Grimme’s xtb program⁶⁴ locally modified to write out the total dipole moment vector as a function of time during MD runs at the GFN-FF level. In contrast to the standard, static approach of diagonalizing a mass-weighted Hessian matrix (normal-mode analysis), this time-dependent IR approach avoids approximating vibrations as uncoupled and purely harmonic, and in contrast to simulated single-molecule gas-phase IR spectra, it directly probes EP vibrations in their relevant environment, i.e., adsorbed to the Pt(111) surface in several different intramolecular structures strongly deviating from the gas phase and in direct neighborhood to several other EP molecules.

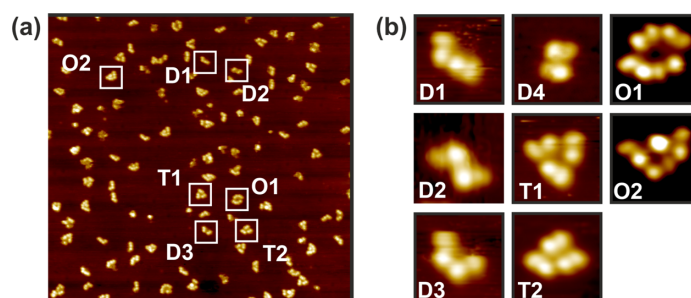


Figure 1. (a) STM image of EP adsorbed on pristine Pt(111) (exposure at 135 K, acquisition temperature 118 K, 611 mV, 0.267 nA, $44.8 \times 42.5 \text{ nm}^2$). (b) Close-up images of different oligomer species: dimers D1, D2, D3, and D4, trimers T1 and T2, and tetramers O1 and O2. Note that the dimer D4 was observed only on the H-covered Pt(111) surface. Reproduced with permission from ref 50.

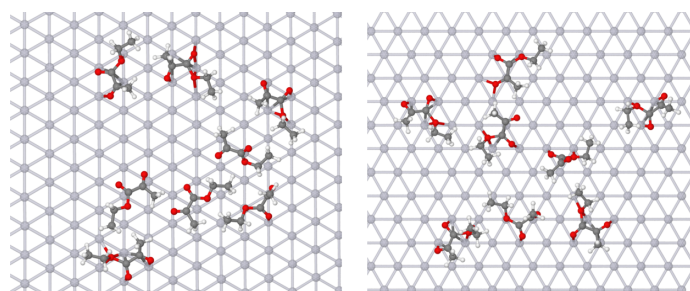


Figure 2. Two typical low-energy structures of eight ethyl pyruvate molecules on Pt(111), shown from above, with the Pt(111) surface in the picture plane. The top-layer Pt-atoms are indicated in transparent-gray.

To extract molecular vibrations corresponding to given IR peaks, we employed a filtering technique similar to the one of ref 65. The full set of $(EP)_n$ nuclear coordinates as a function of time was Fourier-transformed to frequency space, the desired, narrow frequency interval of one IR spectral peak (taken from visual inspection of the IR spectrum) was filtered out with a narrow, Gaussian-shaped band-pass function, and Fourier-transformed back to coordinate space, resulting in a trajectory in which only the atoms involved in this vibrational mode move significantly. This technique and our implementation of it were verified by extracting IR-peak-specific motions for well-known test molecules like water. An artifact that is hard to avoid arises from terminal methyl groups that start and stop to rotate around their central, C-bonded axis in a seemingly random manner in typical MD trajectories. These terminal methyl groups tend to appear with H-atoms collapsed upon their C-atoms in the band-pass-filtered trajectories. Fortunately, however, this does not affect the IR spectra themselves but only the peak-dependent motion extraction, and within that only the appearance of the terminal methyl groups in the filtered trajectories. In fact, these methyl group rotations are of no interest for the present study of EP on Pt(111).

To avoid artifacts from special initial conditions and limited MD times, we have averaged IR spectra over at least 10 trajectories, with initial atom velocities randomly sampled from a room-temperature distribution with pseudorandomized random seeds.

Unless noted otherwise, figures of molecules in vacuo or on surfaces were generated with Jmol.⁶⁶

Experimental Procedures. Experimental procedures were already described in ref 50; for completeness, we repeat relevant parts here briefly.

All experiments were performed in two independent ultra-high vacuum (UHV) apparatuses, UHV-infrared reflection/absorption spectroscopy (IRAS)/molecular beam and UHV-STM, each equipped with a dedicated preparation chamber. After preparation, the samples were transferred in situ into the main part of each apparatus.

Sample Preparation. The Pt(111) single crystal (MaTeck GmbH) was cleaned prior to use in a dedicated preparation chamber (base pressure better than 2×10^{-10} mbar) by repeated cycles of Ar^+ ion bombardment at room temperature, followed by annealing at 1200 K and subsequent oxidation in 1×10^{-7} mbar O_2 at 650–750 K, to remove residual carbon. The last step contains a rapid flash of the sample to 1000 K. Shortly before each experiment the sample was flashed to 600–800 K before cooling to the required temperature to remove CO adsorbates. The long-range order and cleanliness of the Pt(111) single-crystal were checked by low-energy electron diffraction (LEED), Auger electron spectroscopy (AES), and additionally by IRAS of adsorbed CO to probe the abundance of adsorption sites.

Ethyl pyruvate (Sigma-Aldrich, purity >97%) was purified prior to each experiment by repeated freeze–pump–thaw cycles.

STM Experiments. The STM measurements were carried out in a UHV (base pressure better than 1×10^{-10} mbar) apparatus by employing a variable temperature (90–300 K) Aarhus 150 SPM (SPECS). All measurements were carried out in a constant current mode, and the bias voltage UT was applied to the sample. The etched W-Tip was commercially produced by SPECS and in situ sharpened by repeated cycles of 1.25 keV Ar^+ -bombardment with 5×10^{-6} mbar back pressure for 5 min. The sharpness of the W-Tip was validated on the pristine Pt(111) surface. The quality of the sample was additionally verified by

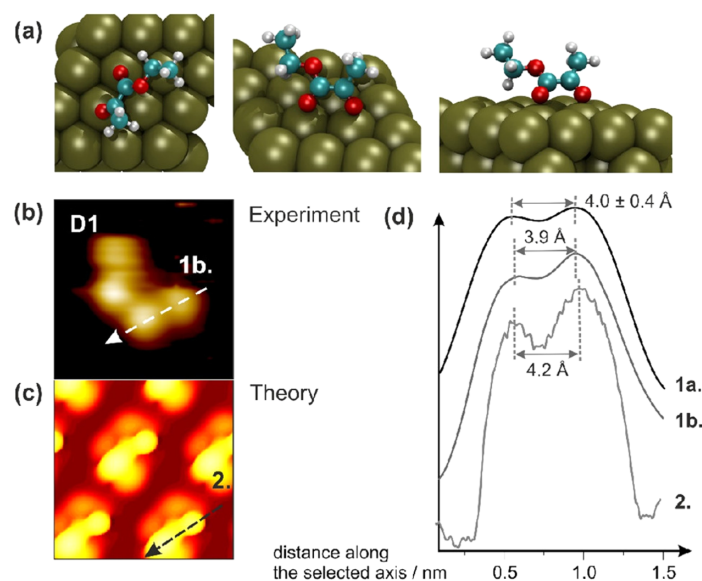


Figure 3. (a) Local minimum-energy geometry of an EP monomer at the DFT level, from 3 different viewpoints. (b) Experimentally measured and (c) theoretically simulated STM images. (d) STM line profiles along the vectors indicated in (b) and (c): (1a) is an average of 14 line profiles of EP molecules in dimers as shown in (b); (1b) was measured for a single EP monomer; (2) is derived from the theoretically simulated STM image shown in (c). Reproduced with permission from ref 50.

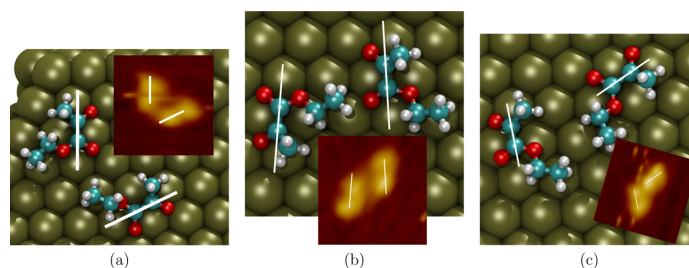


Figure 4. Comparisons of experimental EP-dimer structures (STM pictures in the insets, cf. Figure 1) with calculated EP dimers from global optimization. (a) dimer D3 and the 2nd best calculated dimer, (b) dimer D2 and the 3rd best calculated dimer, (c) dimer D1 and the 4th best calculated dimer. White lines are drawn along the same molecular axes as in Figure 3.

acquiring STM images prior to the deposition at 293 K. EP was dosed through an individual gas doser onto the Pt(111) surface, kept at the desired deposition temperature, and then transferred to the STM chamber for measurements.

RESULTS AND DISCUSSION

In a previous study employing a similar global structure optimization approach,³⁴ we could computationally confirm the repeated experimental finding that TATA molecules on

Table 1. Comparison of Theoretical and Experimental Distances and Angles^a

| dimer | exp. dist. (Å) | theor. dist. (Å) | exp. angle (deg) | theor. angle (deg) |
|-------|----------------|------------------|------------------|--------------------|
| D3 | 7.1 ± 0.2 | 7.24 | 181 ± 2 | 167.19 |
| D2 | 8.2 ± 1.1 | 7.59 | 61 ± 6 | 59.22 |
| D1 | 7.6 ± 0.4 | 7.92 | 106 ± 4 | 147.92 |

^aThe experimental values are an average of 5 exemplary individuals from the STM images.

Au(111) form closely spaced, regular superstructures with fixed relation to the underlying Au top layer.

In stark contrast, a quick look at any STM image of EP molecules on Pt(111) (cf. “Disorder” section) reveals several qualitative but robust observations that are very different: EP molecules neither form regular superstructures on Pt(111) nor do they tend toward close packing, and their positions and orientations do not seem to be related to the Pt atom grid. However, there appears to be a tendency to form dimers, trimers, and tetramers, with several specific versions of each, and the interoligomer distances are much larger than the intraoligomer ones.

With our global structure optimization approach, we find exactly the same qualitative tendencies. Note that we have not biased the global search in any way toward this result; instead, we have used the same global optimization strategy as in ref 34, where it produced regular, closely spaced superstructures. In our optimized EP oligomers on Pt(111), we can identify dimer, trimer, and tetramer arrangements very similar to those seen experimentally by STM.

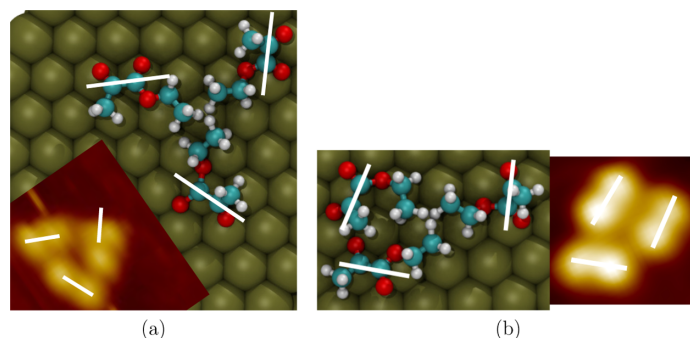


Figure 5. Comparisons of experimental EP trimer structures (STM pictures in the insets, cf. Figure 1) with calculated EP trimers from global optimization. (a) trimer T1 and the best calculated trimer, (b) trimer T2 and the 2nd best calculated trimer.

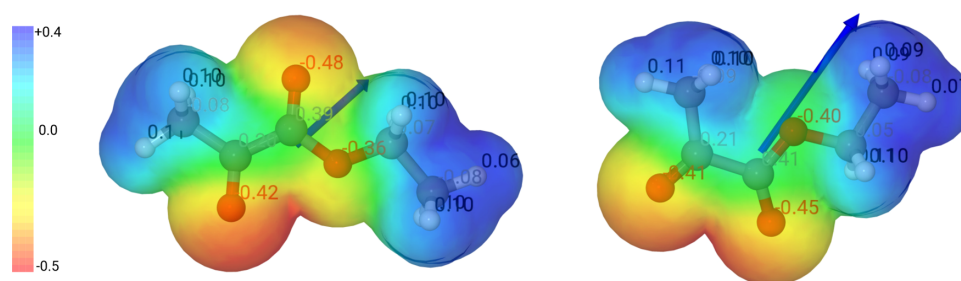


Figure 6. Trans and cis minimum-energy structures of ethyl pyruvate in vacuo, with the molecular electrostatic potential color-coded from positive (blue) to negative (red) on a solvent-accessible molecular surface. Additionally, atomic partial charges are shown as atomic labels, and the molecular dipole as a vector originating from the center of charges. All heavy atoms and the dipole moment vectors are in the drawing plane.

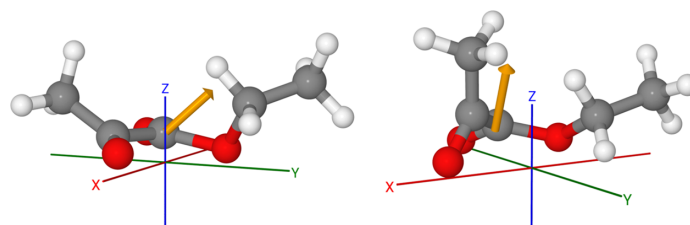


Figure 7. Two typical examples of ethyl pyruvate molecules adsorbed on Pt(111), taken from global optimizations with 8 EP molecules. For clarity, the Pt surface is not shown; it is parallel to the xy-plane (x-axis: red, y-axis: green, z-axis: blue). Molecular dipole moments are shown as orange vectors.

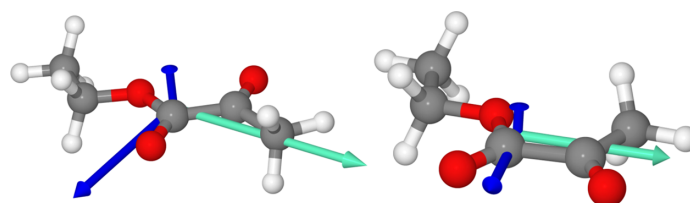


Figure 8. Eigenvalue-scaled quadrupole eigenvectors of cis and trans pyruvate molecules in the gas phase. Blue and green vectors have different eigenvalue signs. For clarity, the cis vectors have been scaled up by 75%.

Furthermore, by examining individual adsorbed EP molecule structures as well as low-order multipoles (molecular charge, dipole, quadrupole) derived from atomic partial charges, we arrive at tentative explanations for all of the EP arrangement observations just mentioned.

Finally, with IR spectra extracted from GFN-FF MD trajectories of multiple EP molecules on Pt(111) and by

examining the vibrational motions corresponding to IR peaks of interest, we provide an alternative interpretation of the characteristic IR spectral features of this system, reported in ref 50.

In the following, we present and discuss all of these findings and explanations in some detail.

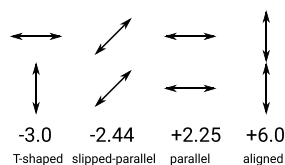


Figure 9. Favorable and unfavorable quadrupole–quadrupole interactions (adapted from ref 51).

Adsorption Conformations. Rotating a single EP molecule in vacuo around the C–C bond between the two carbonyl C-atoms only has a small energy barrier of about 10.5 kJ/mol, and the trans and cis minima differ by only 5.25 kJ/mol (as an order-of-magnitude estimate, both at B97-D3/cc-pVDZ, using a relaxed scan in Gaussian09;⁵⁷ at the GFN-FF level, the minima differ by 8.9 kJ/mol and the barrier is 12.7 kJ/mol). For comparison, one single hydrogen bond between two water molecules has a greater bonding energy of about 21 kJ/mol. In all of our optimized adsorption structures, there are several bond-like Pt–C and Pt–O interactions per EP molecule. At the GFN-FF level, we used for global adsorption structure optimizations, the adsorption energy of one EP molecule that is at least 16 kJ/mol (in the most unfavorable adsorption conformation); more typical values are around 300 kJ/mol (with sometimes two but in most cases three bond-like Pt–O interactions per EP molecule).

In other words, even in comparatively unfavorable adsorption geometries, the interaction energy between the Pt surface and an EP molecule is much larger than the energy needed to twist the EP molecule internally. Therefore, it is not surprising that EP molecules do not adsorb in their planar trans or cis conformations (gas-phase minimum-energy structures) but in strongly distorted ones. Additionally, it appears reasonable that at temperatures significantly above zero Kelvin (100–150 K), there is not one single distorted adsorption structure for EP but many different ones. This is not only consistent with all experimental STM pictures (cf. the following subsections for a few examples) but also with our theoretical global optimizations.

Disorder (and Some Order). The spatial distribution of EP molecules on Pt(111) was investigated experimentally by STM on a well-defined Pt(111) model surface under UHV conditions. Figure 1 shows an STM image displaying typical different surface assemblies formed at cryogenic temperatures on the pristine Pt(111) surface.⁵⁰ Note that, on the one hand, no self-ordering of EP was observed on Pt(111) in a broad range of temperature conditions as well as in the presence of coadsorbed hydrogen. On the other hand, nearly all adsorbed EP molecules are agglomerated in oligomers comprising two, three, or four individual molecules. Close-up images of all types of observed

oligomers measured with the submolecular resolution are shown in Figure 1b. Specifically, four types of dimers (D1–D4), two types of trimers (T1, T2), and two types of tetramers (O1, O2) can be identified. Note that dimer D4 was not observed on pristine Pt(111); it evolves only on an H-precovered surface.⁵⁰

These experimental observations are qualitatively very similar to what we find by our global structure optimizations. Figure 2 shows two typical lowest-energy final structures from our global optimization runs (i.e., possible candidates for global minima), here for a total of eight EP molecules. Again, there is no propensity toward forming regular superstructures, in stark contrast to our findings for TATA molecules on Au(111),³⁴ where we used the same global optimization strategy. There also is a clear tendency to form short-distance, few-membered oligomers with bigger distances between them. Further details are successively discussed in the following subsections.

Oligomer Structures. Already in our previous study,⁵⁰ the intensity distribution across an individual EP molecule measured experimentally by STM was compared to STM-image simulations with the Tersoff–Hamann approach, based on a locally optimized EP structure on Pt(111), employing the PBE functional and projector-augmented-wave pseudopotentials. For further technical details, we refer to ref 50 but reproduce the main result here for completeness. Figure 3a shows the employed EP monomer structure from different perspectives, Figure 3c shows the simulated (2D-periodic) STM image, and Figure 3b shows an experimental EP-dimer STM image. Figure 3d compares two experimental STM line profiles with the simulated one, with these line profiles indicated as arrows in panels (b) and (c).

The black arrow in the simulated image of Figure 3c is drawn along the main axis of the molecule, containing the two carbon atoms involved in the two carbonyl groups. Since the experimental and simulated images show excellent agreement in their intensity distributions and line profiles, it may be concluded that the main axis is drawn in an identical way along the individual protrusion in the experimental STM image (white arrow in Figure 3b) also connects the same two carbonyl carbon atoms.

Based on the above analysis, and assuming that the electronic structure of EP molecules in oligomers is similar to that in the monomer, globally optimized clusters of EP and the STM images can be compared directly, which we do for representative examples in the remainder of this subsection.

For the dimer structures, three of the four best candidates from our global optimization runs can be matched directly with the typical three dimers found in the STM images, cf. Figure 4.

Table 1 shows a quantitative comparison of the angles and distances in these computational minimum-energy structures and the experimental STM images.

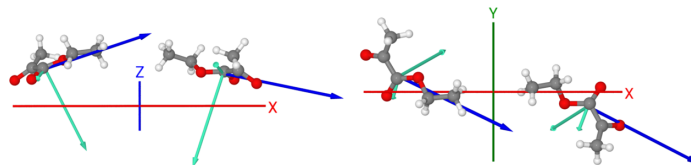


Figure 10. Eigenvalue-scaled quadrupole eigenvectors of pyruvate molecules adsorbed on Pt(111) for the best isolated EP dimer in our global optimizations. For clarity, the Pt surface is not shown; it is parallel to the *xy*-plane (*x*-axis: red, *y*-axis: green, *z*-axis: blue). Blue and green quadrupole vectors have different eigenvalue signs. Left: side view along the *y*-axis (vacuum top, surface bottom); right: top view along the *z*-axis (from the vacuum onto the surface).

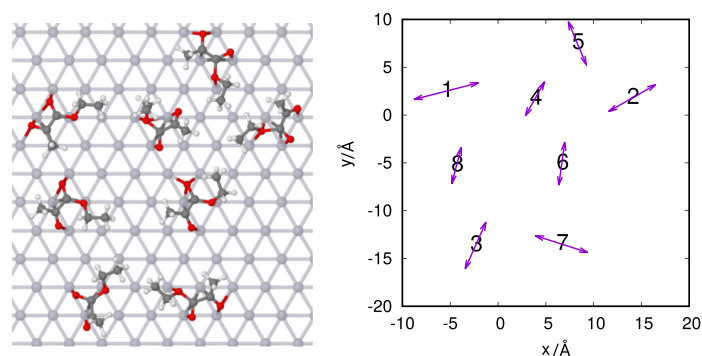


Figure 11. For the low-energy structure of 8 ethyl pyruvate molecules shown in the left panel, the right panel displays the in-plane quadrupole eigenvector of the largest eigenvalue, scaled by this eigenvalue and centered at the molecular partial-charge center, indicated by the (randomly assigned) molecule number. T-shaped configurations are visible for the pairs 2–5 and 3–7, slipped-parallel configurations for the pairs 3–8 and 4–6.

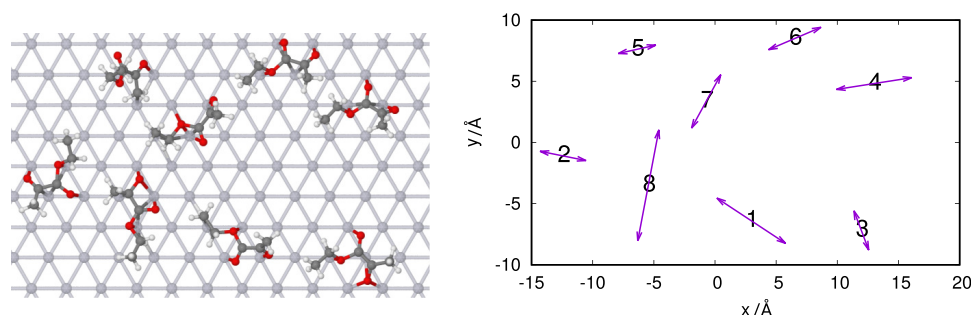


Figure 12. Another low-energy structure of 8 ethyl pyruvate molecules and its quadrupole pattern, displayed as in Figure 11. T-shaped configurations are formed by the pairs 1–8 and 2–8, slipped-parallel configurations by the pairs 4–6 and 7–8. The quadrupole eigenvectors of molecule 5 are less well aligned with the Pt surface.

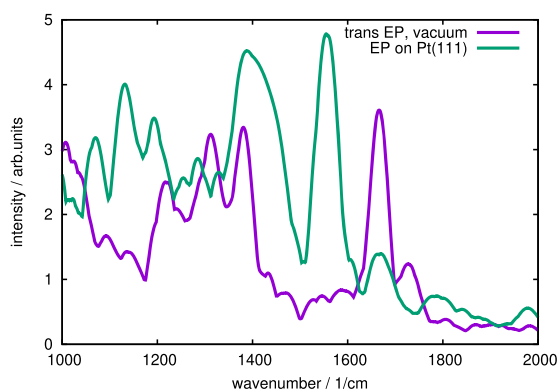


Figure 13. Simulated IR spectra in the wavenumber region of interest, comparing trans ethyl pyruvate in vacuo with the EP octamer of Figure 12.

Similar direct comparisons can be made for the trimers, cf. Figure 5, again resulting in a very good qualitative agreement in one case but some visible deviations in the other, where relative positions and angles of two of the three EP molecules are quite good, but the third one is in a shifted position.

Molecular Charge. At the GFN-FF level, EP molecules physisorbed onto Pt(111) only via van der Waals interaction are charge-neutral. If actually bound to the surface via O-atoms (as

is the case for all structures shown below), however, EP molecules exhibit a net charge ranging from -0.8 to -1.2 . Considering electronegativity values, this makes sense. On the Pauling scale, we have 3.44 for O-atoms, 2.55 for C-atoms, 2.20 for H-atoms, and 2.28 for Pt-atoms. On the Allen scale, we have 3.61 for O-atoms, 2.54 for C-atoms, 2.30 for H-atoms, and 1.72 for Pt-atoms. Hence, in any case, partial charges on O-atoms should be negative, compared to Pt and the alkyl groups.

In the EP@Pt(111) DFT calculations performed for our previous paper,⁵⁰ we found an EP net charge of $+0.95$ using the Mulliken scheme and -0.17 using atoms-in-molecules (AIM) charges for the very same DFT calculation, although a GFN-FF single-point calculation of this locally optimized DFT geometry produces (again) a total EP charge of -1.04 . These discrepancies also translate into strongly different dipole moment magnitudes, ranging from 1.79 Debye for GFN-FF to 2.87 Debye for DFT/Mulliken and 13.9 Debye for DFT/AIM. This illustrates that getting atomic partial charges right in first-principles calculations for a molecule on a metal surface is nontrivial⁵⁷ and that (as expected) different partial-charge prescriptions have a big influence on the outcome.

The directional properties of vectors and tensors, however, are affected much less. For this same DFT-optimized EP monomer geometry on Pt(111) (shown in Figure 3a), all molecular dipole moment directions are within 7 – 18° of each other, for GFN-FF, DFT/Mulliken, and DFT/AIM. Quadrupole moment eigenvector directions differ between 10 and 30° .

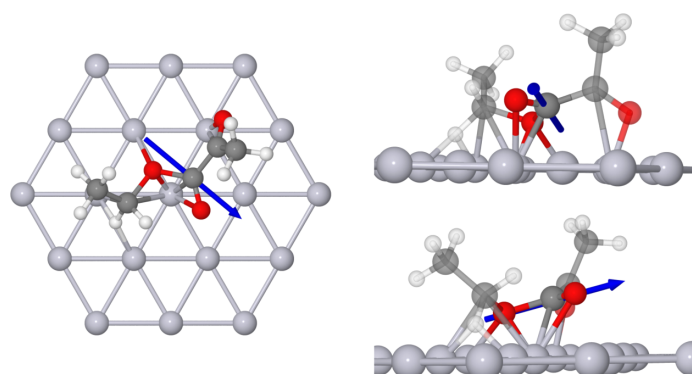


Figure 14. Three different views of the same Pt-adsorbed ethyl pyruvate molecule, the one with the largest contribution to the 1560 cm^{-1} band in the ethyl pyruvate octamer IR spectrum shown in Figure 13. For clarity, only a small section of the topmost Pt layer is shown. The blue arrow indicates the displacement direction of the central C atom in the ester group, which is by far the largest component of this collective vibration. Sticks between the ethyl pyruvate molecule and Pt atoms indicate small distances, not bonds.

Hence, it can be expected that the directional issues discussed below, obtained at the GFN-FF level, are qualitatively reliable.

Dipole Moments. In line with our global structure optimization calculations, we report dipole and quadrupole moments for EP molecules on Pt(111) at the GFN-FF level. To provide a gauge for the reliability of these results, at this same level, a single water molecule in vacuo has a dipole moment of 1.72 Debye, which is in fairly good agreement with the accepted literature value of 1.8546 Debye.⁶⁸ In clusters and condensed phases, the dipole moment of water is enhanced up to around 2.5 Debye due to polarization by the surrounding water molecules.^{69,70}

In the gas phase, EP has two planar minimum-energy structures, trans and cis with respect to the two carbonyl groups, twisted by 180° around the central carbon–carbon bond between the two carbonyl C-atoms. For symmetry reasons, the molecular dipole moment vectors also have to be in-plane, as shown in Figure 6.

The dipole moment values for trans and cis are 2.48 and 7.91 Debye, respectively. Although the EP molecule is substantially larger than the above-mentioned water molecule, the dipole moment of trans-EP is very similar to that of water, simply because the alternating alkyl-carbonyl-alkyl arrangement in the trans-EP molecule leads to compensation effects for the dipole. In cis-EP, the partial-charge distribution is less alternating and, in fact, similar to that in water, leading to a larger dipole moment because of the larger molecular size.

As mentioned above in the Adsorption Conformations section, EP molecules adsorb on the Pt surface in many differently distorted, nonplanar conformations. Interestingly, however, all of these different structures lead to similar changes in the molecular dipole moments, as depicted in Figure 7.

As is qualitatively obvious from Figure 7, the EP molecules tend to bind to the Pt surface via some or all of their oxygen atoms. In many cases, this leads to central C–C dihedral angles rotated by $45\text{--}135^\circ$. However, even for adsorption conformations with a nearly planar CO–COO core of the EP molecule, the somewhat bulky methyl and ethyl moieties need to be distorted away from the Pt surface. All of this results in negatively polarized O-atoms being closer to the Pt surface and positively polarized methyl/ethyl group being farther away. This translates into a dipole moment vector that is not in the (frequently ill-defined) molecular plane anymore but acquires a

significant component perpendicular to the Pt surface (perpendicular to the xy -plane).

The left panel of Figure 7 shows a case with an almost-planar, central CO–COO moiety. Here, collision avoidance between the methyl and ethyl groups and the Pt surface suffices to twist the dipole moment vector out of the (approximate) CO–COO plane (the xy -plane) into forming an angle of 54.6° with the z -axis. Since the methyl and ethyl groups cannot distort away from the Pt surface very far, a fairly small dipole moment of 2.8 Debye results, even smaller than for the gas-phase trans structure. The xy -plane component of it (along the Pt surface) is 2.4 Debye.

In the right panel of Figure 7, the almost 90° twist around the central C–C bond places the methyl group much farther away from the surface, leading to a somewhat stronger dipole moment of 3.4 Debye. Additionally, the dipole moment direction is closer to perpendicular to the Pt surface, with an angle of 24.3° to the z -axis. This leaves a residual dipole moment component in the xy -plane of only 1.74 Debye, even smaller than for the structure in the left panel.

Note that including the Pt surface in these calculations does not change these findings significantly since the amount of partial charge on every Pt atom is very small. Also, these findings shown here are representative of the many different EP adsorption conformations we have seen in our calculations. Upon adsorption, EP molecules develop dipole moment vectors with a significant component perpendicular to the Pt surface through intramolecular distortions alone. Dipole moments with a larger remaining component in the xy -plane (parallel to the Pt surface) are smaller, while larger dipole moments are closer to being perpendicular to the Pt surface, hence leaving a smaller xy -component.

All of this suggests that surface-parallel dipole moment components (in the xy -plane) possibly do not play a major role in the intermolecular ordering phenomena of EP molecules on the Pt surface. They could provide attractive interactions but presumably simply are too small in magnitude. Surface-perpendicular dipole moment components (along the z -axis) are larger but necessarily parallel to each other and of the same directionality (negatively polarized O-atoms down, positively polarized alkyl groups up), resulting in a repulsive dipole interaction between two neighboring EP molecules, in addition to repulsions from overall molecular charges.

Quadrupole Moments. In contrast to molecular charges and dipoles, EP quadrupoles can and do lead to attractive EP–EP interactions. Traceless quadrupole moments are shown here as their 3D eigenvectors, with eigenvector length scaled by the corresponding eigenvalue and color-coded by eigenvector sign. For cis- and trans-EP in vacuo, the quadrupole eigenvector orientations are determined by symmetry, with two of them in the molecular plane and the third one perpendicular to it, as shown in Figure 8. While alternating positively and negatively charged molecular regions partially cancel in the dipole moment, as argued above, they can and do directly contribute to the quadrupole moment. Hence, while dipole moments of water and EP are similar, the quadrupole eigenvalues of EP are factors of 10 and 20 larger than those of water, for cis and trans, respectively. The partial-charge alternation character and with it the quadrupole moment is larger in the trans geometry than in cis, as shown in Figure 8 (note the scaled-up vectors for cis), while for the same reason the dipole moment of cis is larger than that of trans, as noted above.

In adsorption structures of EP, the magnitude of the quadrupole eigenvalues remains the same, but we observe reorientations of the quadrupole eigenvectors, even more strongly determined by the Pt surface than for the dipole vectors. In all cases, we find one quadrupole eigenvector almost exactly perpendicular to the Pt surface and the other two parallel to it. As argued above, this effect can be understood qualitatively by the negatively polarized O-atoms being closer to the Pt surface and the positively polarized alkyl groups being farther away from it. As an overall qualitative result, EP molecules adsorbed on Pt(111) have small in-plane dipole components that are not very effective for inducing multi-EP ordering, but they exhibit large in-plane quadrupole moments that may have an influence on this ordering.

For easy reference, Figure 9 displays a few characteristic quadrupole–quadrupole configurations, with their relative favorable or unfavorable energy contributions, adapted from ref 51.

Such a quadrupole influence on EP molecule ordering can indeed be seen for EP molecules that are not too far away from each other (due to repulsion of their overall charges). As one example, Figure 10 shows quadrupole eigenvectors for the best isolated EP dimer from our global optimization runs. The two blue eigenvectors are in a favorable “slipped-parallel” arrangement.⁵¹ The long green eigenvectors (corresponding to big eigenvalues) are largely perpendicular to the Pt surface (which is in the *xy*-plane), and the short green eigenvectors are largely parallel to the Pt surface but correspond to small eigenvalues.

In surface-adsorbed oligomers of more EP molecules, alignment of the quadrupole eigenvectors parallel and perpendicular to the Pt surface tends to be close to perfect, and for a significant portion of close EP pairs, typical good quadrupole–quadrupole interactions can be found, either slipped-parallel (as above) or T-shaped. Figure 11 displays the first example with one of the best (EP)₈ structures from our global optimizations. In each of its EP molecules, one quadrupole eigenvector is very close to surface-perpendicular, with *z*-axis angles ranging from 10.9° to 0.4°. From the two in-plane quadrupole eigenvectors, we focus on the one for the larger eigenvalue; the other eigenvalue is smaller by a factor between 3.6 and 14.3. Two slipped-parallel and two T-shaped close-pair configurations can be discerned. Of similar significance is that the worst quadrupole–quadrupole interaction configurations (parallel and aligned)⁵¹ are completely avoided.

Figure 12 shows a second example, again one of the best (EP)₈ structures from our global optimizations. Here, the quadrupole eigenvectors of molecule 5 are less well aligned with the Pt surface, deviating by 36.4° from the surface normal. Most of the other EP molecules, however, do exhibit a significant degree of quadrupole–quadrupole ordering. The most unfavorable quadrupole interactions are again absent.

Figure S4 shows yet another example to further illustrate that these are not singular observations but rather the general behavior found in all of our global optimizations.

Note that the (EP)₈@Pt(111) structures shown in Figures 11, 12, and S4 differ by only 0.4% in their optimized energies. In fact, in our global optimizations with more than just a few EP molecules, we find a huge set of low-energy structures of similar energies. This may suggest that the energy landscape presumably is not a rugged funnel that, despite its ruggedness, can direct the system to a unique structure, significantly lower in energy than all others (as surmised in the folding of well-ordered proteins), but rather has a “Banyan tree” shape,⁷¹ in which barriers between low-energy minima are significantly larger than the very small energy differences between them.

Infrared Spectra. IR spectra were simulated as described in the “Methods: Infrared Spectra” section. Figure 13 shows a direct comparison between IR spectra generated for trans-IP in vacuo and for the (EP)₈@Pt(111) case of Figure 12.

In vacuo, the bands at 1666 and 1730 cm⁻¹ correspond to combinations of free ester carbonyl and keto carbonyl vibrations, while those between 1200 and 1400 cm⁻¹ exclusively involve vibrations of the methyl and ethyl groups. In the adsorbed situation, a new absorption band appears in the region 1530–1560 cm⁻¹ (depending on which (EP)₈ we use). This coincides with the same observation in the experiment,⁵⁰ where such an additional band was reported at 1530 cm⁻¹ and assigned to the ester carbonyl (not the keto one) via ¹³C-isotopic labeling. Fourier-filtering analysis of the MD trajectories used for IR spectra simulation, centered at this wavenumber value, reveals that this band corresponds to what can be called a Pt-bound ester carbonyl vibration. A more accurate description would be a central C-atom displacement in a Pt–O–C–O–Pt’ group (cf. Figure 14), resulting in an antisymmetric vibration of these two CO groups.

In our Pt-adsorbed (EP)₈ cases, not all EP molecules contribute to this vibration. One reason for this simply is that not all EP molecules are adsorbed to the underlying Pt-atoms in a way that forms such a Pt–O–C–O–Pt’ group, with the central C-atom having sufficient remaining freedom to oscillate significantly. Additionally, the metal-surface selection rule^{72,73} is operative, which we can enforce in our IR spectra simulation by Fourier-transforming only the *z*-component of the dipole moment vector (perpendicular to the metal surface); in other words, those CO bond directions need a significantly non-zero *z*-component to be able to contribute to the IR spectrum.

CONCLUSIONS

In summary, with unconstrained global structure optimization of EP clusters on Pt(111) at the GFN-FF level, we have assembled a consistent set of possible explanations for the key experimental observations of EP@Pt(111). The EP–Pt interaction is fairly strong, and intramolecular energy barriers between different EP conformations are quite small; this favors EP attachment to Pt surfaces in several different conformations, which in turn disfavors the formation of regular patterns. Additionally, each EP molecule on Pt may have a substantial

non-zero total charge (at least in the submonolayer conditions considered here); this is a possible explanation for large distances between most adsorbed EP molecules. Due to its molecular constitution, EP contains both rather rigid molecular parts (e.g., the ester group) and floppy degrees of freedom (e.g., the bond between the two carbonyl C-atoms), such that the intramolecular conformation changes upon adsorption are present but rather systematic. According to these systematics, EP dipoles are relatively small and tend to have a large component perpendicular to the surface in typical adsorption configurations, leading to another repulsion contribution. However, EP quadrupoles are rather large, and although they also tend to align to the surface normal, their tensorial nature leaves the other quadrupole components aligned parallel to the surface. In our global (EP)_n@Pt(111) optimizations, these surface-parallel quadrupole components avoid repulsive arrangements and favor attractive ones. Hence, quadrupole interactions may be responsible for the residual tendency to form aggregates of a few EP molecules, with small EP–EP distances and with a small set of intermolecular orientational preferences. Last but not least, while GFN-FF-based simulated IR spectra of these systems certainly cannot claim quantitative accuracy, they do offer an explanation for the additional ester carbonyl absorption band observed experimentally⁵⁰ for EP@Pt(111).

Overall, while regular surface adsorption patterns may be aesthetically more pleasing and easier to analyze, this study shows that there may also be ways to interpret and understand disordered adsorbate submonolayers. Of course, the first steps made here at a rather low level of theory should be confirmed by higher-level follow-up studies, but the many points of agreement between theory and experiment already are encouraging. In any case, the present work indicates further avenues to explore when choosing and designing adsorbed molecular assemblies for on-surface synthesis and heterogeneous catalysis.

■ ASSOCIATED CONTENT

SI Supporting Information

The Supporting Information is available free of charge at <https://pubs.acs.org/doi/10.1021/acs.jpcc.1c07058>.

Convergence with respect to the number of Pt layers; relaxation of Pt atoms; and further example of quadrupole interactions of EP@Pt(111) (PDF)

■ AUTHOR INFORMATION

Corresponding Author

Bernd Hartke – Institute for Physical Chemistry, Christian-Albrechts-University, 24098 Kiel, Germany; orcid.org/0000-0001-8480-0862; Email: hartke@pctc.uni-kiel.de

Authors

Christopher Witt – Institute for Physical Chemistry, Christian-Albrechts-University, 24098 Kiel, Germany

Marvin-Christopher Schmidt – Institute for Physical Chemistry, Christian-Albrechts-University, 24098 Kiel, Germany

Carsten Schröder – Institute for Physical Chemistry, Christian-Albrechts-University, 24098 Kiel, Germany

Swetlana Schaueremann – Institute for Physical Chemistry, Christian-Albrechts-University, 24098 Kiel, Germany; orcid.org/0000-0002-9390-2024

Complete contact information is available at:

<https://pubs.acs.org/10.1021/acs.jpcc.1c07058>

Notes

The authors declare no competing financial interest.

■ ACKNOWLEDGMENTS

B.H. thanks Dr. Johannes M. Dieterich for his continuing care for the OGOLEM program package and is grateful for funding by the Deutsche Forschungsgemeinschaft DFG via project Ha2498/16-2.

■ REFERENCES

- (1) Schlögl, R. Heterogeneous Catalysis. *Angew. Chem., Int. Ed.* **2015**, *54*, 3465–3520.
- (2) Clair, S.; de Oteyza, D. G. Controlling a Chemical Coupling Reaction on a Surface: Tools and Strategies for On-Surface Synthesis. *Chem. Rev.* **2019**, *119*, 4717–4776.
- (3) Wang, T.; Zhu, J. Confined on-surface organic synthesis: Strategies and mechanisms. *Surf. Sci. Rep.* **2019**, *74*, 97–140.
- (4) Fan, Q.; Martin-Jimenez, D.; Werner, S.; Ebeling, D.; Koehler, T.; Vollgraff, T.; Sundermeyer, J.; Hieringer, W.; Schirmeisen, A.; Gottfried, J. M. On-Surface Synthesis and Characterization of a Cycloarene: C₁₀₈ Graphene Ring. *J. Am. Chem. Soc.* **2020**, *142*, 894–899.
- (5) Laporte, S.; Finocchi, F.; Paulatto, L.; Blanchard, M.; Balan, E.; Guyot, F.; Saitta, A. M. Strong electric fields at a prototypical oxide/water interface probed by ab initio molecular dynamics: MgO(001). *Phys. Chem. Chem. Phys.* **2015**, *17*, 20382–20390.
- (6) Attia, S.; Schmidt, M.-C.; Schröder, C.; Pessier, P.; Schaueremann, S. Surface-Driven Keto-Enol Tautomerization: Atomistic Insights into Enol Formation and Stabilization Mechanisms. *Angew. Chem., Int. Ed.* **2018**, *57*, 16659–16664.
- (7) Schaueremann, S. Partial Hydrogenation of Unsaturated Carbonyl Compounds: Toward Ligand-Directed Heterogeneous Catalysis. *J. Phys. Chem. Lett.* **2018**, *9*, 5555–5566.
- (8) Schröder, C.; Schmidt, M. C.; Haugg, P. A.; Baumann, A.-K.; Smyczek, J.; Schaueremann, S. Understanding Ligand-Directed Heterogeneous Catalysis: When the Dynamically Changing Nature of the Ligand Layer Controls the Hydrogenation Selectivity. *Angew. Chem., Int. Ed.* **2021**, *60*, 16349–16354.
- (9) Goronzy, D. P.; Ebrahimi, M.; Rosei, F.; Arramel, Fang, Y.; de Feyter, S.; Tait, S. L.; Wang, C.; Beton, P. H.; Wee, A. T. S.; Weiss, P. S.; Perepichka, D. F. Supramolecular Assemblies on Surfaces: Nanopatterning, Functionality, and Reactivity. *ACS Nano* **2018**, *12*, 7445–7481.
- (10) Xing, L.; Peng, Z.; Li, W.; Wu, K. On Controllability and Applicability of Surface Molecular Self-Assemblies. *Acc. Chem. Res.* **2019**, *52*, 1048–1058.
- (11) Bouju, X.; Mattioli, C.; Franc, G.; Pujol, A.; Gourdon, A. Bicomponent Supramolecular Architectures at the Vacuum-Solid Interface. *Chem. Rev.* **2017**, *117*, 1407–1444.
- (12) Stadler, C.; Hansen, S.; Kröger, I.; Kumpf, C.; Umbach, E. Tuning intermolecular interaction in long-range-ordered submonolayer organic films. *Nat. Phys.* **2009**, *5*, 153–158.
- (13) Hohman, J. N.; Zhang, P.; Morin, E. I.; Han, P.; Kim, M.; Kurland, A. R.; McClanahan, P. D.; Balema, V. P.; Weiss, P. S. Self-Assembly of Carboranethiol Isomers on Au(111): Intermolecular Interactions Determined by Molecular Dipole Orientations. *ACS Nano* **2009**, *3*, 527–536.
- (14) Nath, K. G.; Ivasenko, O.; MacLeod, J. M.; Miwa, J. A.; Wuest, J. D.; Nanci, A.; Perepichka, D. F.; Rosei, F. Crystal Engineering in Two Dimensions: An Approach to Molecular Nanopatterning. *J. Phys. Chem. C* **2007**, *111*, 16996–17007.
- (15) Chen, B. W. J.; Xu, L.; Mavrikakis, M. Computational Methods in Heterogeneous Catalysis. *Chem. Rev.* **2021**, *121*, 1007–1048.
- (16) Morales-García, A.; Viñes, F.; Gomes, J. R. B.; Illas, F. Concepts, models, and methods in computational heterogeneous catalysis

illustrated through CO₂ conversion. *WIREs Comput. Mol. Sci.* **2021**, *11*, No. e1530.

(17) Grajciar, L.; Heard, C. J.; Bondarenko, A. A.; Polynski, M. V.; Meeprasert, J.; Pidko, E. A.; Nachtigall, P. Towards operando computational modeling in heterogeneous catalysis. *Chem. Soc. Rev.* **2018**, *47*, 8307–8348.

(18) Järvi, J.; Rinke, P.; Todorović, M. Detecting stable adsorbates of (1S)-camphor on Cu(111) with Bayesian optimization. *Beilstein J. Nanotechnol.* **2020**, *11*, 1577–1589.

(19) Ibenskas, A.; Šiménas, M.; Tornau, E. E. Numerical Engineering of Molecular Self-Assemblies in a Binary System of Trimesic and Benzenetribenzoic Acids. *J. Phys. Chem. C* **2016**, *120*, 6669–6680.

(20) Gdula, K.; Nieckarz, D. On-Surface Self-Assembly of Metal-Organic Architectures: Insights from Computer Simulations. *J. Phys. Chem. C* **2020**, *124*, 20066–20078.

(21) Fortuna, S.; Johnston, K. Influence of Molecule-Surface and Molecule-Molecule Interactions on Two-Dimensional Patterns Formed by Functionalized Aromatic Molecules. *J. Phys. Chem. C* **2018**, *122*, 14459–14466.

(22) Hörmann, L.; Jeindl, A.; Egger, A. T.; Scherbela, M.; Hofmann, O. T. SAMPLE: Surface structure search enabled by coarse graining and statistical learning. *Comput. Phys. Commun.* **2019**, *244*, 143–155.

(23) Jeindl, A.; Domke, J.; Hörmann, L.; Sojka, F.; Forker, R.; Fritz, T.; Hofmann, O. T. Nonintuitive surface self-assembly of functionalized molecules on Ag(111). *ACS Nano* **2021**, *15*, 6723–6734.

(24) Hartke, B. Structural transitions in clusters. *Angew. Chem., Int. Ed.* **2002**, *41*, 1468–1487.

(25) Hartke, B. Global optimization. *WIREs Comput. Mol. Sci.* **2011**, *1*, 879–887.

(26) Zhao, J.; Xie, R.-H. Genetic Algorithms for the Geometry Optimization of Atomic and Molecular Clusters. *J. Comput. Theor. Nanosci.* **2004**, *1*, 117–131.

(27) Jaeger, M.; Schaefer, R.; Johnston, R. L. First principles global optimization of metal clusters and nanoalloys. *Adv. Phys. X* **2018**, *3*, No. 1516514.

(28) Zhang, J.; Glezakou, V.-A. Global optimization of chemical cluster structures: Methods, applications, and challenges. *Int. J. Quantum Chem.* **2021**, *121*, No. e26553.

(29) Srivastava, R. Application of Optimization Algorithms in Clusters. *Front. Chem.* **2021**, *9*, No. 637286.

(30) Hartke, B. Global geometry optimization of clusters using genetic algorithms. *J. Phys. Chem. A* **1993**, *97*, 9973–9976.

(31) Li, Y.; Hartke, B. Assessing Solvation Effects on Chemical Reactions with Globally Optimized Solvent Clusters. *Chem. Phys. Chem.* **2013**, *14*, 2678–2686.

(32) Simm, G. N.; Tuertscher, P. L.; Reiher, M. Systematic microsolvation approach with a cluster-continuum scheme and conformational sampling. *J. Comput. Chem.* **2020**, *41*, 1144–1155.

(33) Witt, C.; Dieterich, J. M.; Hartke, B. Cluster structures influenced by interaction with a surface. *Phys. Chem. Chem. Phys.* **2018**, *20*, 15661–15670.

(34) Freibert, A.; Dieterich, J. M.; Hartke, B. Exploring self-organization of molecular tether molecules on a gold surface by global structure optimization. *J. Comput. Chem.* **2019**, *40*, 1978–1989.

(35) Dittner, M.; Hartke, B. Globally Optimal Catalytic Fields - Inverse Design of Abstract Embeddings for Maximum Reaction Rate Acceleration. *J. Chem. Theory Comput.* **2018**, *14*, 3547–3564.

(36) Dittner, M.; Hartke, B. Globally optimal catalytic fields for a Diels-Alder reaction. *J. Chem. Phys.* **2020**, *152*, No. 114106.

(37) Hartl, B.; Sharma, S.; Briüner, O.; Mertens, S. F. L.; Walter, M.; Kahl, G. Reliable Computational Prediction of the Supramolecular Ordering of Complex Molecules under Electrochemical Conditions. *J. Chem. Theory Comput.* **2020**, *16*, 5227–5243.

(38) Deshpande, S.; Maxson, T.; Greeley, J. Graph theory approach to determine configurations of multidentate and high coverage adsorbates for heterogeneous catalysis. *NPJ Comput. Mater.* **2020**, *6*, No. 79.

(39) Zhai, H.; Sautet, P.; Alexandrova, A. N. Global Optimization of Adsorbate Covered Supported Cluster Catalysts: The Case of Pt₇H₁₀CH₃ on α -Al₂O₃. *ChemCatChem* **2020**, *12*, 762–770.

(40) Garvey, M.; Bai, Y.; Boscoboinik, J. A.; Burkholder, L.; Sorensen, T. E.; Tysoe, W. T. Identifying Molecular Species on Surfaces by Scanning Tunneling Microscopy: Methyl Pyruvate on Pd(111). *J. Phys. Chem. C* **2013**, *117*, 4505–4514.

(41) Mahapatra, M.; Burkholder, L.; Garvey, M.; Bai, Y.; Saldin, D. K.; Tysoe, W. T. Enhanced hydrogenation activity and diastereomeric interactions of methyl pyruvate co-adsorbed with R-1-(1-naphthyl)-ethylamine on Pd(111). *Nat. Commun.* **2016**, *7*, No. 12380.

(42) Burkholder, L.; Tysoe, W. T. Structure and Reaction Pathways of Methyl Pyruvate on Pd(111). *J. Phys. Chem. C* **2009**, *113*, 15298–15306.

(43) Lavoie, S.; Laliberté, M.-A.; Mahieu, G.; Demers-Carpentier, V.; McBreen, P. Keto-Enol Driven Assembly of Methyl Pyruvate on Pt(111). *J. Am. Chem. Soc.* **2007**, *129*, 11668–11669.

(44) Bürgi, T.; Atamny, R.; Knop-Gericke, A.; Hävecker, M.; Schedel-Niedrig, T.; Schlögl, R.; Baiker, A. Adsorption mode of ethyl pyruvate on platinum: an in situ XANES study. *Catal. Lett.* **2000**, *66*, 109–112.

(45) Bonello, J. M.; Williams, F. J.; Santra, A. K.; Lambert, R. M. Fundamental Aspects of Enantioselective Heterogeneous Catalysis: the Surface Chemistry of Methyl Pyruvate on Pt(111). *J. Phys. Chem. B* **2000**, *104*, 9696–9703.

(46) Lavoie, S.; Laliberté, M.-A.; McBreen, P. H. Adsorption States and Modifier-Substrate Interactions on Pt(111) Relevant to the Enantioselective Hydrogenation of Alkyl Pyruvates in the Orito Reaction. *J. Am. Chem. Soc.* **2003**, *125*, 15756–15757.

(47) Bürgi, T.; Atamny, F.; Schlögl, R.; Baiker, A. Adsorption of Ethyl Pyruvate on Pt(111) Studied by XPS and UPS. *J. Phys. Chem. B* **2000**, *104*, 5953–5960.

(48) Bonello, J. M.; Lambert, R. M.; Künzle, N.; Baiker, A. Platinum-Catalyzed Enantioselective Hydrogenation of α -Ketoesters: An Unprecedented Surface Reaction of Methyl Pyruvate. *J. Am. Chem. Soc.* **2000**, *122*, 9864–9865.

(49) Meemken, F.; Baiker, A. Recent progress in heterogeneous asymmetric hydrogenation of C=O and C=C bonds on supported noble metal catalysts. *Chem. Rev.* **2017**, *117*, 11522–11569.

(50) Schröder, C.; Schmidt, M. C.; Witt, C.; Attia, S.; Weber, J.; Baumann, A. K.; Hartke, B.; Schauermann, S. Tuning the strength of molecular bonds in oxygenates via surface-assisted intermolecular interactions: atomistic insights. *J. Phys. Chem. C* **2020**, *124*, 28159–28168.

(51) Stone, A. *The Theory of Intermolecular Forces*, 2nd ed.; Oxford University Press: Oxford, 2013.

(52) Chipot, C.; Jaffe, R.; Maigret, B.; Pearlman, D. A.; Kollman, P. A. Benzene Dimer: A Good Model for π - π Interactions in Proteins? A Comparison between the Benzene and the Toluene Dimers in the Gas Phase and in an Aqueous Solution. *J. Am. Chem. Soc.* **1996**, *118*, 11217–11224.

(53) Dieterich, J. M.; Hartke, B. OGOLEM: Global cluster structure optimisation for arbitrary mixtures of flexible molecules. A multiscale, object-oriented approach. *Mol. Phys.* **2010**, *108*, 279–291.

(54) OGOLEM, Framework for GA-Based Global Optimization. <https://www.ogolem.org/> (accessed November 16, 2021).

(55) OGOLEM Framework, GA-Based Global Optimization of Chemical Problems. <https://github.com/ogolem/ogolem> (accessed November 16, 2021).

(56) Jäger, M.; Schäfer, R.; Johnston, R. L. GIGA: a versatile genetic algorithm for free and supported clusters and nanoparticles in the presence of ligands. *Nanoscale* **2019**, *11*, 9042–9052.

(57) Hofmann, O. T.; Zojer, E.; Hörmann, L.; Jeindl, A.; Maurer, R. J. First-principles calculations of hybrid inorganic-organic interfaces: from state-of-the-art to best practice. *Phys. Chem. Chem. Phys.* **2021**, *23*, 8132–8180.

(58) Janesko, B. G. Strong correlation in surface chemistry. *Mol. Simul.* **2017**, *43*, 394–405.

(59) Bannwarth, C.; Caldeweyher, E.; Ehlert, S.; Hansen, A.; Pracht, P.; Seibert, J.; Spicher, S.; Grimme, S. Extended tight-binding quantum chemistry methods. *WIREs Comput. Mol. Sci.* **2021**, *11*, No. e1493.

(60) Spicher, S.; Grimme, S. Robust Atomistic Modeling of Materials, Organometallic, and Biochemical Systems. *Angew. Chem., Int. Ed.* **2020**, *59*, 15665–15673.

(61) Thomas, M.; Brehm, M.; Figg, R.; Vöringer, P.; Kirchner, B. Computing vibrational spectra from ab initio molecular dynamics. *Phys. Chem. Chem. Phys.* **2013**, *15*, 6608–6622.

(62) Ivanov, S. D.; Witt, A.; Marx, D. Theoretical spectroscopy using molecular dynamics: theory and application to CH_3^+ and its isotopologues. *Phys. Chem. Chem. Phys.* **2013**, *15*, 10270–10299.

(63) von der Esch, B.; Peters, L. D. M.; Sauerland, L.; Ochsenfeld, C. Quantitative comparison of experimental and computed IR spectra extracted from ab initio molecular dynamics. *J. Chem. Theory Comput.* **2021**, *17*, 985–995.

(64) Semiempirical Extended Tight-Binding Program Package. <https://github.com/grimme-lab/xtb> (accessed November 16, 2021).

(65) Massarczyk, M.; Rudack, T.; Schlitter, J.; Kuhne, J.; Kötting, C.; Gerwert, K. Local mode analysis: decoding IR spectra by visualizing molecular details. *J. Phys. Chem. B* **2017**, *121*, 3483–3492.

(66) Jmol: An Open-Source Java Viewer for Chemical Structures in 3D. <http://www.jmol.org/> (accessed November 16, 2021).

(67) Frisch, M. J.; Trucks, G. W.; Schlegel, H. B.; Scuseria, G. E.; Robb, M. A.; Cheeseman, J. R.; Scalmani, G.; Barone, V.; Petersson, G. A.; Nakatsuji, H. et al. *Gaussian 09*, revision D.01; Gaussian, Inc.: Wallingford, CT, 2016.

(68) Clough, S. A.; Beers, Y.; Klein, G. P.; Rothman, L. S. Dipole moment of water from Stark measurements of H_2O , HDO and D_2O . *J. Chem. Phys.* **1973**, *59*, 2254–2259.

(69) Gregory, J. K.; Clary, D. C.; Liu, K.; Brown, M. G.; Saykally, R. J. The water dipole moment in water clusters. *Science* **1997**, *275*, 814–817.

(70) Zhu, T.; van Voorhis, T. Understanding the dipole moment of liquid water from a self-attractive Hartree decomposition. *J. Phys. Chem. Lett.* **2021**, *12*, 6–12.

(71) Wales, D. J. *Energy Landscapes, with Applications to Clusters, Biomolecules and Glasses*; Cambridge University Press: Cambridge, 2003.

(72) Pearce, H. A.; Sheppard, N. Possible importance of a metal-surface selection rule in the interpretation of the infrared spectra of molecules adsorbed on particulate metals; infrared spectra from ethylene chemisorbed on silica-supported metal catalysts. *Surf. Sci.* **1976**, *59*, 205–217.

(73) Greenler, R. G.; Snider, D. R.; Witt, D.; Sorbello, R. S. The metal-surface selection rule for infrared spectra of molecules adsorbed on small metal particles. *Surf. Sci.* **1982**, *118*, 415–428.

8.6 Surface-Driven Keto-Enol Tautomerization: Atomistic Insights into Enol Formation and Stabilization Mechanisms

Publication Data and Reprint

Reference: Smadar Attia, Marvin-Christopher Schmidt,
Carsten Schröder, Pascal Pessier, Swetlana
Schauermann

DOI: 10.1002/anie.201808453

Submitted: 23.07.2018

Accepted: 12.10.2018

Contribution: IRAS measurements, scientific discussions,
preparation of parts of the manuscript

Copyright: Reprinted with permission from Angewandte
Chemie International Edition from Ref.[236].
Copyright 2018 John Wiley and Sons.

Keto–enol Tautomerization

International Edition: DOI: 10.1002/anie.201808453
German Edition: DOI: 10.1002/ange.201808453

Surface-Driven Keto–Enol Tautomerization: Atomistic Insights into Enol Formation and Stabilization Mechanisms

Smadar Attia, Marvin-Christopher Schmidt, Carsten Schröder, Pascal Pessier, and Swetlana Schauer mann*

Abstract: Tautomerisation of simple carbonyl compounds to their enol counterparts on metal surfaces is envisaged to enable an easier route for hydrogenation of the C=O bond in heterogeneously catalyzed reactions. To understand the mechanisms of enol formation and stabilization over catalytically active metal surfaces, we performed a mechanistic study on keto–enol tautomerization of a monocarbonyl compound acetophenone over Pt(111) surface. By employing infrared reflection adsorption spectroscopy in combination with scanning tunneling microscopy, we found that enol can be formed by building a ketone–enol dimer, in which one molecule in the enol form is stabilized through hydrogen bonding to the carbonyl group of the second ketone molecule. Based on the investigations of the co-adsorption behavior of acetophenone and hydrogen, we conclude that keto–enol tautomerization occurs in the intramolecular process and does not involve hydrogen transfer through the surface hypothesized previously.

Chemical transformations of carbonyl compounds is an important step in many applications in heterogeneous catalysis, such as selective hydrogenation of unsaturated ketones, enantioselective hydrogenation of ketoesters, aldol condensation, and others.^[1] This class of reactions is, however, experimentally highly challenging as it requires the activation of a normally very stable C=O bond to be hydrogenated to a C–O bond. There are only a few atomistic-level studies on surfaces, in which the product of direct hydrogenation of the C=O bond with H was confirmed spectroscopically.^[2]

There is an ongoing discussion on an alternative feasible mechanism to activate the C=O bond, which involves keto–enol tautomerization as a first step. In this mechanism, a H atom transfers to oxygen in an intramolecular process to produce a C–O(H) single bond, leaving behind a C=C double bond and forming the enol species. Several theoretical studies predict a significantly lower activation barrier for hydrogenation of the C=C bond in enol as compared to the direct hydrogenation of the C=O bond in ketone for different

classes of mono- and dicarbonyl compounds.^[3] In line with these predictions, keto–enol tautomerization was frequently discussed as a first step in heterogeneously catalyzed hydrogenation of the C=O bond.^[4] A microscopic-level confirmation of this mechanism and a detailed understanding of the elementary steps leading to keto–enol tautomerization on surfaces is still largely missing. To approach the rational design of the catalytic processes involving keto–enol tautomerization as a first step in activation of carbonyl compounds on surfaces, enol formation and stabilization need to be understood at the atomistic scale.

Generally, the ketone form of neutral carbonyl compounds is more stable than the enol form,^[5] therefore the formation of enol species usually requires stabilization by for example, hydrogen bonding. The most commonly discussed mechanism of the enol stabilization is related to diketones or ketoesters containing two carbonyl groups. In these compounds, a chelated ring-like keto–enol tautomer can be formed with one of the carbonyls being transformed to a –C–O–H entity and the other carbonyl participating in the stabilization of the enol part of the molecule through hydrogen bonding between the –C=O and H–O–C– functional groups. Numerous studies provided solid experimental proof for the mechanism leading to formation of chelated keto–enol tautomers in diketones and ketoesters.^[6]

While the enol stabilization is well understood for the compounds comprising two carbonyls, significantly less is known about the enol formation and stabilization for monocarbonyls, in which the intramolecular stabilization is not possible. In a recent study by Demers-Carpentier et al.^[7] on monocarbonyls adsorbed on Pt, an interesting observation on formation of different oligomers, consisting of two or three acetophenone molecules, was reported, which were interpreted as structures comprising exclusively the enol species. As thermal activation, up to 300 K was needed to obtain these enol-containing oligomers, the authors put forward a dissociative type of keto–enol tautomerization mechanism, involving dissociation of a C–H bond in methyl group followed by a H diffusion through the Pt surface to the C=O group.^[7] The experimental verification of this hypothesized dissociative mechanism is not available yet.

In order to obtain a microscopic-level understanding of the enol formation and stabilization mechanisms on surfaces, we performed a mechanistic study on the interaction of acetophenone with well-defined Pt(111) surface in a broad range of temperature and coverage conditions. We employed a unique combination of surface sensitive techniques including infrared reflection absorption spectroscopy (IRAS), scanning tunneling microscopy (STM), and molecular beam

[*] S. Attia, M.-C. Schmidt, C. Schröder, P. Pessier, S. Schauer mann
Institute of Physical Chemistry, Christian-Albrechts-University Kiel,
Max-Eyth-Str. 2, 24118 Kiel (Germany)
E-mail: schauer mann@pctc.uni-kiel.de

S. Attia
Department of Chemical Physics, Fritz-Haber-Institut der Max-
Planck-Gesellschaft
Faradayweg 4–6, 14195 Berlin (Germany)

Supporting information and the ORCID identification number(s) for
the author(s) of this article can be found under:
<https://doi.org/10.1002/anie.201808453>.

techniques to address the chemical nature of the formed surface species and to obtain the real space information on their distribution over the surface and on the intermolecular interactions between the individual molecules. Two independent molecular beams were employed to controllably deposit acetophenone and the second reactant of interest (H_2) to scrutinize the intermolecular interactions involved in keto-enol tautomerization on pristine and H-containing Pt surface. Specifically, it was observed that above 140 K acetophenone forms dimers; this process is accompanied by the evolution of new vibrational bands detected by IRAS, which are related to the enol tautomer. The stabilization of the enol species occurs by intermolecular interaction with the second molecule, that is the ketone form of acetophenone, through hydrogen bonding resulting in surface dimers. The second observed type of surface dimers involves two ketone molecules. Surprisingly, the presence of large amounts of H on Pt was found to destabilize both types of dimers leading to formation of acetophenone monomers in the ketone form. A concomitant vanishing of all vibrational bands related to enol species was detected on H-containing surface. This finding clearly disproves the previously hypothesized dissociative-type tautomerization mechanism based on the H-transfer through the Pt surface. Instead, it points to an intramolecular H-transfer to form the enol tautomer, which exists only if stabilized by hydrogen bonding to a neighboring ketone molecule. Obtained atomistic-level details on intermolecular ketone-enol interactions provide important insights into the mechanisms of enol formation and stabilization for single-carbonyl compounds on surfaces, which were not available so far.

Experimentally, interaction of acetophenone with Pt(111) surface was investigated in the temperature range from 115 to 300 K, both on pristine and H-precovered surfaces. The STM images of acetophenone obtained on the pristine surface (Figure 1a) show that the majority of the molecules (82%) form dimer species at 200 K. A large fraction of the dimers (about 84%) are imaged as two identical elongated protrusions with a bright feature at one end (the species D1 in the insert of Figure 1a), which are interacting by the ends containing the bright spots. The other type of the dimers consists of two unequal species, an elongated protrusion with a bright spot and an elongated structure without a bright feature (species D2 in the insert of Figure 1a). A small fraction of the surface species are monomers (species M, 18% of all adsorbed molecules) imaged as an elongated protrusion with a bright spot at one end, which appear to be identical to a half of the dimer D1.

To clarify the chemical nature of the imaged species, infrared spectra were obtained on this surface, which are shown in Figure 1c. The spectra (1) and (2) are related to acetophenone adsorbed at different sub-monolayer coverages, while the spectrum (3) was recorded on acetophenone multilayer and is shown as a reference for unperturbed molecules. The most prominent bands in the multilayer spectrum comprise the C=O stretching vibration at 1683 cm^{-1} and several vibrational bands in the range $1260\text{--}1450\text{ cm}^{-1}$ related to deformation vibrations of the methyl and benzene groups^[8] (for more details see the Supporting Information). The same vibrational frequencies (marked with the grey dotted lines) are also observed in the spectra (1) and (2)

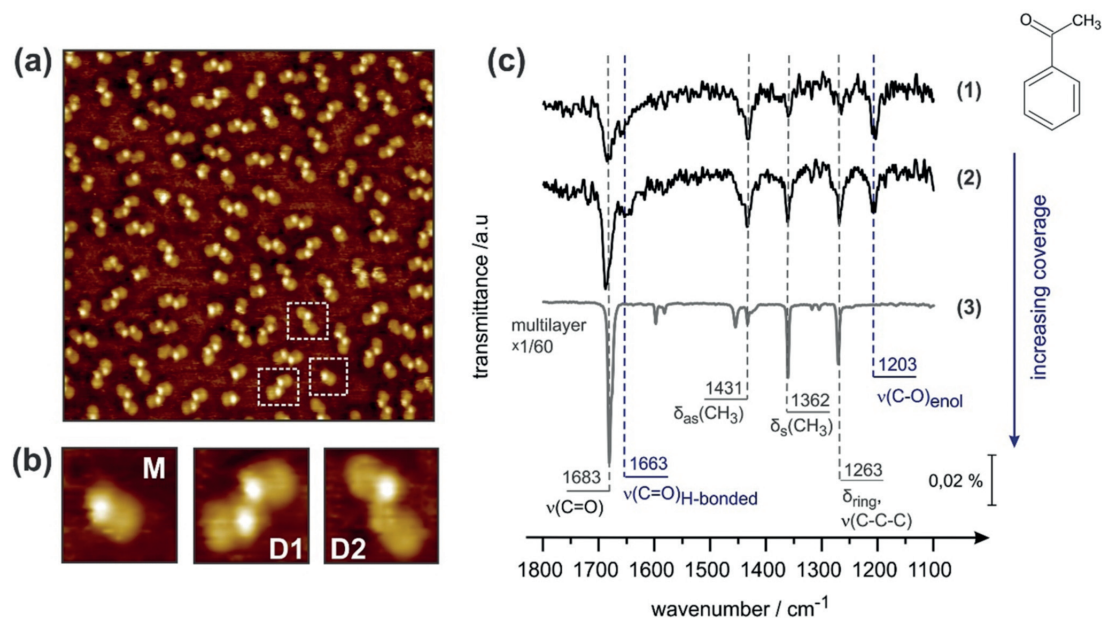


Figure 1. a) STM image of acetophenone on pristine Pt(111) (exposure at 200 K, acquisition temperature 115 K, 1 V, 0.29 nA, $15 \times 15\text{ nm}^2$). b) Close-up images of a monomer (M) and two types of dimers (D1 and D2). c) (1) and (2): IR spectra of acetophenone adsorbed on pristine Pt(111) at different sub-monolayer coverages at 170 K; (3) the spectrum of a multilayer (for the details see the Supporting Information).

obtained at sub-monolayer coverages. Remarkably, the interaction of acetophenone with Pt almost does not affect the frequencies of these bands, pointing to weak interaction of the ketone species with the underlying metal. Besides of the ketone-specific vibrations, two new prominent bands appear at 1203 and 1663 cm^{-1} (marked with blue lines) at sub-monolayer coverages, which are present neither in multilayer of acetophenone nor in the gas phase spectra.^[8]

The evolution of the IR spectra investigated as a function of acetophenone coverage suggests that at least two types of surface species exist on the surface: a) the species exhibiting a combination of the bands at 1203 and 1663 cm^{-1} ; and b) the species showing the bands characteristic for largely unperturbed acetophenone with the most prominent band at 1683 cm^{-1} . Figure 2 shows the IR spectra obtained at different

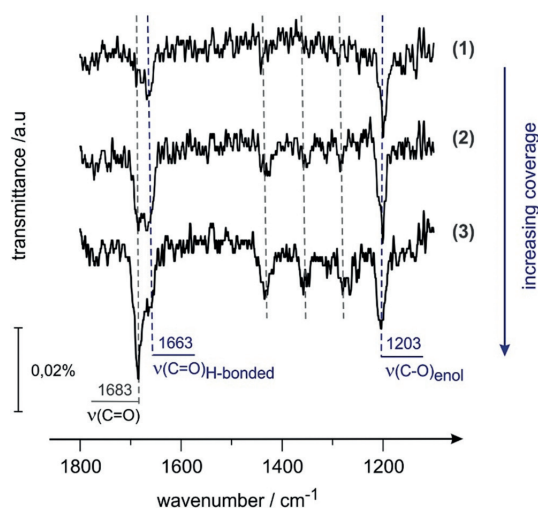


Figure 2. IR spectra of acetophenone adsorbed on pristine Pt(111) recorded at 200 K at different exposures (for the details see the Supporting Information).

coverages at 200 K. The uppermost spectrum (1, lowest coverage) shows almost exclusive formation of the species containing the bands at 1203 and 1663 cm^{-1} , whose intensity grows simultaneously with growing coverages and finally saturates. In the spectrum (2), the onset of the vibration at 1683 cm^{-1} is detected; this band further grows in intensity and finally dominates the spectra in the high coverage range. A similar coverage-dependent trend can be also observed in the spectra shown in Figures 3 a and b obtained for normal and isotopically labelled acetophenone. While the appearance of the bands at 1203 and 1663 cm^{-1} and their intensities are strongly correlated in all datasets, the band at 1683 cm^{-1} develops fully independently: it is less pronounced at low coverages and has the highest intensity in the high coverage range. Based on this strikingly different coverage dependence, we assign the combination of the bands at 1203 and 1663 cm^{-1} to one type of surface species, and the band at 1683 cm^{-1} to a different type of adsorbates.

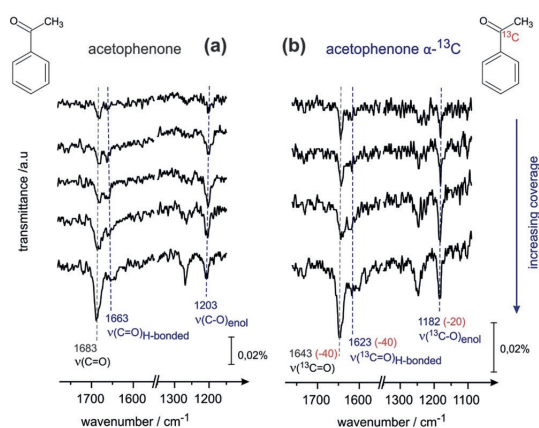


Figure 3. IR spectra: a) acetophenone and b) acetophenone isotopically labelled with ^{13}C at carbonyl-carbon position recorded at different exposures at 170 and 155 K, correspondingly (for the details see the Supporting Information).

The species exhibiting the prominent band at 1683 cm^{-1} can be safely assigned to the largely unperturbed ketone form of acetophenone as the related frequencies coincide with that once of acetophenone ice. Considering the fact that the majority of acetophenone molecules is combined in dimers and two different types of dimers are imaged by STM, we assume that one of these dimer species consists of two ketone molecules and the intermolecular interaction between them does not strongly affect their vibrational frequencies. Note that the monomers, which are also present in small amounts, are expected to have the same vibrational frequencies.

The vibrational range 1050–1250 cm^{-1} is typical for the stretching vibration of a single C–O bond in alcohols and alkoxy groups.^[9] Taking into account feasible keto–enol tautomerization in carbonyl compounds, we assign the band at 1203 cm^{-1} to the stretching vibration of the C–O single bond in the enol form of acetophenone. This assignment is in a close agreement with the previous theoretical and experimental studies on enol formation for a broad class of carbonyl compounds including acetone, diketones and ketoesters.^[6d,10]

The bands in the vibrational range close to 1663 cm^{-1} were previously observed in experimental studies on keto–enol tautomerization in diketones and ketoesters and explained theoretically by formation of a chelated ring-like keto–enol tautomers, in which one carbonyl group transforms into the C–O(H) bond to form enol, while the O atom of the second carbonyl group stabilizes the newly formed OH group of the enol by hydrogen bonding leading to the $-\text{C}=\text{O}\cdots\text{H}-\text{O}-$ structure.^[6d,10b,11] In these type of chelated keto–enol species, two phenomena can affect the C=O frequency: 1) the mixing of the C=O and C=C stretching vibrations, which was theoretically predicted to shift the C=O vibrational band by about 20 cm^{-1} to 1660 cm^{-1} in keto–enol tautomerized β -dicarbonyl compounds;^[11a] and 2) hydrogen bonding between the $-\text{C}=\text{O}$ bond and H–O– group of the enol part of the molecule, which was shown to result in downward shift of the

C=O vibrational frequency for carbonyl compounds.^[12] The latter phenomenon of a frequency shift due to donor-acceptor hydrogen bonding, has a general nature and is predicted to obey the following trend: the higher the acidity of the donor (in this case H–O group) the larger the frequency shift of the acceptor (–C=O group).^[12,13] For this reason, the frequency shifts of the C=O group are expected to be largest when it interacts with the OH group and significantly lower when it is hydrogen-bonded to, for example, a H of a methyl group.

Taking into account the fact that the majority of the surface species are involved in dimers and based on the previous theoretical calculations for β -dicarbonyl compounds,^[11a] we assign the combination of the vibrational bands at 1203 and 1663 cm^{-1} to a dimer, containing one enol and one ketone molecule, which are interacting through hydrogen bonding. The vibration at 1203 cm^{-1} is related to a single C–O bond in enol, while the vibrational band at 1663 cm^{-1} can be assigned to the C=O in ketone with O atom being involved in hydrogen bonding with the OH group of enol. The latter conclusion is based on the fact that the individual acetophenone molecules are not covalently bonded in the dimer, and therefore the downward frequency shift of the C=O bond in ketone most likely originates from the hydrogen bonding with the OH group of the enol and not due to the strong mixing between the C=C and C=O vibrations as calculated for chelated keto–enol dicarbonyls,^[11a] in which the ketone and the enol parts of the same molecule are connected covalently.

To further verify the assignment of these new vibrations, adsorption of acetophenone isotopically labelled with ^{13}C at carbonyl-carbon position was investigated by IRAS. Figures 3a and b show two sets of coverage-dependent IR spectra obtained for two isotopes. The band at 1683 cm^{-1} related to the C=O stretching vibration in the nearly undisturbed ketone shifts downwards by 40 cm^{-1} upon isotopic labelling, agreeing with the estimated shift of about 38 cm^{-1} in the scope of harmonic approximation. Importantly, both new bands also shift upon replacement of the carbonyl-carbon by ^{13}C : the band at the 1663 cm^{-1} shifts by 40 cm^{-1} , while the vibrational frequency 1203 cm^{-1} decreases by 20 cm^{-1} . Both downward shifts confirm the assignment to the bonds involving the α -carbon of acetophenone. Additionally, the shift of the band at 1663 cm^{-1} assigned to the ketone–enol dimer, is identical to the shift of the band at 1683 cm^{-1} related to the C=O vibration in the largely unperturbed ketone–ketone dimers and ketone monomers, additionally supporting our assignment of the band at 1663 cm^{-1} to the stretching vibration mainly exhibiting the C=O character.

Combining the spectroscopic and microscopic information, we conclude that two different types of dimers can be formed on Pt(111). Figure 4a and b shows the most feasible dimer structures, which are consistent with all experimental observations.

The first type of dimers consists of two largely unperturbed ketone molecules, as suggested by the IR frequencies, and dominates the spectra at high coverages. Most likely, the most abundant dimer D1, comprising two identical protrusions with a bright spot close to the contact position (Figure 1a),

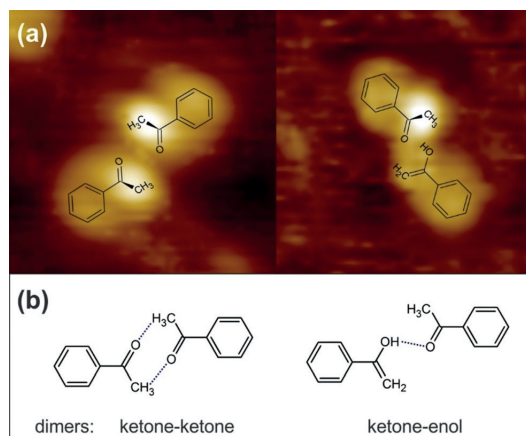


Figure 4. a) Suggested structures of two types of surface dimers: D1: ketone–ketone dimer; D2: ketone–enol dimer superimposed with the STM images from Figure 1. b) Schematics of the suggested structures; the hydrogen bonds are indicated by blue dotted lines.

can be ascribed to these ketone–ketone dimer species. It can be speculated that the elongated protrusion is related to the phenyl group and the bright spot to either CH_3 or C=O groups sticking out of the surface plane, with the lifted CH_3 group being a more likely configuration. It should be pointed out that the monomeric species are also imaged by STM as elongated protrusions with a bright spot, which is identical to the half of the ketone–ketone dimer. This STM pattern is likely related to the ketone form of acetophenone since no stabilization mechanism for enol is available for monomers. This observation additionally supports the assignment of the species D1 to ketone–ketone dimer as it consists of the same building blocks as the ketone monomeric species.

Based on the observation that the individual molecules in this type of dimers are connected at the positions containing the bright spots, and in view of the fact that the vibrational frequencies of the C=O bonds are hardly affected by dimer formation, we believe that two ketone molecules interact through hydrogen bonding between the carbonyls and the H atoms involved in the methyl group. As discussed above, rather weak hydrogen bonding is expected between the C=O and the methyl groups, resulting in a negligible effect on the C=O vibrational frequency.

The dimer D2 consists of one acetophenone molecule in the enol form, and one in the ketone form with the H atom of the OH group of the enol being involved in hydrogen bonding with the O atom of the ketone. The strong hydrogen bonding between the C=O and OH groups leads to a downward frequency shift of the C=O bond to 1663 cm^{-1} as compared to the largely unperturbed ketone form of acetophenone (1683 cm^{-1}). The formation of the C–O single bond results in the vibrational band at 1203 cm^{-1} . The chemical structure of such ketone–enol dimer, consisting of two different forms of acetophenone, most likely establishes itself in non-symmetric dimers D2 displayed in Figure 1b and Figure 4b.

Generally, two major phenomena can be responsible for enol formation on Pt surface: 1) reduction of the activation barrier for the intramolecular H transfer from the methyl to the carbonyl group, for example, due to weakening of the C–H bonds, and/or 2) energetic stabilization of the otherwise unstable enol form by the formation of surface dimers through H-bonding between O–H and C=O groups of the enol and ketone species, correspondingly. The detailed discussion on the feasibility of these mechanisms is provided in the Supporting Information.

It should be noted, that formation of surface dimers and trimers of acetophenone on Pt was previously observed by the group of McBreen^[7] at room temperature and they were assigned exclusively to enol–enol oligomers. Further, the dissociative mechanism of enol formation was hypothesized in this study, which is based on the assumption that a H atom of a methyl group is abstracted by the underlying metal and transfers to the carbonyl group through the Pt surface. The authors discussed the probability of enol formation as being related to the availability of H atoms on the metal surface.

To clarify this feasibility of this mechanism, we investigated keto–enol tautomerization on H-precovered Pt(111). Figures 5 a and b show the STM image obtained on Pt surface saturated with H after adsorption of acetophenone and the IR spectra recorded on this surface, correspondingly. Remarkably, predominantly monomers could be observed on this surface by STM, which appear as elongated protrusions with a bright spot. In line with this observations, only vibrational bands related to the unperturbed form of acetophenone were found, while the vibrations characteristic to ketone–enol dimers (1203 and 1663 cm^{-1}) did not appear. Obviously, formation of the enol form of acetophenone as well as of ketone–enol surface dimers does not occur at this surface. Possible reasons for this observation might include 1) weaker perturbation of the electronic structure of the acetophenone on H-covered Pt, resulting in stronger C–H bonds of the methyl group and hindered intramolecular H-transfer to the carbonyl or/and 2) hindered ketone–enol dimer formation

due to the fact that co-adsorbed H might compete with the O–H group of the enol species for hydrogen bonding to the C=O group of the ketone (see the Supporting Information for detailed discussion).

It becomes also apparent that enol formation on pristine Pt cannot be linked merely to the availability of adsorbed H originating from H-transfer through the surface suggested by Demers-Carpentier et al.,^[7] but rather relies on the intramolecular process involving H-transfer to the carbonyl group to form a C–O–H entity, which is stabilized by hydrogen bonding with the neighboring ketone molecule (see the Supporting Information for detailed discussion). With this, the enol formation and stabilization mechanism of monocarbonyl compounds on surface is similar to that occurring in the intramolecular process in dicarbonyl molecules.

Summarizing, we investigated the surface-driven keto–enol tautomerization in single carbonyl compound acetophenone by combination of microscopic, spectroscopic, and molecular beam techniques on Pt(111) to scrutinize the mechanisms of enol formation and stabilization on catalytically-relevant metal surfaces. It was found that enol species exist not as monomers but are stabilized by the intermolecular interaction with a ketone form of acetophenone and form ketone–enol dimers. The spectroscopic signatures of this dimer point to a significant perturbation of the electronic structure of the involved molecules and suggest strong hydrogen bonding between the –OH group of the enol and the C=O entity of the ketone form of acetophenone. Additionally, a second type of the surface dimers, consisting of two largely unperturbed ketone molecules, was found as well as a small fraction of monomeric species. Co-adsorbed H destabilize both types of dimers leading to predominant formation of ketone monomers and a concomitant vanishing of all vibrational bands related to ketone–enol dimers. This finding suggests that the previously hypothesized dissociative type of enol formation depending on H transfer through the metal surface is rather improbable and this process more likely proceeds by intramolecular H-transfer from the methyl to the carbonyl group.

Obtained atomistic-level insights into mechanisms of enol stabilization for single-carbonyl compounds highlight the exceptional importance of intermolecular interactions in this processes. It can be feasibly tuned by co-adsorption of stable well-ordered layers of foreign molecules, such as specifically designed different types of carbonyl compounds, which would be able to stabilize enols even in presence of hydrogen. Related effects are envisaged to play a key role in controlling the keto–enol tautomerization of simple carbonyls to enable low-barrier chemical transformations and hold a great potential for further development of new catalytic materials, such as for instance, ligand-modified catalysts optimized for enol stabilization.

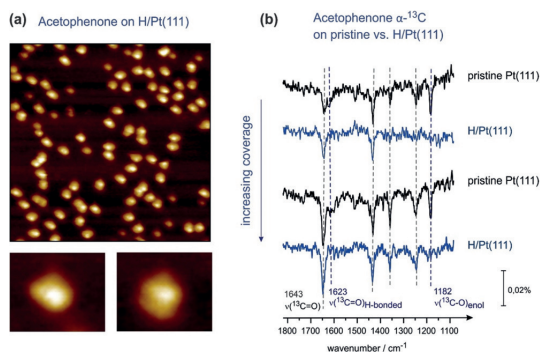


Figure 5. a) STM image of acetophenone adsorbed at H-precovered Pt(111) (exposure at 175 K, acquisition temperature 115 K, 1 V, 0.29 nA, $15 \times 15 \text{ nm}^2$). b) Blue lines: IR spectra of acetophenone α - ^{13}C adsorbed on H-precovered Pt(111) obtained at two different submonolayer coverages; black lines: IRAS spectra of acetophenone α - ^{13}C adsorbed on pristine Pt(111).

Acknowledgements

This work has been supported by European Research Council (Starting Grant ENREMOS 335205). The authors thank Evan Spadafora for valuable discussions.

Conflict of interest

The authors declare no conflict of interest.

Keywords: carbonyl compounds · keto-enol tautomerization on metals · model heterogeneous catalysis · scanning tunneling microscopy · vibrational spectroscopy on surfaces

How to cite: *Angew. Chem. Int. Ed.* **2018**, *57*, 16659–16664
Angew. Chem. **2018**, *130*, 16901–16906

- [1] a) P. Mäki-Arvela, et al., *Appl. Catal. A* **2005**, *292*, 1–49; b) F. Meemken, A. Bäker, *Chem. Rev.* **2017**, *117*, 11522–11569.
- [2] a) K.-H. Dostert, et al., *J. Am. Chem. Soc.* **2015**, *137*, 13496–13502; b) C. J. Kliewer, et al., *J. Am. Chem. Soc.* **2009**, *131*, 9958–9966.
- [3] a) B. Yang, et al., *Phys. Chem. Chem. Phys.* **2011**, *13*, 21146–21152; b) A. M. H. Rasmussen, et al., *ACS Catal.* **2014**, *4*, 1182–1188; c) B. Bandyopadhyay, et al., *J. Phys. Chem. A* **2012**, *116*, 3836–3845.
- [4] a) K. H. Schulz, D. F. Cox, *J. Phys. Chem.* **1993**, *97*, 3555–3564; b) W.-S. Sim, et al., *J. Am. Chem. Soc.* **2002**, *124*, 4970–4971; c) M. Mahapatra, et al., *Nat. Commun.* **2016**, *7*, 12380.
- [5] Z. Rappoport, *The Chemistry of Enols*, Wiley, Chichester, **1990**.
- [6] a) V. Humblot, et al., *Surf. Sci.* **2003**, *537*, 253–264; b) M. Garvey, et al., *J. Phys. Chem. C* **2013**, *117*, 4505–4514; c) T. E. Jones, C. J. Baddeley, *Langmuir* **2006**, *22*, 148–152; d) T. E. Jones, C. J. Baddeley, *J. Phys. Chem. C* **2007**, *111*, 17558–17563; e) D. B. Skliar, et al., *Surf. Sci.* **2007**, *601*, 2887–2895; f) J. Ontaneda, et al., *J. Phys. Chem. C* **2016**, *120*, 27490–27499.
- [7] V. Demers-Carpentier, et al., *J. Phys. Chem. C* **2010**, *114*, 7291–7298.
- [8] A. Gambi, et al., *Spectrochim. Acta A* **1980**, *36*, 871–878.
- [9] a) W. J. Mitchell, et al., *J. Am. Chem. Soc.* **1995**, *117*, 2606–2617; b) M. K. Weldon, C. M. Friend, *Chem. Rev.* **1996**, *96*, 1391–1412.
- [10] a) M. Xu, et al., *Ind. Eng. Chem. Res.* **2014**, *53*, 5451–5454; b) T. P. Roubin, et al., *Chem. Phys. Lett.* **1990**, *175*, 655–659.
- [11] a) N. V. Belova, et al., *J. Phys. Chem. A* **2004**, *108*, 3593–3597; b) E. I. Matrosov, M. I. Kabachnik, *Spectrochim. Acta Part A* **1972**, *28*, 191–196.
- [12] S. D. Fried, et al., *J. Am. Chem. Soc.* **2013**, *135*, 11181–11192.
- [13] M. M. Nolasco, P. J. Ribeiro-Claro, *ChemPhysChem* **2005**, *6*, 496–502.

Manuscript received: July 23, 2018

Revised manuscript received: September 7, 2018

Accepted manuscript online: October 12, 2018

Version of record online: November 25, 2018

8.7 Formation and Stabilization Mechanisms of Enols on Pt through Multiple Hydrogen Bonding

Publication Data and Reprint

Reference: Smadar Attia, Marvin C. Schmidt, Carsten Schröder, Swetlana Schauerermann

DOI: 10.1021/acscatal.9b01481

Submitted: 10.04.2019

Accepted: 05.07.2019

Contribution: IRAS measurements, scientific discussions, preparation of parts of the manuscript

Copyright: Reprinted with permission from ACS Catalysis from Ref.[237]. Copyright 2019 American Chemical Society.

Formation and Stabilization Mechanisms of Enols on Pt through Multiple Hydrogen Bonding

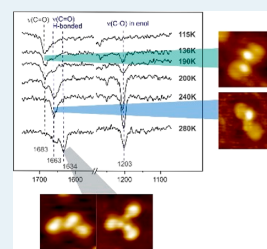
Smadar Attia, Marvin C. Schmidt, Carsten Schröder, and Swetlana Schauer mann*[✉]

Institut für Physikalische Chemie, Christian-Albrechts-Universität zu Kiel, Max-Eyth-Strasse 2, 24118 Kiel, Germany

Supporting Information

ABSTRACT: Lateral interactions between coadsorbed molecules on surfaces might trigger specific reaction pathways and stabilize otherwise energetically unstable reaction intermediates. These phenomena can crucially affect the overall activity and selectivity of catalytic processes and can be employed for purposeful functionalization of surfaces to improve their catalytic efficiency. In this report, we present a study on the atomistic-level details of intermolecular interactions between acetophenone adsorbates on Pt. We show that these interactions trigger an important reaction of keto–enol tautomerization producing an enol reaction intermediate, which is envisaged to enable low-barrier hydrogenation of simple carbonyl compounds. By combining scanning tunneling microscopy and infrared reflection–absorption spectroscopy, we found that several types of hydrogen-bonded oligomer species can be formed, including ketone–enol dimers and ketone–enol–enol trimers. Their evolution exhibits a strong temperature dependence, suggesting that oligomer formation promotes keto–enol tautomerization by lowering the activation barrier for hydrogen transfer from the methyl to the carbonyl group. This process occurs most likely in a concerted way, in which the energy barrier for hydrogen transfer can be compensated by formation of strong hydrogen bonds between enol and ketone species assembled in an oligomer. Additionally, hydrogen bonding between the ketone and the enol parts of surface-adsorbed oligomers stabilizes the otherwise unstable enol species, making them accessible for further reaction steps. Importantly, formation of more than one enol molecule per one ketone species through multiple hydrogen bonding was proven—a finding which might contribute to the rational design of functionalized surfaces capable of enol formation and stabilization at high surface concentrations.

KEYWORDS: keto–enol tautomerization, model heterogeneous catalysis, carbonyl compounds, surface dimers, infrared spectroscopy, scanning tunneling microscopy, Pt(111), surface reactivity



INTRODUCTION

Lateral interactions between different coadsorbed surface species may play a crucial role in controlling reactivity on surfaces. In particular, for multipathway heterogeneously catalyzed reactions, the selectivity depends oftentimes on small differences in the activation barriers of different reaction pathways.¹ These barriers are determined not only by the interaction of the reactants and the reaction intermediates with the underlying catalytic surface but also by their intermolecular interactions with the surrounding adsorbates, which can significantly modify the overall energy landscape and with this dramatically affect the selectivity toward individual reaction pathways. While the intermolecular interactions have been successfully employed in many homogeneous catalysts to control the selectivity,^{2,3} e.g., via modification of an active metal site with specific organic ligands, only a limited number of studies on heterogeneous catalysts relying on this principle have been reported. The majority of the reported studies in this field is related to enantioselective heterogeneous catalysis on surfaces functionalized with chiral adsorbates, which exhibit enantiospecific interaction with a pro-chiral reactant and by this direct the catalytic process toward formation of only one enantiomeric form of the product.^{4–7} Besides enantioselective heterogeneous catalysis, ligand-induced catalysis for nonchiral

systems is gaining more importance in the recent decade.^{8–13} This type of catalytic process is based on the lateral adsorbate–adsorbate interactions between a preadsorbed ligand and a reactant molecule, which makes the surface highly chemo-selective.^{14–20} Mechanistically, two types of interactions are typically invoked to explain the ligand-induced effects: building of individual 1:1 complexes between a ligand and the reactant⁴ and formation of extended well-ordered overlayers of adsorbed ligands offering reactive pockets for the reactant.^{8,9,11} In both types of discussed mechanisms, the lateral interactions between the ligand (or the ligand overlayer) and the reactant affect the reactant's electronic structure and/or its adsorption geometry to trigger the desired chemical transformations.

Despite these recent impressive developments, the atomistic-level understanding of the intermolecular interactions between coadsorbed molecular species on surfaces is rather limited. Further progress in understanding the mechanisms and energetics of intermolecular interaction need to be made in order to approach rational design of functionalized surfaces with tailor-made catalytic properties. Toward this goal, we

Received: April 10, 2019

Revised: June 20, 2019

Published: July 5, 2019

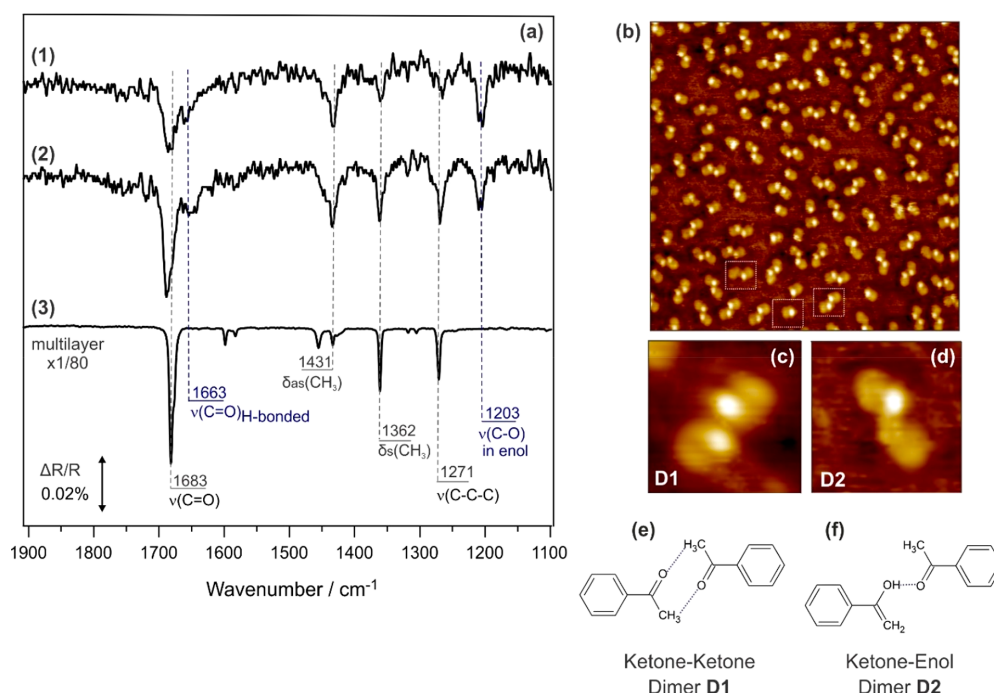


Figure 1. (a) (1 and 2) IR spectra of acetophenone adsorbed at different submonolayer coverages obtained on pristine Pt(111) at 170 K (exposures are as follows: (1) 4.5×10^{15} , (2) 6.1×10^{15} molecules·cm⁻²). (3) Spectrum of a multilayer. (b) STM image of acetophenone on Pt(111) (exposure at 200 K; acquisition temperature 115 K; 1 V, 0.29 nA, 15×15 nm²). Reproduced with permission from ref 29. Copyright 2018 Wiley). (c and d) Close-up images of two types of dimers (D1 and D2). (e and f) Proposed structures of the dimer species D1 and D2, respectively.

report a combined spectroscopic and microscopic study on lateral interactions between acetophenone molecules adsorbed on a well-defined Pt(111) surface. In this paper, we specifically address acetophenone transformation to its enol form, which is assisted by the intermolecular interaction with the ketone counterpart. The process of keto–enol tautomerization of normally more energetically stable ketones to less stable enols²¹ is theoretically predicted to play a decisive role in hydrogenation of the C=O bond in simple carbonyl compounds.^{22–25} The activation barrier is normally rather high to directly hydrogenate the C=O bond; however, it is predicted to be reduced if the process would occur via two consecutive steps including (i) keto–enol tautomerization to form enol species followed by (ii) low-barrier hydrogenation of the C=C bond. For this reason, formation and stabilization of the enol form of simple carbonyls can potentially be one of the most crucial steps in hydrogenation of carbonyl compounds. In line with the theoretical predictions, keto–enol tautomerization as a first step in catalytic hydrogenation of the C=O bond is a subject of ongoing discussion in catalytic studies on real powdered materials.^{26–28}

It should be pointed out that the enol-based mechanism of hydrogenation of carbonyl compounds relies on two largely independent processes: (i) formation and stabilization of normally energetically unstable enol species followed by (ii) hydrogenation of the C=C bond. In order to experimentally realize this predicted low-barrier hydrogenation pathway, both parts of the problem need to be solved in a catalytic process. In particular, formation and stabilization of enol species as a reaction intermediate is a highly challenging task, as enols

normally undergo the reverse process to form a more stable ketone form of the molecule.²¹

In this report, we address the first issue—stabilization of enols on a catalytic surface under the reaction conditions—and demonstrate that enols can be formed and stabilized on Pt by hydrogen bonding with the coadsorbed ketone form of the same molecule. Importantly, we provide clear spectroscopic evidence that multiple hydrogen bonds can be formed with a single carbonyl group resulting in formation and stabilization of more than one enol per single ketone molecule. Formation of different types of ketone–enol oligomers—dimers and trimers—was observed in this study, where evolution exhibits a strong temperature dependence pointing to the decisive role of the kinetic effects in these processes. Obtained results provide important insights into the mechanisms of formation and stabilization of enols on transition metal surfaces, which can be applied for purposeful functionalization of catalytic surfaces to make them capable of stabilizing large amounts of enol intermediates.

RESULTS AND DISCUSSION

In order to obtain these microscopic insights, we carried out a mechanistic study on acetophenone adsorption and chemical transformations over Pt(111) surface in a broad range of temperature conditions. We employed a unique combination of experimental techniques including molecular beams, scanning tunneling microscopy (STM), and infrared reflection absorption spectroscopy (IRAS) capable of providing both microscopic real space information on the distribution of surface species as well as the spectroscopic information on

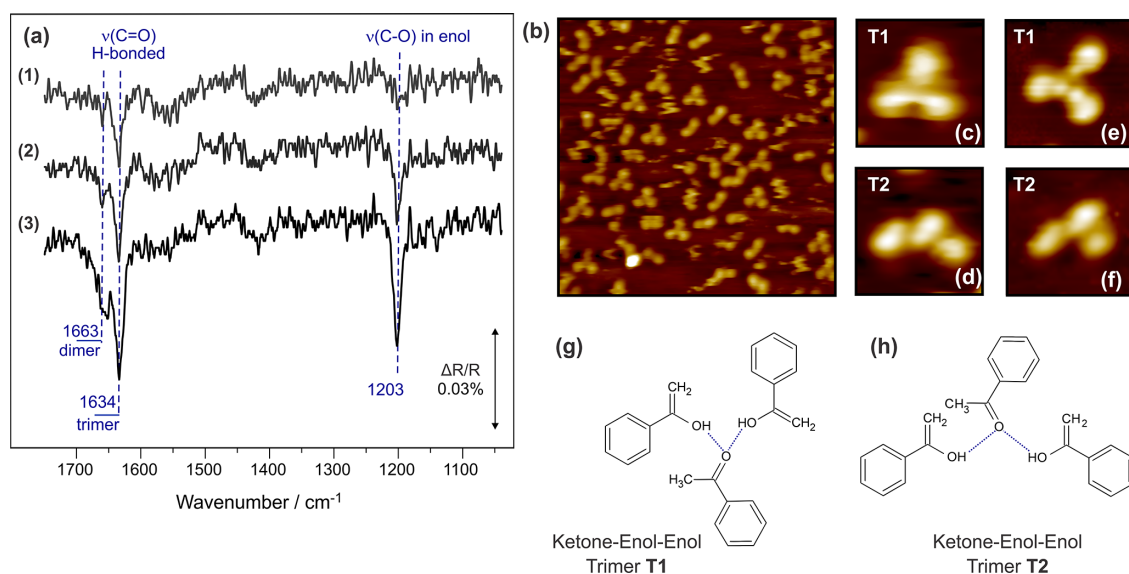


Figure 2. (a) (1–3) IR spectra of acetophenone obtained for different submonolayer coverages recorded on Pt(111) at 280 K (exposures are (1) 1.3×10^{14} , (2) 2.7×10^{14} , and (3) 9.0×10^{14} molecules- cm^{-2}). (b) STM image of acetophenone on Pt(111) (exposure at 285 K; acquisition temperature 285 K; 1 V, 0.29 nA, $15 \times 15 \text{ nm}^2$). (c and d) Close-up images of two type of trimers (T1 and T2) obtained under the conditions described in b. (e and f) Close-up images of two type of trimers (T1 and T2) obtained after exposure at 285 K followed by the acquisition at 115 K. (g and h) Proposed structures of the trimer species T1 and T2, correspondingly.

their chemical nature. Acetophenone was chosen as a model molecule, which can undergo ketone–enol tautomerization, has a relatively high binding energy on Pt(111) to remain on the surface under the high-temperature reaction conditions, and exhibits quite simple chemical structure resembling a large variety of carbonyl compounds. In our earlier studies performed in the low-temperature range, formation of two different types of dimers was detected.²⁹ Figure 1 summarizes the most important observations of this study, which are relevant for further discussion. Briefly, above ca. 200 K the majority of acetophenone molecules are agglomerated to dimers on Pt(111). Two types of dimer species can be imaged by STM, which are shown in the inset of the Figure 1b. The first and more abundant type of dimer (D1) consists of two identical protrusions, each of them exhibiting a bright spot related to an acetyl group and a darker area related to the aromatic ring. The second dimer (D2) is imaged as asymmetric species, with one-half being identical to one-half of the dimer D1 and the other half not exhibiting the bright spot. A small fraction (16%) of acetophenone is adsorbed as monomers and imaged as a protrusion with a bright spot and a darker area, which is identical to the half of the symmetric dimer D1. The IRAS spectra shown in Figure 1a allowed for spectroscopic identification of both types of dimers. Spectra (1 and 2) obtained at submonolayer acetophenone coverages show in general the same vibrational bands as the spectrum obtained for acetophenone multilayer (3) representing non-perturbed molecular species. The most prominent vibrational band at 1683 cm^{-1} is related to the C=O stretching bond vibration in acetophenone.³⁰ At submonolayer coverages, there are two new vibrational bands, which are not present in the unperturbed spectrum of the multilayer: the band at 1203 cm^{-1} , which is typical for a single C–O bond in alkoxy groups and alcohols,^{31,32} and the band at 1663 cm^{-1} , which can be

attributed to the C=O bond involved in hydrogen bonding.^{33–36} The observed strong correlation in the appearance of these two new bands allows us to conclude that they are related to the dimer species, in which one of the molecules is transformed to the enol form as indicated by a vibration of the C–O single bond (1203 cm^{-1}), and the other molecule is present in the ketone form, in which the carbonyl group is involved in hydrogen bonding with the OH group of the enol and therefore is strongly red shifted to 1663 cm^{-1} .²⁹ This latter assignment is in an excellent agreement with the earlier experimental and theoretical studies on the keto–enol tautomerization in diketones and ketoesters leading to formation of chelated ring-like ketone/enol tautomers.^{33–36} In these structures, one carbonyl group converts to the C–O(H) bond and forms enol while the oxygen atom of the second carbonyl group stabilizes the OH group of the newly formed enol by H bonding, thus resulting in the $-\text{C}=\text{O} \cdots \text{H}-\text{O}-$ structure. Generally, two phenomena can lead to a red shift of the C=O bond in these types of keto–enol species: (i) mixing of the C=C and the C=O stretching vibrations and (ii) H bonding between the $-\text{C}=\text{O}$ and $\text{H}-\text{O}-$ groups in the dimer, which results in a downward shift of the C=O stretching frequency for different carbonyl compounds.³⁷ This latter effect is related to the donor–acceptor nature of H bonding and was predicted to comply with the following trend: the higher acidity of the donor participating in the hydrogen bond ($\text{H}-\text{O}$ group) results in the larger frequency shift of the acceptor ($-\text{C}=\text{O}$ group).^{37,38} Since the dimers discussed in this study consist of two individual molecules and the mixing of the C=C and C=O bonds is not possible to the same extent as it would be feasible for a single ring-like ketone/enol tautomer of diketones and ketoesters, the observed strong frequency shift (20 cm^{-1}) can be mostly related to hydrogen bonding between the acidic hydrogen of the OH group in the

enol and the oxygen involved in the carbonyl group of the ketone. The other type of dimers (D1) as well as the monomers exhibit a vibrational frequency of the C=O bond at 1683 cm^{-1} , which is close to the unperturbed value detected in the multilayer spectra and in the gaseous acetophenone.³⁰ This observation allows us to suggest that the dimer D1 consists of two ketone molecules, which are not strongly perturbed by the intermolecular interaction and which interact most likely via the hydrogen bonding between the carbonyl group and the hydrogen atoms of the methyl groups. These hydrogen atoms are considerably less acidic than that involved in the OH group, and therefore, their interaction with the carbonyl group does not significantly shift the vibrational frequency of the C=O bond. The hypothesized structures of both types of dimers are shown as the insert in Figure 1e and 1f. It should be emphasized that the vibrational spectrum (3) of acetophenone multilayer is related to the ketone form acetophenone as it is the thermodynamically most stable configuration,²¹ and for this reason it does not contain spectroscopic signatures of the enol species. To form and stabilize the normally unstable enol form of acetophenone, an interaction with the underlying metal surface is required, which is most likely responsible for two processes: (i) perturbation of the electronic structure which promotes H transfer to form the enol and (ii) providing two adjacent adsorption sites to enable ketone–enol dimer formation in which the enol species is stabilized by strong hydrogen bonding to the carbonyl group of the ketone.

It is interesting to note that the dimers D1 are found in two enantiomeric forms as *S,S* and *R,R* dimers according to the definition given in ref 39, while dimers D2 are heterochiral. For more extended discussion on the chirality of the both dimers see the Supporting Information.

With increasing temperature, new species appear on the surface as evidenced both by vibrational spectra as well as by STM. Figure 2a displays the IR spectra obtained at different submonolayer coverages at 280 K, which show the appearance of a new vibrational band at 1634 cm^{-1} . This band is strongly shifted by 49 cm^{-1} with respect to the frequency of the C=O vibration in the unperturbed molecule (1683 cm^{-1}) and by 29 cm^{-1} with respect to the C=O bond involved in hydrogen bonding with a single enol molecule (1663 cm^{-1}) as discussed above. This new band appears already at the lowest coverage as the most prominent vibration simultaneously with the band at 1203 cm^{-1} , which is related to the stretching mode of the single C–O bond in the enol form of acetophenone. With increasing coverage, both bands grow in intensity and the additional band at 1663 cm^{-1} evolves and becomes more pronounced. Taking into account the fact that the C=O double bond strongly shifts when involved in hydrogen bonding with acidic hydrogen and there are no other possible prominent vibrations, i.e., exhibiting a large dynamic dipole moment, in this vibrational region other than the C=O bond, the band at 1634 cm^{-1} can be most likely assigned to the stretching mode of the C=O bond, which is involved in hydrogen bonding with two enol molecules via the HO groups. This hypothesis is corroborated by the microscopic observations. Figure 2b shows the STM images obtained after acetophenone deposition at 285 K followed by the image acquisition at the same temperature. It can be clearly seen that a new type of surface species—acetophenone trimers—are populated under these conditions. Two types of trimers were observed in our study, which are indicated as T1 (Figure 2c) and T2 (Figure 2d) with T1 exhibiting a flower-shaped form,

while the trimer T2 appears as a hat-shaped species. Note that the surface species are very mobile at room temperature, which results in quite noisy STM images. For this reason, the intramolecular structure of the surface trimers could not be resolved at the high-temperature conditions. When the surface was cooled to 115 K, the trimer species appear less noisy (Figure 2e and 2f); however, it should be kept in mind that the intermolecular structure observed at low temperature might deviate from the structure of the trimers under the high-temperature conditions. The strong shift of the C=O stretching mode in the trimers is in excellent agreement with the previous spectroscopic observations obtained for the danthron molecule,⁴⁰ which is shown in the Figure 3. In this

Danthron

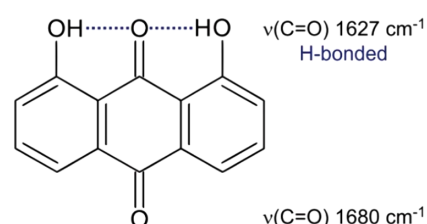


Figure 3. Molecular structure of danthron molecule. Vibrational frequencies of a free-standing and double H-bonded C=O group are given as numbers on the right.⁴⁰

molecule, the free-standing C=O double bond exhibits a stretching mode at 1680 cm^{-1} , which is typical for carbonyl compounds. On the other hand, the second carbonyl group involved in hydrogen bonding with two neighboring hydroxyl groups shows a strong red shift by 53 cm^{-1} . This observation obeys the vibrational frequency shift rule discussed above: the stronger the hydrogen bonding interaction, the stronger the shift of the C=O vibrational band. The very similar frequency shifts— 49 cm^{-1} in this study and 53 cm^{-1} for the C=O bond involved in hydrogen bonding with two hydroxyl groups in danthron—additionally support the assignment of the vibrational peak at 1634 cm^{-1} to the stretching vibration of the carbonyl group involved into H bonding with two enol molecules. The schematic representation of the possible trimer structures based on both the spectroscopic and the microscopic information is shown in Figure 2g and 2h.

Previously, formation of acetophenone oligomers was reported by Demers-Carpentier et al.⁴¹ at room temperature, who hypothesized formation of trimers consisting of solely enol molecules based on the STM and HREELS results. The most intense vibrational band at 1640 cm^{-1} observed in their study was assigned to a C=C stretching vibration of enol species, which is, however, quite unlikely as this bond exhibits a small dynamic dipole moment resulting in low-intensity bands as compared to the C=O and C–O vibrations. Taking into account the highest intensity of the vibration at 1640 cm^{-1} and lower resolution of HREELS, we hypothesize that this band might be rather related to C=O stretching vibration involved into hydrogen bonding with two enol molecules.

Thus, two types of surface species containing enols were observed in our study at Pt(111) at room temperature: (i) ketone–enol–enol trimers, characterized by the vibrational modes at 1634 and 1203 cm^{-1} , which are related to the double

hydrogen-bonded C=O bond in the ketone form of acetophenone and the C–O single bonds in two enol molecules, correspondingly, and (ii) ketone–enol dimers exhibiting the bands at 1663 and 1203 cm^{-1} , related to the hydrogen-bonded carbonyl of the ketone and the C–O vibration of a single enol molecule, respectively. No ketone–ketone dimers or monomers are present above 240 K on the surface as evidenced by the missing band at 1683 cm^{-1} related to these mostly unperturbed surface species.

It should be emphasized that we obtained spectroscopic evidence that a single ketone molecule is able to stabilize multiple enol molecules on surfaces: the phenomenon, which is to the best of our knowledge not known for single carbonyl compounds for the liquid and gas phase. This phenomenon can be potentially based on different surface-related effects including (i) kinetic effects, i.e., the decrease of the energy barrier for the intramolecular H transfer from the CH_3 to the carbonyl group to form enol and/or (ii) energetic stabilization of the otherwise unstable enol form via formation of trimer species (or dimers as observed in the lower temperature range) through hydrogen bonding between O–H and C=O groups of the enol and ketone species, correspondingly.

The reduction of the energy barrier for intramolecular hydrogen transfer can potentially arise for two reasons: first, the interaction with the underlying metal might strongly weaken the C–H bond of the methyl group so that hydrogen can be easier transferred to the carbonyl group. A similar effect was previously reported, e.g., for alkanes adsorbed on transition metals as evidenced by appearance of soft C–H stretching vibrational modes in IR spectra,^{42–44} which, however, were not observed in this study. Second, the activation barrier might be potentially reduced due to the formation of oligomer species (trimers or dimers) interacting via hydrogen bonding, as it was recently demonstrated, e.g., for the gaseous dimers of β -cyclohexandione⁴⁵ and cyclopentanone.⁴⁶ In such concerted process, high energy costs for H transfer to the carbonyl group is compensated by simultaneous establishing strong hydrogen bonding between an OH group of the enol and the C=O group of the ketone. In this case, the surface can provide adjacent adsorption sites enabling oligomer formation and by this assisting the keto–enol tautomerization process.

The next feasible phenomenon—energetic stabilization of the enol species by H bonding in an oligomer—is related to the fact that the enol form is usually energetically less favorable than the ketone one.²¹ However, the interaction between the carbonyl group of the ketone and the OH group of the enol can potentially stabilize the latter species on the surface via strong hydrogen bonding. In this scenario, the surface also acts as a support providing adjacent adsorption sites.

It should be pointed out that all three mechanisms might potentially contribute to the formation and/or stabilization of the enol species on the surface. Even though the degree of their contributions to the overall process is not clear so far, it can be quite reliably claimed that at least one of the mechanisms related to dimer/trimer formation must be acting since the enol form was observed spectroscopically only if oligomers were present on the surface.

In order to obtain more insights into the formation mechanisms of dimer and trimer species, we performed spectroscopic studies systematically varying the temperature in the range from 115 to 280 K. The corresponding IR spectra related to the coverages close to saturation are shown in the Figure 4. At the lowest temperature (115 K), only the band at

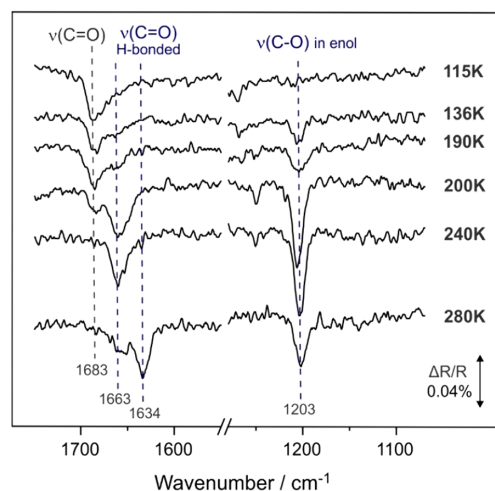


Figure 4. IR spectra of acetophenone adsorbed on Pt(111) at the temperatures indicated at the right side. Only the C=O and C–O stretching regions are shown. All spectra were obtained at submonolayer coverages after acetophenone exposures of 2.3×10^{15} (115 K), 3.8×10^{14} (136 K), 1.0×10^{16} (190 K), 6.5×10^{14} (200 K), 4.0×10^{14} (240 K), and 9.0×10^{14} (280 K) molecules- cm^{-2} .

1683 cm^{-1} can be observed, which is related to the C=O stretching vibrational frequency of a nearly unperturbed molecule. At this temperature acetophenone is present on the surface only as monomer species as evidenced by STM (not shown). Starting from 136 to 190 K, two new bands evolve—at 1663 cm^{-1} , which appears first as a shoulder, and at 1203 cm^{-1} —pointing to formation of ketone–enol dimers. These bands gain in absolute and relative intensity with increasing temperature and become the most prominent vibrational peaks in the temperature range 200–240 K. It should be noted that at least up to 200 K not only ketone–enol dimers but also ketone–ketone dimers are present on the surface as seen by STM and IRAS (see Figure 1). In the temperature range 240–280 K, the vibrational band at 1634 cm^{-1} evolves pointing to the formation of the ketone–enol–enol trimers, which coexist with the ketone–enol dimers as suggested both by IRAS and by STM.

On the basis of the strong temperature dependence observed for the evolution of the ketone–enol(s) dimers and trimers on Pt surface and taking into account the above discussion on the possible mechanisms of the ketone–enol(s) oligomer formation, it can be concluded that the kinetic effects play most likely the major role in this process. Obviously, a kinetic barrier for hydrogen transfer to form the enol species must be overcome in the reaction of keto–enol tautomerization. This becomes possible above ca. 136 K (as evidenced by IRAS) to form the first enol molecule involved in a ketone–enol dimer and at around 280 K to form the second enol molecule accommodated in a ketone–enol–enol trimer. This significant difference in the activation barriers for the formation of the first and second enols involved in a dimer or trimer, correspondingly, indicates that keto–enol tautomerization occurs most likely in a concerted process within a complex of molecules (dimers or trimers) and not in an individual acetophenone monomer adsorbed on the surface. If the opposite were true and the rate-limiting step (i.e.,

exhibiting the highest activation barrier) of the overall process would be keto–enol tautomerization in the adsorbed monomer species followed by an easier (i.e., considerably less activated) attachment of the formed enol to the carbonyl group of the ketone, very similar activation barriers for dimers and trimers formation can be expected, which strongly contradicts the experimental observation. On the contrary, the concerted process suggests formation of a surface dimer (trimer), in which high energy costs for H transfer from the methyl to the carbonyl group are compensated by simultaneous formation of hydrogen bonds between an OH group of the enol and the C=O group of the ketone. In this case, different activation energies can be expected for dimer and trimer formation since significantly different reacting species are involved in the concerted tautomerization process: two individual monomer species for ketone–enol dimer formation vs dimer and monomer species for building a ketone–enol–enol trimer. In the latter process, formation of a trimer can be expected to have a higher overall activation barrier since the formation of a second hydrogen bond—between a second enol and a carbonyl group of the ketone–enol dimer—might compensate for the barrier for hydrogen transfer most likely only to a low extent since the C=O bond is already involved in H bonding with the first enol molecule. In contrast, formation of ketone–enol dimer involves strong hydrogen bonding of the enol to a nonbonded carbonyl group, which can compensate for the energy barrier for H transfer to a greater extent and therefore might result in a lower apparent activation energy.

It should be pointed out that at all investigated temperatures the enol form of acetophenone was observed always as a complex with a ketone molecule—either in a dimer or in a trimer. Individually adsorbed enol species were detected neither by IRAS nor by STM at all investigated reaction conditions, suggesting that the enol form can be present on the surface only if stabilized via hydrogen bonding with the carbonyl group of the ketone species. Thus, two phenomena might be considered as being most likely responsible for enol evolution on Pt: (i) formation of the enol species in the concerted process within a dimer (trimer) complex and (ii) energetic stabilization of the enol form of acetophenone via H bonding between the OH group(s) of the enol(s) and the carbonyl group of the ketone.

CONCLUSIONS

In summary, formation of acetophenone oligomers—dimers and trimers—was observed on Pt(111) in a broad range of temperature conditions by STM. The spectroscopic studies performed by IRAS on these oligomer-containing surfaces revealed the chemical structure of the adsorbed species. The trimer species most likely consist of one ketone molecule attached to two enol molecules via hydrogen bonding between the carbonyl group of the ketone and the OH groups of the enols. This strong interaction between the carbonyl group and two hydroxyl groups results in a pronounced characteristic frequency shift of the C=O bond by 49 cm^{-1} . Additionally, two types of dimer species—ketone–ketone and ketone–enol dimers—were detected. A strong temperature dependence of dimers and trimers formation was observed in this study, providing atomistic-level details on the surface-assisted keto–enol tautomerization process. Most likely, hydrogen transfer from the methyl group to the carbonyl group to produce enol is the rate-limiting step, which might occur in a concerted way

within a complex of either two or three acetophenone molecules. In this process, the energy barrier for hydrogen transfer can be potentially compensated by simultaneous formation of a hydrogen bond between the OH group of the enol and the carbonyl group of the ketone. Importantly, enol species were detected only as a part of dimers or trimers, suggesting that energetic stabilization of the normally less stable enol form of acetophenone via hydrogen bonding with a ketone molecule plays an important role in the overall process. One of the most important results of this study is obtaining clear microscopic and spectroscopic evidence that one ketone molecule can participate in formation and energetic stabilization of more than one enol molecule via multiple hydrogen bonding. This type of interaction might be utilized for purposeful functionalization of catalytic surfaces with carbonyl-containing species, which can promote formation and stabilize multiple enols per single carbonyl group. These types of surfaces are envisaged to have a high potential for enabling a low-barrier hydrogenation route of carbonyl compounds relying on keto–enol tautomerization as a first step followed by low-barrier hydrogenation of the C=C bond. The results of this study provide important atomistic-level insights contributing to rational design of such type of functionalized catalytic surfaces.

ASSOCIATED CONTENT

Supporting Information

The Supporting Information is available free of charge on the ACS Publications website at DOI: 10.1021/acscatal.9b01481.

Experimental details and figure (PDF)

AUTHOR INFORMATION

Corresponding Author

*E-mail: schauermann@pctc.uni-kiel.de.

ORCID

Swetlana Schauermann: 0000-0002-9390-2024

Notes

The authors declare no competing financial interest.

ACKNOWLEDGMENTS

Support from the European Research Council (ERC Starting Grant ENREMOS, project no. 335205) is gratefully acknowledged.

REFERENCES

- (1) Somorjai, G. A. *Introduction to Surface Chemistry and Catalysis*, 2nd ed.; John Wiley & Sons: New York, 2010.
- (2) Collman, J. P.; Wang, Z.; Straumanis, A.; Quelquejeu, M.; Rose, E. An Efficient Catalyst for Asymmetric Epoxidation of Terminal Olefins. *J. Am. Chem. Soc.* **1999**, *121*, 460–461.
- (3) Taylor, M. S.; Jacobsen, E. N. Asymmetric Catalysis by Chiral Hydrogen-Bond Donors. *Angew. Chem., Int. Ed.* **2006**, *45*, 1520–1543.
- (4) Mallat, T.; Orglmeister, E.; Baiker, A. Asymmetric Catalysis at Chiral Metal Surfaces. *Chem. Rev.* **2007**, *107*, 4863–4890.
- (5) Meemken, F.; Baiker, A. Recent Progress in Heterogeneous Asymmetric Hydrogenation of C=O and C=C Bonds on Supported Noble Metal Catalysts. *Chem. Rev.* **2017**, *117*, 11522–11569.
- (6) Gellman, A. J.; Tysoe, W. T.; Zaera, F. Surface Chemistry for Enantioselective Catalysis. *Catal. Lett.* **2015**, *145*, 220–232.
- (7) Rodríguez-García, L.; Hungerbühler, K.; Baiker, A.; Meemken, F. The Critical Role of Tilted Cinchona Surface Species for Enantioselective Hydrogenation. *ACS Catal.* **2017**, *7*, 3799–3809.

- (8) Marshall, S. T.; O'Brien, M.; Oetter, B.; Corpuz, A.; Richards, R. M.; Schwartz, D. K.; Medlin, J. W. Controlled Selectivity for Palladium Catalysts Using Self-Assembled Monolayers. *Nat. Mater.* **2010**, *9*, 853–858.
- (9) Marshall, S. T.; Medlin, J. W. Surface-Level Mechanistic Studies of Adsorbate–Adsorbate Interactions in Heterogeneous Catalysis by Metals. *Surf. Sci. Rep.* **2011**, *66*, 173–184.
- (10) Sonstrom, P.; Baumer, M. Supported Colloidal Nanoparticles in Heterogeneous Gas Phase Catalysis: On the Way to Tailored Catalysts. *Phys. Chem. Chem. Phys.* **2011**, *13*, 19270–19284.
- (11) Lien, C.-H.; Medlin, J. W. Control of Pd Catalyst Selectivity with Mixed Thiolate Monolayers. *J. Catal.* **2016**, *339*, 38–46.
- (12) Hutchings, G. J.; King, F.; Okoye, I. P.; Padley, M. B.; Rochester, C. H. Selectivity Enhancement in the Hydrogenation of A, B-Unsaturated Aldehydes and Ketones Using Thiophene-Modified Catalysts. *J. Catal.* **1994**, *148*, 453–463.
- (13) Chiu, M. E.; Kyriakou, G.; Williams, F. J.; Watson, D. J.; Tikhov, M. S.; Lambert, R. M. Sulfur, Normally a Poison, Strongly Promotes Chemoselective Catalytic Hydrogenation: Stereochemistry and Reactivity of Crotonaldehyde on Clean and S-Modified Cu(111). *Chem. Commun.* **2006**, 1283–1285.
- (14) Wu, B.; Huang, H.; Yang, J.; Zheng, N.; Fu, G. Selective Hydrogenation of A,B-Unsaturated Aldehydes Catalyzed by Amine-Capped Platinum-Cobalt Nanocrystals. *Angew. Chem., Int. Ed.* **2012**, *51*, 3440–3443.
- (15) Kwon, S. G.; Krylova, G.; Sumer, A.; Schwartz, M. M.; Bunel, E. E.; Marshall, C. L.; Chattopadhyay, S.; Lee, B.; Jellinek, J.; Shevchenko, E. V. Capping Ligands as Selectivity Switchers in Hydrogenation Reactions. *Nano Lett.* **2012**, *12*, 5382–5388.
- (16) Pang, S. H.; Medlin, J. W. Controlling Catalytic Selectivity Via Adsorbate Orientation on the Surface: From Furfural Deoxygenation to Reactions of Epoxides. *J. Phys. Chem. Lett.* **2015**, *6*, 1348–1356.
- (17) Ernst, J. B.; Muratsugu, S.; Wang, F.; Tada, M.; Glorius, F. Tunable Heterogeneous Catalysis: N-Heterocyclic Carbenes as Ligands for Supported Heterogeneous Ru/K-Al₂O₃ Catalysts to Tune Reactivity and Selectivity. *J. Am. Chem. Soc.* **2016**, *138*, 10718–10721.
- (18) Ernst, J. B.; Schwermann, C.; Yokota, G.-i.; Tada, M.; Muratsugu, S.; Doltsinis, N. L.; Glorius, F. Molecular Adsorbates Switch on Heterogeneous Catalysis: Induction of Reactivity by N-Heterocyclic Carbenes. *J. Am. Chem. Soc.* **2017**, *139*, 9144–9147.
- (19) Dostert, K.-H.; O'Brien, C. P.; Ivars-Barceló, F.; Schauermaann, S.; Freund, H.-J. Spectators Control Selectivity in Surface Chemistry: Acrolein Partial Hydrogenation over Pd. *J. Am. Chem. Soc.* **2015**, *137*, 13496–13502.
- (20) Schauermaann, S. Partial Hydrogenation of Unsaturated Carbonyl Compounds: Toward Ligand-Directed Heterogeneous Catalysis. *J. Phys. Chem. Lett.* **2018**, *9*, 5555–5566.
- (21) Rappoport, Z. *The Chemistry of Enols (Chemistry of Functional Groups Series)*; John Wiley & Sons Ltd.: Chichester, 1990.
- (22) Rasmussen, A. M. H.; Groves, M. N.; Hammer, B. Remote Activation of Chemical Bonds in Heterogeneous Catalysis. *ACS Catal.* **2014**, *4*, 1182–1188.
- (23) Yang, B.; Wang, D.; Gong, X.-Q.; Hu, P. Acrolein Hydrogenation on Pt(211) and Au(211) Surfaces: A Density Functional Theory Study. *Phys. Chem. Chem. Phys.* **2011**, *13*, 21146–21152.
- (24) De Vrieze, J. E.; Thybaut, J. W.; Saeys, M. Role of Keto–Enol Tautomerization in the Copper-Catalyzed Hydrogenation of Ketones. *ACS Catal.* **2019**, *9*, 3831.
- (25) De Vrieze, J. E.; Thybaut, J. W.; Saeys, M. Role of Keto–Enol Tautomerization in the Copper-Catalyzed Hydrogenation of Ketones. *ACS Catal.* **2019**, *9*, 3831–3839.
- (26) Schulz, K. H.; Cox, D. F. Surface Reactions of Acrolein and Propionaldehyde on Cuprous Oxide(100): Nonselective Oxidation and Enolate-Mediated Side Reactions to C3 Products. *J. Phys. Chem.* **1993**, *97*, 3555–3564.
- (27) Sim, W.-S.; Li, T.-C.; Yang, P.-X.; Yeo, B.-S. Isolation and Identification of Surface-Bound Acetone Enolate on Ni(111). *J. Am. Chem. Soc.* **2002**, *124*, 4970–4971.
- (28) Mahapatra, M.; Burkholder, L.; Garvey, M.; Bai, Y.; Saldin, D. K.; Tysoe, W. T. Enhanced Hydrogenation Activity and Diastereomeric Interactions of Methyl Pyruvate Co-Adsorbed with R-1-(1-Naphthyl)Ethylamine on Pd(111). *Nat. Commun.* **2016**, *7*, 12380.
- (29) Attia, S.; Schmidt, M.-C.; Schröder, C.; Pessier, P.; Schauermaann, S. Surface-Driven Keto–Enol Tautomerization: Atomistic Insights into Enol Formation and Stabilization Mechanisms. *Angew. Chem., Int. Ed.* **2018**, *57*, 16659–16664.
- (30) Gambi, A.; Giorgianni, S.; Passerini, A.; Visinoni, R.; Gheretti, S. Infrared Studies of Acetophenone and Its Deuterated Derivatives. *Spectrochimica Acta Part A: Molecular Spectroscopy* **1980**, *36*, 871–878.
- (31) Mitchell, W. J.; Xie, J.; Jachimowski, T. A.; Weinberg, W. H. Carbon Monoxide Hydrogenation on the Ru(001) Surface at Low Temperature Using Gas-Phase Atomic Hydrogen: Spectroscopic Evidence for the Carbonyl Insertion Mechanism on a Transition Metal Surface. *J. Am. Chem. Soc.* **1995**, *117*, 2606–2617.
- (32) Weldon, M. K.; Friend, C. M. Probing Surface Reaction Mechanisms Using Chemical and Vibrational Methods: Alkyl Oxidation and Reactivity of Alcohols on Transitions Metal Surfaces. *Chem. Rev.* **1996**, *96*, 1391–1412.
- (33) Jones, T. E.; Baddeley, C. J. Influence of Modification Conditions on the Interaction of Methylacetoacetate with (R,R)-Tartaric Acid-Modified Ni{111}. *J. Phys. Chem. C* **2007**, *111*, 17558–17563.
- (34) Roubin, P.; Chiavassa, T.; Verlaque, P.; Pizzala, L.; Bodot, H. Ft-Ir Study of Uv-Induced Isomerization of Intramolecularly Hydrogen-Bonded Carbonyl Compounds Isolated in Xenon Matrices. *Chem. Phys. Lett.* **1990**, *175*, 655–659.
- (35) Belova, N. V.; Oberhammer, H.; Girichev, G. V. Tautomeric and Conformational Properties of Methyl Acetoacetate, CH₃OC(O)–CH₂–C(O)CH₃: Electron Diffraction and Quantum Chemical Study. *J. Phys. Chem. A* **2004**, *108*, 3593–3597.
- (36) Matrosov, E. I.; Kabachnik, M. I. Characteristics of the Cis and Trans Enolic Structures in the I.R. Spectra. *Spectrochimica Acta Part A: Molecular Spectroscopy* **1972**, *28*, 191–196.
- (37) Fried, S. D.; Bagchi, S.; Boxer, S. G. Measuring Electrostatic Fields in Both Hydrogen-Bonding and Non-Hydrogen-Bonding Environments Using Carbonyl Vibrational Probes. *J. Am. Chem. Soc.* **2013**, *135*, 11181–11192.
- (38) Nolasco, M. M.; Ribeiro-Claro, P. J. A. C-H···O Hydrogen Bonds in Cyclohexenone Reveal the Spectroscopic Behavior of C_{sp}³-H and C_{sp}²-H Donors. *ChemPhysChem* **2005**, *6*, 496–502.
- (39) Demers-Carpentier, V.; Goubert, G.; Masini, F.; Dong, Y.; Rasmussen, A. M. H.; Hammer, B.; McBreen, P. H. Scanning Tunneling Microscopy Measurements of the Full Cycle of a Heterogeneous Asymmetric Hydrogenation Reaction on Chirally Modified Pt(111). *J. Phys. Chem. Lett.* **2012**, *3*, 92–96.
- (40) Madsen, F.; Terpager, I.; Olksær, K.; Spanget-Larsen, J. Ultraviolet-Visible and Infrared Linear Dichroism Spectroscopy of 1,8-Dihydroxy-9,10-Anthraquinone Aligned in Stretched Polyethylene. *Chem. Phys.* **1992**, *165*, 351–360.
- (41) Demers-Carpentier, V.; Laliberté, M.-A.; Lavoie, S.; Mahieu, G.; McBreen, P. H. Two-Dimensional Self-Assembly and Catalytic Function: Conversion of Chiral Alcohols into Self-Assembled Enols on Pt(111). *J. Phys. Chem. C* **2010**, *114*, 7291–7298.
- (42) Demuth, J. E.; Ibach, H.; Lehwald, S. Ch Vibration Softening and the Dehydrogenation of Hydrocarbon Molecules on Ni(111) and Pt(111). *Phys. Rev. Lett.* **1978**, *40*, 1044–1047.
- (43) Fossier, K. A.; Nuzzo, R. G.; Bagus, P. S.; Wöll, C. The Adsorption of Cyclopropane and Cyclohexane on Cu(111): An Experimental and Theoretical Investigation on the Nature of the Ch–Metal Interaction. *Angew. Chem., Int. Ed.* **2002**, *41*, 1735–1737.
- (44) Hostetler, M. J.; Manner, W. L.; Nuzzo, R. G.; Girolami, G. S. Two-Dimensional Melting Transitions of Rod-Like Molecules Analyzed by Reflection-Absorption Infrared Spectroscopy. *J. Phys. Chem.* **1995**, *99*, 15269–15278.
- (45) Bandyopadhyay, B.; Pandey, P.; Banerjee, P.; Samanta, A. K.; Chakraborty, T. CH···O Interaction Lowers Hydrogen Transfer

Barrier to Keto–Enol Tautomerization of β -Cyclohexanedione: Combined Infrared Spectroscopic and Electronic Structure Calculation Study. *J. Phys. Chem. A* **2012**, *116*, 3836–3845.

(46) Ghosh, A. K.; Chatterjee, P.; Chakraborty, T. Keto–Enol Tautomerization and Intermolecular Proton Transfer in Photoionized Cyclopentanone Dimer in the Gas Phase. *J. Chem. Phys.* **2014**, *141*, 044303.

8.8 Keto–Enol Tautomerization as a First Step in Hydrogenation of Carbonyl Compounds

Publication Data and Reprint

Reference: Smadar Attia, Marvin C. Schmidt, Carsten Schröder, Jann Weber, Ann-Katrin Baumann, Swetlana Schauermann

DOI: 10.1021/acs.jpcc.9b10181

Submitted: 30.10.2019

Accepted: 12.11.2019

Contribution: IRAS measurements, scientific discussions, preparation of parts of the manuscript

Copyright: Reprinted with permission from JPC C from Ref.[238]. Copyright 2020 American Chemical Society.

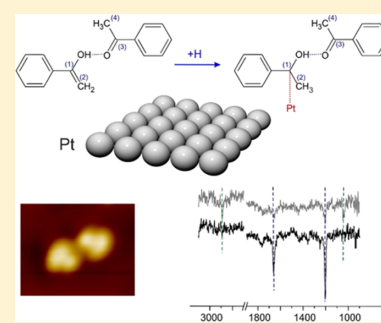
Keto–Enol Tautomerization as a First Step in Hydrogenation of Carbonyl Compounds

Smadar Attia, Marvin C. Schmidt, Carsten Schröder, Jann Weber, Ann-Katrin Baumann, and Swetlana Schauermaⁿ*

Institute of Physical Chemistry, Christian-Albrechts-University Kiel, Max-Eyth-Street 2, 24118 Kiel, Germany

Supporting Information

ABSTRACT: Keto–enol tautomerization of carbonyl compounds to their enol form is theoretically predicted to enable a low-barrier pathway for hydrogenation of normally very stable C=O bond. In the scope of this anticipated mechanism, the reaction can proceed via two consecutive steps, including the formation of enol followed by an H insertion into the enolic C=C bond, and exhibits a lower activation barrier than the direct H insertion into the carbonyl group. Here, we present an experimental study on atomistic level details of hydrogenation of a simple carbonyl compound acetophenone over Pt(111) providing experimental evidence that keto–enol tautomerization plays a crucial role in this reaction. By employing a combination of spectroscopic and imaging techniques, we show that acetophenone forms ketone–enol dimers, in which the normally unstable form of enol is stabilized by H-bonding with the carbonyl group of the neighboring acetophenone molecule. These ketone–enol dimers can attach an H atom to form a reaction intermediate consisting of a partly hydrogenated acetophenone species and nonhydrogenated acetophenone. Based on the spectroscopic assignment of the reaction intermediate, we conclude that H atom can be attached either to the C=C bond of the enol part, or to the strongly weakened C=O bond of the ketone part of the ketone–enol dimer. In both cases, the formation of ketone–enol dimer species was found to be a crucial step in acetophenone hydrogenation. Observed phenomena provide atomistic level insights into the mechanisms of heterogeneously catalyzed hydrogenation of simple carbonyl compounds and can be employed for purposeful modification of catalysts with functional groups capable of stabilizing the enol species.



INTRODUCTION

Heterogeneously catalyzed hydrogenation of carbonyl compounds is an important step for many technically relevant applications, such as aldol condensation, enantioselective hydrogenation of ketoesters, selective hydrogenation of unsaturated ketones, and others.^{1,2} Despite the significance of this process, the mechanistic aspects of C=O bond hydrogenation are poorly understood and were addressed only in a limited number of microscopic level studies.^{3–7} Generally, this class of reactions is highly challenging since it requires the activation of a normally very stable C=O bond for further chemical transformations with hydrogen and hence relies on the catalytic materials capable of effective weakening of the carbonyl bond.

Recently, an alternative low-barrier mechanism for hydrogenation of carbonyl compounds was suggested in a number of theoretical studies, which involves keto–enol tautomerization as a first step.^{8–11} In the scope of this mechanism, the H atom attached to the neighboring α -carbon transfers to the oxygen atom of the carbonyl group in an intramolecular process to form a C–O(H) single bond. Simultaneously, a C=C double bond is formed on the neighboring α -carbon thus producing the enol species. According to the theoretical predictions, the activation barrier to hydrogenate the C=C bond in enol can be significantly lower than the activation barrier for direct

hydrogenation of the C=O bond for different classes of mono- and dicarbonyl compounds.^{8–11} Thus, the overall process might proceed via two consecutive steps involving keto–enol tautomerization followed by hydrogenation of the C=C bond with both of them exhibiting lower energy barriers than the direct hydrogenation of the carbonyl group. This scenario would result in an alternative low-barrier hydrogenation pathway and was frequently discussed as a conceivable mechanism for hydrogenation of carbonyl compounds over powdered catalytic materials.^{12–14} However, the experimental confirmation of this mechanistic picture and a detailed understanding of the individual elementary steps involved are largely missing.

The major problem of this mechanism is related to the instability of enol species that, even if formed, would readily convert to normally more stable ketone form.¹⁵ In our recent studies on acetophenone interaction with Pt(111), we demonstrated that the enol species can be produced on this surface. However, they exist only in the form of ketone–enol dimers¹⁶ or ketone–enol–enol trimers¹⁷ (Supporting Information), in which strong hydrogen bonding between the

Received: October 30, 2019

Revised: November 6, 2019

Published: November 12, 2019

OH group of the enol and the C=O group of the ketone ensures stabilization of the enol species. The stabilization mechanisms of enols on surfaces in the form of dimers and trimers found in these studies are similar to those previously described for chelated ketone/enol tautomers in diketones and ketoesters in the gas phase and solutions.^{18–23}

Despite this recent progress in the understanding of the stabilization mechanisms of adsorbed enol species, no experimental evidence of the involvement of enols into the low-barrier hydrogenation pathway of carbonyl compounds was reported so far. To address this issue, we performed a mechanistic study on hydrogenation of acetophenone over well-defined Pt(111) surface in a broad range of temperature and coverage conditions. We employed a unique combination of surface sensitive techniques including infrared reflection absorption spectroscopy (IRAS), scanning tunneling microscopy (STM), and molecular beam techniques, allowing to address the chemical nature of the surface species and to obtain the real-space information on the intermolecular interactions between the individual molecules. We demonstrate that the formation and stabilization of enol species are strongly dependent on the presence of two different types of adsorbed hydrogen species, weakly bound β_1 and strongly bound β_2 , on the Pt surface reported in earlier studies.²⁴ When both H species are present, no formation of ketone–enol dimers could be observed, neither spectroscopically nor by imaging techniques. However, if the weakly bound β_1 -H is selectively removed and only strongly bound β_2 -H remains on the surface, acetophenone forms ketone–enol dimers, as well as a second type of surface species is formed, which can be spectroscopically assigned to partly hydrogenated form of acetophenone involved in a dimer with the second acetophenone molecule. These observations indicate that (i) the weakly bound β_1 -H species prevent the formation and/or stabilization of enol form of acetophenone, while ketone–enol species can be formed in the presence of strongly bound β_2 -H; (ii) the first hydrogenation step involves ketone–enol dimer species, suggesting that keto–enol tautomerization plays indeed an important role in opening up a low-barrier hydrogenation pathway of carbonyl compounds. The spectroscopically derived reaction intermediates suggest two feasible mechanisms that might be responsible for dimer-induced hydrogenation: (i) formation of the C=C bond in the enol part of the dimer, which might exhibit a lower activation barrier for hydrogenation according to theoretical predictions,^{8–11} and (ii) weakening of the C=O bond in the ketone part of the dimer due to the strong interaction with the acidic hydrogen of the OH group of the enol, which might potentially result in easier H insertion into this highly perturbed carbonyl group.

Obtained atomistic level details on partial hydrogenation of carbonyl compounds provide important insights into the mechanisms of this technologically highly relevant class of reactions. Related phenomena can be employed for controlling keto–enol tautomerization of single carbonyl compounds to enable their low-barrier chemical transformations via e.g., controllable surface functionalization with carbonyl-containing ligands capable of effective stabilization of enol form of ketones and aldehydes.

RESULTS AND DISCUSSION

To investigate adsorption and reactivity of acetophenone on Pt(111), we employed a combination of molecular beam

techniques, IRAS and STM to obtain detailed information on the nature of the adsorbed surface species and their spatial distribution under the isothermal reaction relevant conditions. Previously, we detected the formation of surface ketone–enol dimers¹⁶ and ketone–enol–enol trimers¹⁷ on this surface. Figure 1 summarizes the most important observations of this

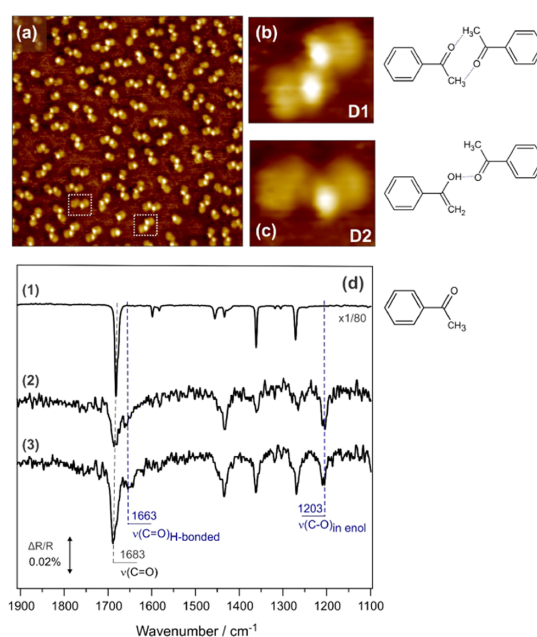


Figure 1. (a) STM image of acetophenone on pristine Pt(111) (exposure at 200 K; acquisition temperature 115 K; 1 V, 0.29 nA, $15 \times 15 \text{ nm}^2$); (b) and (c) close-up images of two types of dimers (D1 and D2); on the right the suggested structures of the ketone–ketone (D1) and ketone–enol (D2) dimers are displayed. (d) (1): IR spectrum of acetophenone multilayers obtained at 156 K, (2, 3): IR spectra of acetophenone adsorbed on pristine Pt(111) at different submonolayer coverages obtained at 170 K.

study, which are relevant for further discussion. Figure 1a shows the STM image of acetophenone adsorbed on Pt(111) at 200 K. The majority of the adsorbed molecules (84%) are agglomerated into dimer species of two different types: (i) the more abundant symmetric D₁ species, consisting of two identical protrusions with a brighter and darker areas (Figure 1b) and (ii) the less abundant asymmetric D₂ dimer (Figure 1c). In the latter species, one half exhibits the same contrast as half of the dimer D₁ (combining the brighter and the darker area), while the second half is lacking this structure. A small fraction (16%) of adsorbed species appear as monomers and imaged as a protrusion with a bright spot and a darker area identical to the half of the symmetric dimer D₁.

To identify the chemical structure of the adsorbed species, IR spectra were obtained at the submonolayer coverages (Figure 1d, spectra (2) and (3)) and at multilayer coverages (Figure 1d, spectrum (1)), with the latter serving as a reference for unperturbed acetophenone species. Most of the vibrational bands observed at submonolayer coverages can be found in the spectrum of acetophenone ice with the most prominent band at 1683 cm^{-1} , which is related to the C=O stretching vibration in unperturbed acetophenone.²⁵ There are, however,

two new bands, appearing at the submonolayer coverages (marked with blue lines in the Figure 1d): the band at 1203 cm^{-1} , which is related to a single C–O bond in enol species, and the band at 1663 cm^{-1} , which was assigned to the C=O bond involved in hydrogen bonding with strongly acidic hydrogen and therefore vibrationally red shifted by 20 cm^{-1} from the unperturbed value.^{21,26–28} Based on the observed strong correlation in the appearance and coverage-dependence of these two bands as well as the microscopic observation that most of the adsorbed molecules are agglomerated in dimers in this temperature range, we concluded that an adsorbed ketone–enol dimer species is formed, in which the enol part of the dimer is stabilized by strong H-bonding between the OH group of the enol and the carbonyl group of the ketone molecules.¹⁶ This assignment was additionally confirmed by obtaining IR spectra for isotopically labeled ^{13}C acetophenone.¹⁶ Note that the frequency shift of the H-bonded carbonyls is generally accepted to obey the following trend:^{29,30} the higher is the acidity of the donor (in this case H–O group), the larger is the frequency shift of the acceptor (–C=O group). Thus, the frequency shifts of the C=O group are expected to be the highest when it interacts with the OH group and significantly low when it is hydrogen-bonded to e.g., an H of a methyl group. The suggested structure of the ketone–enol dimer is shown in Figure 1 (right). The ketone–enol dimer is most likely related to the asymmetric dimer species D_2 imaged by STM (Figure 1c) and is characterized by a unique combination of the vibrational bands at 1203 and 1663 cm^{-1} . The other type of dimer – D_1 – was assigned to a combination of two ketone molecules, which are connected via H-bonding between a carbonyl group of one molecule and the nonacidic H of the methyl group of the other molecule. In this case, no or very small vibrational shift of the C=O bond from the unperturbed value (1683 cm^{-1}) is expected due to the low acidity of methyl-H,^{29,30} which is observed experimentally. A more detailed discussion on the assignment of different types of dimers can be found elsewhere.¹⁶

It should be noted that the formation of ketone–enol dimers exhibits a strong temperature dependence: with increasing temperature the fraction of the ketone–enol dimers grows and at the temperature 240 K only ketone–enol dimers are spectroscopically observed¹⁷ (see also Figure S1 in the Supporting Information). Additionally, the third type of acetophenone oligomers appears above 280 K , in which one carbonyl group of the ketone form of acetophenone is connected to two OH groups of the enols. This interaction results in a further frequency shift of the H-bonded C=O vibration to 1634 cm^{-1} .

To obtain more atomistic level insights into initial steps of acetophenone hydrogenation on Pt(111), its adsorption and reactivity behavior were investigated on H-precovered Pt(111) surface. Previously, H adsorption on the Pt(111) surface was comprehensively studied by temperature-programmed desorption (TPD); the review by Christmann^{24,31} summarizes the most important conclusions of this study. Briefly, H forms two distinct states on Pt (111) – the weakly bound β_1 -H state, exhibiting the maximum of the desorption rate at about 225 K , and the strongly bound β_2 -H state, desorbing at approximately 325 K .

To understand how the nature of adsorbed hydrogen affects the adsorption and reactivity behavior of acetophenone, coadsorption of these species was studied on two types of surfaces: (i) Pt containing both β_1 - and β_2 -H states and (ii) Pt

precovered with the β_2 -H only. The latter surface was produced by H adsorption at 150 K , at which both states are populated, followed by heating the surface to 240 K , at which the weakly bound β_1 -H desorbs, while the stronger bound β_2 -H remains on the surface.

Figure 2 shows the results of STM and IRAS studies carried out on H-precovered Pt(111) in the temperature range 190 –

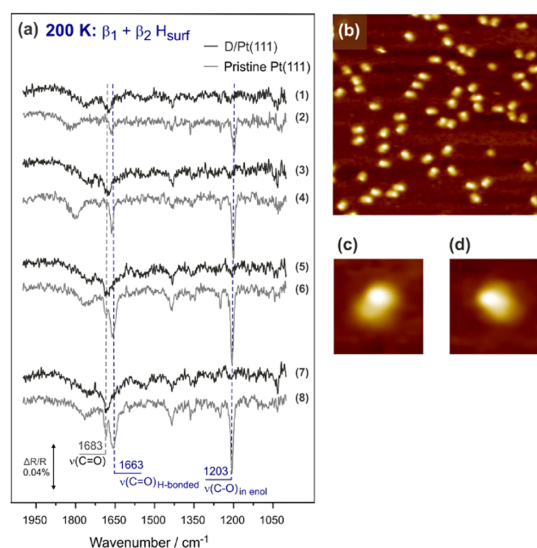


Figure 2. (a) IR spectra of acetophenone obtained on pristine (grey lines) and D-precovered (black lines) Pt(111) at different submonolayer coverages at 200 K . Acetophenone exposure (grey lines) (1) 1.7×10^{14} molecules cm^{-2} , (2) 2.1×10^{14} molecules cm^{-2} , (3) 6.5×10^{14} molecules cm^{-2} , and (4) 1.2×10^{15} molecules cm^{-2} ; (black lines) (1) 3.1×10^{14} molecules cm^{-2} , (2) 5.8×10^{14} molecules cm^{-2} , (3) 2.0×10^{15} molecules cm^{-2} , and (4) 3.9×10^{15} molecules cm^{-2} ; (b–d) STM image of acetophenone adsorbed at H-precovered Pt(111) (H_2 exposure at 150 K ; acetophenone exposure at 190 K ; acquisition temperature 115 K , 1 V , 0.29 nA , (b): $23 \times 23\text{ nm}^2$).

200 K , in which both β_1 - and β_2 -H states are populated. It can be clearly seen that the majority of the surface species on this surface are monomers, which appear as elongated protrusions with a bright spot (Figure 2b–d), similar to those observed on the pristine Pt surface. In line with this observation, the vibrational spectra exhibit only the vibrational features characteristic for unperturbed acetophenone in the ketone form with the most prominent band at 1683 cm^{-1} related to a C=O bond (Figure 2a). Both vibrational features characteristic for ketone–enol dimer (1203 and 1663 cm^{-1}) are absent on the H-precovered surface suggesting the inhibition of dimer formation by coadsorbed hydrogen.

There are several reasons that can be invoked as a possible explanation of this phenomenon. First, the formation of any kind of dimers—either ketone–enol or ketone–ketone ones—requires the formation of hydrogen bonds between the carbonyl group of the ketone and a hydrogen atom of the neighboring molecule, incorporated either into the OH group in case of ketone–enol or into the CH_3 group in case of ketone–ketone species. If H is present on the surface, it might interact with the carbonyl groups via a bond similar to hydrogen bonding thus preventing hydrogen bonding between

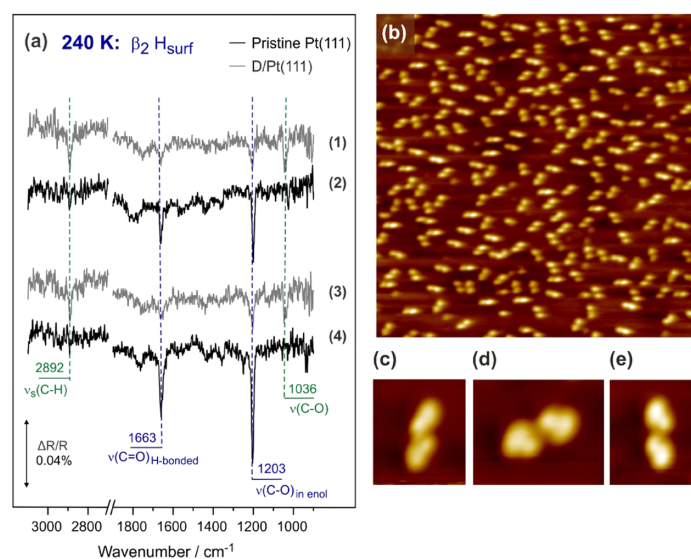


Figure 3. (a) IR spectra of acetophenone adsorbed on pristine (black lines) and D-precovered (grey lines) Pt(111) obtained at 240 K at different submonolayer coverages. Acetophenone exposure: (1) 4.0×10^{14} molecules cm^{-2} , (3) 5.4×10^{14} molecules cm^{-2} ; (black lines), (2) 2.7×10^{14} molecules cm^{-2} , and (4) 4.0×10^{14} molecules cm^{-2} ; (b–e) STM image of acetophenone adsorbed at H-precovered Pt(111) (H_2 exposure at 150 K followed by heating to 240 K; acetophenone exposure at 240 K; acquisition temperature 115 K, 1 V, 0.29 nA, (b): $30 \times 30 \text{ nm}^2$).

neighboring molecules. Second, the formation of ketone–enol species relies on H transfer from the CH_3 group to the O atom of the carbonyl group to form the enol part of the dimer. This process might require considerable perturbation of the molecule's electronic structure by the underlying metal, which might occur effectively on pristine Pt(111) but be hindered on the H-containing surface as a result of weaker interaction between acetophenone and H-precovered Pt. In this case, the inhibition of intramolecular H transfer in acetophenone by coadsorbed H can be a potential reason for missing ketone–enol dimer formation but not the fact that the ketone–ketone dimers are also not formed. For this reason, the first explanation based on hindered intermolecular hydrogen bonding due to competition with adsorbed hydrogen seems to be a more likely scenario as it could account for the lack of the formation of both types of dimers.

In the next step, the surface containing only one type of hydrogen—strongly bound β_2 -H species—was investigated with respect to the interaction with acetophenone. Figure 3a shows the comparison of the vibrational spectra obtained on this surface at 240 K with those recorded at the same temperature on pristine Pt(111). Note that on the pristine Pt(111) surface only ketone–enol dimers are populated at 240 K as evidenced by the presence of the bands at 1203 and 1663 cm^{-1} and the absence of the band at 1683 cm^{-1} (black lines, see also Figure S1). The STM image obtained on β_2 -H-containing Pt(111) is displayed in Figure 3b–d. It can be clearly seen that acetophenone dimers are formed on this surface again and the absolute majority of the adsorbates is accommodated in dimer species. The IR spectra reveal the formation of ketone–enol dimers on the β_2 -H-covered surface as evidenced by the presence of the vibrational bands at 1203 and 1663 cm^{-1} . Importantly, a new and very prominent band at 1036 cm^{-1} appears on this surface, which is present neither

on the pristine Pt(111) surface nor on the surface containing a combination of β_1 - and β_2 -H species. The intensity of this band is comparable to the intensity of the C–O single bond in the ketone–enol dimers (1203 cm^{-1}) suggesting that noticeable amounts of the new species are formed. The vibrational range 1000–1200 cm^{-1} is typical for a single C–O bond, which was reported for gaseous species and a number of oxygenates on different surfaces.^{32–34} Note that the frequency of the new band is approximately 150 cm^{-1} lower than the frequency of 1203 cm^{-1} found ketone–enol dimers, suggesting that the chemical environment of this bond strongly differs from that one existing in the enol form. One of the most likely explanations for this strong frequency shift could be the fact that the C atom connected to O is not involved in the C=C double bond on the other side as in the case of enol species. Indeed, typical C–O vibrational frequencies in saturated alcohols lie in the range 1000–1150 cm^{-1} .³² More specifically, the C–O(H) bond in the nondissociated form of 1-phenylethanol—the hydrogenation product of acetophenone—exhibits a vibrational frequency at 1082 cm^{-1} ,³⁵ which is close to our experimentally observed value of 1036 cm^{-1} . Concomitantly with the appearance of a new C–O single bond, a strong vibrational band evolves at 2892 cm^{-1} , which is typically assigned to C–H stretching vibrations in methyl ($-\text{CH}_3$) or methylene-bridge ($-\text{CH}_2-$) groups^{5,34} and nearly coincides with the C–H stretching frequency of the methyl group in 1-phenylethanol (2886 cm^{-1}).³⁵ Importantly, this frequency is typical for C–H vibrations with C atom being involved in the C–C single bond. In contrast, if the C atom would be involved in the C=C double bond, the =C–H stretching vibration would appear at significantly higher frequencies in the range 2960–3060 cm^{-1} .⁵

Simultaneous evolution of new intense vibrational bands related to (i) C–O single bond and (ii) C–H single bonds with C atom not being involved into the C=C double bond strongly suggests the formation of a new type of surface

species, which most likely originates from partial hydrogenation of acetophenone with one H atom. It should be emphasized that the formation of hydrogenated species occurs in the temperature regime, where the absolute majority of the adsorbates is associated to dimers. Thus, at 240 K the pristine Pt(111) surface contains only ketone–enol dimers but no ketone–ketone dimers or monomers since the bands at 1203 and 1663 cm^{-1} are observed, while the band at 1683 cm^{-1} is not present. At β_2 -H-containing surface, a fraction of these dimers is still present in the ketone–enol form according to spectroscopic observations, while the rest of the dimers—roughly a similar amount as judged by the similar intensities of two C–O single bonds (1203 vs 1036 cm^{-1})—undergoes partial hydrogenation forming H-bonded dimer species consisting of one half-hydrogenated acetophenone molecule and one original acetophenone. Note that since the reactants—the ketone–enol dimers—and the products—the partly hydrogenated acetophenone forming a dimer with the original acetophenone molecule—are found on the surface only in the form of dimers, the hydrogenation step occurs most likely in dimers and not in monomers. Note that the conclusion on the partial hydrogenation of the surface species was deduced from the new spectroscopic signature appearing in the infrared spectra shown in Figure 3a and not from the STM images. The possible full hydrogenation product—1-phenylethanol—was not observed in the gas phase, most likely due to two reasons: (1) the second half-hydrogenation step might require higher reaction temperatures and (2) the detection of the product might be difficult in view of the fact that such heavy molecules as 1-phenylethanol stick to the chamber walls and cannot desorb to eventually reach the mass spectrometer.

Based on the spectroscopic observations, the new species contains a C–O single bond and the C–H bonds with C atom not being involved in the C=C double bond. If this scenario is true, there are two possible reaction mechanisms resulting in the partially hydrogenated product, which is consistent with all spectroscopic and microscopic observations: (1) H insertion into the C=C bond of the enol molecule and (2) H insertion into the C=O bond of the ketone molecule, which is involved into H bonding with OH group of enol. Figure 4 shows the feasible reaction mechanisms that can potentially result in the observed product. Note that H-bonding between two halves of the product dimer should be possible in order to ensure the stability of the newly formed dimer species under the reaction conditions.

Insertion of H into the C=C bond of enol can occur along two pathways: (i) if H attaches to the C(2) atom, a methyl group is formed, while the C(1) atom becomes connected to Pt (Figure 4, species A) and (ii) if H connects to C(1) atom, a $-\text{CH}_2-$ bridge group is produced with C(2) being attached to the surface (Figure 4, species B). Both possible species should generally produce a similar spectroscopic pattern consistent with the spectroscopic observations. However, the species A seems to be more likely as its structure better explains the strong downward shift of the C–O single bond observed experimentally. If the involved carbon C(1) is directly attached to the metal, the reduced mass of the C–O entity strongly increases, which should result in a noticeable decrease of the related vibrational frequency.³⁶ Also, the newly formed CH_3 group of the species A should have high flexibility with respect to the surface so that it can principally attain a close-to-upright configuration with respect to the surface resulting in the high

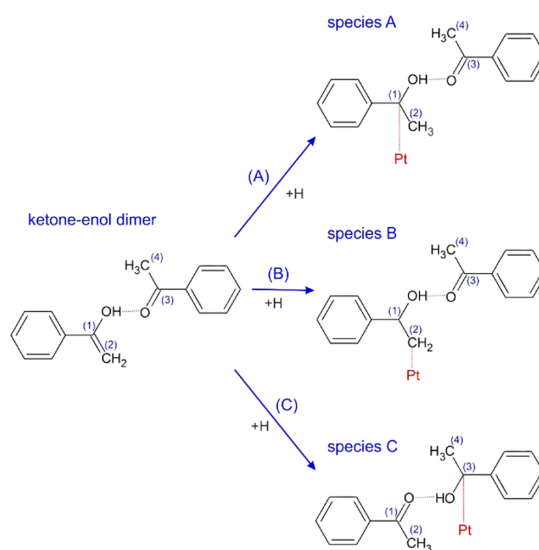


Figure 4. Proposed reaction mechanisms leading to H insertion into the ketone–enol dimer on Pt(111) surface.

intensity of the C–H stretching vibrations in accordance with the metal surface selection rule (MSSR).³⁶ In species B, the C–H vibrations of the methylene-bridge group, in which a C(2) atom is connected to Pt, are expected to be more parallel to the underlying metal surface and therefore to exhibit low or no intensity in this vibrational region.

The ketone part of the ketone–enol dimer can be principally hydrogenated on the C=O bond—either at the O or C(3) position—producing either Pt–C(3)–OH entity (species C in Figure 4) or $-\text{HC}(3)-\text{O}-\text{Pt}$ entity (not shown). In both cases, the carbonyl group of the ketone molecule will not be available for H-bonding with the neighboring molecule anymore and the dimers should fall apart. At this stage, the enol form of the original dimer can possibly transfer back to ketone and build a dimer with the newly formed Pt–C(3)–OH entity to form the species C. Note that the species C is identical to the species A and its structure is also consistent with the experimental observations. In contrast, the formation of the $-\text{HC}(3)-\text{O}-\text{Pt}$ entity can be excluded as in this case the molecule has no possibility to form H-bonded dimers (between the C=O and HO– groups) and should appear as a monomer on the surface, which contradicts the experimental observations.

In both discussed cases, the dimer consisting of one ketone and one partly hydrogenated molecule containing an OH-group is produced; however, it cannot be unambiguously deduced from our experimental observations if the H atom is inserted into the C=C double bond of the enol form or into the H-bonded C=O bond of the ketone form. H insertion into the enol form of acetophenone seems to be more likely based both on the theoretical predictions and frequently experimentally observed easier hydrogenation of olefins. However, the electronic structure perturbation of the C=O bond via H-bonding with the neighboring HO– group can be quite substantial, as indicated by the strong red shift of the carbonyl frequency from 1683 to 1663 cm^{-1} upon H-bonding with enol. This strong interaction between acidic hydrogen of the enol and the carbonyl group of the ketone part of the

dimer weakens the C=O bond quite significantly and with this can potentially lower the activation barrier for H insertion into the carbonyl group. Thus, both mechanisms can potentially lead to the spectroscopically observed reaction intermediates.

It should be pointed out, however, that the formation of ketone–enol dimers appears to be crucial for the first hydrogenation step in this reaction as both the reactants (ketone–enol dimers) and the products (dimers consisting of a ketone and partly hydrogenated acetophenone) are present on the surface in the dimer form. The mechanisms described above can be enabled only via dimer formation: (i) either due to the formation and stabilization of the C=C bond, which can be hydrogenated with the low activation barrier, or (ii) due to weakening of the C=O bond as a result of strong hydrogen bonding with the acidic hydrogen of the enol species.

CONCLUSIONS

In summary, the mechanisms of acetophenone hydrogenation were investigated on Pt(111) using a unique combination of molecular beam techniques, in operando IRAS and STM under well-defined UHV conditions. The absolute majority of acetophenone was found to form ketone–enol dimers under the reaction-relevant conditions, in which one molecule undergoes keto–enol tautomerization to produce the enol form, while the other remains present as ketone. The normally unstable enol form of acetophenone is stabilized on the surface by strong hydrogen bonding between the OH group of the enol and the C=O group of the ketone. We show that the target process—hydrogenation of the carbonyl group—occurs in the ketone–enol dimers and results in the formation of a partly hydrogenated acetophenone species attached via hydrogen bonding to the second acetophenone molecule. This observation suggests that dimers are preserved during the hydrogenation process. The spectroscopically derived reaction intermediates suggest that two possible mechanisms can be responsible for dimer-induced hydrogenation of the carbonyl group: (i) formation of the C=C bond in the enol part of the dimer, which might exhibit a lower activation barrier for hydrogenation according to theoretical predictions, and (ii) weakening of the C=O bond in the ketone part of the dimer due to the strong interaction with the acidic hydrogen of enol, which might potentially result in easier H insertion into this highly perturbed carbonyl group. The formation of ketone–enol dimers was found to crucially depend on the presence of different hydrogen species that can be populated on the Pt surface. While weakly bound β_1 -H prevents the formation of dimers, most likely due to competition for H-bonding with the carbonyl groups, strongly bound β_2 -H does not exhibit such an effect and participates in the hydrogenation of acetophenone dimers.

Obtained mechanistic insights into hydrogenation of carbonyl compounds highlight the exceptional importance of intermolecular interactions in governing the catalytic activity. Observed phenomena can be employed for purposeful functionalization of catalytic surfaces by coadsorption of layers of functional groups capable of effective stabilization of enol species to enable low-barrier hydrogenation pathways. Related effects are expected to play the key role in controlling hydrogenation of all types of carbonyl compounds and hold great potential for further development of new powdered catalysts such as ligand-functionalized catalytic materials.

ASSOCIATED CONTENT

Supporting Information

The Supporting Information is available free of charge at <https://pubs.acs.org/doi/10.1021/acs.jpcc.9b10181>.

Experimental details and temperature dependence of acetophenone oligomer formation (PDF)

AUTHOR INFORMATION

Corresponding Author

*E-mail: schauerma@pctc.uni-kiel.de.

ORCID

Swetlana Schauerma: 0000-0002-9390-2024

Notes

The authors declare no competing financial interest.

ACKNOWLEDGMENTS

Financial support by the German Science Foundations (DFG, Grant SCHA 1477/3-1) is gratefully acknowledged.

REFERENCES

- (1) Meemken, F.; Baiker, A. Recent Progress in Heterogeneous Asymmetric Hydrogenation of C=O and C=C Bonds on Supported Noble Metal Catalysts. *Chem. Rev.* **2017**, *117*, 11522–11569.
- (2) Mäki-Arvela, P.; Hájek, J.; Salmi, T.; Murzin, D. Y. Chemo-selective Hydrogenation of Carbonyl Compounds over Heterogeneous Catalysts. *Appl. Catal., A* **2005**, *292*, 1–49.
- (3) Dostert, K.-H.; O'Brien, C. P.; Ivars-Barceló, F.; Schauerma, S.; Freund, H.-J. Spectators Control Selectivity in Surface Chemistry: Acrolein Partial Hydrogenation over Pd. *J. Am. Chem. Soc.* **2015**, *137*, 13496–13502.
- (4) Dostert, K.-H.; O'Brien, C. P.; Mirabella, F.; Ivars-Barceló, F.; Attia, S.; Spadafora, E.; Schauerma, S.; Freund, H.-J. Selective Partial Hydrogenation of Acrolein on Pd: A Mechanistic Study. *ACS Catal.* **2017**, *7*, 5523–5533.
- (5) Kliewer, C. J.; Bieri, M.; Somorjai, G. A. Hydrogenation of the α,β -Unsaturated Aldehydes Acrolein, Crotonaldehyde, and Prenal over Pt Single Crystals: A Kinetic and Sum-Frequency Generation Vibrational Spectroscopy Study. *J. Am. Chem. Soc.* **2009**, *131*, 9958–9966.
- (6) Kennedy, G.; Baker, L. R.; Somorjai, G. A. Selective Amplification of C=O Bond Hydrogenation on Pt/TiO₂: Catalytic Reaction and Sum-Frequency Generation Vibrational Spectroscopy Studies of Crotonaldehyde Hydrogenation. *Angew. Chem., Int. Ed.* **2014**, *53*, 3405–3408.
- (7) Zaera, F. The Surface Chemistry of Metal-Based Hydrogenation Catalysis. *ACS Catal.* **2017**, *7*, 4947–4967.
- (8) Rasmussen, A. M. H.; Groves, M. N.; Hammer, B. Remote Activation of Chemical Bonds in Heterogeneous Catalysis. *ACS Catal.* **2014**, *4*, 1182–1188.
- (9) Yang, B.; Wang, D.; Gong, X.-Q.; Hu, P. Acrolein Hydrogenation on Pt(211) and Au(211) Surfaces: A Density Functional Theory Study. *Phys. Chem. Chem. Phys.* **2011**, *13*, 21146–21152.
- (10) De Vrieze, J. E.; Thybaut, J. W.; Saeys, M. Role of Keto–Enol Tautomerization in the Copper-Catalyzed Hydrogenation of Ketones. *ACS Catal.* **2019**, *9*, 3831–3839.
- (11) Bandyopadhyay, B.; Pandey, P.; Banerjee, P.; Samanta, A. K.; Chakraborty, T. C–O Interaction Lowers Hydrogen Transfer Barrier to Keto–Enol Tautomerization of β -Cyclohexanedione: Combined Infrared Spectroscopic and Electronic Structure Calculation Study. *J. Phys. Chem. A* **2012**, *116*, 3836–3845.
- (12) Schulz, K. H.; Cox, D. F. Surface Reactions of Acrolein and Propionaldehyde on Cuprous Oxide(100): Nonselective Oxidation and Enolate-Mediated Side Reactions to C₃ Products. *J. Phys. Chem. A* **1993**, *97*, 3555–3564.

- (13) Sim, W.-S.; Li, T.-C.; Yang, P.-X.; Yeo, B.-S. Isolation and Identification of Surface-Bound Acetone Enolate on Ni(111). *J. Am. Chem. Soc.* **2002**, *124*, 4970–4971.
- (14) Mahapatra, M.; Burkholder, L.; Garvey, M.; Bai, Y.; Saldin, D. K.; Tysoe, W. T. Enhanced Hydrogenation Activity and Diastereomeric Interactions of Methyl Pyruvate Co-Adsorbed with R-1-(1-Naphthyl)Ethylamine on Pd(111). *Nat. Commun.* **2016**, *7*, No. 12380.
- (15) Rappoport, Z. *The Chemistry of Enols (Chemistry of Functional Groups Series)*; John Wiley & Sons Ltd: Chichester, 1990.
- (16) Attia, S.; Schmidt, M.-C.; Schröder, C.; Pessier, P.; Schauermann, S. Surface-Driven Keto–Enol Tautomerization: Atomistic Insights into Enol Formation and Stabilization Mechanisms. *Angew. Chem., Int. Ed.* **2018**, *57*, 16659–16664.
- (17) Attia, S.; Schmidt, M. C.; Schröder, C.; Schauermann, S. Formation and Stabilization Mechanisms of Enols on Pt through Multiple Hydrogen Bonding. *ACS Catal.* **2019**, *9*, 6882–6889.
- (18) Humblot, V.; et al. Synchrotron Far-Infrared Rairs Studies of Complex Molecules on Cu(110). *Surf. Sci.* **2003**, *537*, 253–264.
- (19) Garvey, M.; Bai, Y.; Boscoboinik, J. A.; Burkholder, L.; Sorensen, T. E.; Tysoe, W. T. Identifying Molecular Species on Surfaces by Scanning Tunneling Microscopy: Methyl Pyruvate on Pd(111). *J. Phys. Chem. C* **2013**, *117*, 4505–4514.
- (20) Jones, T. E.; Baddeley, C. J. Investigating the Mechanism of Chiral Surface Reactions: The Interaction of Methylacetoacetate with (S)-Glutamic Acid Modified Ni{111}. *Langmuir* **2006**, *22*, 148–152.
- (21) Jones, T. E.; Baddeley, C. J. Influence of Modification Conditions on the Interaction of Methylacetoacetate with (R,R)-Tartaric Acid-Modified Ni{111}. *J. Phys. Chem. C* **2007**, *111*, 17558–17563.
- (22) Skliar, D. B.; Gelmi, C.; Ogunnaike, T.; Willis, B. G. Interaction of 2,2,6,6-Tetramethyl-3,5-Heptanedione with the Si(100)-2×1 Surface: Scanning Tunneling Microscopy and Density Functional Theory Study. *Surf. Sci.* **2007**, *601*, 2887–2895.
- (23) Ontaneda, J.; Nicklin, R. E. J.; Cornish, A.; Roldan, A.; Grau-Crespo, R.; Held, G., Adsorption of Methyl Acetoacetate at Ni{111}: Experiment and Theory. *J. Phys. Chem. C* **2016**, *120*, 27490–27499. DOI: 10.1021/acs.jpcc.6b10023.
- (24) Christmann, K. Interaction of Hydrogen with Solid Surfaces. *Surf. Sci. Rep.* **1988**, *9*, 1–163.
- (25) Gambi, A.; Giorgianni, S.; Passerini, A.; Visinoni, R.; Ghersetti, S. Infrared Studies of Acetophenone and Its Deuterated Derivatives. *Spectrochim. Acta, Part A* **1980**, *36*, 871–878.
- (26) Roubin, P.; Chiavassa, T.; Verlaque, P.; Pizzala, L.; Bodot, H. Ft-IR Study of Uv-Induced Isomerization of Intramolecularly Hydrogen-Bonded Carbonyl Compounds Isolated in Xenon Matrices. *Chem. Phys. Lett.* **1990**, *175*, 655–659.
- (27) Belova, N. V.; Oberhammer, H.; Girichev, G. V. Tautomeric and Conformational Properties of Methyl Acetoacetate, $\text{CH}_3\text{OC}(\text{O})\text{CH}_2\text{C}(\text{O})\text{CH}_3$: Electron Diffraction and Quantum Chemical Study. *J. Phys. Chem. A* **2004**, *108*, 3593–3597.
- (28) Matrosov, E. I.; Kabachnik, M. I. Characteristics of the Cis and Trans Enolic Structures in the I.R. Spectra. *Spectrochim. Acta, Part A* **1972**, *28*, 191–196.
- (29) Fried, S. D.; Bagchi, S.; Boxer, S. G. Measuring Electrostatic Fields in Both Hydrogen-Bonding and Non-Hydrogen-Bonding Environments Using Carbonyl Vibrational Probes. *J. Am. Chem. Soc.* **2013**, *135*, 11181–11192.
- (30) Nolasco, M. M.; Ribeiro-Claro, P. J. A. C–H...O Hydrogen Bonds in Cyclohexenone Reveal the Spectroscopic Behavior of Csp³–H and Csp²–H Donors. *ChemPhysChem* **2005**, *6*, 496–502.
- (31) Christmann, K.; Ertl, G.; Pignet, T. Adsorption of Hydrogen on a Pt(111) Surface. *Surf. Sci.* **1976**, *54*, 365–392.
- (32) Bellamy, L. *The Infra-Red Spectra of Complex Molecules*; Springer Science & Business Media, 2013.
- (33) Mitchell, W. J.; Xie, J.; Jachimowski, T. A.; Weinberg, W. H. Carbon Monoxide Hydrogenation on the Ru(001) Surface at Low Temperature Using Gas-Phase Atomic Hydrogen: Spectroscopic Evidence for the Carbonyl Insertion Mechanism on a Transition Metal Surface. *J. Am. Chem. Soc.* **1995**, *117*, 2606–2617.
- (34) Weldon, M. K.; Friend, C. M. Probing Surface Reaction Mechanisms Using Chemical and Vibrational Methods: Alkyl Oxidation and Reactivity of Alcohols on Transitions Metal Surfaces. *Chem. Rev.* **1996**, *96*, 1391–1412.
- (35) Linstrom, P. J.; Mallard, W. G. E., *Nist Chemistry Webbook, Nist Standard Reference Database Number 69*; National Institute of Standards and Technology: Gaithersburg MD, p 20899.
- (36) Hoffmann, F. M. Infrared Reflection-Absorption Spectroscopy of Adsorbed Molecules. *Surf. Sci. Rep.* **1983**, *3*, 107–192.

8.9 Temperature-Dependent Formation of Acetophenone Oligomers Accompanied by Keto-Enol Tautomerism: Real Space Distribution

Publication Data and Reprint

Reference: Marvin C. Schmidt, Smadar Attia, Carsten Schröder, Ann-Katrin Baumann, Pascal Pessier, and Svetlana Schauermann

DOI: 10.1021/acs.jpcc.0c04343

Submitted: 14.05.2020

Accepted: 04.06.2020

Contribution: IRAS measurements, scientific discussions, preparation of parts of the manuscript

Copyright: Reprinted with permission from JPC C from Ref.[235]. Copyright 2020 American Chemical Society.

Temperature-Dependent Formation of Acetophenone Oligomers Accompanied by Keto–Enol Tautomerism: Real Space Distribution

Marvin C. Schmidt, Smadar Attia, Carsten Schröder, Ann-Katrin Baumann, Pascal Pessier, and Svetlana Schauermaⁿ*



Cite This: *J. Phys. Chem. C* 2020, 124, 14262–14271



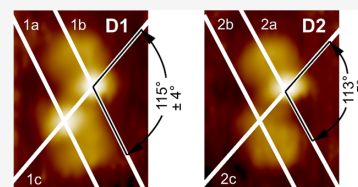
Read Online

ACCESS |

Metrics & More

Article Recommendations

ABSTRACT: We present a mechanistic study addressing formation, adsorption configuration, and stability of acetophenone oligomers on a catalytically active Pt(111) surface by a combination of scanning tunneling microscopy (STM) and infrared reflected absorption spectroscopy. Different types of acetophenone dimers and trimers were observed, with formation and relative distribution strongly depending on the surface temperature. In a low-temperature range, acetophenone is adsorbed mostly in the form of monomer species, while with increasing temperature, trans-dimers are formed starting from about 140 K followed by evolution of cis-dimers as well as symmetric and asymmetric trimers at 300 K. Spectroscopically, we can distinguish between ketone–ketone and ketone–enol dimers. In the latter species, the enol form of acetophenone is stabilized via hydrogen bonding to the carbonyl group of the ketone counterpart. Trimers consist mostly of one ketone molecule interacting via hydrogen bonding with two enol species and can form two different adsorption configurations on the surface—symmetric and asymmetric. The ketone–ketone dimers are the predominant species at 170–200 K, while at 240 K, all dimer adsorbates convert to ketone–enol species. The adsorption configuration of different types of oligomers with respect to the underlying metal surface was determined with atomic resolution. The stability and mobility of oligomers were addressed by STM in the low- and high-temperature range. At 115 K, the trans-dimers appear to be immobile on Pt(111), while the monomers can undergo frustrated rotation of the acetyl group with respect to the phenyl moiety. At 300 K, the transformation of the trans-dimer to the symmetric trimer by attaching a neighboring acetophenone molecule was observed followed by the rearrangement to the asymmetric trimer and its disintegration to a trans-dimer and a monomer. The interconversion of the symmetric to the asymmetric trimer appears to occur as an intramolecular restructuring without losing the integrity of the whole complex.



INTRODUCTION

Lateral interactions between hydrocarbon species adsorbed on catalytically active surfaces might greatly affect their chemical transformations along competing reaction pathways. There are a large number of reports on the strongly altered catalytic activity of transition-metal catalysts induced by coadsorption of different types of hydrocarbon-based surface modifiers, including, e.g., chiral adsorbates to trigger asymmetric hydrogenation catalysis^{1–4} or adsorbed organic ligands to induce chemoselective hydrogenation of multi-unsaturated carbonyl compounds.^{5–17} In these studies, the efficiency of heterogeneously catalyzed reactions in terms of activity and selectivity is controlled via tuning the lateral interactions between the adsorbed organic modifier and the reactant, which is typically achieved by varying the chemical nature and adjusting the adsorption geometry and coverage of the adsorbed surface ligands. This concept opens up a new prospect of controllable tuning the catalytic activity and selectivity of heterogeneously catalyzed transformations of hydrocarbons, especially those relying on subtle differences in the activation barriers of competing reactions pathways, which is otherwise very difficult to control.¹⁸ The atomistic-level

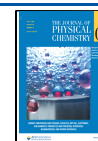
understanding of the lateral interaction between different types of hydrocarbons on catalytically active surfaces is therefore of crucial importance for developing knowledge-based design of catalytic materials with tailor-made properties.

Our recent studies on hydrogenation of simple carbonyl compounds including simple and multi-unsaturated aldehydes and ketones, such as acetophenone,^{19–22} isophorone,^{23–26} and acrolein,^{16,17,27–30} over transition-metal surfaces (Pd and Pt) also demonstrate that lateral interactions between the neighboring molecules can critically control their adsorption geometry and induce formation of new reaction intermediates and alternative catalytic routes, which are not possible in the absence of adsorbate–adsorbate interactions. Particularly, acetophenone was shown to form surface dimers and trimers,^{19,20} in which at least one molecule undergoes keto–

Received: May 14, 2020

Revised: June 4, 2020

Published: June 4, 2020



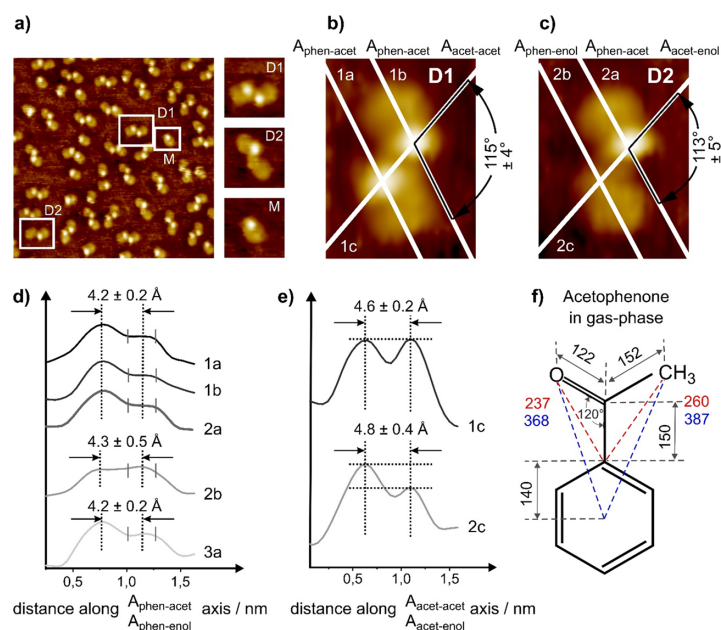


Figure 1. (a) STM image of acetophenone on pristine Pt(111) (exposure at 200 K, acquisition temperature of 115 K, 1 V, 0.29 nA, 13.1×13.1 nm²). (b and c) Close-up images of two types of dimers D1 and D2, respectively, indicating the selected axes. (d and e) Comparison of the line profiles obtained along the selected axes indicated in (b) and (c) (see text for details). (f) Structure and characteristic distances of acetophenone in the gas phase (from NIST⁵³). All distances are given in pm.

enol tautomerism to form the enol form of acetophenone. In this process, a H atom of the methyl group is transferred to the C=O group of the same molecule to form the C–OH entity and leaving behind the C=C double bond. The enol species, which is normally highly unstable in the gas phase and readily converts back to ketone,³¹ is stabilized on the surface via formation of a strong hydrogen bond between the HO- group of enol and the C=O group of the ketone form of acetophenone involved in the ketone–enol dimer.¹⁹ The ketone–enol dimers turned out to be the crucial reaction intermediate in hydrogenation of the carbonyl bond of acetophenone.²² This observation is in line with the recent theoretical predictions on hydrogenation of simple carbonyl compounds, which suggest that a low-barrier reaction pathway occurs via two consecutive steps: keto–enol tautomerism producing a C=C bond, which can be easily hydrogenated by insertion of atomic hydrogen.^{32–34} This consecutive mechanism was computed to result in a lower activation barrier than the direct hydrogenation of the carbonyl group for a broad class of carbonyl compounds.

In view of these striking results demonstrating the crucial role of dimer formation in hydrogenation of the carbonyl compounds, it becomes evident that oligomer formation and stabilization mechanisms of the thermodynamically unstable enol species need to be understood at the atomistic level. Currently, only a limited number of studies are available dealing with the stabilization mechanisms of oligomers consisting of simple carbonyl compounds on transition-metal surfaces. McBreen et al.^{35–37} reported formation of different types of oligomers, including dimers and trimers, for 2,2,2-trifluoroacetophenone on Pt(111), which are stabilized via H bonding between the carbonyl group and a H atom of the phenyl ring of the adjacent molecule. More recently, formation

of acetophenone dimers and trimers was reported by the same group³⁸ at room temperature, who hypothesized formation of both types of oligomers consisting of solely enol molecules.

To address the details of the lateral interactions between carbonyl compounds, we performed an atomistic-level study on formation of acetophenone oligomers on a catalytically active Pt(111) surface under a broad range of temperature and coverage conditions by employing a combination of STM (scanning tunneling microscopy) and IRAS (infrared reflection absorption spectroscopy). Particularly, we show that the abundance and the relative distribution of different types of acetophenone dimers and trimers strongly depend on the surface temperature. In a low-temperature range, oligomer formation starts with evolution of trans-dimer species above ca. 140 K, which can exist in the form of ketone–ketone or ketone–enol dimers. At elevated temperatures, new types of oligomers are formed including cis-dimers as well as two types of trimers, with the latter species being adsorbed in symmetric or asymmetric configuration. We report the adsorption configuration of different types of oligomers with respect to the underlying metal surface determined with atomic resolution. The stability and mobility of oligomers were addressed by STM in the low- and high-temperature range. At low temperatures, the trans-dimers appear to be immobile on Pt(111), while the monomers can undergo frustrated rotation of the acetyl group with respect to the phenyl moiety. Close to room temperature, the transition between different oligomers—a trans-dimer and monomer to a symmetric trimer followed by its interconversion to an asymmetric trimer without losing the integrity of the whole complex—was also detected as a function of time. The obtained results provide important atomistic-level insights into the intermolecular lateral interaction of adsorbed carbonyl compounds.

EXPERIMENTAL SECTION

Sample Preparation. The Pt(111) single crystal (MaTeck GmbH) was cleaned prior to use in ultrahigh vacuum (UHV) chambers by repeated cycles of Ar⁺-ion bombardment at room temperature followed by annealing at 1150 K and subsequent oxidation in 1×10^{-7} mbar O₂ at 650–750 K to remove residual carbon. The last step involves the rapid flash of the sample to 1000 K. Shortly before each experiment, the sample was flashed to 600 K before cooling to the required temperature to remove CO adsorbates. The long range order and cleanliness of the Pt(111) single crystal were examined by low-energy electron diffraction, Auger electron spectroscopy, and additionally (in the case of IRAS apparatus) IRAS of adsorbed CO to probe the abundance of adsorption sites.

STM. The STM measurements were carried out in a UHV (base pressure better than 1×10^{-10} mbar) apparatus by employing a variable temperature (90–300 K) Aarhus 150 SPM (SPECS). All measurements were carried out in constant current mode, and the bias voltage U_T was applied to the sample. The etched W-tip was commercially produced by SPECS and in situ sharpened by repeated cycles of 3 keV Ar⁺ bombardment with 5×10^{-6} mbar back pressure for 5 min. The sharpness of the W-tip was validated on the pristine Pt(111) surface.

The Pt(111) single crystal was cleaned according to the cleaning procedure described above. The quality of the sample was additionally verified by acquiring STM images prior to the deposition at 293 K. Acetophenone (Sigma-Aldrich, purity of $\geq 99.5\%$) was purified prior to the experiments by repeated freeze–pump–thaw cycles, dosed through an individual gas doser onto the Pt(111) surface, which was held at various temperatures ranging from 160 to 300 K, and then transferred to the STM chamber for measurements.

IRAS. The IRAS experiments were performed in a specially designed UHV apparatus (base pressure of $2 \cdot 10^{-10}$ mbar) containing two effusive doubly differentially pumped multi-channel array sources and a supersonic beam operated at room temperature.³⁹ IRAS data have been acquired using a vacuum Fourier transform infrared (FT-IR) spectrometer (Bruker Vertex 80v) with a spectral resolution of 2 cm^{-1} and a mid-infrared polarizer and p-polarized IR light. The spectrometer is equipped with a narrow-band mercury–cadmium–telluride detector. IR spectra were acquired at the same surface temperature that was used for acetophenone deposition (115–300 K). An automated quadrupole mass spectrometer system (Hiden, HAL 301/3F) was employed for the continuous monitoring of the partial pressures of gaseous species during acetophenone deposition.

RESULTS AND DISCUSSION

Adsorption of acetophenone was investigated on a well-defined Pt(111) surface under UHV conditions in the temperature range 115–300 K by combination of STM and IRAS. Acetophenone was dosed either via a dedicated gas doser in an STM apparatus or via an effusive molecular beam in a molecular beam/IRAS apparatus at constant flux. Figure 1a shows the STM image obtained at 115 K after exposure to acetophenone at 200 K. The acetophenone coverage corresponds to approximately 4×10^{13} molecules·cm⁻². Three different types of surface adsorbates can be distinguished on this surface, which are shown enlarged in the close-up images on the right: monomers (M), symmetric trans-

dimers (D1), and asymmetric trans-dimers (D2). Here, the term “trans” is related to the relative position of the individual molecules, which are situated at the opposite sides of the axes $A_{\text{acet-acet}}$ (Figure 1b) and $A_{\text{acet-enol}}$ (Figure 1c) connecting the smaller protrusions, i.e., the interacting parts of the molecules. The more abundant symmetric trans-dimer D1 consists of two identical protrusions, each enclosing a brighter and darker area (Figure 1b). The brighter area appears as a small spot, while the darker area is somewhat larger in size. These identical molecular species are connected to each other via the functional groups appearing brighter in STM, particularly acetyl groups, as shown previously based on a combination of spectroscopic and microscopic observations (see ref 19 and the discussion below). The acetyl groups form strong hydrogen bonds between the H atoms of the methyl group of one molecule and the O atom of the carbonyl group of the neighboring molecule. In the less abundant asymmetric trans-dimer D2 (Figure 1c), one of the molecules also appears as a combination of the brighter and darker areas and exhibits the same contrast as the half of the trans-dimer D1. The second molecule in D2 has approximately the same shape—a combination of a larger and smaller spots—but the intensity of both moieties is similar. This dimer D2 was previously assigned to a combination of a ketone and an enol acetophenone species, in which a normally unstable enol is stabilized via H bonding between the OH group of enol and the carbonyl group of ketone.¹⁹ The majority of monomers M exhibits the same contrast as the half of the trans-dimer D1, showing a small bright protrusion at one end and the larger darker area at the other, suggesting the ketone form of the monomer species.

The exact chemical nature of the trans-dimers D1 and D2 was previously identified by infrared spectroscopy. Figure 2

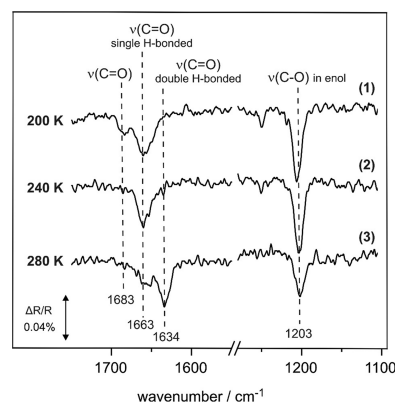


Figure 2. IR spectra of acetophenone adsorbed on Pt(111) at 200, 240, and 280 K. Only the C=O and C–O stretching regions are shown. All spectra are related to sub-monolayer coverages and were obtained after exposures to 6.5×10^{14} (200 K), 4.0×10^{14} (240 K), and 9.0×10^{14} (280 K) molecules·cm⁻².

summarizes the most important observations of this study, which are relevant for further discussion of the STM data. The spectrum 1 shows the fingerprint region of acetophenone with the main vibrational bands at 1683, 1663, and 1203 cm⁻¹. The vibrational band at 1683 cm⁻¹ is assigned to the C=O vibration of acetophenone, either in a monomer or in a ketone–ketone trans-dimer D1, in which the C=O bond is

not strongly perturbed by H bonding between the carbonyl group and the methyl group of the neighboring molecules.^{19,21} For this reason, this vibrational frequency coincides with that one of the nonperturbed acetophenones in the gas phase⁴⁰ or adsorbed in the multilayers (1683 cm⁻¹). The combination of the vibrational bands at 1203 and 1663 cm⁻¹, which always appear in a correlated fashion, is related to the C–O single bond in the enol form of acetophenone and the C=O double bond in the ketone form, respectively.¹⁹ These vibrational bands were assigned to a ketone–enol dimer D2, in which the H atom of the OH group of enol is hydrogen-bonded to the O atom of the carbonyl group of the ketone. This strong interaction stabilizes the normally unstable enol form of acetophenone, which would otherwise quickly transfer back to ketone. The large shift of the C=O vibrational frequency (20 cm⁻¹ as compared to an unperturbed value of 1683 cm⁻¹ observed in the gas phase and acetophenone multilayers) in the ketone part of the ketone–enol dimer D2 is related to the fact that the carbonyl group is hydrogen-bonded to highly acidic H of the enol, which is known to result in pronounced changes in carbonyl vibrational frequency.^{41,42} Further details on the spectroscopic assignment of the surface species can be found elsewhere.^{19,20} The assignment of the bright protrusions seen in STM to the acetyl group and the darker areas to the phenyl moiety is consistent with the spectroscopic data, showing that the acetyl group of the ketone and the HO group of the enol are directly involved in hydrogen bonding. The particular structure of both trans-dimers in the form of a ball model can be found in our previous report.¹⁹

The largest fraction of the surface species is related to the symmetric ketone–ketone trans-dimer D1 (69%), while the abundance of the asymmetric ketone–enol trans-dimers D2 (13%) and monomers M (18%) is significantly lower at this temperature (Figure 1a). Figure 1d,e shows the line profiles for different types of surface dimers (D1 and D2) along the selected axes $A_{\text{acet-acet}}$ and $A_{\text{phen-acet}}$ (Figure 1b) and $A_{\text{acet-enol}}$, $A_{\text{phen-acet}}$, and $A_{\text{phen-enol}}$ (Figure 1c) shown in the close-up images for the species D1 and D2, respectively. The axes $A_{\text{phen-acet}}$ (Figure 1b) are drawn between the centers of the phenyl ring and the acetyl group (Figure 1b, dimer D1) and are rotated by $115 \pm 4^\circ$ with respect to the axis $A_{\text{acet-acet}}$. The axes $A_{\text{phen-acet}}$ and $A_{\text{phen-enol}}$ (Figure 1c, dimer D2) are drawn between the centers of the phenyl ring and the acetyl group or the ethenol group, for ketone and enol, respectively, and are rotated by $113 \pm 5^\circ$ with respect to the axis $A_{\text{acet-enol}}$.

Figure 1d,e shows the line profiles measured along the above described axes. For the symmetric trans-dimer D1, the line profiles along both the axes $A_{\text{phen-acet}}$ of the two individual ketone molecules (Figure 1d, lines 1a and 1b) look very similar, showing a plateau-like region related to the phenyl group and a maximum at the position of the bright spot corresponding to the acetyl group. The characteristic distances between the center of the phenyl ring and the maximum of the bright protrusion $d_{\text{phen-acet}}$ amounts to $4,2 \pm 0,2$ Å. Based on our experimental results, it is difficult to unambiguously determine which part of the acetyl group is imaged as a bright protrusion. In our previous IRAS studies on adsorption configuration of the acetophenone monomer species, which was determined to be consistent with the $\eta^1(\text{O})$ geometry,²¹ we hypothesized that most likely the methyl group is imaged as a bright spot. If this assumption is true also for the species investigated in this study (both monomers and dimers), the measured characteristic distance $d_{\text{phen-acet}} = 4,2 \pm 0,2$ Å is close

to the distance 3,87 Å between the center of the phenyl ring and the methyl group of a free-standing acetophenone molecule (see calculated characteristic distances for gas-phase acetophenone in Figure 1f, blue numbers). It should be noted, however, that also the distance between the center of the phenyl ring and the O atom (3,68 Å, Figure 1f) is quite similar to the experimentally measured value ($d_{\text{phen-acet}} = 4,2 \pm 0,2$ Å). In view of the possible distortion of the adsorbed acetophenone species, e.g., elongation of the molecular bonds or changing angles, the experimentally measured distance $d_{\text{phen-acet}}$ was found to be in good quantitative agreement with the corresponding characteristic dimensions of gas-phase acetophenone, i.e., the distance between the center of the phenyl ring and the methyl group or the O atom of the carbonyl group.

The line profiles measured along the axis $A_{\text{acet-acet}}$ connecting two acetyl groups in the D1 dimer (Figure 1e, line 1c) exhibit two maxima with the distance between them $d_{\text{acet-acet}}$ being equal to $4,6 \pm 0,2$ Å. This relatively short distance, which is comparable to the characteristic length of the molecule (e.g., $d_{\text{phen-acet}} = 4,2$ Å), additionally confirms a strong interaction between both parts of dimers capable of bringing the individual molecules in very close contact.

The line profile measured along the central axis $A_{\text{phen-acet}}$ for the ketone part of the asymmetric trans-dimer D2 (Figure 1d, line 2a) shows the same dimensions and a very similar shape to the line profile of a ketone molecule in the symmetric trans-dimer D1. Specifically, it exhibits a plateau-like region at the position of the phenyl ring and a maximum at the acetyl group. The characteristic distance $d_{\text{phen-acet}}$ in this line profile ($4,2 \pm 0,2$ Å) is the same as the distance in the individual ketone molecules in the ketone–ketone trans-dimer D1. In contrast, the line profile along the central axis $A_{\text{phen-enol}}$ in the enol part of D2 (Figure 1d, line 2b) shows a clearly different shape without a maximum at the position of the ethenol group. However, the characteristic distance $d_{\text{phen-enol}} = 4,3 \pm 0,5$ Å remains close to the distance $d_{\text{phen-acet}}$ measured for the ketone part of the molecule. The line profile connecting the centers of the acetyl and ethenol groups (Figure 1e, line 2c) also exhibits a different shape in the ketone–enol trans-dimer D2 as compared to ketone–ketone trans-dimer D1, showing a pronounced maximum at the position of acetyl and a significantly less intense peak at the position of the ethenol group. Interestingly, the distance between these groups $d_{\text{acet-enol}}$ ($4,8 \pm 0,4$ Å) is nearly the same as the characteristic distance $d_{\text{acet-acet}}$ ($4,6 \pm 0,2$ Å) measured for the ketone–ketone trans-dimer D1. This observation suggests a strong interaction also between two individual molecules in the ketone–enol trans-dimer D2 capable of bringing two species in close contact.

For the monomer M, the line profile along the central axis appears to be identical to the half of the ketone–ketone trans-dimer. The characteristic distance $d_{\text{phen-acet}}$ amounts to $4,2 \pm 0,2$ Å (Figure 1d, line 3a), which is very close to the corresponding value measured in the individual molecules of the ketone–ketone trans-dimer D1 and the ketone part of the ketone–enol trans-dimer D2.

The distribution of the surface species between monomers and dimers exhibits very strong temperature dependence. Figure 3a shows the STM images of acetophenone at similar surface coverages obtained after exposure in the temperature range 160–200 K while imaging was performed at 115 K. The statistical evaluation of the distribution of different adsorbates is displayed in Figure 3b. A clear trend can be observed here:

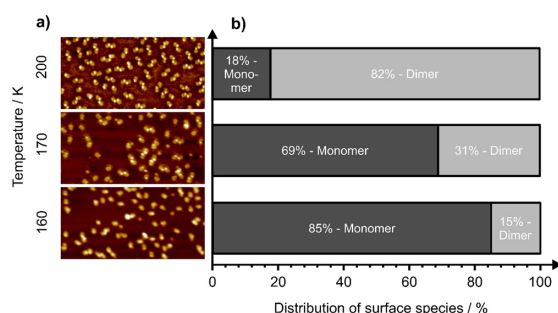


Figure 3. (a) STM images ($20 \times 10 \text{ nm}^2$) of acetophenone adsorbed on pristine Pt(111) at different temperatures. The images were obtained at 105–115 K after exposure to acetophenone at the temperatures indicated on the left. Imaging conditions: 1 V and typical current of 0.26–0.31 nA. (b) Statistical evaluation of the distribution of different surface species obtained on larger STM scans.

the fraction of the dimer species significantly grows with increasing temperature from 15% at 160 K to 82% at 200 K. Generally, two conditions have to be fulfilled to form a ketone–ketone dimer, which is the prevalent form of dimers at 200 K: (i) two individual molecules have to be able to diffuse to approach each other and (ii) a hydrogen bond between two acetyl groups has to be established. The low abundance of dimer species at 160 K can be most likely related to the limited diffusion of the adsorbed species since establishing of hydrogen bonding is usually an easy and less activated process, which was previously observed for carbonyl compounds under cryogenic conditions.⁴³ The increasing surface temperature has a pronounced effect not only on the relative distribution between the monomer and dimer species but also on the relative amounts of the ketone–ketone (D1) and ketone–enol (D2) trans-dimers.²⁰ The fraction of the latter species grows significantly with increasing temperature, and the ketone–enol trans-dimers D2 become the only species at around 240 K. This observation clearly indicates that keto–enol tautomerism is an activated process and the ketone–enol dimers D2 are more stable surface species than ketone–ketone dimers D1. It should be also noted that van der Waals interaction plays an important role in adsorption of organic molecules on metal surfaces, as shown in a number of recent theoretical studies.^{44,45} We expect that the formation and stability of oligomer species studied here might be also greatly affected by the dispersive interactions with the underlying metal support. Further theoretical studies are needed to shed light on the atomistic details of these processes.

In the next step, the mobility of different surface species—dimers vs. monomers—was investigated by continuous imaging the adsorbate-covered surface for 32 min. Figure 4a shows the composition of the surface produced by acetophenone exposure at 170 K followed by cooling down to the imaging temperature 115 K, at which the mobility of the surface species was investigated. The close-up images on the right show the time evolution of different species marked with the symbols D1, M1, and M2, related to the ketone–ketone trans-dimer and two different types of monomers, respectively. The species D1 remain immobile during the entire observation time (Figure 4b), suggesting the strong binding energy of the ketone–ketone trans-dimer D1 on the Pt(111) surface, which prevents its movement or rotation at 115 K. Interestingly,

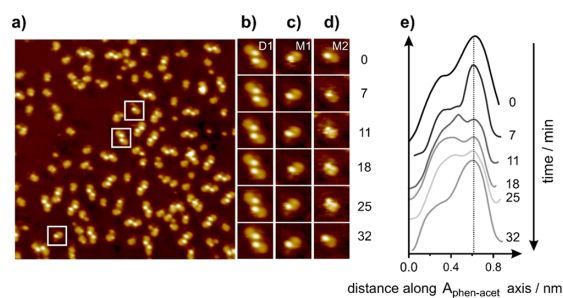


Figure 4. (a) STM image ($19 \times 19 \text{ nm}^2$) of acetophenone on Pt(111) (exposure at 170 K, acquisition temperature of 118 K, 1 V, 0.3 nA). (b–d) Consecutive close-up images of a trans-dimer (D1) and two monomer species (M1 and M2) obtained after a time interval indicated on the right: 0, 7, 11, 18, 25, and 32 min. (e) Corresponding line profiles measured along the $A_{\text{phen-acet}}$ axis of the monomer species shown in (d). The numbers on the right show the time interval (the same as indicated in the close-up images).

some of the monomers also appear to be immobile on the time scale of the experiment, while others show frustrated rotation of the acetyl group, which can be either thermally driven⁴⁶ or induced by electrons ejected from the STM tip, as shown previously for various atoms and molecules adsorbed on metal substrates.^{47,48} The series of close-up images shown in Figure 4c provide an example of the immobile monomer species, which preserve their position on the surface and the adsorption configuration— as deduced from the relative positions of the acetyl and phenyl groups— during the observation time. The time evolution of the second monomer is displayed in Figure 4d, clearly showing a change in the position of the acetyl group with respect to the phenyl ring between 7 and 11 min as well as its flip back between 25 and 32 min. If the frustrated rotation is a thermally driven process, this observation implies that the corresponding activation barrier in acetophenone monomers can be overcome at 115 K. Note that this process cannot be related to keto–enol tautomerism under these temperature conditions, as the onset of enol formation was detected by IRAS only above 140 K. The line profiles for the flipping molecule along the phenyl–acetyl axis $A_{\text{phen-acet}}$ are displayed in Figure 4e. The first two lines exhibit a profile characteristic for a more abundant adsorption configuration of acetophenone monomer M1, containing a plateau-like region and a maximum at the position of the acetyl group. In the time range between 7 and 11 min, the profile changes drastically and the maximum becomes less pronounced, pointing to a change in the relative position of the acetyl group with respect to the phenyl ring. After 25 min, the original form of the line profiles is restored, suggesting that the ketone acquires the initial most abundant adsorption configuration M1. Earlier literature reports suggested the $\eta^1(\text{O})$ configuration (with the O atom of the carbonyl group pointing down to the metal surface and the methyl group pointing away) being the most stable adsorption configuration for a variety of different carbonyl compounds.^{49–52} Our more recent IRAS studies on the adsorption configuration of acetophenone monomers on Pt(111) at 115 K were consistent with this model.²¹ It can be speculated that acetophenone molecules, normally adsorbed in $\eta^1(\text{O})$ configuration, might gain enough energy—either thermally or through electronic excitation—to perform the frustrated rotation of the acetyl group and transfer it into a different less

stable position, e.g., with the O atom pointing upwards or with the entire acetyl group adopting a flat-lying configuration on the surface. With time, the acetyl group flips back to the stable and more abundant $\eta^1(\text{O})$ configuration M1.

Figure 5a shows the distribution of surface species on Pt(111) after acetophenone exposure at 300 K and cooling

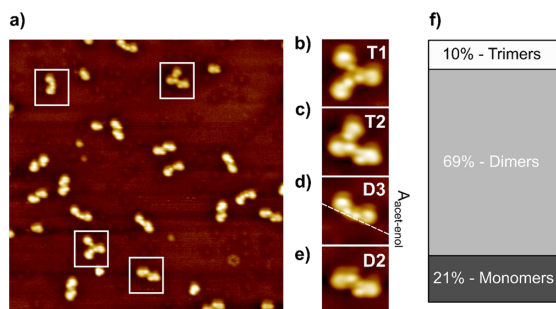


Figure 5. (a) STM image of acetophenone adsorbed on Pt(111) obtained after exposure at 293 K ($20.4 \times 20.4 \text{ nm}^2$, acquisition temperature of 123 K, imaging conditions: 1 V, 0.5 nA). (b–e) Close-up images of different surface species (trimers T1 and T2, cis-dimer D3, and trans-dimer D2, respectively). (f) Statistical evaluation of the distribution of different surface species obtained on larger STM scans ($40 \times 40 \text{ nm}^2$).

down to the acquisition temperature 115 K. At 300 K, a new type of adsorbate evolves, containing three molecules appearing as a combination of large and small protrusions, attached to each other via the acetyl groups or their derivatives. Figure 5b–e displays the close-up images of the individual oligomer species found on the surface, while Figure 5f shows the statistical distribution of the monomer, dimer, and trimer species obtained from a larger STM scan. The spectrum 3 in Figure 2 shows the chemical nature of the surface species at room temperature. Since only three characteristic bands at 1203, 1663, and 1634 cm^{-1} are observed and the band at 1683 cm^{-1} related to the ketone–ketone dimers D1 and monomers is absent, it can be concluded that all oligomer species contain a combination of ketone and enol species. Based on the analysis of the IRAS data, it was concluded that ketone–enol dimer species and ketone–enol–enol trimer species are populated on the surface at 300 K.²⁰ In the latter case, a single carbonyl group forms hydrogen bonds with two OH groups of two enol species, which results in a new C=O vibrational band at 1634 cm^{-1} shifted by 49 cm^{-1} from the unperturbed value. The vast majority of the oligomer species at 300 K are dimers (69%). Two different types of dimers can be observed, which differ in the position of the phenyl group with respect to the axis connecting the acetyl and ethenol groups ($A_{\text{acet-enol}}$): (i) the trans-dimers showing the same adsorption configuration as in the low-temperature range (close-up image (e), D2 trans-dimer), in which the phenyl rings are positioned on the different sides of the axis $A_{\text{acet-enol}}$ and (ii) a new type of dimer—cis-dimer D3 (close-up image (d))—exhibiting a new adsorption configuration with both phenyl rings lying on the same side with respect to the $A_{\text{acet-enol}}$ axis. Since the dimer D3 is observed only at the elevated temperatures, its formation should occur in the activated process with the energy barrier being higher than that one associated with the formation of the trans-dimer D2. Most likely the steric hindrance between two

phenyl groups situated in the cis-position is responsible for higher activation energy of D3 formation.

Two types of ketone–enol–enol trimers are shown in the close-up images in Figure 5b,c, with one exhibiting nearly three-fold symmetry (T1) and the second being asymmetric (T2). In both types of configuration, one ketone molecule is connected via hydrogen bonding to two enol species, as deduced from the spectroscopic observation of two characteristic bands:²⁰ (1) the C=O bond hydrogen-bonded to two OH groups at 1634 cm^{-1} and (2) the C–O bond in enol appeared at 1203 cm^{-1} . The shape of these species depends on the particular orientation of two OH groups involved in the trimer with respect to the carbonyl group. For the asymmetric trimer T2, it can be quite safely concluded that the central molecule should be related to the ketone species, while the two molecules on both sides are enols, as only the central molecule is bonded to two neighbors. The simultaneous appearance at 300 K and coexistence of both types of trimers suggest their similar energetic stability on Pt(111).

Previously, the formation of acetophenone oligomers on Pt(111), including dimers and trimers, was reported by McBreen et al.³⁸ at 300 K. Based on the vibrational spectra obtained by high-resolution electron energy loss spectroscopy (HREELS), the authors hypothesized the formation of dimers and trimers consisting of solely enol molecule interaction via OH groups. The vibrational band at 1640 cm^{-1} observed in their study was assigned to a C=C stretching vibration of enol species. This assignment seems to be quite unlikely to us as this bond exhibits a small dynamic dipole moment resulting in low-intensity bands as compared to the C=O and C–O stretching vibrations. Taking into account the observed high intensity of the vibration at 1640 cm^{-1} and lower resolution of HREELS, we hypothesize that this band might be rather related to the C=O stretching vibration involved in hydrogen bonding with the two enol molecules described above (the band at 1634 cm^{-1} in our study).

The orientation of different types of oligomer species with respect to the underlying metal substrate was determined based on atomically resolved STM images, in which the oligomer molecules and the individual underlying Pt atoms could be resolved. A typical example of such an image is shown in Figure 6a. The positions of single Pt atoms are indicated with a grid corresponding to the hexagonal symmetry of the underlying Pt(111) surface. Note that due to the tip convolution effects, the small objects appear in STM larger than they are in reality. It can be recognized that each individual acetophenone molecule in all oligomers has a similar footprint on the underlying metal including three Pt atoms, which is shown in the close-up images of Figure 6b–d. The footprint of the individual acetophenone molecules is indicated with red dots for each oligomer. Two axes drawn via these three atoms (indicated as (1) and (2) in Figure 6b) are inclined with respect to each other at 120° . Figure 1f displays selected characteristic dimensions of a free-standing acetophenone molecule in the gas phase.⁵³ Due to the tip convolution effect making the molecules appear larger, it is difficult to unambiguously attribute the position of the individual functional group in acetophenone to particular adsorption sites on Pt(111). However, it can be seen that the phenyl groups typically cover two Pt atoms, i.e., the most bright part of the ring lies between two metal atoms at the bridge position. The characteristic size of the carbon framework in the phenyl ring amounts to 2.80 \AA (Figure 1f), which fits well the distance

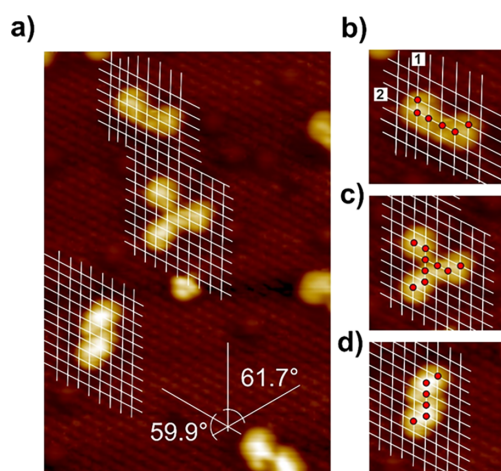


Figure 6. (a) STM image of acetophenone adsorbed on Pt(111) with atomically resolved underlying Pt lattice obtained after exposure at 293 K ($7.1 \times 11.2 \text{ nm}^2$, acquisition temperature of 123 K, 1 V, 0.5 nA). The white grid indicates the positions of the individual Pt atoms. (b–d) Close-up images of individual oligomers—cis-dimer D3, symmetric trimer T1, and trans-dimer D2—shown together with the Pt grid. The red dots show the footprint of the corresponding species on the surface. Each monomer, constituting different types of oligomers, covers three Pt atoms. The axes 1 and 2 drawn through these atoms (see (b)) are tilted with respect to each other by 120° .

between two lattice Pt atoms of 2.78 \AA . With this, qualitatively very good agreement is found between the experimentally observed footprint of the phenyl group, corresponding approximately to the interatomic distance of Pt atoms, and the size of the phenyl group in the gas-phase acetophenone. The exact position of the acetyl/ethenol group is more difficult to deduce based on the available STM data set. The models of the footprint shown in Figure 6b–d suggest two feasible adsorption sites for acetyl/ethenol group: either (i) it occupies a space approximately between two Pt atoms, e.g., 2.78 \AA , or (ii) it is positioned above a single Pt atom in on-top configuration. Figure 1f shows the characteristic dimensions of the acetyl group in the gas phase according to NIST database,⁵³ with a characteristic value lying in the range 2.37 – 2.60 \AA (red numbers; the distance between the C atom of the phenyl group and the O atom (2.37 \AA) and the distance between the C atom of the phenyl group and the methyl group (2.60 \AA)). Note that the exact dimensions of the acetyl/ethenol group footprint on the surface might strongly depend on the particular adsorption geometry of the related molecules in the dimers or trimers as well as on the possible elongation of the molecular bonds due to an interaction with the underlying metal. The characteristic range 2.37 – 2.60 \AA deduced for unperturbed acetophenone in the gas phase is quite close to the distance between two Pt atoms (2.78 \AA), with this fairly fitting the footprint model shown in Figure 6b–d. Further theoretical work is needed to address the adsorption geometry of acetophenone oligomers in more detail, which is not available so far to the best of our knowledge. Previous theoretical studies employing density function theory addressed adsorption of an acetophenone derivative (2,2,2-trifluoroacetophenone, TFAP) on Pt(111), in which the H atoms of the methyl group are substituted by three fluoro

atoms.^{32,37} The reported most stable adsorption configuration is related to a so-called bridge30 site.³⁷ In this adsorption site, the aromatic ring lies flat on the surface and is centered over a Pt–Pt bridge site with the aromatic C–C bonds at an approximate angle of 30° or 90° to the close-packed directions within the surface. This result is in agreement with the earlier computational studies carried out for different aromatic molecules.^{54–57} The calculated adsorption position of the phenyl ring in TFAP is in excellent agreement with the adsorption site deduced in our STM study, wherein the position of the ring center was identified as a bridge site between two Pt atoms. For the position of the trifluoroacetyl group with respect to the phenyl ring, a few different adsorption configurations were computed, exhibiting slightly different energies with respect to the most stable configuration.³⁷ The direct comparison of the computed configurations with our experimentally derived model is rather difficult because of the different chemical nature of the acetyl vs trifluoroacetyl groups and their different space requirements. However, for the most stable adsorption configuration with the trifluoroacetyl group occupying mostly the on-top Pt position, the footprint produced by TFAP turns out to be in good qualitative agreement with the footprint derived from our experimental images (with the acetyl group also likely occupying a neighboring on-top site), even though this result should be taken with precaution.

Thus, the comparison of the adsorption model theoretically computed for TFAP^{32,37} and experimentally determined for acetophenone in our study shows excellent agreement in the position of the phenyl ring and good qualitative agreement in the overall footprint of both molecules. It should be noted, however, that the footprint of acetophenone determined in our study was derived not from individually adsorbed molecules but from the dimer and trimer species. Even though the footprint of the monomers seems to be identical in all oligomer species, some changes in the adsorption configuration of monomers, especially the acetyl groups, due to intermolecular interactions cannot be completely excluded. Further theoretical work is needed to obtain more insights into the details of adsorption configurations of acetophenone oligomers.

The dynamic behavior of different types of oligomers was monitored at 300 K within several tens of minutes. Figure 7 shows the set of images, which were selected from a consecutively acquired STM scan at 300 K. Here, three typical oligomers are marked and shown on the close-up images on the right: symmetric trimer T1 (Figure 7a-I), trans-dimer D2 (Figure 7a-II), and cis-dimer D3 (Figure 7a-III). Note that the somewhat worse quality of the images is related to the higher-temperature instability of STM at 300 K and higher diffusion of acetophenone at elevated temperatures. Interestingly, the positions and the shape of the first two species, symmetric trimer T1 and cis-dimer D3, do not notably change on the experimental time scale. In contrast, the adsorbate appearing as a trans-dimer D1 in the first image (0 min, Figure 7a-II) undergoes considerable transformations. First, in the image related to 10 min of observation, it picks up a neighboring acetophenone molecule and becomes a symmetric trimer T1 (Figure 7c-II). After 15 min, this species converts to asymmetric trimer T2 (Figure 7d-II), and after 20 minutes, it loses one of the molecule to become a trans-dimer D2 (Figure 7e-II). This observation demonstrates that dimers and trimers can interconvert into each other at 300 K, attaching or losing a neighboring acetophenone molecule. It appears also

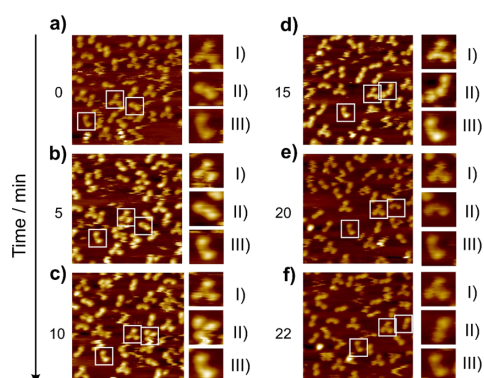


Figure 7. (a–f) Consecutive STM images of acetophenone adsorbed on Pt(111) obtained after exposure at 293 K. The acquisition temperature is the same ($7 \times 7 \text{ nm}^2$, 1 V, 0.52 nA). The numbers on the left indicate the time interval after the beginning of acquisition (0, 5, 10, 15, 20, and 22 min). Close-up images on the right show the time evolution of three individual oligomers: symmetric trimer T1 (I), trans-dimer D2 (II) undergoing structural transformations, and cis-dimer D3 (III).

likely that trimers interconvert into each other without losing their integrity as a trimer species, i.e., without intermediate disintegration to a dimer and monomer and attaching the monomer at a different position. This hypothesis, if true, suggests the ability of the ketone–enol–enol trimer to undergo complex restructuring in an intramolecular process.

CONCLUSIONS

Summarizing, we present a combined STM and IRAS study addressing the mechanisms of formation, adsorption configuration, and stability of different types of acetophenone oligomers on the catalytically active Pt(111) surface in a broad range of temperature and coverage conditions. We show that acetophenone can exist in the form of monomers, dimers, and trimers, with formation and relative distribution strongly depending on the surface temperature. Below 160 K, mostly monomers are observed, while above 200 K, trans-dimers represent the majority of surface species. Two types of trans-dimers could be identified spectroscopically at 200 K: the ketone–ketone species (D1), accounting for the largest fraction of trans-dimers, and ketone–enol trans-dimers (D2), in which the normally unstable enol form of acetophenone is stabilized via hydrogen bonding with the carbonyl group of the ketone counterpart. The trans-dimers appear to be immobile on this surface at 115 K, while the monomers can undergo frustrated rotation of the acetyl group with respect to the phenyl ring. With increasing temperature, the ketone–ketone dimers transform to ketone–enol species, which becomes the only surface species at 240 K.

At 300 K, three new types of oligomers are formed on the surface including symmetric (T1) and asymmetric (T2) trimers and a new type of cis-dimer (D3). Spectroscopically, the trimers are identified as ketone–enol–enol species, in which one carbonyl group is connected via H bonding to two enol species. Both types of dimers—cis and trans—exist in the form of ketone–enol species in this temperature range. The position of different types of dimers and trimers with respect to the underlying metal surface was determined with atomic precision. The monomers constituting different types of

oligomers have a similar footprint on the underlying metal surface. The phenyl ring was determined to be situated between two Pt atoms in a bridge position, which is in excellent agreement with the theoretical predictions made for a structurally similar acetophenone derivative TFAP. Finally, the stability of different adsorption configurations of dimers and a symmetric trimer was monitored by obtaining consecutive STM images. Particularly, the transformation of the trans-dimer (D2) to the symmetric trimer (T1) by attaching a neighboring acetophenone molecule was observed followed by the transformation of this species to the asymmetric trimer (T2) and its disintegration to a trans-dimer (D1) and a monomer. Specifically, the interconversion of the symmetric to asymmetric trimer appears to occur without disintegration into a dimer and a monomer, pointing to the possibility of the ketone–enol–enol trimer species to undergo complex intramolecular restructuring without losing the integrity of the whole complex.

The obtained results provide important atomistic-level insight into lateral interactions between acetophenone molecules on the catalytically active Pt surface.

AUTHOR INFORMATION

Corresponding Author

Swetlana Schauer mann – Institute of Physical Chemistry, Christian Albrechts University Kiel, 24118 Kiel, Germany; orcid.org/0000-0002-9390-2024; Email: schauer mann@pctc.uni-kiel.de

Authors

Marvin C. Schmidt – Institute of Physical Chemistry, Christian Albrechts University Kiel, 24118 Kiel, Germany
Smadar Attia – Institute of Physical Chemistry, Christian Albrechts University Kiel, 24118 Kiel, Germany
Carsten Schröder – Institute of Physical Chemistry, Christian Albrechts University Kiel, 24118 Kiel, Germany
Ann-Katrin Baumann – Institute of Physical Chemistry, Christian Albrechts University Kiel, 24118 Kiel, Germany
Pascal Pessier – Institute of Physical Chemistry, Christian Albrechts University Kiel, 24118 Kiel, Germany

Complete contact information is available at: <https://pubs.acs.org/10.1021/acs.jpcc.0c04343>

Notes

The authors declare no competing financial interest.

ACKNOWLEDGMENTS

Financial support by the German Science Foundations (DFG, grant SCHA 1477/3-1) is gratefully acknowledged.

REFERENCES

- (1) Mallat, T.; Orglmeister, E.; Baiker, A. Asymmetric Catalysis at Chiral Metal Surfaces. *Chem. Rev.* **2007**, *107*, 4863–4890.
- (2) Meemken, F.; Baiker, A. Recent Progress in Heterogeneous Asymmetric Hydrogenation of C=O and C=C Bonds on Supported Noble Metal Catalysts. *Chem. Rev.* **2017**, *117*, 11522–11569.
- (3) Gellman, A. J.; Tysoe, W. T.; Zaera, F. Surface Chemistry for Enantioselective Catalysis. *Catal. Lett.* **2015**, *145*, 220–232.
- (4) Rodríguez-García, L.; Hungerbühler, K.; Baiker, A.; Meemken, F. The Critical Role of Tilted Cinchona Surface Species for Enantioselective Hydrogenation. *ACS Catal.* **2017**, *7*, 3799–3809.
- (5) Marshall, S. T.; O'Brien, M.; Oetter, B.; Corpuz, A.; Richards, R. M.; Schwartz, D. K.; Medlin, J. W. Controlled Selectivity for

Palladium Catalysts Using Self-Assembled Monolayers. *Nat. Mater.* **2010**, *9*, 853–858.

(6) Marshall, S. T.; Medlin, J. W. Surface-Level Mechanistic Studies of Adsorbate–Adsorbate Interactions in Heterogeneous Catalysis by Metals. *Surf. Sci. Rep.* **2011**, *66*, 173–184.

(7) Sonström, P.; Bäumer, M. Supported Colloidal Nanoparticles in Heterogeneous Gas Phase Catalysis: On the Way to Tailored Catalysts. *Phys. Chem. Chem. Phys.* **2011**, *13*, 19270–19284.

(8) Lien, C.-H.; Medlin, J. W. Control of Pd Catalyst Selectivity with Mixed Thiolate Monolayers. *J. Catal.* **2016**, *339*, 38–46.

(9) Hutchings, G. J.; King, F.; Okoye, I. P.; Padley, M. B.; Rochester, C. H. Selectivity Enhancement in the Hydrogenation of A, B-Unsaturated Aldehydes and Ketones Using Thiophene-Modified Catalysts. *J. Catal.* **1994**, *148*, 453–463.

(10) Chiu, M. E.; Kyriakou, G.; Williams, F. J.; Watson, D. J.; Tikhov, M. S.; Lambert, R. M. Sulfur, Normally a Poison, Strongly Promotes Chemoselective Catalytic Hydrogenation: Stereochemistry and Reactivity of Crotonaldehyde on Clean and S-Modified Cu(111). *Chem. Commun.* **2006**, *12*, 1283–1285.

(11) Wu, B.; Huang, H.; Yang, J.; Zheng, N.; Fu, G. Selective Hydrogenation of α,β -Unsaturated Aldehydes Catalyzed by Amine-Capped Platinum-Cobalt Nanocrystals. *Angew. Chem., Int. Ed.* **2012**, *51*, 3440–3443.

(12) Kwon, S. G.; Krylova, G.; Sumer, A.; Schwartz, M. M.; Bunel, E. E.; Marshall, C. L.; Chattopadhyay, S.; Lee, B.; Jellinek, J.; Shevchenko, E. V. Capping Ligands as Selectivity Switchers in Hydrogenation Reactions. *Nano Lett.* **2012**, *12*, 5382–5388.

(13) Pang, S. H.; Medlin, J. W. Controlling Catalytic Selectivity Via Adsorbate Orientation on the Surface: From Furfural Deoxygenation to Reactions of Epoxides. *J. Phys. Chem. Lett.* **2015**, *6*, 1348–1356.

(14) Ernst, J. B.; Muratsugu, S.; Wang, F.; Tada, M.; Glorius, F. Tunable Heterogeneous Catalysis: N-Heterocyclic Carbenes as Ligands for Supported Heterogeneous Ru/K-Al₂O₃ Catalysts to Tune Reactivity and Selectivity. *J. Am. Chem. Soc.* **2016**, *138*, 10718–10721.

(15) Ernst, J. B.; Schwermann, C.; Yokota, G.-I.; Tada, M.; Muratsugu, S.; Doltsinis, N. L.; Glorius, F. Molecular Adsorbates Switch on Heterogeneous Catalysis: Induction of Reactivity by N-Heterocyclic Carbenes. *J. Am. Chem. Soc.* **2017**, *139*, 9144–9147.

(16) Dostert, K.-H.; O'Brien, C. P.; Ivars-Barceló, F.; Schauer mann, S.; Freund, H.-J. Spectators Control Selectivity in Surface Chemistry: Acrolein Partial Hydrogenation over Pd. *J. Am. Chem. Soc.* **2015**, *137*, 13496–13502.

(17) Schauer mann, S. Partial Hydrogenation of Unsaturated Carbonyl Compounds: Toward Ligand-Directed Heterogeneous Catalysis. *J. Phys. Chem. Lett.* **2018**, *9*, 5555–5566.

(18) Somorjai, G. A. *Introduction to Surface Chemistry and Catalysis*, 2nd Ed.; John Wiley & Sons: New York, 2010.

(19) Attia, S.; Schmidt, M.-C.; Schröder, C.; Pessier, P.; Schauer mann, S. Surface-Driven Keto–Enol Tautomerization: Atomistic Insights into Enol Formation and Stabilization Mechanisms. *Angew. Chem., Int. Ed.* **2018**, *57*, 16659–16664.

(20) Attia, S.; Schmidt, M. C.; Schröder, C.; Schauer mann, S. Formation and Stabilization Mechanisms of Enols on Pt through Multiple Hydrogen Bonding. *ACS Catal.* **2019**, *9*, 6882–6889.

(21) Attia, S.; Schauer mann, S. Coverage-Dependent Adsorption Geometry of Acetophenone on Pt(111). *J. Phys. Chem. C* **2020**, *124*, 557–566.

(22) Attia, S.; Schmidt, M. C.; Schröder, C.; Weber, J.; Baumann, A.-K.; Schauer mann, S. Keto–Enol Tautomerization as a First Step in Hydrogenation of Carbonyl Compounds. *J. Phys. Chem. C* **2019**, *123*, 29271–29277.

(23) Dostert, K.-H.; O'Brien, C. P.; Liu, W.; Riedel, W.; Savara, A.; Tkatchenko, A.; Schauer mann, S.; Freund, H.-J. Adsorption of Isophorone and Trimethyl-Cyclohexanone on Pd(111): A Combination of Infrared Reflection Absorption Spectroscopy and Density Functional Theory Studies. *Surf. Sci.* **2016**, *650*, 149–160.

(24) Dostert, K.-H.; O'Brien, C. P.; Riedel, W.; Savara, A.; Liu, W.; Oehzelt, M.; Tkatchenko, A.; Schauer mann, S. Interaction of

Isophorone with Pd(111): A Combination of Infrared Reflection–Absorption Spectroscopy, near-Edge X-Ray Absorption Fine Structure, and Density Functional Theory Studies. *J. Phys. Chem. C* **2014**, *118*, 27833–27842.

(25) Liu, W.; Jiang, Y.; Dostert, K.-H.; O'Brien, C. P.; Riedel, W.; Savara, A.; Schauer mann, S.; Tkatchenko, A. Catalysis Beyond Frontier Molecular Orbitals: Selectivity in Partial Hydrogenation of Multi-Unsaturated Hydrocarbons on Metal Catalysts. *Sci. Adv.* **2017**, *3*, No. e1700939.

(26) Liu, W.; Savara, A.; Ren, X.; Ludwig, W.; Dostert, K.-H.; Schauer mann, S.; Tkatchenko, A.; Freund, H.-J.; Scheffler, M. Toward Low-Temperature Dehydrogenation Catalysis: Isophorone Adsorbed on Pd(111). *J. Phys. Chem. Lett.* **2012**, *3*, 582–586.

(27) Dostert, K.-H.; O'Brien, C. P.; Mirabella, F.; Ivars-Barceló, F.; Schauer mann, S. Adsorption of Acrolein, Propanal, and Allyl Alcohol on Pd(111): A Combined Infrared Reflection–Absorption Spectroscopy and Temperature Programmed Desorption Study. *Phys. Chem. Chem. Phys.* **2016**, *18*, 13960–13973.

(28) Dostert, K.-H.; O'Brien, C. P.; Mirabella, F.; Ivars-Barceló, F.; Attia, S.; Spadafora, E.; Schauer mann, S.; Freund, H.-J. Selective Partial Hydrogenation of Acrolein on Pd: A Mechanistic Study. *ACS Catal.* **2017**, *7*, 5523–5533.

(29) O'Brien, C. P.; Dostert, K.-H.; Schauer mann, S.; Freund, H.-J. Selective Hydrogenation of Acrolein over Pd Model Catalysts: Temperature and Particle-Size Effects. *Chem. - Eur. J.* **2016**, *22*, 15856–15863.

(30) O'Brien, C. P.; Dostert, K. H.; Hollerer, M.; Stiehler, C.; Calaza, F.; Schauer mann, S.; Shaikhtudinov, S.; Sterrer, M.; Freund, H. J. Supports and Modified Nano-Particles for Designing Model Catalysts. *Faraday Discuss.* **2016**, *188*, 309–321.

(31) Rappoport, Z. *The Chemistry of Enols (Chemistry of Functional Groups Series)*; John Wiley & Sons Ltd Chichester: 1990.

(32) Rasmussen, A. M. H.; Groves, M. N.; Hammer, B. Remote Activation of Chemical Bonds in Heterogeneous Catalysis. *ACS Catal.* **2014**, *4*, 1182–1188.

(33) Yang, B.; Wang, D.; Gong, X.-Q.; Hu, P. Acrolein Hydrogenation on Pt(211) and Au(211) Surfaces: A Density Functional Theory Study. *Phys. Chem. Chem. Phys.* **2011**, *13*, 21146–21152.

(34) De Vrieze, J. E.; Thybaut, J. W.; Saeys, M. Role of Keto–Enol Tautomerization in the Copper-Catalyzed Hydrogenation of Ketones. *ACS Catal.* **2019**, *9*, 3831–3839.

(35) Laliberté, M.-A.; Lavoie, S.; Hammer, B.; Mahieu, G.; McBreen, P. H. Activation in Prochiral Reaction Assemblies on Pt(111). *J. Am. Chem. Soc.* **2008**, *130*, 5386–5387.

(36) Demers-Carpentier, V.; McBreen, P. H. Surface Vibrational Spectroscopy Study of Benzene and 2,2,2-Trifluoroacetophenone on Pt(111). *J. Phys. Chem. C* **2011**, *115*, 6513–6520.

(37) Goubert, G.; Rasmussen, A. M. H.; Dong, Y.; Groves, M. N.; McBreen, P. H.; Hammer, B. Walking-Like Diffusion of Two-Footed Asymmetric Aromatic Adsorbates on Pt(111). *Surf. Sci.* **2014**, *629*, 123–131.

(38) Demers-Carpentier, V.; Laliberté, M.-A.; Lavoie, S.; Mahieu, G.; McBreen, P. H. Two-Dimensional Self-Assembly and Catalytic Function: Conversion of Chiral Alcohols into Self-Assembled Enols on Pt(111). *J. Phys. Chem. C* **2010**, *114*, 7291–7298.

(39) Attia, S.; Spadafora, E. J.; Hartmann, J.; Freund, H.-J.; Schauer mann, S. Molecular Beam/Infrared Reflection–Absorption Spectroscopy Apparatus for Probing Heterogeneously Catalyzed Reactions on Functionalized and Nanostructured Model Surfaces. *Rev. Sci. Instrum.* **2019**, *90*, No. 053903.

(40) Gambi, A.; Giorgianni, S.; Passerini, A.; Visinoni, R.; Gheretti, S. Infrared Studies of Acetophenone and Its Deuterated Derivatives. *Spectrochim. Acta, Part A* **1980**, *36*, 871–878.

(41) Fried, S. D.; Bagchi, S.; Boxer, S. G. Measuring Electrostatic Fields in Both Hydrogen-Bonding and Non-Hydrogen-Bonding Environments Using Carbonyl Vibrational Probes. *J. Am. Chem. Soc.* **2013**, *135*, 11181–11192.

(42) Nolasco, M. M.; Ribeiro-Claro, P. J. A. C-H...O Hydrogen Bonds in Cyclohexenone Reveal the Spectroscopic Behavior of C_{sp3}-H and C_{sp2}-H Donors. *Chem. Phys. Chem.* **2005**, *6*, 496–502.

(43) Bandyopadhyay, B.; Pandey, P.; Banerjee, P.; Samanta, A. K.; Chakraborty, T. CH-O Interaction Lowers Hydrogen Transfer Barrier to Keto–Enol Tautomerization of B-Cyclohexanedione: Combined Infrared Spectroscopic and Electronic Structure Calculation Study. *J. Phys. Chem. A* **2012**, *116*, 3836–3845.

(44) Stöhr, M.; Van Voorhis, T.; Tkatchenko, A. Theory and Practice of Modeling Van Der Waals Interactions in Electronic-Structure Calculations. *Chem. Soc. Rev.* **2019**, *48*, 4118–4154.

(45) Su, G.; Yang, S.; Jiang, Y.; Li, J.; Li, S.; Ren, J.-C.; Liu, W. Modeling Chemical Reactions on Surfaces: The Roles of Chemical Bonding and Van Der Waals Interactions. *Prog. Surf. Sci.* **2019**, *94*, 100561.

(46) Gimzewski, J. K.; Joachim, C.; Schlittler, R. R.; Langlais, V.; Tang, H.; Johannsen, I. Rotation of a Single Molecule within a Supramolecular Bearing. *Science* **1998**, *281*, 531–533.

(47) Schaffert, J.; Cottin, M. C.; Sonntag, A.; Bobisch, C. A.; Möller, R.; Gauyacq, J.-P.; Lorente, N. Tunneling Electron Induced Rotation of a Copper Phthalocyanine Molecule on Cu (111). *Phys. Rev. B* **2013**, *88*, No. 075410.

(48) Mo, Y. W. Reversible Rotation of Antimony Dimers on the Silicon (001) Surface with a Scanning Tunneling Microscope. *Science* **1993**, *261*, 886–888.

(49) Avery, N. R. EELS Identification of the Adsorbed Species from Acetone Adsorption on Pt (111). *Surf. Sci.* **1983**, *125*, 771–786.

(50) Vannice, M. A.; Erley, W.; Ibach, H. A RAIRS and HREELS Study of Acetone on Pt (111). *Surf. Sci.* **1991**, *254*, 1–11.

(51) Delbecq, F.; Sautet, P. Adsorption of Aldehydes and Ketones on Platinum and Palladium: Influence of Steps, Open Faces and Metal Nature: A Theoretical Study. *Surf. Sci.* **1993**, *295*, 353–373.

(52) Vargas, A.; Bürgi, T.; Baiker, A. Adsorption of Activated Ketones on Platinum and Their Reactivity to Hydrogenation: A DFT Study. *J. Catal.* **2004**, *222*, 439–449.

(53) Johnson, R. D., III Nist Computational Chemistry Comparison and Benchmark Database. In *NIST Standard Reference Database Number 101*; NIST: Release 20, August 2019.

(54) Honkela, M. L.; Björk, J.; Persson, M. Computational Study of the Adsorption and Dissociation of Phenol on Pt and Rh Surfaces. *Phys. Chem. Chem. Phys.* **2012**, *14*, 5849–5854.

(55) Morin, C.; Simon, D.; Sautet, P. Trends in the Chemisorption of Aromatic Molecules on a Pt(111) Surface: Benzene, Naphthalene, and Anthracene from First Principles Calculations. *J. Phys. Chem. B* **2004**, *108*, 12084–12091.

(56) Rasmussen, A. M. H.; Hammer, B. Adsorption, Mobility, and Dimerization of Benzaldehyde on Pt(111). *J. Chem. Phys.* **2012**, *136*, 174706.

(57) Jenkins, S. J. Aromatic Adsorption on Metals Via First-Principles Density Functional Theory. *Proc. R. Soc. A* **2009**, *465*, 2949–2976.

8.10 Formation and Real-Space Distribution of Acetophenone Dimers on H-containing Pt(111)

Publication Data and Reprint

Reference: Marvin C. Schmidt, Smadar Attia, Carsten Schröder, Ann-Katrin Baumann and Swetlana Schauermann

DOI: 10.1021/acs.jpcc.1c05707

Submitted: 28.06.2021

Accepted: 17.08.2021

Contribution: IR measurements, scientific discussions, preparation of parts of the manuscript

Copyright: Reprinted with permission from JPC C from Ref.[239]. Copyright 2021 American Chemical Society.

Formation and Real-Space Distribution of Acetophenone Dimers on H-containing Pt(111)

Marvin C. Schmidt, Smadar Attia, Carsten Schröder, Ann-Katrin Baumann, and Svetlana Schauerma^{*}

Cite This: *J. Phys. Chem. C* 2021, 125, 19311–19324

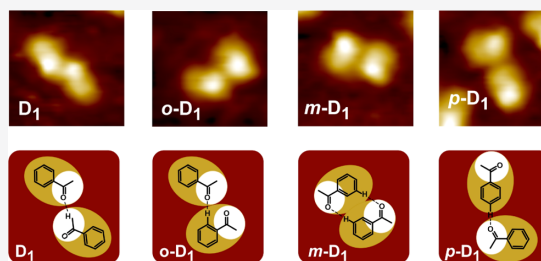
Read Online

ACCESS |

Metrics & More

Article Recommendations

ABSTRACT: We present a mechanistic study on the formation and real-space distribution of acetophenone dimers on the H-containing Pt(111) surface. Their geometric configuration and the specific chemical nature are addressed by a combination of scanning tunneling microscopy (STM) and infrared reflected absorption spectroscopy (IRAS). The formation of different types of acetophenone dimers is reported here, which critically depends on the surface coverage of H species. When the surface coverage of H is close to a monolayer (ML), acetophenone is adsorbed mainly as monomer species, while only a small amount of adsorbates are agglomerated into dimers. In these dimers, the majority of species are related to acetyl/phenyl dimers, in which a carbonyl group of one molecule interacts with a H atom involved in the phenyl ring of the neighboring molecule. Depending on the position of this ring, H atom, *ortho*-, *meta*-, and *para*-dimers can be formed with comparable probabilities. On the surface precovered with a lower concentration of H (close to 0.5 ML) only, a new class of dimers prevail, which interacts via two acetyl groups forming ketone–enol dimers or partly hydrogenated dimers. Specifically, in the ketone–enol dimers, one molecule undergoes keto–enol tautomerization and a newly formed OH group becomes involved in H bonding with the neighboring carbonyl entity. In this way, a normally unstable enol species can be stabilized on the surface. The interaction between the carbonyl group and the phenyl ring becomes negligible on this type of surface. Additionally, a large fraction of the ketone–enol dimers becomes partly hydrogenated on this surface, producing a direct reaction intermediate toward hydrogenation of the carbonyl group in acetophenone. We discuss the chemical nature as well as the structure of all formed surface species observed on H-containing Pt.

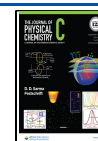


INTRODUCTION

Heterogeneously catalyzed hydrogenation of carbonyl compounds is a highly challenging process relying on the activation of a typically strong C=O double bond.^{1,2} Usually, transition metal catalysts working under high-temperature conditions are employed for this type of reaction to promote hydrogen insertion into the stable carbonyl group. As an alternative to this direct reaction pathway, a different type of the reaction mechanism was recently predicted theoretically,^{3–5} which relies on two consecutive reaction steps: (i) keto–enol tautomerization, in which the C–OH and C=C groups are formed in the enol form of the reactant, followed by (ii) hydrogen insertion into the newly formed C=C bond. The activation barriers for both of these reaction steps were predicted to be significantly lower as compared to direct hydrogen insertion into the strongly bound carbonyl group. This predicted reaction mechanism based on keto–enol tautomerization could open up a prospect to a new low-temperature hydrogenation route of carbonyl compounds. The major problem of this process, however, is the instability of enol species, which are usually thermodynamically less favorable forms of carbonyl compounds.⁶ Thus, the practical

realization of this potentially highly promising catalytic route relies on finding a way to stabilize the enol form of the reactant on the catalytic surface, making it capable of entering the second reaction step. In our recent mechanistic studies on the hydrogenation of acetophenone over Pt(111), we provided experimental evidence for this predicted reaction pathway.⁷ Specifically, it was shown that hydrogenation of this compound can occur already at 240 K. Importantly, the direct precursor for this reaction pathway was identified as a ketone–enol dimer, containing an enol form of the molecule, in which the OH group is stabilized by hydrogen bonding with the C=O group of the neighboring acetophenone molecule in the ketone form. The combination of spectroscopic and microscopic observations^{7–12} allowed us to conclude that stabilization of

Received: June 28, 2021
Revised: August 17, 2021
Published: August 27, 2021



enol species in the form of ketone–enol dimers plays a crucial role in the formation of the desired enol-containing reaction intermediates and in promoting the enol-based hydrogenation pathway.

Even though these studies^{7–12} provided first insights into the related surface processes, the details of enol formation and stabilization on H-containing transition metal surfaces are not fully understood yet. In view of the striking results demonstrating the crucial role of stabilized enol species in the hydrogenation of carbonyl compounds, it becomes evident that the related elementary processes need to be understood at the microscopic level under the catalytically relevant conditions.

Previously, the formation of surface dimers of carbonyl compounds was reported in a number of studies carried out on pristine transition metal surfaces. McBreen et al.^{13–16} reported the formation of different types of oligomers, including dimers and trimers, for 2,2,2-trifluoroacetophenone (TFAP) on Pt(111) at low temperatures. The authors proposed a stabilization mechanism of the oligomer species based on H bonding between the carbonyl group and a hydrogen atom involved in the phenyl ring of the neighboring molecule. The same authors observed the formation of acetophenone dimers and trimers¹⁷ at room temperature, which was explained by the formation of different types of oligomers consisting of solely enol molecules. More recently, we investigated the interaction of acetophenone with the pristine Pt(111) surface,^{7–12} which was shown to form ketone–ketone and ketone–enol dimers as well as ketone–enol–enol trimers depending on the surface temperature. In all observed cases, the individual molecules were connected to each other via the acetyl groups: (i) either via a C=O group and a H atom of the methyl groups (in ketone–ketone dimers) or (ii) via the C=O group of the ketone and the H of the –OH group of the enol form of acetophenone. Importantly, the formation of enol species was found to be an activated process occurring only above a threshold surface temperature lying close to 140 K.^{9,10} In the temperature range of around 240 K, the ketone–enol dimer is the most populated surface species, while close to 300 K, the ketone–enol–enol trimers start to evolve.¹⁰ Generally, the stabilization mechanisms of enols on surfaces in the form of dimers and trimers found in these studies are similar to those previously described for chelated ketone/enol tautomers in diketones and ketoesters in the gas phase and solutions.^{18–23} To the best of our knowledge, no systematic mechanistic studies on enol formation and stabilization on the surfaces containing hydrogen was reported so far in the literature.

To address the details of enol formation and stabilization on hydrogen-containing catalytic surfaces, we performed a mechanistic study on the interaction of acetophenone with a model Pt(111) surface precovered with hydrogen in a broad range of temperature and coverage conditions. In this study, we employ a combination of scanning tunneling microscopy (STM) and infrared reflection absorption spectroscopy (IRAS) with a particular focus on the investigation of the microscopic structures of acetophenone dimers formed on hydrogen-containing surfaces as well as on the effects related to the concentration of adsorbed H species.

Specifically, we show that on the Pt(111) surface containing H at high surface coverage $\Theta_{\text{H}} \approx 1$ ML, mainly the monomer form of acetophenone is present, while only a minor fraction of adsorbates are agglomerated in dimers. The absolute majority of these dimer species exhibit an interaction based on H

bonding between an O atom of a carbonyl group and a H atom involved in the phenyl ring of neighboring acetophenone molecules. Three different types of dimers involving the acetyl/phenyl interaction were found on this surface, corresponding to three different positions of H in the phenyl ring with respect to the acetyl group. A very minor fraction of the dimers populated on this surface is the species in which intermolecular bonding is realized via two acetyl groups, interacting via a carbonyl O and a H atom involved in a CH₃ entity.

The chemical composition and the distribution of dimer species strongly change when the H surface coverage decreases to about half of the monolayer, which can be achieved by increasing the temperature to 240–250 K.^{24–26} Nearly all adsorbed acetophenone molecules become agglomerated in dimers; two chemically different dimer structures can be observed. In both types of dimers, the interaction between the two acetyl groups prevails on this surface, in contrast to Pt precovered with $\Theta_{\text{H}} \approx 1$ ML, containing mainly acetyl/phenyl dimers. The first type of observed species is the ketone–enol dimer, with one molecule being present in the enol form, which is H-bonded to the carbonyl group of the second acetophenone molecule. The normally energetically unstable enol species are stabilized by this strong intermolecular interaction with neighboring ketones. The second type of dimers on this surface results from partial hydrogenation of the ketone–enol dimer to produce a partly hydrogenated reaction intermediate, exhibiting a characteristic vibrational signature in IRAS. We provide detailed structural and chemical analysis of all acetophenone-related species observed on the H-precovered Pt(111) surfaces.

The atomistic-level details obtained on lateral interactions between the carbonyl compounds on catalytically relevant H-containing surfaces provide important insights into the mechanisms of low-barrier hydrogenation of aldehydes and ketones. The related phenomena can be employed for purposeful surface functionalization with stable carbonyl-containing compounds capable of energetic stabilization of the enol form of ketones and aldehydes and thus promoting the low-barrier enol-based hydrogenation pathway.

METHODS

Sample Preparation. The Pt(111) single-crystal (MaTeck GmbH) was cleaned prior to use in ultra-high vacuum (UHV) chambers by repeated cycles of Ar⁺ ion bombardment at room temperature, followed by annealing at 1150 K and subsequent oxidation in 1×10^{-7} mbar O₂ at 650–750 K to remove residual carbon. The last step contains the rapid flash of the sample to 1000 K. Shortly before each experiment, the sample was flashed to 600 K before cooling to the required temperature to remove CO adsorbates. The long-range order and cleanliness of the Pt(111) single-crystal were checked by low energy electron diffraction (LEED), Auger electron spectroscopy (AES), and additionally by IRAS of adsorbed CO to probe the abundance of adsorption sites.

STM. The STM measurements were carried out in an ultra-high vacuum (UHV, base pressure better than 1×10^{-10} mbar) apparatus by employing a variable temperature (90–300 K) Aarhus 150 SPM (SPECS). All measurements were carried out in a constant current mode, and the bias voltage U_{T} was applied to the sample. The etched W-Tip was commercially produced by SPECS and *in situ* sharpened by repeated cycles of 1.25 keV Ar⁺-bombardment with 5×10^{-6} mbar back

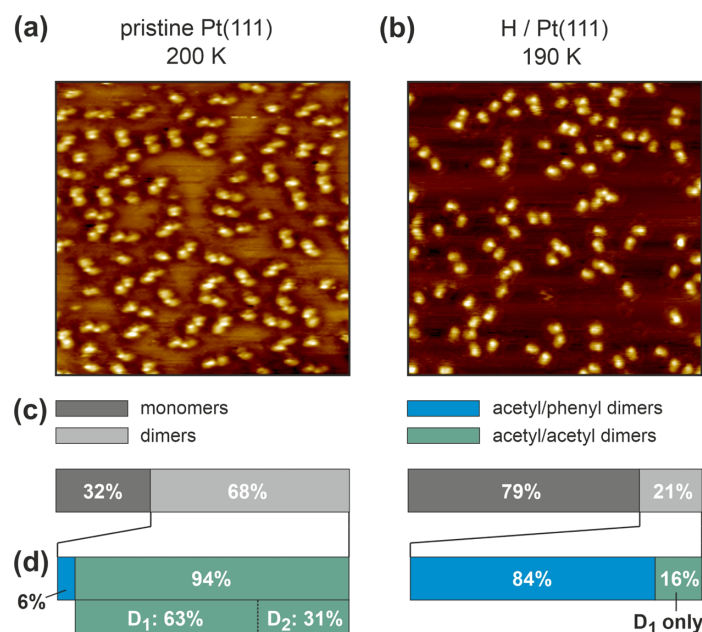


Figure 1. STM images of acetophenone (a) adsorbed on pristine Pt(111) (exposure at 200 K, acquisition temperature 125 K, 1 V, 0.29 nA, $19 \times 19 \text{ nm}^2$) and (b) H-precovered Pt(111) surfaces, $\Theta_{\text{H}} \approx 0.95 \text{ ML}$ (exposure at 190 K, acquisition temperature 120 K, 0.5 V, 0.30 nA, $20 \times 20 \text{ nm}^2$). (c) Statistical evaluation of the distribution of monomer vs dimer surface species. (d) Statistical distribution of acetyl/acetyl vs acetyl/phenyl dimer species. Both statistical evaluations shown in (c) and (d) were performed on larger STM scans.

pressure for 5 min. The sharpness of the W-Tip was validated on the pristine Pt(111) surface.

The Pt(111) single-crystal was cleaned according to the cleaning procedure described above. The quality of the sample was additionally verified by acquiring STM images prior to the deposition at 293 K. H_2 (Linde HiQ 6.0) was backfilled into the chamber via an individual gas doser with a pressure in the preparation chamber of 2×10^{-6} mbar for 3 min to ensure complete saturation of the Pt(111) surface. Acetophenone (Sigma-Aldrich, purity $\geq 99.5\%$) was purified prior to the experiments by repeated freeze–pump–thaw cycles. Acetophenone was dosed through an individual gas doser onto the Pt(111) surface, kept at the desired deposition temperature, and then transferred to the STM chamber for measurements.

IRAS. The IRAS experiments were performed in a specially designed UHV apparatus²⁷ (base pressure 2×10^{-10} mbar) containing two effusive doubly differentially pumped multi-channel array sources and a supersonic beam operated at room temperature. Acetophenone (Sigma-Aldrich, purity 99%) was dosed onto the sample via an effusive source at a typical flux of 2×10^{12} molecules·cm⁻²·s⁻¹ controlled by a pneumatic valve and a shutter. The source was operated at room temperature, and the beam diameter was chosen to exceed the sample size. Acetophenone was purified prior to the experiments by repeated freeze–pump–thaw cycles. H_2 (Linde HiQ 6.0) was dosed via an independent molecular beam without further purification at a typical flux of 8.5×10^{14} molecules·cm⁻²·s⁻¹. IRAS data have been acquired using a vacuum Fourier transform infrared (FT-IR) spectrometer (Bruker Vertex 80v) with a spectral resolution of 2 cm^{-1} and a mid-infrared (MIR) polarizer and p-polarized IR light. The spectrometer is equipped with a narrow band Mercury–Cadmium–Telluride

(MCT) detector. IRAS spectra were acquired at the same surface temperature that was used for deposition. An automated quadrupole mass spectrometer (QMS) system (Hiden, HAL 301/3F) was employed for the continuous monitoring of the partial pressures of gaseous species.

RESULTS AND DISCUSSION

Acetophenone adsorption on a well-defined Pt(111) surface precovered with hydrogen was investigated by STM and IRAS under UHV conditions in a temperature range of 190–260 K. Figure 1 displays the STM images obtained on pristine and H-precovered Pt surface obtained after the deposition of acetophenone at 200 and 190 K, respectively. The acetophenone coverage corresponds to approximately 2.8×10^{13} and 4.2×10^{13} molecules·cm⁻², respectively (calculated directly from STM images). In this temperature range, a near-saturation coverage of H on Pt(111) can be achieved, as shown by Poelsema and Comsa.²⁴ Using their reported temperature-programmed desorption (TPD) data obtained on Pt(111), we estimated the H coverage at 190 K as $\Theta_{\text{H}} \approx 0.95 \text{ ML}$. Note that the monolayer of H is defined as the number of adsorbed H atoms divided by the number of surface Pt atoms, i.e., one H atom is adsorbed per one Pt atom in saturation.^{24,28} The surface concentration of adsorbed acetophenone species is significantly lower and corresponds to approx. 0.02–0.03 acetophenone molecules per surface Pt atom.

On the pristine Pt(111) surface at 200 K (Figure 1a), three major types of surface species can be discriminated, which were extensively discussed in our previous reports.^{7–10,12} Briefly, about 68% of surface species are dimers and 32% are related to monomers of acetophenone. Combining microscopic observations with infrared spectroscopy, we were able to

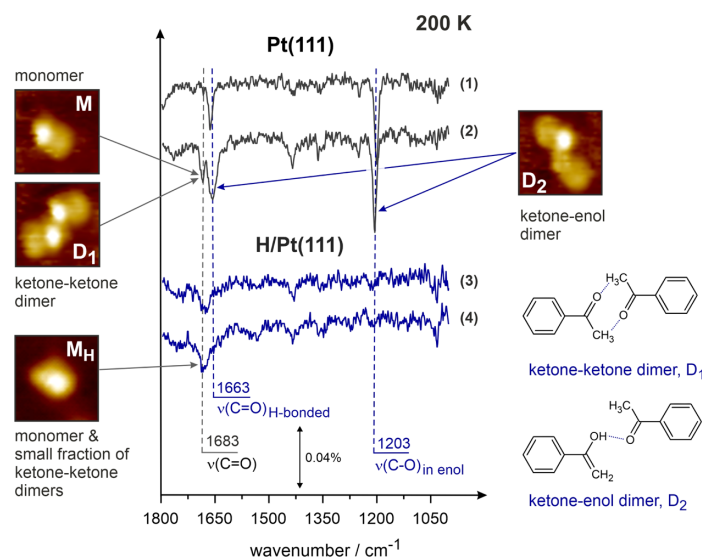


Figure 2. IR spectra of acetophenone adsorbed on pristine (spectra 1 and 2) and H-precovered Pt(111), $\Theta_{\text{H}} \approx 0.95$ ML (spectra 3 and 4) obtained at 200 K. All spectra are related to submonolayer coverages and were obtained after acetophenone exposures to (1) 2.1×10^{14} , (2) 1.2×10^{15} , (3) 5.8×10^{14} , and (4) 3.9×10^{15} molecules- cm^{-2} .

show that in this temperature range, the acetophenone dimers can be related to two chemically different surface species: ketone–ketone (D_1) and ketone–enol (D_2) species. The related IR spectra and the close-up STM images of these surface species are shown in Figure 2: spectra (1) and (2) obtained on pristine Pt(111) and the related STM close-up images. The more abundant (63%) symmetric dimer D_1 consists of two identical protrusions, each enclosing a brighter and a darker area. The brighter area was previously identified as an acetyl group so that the intermolecular interaction in this type of dimer occurs via two acetyl groups, most likely via a H bonding between the C=O group of one acetophenone molecule and a H atom of the CH_3 - group of the neighboring acetophenone species. In the less abundant (31%) asymmetric dimer D_2 , one of the molecules also appears as a combination of the brighter and darker areas (similarly to the individual molecules constituting the dimer D_1 and to the monomer species M, also shown in a close-up image in Figure 2). In contrast, the second half of the dimer in D_2 species shows a nearly uniform intensity across the molecule. Based on the combination of microscopic and spectroscopic results, we assigned this dimer to the combination of a ketone and an enol form of acetophenone, in which a normally unstable enol is stabilized via H bonding between the OH group of the enol and the carbonyl group of the ketone. The detailed assignment of the related IR spectra was performed earlier;^{9,10} here, we will only briefly summarize the most important vibrational bands, which are relevant for the further discussion of acetophenone adsorption on the H-precovered surface.

The spectra (1) and (2) obtained at submonolayer acetophenone coverages (Figure 2) show the three most prominent vibrational bands: (i) the band at 1683 cm^{-1} is related to the C=O stretching bond vibration, which is characteristic to a nearly unperturbed acetophenone;²⁹ (ii) the band at 1203 cm^{-1} , arising from a single C–O bond in the enol form of acetophenone, and (iii) the band at 1663 cm^{-1} , which is assigned to the C=O bond of the ketone form

involved in hydrogen bonding.^{8–10} The latter two bands always appear and evolve in a correlated manner (as it can be seen, e.g., in the spectra (1) and (2) of Figure 2) and can be therefore assigned to the same surface species, particularly to the ketone–enol dimer D_2 . In this dimer, the carbonyl group of the ketone is involved in hydrogen bonding with the OH group of the enol and, therefore, is strongly red-shifted from 1683 cm^{-1} (in the nonperturbed acetophenone) to 1663 cm^{-1} .⁹ This assignment is in an excellent agreement with the earlier reports on keto-enol tautomerization in diketones and ketoesters resulting in the formation of a chelated ring-like ketone/enol tautomers.^{21,30–32} It is important to note that the strong frequency shift of the carbonyl band in the ketone–enol dimer is related to the strong interaction between this group and acidic hydrogen of the –OH group in the enol. This effect based on the donor–acceptor hydrogen bonding has a general nature and is predicted to obey the following trend: the higher the acidity of the donor involved in the hydrogen bond (in our case, hydrogen in the OH group), the larger is the resulting frequency shift of the acceptor (i.e., in the –C=O group).^{33,34} For this reason, the dimers formed via hydrogen bonding with nonacidic hydrogen (e.g., H involved in the – CH_3 entity of the ketone form) are not expected to show any noticeable frequency shifts. Therefore, the band at 1683 cm^{-1} can be assigned to the carbonyl stretching vibration in the ketone–ketone dimers D_1 , in which a nonacidic hydrogen is involved in bonding, and in acetophenone monomers M, as the latter species experience no lateral interactions with the neighbors.

Figure 1b shows the STM image of acetophenone adsorbed on Pt(111) precovered with H at 190 K. It can be clearly seen that the distribution between the monomer and dimer species drastically change on the surface precovered with H at $\Theta_{\text{H}} \approx 0.95$ ML: the majority of the surface species (79%) are now monomers, while dimers account only for 21% of adsorbates. Spectroscopically, it can be seen that no ketone–enol dimers D_2 are formed on this surface as indicated by the absence of the vibrational bands at 1203 and 1663 cm^{-1} (spectra (3) and

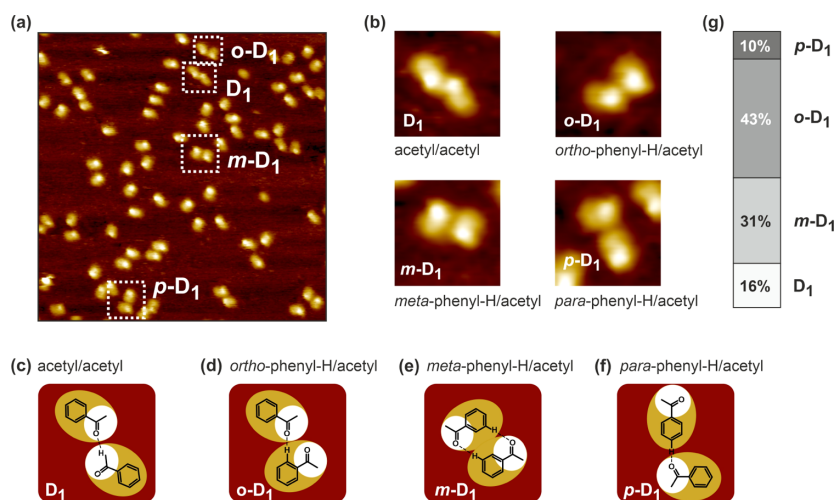


Figure 3. (a) STM image of acetophenone adsorbed on the H-precured Pt(111) surface, $\Theta_{\text{H}} \approx 0.95$ ML, (exposure at 190 K, acquisition temperature 120 K, 0.12 V, 0.49 nA, 19×19 nm²). (b) Close-up images of different surface species (acetyl/acetyl dimer D_1 , *ortho*-phenyl-H/acetyl dimer $o\text{-}D_1$, *meta*-phenyl-H/acetyl dimer $m\text{-}D_1$, *para*-phenyl-H/acetyl dimer $p\text{-}D_1$) present on the surface. (c)–(f) Proposed structures of dimer species shown in (b). (g) Statistical distribution of different acetyl/phenyl and acetyl/acetyl dimer species. The statistical evaluation was performed on a larger STM scan.

(4) in Figure 2), related to the C–O single bond in the enol and H bonded C=O bond in the ketone part of the ketone–enol dimer D_2 , respectively. Only the vibrational band at 1683 cm⁻¹ is present in the IR spectra on this surface, which is related to acetophenone monomers (indicated further as M_{H}) and to the small fraction of ketone–ketone dimers. The combination of these observations suggests that the ketone–enol dimers do not exist on the Pt surface covered with $\Theta_{\text{H}} \approx 0.95$ ML hydrogen, which can occur either (i) because of hindered formation of the enol species or (ii) due to energetic destabilization of ketone–enol dimers. The latter scenario can occur, e.g., if the interaction strength between the enol and ketone species in the presence of highly abundant H becomes lower than the interaction strength between the ketone species and coadsorbed H atoms so that quasi-hydrogen bonding with the surface-adsorbed atomic H is formed. The specific reasons for this observed scenario are currently being investigated in theoretical studies.

It is important to point out that the ketone–ketone dimers can still be formed on the H-containing surface at $\Theta_{\text{H}} \approx 0.95$ ML; however, their structure undergoes strong changes as compared to pristine Pt(111). Figure 3a,b shows the four types of ketone–ketone species observed on the H-precured Pt(111) at 190 K. The dimer D_1 is the same type of dimer, which is present on the pristine Pt(111) surface under the same temperature conditions (see Figures 1 and 2). In this species, an O atom involved in the carbonyl group of one molecule is hydrogen bonded to a H atom of the $-\text{CH}_3$ group of the neighboring molecule. Figure 3c shows the proposed configuration of the acetyl/acetyl dimer D_1 . Note that in this case, intermolecular bonding occurs between the acetyl groups of both acetophenone molecules. This type of interaction will be further indicated as the acetyl/acetyl interaction and the related dimers as acetyl/acetyl dimers. Also, note that even if one of the acetyl groups undergoes chemical transformation, e.g., keto–enol tautomerization or partial hydrogenation, the interaction occurring via this former acetyl group with another

acetyl group will also be indicated as the acetyl/acetyl interaction.

In contrast, three other types of surface dimers exhibit a different type of interaction, in which a H atom of the phenyl ring is involved. The STM close-up images shown in Figure 3b (dimers indicated as $o\text{-}D_1$, $m\text{-}D_1$, and $p\text{-}D_1$) demonstrate that in each of these cases, the bright protrusion of one molecule (acetyl group) is situated in close vicinity to the darker protrusion of the other molecule (phenyl ring). This observation suggests that an O atom of the carbonyl group most likely interacts with a H atom involved in the phenyl ring of the neighboring molecule. This type of bonding between a carbonyl group and a H atom of the phenyl ring was previously reported by McBreen et al. for trifluoroacetophenone (TFAP) adsorbed on Pt(111) at 300 K.¹⁶ In the following, this class of dimers, comprising *o*-, *m*-, and *p*- D_1 dimer species, will be indicated as acetyl/phenyl dimers. It is important to note that three different configurations of the acetyl/phenyl dimers correspond to three possible positions of H atoms in the phenyl ring with respect to the acetyl group. Figure 3d–f shows the proposed configurations of these dimer species and the H atoms involved in hydrogen bonding. The scheme displayed in Figure 3d is related to the case when a H atom situated in the *ortho*-position with respect to the acetyl group is involved in hydrogen bonding with the neighboring carbonyl. According to this position, the related dimer is denoted as the *ortho*-phenyl-H/acetyl ($o\text{-}D_1$) dimer. For the hydrogen atoms in *meta*- and *para*- positions, the related dimers are shown in Figure 3e–f, respectively, and denoted as *meta*-phenyl-H/acetyl ($m\text{-}D_1$) and *para*-phenyl-H/acetyl ($p\text{-}D_1$). Note that the proposed configurations of the acetyl/phenyl dimers based just on the positions of three different types of H atoms correspond exactly to the shape of the dimers *o*-, *m*-, and *p*- D_1 observed experimentally (Figure 3b).

The statistics showing the distribution of different types of dimers on the H-precured Pt(111) surface at $\Theta_{\text{H}} \approx 0.95$ ML is displayed in Figure 3d: only about 16% of all dimers are

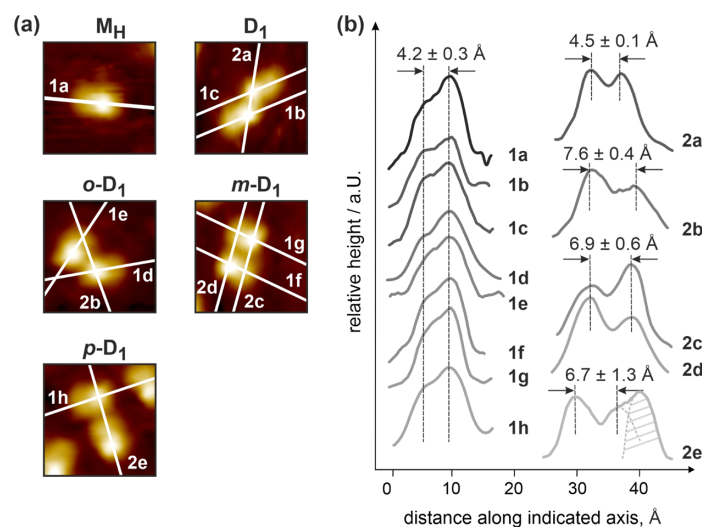


Figure 4. (a) Close-up images of the observed monomer M_H and dimers D_1 , o - D_1 , m - D_1 , and p - D_1 on the H-precovered Pt(111) surface, $\Theta_H \approx 0.95$ ML, at 190 K. (b) STM line profiles obtained from the species shown in (a) along the axes indicated on the close-up images. The distances reported above the line profiles are obtained as an average from typically 10 measurements.

present in the form of acetyl/acetyl species (D_1), while 84% of all dimers are acetyl/phenyl species. Among the latter types of dimers, the most populated is the o - D_1 dimer (43%), followed by the m - D_1 (31%) and p - D_1 (10%) dimers. It should be noted that each acetophenone molecule contains only one H atom in the *para*-position, while there are two H atoms in the *ortho*- and *meta*-position each. This higher absolute amount of *ortho*- and *meta*-H is most likely responsible for the higher abundance of o - D_1 and m - D_1 dimer species as compared to p - D_1 . Additionally, the *ortho*-H is the most acidic H atom in acetophenone, which makes it capable of making the strongest H bonding to the carbonyl group of the neighboring acetophenone molecule. This effect together with the high population of *ortho*-H atoms might be responsible for the highest relative population of o - D_1 species.

Figure 1d shows the distribution of different surface species on the H-precovered ($\Theta_H \approx 0.95$ ML) vs pristine Pt(111) surface. On the pristine Pt(111) surface, the most populated dimer species are acetyl/acetyl dimers D_1 and D_2 , totally amounting to 94% of all dimer species. Note that within this amount, 63% accounts for acetyl/acetyl ketone–ketone dimers D_1 and 31% for acetyl/acetyl ketone–enol species D_2 . Only 6% of all dimer species are related to acetyl/phenyl dimers on pristine Pt. On the H-precovered Pt(111) surface at $\Theta_H \approx 0.95$ ML, this distribution strongly changes: only 21% of all surface species are dimers, and the absolute majority of them (84%) is related to acetyl/phenyl dimers. Thus, the presence of highly abundant H ($\Theta_H \approx 0.95$ ML) not only leads to the disappearance of keto-enol species D_2 and formation of mostly monomers on the surface but also the distribution of the dimer species switches from mostly acetyl/acetyl dimers on the pristine surface to a predominant population of the acetyl/phenyl dimers on the H-precovered surface at high H coverage.

Summarizing, the combination of these observations suggests that principally different types of intermolecular interactions are acting on pristine vs H-precovered Pt(111) at high H coverages ($\Theta_H \approx 0.95$ ML) in the temperature range 190–200 K. On the pristine Pt(111) surface, acetyl/acetyl

interactions dominate and two main types of dimers are formed: (1) the ketone–ketone dimer D_1 , in which the intermolecular interaction is realized via bonding between the two acetyl groups, and (2) the ketone–enol dimer D_2 , in which one acetyl group undergoes keto-enol tautomerization and the newly formed OH group becomes involved in H bonding with the acetyl group (i.e., C=O entity) of the second ketone molecule. In contrast, on the H-precovered Pt(111) surface at $\Theta_H \approx 0.95$ ML, the absolute majority of adsorbed acetophenone is present in the form of monomers. The smaller fraction of dimers shows a strongly different distribution of possible geometric configurations. The predominant intermolecular interaction in these dimers switches to the interaction between the phenyl-H involved in the phenyl ring and the acetyl group of the neighboring species. Three different types of acetyl/phenyl dimers were observed experimentally, which correspond to three possible positions of H in the phenyl ring of acetophenone. It should also be noted that one form of the acetyl/acetyl dimer was also observed on this surface—the ketone–ketone species D_1 —however, in very small amounts.

The origin of the observed switch in the predominant intermolecular interactions is not a quite clear jet. The fact that most of the dimers fall apart on the surface nearly saturated with H might be explained by binding of the individual acetophenone molecules to H atoms adsorbed on the surface, thus establishing a quasi H bonding with the coadsorbed H instead of H bonding with neighboring acetophenone molecules. The bonding strength to the surface-adsorbed H might be greater than bonding between two acetyl groups in the D_1 and D_2 dimers, which results in the predominant formation of the monomer species on the surface nearly saturated with H. It is even less clear, however, why a drastic switch from the acetyl/acetyl interaction to the acetyl/phenyl interaction occurs on the H-containing surface. This experimental observation suggests that the acetyl/phenyl interaction is more stable than the acetyl/acetyl interaction at H surface coverage close to a monolayer, while on the

pristine Pt(111), an opposite trend exists: the acetyl/acetyl prevails over the acetyl/phenyl interaction. It should be kept in mind, however, that not only the binding energy between the different functional groups changes in the presence of H but also the overall binding energy of the entire molecule to the surface might strongly decrease on the H-containing surface. It can be speculated that the switch in the intermolecular bonding from acetyl/acetyl to acetyl/phenyl might be a complex interplay of different parameters, comprising the change of the overall binding energy between a molecule and the underlying metal, the possibility to make a *quasi H bonding* with the surface-adsorbed H, possible change of the adsorption site on the H-covered surface, etc. Based on the available experimental data, it appears to be difficult to judge about the relative contributions of these factors, which need to be addressed in more detail in computational studies.

Figure 4 shows the more detailed analysis of different types of dimers as well as the monomer M_H on the H-precovered Pt(111) surface at $\Theta_H \approx 0.95$ ML. Here, the STM line profiles measured across the individual surface species are analyzed in a quantitative way. Figure 4a displays the axes (1a–1h and 2a–2e), along which the STM line profiles were obtained. These axes are drawn either along the main molecular axis of the individual acetophenone molecules (axes 1a–1h) or along two individual interacting acetyl groups in the acetyl/acetyl dimer D_1 (2a) or along two interacting groups—the acetyl and the phenyl group—in the acetyl/phenyl dimers *o*-, *m*-, and *p*- D_1 (2b–2e). The latter axes 2a–2e are chosen to characterize the typical distance between the interacting functional groups in the dimers on the H-containing surface. Note that for the acetyl/phenyl type of dimers, the line is drawn between the acetyl group and the center of the phenyl ring and not between the acetyl and the phenyl-H as the H atoms cannot be atomically resolved.

The line profiles 1a–1h measured across the individual acetophenone molecules are very similar for all present species. They exhibit two maxima, and the average distance between these maxima amounts to 4.2 ± 0.3 Å. Note that this value does not correspond to the size of the molecule, which cannot be exactly determined by STM due to tip convolution effects, but shows merely the distance between the two maxima in the electron density distribution in acetophenone. This value is in an excellent agreement with the same value measured for acetophenone adsorbed on pristine Pt(111) of 4.2 ± 0.2 Å. Both values agree well with the typical distances between the acetyl group and the phenyl ring calculated for the gaseous acetophenone molecule: 3.9 Å for the distance between the methyl group and the center of the phenyl ring and 3.7 Å between the O atoms and the ring center (for more details see ref 12). This observation indicates that the intramolecular structure of the individual acetophenone molecules does not noticeably change due to the interaction with the H-precovered Pt(111) surface at high hydrogen coverage ($\Theta_H \approx 0.95$ ML) as compared to pristine Pt(111).

The line 2a displays the line profile obtained along the axis connecting two interacting acetyl groups in the acetyl/acetyl dimer D_1 . The measured distance between the two maxima amounts to 4.5 ± 0.1 Å, which is in a very good agreement with the value of 4.6 ± 0.2 Å measured for the same type of dimer D_1 on pristine Pt(111).¹² Also, this observation indicates that the bonding between the two ketone species via two acetyl groups does not undergo noticeable changes when the Pt surface is precovered with H.

For the acetyl/phenyl dimers, the characteristic distance between the two interacting groups is significantly larger than that for the acetyl/acetyl dimers. Thus, for the *ortho*-, *meta*-, and *para*-dimers, the distances between the two peaks in the line profiles (line 2b for *ortho*-, lines 2c and d for *meta*-, and line 2e for *para*-dimers in Figure 4b) are quite similar: 7.6 ± 0.4 , 6.9 ± 0.6 , and 6.7 ± 1.3 Å for *o*- D_1 , *m*- D_1 , and *p*- D_1 , respectively. It should be noted that the axis 2e, connecting the interacting acetyl and phenyl groups in *p*- D_1 , also crosses the second noninteracting acetyl group, giving rise to an additional peak in the STM line profile, which is shown in Figure 4b as a dashed area for clarity. Note that while the distance for the *o*- D_1 seems to be somewhat larger than for *m*- and *p*- D_1 , all values lie within the same error interval.

It is interesting to estimate the distance between the acetyl group and the phenyl-H atom directly involved in H bonding, which can be done by subtracting the distance between the ring center and the phenyl-H (1.4 Å according to the gas phase calculation¹²) from the value measured between the acetyl group and the center of the phenyl ring. These estimated distances between the acetyl group and the phenyl-H atom amount to approx. 6.0 ± 0.4 , 5.5 ± 0.6 , 5.3 ± 1.3 Å for *o*- D_1 , *m*- D_1 , and *p*- D_1 , respectively. In all cases, these distances are somewhat greater than the characteristic distance between the two interacting acetyl groups in the acetyl/acetyl dimer D_1 4.2 ± 0.3 Å (except for the very last case, in which the lowest limit of the error interval 5.3 ± 1.3 Å overlaps with the error interval 4.2 ± 0.3 Å for acetyl/acetyl dimer D_1). Generally, it can be concluded that the characteristic distances between the two interacting groups in the acetyl/phenyl dimers are 25–40% larger than this distance in the acetyl/acetyl dimer. This observation might be indicative of a weaker interaction between the individual molecular species in acetyl/phenyl dimers but can also be related merely to differences in the adsorption sites on the underlying Pt(111).

Having investigated intermolecular bonding in acetophenone dimers on H-precovered Pt(111) at $\Theta_H \approx 0.95$ ML, we performed a similar study in the higher temperature range (240 and 260 K), in which H concentration is significantly lower. The estimate of the H surface concentration was performed based on the TPD study by Poelsema and Comsa in the same way as for the temperature 190 K discussed above.²⁴ Specifically, the H surface coverage was estimated to amount to $\Theta_H \approx 0.57$ ML for 240 K and $\Theta_H \approx 0.5$ ML for 260 K. The TPD data reported by other groups^{25,26} result in similar estimated coverages close to half of a monolayer. It should be noted that earlier reports on H adsorption over Pt(111) put forward the formation of two different types of H species, which are indicated as weakly bound β_1 -H and strongly bound β_2 -H species³⁵ appearing as two distinct peaks in TPD. In the more recent studies on that topic, it was shown that the appearance of two desorption states is an artifact connected most likely to the presence of irregular surface sites, e.g., steps.^{24,36} This hypothesis was additionally confirmed in hydrogen adsorption studies on vicinal Pt surfaces showing the evolution of new high-temperature desorption peaks upon variation of the step density.^{37,38} The current general opinion is that there is only one smooth desorption peak in TPD on Pt(111), implying a smooth continuous growth of the H binding energy with the decreasing H surface concentration. The latter observation as well as the results of studies directly measuring H binding energy by isosteric heat of adsorption measurements²⁴ reveal a rather strong repulsive interaction

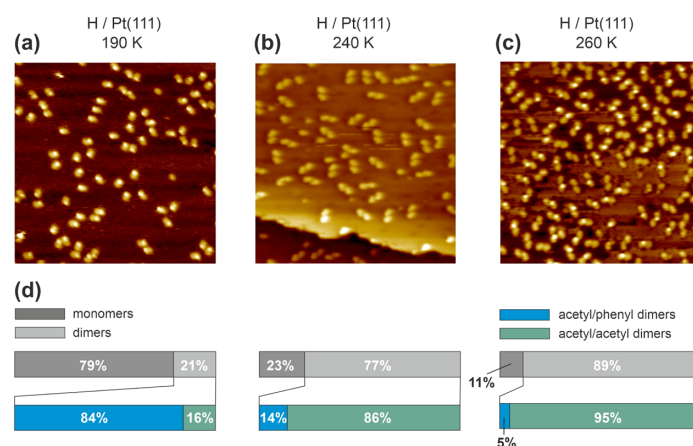


Figure 5. (a) STM image of acetophenone adsorbed on the H-precovered Pt(111) surface, $\Theta_H \approx 0.95$ ML, (exposure at 190 K, acquisition temperature 120 K, 0.12 V, 0.49 nA, 19×19 nm²). (b, c) STM images of acetophenone adsorbed on the H-containing Pt(111) surface ((b): $\Theta_H \approx 0.57$ ML, exposure at 240 K, acquisition temperature 120 K, 1 V, 0.1 nA, 20×20 nm²; (c) $\Theta_H \approx 0.5$ ML, exposure at 260 K, acquisition temperature 150 K, 1 V, 0.32 nA, 20×20 nm²); and (d) statistical distribution of monomers vs dimers (gray bars) and acetyl/acetyl vs acetyl/phenyl dimers (blue and green bars) for STM scans shown in (a–c). All statistical evaluations are done on larger STM scans.

between the adsorbed H atoms. In terms of a simple model developed by Poelsema and Comsa, this pairwise H–H repulsive interaction is estimated to be close to $5 \text{ kJ}\cdot\text{mol}^{-1}$,²⁴ while the binding energy of H atoms changes from approx. 50 to $75 \text{ kJ}\cdot\text{mol}^{-1}$ with decreasing H coverage from $\Theta_H \approx 1$ to $\Theta_H \approx 0$ ML, respectively.²⁴

Figure 5 shows a series of STM images obtained in the low (190 K Figure 5a) and high (240 and 260 K, Figure 5b,c) temperature range on H-precovered surfaces. In both images related to the higher temperatures (240 and 260 K), it can be clearly seen that dimers become the majority of the surface species (77 and 89% of surface species are dimers, respectively), and the distribution of these dimers strongly shifts to acetyl/acetyl dimers (86 and 95%, respectively). Thus a strong difference in the composition of acetophenone species was revealed for different H surface coverages: (1) in the low coverage regime ($\Theta_H \approx 0.5$ – 0.57 ML), the acetyl/acetyl interactions are favored and the dimers are energetically more stable than monomers; (2) in contrast, at the H coverage close to saturation ($\Theta_H \approx 0.95$ ML), the monomer form of acetophenone is the most stable type of surface species and in the small fraction of dimers, which are still formed on this surface, the acetyl/phenyl type of interaction prevails over the acetyl/acetyl interaction. From this observation, it can also be concluded that the effects observed in the low-temperature range—strong reduction of the population of surface dimers and switch to the acetyl/phenyl type of intermolecular interaction—must be related to the higher H coverages. Once approx. 40–50% of H is removed (high-temperature regime), the surface behaves more similar to pristine Pt(111): dimers constitute the majority of the surface species and the acetyl/acetyl intermolecular interactions prevail.

The exact reason responsible for the drastic switch in the dimer population and their structures upon transition from the H-saturated surface ($\Theta_H \approx 0.95$ ML) to the surface covered with approx. half of the saturation coverage ($\Theta_H \approx 0.5$ – 0.57 ML) cannot be unambiguously deduced from our experimental datasets. Generally, there are two possible scenarios that might explain this strong switch. First, the binding energy of adsorbed

H is a strong function of H surface coverage. According to the study on isosteric heats of adsorption by Poelsema and Comsa,²⁴ the binding energy of H amounts on average to $48 \text{ kJ}\cdot\text{mol}^{-1}$ for saturated surface ($\Theta_H \approx 0.95$ ML) and $63 \text{ kJ}\cdot\text{mol}^{-1}$ for the surface covered with $\Theta_H \approx 0.5$ ML. The weaker binding H species populated at low temperatures (190–200 K) might be able to undergo a quasi H bonding with a carbonyl group of acetophenone, thus preventing the formation of intermolecular bonds required for the formation of dimers. In contrast, stronger bonded H species populated in the high-temperature regime (240–260 K) might be bonded too strong to the surface and, therefore, not capable of establishing bonds with coadsorbed acetophenone, thus preventing dimer formation. The same differences in H binding energies might be principally also responsible for the switch from acetyl/phenyl to acetyl/acetyl type of interaction upon transition from the saturated surface to hydrogen coverage $\Theta_H \approx 0.5$ ML. Here, the stability of different types of dimers—acetyl/acetyl vs acetyl/phenyl—can depend on a complex interplay of different parameters varying as a function of H binding energy, such as, e.g., the change of the overall binding energy between a molecule and the underlying H-covered Pt, the possibility to establish a *quasi H bonding* with the surface-adsorbed H, possible change of the adsorption site for dimers with a varying binding energy of H, etc. The exact role of these parameters can be addressed in theoretical studies.

The second potentially possible reason for the observed phenomena could be the inhomogeneous distribution of H at lower coverages, resulting in the formation of dense H islands and empty metal patches. If acetophenone dimers would preferentially adsorb at free metal patches in this scenario, the same structures would be built on the free metal areas as on the pristine Pt(111) surface, which is indeed observed experimentally. While this scenario would be an easy explanation for the observed acetophenone structures, the formation of densely packed H islands and free metal patches is rather unlikely since coadsorbed H atoms exhibit a substantial pairwise repulsive interaction on Pt(111)^{24,36} and

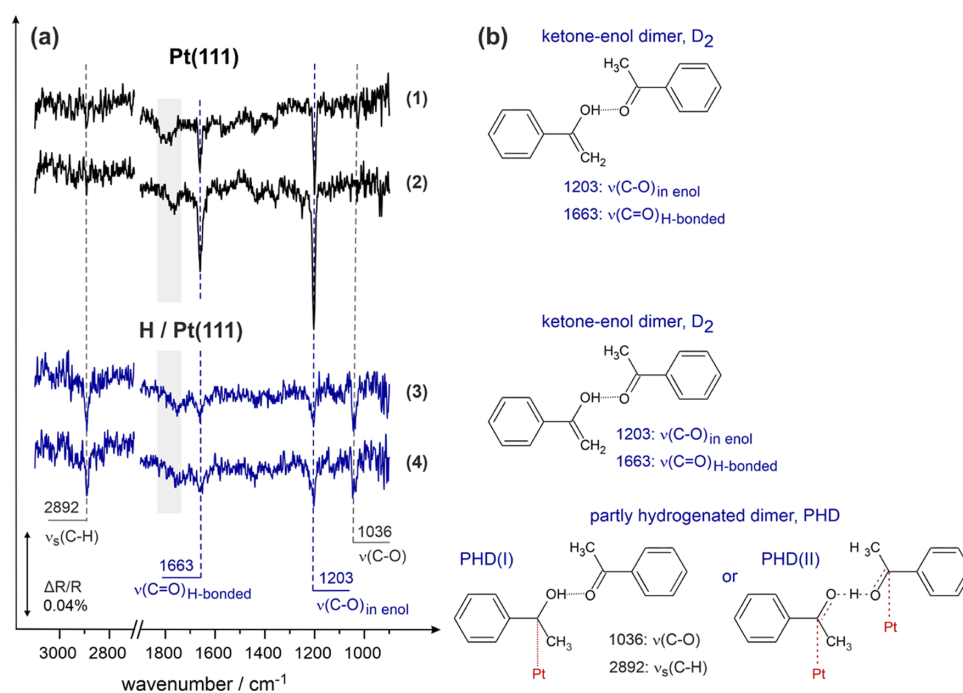


Figure 6. (a) IR spectra of acetophenone adsorbed on pristine (spectra 1 and 2) and H-precovered Pt(111), $\Theta_{\text{H}} \approx 0.57$ ML (spectra 3 and 4) obtained at 240 K. All spectra are related to submonolayer coverages and were recorded after acetophenone exposure to (1) 2.7×10^{14} , (2) 4.0×10^{14} , (3) 4.0×10^{14} , and (4) 5.4×10^{14} molecules·cm⁻². See the related text for further details; (b) proposed structural models for dimers D₂ and PHD based on the combination of spectroscopic and microscopic observations.

should maximize the interatomic distances resulting in rather homogeneous distribution across the surface. Under our experimental conditions (relatively high H coverages: approx. 0.5–0.6 H atoms per surface Pt atom; and very low acetophenone coverages: approx. 0.02–0.03 acetophenone molecules per surface Pt atom), it is also unlikely that very small amounts of coadsorbed acetophenone can substantially effect H distribution across the surface. Based on these considerations, we believe that hydrogen at $\Theta_{\text{H}} \approx 0.5$ ML should be distributed rather homogeneously and the differences in the adsorption structures of acetophenone are more likely related to the change in the H binding energy upon transition from the saturation coverage to $\Theta_{\text{H}} \approx 0.5$ ML.

At 260 K, it turned out to be possible to achieve intramolecular resolution of different dimer species. To obtain more atomistic-level insight into their chemical structure, an IR study was also performed in the high-temperature range. Figure 6 shows the comparison of IR spectra obtained on pristine (spectra (1) and (2)) vs H-containing Pt(111) with the $\Theta_{\text{H}} \approx 0.57$ ML (spectra (3) and (4)) surface at 240 K. On pristine Pt(111), two intense characteristic bands are observed at 1203 and 1663 cm⁻¹, indicating the formation of ketone-enol dimers D₂. It should be emphasized that the band at 1683 cm⁻¹, which was assigned to either ketone–ketone dimers or monomers,^{9,10} is not present in the spectra recorded at 240 K. This observation suggests that nearly all acetophenone molecules transform to ketone-enol dimers (D₂) on the pristine Pt(111) surface. Note that the broad band around 1800 cm⁻¹ highlighted with the gray color is typical for CO molecules adsorbed at very low concentrations (less than 1% of

surface coverage).³⁹ It might originate either from unwanted coadsorption of CO from the background or from minor acetophenone decomposition.

On the H-precovered surface with $\Theta_{\text{H}} \approx 0.57$ ML, the spectra ((3) and (4)) undergo noticeable changes as compared to the pristine surface. The bands at 1203 and 1663 cm⁻¹ still remain visible and intense, indicating the presence of ketone-enol dimers D₂. On the other hand, a new band at 1036 cm⁻¹ appears on this surface, which was observed neither on the pristine Pt(111) surface nor on the surface containing a full H monolayer. In our previous study,⁷ this band, which is red-shifted from the C–O single bond vibration in enol (1203 cm⁻¹) by about 150 cm⁻¹, was assigned to the partly hydrogenated dimer (PHD), in which a H atom is inserted into the C=C double bond of the enol to produce the reaction intermediate shown in Figure 6 (PHD dimer). The assignment was made mostly based on two considerations: (i) the typical C–O vibrational frequencies in saturated alcohols lie in the range of 1000–1150 cm⁻¹;⁴⁰ and (ii) specifically for the nondissociated form of 1-phenylethanol, which is the full hydrogenation product of acetophenone, the C–O(H) bond exhibits a vibrational frequency at 1082 cm⁻¹,⁴¹ which is close to our experimentally observed value of 1036 cm⁻¹. Simultaneously with the evolution of a new C–O single bond at 1036 cm⁻¹, a strong vibrational band appears at 2892 cm⁻¹, which can be assigned to C–H stretching vibrations in methyl (–CH₃) or methylene-bridge (–CH₂–) groups.^{42,43} The position of this band is in excellent agreement with the C–H stretching frequency of the –CH₃ group in 1-phenylethanol (2886 cm⁻¹).⁴¹ The simultaneous appearance

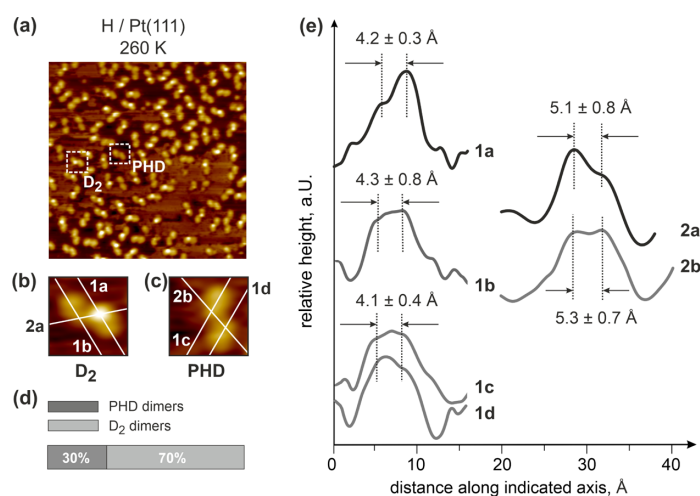


Figure 7. (a) STM image of acetophenone adsorbed on the H-precovered Pt(111) surface, $\Theta_{\text{H}} \approx 0.5$ ML, (exposure at 260 K, acquisition temperature 150 K, 1 V, 0.32 nA, 20×20 nm²). (b, c) Close-up images of the observed dimers D₂ and PHD. (d) Statistical distribution of D₂ and PHD dimers on the H-precovered Pt(111) surface, $\Theta_{\text{H}} \approx 0.5$ ML, at 260 K. Statistical distribution was obtained on a larger STM scan. (e) Comparison of the line profiles measured for D₂ and PHD dimers along the axes indicated in (b) and (c). The distances reported above the line profiles are obtained as an average from typically 10 measurements.

of a new C–O single bond (1036 cm⁻¹), which is not conjugated to a C=C double bond, and the –CH₃ groups can be interpreted as the formation of the PHD dimer shown in Figure 6, which possesses both proposed entities. A more detailed discussion of the IR spectra related to the PHD dimer can be found elsewhere.⁷ Here, we would only briefly summarize the main points, which are relevant for further discussion. First, the intensity of the band at 1203 cm⁻¹ is by about a factor of two reduced on H-containing Pt(111) with $\Theta_{\text{H}} \approx 0.57$ ML as compared to the pristine surface. On the other hand, a new band at 1036 cm⁻¹ exhibits the intensity, which is comparable to the intensity of the band at 1203 cm⁻¹ on the same surface. The combination of these observations suggests that a large fraction of the original ketone–enol dimers D₂ become partly hydrogenated to PHD under these temperature conditions on the surface containing lower concentrations of H ($\Theta_{\text{H}} \approx 0.57$ ML). Comparable intensities of both bands lying in the range of the single C–O bond vibrations most likely indicate that the amounts of the related species are also similar. It should be, however, kept in mind that IRAS is not a strictly quantitative method, i.e., the band intensity might not be directly proportional to the concentration of the adsorbed surface species, and the resulting intensity of a vibrational band can be strongly affected by the adsorption geometry due to the metal surface selection rule and the dipole coupling effects.⁴⁴

Thus, two major observations based on the spectroscopic and microscopic results can be done for the H-precovered Pt(111) surface with $\Theta_{\text{H}} \approx 0.57$ ML. First, the absolute majority of the acetophenone is accommodated in dimer species, specifically ketone–enol dimers D₂ and partly hydrogenated PHD dimers, which are related to acetyl/acetyl dimers interacting via acetyl/former acetyl groups. This is in sharp contrast to the surface precovered by a full monolayer of H species, where the major amount of acetophenone was found in the form of monomers and the smaller fraction of dimers comprising mostly acetyl/phenyl dimer species.

Second, comparable amounts of ketone–enol D₂ and partly hydrogenated PHD species were found on this surface, suggesting that the H species populated in the lower coverage range is capable of hydrogenating acetophenone at the reaction temperature above 240 K. It should be emphasized that both before and after hydrogenation event, the reaction intermediates exist in the form of dimer species, pointing to an important role of intermolecular interactions in the elementary hydrogenation step. More details on the feasible reaction mechanisms of this surface process are discussed elsewhere.⁷ Here, we would like to focus on the atomistic structure of the PHD reaction intermediate, which was further investigated by STM.

Figure 7a shows the STM image obtained at 260 K on the surface precovered with H at $\Theta_{\text{H}} \approx 0.5$ ML. On this surface, it was possible to obtain an intramolecular resolution of acetophenone adsorbates. Specifically, two different types of surface structures were found here, which are shown in Figure 7b,c.

The structure displayed in Figure 7b accounts for 70% of all surface species and combines two protrusions exhibiting different intensity distributions. One-half of the dimer consists of a combination of a brighter and a darker area, while the second half shows a uniform intensity distribution at a relatively low intensity. The combination of these protrusions was also observed on pristine Pt(111) in the low-temperature range (see the close-up image of the D₂ dimer in Figure 2) and was assigned to the ketone–enol dimers D₂.^{9,10} Similarly to D₂ dimers observed on the pristine surface, the ketone–enol dimers formed at 260 K on the H-precovered surface at $\Theta_{\text{H}} \approx 0.5$ ML interact via the acetyl groups (and are therefore formally related to acetyl/acetyl dimers). This observation is also in an excellent agreement with the IR spectra shown in Figure 6, suggesting the formation of ketone–enol dimers in this temperature range. The strong interaction between the –OH and C=O entities is evidenced by the shift of the C=O vibrational frequency to 1663 cm⁻¹, typical for H-bonded C=

O. The line profiles measured for the D₂ dimer on this surface are shown in Figure 7e. The axes 1a and 1b are drawn along the main molecular axis of individual acetophenone molecules in the ketone and the enol part of the D₂ dimer, respectively. The axis 2a connects two interacting acetyl/former acetyl groups. The line profile measured along the 1a axis exhibits two maxima, with one of them being considerably stronger in intensity; the characteristic distance between the maxima amounts to 4.2 ± 0.3 Å. The line profile along the protrusion with a nearly uniform intensity distribution (1b) shows a plateau with a typical width of 4.1 ± 0.8 Å. Note that the statistic was collected on a large number (typically 10) of D₂ dimers. The characteristic distance between the two interacting acetyl groups was obtained for the line profile 2a, which amounts to 5.1 ± 0.8 Å. The latter value is comparable within the characteristic dimensions of acetophenone,¹² suggesting that a strong interaction between both parts of the dimer D₂ exists, bringing the molecules in close vicinity at a distance comparable with the characteristic length of a molecular species. All parameters measured for the D₂ dimer formed on the H-containing surface at $\Theta_{\text{H}} \approx 0.5$ ML are in an excellent agreement with the same parameters measured for the D₂ dimer formed on pristine Pt(111): 4.2 ± 0.2 Å (along the main axis in ketone), 4.3 ± 0.5 Å (along the main axis in enol), and 4.8 ± 0.4 Å (between both acetyl groups) (for more details, see ref 12). This good agreement suggests that ketone–enol dimers D₂ are very similar in structure when formed on pristine vs H-containing Pt(111) at $\Theta_{\text{H}} \approx 0.5$ ML and also intermolecular bonding between the two interacting entities is not drastically affected by coadsorbed H. This latter conclusion is also supported by the IR results, showing that the combination of the vibrational frequencies characteristic for the ketone–enol dimer (1203 and 1663 cm⁻¹) remain the same on both types of surfaces.

The second observed structure (Figure 7c) accounts for about 30% of surface species and can be very likely related to the PHD dimer as suggested by the IR results, showing that a partly hydrogenated acetophenone species exists on the surface in this temperature range (the combination of the bands at 1036 and 2892 cm⁻¹). The line profiles measured for this surface species are shown in Figure 7e. The axes 1c and 1d were drawn along the main axes of the individual molecules, and the axis 2b connects two centers of the interacting entities, which are the acetyl and the partly hydrogenated acetyl groups. Both line profiles along the axis 1c and 1d show rather broad plateaus with a characteristic width of 4.1 ± 0.4 Å. This dimension is in good agreement with the characteristic dimensions of the individual molecules (4.2 ± 0.3 Å) measured for the other types of dimers (D₁, *o*-D₁, *m*-D₁, *p*-D₁), as shown in Figure 4b. The line profile along the axis 2b shows two peaks with an average distance between them amounting to 5.3 ± 0.7 Å. This distance is of the same range as the corresponding distances of all acetyl/acetyl dimers: 4.5 ± 0.1 Å for D₁ (Figure 4b, line 2a) and 5.1 ± 0.8 Å (Figure 7e, line 2a) for D₂ dimers. With this, the newly formed PHD dimer exhibits typical distances both along the main molecular axes as well as between the interacting entities, which were also determined for the other types of acetyl/acetyl dimers. It is important to note that after a hydrogenation event, the absolute majority of the surface reaction intermediates—PHD dimers—remains adsorbed in the form of the dimer and the characteristic distance between two individual molecules remain nearly the same (within the measured error interval)

as in the nonhydrogenated acetyl/acetyl dimers D₁ and D₂. This observation indicates that the partly hydrogenated molecules must still be strongly interacting with the second acetophenone species even after the hydrogenation event. The possible structure of the PHD dimer (PHD(I)) shown in Figure 6 illustrates this interaction: the –OH group belonging to the hydrogenated part of PHD is H-bonded with the carbonyl group of the neighboring acetophenone molecule. It should be noted, however, that this structure can be expected to give rise to an STM image with a nonuniform distribution of the electron density for individual monomers constituting the PHD dimer. However, the experimentally obtained STM images rather suggest a homogeneous distribution of the electron density in the PHD surface species (Figure 7b). This scenario can be realized in the alternative structure of the PHD species shown in Figure 6b (PHD(II)): here, the H atom is equally distributed between the two oxygen atoms of the neighboring acetophenone molecules so that the two identical entities develop, which might give rise to a uniform intensity distribution observed experimentally. Based on the experimentally available datasets, it appears to be impossible to unambiguously distinguish between these two proposed forms of the PHD species. Further theoretical studies are necessary to resolve the detailed structure of this species under the catalytically relevant hydrogenation conditions.

There is a large body of previously reported experimental studies related to the effects of preadsorbed hydrogen on the interaction of hydrocarbons and other molecular adsorbates, such as, e.g., water, with the underlying metal surface. Specifically, Petrik and Kimmel have demonstrated a strong dependence of water-binding energy on Pt(111) on coverage of preadsorbed deuterium:⁴⁵ with the increasing D coverage, the water desorption peak shifts to lower temperatures, suggesting weaker interaction strength with the underlying D-covered metal. Even more pronounced effects of preadsorbed H on adsorption, desorption, and reactivity of water were revealed in studies by Juurlink et al.^{46–48} carried out on vicinal Pt surfaces. Specifically, the authors demonstrated that the step type and orientation have a dramatic effect on the water interaction with Pt in the presence of coadsorbed hydrogen. The observed effects were found to be of a long-range nature. Thus, while water is able to form two-dimensional (2D) networks interacting through bonding on the saturated D/Pt(111) surface, the saturated D/Pt(533) and D/Pt(977) surfaces showed a hydrophobic character and did not enable the formation of the extended 2D structures. Based on these results, the authors concluded that the (100) steps have a very strong and long-ranged influence on the surface hydrophobicity, i.e., the ability of water to establish extended 2D networks connected via hydrogen bonding when the surface was precovered with D.⁴⁹

Similar effects of preadsorbed H on the binding strength of adsorbates were also demonstrated for hydrocarbon compounds. Thus, Mullins et al. have shown that a preadsorbed layer of hydrogen dramatically affects the interaction strength of methanol with Au(111).⁵⁰ Specifically, by studying methanol adsorption at different coverages, including multilayers, the authors observed that the desorption temperature of the amorphous phase on top of the monolayer increases if the gold surface was saturated with hydrogen prior to methanol exposure. This stronger bonding of the methanol amorphous layer to the methanol monolayer was attributed to a change of the methanol monolayer network, which was induced by its

interaction with the underlying metal precovered with hydrogen. Interestingly, H was observed not only to affect the binding strength of the molecular species to the underlying metal but was also shown to disturb the hydrogen-bonded networks of organic compounds existing on pristine metals. Thus, Trenary et al. have shown that hydrogen bonding between neighboring surface species aminomethylidyne on Pt(111) can be disrupted by coadsorbed atomic hydrogen.⁵¹ The authors put forward possible site blocking by coadsorbed hydrogen, which prevents the organic adsorbates from getting close enough to establish hydrogen bonds. The major observations made in our study—the strong change of the intermolecular interactions involving hydrogen bonding due to the presence of coadsorbed H—are in good agreement with the previous reports on H-precovered surfaces, both for water and hydrocarbon adsorption studies. The related phenomena seem to have a general nature and call for further atomistic-level investigations, which can potentially open up a prospect of controlling the properties of adsorption systems in H-containing environments.

CONCLUSIONS

Summarizing, we present a mechanistic study on the formation of different types of acetophenone dimers and their derivatives over the H-containing Pt(111) surface. Depending on the surface coverage of H—a nearly saturated monolayer vs intermediate coverage close to half the monolayer—strongly different behavior in dimer formation was observed.

In the low-temperature range with $\Theta_{\text{H}} \approx 0.95$ ML, most of the acetophenone was found in the form of monomers and only a small fraction of dimers was present. This behavior is in sharp contrast to the pristine Pt(111) surface, on which, in the same temperature range, the majority of acetophenone species are agglomerated in dimers: ketone–ketone D_1 and ketone–enol D_2 dimers, both interacting via acetyl groups. Additionally, a small fraction of dimers still populated on this nearly saturated surface exhibit strongly different lateral interactions as compared to the pristine surface. While on the pristine surface, the absolute majority of the dimers are formed due to lateral interaction between two acetyl groups—either $\text{C}=\text{O}\cdots\text{H}_3\text{C}$ —in ketone–ketone dimers D_1 or $-\text{OH}\cdots\text{O}=\text{CH}$ —in the ketone–enol dimer D_2 —this type of interaction does not prevail on the H-covered surface with $\Theta_{\text{H}} \approx 0.95$ ML. The major fraction of dimer species is formed due to the H bonding between an acetyl group of one acetophenone and a H atom involved in the phenyl ring of the neighboring molecule (acetyl/phenyl dimers). Only a minor fraction of the dimers is related to the acetyl–acetyl dimer D_1 , while the ketone–enol dimers D_2 completely disappear on this surface. Three different types of acetyl/phenyl dimers—*ortho*-, *meta*-, and *para*- D_1 -dimers—were observed here, which result from different positions of phenyl-H atoms involved in H bonding with respect to the acetyl group. The most populated acetyl/phenyl species are *o*- D_1 dimers, with phenyl-H being in the *ortho*-position with respect to the acetyl group. This observation might result from the highest acidity and high population of *ortho*-H.

When the H concentration decreases to the range $\Theta_{\text{H}} \approx 0.5$ – 0.57 ML, the intermolecular lateral interaction and, as a consequence, the composition of the oligomer species change dramatically. In this case, the majority of adsorbates (77% for 240 K and 89% for 240 K) again become agglomerated in dimers, interacting via two acetyl groups. However, at least one

of these acetyl groups undergoes chemical transformation. In one type of the observed dimers (D_2), keto–enol tautomerization occurs, transferring acetophenone in the enol form. The newly formed OH group interacts with the $\text{C}=\text{O}$ group of the neighboring molecule via H bonding, thus energetically stabilizing the normally unstable enol species. The second type of dimer (PHD) results from partial hydrogenation of the ketone–enol species, in which a newly formed C–O single bond exhibits a characterizing vibrational frequency, which is strongly red-shifted from the vibrational frequency of the C–O bond in enol.

Thus, a high H concentration exerts a strong negative effect on the population of the acetyl–acetyl dimers: (i) it completely prevents the formation of ketone–enol dimers D_2 and (ii) strongly inhibits the formation of the ketone–ketone dimers D_1 . On the other hand, in the presence of a nearly saturated H layer, the formation of the acetyl/phenyl dimers is promoted, which are either not formed or formed only in negligible amounts on pristine and the H-containing Pt(111) surface at lower H concentrations ($\Theta_{\text{H}} \approx 0.5$ – 0.57 ML).

We report the detailed structural analysis of all observed dimer species on different types of surfaces. In general, all types of acetyl/acetyl dimers, including partly hydrogenated dimer PHD, exhibit similar structural parameters of the individual molecules along the main acetophenone axis. The distances between the acetyl groups (and acetyl/former acetyl groups) are comparable to the characteristic length of the molecules, pointing thus to a strong intermolecular interaction between both acetyl entities. In the acetyl/phenyl dimers, the characteristic length of the molecular species along the main axis is found to be the same as in an acetophenone standing alone; however, the typical distance between the acetyl group and the H atom of the phenyl ring appears to be slightly larger than the distance between the two acetyls in acetyl/acetyl dimers.

The obtained results provide important atomistic-level insight into lateral interactions between acetophenone molecules on the catalytically relevant Pt surface precovered with different types of H species.

AUTHOR INFORMATION

Corresponding Author

Swetlana Schauer mann – Institute of Physical Chemistry,
Christian Albrechts University Kiel, 24118 Kiel, Germany;
orcid.org/0000-0002-9390-2024;
Email: schauer mann@pctc.uni-kiel.de

Authors

Marvin C. Schmidt – Institute of Physical Chemistry,
Christian Albrechts University Kiel, 24118 Kiel, Germany
Smadar Attia – Institute of Physical Chemistry, Christian
Albrechts University Kiel, 24118 Kiel, Germany
Carsten Schröder – Institute of Physical Chemistry, Christian
Albrechts University Kiel, 24118 Kiel, Germany
Ann-Katrin Baumann – Institute of Physical Chemistry,
Christian Albrechts University Kiel, 24118 Kiel, Germany

Complete contact information is available at:
<https://pubs.acs.org/10.1021/acs.jpcc.1c05707>

Notes

The authors declare no competing financial interest.

ACKNOWLEDGMENTS

Financial support by the German Science Foundations (DFG, Grants SCHA 1477/6–1 and INST 257/543–1 FUGG) is gratefully acknowledged.

REFERENCES

- (1) Meemken, F.; Baiker, A. Recent Progress in Heterogeneous Asymmetric Hydrogenation of C=O and C=C Bonds on Supported Noble Metal Catalysts. *Chem. Rev.* **2017**, *117*, 11522–11569.
- (2) Mäki-Arvela, P.; Hájek, J.; Salmi, T.; Murzin, D. Y. Chemo-selective Hydrogenation of Carbonyl Compounds over Heterogeneous Catalysts. *Appl. Catal., A* **2005**, *292*, 1–49.
- (3) Rasmussen, A. M. H.; Groves, M. N.; Hammer, B. Remote Activation of Chemical Bonds in Heterogeneous Catalysis. *ACS Catal.* **2014**, *4*, 1182–1188.
- (4) Yang, B.; Wang, D.; Gong, X.-Q.; Hu, P. Acrolein Hydrogenation on Pt(211) and Au(211) Surfaces: A Density Functional Theory Study. *Phys. Chem. Chem. Phys.* **2011**, *13*, 21146–21152.
- (5) De Vrieze, J. E.; Thybaut, J. W.; Saeys, M. Role of Keto–Enol Tautomerization in the Copper-Catalyzed Hydrogenation of Ketones. *ACS Catal.* **2019**, *9*, 3831–3839.
- (6) Rappoport, Z. *The Chemistry of Enols (Chemistry of Functional Groups Series)*; John Wiley & Sons Ltd.: Chichester, 1990.
- (7) Attia, S.; Schmidt, M. C.; Schröder, C.; Weber, J.; Baumann, A.-K.; Schaueremann, S. Keto–Enol Tautomerization as a First Step in Hydrogenation of Carbonyl Compounds. *J. Phys. Chem. C* **2019**, *123*, 29271–29277.
- (8) Attia, S.; Schaueremann, S. Coverage-Dependent Adsorption Geometry of Acetophenone on Pt(111). *J. Phys. Chem. C* **2020**, *124*, 557–566.
- (9) Attia, S.; Schmidt, M.-C.; Schröder, C.; Pessier, P.; Schaueremann, S. Surface-Driven Keto–Enol Tautomerization: Atomistic Insights into Enol Formation and Stabilization Mechanisms. *Angew. Chem., Int. Ed.* **2018**, *57*, 16659–16664.
- (10) Attia, S.; Schmidt, M. C.; Schröder, C.; Schaueremann, S. Formation and Stabilization Mechanisms of Enols on Pt through Multiple Hydrogen Bonding. *ACS Catal.* **2019**, *9*, 6882–6889.
- (11) Attia, S.; Spadafora, E. J.; Schmidt, M. C.; Schröder, C.; Baumann, A.-K.; Schaueremann, S. Adsorption Geometry and Self-Assembling of Chiral Modifier (R)-(+)-1-(1-Naphthylethylamine) on Pt(111). *Phys. Chem. Chem. Phys.* **2020**, *22*, 15696–15706.
- (12) Schmidt, M. C.; Attia, S.; Schröder, C.; Baumann, A.-K.; Pessier, P.; Schaueremann, S. Temperature-Dependent Formation of Acetophenone Oligomers Accompanied by Keto–Enol Tautomerism: Real Space Distribution. *J. Phys. Chem. C* **2020**, *124*, 14262–14271.
- (13) Laliberté, M.-A.; Lavoie, S.; Hammer, B.; Mahieu, G.; McBreen, P. H. Activation in Prochiral Reaction Assemblies on Pt(111). *J. Am. Chem. Soc.* **2008**, *130*, 5386–5387.
- (14) Demers-Carpentier, V.; McBreen, P. H. Surface Vibrational Spectroscopy Study of Benzene and 2,2,2-Trifluoroacetophenone on Pt(111). *J. Phys. Chem. C* **2011**, *115*, 6513–6520.
- (15) Goubert, G.; Rasmussen, A. M. H.; Dong, Y.; Groves, M. N.; McBreen, P. H.; Hammer, B. Walking-Like Diffusion of Two-Footed Asymmetric Aromatic Adsorbates on Pt(111). *Surf. Sci.* **2014**, *629*, 123–131.
- (16) Demers-Carpentier, V.; Laliberté, M.-A.; Pan, Y.; Mahieu, G.; Lavoie, S.; Goubert, G.; Hammer, B.; McBreen, P. H. Tuning Aryl–CH...O Intermolecular Interactions on Pt(111). *J. Phys. Chem. C* **2011**, *115*, 1355–1360.
- (17) Demers-Carpentier, V.; Laliberté, M.-A.; Lavoie, S.; Mahieu, G.; McBreen, P. H. Two-Dimensional Self-Assembly and Catalytic Function: Conversion of Chiral Alcohols into Self-Assembled Enols on Pt(111). *J. Phys. Chem. C* **2010**, *114*, 7291–7298.
- (18) Humblot, V.; Bingham, C. J. A.; Le Roux, D.; Mateo Marti, E.; McNutt, A.; Nunn, T. S.; Ortega Lorenzo, M.; Roberts, A. J.; Williams, J.; Surman, M.; et al. Synchrotron Far-Infrared Raman Studies of Complex Molecules on Cu(110). *Surf. Sci.* **2003**, *537*, 253–264.
- (19) Garvey, M.; Bai, Y.; Boscoboinik, J. A.; Burkholder, L.; Sorensen, T. E.; Tysøe, W. T. Identifying Molecular Species on Surfaces by Scanning Tunneling Microscopy: Methyl Pyruvate on Pd(111). *J. Phys. Chem. C* **2013**, *117*, 4505–4514.
- (20) Jones, T. E.; Baddeley, C. J. Investigating the Mechanism of Chiral Surface Reactions: The Interaction of Methylacetacetate with (S)-Glutamic Acid Modified Ni{111}. *Langmuir* **2006**, *22*, 148–152.
- (21) Jones, T. E.; Baddeley, C. J. Influence of Modification Conditions on the Interaction of Methylacetacetate with (R,R)-Tartaric Acid-Modified Ni{111}. *J. Phys. Chem. C* **2007**, *111*, 17558–17563.
- (22) Skliar, D. B.; Gelmi, C.; Ogunnaike, T.; Willis, B. G. Interaction of 2,2,6,6-Tetramethyl-3,5-Heptanedione with the Si(100)-2 × 1 Surface: Scanning Tunneling Microscopy and Density Functional Theory Study. *Surf. Sci.* **2007**, *601*, 2887–2895.
- (23) Ontaneda, J.; Nicklin, R. E. J.; Cornish, A.; Graucrespo, R.; Held, G. Adsorption of Methyl Acetoacetate at Ni{111}: Experiment and Theory. *J. Phys. Chem. C* **2016**, *120*, 27490–27499.
- (24) Poelsema, B.; Lenz, K.; Comsa, G. The Dissociative Adsorption of Hydrogen on Defect-Free Pt(111). *J. Phys.: Condens. Matter* **2010**, *22*, No. 304006.
- (25) Samson, P.; Nesbitt, A.; Koel, B. E.; Hodgson, A. Deuterium Dissociation on Ordered Sn/Pt(111) Surface Alloys. *J. Chem. Phys.* **1998**, *109*, 3255–3264.
- (26) Voss, M. R.; Busse, H.; Koel, B. E. Adsorption of Thermal D Atoms on Sn/Pt(111) Surface Alloys. *Surf. Sci.* **1998**, *414*, 330–340.
- (27) Attia, S.; Spadafora, E. J.; Hartmann, J.; Freund, H.-J.; Schaueremann, S. Molecular Beam/Infrared Reflection-Absorption Spectroscopy Apparatus for Probing Heterogeneously Catalyzed Reactions on Functionalized and Nanostructured Model Surfaces. *Rev. Sci. Instrum.* **2019**, *90*, No. 053903.
- (28) Norton, P. R.; Davies, J. A.; Jackman, T. E. Absolute Coverage and Isosteric Heat of Adsorption of Deuterium on Pt(111) Studied by Nuclear Microanalysis. *Surf. Sci.* **1982**, *121*, 103–110.
- (29) Gambi, A.; Giorgianni, S.; Passerini, A.; Visinoni, R.; Gherseti, S. Infrared Studies of Acetophenone and Its Deuterated Derivatives. *Spectrochim. Acta, Part A* **1980**, *36*, 871–878.
- (30) Belova, N. V.; Oberhammer, H.; Girichev, G. V. Tautomeric and Conformational Properties of Methyl Acetoacetate, CH₃OC(O)–CH₂–C(O)CH₃: Electron Diffraction and Quantum Chemical Study. *J. Phys. Chem. A* **2004**, *108*, 3593–3597.
- (31) Roubin, P.; Chiavassa, T.; Verlaque, P.; Pizzala, L.; Bodot, H. Ft-IR Study of Uv-Induced Isomerization of Intramolecularly Hydrogen-Bonded Carbonyl Compounds Isolated in Xenon Matrices. *Chem. Phys. Lett.* **1990**, *175*, 655–659.
- (32) Matrosov, E. I.; Kabachnik, M. I. Characteristics of the Cis and Trans Enolic Structures in the I.R. Spectra. *Spectrochim. Acta, Part A* **1972**, *28*, 191–196.
- (33) Fried, S. D.; Bagchi, S.; Boxer, S. G. Measuring Electrostatic Fields in Both Hydrogen-Bonding and Non-Hydrogen-Bonding Environments Using Carbonyl Vibrational Probes. *J. Am. Chem. Soc.* **2013**, *135*, 11181–11192.
- (34) Nolasco, M. M.; Ribeiro-Claro, P. J. A. C–H...O Hydrogen Bonds in Cyclohexenone Reveal the Spectroscopic Behavior of Csp³–H and Csp²–H Donors. *Chem. Phys. Chem.* **2005**, *6*, 496–502.
- (35) Christmann, K. Interaction of Hydrogen with Solid Surfaces. *Surf. Sci. Rep.* **1988**, *9*, 1–163.
- (36) Poelsema, B.; Lenz, K.; Comsa, G. The Dissociative Adsorption of Hydrogen on Pt(111): Actuation and Acceleration by Atomic Defects. *J. Chem. Phys.* **2011**, *134*, No. 074703.
- (37) van der Niet, M. J. T. C.; den Dunnen, A.; Juurlink, L. B. F.; Koper, M. T. M. The Influence of Step Geometry on the Desorption Characteristics of O₂, D₂, and H₂O from Stepped Pt Surfaces. *J. Chem. Phys.* **2010**, *132*, No. 174705.
- (38) Kolb, M. J.; Garden, A. L.; Badan, C.; Garrido Torres, J. A.; Skúlason, E.; Juurlink, L. B. F.; Jónsson, H.; Koper, M. T. M. Elucidation of Temperature-Programmed Desorption of High-Coverage Hydrogen on Pt(211), Pt(221), Pt(533) and Pt(553) Based on

Density Functional Theory Calculations. *Phys. Chem. Chem. Phys.* **2019**, *21*, 17142–17151.

(39) Steininger, H.; Lehwald, S.; Ibach, H. On the Adsorption of Co on Pt(111). *Surf. Sci.* **1982**, *123*, 264–282.

(40) Bellamy, L. *The Infra-Red Spectra of Complex Molecules*; Springer Science & Business Media, 2013.

(41) Linstrom, P. J.; Mallard, W.G. *Nist Chemistry Webbook, Nist Standard Reference Database Number 69*; National Institute of Standards and Technology: Gaithersburg MD, 20899.

(42) Kliewer, C. J.; Bieri, M.; Somorjai, G. A. Hydrogenation of the A,B-Unsaturated Aldehydes Acrolein, Crotonaldehyde, and Prenal over Pt Single Crystals: A Kinetic and Sum-Frequency Generation Vibrational Spectroscopy Study. *J. Am. Chem. Soc.* **2009**, *131*, 9958–9966.

(43) Weldon, M. K.; Friend, C. M. Probing Surface Reaction Mechanisms Using Chemical and Vibrational Methods: Alkyl Oxidation and Reactivity of Alcohols on Transitions Metal Surfaces. *Chem. Rev.* **1996**, *96*, 1391–1412.

(44) Hoffmann, F. M. Infrared Reflection-Absorption Spectroscopy of Adsorbed Molecules. *Surf. Sci. Rep.* **1983**, *3*, 107–192.

(45) Petrik, N. G.; Kimmel, G. A. Electron-Stimulated Reactions in Thin D₂O Films on Pt(111) Mediated by Electron Trapping. *J. Chem. Phys.* **2004**, *121*, 3727–3735.

(46) van der Niet, M. J.; Dominicus, I.; Koper, M. T.; Juurlink, L. B. Hydrophobic Interactions between Water and Pre-Adsorbed D on the Stepped Pt(533) Surface. *Phys. Chem. Chem. Phys.* **2008**, *10*, 7169–7179.

(47) den Dunnen, A.; van der Niet, M. J. T. C.; Koper, M. T. M.; Juurlink, L. B. F. Interaction between H₂O and Preadsorbed D on the Stepped Pt(533) Surface. *J. Phys. Chem. C* **2012**, *116*, 18706–18712.

(48) van der Niet, M. J.; den Dunnen, A.; Koper, M. T.; Juurlink, L. B. Tuning Hydrophobicity of Platinum by Small Changes in Surface Morphology. *Phys. Rev. Lett.* **2011**, *107*, No. 146103.

(49) den Dunnen, A.; van der Niet, M. J.; Badan, C.; Koper, M. T.; Juurlink, L. B. Long-Range Influence of Steps on Water Adsorption on Clean and D-Covered Pt Surfaces. *Phys. Chem. Chem. Phys.* **2015**, *17*, 8530–8537.

(50) Brush, A. J.; Pan, M.; Mullins, C. B. Methanol O–H Bond Dissociation on H-Precovered Gold Originating from a Structure with a Wide Range of Surface Stability. *J. Phys. Chem. C* **2012**, *116*, 20982–20989.

(51) Celio, H.; Mills, P.; Jentz, D.; Trenary, M. The Influence of Hydrogen on the Aggregation of Aminomethyldyne on Pt(111). *Surf. Sci.* **1997**, *381*, 65–76.

8.11 Adsorption geometry and self-assembling of chiral modifier (R)-(+)-1-(1-naphthylethylamine) on Pt(111)

Publication Data and Reprint

Reference: Smadar Attia, Evan J. Spadafora, Marvin C. Schmidt, Carsten Schröder, Ann-Katrin Baumann, Svetlana Schauerermann

DOI: 10.1039/d0cp01946a

Submitted: 10.04.2020

Accepted: 30.06.2020

Contribution: IRAS measurements, scientific discussions, DFT calculation, developing a procedure for measuring molecules with low vapor pressure, preparation of parts of the manuscript

Copyright: Reproduced from Ref.[286] with permission from the PCCP Owner Societies. Copyright 2020 Royal Society of Chemistry.


 Cite this: *Phys. Chem. Chem. Phys.*, 2020, 22, 15696

Adsorption geometry and self-assembling of chiral modifier (*R*)-(+)-1-(1-naphthylethylamine) on Pt(111)[†]

 Smadar Attia, Evan J. Spadafora,  Marvin C. Schmidt, Carsten Schröder, Ann-Katrin Baumann and Swetlana Schauer mann *

A mechanistic study on interaction of a chiral modifier – (*R*)-(+)-1-(1-naphthylethylamine) (*R*-NEA) – with a single crystalline Pt(111) surface is reported. The details of the adsorption geometry of individual *R*-NEA molecules and their intermolecular interactions are addressed by combination of infrared reflection absorption spectroscopy (IRAS) and scanning tunneling microscopy (STM). The spectroscopic observations suggest that the molecules are tilted with respect to the underlying metal substrate with the long axis of the naphthyl ring being parallel and the short axis tilted with respect to the surface. In the medium coverage range, formation of directed 3–5 membered chains was observed by STM for the first time, which points to intermolecular bonding between individual molecules and might account for an unusual tilted adsorption geometry deduced from the IR spectra. Based on the STM images revealing the atomic structure of the Pt grid close to the *R*-NEA chains, we propose the adsorption configuration of NEA fitting both the IRAS and STM data. The obtained results suggest that this strong intermolecular interaction energetically stabilizes the tilted adsorption geometry of the naphthyl ring, which otherwise would be expected to lie flat on the metal to maximize the dispersive interactions. At the coverage close to saturation, *R*-NEA builds a self-assembled overlayer with hexagonal symmetry, exhibiting intermolecular distances larger than in the directed chains.

 Received 10th April 2020,
Accepted 30th June 2020

DOI: 10.1039/d0cp01946a

rsc.li/pccp

Introduction

Producing and purifying enantiopure chemicals is a topic of immense practical importance arising from the fact that all biologically important molecules are chiral. The tremendous progress in the development of homogeneous chiral catalysts opened up a major new field in chemistry for production of enantiomerically pure pharmaceuticals. By comparison, effective heterogeneously catalyzed enantioselective processes are still rare, despite their huge potential importance. Besides the major operational advantage offered by heterogeneous over homogeneous catalysis, allowing exclusion of expensive separation steps, the combination of chiral media to induce enantioselectivity with the highly catalytically active metal nanoparticles can result in tremendous synergetic effects. For example, rapid dissociation of molecular oxygen or hydrogen can be ensured on metal surfaces – the reaction step that commonly limits the homogeneously catalyzed routes. There is a rapidly emerging new research field, which focuses on development of chirally-modified catalytic

surfaces that can be used as chiral media to induce enantioselectivity in heterogeneously catalyzed reactions.^{3–5} Such catalysts, combining high catalytic activity and stereochemical control, can be produced by a variety of methods, including *e.g.*, chiral templating by formation of long-range ordered patterns of chiral molecules on the metal surfaces (supramolecular chirality)⁴ or adsorption of chiral organic molecules (chiral modifiers) that build a 1 : 1 complex with a pro-chiral substrate.³ Among these methods, imparting chirality by adsorption of chiral modifiers seems to be one of the most promising.³ Typically, such chiral modifiers are adsorbed *via* dispersive interaction with an anchoring moiety, *e.g.*, naphthyl ring, and the chiral functional group responsible for chiral 1 : 1 interaction with the prochiral reactant is lifted above the surface plane. Specifically in the hydrogenation of C=O and C=C functions, such chirally modified supported metal catalysts represent a successful approach with high synthetic potential demonstrated in batch and continuous-flow reactors.^{6–8}

Despite the impressive development in this field in the past years, the mechanistic details of the underlying microscopic processes are still under debate. In addition, the complexity of the known effectively operating systems limits their extension to other classes of reactants or other catalysts. The successful cases are quite sensitive to changes in the reaction participants in ways that are difficult to predict. At this stage, microscopic

Institute of Physical Chemistry, Christian-Albrechts-University, Kiel Max-Eyth-Str. 2, 24118 Kiel, Germany. E-mail: schauer mann@pctc.uni-kiel.de

[†] Electronic supplementary information (ESI) available. See DOI: 10.1039/d0cp01946a

understanding of enantioselective heterogeneous catalysis strongly gains importance in order to further advance this field and to develop new concepts for rational design of new catalytic materials from first principles.

The chiral organic compound (*R*)-(+)-1-(1-naphthylethylamine) (*R*-NEA) proved itself to be a very promising surface modifier in heterogeneous chiral catalysis.^{9–12} There is no general agreement in the literature on the adsorption geometry of this molecule on metal surfaces. In the recent studies on *R*-NEA/Pt(111)^{13–17} and *R*-NEA/Pd(111) surfaces,¹⁸ the *R*-NEA ligand was suggested to undergo a combination of naphthyl/Pt π - and amine/Pt dative-bonding, meaning that the aromatic moiety lies flat on the surface and acts as a chemical anchor, similarly to observations made for another prominent chiral modifier cinchonine.^{19,20} Similarly, McBreen and co-workers have shown that π -bound *R*-NEA is prevalent on Pt(111).²¹ On the other hand, some reports disagree with this view, suggesting that neither *R*-NEA, nor cinchonine are adsorbed with the naphthyl group π -bonded to the catalyst surface. Specifically, Meemken *et al.*²² reported a strongly tilted adsorption geometry for cinchonine, which was put forward to play an important role in the enantioselective step in hydrogenation processes. Zaera and co-workers²³ reported the adsorption structure with *R*-NEA being bound to the surface *via* the aminic N based on the infrared reflection absorption spectroscopy (IRAS) studies on a polycrystalline Pt surface. This result is in line with an earlier study from the same group on *R*-NEA/Pt(111)² suggesting the transition from the flat-lying to strongly tilted adsorption geometry of the naphthalene ring with increasing coverage. In contrast to the findings of Zaera *et al.*,^{2,23} McBreen and co-workers have shown that π -bound *R*-NEA is prevalent on Pt(111).²¹ A recent review²⁴ provides a comprehensive discussion on the currently available literature reports.

Here, we report a mechanistic study on interaction of a chiral modifier *R*-NEA with single crystalline Pt(111) surface. By combining IRAS and scanning tunneling microscopy (STM), we address the details of the adsorption geometry of individual molecules and the intermolecular lateral interactions between them resulting in formation of a self-assembled layer. The spectroscopic observations suggest that the molecules are tilted with respect to the underlying metal substrate with the long axis of the naphthyl ring being parallel to the surface. In the medium coverage range, formation of directed chains of *R*-NEA molecules was observed for the first time. This phenomenon most likely results from intermolecular bonding between individual molecules and might account for an unusual tilted adsorption geometry deduced from the spectroscopic observations. Based on the STM images revealing the atomic resolution of the Pt grid close to the *R*-NEA chains and previously reported theoretical calculations, we show that every second Pt atom is covered by the ethylamine moiety. We propose an adsorption configuration accounting for this observation, which is in agreement with the tilted adsorption geometry derived from IRAS spectra and which can be stabilized by intermolecular bonding of neighboring *R*-NEA species. The obtained results point to a strong intermolecular interaction between individual molecules, which energetically stabilizes the tilted geometry of the naphthyl ring. In a coverage range close to a monolayer, the

adsorbates form a densely packed overlayer with the larger intermolecular distances than in the chains pointing to increasing contribution of the repulsive interactions between co-adsorbed species.

Experimental section

The IRAS experiments were performed in a specially designed UHV apparatus (base pressure 2×10^{-10} mbar) equipped with a dedicated chamber for deposition of organic molecules *via* a gas doser or Knudsen effusive cell. Further details on the apparatus can be found elsewhere.²⁵

Sample preparation

The Pt(111) single crystal (MaTeck GmbH) was cleaned prior to use by repeated cycles of Ar⁺ ion bombardment at room temperature, followed by oxidation in 1×10^{-6} mbar O₂ at 750–800 K to remove residual carbon and subsequent annealing at 1150 K. The last cleaning cycle contained reduction of the surface with 1×10^{-6} mbar CO at 400–450 K. Shortly before each experiment the sample was flashed to 600 K before cooling to the required temperature to remove CO adsorbates. The long range order and cleanliness of the Pt(111) single-crystal were checked by Low Energy Electron Diffraction (LEED), Auger Electron Spectroscopy (AES) and additionally by IRAS of adsorbed CO to probe the abundance of adsorption sites.

(*R*)-(+)-1-(1-Naphthyl)ethylamine (*R*-NEA, Sigma-Aldrich, purity 99%) was deposited onto the sample *via* a gas doser controlled by a leak valve at a typical pressure of 5×10^{-8} mbar. During deposition the sample was held at 160 K. *R*-NEA was purified prior to the experiments by repeated freeze–pump–thaw cycles.

IRAS

IRAS data have been acquired using a vacuum Fourier transform infrared (FT-IR) spectrometer (Bruker Vertex 80v) with a spectral resolution of 2 cm^{-1} and a mid-infrared (MIR) polarizer and *p*-polarized IR light. The spectrometer is equipped with a narrow band Mercury–Cadmium–Telluride (MCT) detector. IRAS spectra were acquired at almost the same surface temperature that was used for *R*-NEA deposition (155–160 K). An automated quadrupole mass spectrometer (QMS) system (Hiden, HAL 301/3F) was employed for the continuous monitoring of the partial pressures of gaseous species.

B3LYP exchange–correlation functional (DFT)

Vibrational frequencies of an isolated *R*-NEA molecule were calculated within the harmonic approximation at the B3LYP/aug-ccpVTZ level of theory, using the Gaussian16 software.²⁶ First estimation for the lowest energy structure was obtained by relaxed potential energy surface scan (PES) of *R*-NEA in the gas phase rotating the ethylamine group with respect to the naphthalene ring, through the C–C bond connecting them. The scan was performed using the smaller 6-31G(d,p) basis set to minimize computer requirements while exploring the conformation space, which provides a sufficient level of accuracy

for this purpose. Next, starting with the obtained lowest energy structure of rotational conformer, we performed geometry optimization and frequency calculations at the B3LYP/aug-ccpVTZ level of theory. The geometry was optimized until all forces were smaller than $0.01 \text{ eV } \text{Å}^{-1}$. Vibrational modes were calculated within the harmonic approximation and visualized with GaussView 05.²⁷ Experimentally, to obtain a reference spectrum for an unperturbed molecule, the IR spectra are first recorded at multilayer coverages at which most of the adsorbed molecules do not directly interact with the surface. The resulting experimental bands are then assigned by comparison to the theoretical spectra and the calculated frequencies are scaled by a factor of 0.967 for best fitting the experimental data.

STM

The STM measurements were carried out in a different UHV (base pressure better than 1×10^{-10} mbar) apparatus by employing a variable temperature (90–300 K) Aarhus 150 SPM (SPECS). All measurements were carried out in a constant current mode and the bias voltage U_T was applied to the sample. The etched W-Tip was commercially produced by SPECS and *in situ* sharpened by an 3 keV Ar^+ -bombardment with 5×10^{-6} mbar back pressure for 5 min.

The Pt(111) single crystal was cleaned according to the cleaning procedure described above. The quality of the sample was additionally verified by acquiring STM images prior to the deposition. *R*-NEA was purified prior to the experiments by repeated freeze–pump–thaw cycles. *R*-NEA (*R*-NEA, Sigma-Aldrich, purity 99%) was dosed through individual gas doser onto the Pt(111) surface (i) kept at 300 K and (ii) pre-cooled in STM to 160 K and then transferred to the preparation chamber for dosing (in the latter case, some temperature rise might have occurred as the sample was placed in a not cooled transfer system). After the deposition the sample was transferred back to the STM.

Results and discussion

Assignment of vibrational bands in *R*-NEA multilayer

In order to address the adsorption geometry of *R*-NEA on Pt(111) at sub-monolayer coverages, we first performed a detailed assignment of individual vibrational bands. For this, a multilayer coverage of *R*-NEA was produced at 160 K. At this coverage, the absolute majority of the molecule does not directly interact with the underlying metal support and therefore can serve as a reference for unperturbed molecular species. The spectrum of these species can be compared to the known literature data for the unperturbed molecules (*e.g.*, in the gas phase or in solutions) to assign the vibrational bands. The experimentally measured IR spectrum of *R*-NEA on Pt(111) at multilayer coverages, acquired at 160 K, is shown in Fig. 1a.

To the best of our knowledge, the assignment of the vibrational bands for *R*-NEA currently available in the literature was performed based on the IR spectra of other structurally similar molecules, such as phenylethylamine,^{28–30} substituted naphthalene,³¹ and ethylamine,³² but not *R*-NEA itself. Also no assignments based on the isotopic labelling of *R*-NEA were reported to far. While the comparison with the structurally

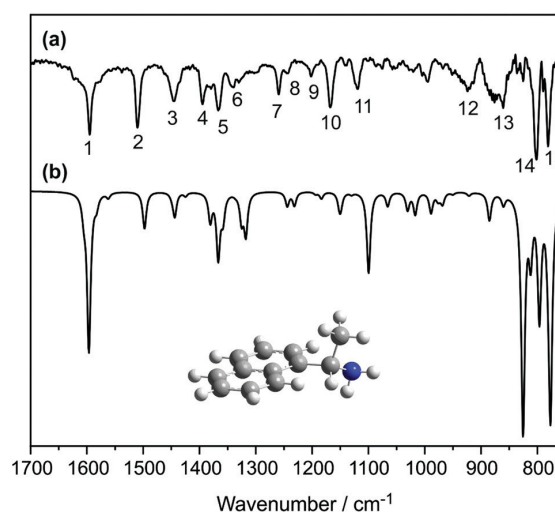


Fig. 1 Experimental IR spectra of *R*-NEA on Pt(111) at multilayer coverages measured at 160 K (a) along with the calculated IR spectra at B3LYP/cc-aug-pVTZ level of theory of an isolated *R*-NEA (b). The frequencies were scaled by factor of 0.967 to obtain the best fit to the experimental data. The calculated bands are labeled from (1) to (15), which correspond to the labels enumerating bands in the Table 1.

similar molecules can provide correct assignment in many cases, there is still some ambiguity for a number of bands, which assignment is less clear. For example, the experimental band at around 1600 cm^{-1} , which was reported by several groups^{2,13,21,23,33} for *R*-NEA on Pt surfaces, was assigned solely to the in-plane (C–C)_{ring} stretching mode of the naphthalene ring. However, theoretical studies^{29,30} on free standing phenylethylamine suggest that this band can be assigned to deformation mode of the $-\text{NH}_2$ group.

To verify the assignment currently available in the literature, we performed theoretical calculations of isolated (gas phase) *R*-NEA using the Gaussian 16 software package.²⁶ The calculation was carried out at the B3LYP/cc-aug-pVTZ level of theory. The calculated frequencies were scaled by a factor of 0.967 for best fitting the experimental data and the assignment was carried out by comparison of the computed and experimental (non-perturbed molecule in *R*-NEA multilayer) spectra. The resulting assignment of the experimentally observed IR bands is summarized in Table 1. The numbers in the left column correspond to the numbers enumerating the vibrational modes shown in Fig. 1a.

The calculated and experimentally measured IR spectra appear fairly similar, both in terms of the position of the bands and the distribution of their intensities. Specifically, the vibrational bands (1)–(6) lying in the region $1350\text{--}1600 \text{ cm}^{-1}$, which are particularly relevant for the further discussion, can be quite safely assigned based on the computed spectra. The vibrational band at 1597 cm^{-1} is assigned to the symmetric deformation of the NH_2 group. The vibrational band at 1512 cm^{-1} band is assigned to the in-plane C–C stretching mode of the naphthalene ring; the corresponding dynamic dipole moment of the later vibration is aligned along the long axis of the naphthalene ring in accordance to previously published data^{2,21,33,34} and will

Table 1 Vibrational frequencies (in cm^{-1}) of NEA and their assignments. Experimental vibrational frequencies (cm^{-1}) of multilayer of NEA are compared with harmonic frequencies calculated at the B3LYP/aug-cc-pVTZ (scaled by 0.967) level of theory. Labels (1)–(15) refer to Fig. 1

| Mode number | Gas phase ^a | Pure liquid ^b | Multilayer ^c | B3LYP/aug-cc-pVTZ, scaled | Assignment |
|-------------|------------------------|--------------------------|-------------------------|---------------------------|---|
| 1 | 1597 | 1595 | 1597 | 1597 | $\delta_s(\text{NH}_2)$ |
| 2 | 1508 | 1510 | 1512 | 1510 | $\nu_{\text{ip}}(\text{CC})_{\text{ring-long}}$ |
| 3 | 1453 | 1446 | 1448 | 1466 | $\delta_{\text{as}}(\text{CH}_3)$ |
| 4 | | 1395 | 1397 | 1380 | $\delta_{\text{ip}}(\text{CH})_{\text{ring-short}}, \delta(\text{C}^*\text{H})_{\text{ethylamine}}$ |
| 5 | 1377 | 1368 | 1369 | 1367 | $\delta_s(\text{CH}_3)$ |
| 6 | 1329 | 1337 | 1342 | 1325 | $\delta(\text{C}^*\text{H})_{\text{ethylamine}}$ |
| 7 | 1242 | 1259 | 1262 | 1245 | $\delta(\text{C}^*\text{H})_{\text{ethylamine}}$ |
| 8 | | 1242 | 1245 | 1232 | Ring breathing |
| 9 | 1204 | 1201 | 1204 | 1185 | Mix modes $\omega(\text{NH}_2)$ |
| 10 | 1167 | 1167 | 1170 | 1151 | mix modes $\nu(\text{C-N})$ |
| 11 | 1117 | 1119 | 1120 | 1100 | Mix modes |
| 12 | 905 | 917 | 927 | 911 | Mix modes $\rho(\text{CH}_3), \rho(\text{NH}_2), \nu(\text{C}^*\text{-C})_{\text{ethylamine-ring}}$ |
| 13 | 856 | 861 | 863 | 862 | $\omega(\text{NH}_2)$ |
| 14 | 795 | | 804 | 790 | $\delta_{\text{oop}}(\text{CH})_{\text{ring}}$ |
| 15 | 773 | | 783 | 765 | $\delta_{\text{oop}}(\text{CH})_{\text{ring}}$ |

^a Gas phase values are adopted from NIST data base for *S*-NEA.¹ ^b Values reported by Zaera for pure liquid NEA.² ^c Obtained experimental values for multilayer of *R*-NEA on Pt(111) at 160 K as shown in Fig. 5a. C* indicates the chiral center.

be denoted as $\nu(\text{C-C})_{\text{ring-long}}$. The vibrational bands at 1448 and 1369 cm^{-1} are assigned to the anti-symmetric and symmetric deformation of the CH_3 group, respectively; the vibrational band at 1397 cm^{-1} can be most likely assigned to deformation vibrations which mainly exhibit the C–H bonds of the naphthalene ring along its short axis (denoted as $\delta(\text{C-H})_{\text{ring-short}}$). The orientation of the computed dynamic dipole moment for these selected bands is shown in Fig. 2. The visualization of the vibrational bands (7)–(10) can be found in the ESI.†

Adsorption of *R*-NEA on Pt(111) at sub-monolayer coverages

Having assigned the most important vibrational bands in non-perturbed *R*-NEA adsorbed in multilayers, we studied the

interaction of this molecule with Pt(111) at submonolayer coverages *via* IRAS. The vibrational spectra obtained in the low coverage regime provide information on the possible perturbation of the chemical bonds due to the interaction with the underlying metal as well as on the adsorption geometry of the adsorbed species. The latter information can be extracted by applying the metal surface selection rule (MSSR) relying on the fact that only vibrations exhibiting a non-zero projection of the dynamic dipole moment onto the surface normal are visible in IRAS.³⁵ In contrast, if the dynamic dipole moment is oriented parallel to the surface, an image dipole is built in the underlying metal that cancels out the dynamic dipole moment resulting in total zero intensity of the corresponding

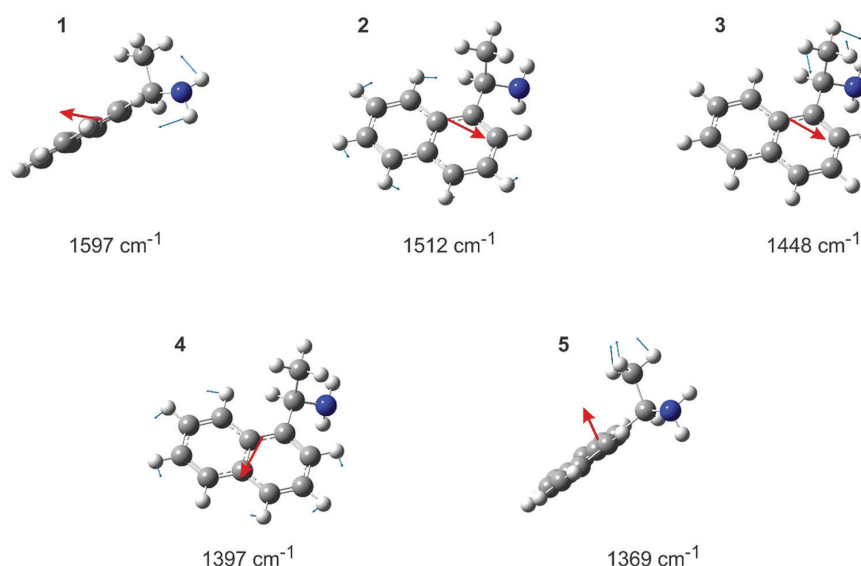


Fig. 2 Visualization of selected vibrational modes of *R*-NEA, with labels (1)–(5) corresponding to the same labels in Fig. 1 and Table 1. The displacement vectors and the resulting dynamic dipole moment for each mode are indicated in blue and red, respectively. The origin of the dynamic dipole moment is placed arbitrary in the *R*-NEA center of mass.

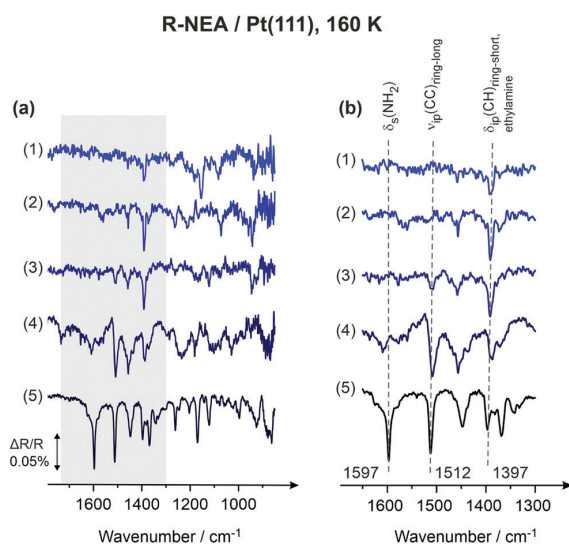


Fig. 3 IRAS spectra of *R*-NEA on Pt(111) recorded at 160 K as a function of *R*-NEA exposure; 5×10^{-8} mbar at 155 K for (1) 1, (2) 1.5, (3) 2, (4) 5, (5) 10 minutes. (b) Enlarged view of the region 1300–1650 cm^{-1} .

vibrational mode. Based on this rule, it is possible to judge about the orientation of the selected vibrational modes in space and, consequently, about the orientation of the molecule with respect to the surface plane.

The IR spectra obtained for submonolayer coverages of *R*-NEA at 160 K are shown in Fig. 3. The Fig. 3a displays the spectral range 900–1800 cm^{-1} , while the Fig. 3b shows the evolution of the selected bands in the range 1300–1650 cm^{-1} in more detail (note that the exact determination of the *R*-NEA coverage is difficult as it requires an accurate sticking coefficient measurement. It can be approximately estimated that the spectra 4 and 5 roughly correspond to a monolayer coverage, while the spectra 1–3 are more close to a half of monolayer). It can be clearly seen that the intensity distribution of the individual vibrational modes strongly changes with increasing coverage. At the lowest coverage (spectrum (1)), only the band at 1397 cm^{-1} is present in the spectrum, which is related mainly to the $\delta_{\text{ip}}(\text{C-H})_{\text{ring-short}}$ with the dynamic dipole moment lying in the plane of the naphthyl ring and being oriented parallel to its short axis (see Fig. 2). This band grows in intensity with growing *R*-NEA exposure and saturates in spectrum (3). Increasing coverage leads to the appearance of the bands at 1448 and 1512 cm^{-1} in spectrum (2), which grow in intensity and saturate in the spectrum (4). The band at 1448 cm^{-1} is assigned to the asymmetric deformation vibration of the methyl group ($\delta_{\text{as}}(\text{CH}_3)$) and the band at 1512 cm^{-1} to the $(\text{C-C})_{\text{ring-long}}$ in-plane stretching vibration ($\nu_{\text{ip}}(\text{C-C})_{\text{ring-long}}$). For both latter bands the dynamic dipole moment lies in plane of the naphthyl ring and is oriented along its long axis (Fig. 2). In spectrum (4), the band at 1597 cm^{-1} appears and grows in intensity with increasing *R*-NEA exposure to finally dominate the spectrum obtained at the highest coverage (spectrum (5)). This band can be assigned to the symmetric deformation

vibration of amine ($\delta_{\text{s}}(\text{NH}_2)$) with the corresponding dynamic dipole moment lying out of plane of the naphthyl ring (Fig. 2).

Taking into account the fact that the frequencies of the vibrational bands observed in the sub-monolayer coverages are similar to those measured for *R*-NEA multilayers, it can be concluded that *R*-NEA is not strongly perturbed by the interaction with Pt in the investigated low temperature range (160 K) and adsorbs molecularly. Further, we make an assumption that the naphthyl ring largely preserves its flat geometry upon adsorption on the metal surface, which seems to be a valid assumption in view of nearly unperturbed vibrational modes in the adsorbed molecules as compared to *R*-NEA multilayer spectra. In this case, some conclusion regarding the orientation of the naphthyl ring with respect to the surface plane of the underlying metal can be made based on the MSSR.

The fact that only the band at 1397 cm^{-1} with the dynamic dipole moment oriented along the short axis of the naphthyl ring can be detected in the lowest coverage range points to an inclined adsorption geometry of *R*-NEA, which is shown in Fig. 4a. In this geometry, the naphthyl ring is oriented in such a way that its long axis is parallel to the surface plane, while the short axis is inclined. This configuration result in a non-zero projection of the dynamic dipole moment related to the band 1397 cm^{-1} onto the surface normal making it visible by IRAS, while the vibrational modes oriented along the long axis of the naphthyl ring (1448 and 1512 cm^{-1}) cannot be seen due to the MSSR (please note that the adsorption configuration shown in Fig. 4a is deduced solely from the IRAS spectra and seems to be counterintuitive for monomer species as the naphthyl ring is expected to lie flat on the surface to maximize dispersive interactions. Later, we will show that the *R*-NEA molecules are not populated as monomers but organized in chains under the investigated temperature conditions, in which the tilted geometry is stabilized by the intermolecular interactions). It should be pointed out that the band at 1597 cm^{-1} , which is assigned to the symmetric deformation of the amine group, is also absent in the spectrum (1). The dynamic dipole moment of this vibration in the gas phase is aligned along the plane spanned by the H–N–H bonds (Fig. 2, (1)). The absence of this band in

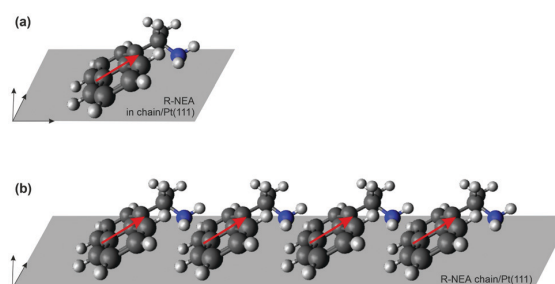


Fig. 4 Schematic drawing of *R*-NEA adsorbed on Pt(111). (a) The aromatic ring is tilted on the surface even at low coverage. The dynamic dipole moment of the band at 1397 cm^{-1} is shown schematically with respect to the surface plane. (b) Schematic representation of *R*-NEA chains on Pt(111) and the proposed intermolecular interaction between the neighboring molecules responsible for tilted adsorption geometry and chain formation.

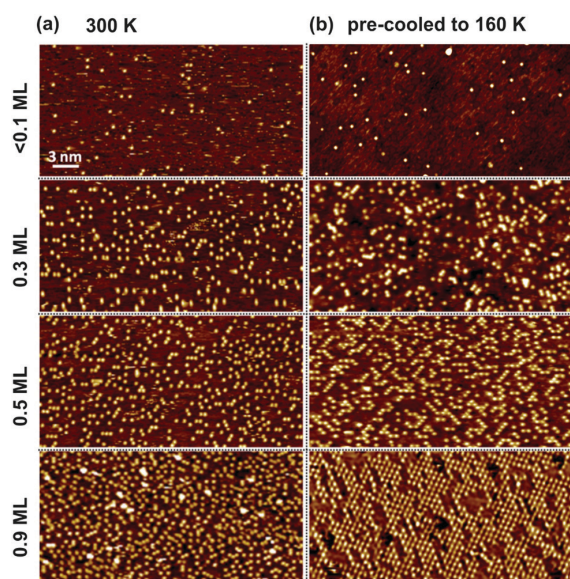


Fig. 5 STM topography images ($36\text{ nm} \times 18\text{ nm}$) of *R*-NEA adsorbed on Pt(111) as a function of coverage deposited at room temperature (a) and at the surface pre-cooled to 160 K prior deposition (b, see Experimental section). The scans (a) were obtained at 300 K; the scans (b) were acquired at 160–165 K. Typical imaging conditions: bias voltage 1–1.1 V, tunneling current 0.11–0.21 nA.

the spectra obtained on Pt suggests that its dynamic dipole moment is parallel to the surface. This scenario can be achieved in two different ways: (i) the amine group might rotate with respect to the surface in such a way, that the entire H–N–H plane becomes parallel to the surface and therefore all vectors lying in this plane are parallel to the underlying metal; (ii) the H–N–H plane is not parallel to the surface but the dynamic dipole moment is oriented on the plane in such a way that it is parallel to the surface. The second scenario seems to be less likely, even though it cannot be excluded based on the available experimental data.

Appearance of the vibrational bands at 1448 and 1512 cm^{-1} at increasing *R*-NEA exposure suggests formation of a different type of surface species or the re-orientation of the already present adsorbates in such a way that the molecules are inclined not only along the short but also along the long axis of the naphthyl ring. At even higher exposures the band at 1597 cm^{-1} becomes also visible suggesting further structural transformations of the adsorbates. If our assumption on the orientation of the H–N–H plane parallel to the surface is true for the low coverage regime, the appearance of the symmetric deformation vibration at 1597 cm^{-1} in the high coverage regime should imply a reorientation of the amine group – and with this the H–N–H plane – with respect to the surface, so that this vibrational mode exhibits a non-zero projection of the dynamic dipole moment along the surface normal. For the further discussion of IR spectra in the full frequency range the reader is referred to ESL.†

Overall, the IR data strongly indicates that *R*-NEA is adsorbed with its naphthyl ring tilted with respect to the surface in the entire coverage range. At lower coverages, the naphthyl

ring is tilted only along the short surface plane, while at higher coverages the naphthyl ring lifts up even more so that both axes – the short and the long ones – become inclined with respect to the surface plane of the underlying metal. This observation is in agreement with a previously reported study by Lambert *et al.*⁷ employing near edge X-ray absorption fine structure spectroscopy (NEXAFS) as well as with the IRAS results of Zaera *et al.*² Generally, adsorption of aromatic compounds on metals is usually discussed to be dominated by dispersive interactions between the aromatic ring(s) and the underlying metal, resulting in a flat-lying adsorption geometry of the ring at low coverages. In view of this typical behavior, the IRAS data pointing to a tilted adsorption geometry even at the lowest coverages are quite surprising.

In order to obtain further insights into the atomistic details of *R*-NEA adsorption on Pt(111), we performed a study employing STM as a tool to obtain real space information on the distribution of the adsorbates at two different temperatures: 300 K and on the sample pre-cooled to 160 K. The recorded STM images are shown in Fig. 5. At 300 K, the majority of *R*-NEA molecules is practically randomly distributed on the surface irrespective of coverage as shown in Fig. 5a. Only a minor fraction of the adsorbates is agglomerated to oligomers, mainly into 3-membered chains as can be seen *e.g.*, in the image related to 0.5 ML coverage at 300 K. In contrast, at low temperature nearly all adsorbates agglomerate in chains, which can be clearly seen in Fig. 5b at intermediate coverage range. The chains typically contain 4–6 members and some of them are agglomerated in more complex hexagonal-like structure corresponding to the hexagonal symmetry of the underlying support. At the coverages close to saturation, *R*-NEA self-assembles into a long-range ordered structure exhibiting a hexagonal symmetry. The oligomer species and the 2D-layer observed at 160 K were stable on the surface within at least two hours after deposition. To the best of our knowledge, neither formation of the directed chains nor self-assembling in the high coverage regime was reported in the literature for NEA adsorbates so far. Previously, the *R*-NEA adsorption was investigated only at room temperature, at which random distribution of the monomeric adsorbed species was detected.³⁶ Note, that no formation of chiral structures was observed at both temperatures, which is in line with the previous report on adsorption configuration of NEA on Pt(111).³⁶

Fig. 6a shows an STM image of a 3-membered *R*-NEA chain revealing the atomic resolution of the underlying Pt surface, which allows to determine the position of individual molecules with respect to the metal atoms. Fig. 6b shows the same 3-membered *R*-NEA chain overlapped with the hexagonal grid displaying the positions of the Pt atoms. By comparison of the Fig. 6a and b, it can be quite clearly seen that every second Pt atom along the $[\bar{1}01]$ axis is covered by a moiety appearing as a bright protrusion. Taking into account the distance between Pt atoms of 2.775 \AA , the separation between the bright spots in the chains can be estimated to be around 5.55 \AA . Previously, *R*-NEA molecules adsorbed on Pt(111) surface were imaged by STM in the study reported by McBreen *et al.*³⁷ Based on the theoretical calculations reported in the same work, the bright spot was assigned to the ethylamine moiety, which can adopt two

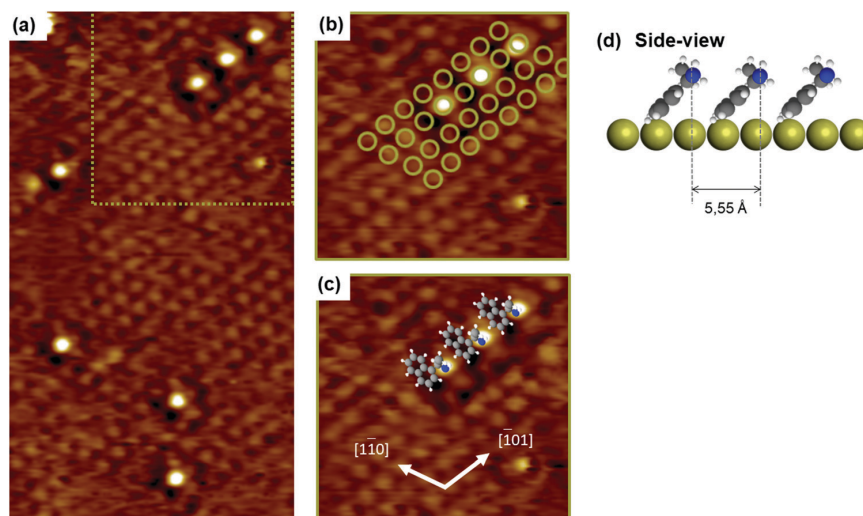


Fig. 6 (a) STM topography image (4.5×7.5 nm, $I_t = 0.12$ nA, $V_t = 1$ V) of *R*-NEA adsorbed on Pt(111) at 300 K revealing the underlying Pt atomic lattice; the scan was acquired at 300 K; close up of the three-membered chain showing the positions of the underlying Pt atoms (b) and the proposed adsorption geometry of the *R*-NEA species with respect to the Pt lattice (c). (d) The side view of the proposed adsorption model.

relative positions with respect to the naphthyl ring resulting in formation of two stable *R*-NEA configurations³⁷ appearing in their study as monomer species at the reported surface temperature of 261 K. No atomic resolution of the metal substrate was achieved in this study, so that the position of the ethylamine group with respect to the underlying Pt atoms was deduced solely from the computational model. The latter model predicts that an ethylamine group occupies a single Pt atom in an on-top position, while the flat lying aromatic ring exhibits a significantly larger footprint. Following these theoretical results and taking into account a large size of the naphthyl ring, we assign the bright spot occupying an on-top Pt atom to the ethylamine group of *R*-NEA. The position of the naphthyl ring cannot be unambiguously deduced from the available STM data. It should be noted that close to each bright spot a depression consisting of two dark circles can be seen, which might be in principle related to the naphthyl ring situated between the ethylamine groups as schematically shown in the ball model displayed in Fig. 6d (note that this model is only a cartoon). However, this depression appears at the same position not only in the 3-membered ring but also in the other *R*-NEA species adsorbed at the surface as monomers. This fact would suggest that all *R*-NEA species seen on this image are oriented in an identical way with respect to the underlying support, which is rather unlikely. Alternatively, the appearance of this depression can be related to a complex interaction between the STM-tip modified by picking up an *R*-NEA molecule and adsorbed *R*-NEA species. In the latter case, appearance of a depression at the same relative position for all adsorbed species can be considered as an artifact related to the scanning procedure and a particular termination of the STM tip. It should be noted that – similarly to the previous report³⁷ – also in our study no evidence for formation of theoretically

predicted two stable configurations of *R*-NEA³⁷ were found. The computed configurations are related to the slightly different orientation of the ethylamine-group with respect to the naphthyl ring in the monomer *R*-NEA species. Since only the ethylamine-group but not the naphthyl ring was imaged in our study, their relative configuration cannot be reliably determined, so that the direct comparison to the calculated modes is not possible.

It is important to note that the computational studies³⁷ were performed for single *R*-NEA molecules lying flat on Pt(111), in which the naphthyl ring was predicted to occupy 6–7 Pt atoms depending on the particular adsorption configuration. If such flat lying molecules were organized in directed chains, only every third Pt atom would be covered by the ethylamine group³⁷ and not every second as observed in our study at low temperatures, at which directed chains are formed. Additionally, all vibrational bands of the naphthyl ring with the dynamic dipole moment lying in plane of the ring would be invisible in IRAS due to MSSR. Thus, both the IRAS and STM results suggest that the experimentally observed formation of the directed chains cannot be explained by flat lying *R*-NEA molecules situated close to each other. This contradiction can be eliminated if we would assume an adsorption model, in which the naphthyl rings are tilted with respect to the surface, so that their footprint on the underlying Pt surface becomes significantly smaller and allows to accommodate an ethylamine group on every second Pt atom. One of the likely models illustrating this scenario is shown in Fig. 6d (side view). Note that this is a cartoon and not a computationally derived model. This model also implies that the dynamic dipole moment of the in-plane ring vibration $\delta_{ip}(\text{C-H})_{\text{ring-short}}$ along the short axis (1397 cm^{-1}) should be visible in IRAS, while the in-plane stretching vibration along the long axis ($\nu_{ip}(\text{C-C})_{\text{ring-long}}$, 1512 cm^{-1}) should

have zero intensity, which is consistent with the experimental observations. Fig. 4b shows the same adsorption geometry as a cartoon, additionally illustrating the direction of the dynamic dipole moment of the band 1397 cm^{-1} , which is visible in IRAS due to its non-zero projection onto the surface normal. For this case, the spectroscopic results suggest that the naphthyl ring is tilted along its short axis (represented by the red arrow in the Fig. 4b), while the long axis is oriented parallel to the surface. Note that this adsorption configuration is the only one fitting both IRAS and STM experimental results. In such adsorption configuration, a H atom involved into the aromatic ring can establish hydrogen bonding with the amino group of the neighboring molecule, thus providing the basis for the formation of the directed chains. Alternatively, a H atom directly bound to the chiral carbon (C^*H group) or belonging to the methyl group of one molecule can be involved in the $\text{H}\cdots\pi$ interaction with the naphthyl ring of the neighboring molecule, resulting in the directed intermolecular interaction and formation of the chains.

The directed interaction between neighboring molecules based on hydrogen bonding between different moieties of the neighboring molecules put forward in this report agrees well with the results of the previously published studies on different types of aromatic compounds, *e.g.*, methylnaphthalene/ethylformate or methylpyruvate/cinchonidine, showing that hydrogens of the naphthyl ring are capable of forming hydrogen bonds on Pt(111).^{38–40} Another possible scenario related to the $\text{H}\cdots\pi$ interaction between a hydrogen involved in either CH_3 or C^*H group (with C^* being a chiral center of *R*-NEA) of one molecule and the naphthyl ring of the neighboring molecule was previously suggested for various complexes of chiral molecules.^{41,42}

In a higher coverage range, at which the *R*-NEA are still organized in chains (and not in the ordered overlayer), the IRAS data suggest that the molecules are inclined along both short and long axes of the naphthalene ring. In this case, the simple model shown in Fig. 4b and 6d becomes more complicated. The naphthyl rings seem to have even weaker interaction with the underlying Pt surface resulting in additional lifting of the aromatic moiety and its stronger inclination with respect to the metal surface. However, this additional upward tilting of the naphthyl ring does not result in the drastic changes of the chain geometry as evidenced by STM, suggesting that the nature of the lateral interactions between neighboring *R*-NEA molecules remain most likely the same. Based on all available data sets, a clear conclusion about the strong intermolecular interaction between the neighboring adsorbates can be drawn, which results in formation of directed chains. It is very likely that this strong intermolecular interaction energetically stabilizes the tilted adsorption configuration of the naphthyl ring, which otherwise would be expected to lie flat on the metal surface to maximize the dispersive interaction.

Fig. 7a shows a close up image of the ordered 2D *R*-NEA layer formed at the coverages close to saturation. The distance between two neighboring bright spots along both indicated axes becomes considerably longer than in the chains and amounts to approximately 9.5 \AA (vs. 5.55 \AA measured in the

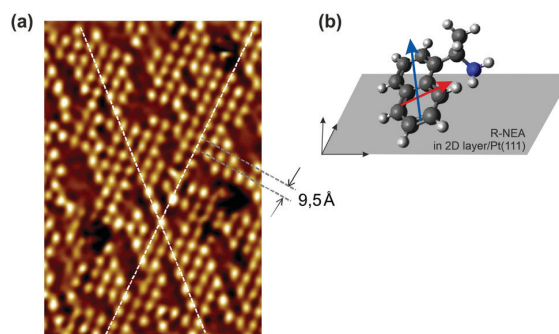


Fig. 7 (a) STM topography image ($12 \times 18\text{ nm}$) of 2D layer formed by *R*-NEA adsorbed on Pt(111) at a close to monolayer coverage. The surface was pre-cooled to 160 K prior deposition. (b) Schematic drawing of a single *R*-NEA molecule incorporated to a 2D layer. The aromatic ring is tilted with respect to the surface plane along both short and long axes of the naphthyl ring; the axes are indicated with the red and blue arrows, correspondingly.

chains), which corresponds to approximately 3.4 times distance between the closest neighboring Pt atoms. It is important to note that according to the IRAS data, all dynamic dipole moments lying in the plane of the naphthyl ring are visible in the highest coverage range roughly corresponding to monolayer. This observation strongly suggests a tilted adsorption configuration of the naphthyl ring with both short and long axes being inclined with respect to the surface plane in the self-organized 2D layer. A cartoon indicating the orientation of the short (red arrow) and long (blue arrow) axes of the naphthyl ring with respect to the underlying surface plane is displayed in Fig. 7b. Here, a single *R*-NEA molecule is shown for clarity, however it should be kept in mind that in this adsorption configuration it is incorporated into the 2D layer. The layer exhibits hexagonal symmetry corresponding to the symmetry of the underlying Pt(111) support. The exact position of the ethylamine groups with respect to Pt atoms cannot be deduced from the presented data as no atomic resolution of the underlying metal could be achieved for this high coverage range. Based on the fact that larger intermolecular distances and self-ordering were observed in this coverage range, it can be assumed that not only attractive interactions described above but also lateral repulsive interactions play a role in the formation of the ordered 2D-layer. The latter interactions most likely result from the repulsion between electron rich moieties of *R*-NEA, *e.g.*, naphthyl rings or the lone pairs of the amine groups. However, the exact origin of repulsion cannot be deduced from the available data. Here, computational work is needed to obtain further insights into the nature of *R*-NEA self-organization on Pt.

It should be noted that the vibrational spectra of *R*-NEA obtained at 300 K show almost no intensity at the positions of all characteristic vibrational bands, especially those related to the prominent vibrations of the naphthyl ring, which are seen at 160 K . Similar observations were made in the study of McBreen *et al.*,³⁶ where no characteristic spectroscopic signatures of *R*-NEA were

observed after NEA adsorption at 300 K on Pt(111). Taking into account the fact that *R*-NEA is present in large quantities at room temperature (see Fig. 5a), this result suggests, that the molecules are lying flat, so that the most prominent vibrational bands are invisible due to the MSSR.⁴³ This hypothesis is in line with our STM observations: (i) at 300 K, the molecules are not involved in lateral interactions with the neighbouring species according to STM and therefore they adopt a flat lying adsorption geometry – most likely due to strong dispersive interactions between the naphthyl ring and the metal – resulting in vanishing of the most prominent vibrational bands due to MSSR;⁴³ (ii) in contrast, once the *R*-NEA species undergo lateral interactions with the neighbours and agglomerate into self-assembled structures – chains or 2-D layer at 160 K – they attain an inclined adsorption configuration and hence many vibrational modes become visible.

Conclusions

Adsorption of *R*-(1-naphthyl)ethylamine (*R*-NEA) on single crystalline Pt(111) surface was investigated by a combination of STM and IRAS over a broad range of coverage and temperature conditions. *R*-NEA molecules adsorbed on Pt(111) at 160 K were observed for the first time to form directed chains at intermediate coverages and self-assemble into a *R*-NEA overlayer at the coverages close to a monolayer. Formation of directed chains at low temperature, typically consisting of 3–5 members, points to a directed intermolecular interaction between the neighboring *R*-NEA molecules. In contrast, adsorption of *R*-NEA at 300 K results in random distribution of the molecules over the entire surface even at the coverages close to saturation.

Assignment of the vibrational bands in the sub-monolayer coverage range was performed based on the *R*-NEA multilayer spectra serving as a reference for unperturbed species as well as IR spectra theoretically calculated at the B3LYP/aug-ccpVTZ level of theory. A very good agreement between the experimentally measured and calculated vibrational spectra was obtained. For the low/intermediate *R*-NEA coverage, the spectroscopic results suggest an adsorption geometry, in which the long axis of the naphthyl ring is oriented parallel to the surface plane, while the short axis of the aromatic ring is inclined with respect to the surface. At the higher coverages, both axes become visible in IR spectra pointing to the changes of the adsorption geometry; specifically, tilting of both long and short axes of the naphthyl ring with respect to the surface plane, most probably due to crowding effects. The unusual inclined adsorption geometry along one axis of the naphthyl ring observed at the intermediate coverages is most likely stabilized by the intermolecular bonding to the neighboring *R*-NEA molecules, resulting in formation of the directed *R*-NEA chains. Likely scenarios of such intermolecular interaction might involve (i) hydrogen bonding between the -amine group of a given molecule and an H atom of the naphthyl ring of its neighbor; (ii) H $\cdots\pi$ interaction between a hydrogen involved in either CH₃ or C^{*}H group of one molecule and the naphthyl ring of the neighboring molecule and (iii) the less likely (due to geometrical constrain)

intermolecular $\pi\cdots\pi$ stacking interaction between the naphthyl rings of neighboring molecules.

Based on the STM images revealing the atomic resolution of the Pt grid close to the *R*-NEA chains and previously reported theoretical calculations, we show that every second Pt atom is covered by the ethylamine moiety. We propose an adsorption configuration accounting for this observation, which is in agreement with the tilted adsorption geometry derived from IRAS spectra and which can be stabilized by intermolecular bonding between neighboring *R*-NEA species. In the coverage range close to a monolayer, formation of a self-organized 2D layer with the distance between repeating units (most likely ethylamine groups) of approximately 9.5 Å is observed. Both the larger intermolecular distances and self-organization point to an increasing contribution of the repulsive lateral interactions – presumably between electron rich moieties of *R*-NEA – in the formation of the overlayer structure.

Obtained results provide important insights into the mechanistic details of interaction of chiral modifiers with the transition metal surfaces relevant for enantioselective heterogeneous catalysis.

Conflicts of interest

There are no conflicts to declare.

Acknowledgements

Financial support by the German Science Foundations (DFG, Grant SCHA 1477/3-1) is gratefully acknowledged.

References

- 1 P. J. Linstrom and W. Mallard, *Nist Chemistry Webbook*, Nist Standard Reference Database No. 69, 2001.
- 2 I. Lee, Z. Ma, S. Kaneko and F. Zaera, 1-(1-Naphthyl) Ethylamine Adsorption on Platinum Surfaces: On the Mechanism of Chiral Modification in Catalysis, *J. Am. Chem. Soc.*, 2008, **130**, 14597–14604.
- 3 F. Meemken and A. Baiker, Recent Progress in Heterogeneous Asymmetric Hydrogenation of C=O and C=C Bonds on Supported Noble Metal Catalysts, *Chem. Rev.*, 2017, **117**, 11522–11569.
- 4 T. Mallat, E. Orglmeister and A. Baiker, Asymmetric Catalysis at Chiral Metal Surfaces, *Chem. Rev.*, 2007, **107**, 4863–4890.
- 5 L. Rodríguez-García, K. Hungerbühler, A. Baiker and F. Meemken, The Critical Role of Tilted Cinchona Surface Species for Enantioselective Hydrogenation, *ACS Catal.*, 2017, **7**, 3799–3809.
- 6 A. Baiker, Progress in Asymmetric Heterogeneous Catalysis: Design of Novel Chirally Modified Platinum Metal Catalysts, *J. Mol. Catal. A: Chem.*, 1997, **115**, 473–493.
- 7 J. M. Bonello, F. J. Williams and R. M. Lambert, Aspects of Enantioselective Heterogeneous Catalysis: Structure and Reactivity of (*S*)-(–)-1-(1-Naphthyl) Ethylamine on Pt{111}, *J. Am. Chem. Soc.*, 2003, **125**, 2723–2729.

- 8 R. L. Augustine, S. K. Taneilyan and L. K. Doyle, Enantioselective Heterogeneous Catalysis I. A Working Model for the Catalyst: Modifier: Substrate Interactions in Chiral Pyruvate Hydrogenations, *Tetrahedron Lett.*, 1993, **4**, 1803–1827.
- 9 K. Szori, K. Balazsik, S. Cserenyi, G. Szollosi and M. Bartok, Inversion of Enantioselectivity in the 2,2,2-Trifluoroacetophenone Hydrogenation over Pt-Alumina Catalyst Modified by Cinchona Alkaloids, *Appl. Catal., A*, 2009, **362**, 178–184.
- 10 M. C. Holland, F. Meemken, A. Baiker and R. Gilmour, Chiral Imidazolidinone and Proline-Derived Surface Modifiers for the Pt-Catalysed Asymmetric Hydrogenation of Activated Ketones, *J. Mol. Catal. A: Chem.*, 2015, **396**, 335–345.
- 11 S. Diezi, T. Mallat, A. Szabo and A. Baiker, Fine Tuning the “Chiral Sites” on Solid Enantioselective Catalysts, *J. Catal.*, 2004, **228**, 162–173.
- 12 J. L. Margitfalvi and E. Tálas, Anomalous Behavior of Rigid Cinchona Alkaloids in the Enantioselective Hydrogenation of Ethyl Pyruvate in an Aprotic Solvent, *Appl. Catal., A*, 2006, **301**, 187–195.
- 13 V. Demers-Carpentier, G. Goubert, F. Masini, R. Lafleur-Lambert, Y. Dong, S. Lavoie, G. Mahieu, J. Boukouvalas, H. Gao and A. M. Rasmussen, Direct Observation of Molecular Preorganization for Chirality Transfer on a Catalyst Surface, *Science*, 2011, **334**, 776–780.
- 14 Y. Dong, G. Goubert, M. N. Groves, J.-C. Lemay, B. Hammer and P. H. McBreen, Structure and Dynamics of Individual Diastereomeric Complexes on Platinum: Surface Studies Related to Heterogeneous Enantioselective Catalysis, *Acc. Chem. Res.*, 2017, **50**, 1163–1170.
- 15 Y. Dong, K. Svane, J.-C. Lemay, M. N. Groves and P. H. McBreen, Stm Study of Ketopantolactone/(*R*)-1-(1-Naphthyl) Ethylamine Complexes on Pt(111): Comparison of Prochiral and Enantiomeric Ratios and Examination of the Contribution of CH \cdots OC Bonding, *ACS Catal.*, 2017, **7**, 1757–1765.
- 16 G. Goubert, Y. Dong, M. N. Groves, J.-C. Lemay, B. Hammer and P. H. McBreen, Monitoring Interconversion between Stereochemical States in Single Chirality-Transfer Complexes on a Platinum Surface, *Nat. Chem.*, 2017, **9**, 531.
- 17 G. Goubert and P. H. McBreen, Surface Diastereomeric Complexes Formed by Methyl Benzoylformate and (*R*)-1-(1-Naphthyl) Ethylamine on Pt(111), *ACS Catal.*, 2014, **4**, 847–854.
- 18 M. Mahapatra, L. Burkholder, M. Garvey, Y. Bai, D. K. Saldin and W. T. Tysoe, Enhanced Hydrogenation Activity and Diastereomeric Interactions of Methyl Pyruvate Co-Absorbed with *R*-1-(1-Naphthyl) Ethylamine on Pd (111), *Nat. Commun.*, 2016, **7**, 12380.
- 19 A. Vargas and A. Baiker, First Principles Study of the Conformations of Cinchonidine on a Pt(111) Surface, *J. Catal.*, 2006, **239**, 220–226.
- 20 J. Kubota and F. Zaera, Adsorption Geometry of Modifiers as Key in Imparting Chirality to Platinum Catalysts, *J. Am. Chem. Soc.*, 2001, **123**, 11115–11116.
- 21 Y. Zeng, F. Masini, A. M. Rasmussen, M. N. Groves, V. Albert, J. Boukouvalas and P. H. McBreen, The Most Stable Adsorption Geometries of Two Chiral Modifiers on Pt(111), *Surf. Sci.*, 2018, **676**, 17–22.
- 22 L. Rodríguez-García, K. Hungerbühler, A. Baiker and F. Meemken, The Critical Role of Tilted Cinchona Surface Species for Enantioselective Hydrogenation, *ACS Catal.*, 2017, **7**, 3799–3809.
- 23 A. D. Gordon and F. Zaera, Adsorption of 1-(1-Naphthyl) Ethylamine from Solution onto Platinum Surfaces: Implications for the Chiral Modification of Heterogeneous Catalysts, *Angew. Chem., Int. Ed.*, 2013, **52**, 3453–3456.
- 24 F. Meemken and A. Baiker, Recent Progress in Heterogeneous Asymmetric Hydrogenation of C=O and C=C Bonds on Supported Noble Metal Catalysts, *Chem. Rev.*, 2017, **117**, 11522–11569.
- 25 S. Attia, E. J. Spadafora, J. Hartmann, H.-J. Freund and S. Schauermaun, Molecular Beam/Infrared Reflection-Absorption Spectroscopy Apparatus for Probing Heterogeneously Catalyzed Reactions on Functionalized and Nanostructured Model Surfaces, *Rev. Sci. Instrum.*, 2019, **90**, 053903.
- 26 M. J. Frisch, *et al.*, *Gaussian 16 Rev. C.01*, Wallingford, CT, 2016.
- 27 R. Dennington, T. Keith and J. Millam, *Gaussview, Version 5*, Semicem Inc., Shawnee Mission, KS, 2009.
- 28 T. B. Freedman, G. A. Balukjian and L. A. Nafie, Enhanced Vibrational Circular Dichroism Via Vibrationally Generated Electronic Ring Currents, *J. Am. Chem. Soc.*, 1985, **107**, 6213–6222.
- 29 C. H. Pollok and C. Merten, Conformational Distortion of *A*-Phenylethyl Amine in Cryogenic Matrices—a Matrix Isolation Vcd Study, *Phys. Chem. Chem. Phys.*, 2016, **18**, 13496–13502.
- 30 C. Merten, M. Amkreutz and A. Hartwig, Vcd Study of *A*-Methylbenzyl Amine Derivatives: Detection of the Unchanged Chiral Motif, *Chirality*, 2010, **22**, 754–761.
- 31 J. Hawkins, E. Ward and D. Whiffen, Characteristic Infra-Red Absorption Frequencies of Substituted Naphthalenes, *Spectrochim. Acta*, 1957, **10**, 105–109.
- 32 Y. Hamada, K. Hashiguchi, A. Y. Hirakawa, M. Tsuboi, M. Nakata, M. Tasumi, S. Kato and K. Morokuma, Vibrational Analysis of Ethylamines: Trans and Gauche Forms, *J. Mol. Spectrosc.*, 1983, **102**, 123–147.
- 33 F. Meemken, T. Steiger, M. C. Holland, R. Gilmour, K. Hungerbühler and A. Baiker, Adsorption and Stability of Chiral Modifiers Based on 1-(1-Naphthyl)-Ethylamine for Pt Catalysed Heterogeneous Asymmetric Hydrogenations, *Catal. Sci. Technol.*, 2015, **5**, 705–715.
- 34 D. Stacchiola, L. Burkholder and W. T. Tysoe, Enantioselective Chemisorption on a Chirally Modified Surface in Ultrahigh Vacuum: Adsorption of Propylene Oxide on 2-Butoxide-Covered Palladium(111), *J. Am. Chem. Soc.*, 2002, **124**, 8984–8989.
- 35 F. M. Hoffmann, Infrared Reflection-Absorption Spectroscopy of Adsorbed Molecules, *Surf. Sci. Rep.*, 1983, **3**, 107–192.

- 36 V. Demers-Carpentier, *et al.*, Direct Observation of Molecular Preorganization for Chirality Transfer on a Catalyst Surface, *Science*, 2011, **334**, 776–780.
- 37 G. Goubert, A. M. H. Rasmussen, Y. Dong, M. N. Groves, P. H. McBreen and B. Hammer, Walking-Like Diffusion of Two-Footed Asymmetric Aromatic Adsorbates on Pt(111), *Surf. Sci.*, 2014, **629**, 123–131.
- 38 S. Lavoie, G. Mahieu and P. H. McBreen, Chemisorption-Induced Double Hydrogen Bonding, Self-Assembly, and Stereoselection, *Angew. Chem., Int. Ed.*, 2006, **45**, 7404–7407.
- 39 S. Lavoie, M.-A. Laliberté, I. Temprano and P. H. McBreen, A Generalized Two-Point H-Bonding Model for Catalytic Stereoselective Hydrogenation of Activated Ketones on Chirally Modified Platinum, *J. Am. Chem. Soc.*, 2006, **128**, 7588–7593.
- 40 S. Lavoie, M.-A. Laliberté and P. McBreen, Adsorption States and Modifier–Substrate Interactions on Pt(111) Relevant to the Enantioselective Hydrogenation of Alkyl Pyruvates in the Orito Reaction, *J. Am. Chem. Soc.*, 2003, **125**, 15756–15757.
- 41 D. Scuderi, K. Le Barbu-Debus and A. Zehnacker, The Role of Weak Hydrogen Bonds in Chiral Recognition, *Phys. Chem. Chem. Phys.*, 2011, **13**, 17916–17929.
- 42 K. Le Barbu-Debus, M. Broquier, A. Mahjoub and A. Zehnacker-Rentien, Chiral Recognition in Jet-Cooled Complexes of (1*r*, 2*s*)-(+)-*cis*-1-Amino-2-Indanol and Methyl Lactate: On the Importance of the CH \cdots II Interaction, *Phys. Chem. Chem. Phys.*, 2009, **11**, 7589–7598.
- 43 F. M. Hoffmann, Infrared Reflection–Absorption Spectroscopy of Adsorbed Molecules, *Surf. Sci. Rep.*, 1983, **3**, 107–192.

Bibliography

- [1] J. G. de Vries, S. D. Jackson, *Catal. Sci. Technol.* **2012**, 2, 2009.
- [2] G. Centi, P. Ciambelli, S. Perathoner, P. Russo, *Catal. Today* **2002**, 75, 3–15.
- [3] P. C. Rao, M. Yoon, *Energies* **2020**, 13.
- [4] R. A. Sheldon, R. S. Downing, *Appl. Catal., A* **1999**, 189, 163–183.
- [5] K. W. Kolasinski, *Surface Science third edition ed.*, Wiley-VCH, **2012**.
- [6] G. Ertl, H. Knözinger, J. Weitkamp, *Handbook of Heterogeneous Catalysis*, John Wiley and Sons, Ltd, **1997**.
- [7] H. S. Taylor, *Proc. R. Soc. A* **1997**, 108, 105–111.
- [8] I. Chorkendorff, J. W. Niemantsverdriet, *Concepts of Modern Catalysis and Kinetics*, John Wiley and Sons, Ltd, **2013**.
- [9] J. K. Nørskov, F. Studt, F. Abild-Pedersen, T. Bligaard, *Fundamental Concepts in Heterogeneous Catalysis*, John Wiley and Sons, **2014**.
- [10] R. Millini, *Science* **2017**, 355, 1028.
- [11] I. G. Clayson, D. Hewitt, M. Hutereau, T. Pope, B. Slater, *Adv. Mater.* **2020**, 32, e2002780.
- [12] M. Moliner, J. M. Serra, A. Corma, E. Argente, S. Valero, V. Botti, *Microporous Mesoporous Mater.* **2005**, 78, 73–81.
- [13] G. Ertl, *Angew. Chem. Int. Ed.* **1976**, 15, 391–400.
- [14] G. Ertl, *Angew. Chem. Int. Ed.* **1990**, 29, 1219–1227.
- [15] H. J. Freund, M. Bäumer, J. Libuda, T. Risse, G. Rupprechter, S. Shaikhutdinov, *J. Catal.* **2003**, 216, 223–235.
- [16] C. T. Campbell, *Surf. Sci. Rep.* **1997**, 27, 1–111.
- [17] P. L. J. Gunter, J. W. Niemantsverdriet, F. H. Ribeiro, G. A. Somorjai, *Catal. Rev. - Sci. Eng.* **1997**, 39, 77–168.
- [18] **2021**. <https://www.basf.com/us/en/media/multimedia/photos.html>.
- [19] S. Spatenka, M. Matzopoulos, Z. Urban, A. Cano, *Ind. Eng. Chem. Res.* **2019**, 58, 12571–12585.

- [20] P. W. Voorhees, *J. Stat. Phys.* **1985**, *38*, 231–252.
- [21] T. W. Hansen, A. T. Delariva, S. R. Challa, A. K. Datye, *Acc. Chem. Res.* **2013**, *46*, 1720–30.
- [22] D. L. Trimm, *Appl. Catal. A: Gen* **2001**, *212*, 153–160.
- [23] J. Libuda, H. J. Freund, *Surf. Sci. Rep.* **2005**, *57*, 157–298.
- [24] H. J. Freund, *Chem. Eur. J.* **2010**, *16*, 9384–97.
- [25] S. Schauer mann, H. J. Freund, *Acc. Chem. Res.* **2015**, *48*, 2775–82.
- [26] A. Schmid, J. S. Dordick, B. Hauer, A. Kiener, M. Wubbolts, B. Witholt, *Nature* **2001**, *409*, 258–68.
- [27] J. Grosskopf, T. Kratz, T. Rigotti, T. Bach, *Chem. Rev.* **2021**.
- [28] S. Kunz, *Top. Catal.* **2016**, *59*, 1671–1685.
- [29] F. Zaera, *Coord. Chem. Rev.* **2021**, *448*, 214179.
- [30] W. Wu, E. V. Shevchenko, *J. Nanopart. Res.* **2018**, *20*.
- [31] L. Lu, S. Zou, B. Fang, *ACS Catal.* **2021**, *11*, 6020–6058.
- [32] K. R. Kahsar, D. K. Schwartz, J. W. Medlin, *J. Am. Chem. Soc.* **2014**, *136*, 520–6.
- [33] B. Wu, H. Huang, J. Yang, N. Zheng, G. Fu, *Angew. Chem. Int. Ed.* **2012**, *51*, 3440–3.
- [34] V. Satagopan, S. B. Chandalia, *J. Chem. Technol. Biotechnol.* **1994**, *59*, 257–263.
- [35] P. Claus, H. Hofmeister, C. Mohr, *Gold Bulletin* **2004**, *37*, 181–186.
- [36] T. B. L. W. Marinelli, S. Nabuurs, V. Ponec, *J. Catal.* **1995**, *151*, 431–438.
- [37] K. Brandt, M. E. Chiu, D. J. Watson, M. S. Tikhov, R. M. Lambert, *J. Am. Chem. Soc.* **2009**, *131*, 17286–90.
- [38] L. E. Murillo, J. G. Chen, *Surf. Sci.* **2008**, *602*, 919–931.
- [39] K. H. Dostert, C. P. O'Brien, F. Ivars-Barcelo, S. Schauer mann, H. J. Freund, *J. Am. Chem. Soc.* **2015**, *137*, 13496–502.
- [40] K. H. Dostert, C. P. O'Brien, F. Mirabella, F. Ivars-Barcelo, S. Schauer mann, *Phys. Chem. Chem. Phys.* **2016**, *18*, 13960–73.
- [41] K.-H. Dostert, C. P. O'Brien, F. Mirabella, F. Ivars-Barceló, S. Attia, E. Spadafora, S. Schauer mann, H.-J. Freund, *ACS Catal.* **2017**, *7*, 5523–5533.
- [42] C. P. O'Brien, K. H. Dostert, S. Schauer mann, H. J. Freund, *Chem. Eur. J.* **2016**, *22*, 15856–15863.

- [43] T. Schalow, B. Brandt, D. E. Starr, M. Laurin, S. Schaueremann, S. K. Shaikhutdinov, J. Libuda, H. J. Freund, *Catal. Lett.* **2006**, *107*, 189–196.
- [44] P. Gallezot, D. Richard, *Catal. Rev. - Sci. Eng.* **1998**, *40*, 81–126.
- [45] P. Mäki-Arvela, J. Hájek, T. Salmi, D. Y. Murzin, *Appl. Catal., A* **2005**, *292*, 1–49.
- [46] C. Decarvalho, M. Dafonseca, *Food Chem.* **2006**, *95*, 413–422.
- [47] W. S. Knowles, *Angew. Chem. Int. Ed.* **2002**, *41*.
- [48] R. Noyori, *Angew. Chem. Int. Ed.* **2002**, *41*.
- [49] K. B. Sharpless, *Angew. Chem. Int. Ed.* **2002**, *41*.
- [50] S. Akabori, S. Sakurai, Y. Izumi, Y. Fujii, *Nature* **1956**, *178*, 323–324.
- [51] M. Heitbaum, F. Glorius, I. Escher, *Angew. Chem. Int. Ed.* **2006**, *45*, 4732–62.
- [52] T. Mallat, E. Orglmeister, A. Baiker, *Chem. Rev.* **2007**, *107*, 4863–90.
- [53] F. Meemken, L. Rodriguez-Garcia, *J. Phys. Chem. Lett.* **2018**, *9*, 996–1001.
- [54] F. Meemken, A. Baiker, *Chem. Rev.* **2017**, *117*, 11522–11569.
- [55] H. U. Blaser, H. P. Jalett, W. Lottenbach, M. Studer, *J. Am. Chem. Soc.* **2000**, *122*, 12675–12682.
- [56] Y. Orito, S. Imai, S. Niwa, *Nippon Kagaku Kaishi* **1979**, 1118–1120.
- [57] J.-C. Lemay, Y. Dong, M. N. Groves, V. Demers-Carpentier, G. Goubert, R. Lafleur-Lambert, J. Boukouvalas, B. Hammer, P. H. McBreen, *Surf. Sci.* **2016**, *646*, 13–18.
- [58] A. Vargas, S. Reimann, S. Diezi, T. Mallat, A. Baiker, *J. Mol. Catal. A: Chem.* **2008**, *282*, 1–8.
- [59] S. Lavoie, P. H. McBreen, *J. Phys. Chem. B* **2005**, *109*, 11986–90.
- [60] E. Rauls, B. Hammer, *Catal. Lett.* **2006**, *106*, 111–114.
- [61] S. Lavoie, M. A. Laliberte, I. Temprano, P. H. McBreen, *J. Am. Chem. Soc.* **2006**, *128*, 7588–93.
- [62] S. Lavoie, M.-A. Laliberté, P. McBreen, *Catal. Lett.* **2004**, *97*, 111–114.
- [63] M. N. Groves, G. Goubert, A. M. H. Rasmussen, Y. Dong, J. C. Lemay, V. Demers-Carpentier, P. H. McBreen, B. Hammer, *Surf. Sci.* **2014**, *629*, 48–56.
- [64] S. Lavoie, M. A. Laliberte, P. H. McBreen, *J. Am. Chem. Soc.* **2003**, *125*, 15756–7.
- [65] S. Lavoie, M. A. Laliberte, G. Mahieu, V. Demers-Carpentier, P. McBreen, *J. Am. Chem. Soc.* **2007**, *129*, 11668–9.
- [66] M. A. Laliberte, S. Lavoie, B. Hammer, G. Mahieu, P. H. McBreen, *J. Am. Chem. Soc.* **2008**, *130*, 5386–7.

- [67] S. Guan, O. Donovan-Sheppard, C. Reece, D. J. Willock, A. J. Wain, G. A. Attard, *ACS Catal.* **2016**, *6*, 1822–1832.
- [68] M. Garvey, Y. Bai, J. A. Boscoboinik, L. Burkholder, T. E. Sorensen, W. T. Tysoe, *J. Phys. Chem. C* **2013**, *117*, 4505–4514.
- [69] Y. Dong, G. Goubert, M. N. Groves, J. C. Lemay, B. Hammer, P. H. McBreen, *Acc. Chem. Res.* **2017**, *50*, 1163–1170.
- [70] G. Goubert, Y. Dong, M. N. Groves, J. C. Lemay, B. Hammer, P. H. McBreen, *Nat. Chem.* **2017**, *9*, 531–536.
- [71] V. Demers-Carpentier, A. M. Rasmussen, G. Goubert, L. Ferrighi, Y. Dong, J. C. Lemay, F. Masini, Y. Zeng, B. Hammer, P. H. McBreen, *J. Am. Chem. Soc.* **2013**, *135*, 9999–10002.
- [72] V. Demers-Carpentier, M.-A. Laliberté, S. Lavoie, G. Mahieu, P. H. McBreen, *J. Phys. Chem. C* **2009**, *114*, 7291–7298.
- [73] M. Castonguay, J. R. Roy, A. Rochefort, P. H. McBreen, *J. Am. Chem. Soc.* **2000**, *122*, 518–524.
- [74] M. Castonguay, J. R. Roy, S. Lavoie, M. A. Laliberté, P. H. McBreen, *J. Phys. Chem. B* **2004**, *108*, 4134–4140.
- [75] L. Burkholder, W. T. Tysoe, *J. Phys. Chem. C* **2009**, *113*, 15298–15306.
- [76] L. Burkholder, M. Garvey, M. Weinert, W. T. Tysoe, *J. Phys. Chem. C* **2011**, *115*, 8790–8797.
- [77] J. M. Bonello, E. C. H. Sykes, R. Lindsay, F. J. Williams, A. K. Santra, R. M. Lambert, *Surf. Sci.* **2001**, *482-485*, 207–214.
- [78] J. M. Bonello, R. M. Lambert, N. Künzle, A. Baiker, *J. Am. Chem. Soc.* **2000**, *122*, 9864–9865.
- [79] M. Mahapatra, L. Burkholder, M. Garvey, Y. Bai, D. K. Saldin, W. T. Tysoe, *Nat. Commun.* **2016**, *7*, 12380.
- [80] J. C. Lemay, Y. Dong, V. Albert, M. Inouye, M. N. Groves, J. Boukouvalas, P. H. McBreen, *ACS Catal.* **2020**, *10*, 3034–3041.
- [81] G. Goubert, P. H. McBreen, *ACS Catal.* **2014**, *4*, 847–854.
- [82] K. R. Hahn, A. Baiker, *J. Phys. Chem. C* **2020**, *124*, 18020–18030.
- [83] A. M. H. Rasmussen, M. N. Groves, B. Hammer, *ACS Catal.* **2014**, *4*, 1182–1188.
- [84] B. Yang, D. Wang, X. Q. Gong, P. Hu, *Phys. Chem. Chem. Phys.* **2011**, *13*, 21146–52.
- [85] J. E. De Vrieze, J. W. Thybaut, M. Saeys, *ACS Catal.* **2019**, *9*, 3831–3839.

- [86] B. Bandyopadhyay, P. Pandey, P. Banerjee, A. K. Samanta, T. Chakraborty, *J. Phys. Chem. A* **2012**, *116*, 3836–3845.
- [87] V. Humblot, C. J. A. Bingham, D. Le Roux, E. Mateo Marti, A. McNutt, T. S. Nunney, M. Ortega Lorenzo, A. J. Roberts, J. Williams, M. Surman, R. Raval, *Surf. Sci.* **2003**, *537*, 253–264.
- [88] T. E. Jones, C. J. Baddeley, *Langmuir* **2006**, *22*, 148–52.
- [89] T. E. Jones, C. J. Baddeley, *J. Phys. Chem. C* **2007**, *111*, 17558–17563.
- [90] J. Ontaneda, R. E. J. Nicklin, A. Cornish, A. Roldan, R. Grau-Crespo, G. Held, *J. Phys. Chem. C* **2016**, *120*, 27490–27499.
- [91] D. B. Skliar, C. Gelmi, T. Ogunnaike, B. G. Willis, *Surf. Sci.* **2007**, *601*, 2887–2895.
- [92] Z. Rappoport, *The Chemistry of Enols (Chemistry of Functional Group Series)*, of *PATAI'S Chemistry of Functional Groups*, John Wiley and Sons Ltd, **1990**.
- [93] K.-H. Meiwes-Broer, *Metal Clusters at Surfaces*, of *Springer Series in Cluster Physics*, Springer-Verlag Berlin Heidelberg, **2000**.
- [94] F. Zaera, *Chem. Rev.* **2012**, *112*, 2920–86.
- [95] D. R. Uhlmann, B. Chalmers, K. A. Jackson, *J. Appl. Phys.* **1964**, *35*, 2986–2993.
- [96] C. Neto, D. R. Evans, E. Bonaccorso, H.-J. Butt, V. S. J. Craig, *Rep. Prog. Phys.* **2005**, *68*, 2859–2897.
- [97] G. M. Nathanson, *Annu. Rev. Phys. Chem.* **2004**, *55*, 231–55.
- [98] A. Oron, S. H. Davis, S. G. Bankoff, *Rev. Mod. Phys.* **1997**, *69*, 931–980.
- [99] K. Wandelt, *Surface and Interface Science, Vol. 1-6*, Wiley-VCH, **2016**.
- [100] M. Bonn, A. W. Kleyn, G. J. Kroes, *Surf. Sci.* **2002**, *500*, 475–499.
- [101] A. W. Kleyn, *Chem. Soc. Rev.* **2003**, *32*, 87–95.
- [102] J. E. Hurst, C. A. Becker, J. P. Cowin, K. C. Janda, L. Wharton, D. J. Auerbach, *Phys. Rev. Lett.* **1979**, *43*, 1175–1177.
- [103] H. Lüth, *Solid Surfaces, Interfaces and Thin Films*, of *Graduate Texts in Physics*, Springer, Cham, **2015**.
- [104] J. E. Lennard-Jones, *Physica* **1937**, *4*, 941–956.
- [105] B. Hammer, J. K. Nørskov, *Adv. Catal.* **2000**, *45*, 71–129.
- [106] G. Brodén, T. N. Rhodin, C. Brucker, R. Benbow, Z. Hurych, *Surf. Sci.* **1976**, *59*, 593–611.
- [107] E. M. Stuve, R. J. Madix, *J. Phys. Chem.* **1985**, *89*, 3183–3185.
- [108] F. Zaera, *ACS Catal.* **2017**, *7*, 4947–4967.

- [109] J. M. Campbell, C. T. Campbell, *Surf. Sci.* **1991**, *259*, 1–17.
- [110] F. Zaera, *Surf. Sci. Rep.* **2017**, *72*, 59–104.
- [111] K. D. Rendulic, A. Winkler, *Surf. Sci.* **1994**, *299-300*, 261–276.
- [112] K. Christmann, *Surf. Sci. Rep.* **1988**, *9*, 1–163.
- [113] T. Mitsui, M. K. Rose, E. Fomin, D. F. Ogletree, M. Salmeron, *Nature* **2003**, *422*, 705–7.
- [114] R. J. Behm, V. Penka, M.-G. Cattania, K. Christmann, G. Ertl, *J. Chem. Phys.* **1983**, *78*, 7486–7490.
- [115] M. Wilde, K. Fukutani, M. Naschitzki, H. J. Freund, *Phys. Rev. B* **2008**, *77*.
- [116] M. Wilde, K. Fukutani, *Phys. Rev. B* **2008**, *78*.
- [117] M. Wilde, K. Fukutani, *Surf. Sci. Rep.* **2014**, *69*, 196–295.
- [118] C. M. Greenlief, S. Akhter, J. M. White, *J. Phys. Chem.* **2002**, *90*, 4080–4083.
- [119] B. Poelsema, K. Lenz, G. Comsa, *J. Phys. Condens. Matter* **2010**, *22*, 304006.
- [120] B. Poelsema, K. Lenz, G. Comsa, *J. Chem. Phys.* **2011**, *134*, 074703.
- [121] S. K. Jo, *Surf. Sci.* **2015**, *635*, 99–107.
- [122] M. J. van der Niet, A. den Dunnen, L. B. Juurlink, M. T. Koper, *J. Chem. Phys.* **2010**, *132*, 174705.
- [123] A. T. Gee, B. E. Hayden, C. Mormiche, T. S. Nunney, *J. Chem. Phys.* **2000**, *112*, 7660–7668.
- [124] I. Langmuir, *J. Am. Chem. Soc.* **1918**, *40*, 1361–1403.
- [125] E. A. Guggenheim, *Thermodynamics*, North-Holland Publishing Co., **1949**.
- [126] M. Temkin, V. Pyzhev, *Acta Phys. Chem. USSR* **1940**, *12*, 327.
- [127] H. Freundlich, *Z. Phys. Chem.* **1907**, *57U*, 385–470.
- [128] P. Kisliuk, *J. Phys. Chem. Solids* **1957**, *3*, 95–101.
- [129] M. Hirsimäki, M. Valden, *J. Chem. Phys.* **2001**, *114*, 2345–2354.
- [130] T. G. A. Youngs, S. Haq, M. Bowker, *Surf. Sci.* **2008**, *602*, 1775–1782.
- [131] S. Brunauer, P. H. Emmett, E. Teller, *J. Am. Chem. Soc.* **1938**, *60*, 309–319.
- [132] M. R. Bhambhani, P. A. Cutting, K. S. W. Sing, D. H. Turk, *J. Colloid Interface Sci.* **1972**, *38*, 109–117.
- [133] J. W. Niemantsverdriet, K. Markert, K. Wandelt, *Appl. Surf. Sci.* **1988**, *31*, 211–219.

- [134] J. W. Niemantsverdriet, P. Dolle, K. Markert, K. Wandelt, *J. Vac. Sci. Technol.* **1987**, *5*, 875–878.
- [135] H. R. Siddiqui, X. Guo, I. Chorkendorff, J. T. Yates, *Surf. Sci.* **1987**, *191*, L813–L818.
- [136] M. J. P. Hopstaken, J. W. Niemantsverdriet, *J. Phys. Chem. B* **2000**, *104*, 3058–3066.
- [137] D. A. King, *Surf. Sci.* **1975**, *47*, 384–402.
- [138] C.-C. Wang, J.-Y. Wu, J.-C. Jiang, *J. Phys. Chem. C* **2013**, *117*, 6136–6142.
- [139] P. J. Barrie, *Phys. Chem. Chem. Phys.* **2008**, *10*, 1688–96.
- [140] D. A. King, *J. Vac. Sci. Technol.* **1980**, *17*, 241–247.
- [141] L. Verstraete, S. De Feyter, *Chem. Soc. Rev.* **2021**, *50*, 5884–5897.
- [142] A. P. van Bavel, M. J. P. Hopstaken, D. Curulla, J. W. Niemantsverdriet, J. J. Lukkien, P. A. J. Hilbers, *J. Chem. Phys.* **2003**, *119*, 524–532.
- [143] I. Fernandez-Torrente, S. Monturet, K. J. Franke, J. Fraxedas, N. Lorente, J. I. Pascual, *Phys. Rev. Lett.* **2007**, *99*, 176103.
- [144] S. T. Marshall, J. W. Medlin, *Surf. Sci. Rep.* **2011**, *66*, 173–184.
- [145] I. Langmuir, *Trans. Faraday Soc.* **1922**, *17*, 607–620.
- [146] C. N. Hinshelwood, *Proc. Math. Phys.* **1926**, *113*, 230–233.
- [147] C. T. Campbell, G. Ertl, H. Kuipers, J. Segner, *J. Chem. Phys.* **1980**, *73*, 5862–5873.
- [148] D. D. Eley, E. K. Rideal, *Nature* **1940**, *146*, 401–402.
- [149] G. I. Jenkins, E. Rideal, *J. Chem. Soc.* **1955**.
- [150] J. Harris, B. Kasemo, *Surf. Sci. Lett.* **1981**, *105*, L281–L287.
- [151] G. Scoles, *Atomic and Molecular Beam Methods, Vol. 1*, Oxford University Press, **1988**.
- [152] W. Demtröder, *Experimentalphysik 1, Vol. 7 of Springer-Lehrbuch*, Springer Spektrum, Berlin, Heidelberg, **2015**.
- [153] S. Wright, R. R. A. Syms, *J. Micromech. Microeng.* **2018**, *28*.
- [154] A. Breuers, M. Herder, P. Kucharczyk, M. Schleberger, K. Sokolowski-Tinten, A. Wucher, *New J. Phys.* **2019**, *21*.
- [155] J. M. Hollas, *Modern Spectroscopy, Vol. 4 of Wiley-VCH*, John Wiley and Sons, **2003**.
- [156] H. Haken, H. C. Wolf, *Molekülphysik und Quantenchemie, of Springer-Lehrbuch*, Springer, Berlin, Heidelberg, **2006**.

- [157] P. Clausing, *Ann. Phys.* **1932**, *404*, 961–989.
- [158] J. H. Gross, *Mass Spectrometry*, Springer, Berlin, Heidelberg, **2011**.
- [159] C. J. Chen, *Introduction to Scanning Tunneling Microscopy*, Oxford Science Publications, **2007**.
- [160] P. R. Griffiths, J. A. de Haseth, *Fourier Transform Infrared Spectrometry*, John Wiley and Sons, Ltd, **2007**.
- [161] J. Reinhold, *Quantentheorie der Moleküle*, Springer Vieweg, Wiesbaden, **2013**.
- [162] M. Born, R. Oppenheimer, *Ann. Phys.* **1927**, *389*, 457–484.
- [163] F. Cotton, *Chemical Applications of Group Theory*, Wiley India, **2003**.
- [164] P. Atkins, J. De Paula, V. Walters, *Physical Chemistry*, Wiley-VCH, Weinheim, **2006**.
- [165] S. A. Khan, S. B. Khan, L. U. Khan, A. Farooq, K. Akhtar, A. M. Asiri, *Fourier Transform Infrared Spectroscopy: Fundamentals and Application in Functional Groups and Nanomaterials Characterization*, Springer International Publishing, **2018**, book section Chapter 9, pp. 317–344.
- [166] P. Jacquinet, *Rep. Prog. Phys.* **1960**, *23*, 267–312.
- [167] M. Bass, E. Van Stryland, W. Wolfe, D. Williams, *Handbook of Optics: Fundamentals, techniques and design*, McGraw-Hill, **1995**.
- [168] F. Hoffmann, *Surf. Sci. Rep.* **1983**, *3*, 107–192.
- [169] R. G. Greenler, *J. Chem. Phys.* **1966**, *44*, 310–315.
- [170] S. A. Francis, A. H. Ellison, *J. Opt. Soc. Am.* **1959**, *49*.
- [171] P. Johnson, R. Christy, *Phys. Rev. B* **1974**, *9*, 5056–5070.
- [172] R. G. Greenler, *J. Vac. Sci. Technol.* **1975**, *12*, 1410–1417.
- [173] S. Attia, E. J. Spadafora, J. Hartmann, H. J. Freund, S. Schaueremann, *Rev. Sci. Instrum.* **2019**, *90*, 053903.
- [174] S. Attia, *PhD Thesis: Ligand-Directed Heterogeneous Catalysis on Model Surfaces*, Technische Universität Berlin, **2019**.
- [175] C. Schröder, M. C. Schmidt, P. A. Haugg, A. K. Baumann, J. Smyczek, S. Schaueremann, *Angew. Chem. Int. Ed.* **2021**, *60*, 16349–16354.
- [176] C. Schröder, P. A. Haugg, A. K. Baumann, M. C. Schmidt, J. Smyczek, S. Schaueremann, *Chem. Eur. J.* **2021**, *27*, 17240–17254.
- [177] C. Schröder, A.-K. Baumann, M. C. Schmidt, J. Smyczek, P. A. Haugg, O.-C. Graap, S. Schaueremann, *J. Phys. Chem. C* **2022**, *126*, 4907–4920.
- [178] E. Barbayanni, G. Kokotos, *ChemCatChem* **2012**, *4*, 592–608.

- [179] K. Honda, M. Kataoka, S. Shimizu, *Appl. Microbiol. Biotechnol.* **2002**, *60*, 288–92.
- [180] T. H. Rod, J. K. Nørskov, *Surf. Sci.* **2002**, *500*, 678–698.
- [181] B. Schmid, O. Einsle, H. J. Chiu, A. Willing, M. Yoshida, J. B. Howard, D. C. Rees, *Biochemistry* **2002**, *41*, 15557–65.
- [182] B. K. Burgess, D. J. Lowe, *Chem. Rev.* **1996**, *96*, 2983–3012.
- [183] D. Sehnal, S. Bittrich, M. Deshpande, R. Svobodova, K. Berka, V. Bazgier, S. Velankar, S. K. Burley, J. Koca, A. S. Rose, *Nucleic Acids Res.* **2021**, *49*, W431–W437.
- [184] J. P. Collman, Z. Wang, A. Straumanis, M. Quelquejeu, E. Rose, *J. Am. Chem. Soc.* **1999**, *121*, 460–461.
- [185] R. L. Augustine, *Catal. Today* **1997**, *37*, 419–440.
- [186] S. Tuokko, P. M. Pihko, K. Honkala, *Angew. Chem. Int. Ed.* **2016**, *55*, 1670–4.
- [187] F. Tureček, *J. Chem. Soc., Chem. Commun.* **1984**, 1374–1375.
- [188] L. Bellarosa, J. Diez, J. Gimeno, A. Lledos, F. J. Suarez, G. Ujaque, C. Vicent, *Chem. Eur. J.* **2012**, *18*, 7749–65.
- [189] C. Mohr, P. Claus, *Sci. Prog.* **2001**, *84*, 311–34.
- [190] B. Hammer, J. K. Nørskov, *Surf. Sci.* **1995**, *343*, 211–220.
- [191] B. Hammer, J. K. Nørskov, *Nature* **1995**, *376*, 238–240.
- [192] N. İnoğlu, J. R. Kitchin, *Mol. Simul.* **2010**, *36*, 633–638.
- [193] B. Li, W. Gao, Q. Jiang, *J. Phys. Energy* **2021**, *3*.
- [194] Y. A. Ryndin, C. C. Santini, D. Prat, J. M. Basset, *J. Catal.* **2000**, *190*, 364–373.
- [195] P. N. Rylander, D. R. Steele, *Tetrahedron Lett.* **1969**, *10*, 1579–1580.
- [196] J. H. Sinfelt, *Acc. Chem. Res.* **2002**, *10*, 15–20.
- [197] M. Muir, D. L. Molina, A. Islam, M. K. Abdel-Rahman, M. Trenary, *J. Phys. Chem. C* **2020**, *124*, 24271–24278.
- [198] G. Chen, C. Xu, X. Huang, J. Ye, L. Gu, G. Li, Z. Tang, B. Wu, H. Yang, Z. Zhao, Z. Zhou, G. Fu, N. Zheng, *Nat. Mater.* **2016**, *15*, 564–9.
- [199] K. Chen, H. Wu, Q. Hua, S. Chang, W. Huang, *Phys. Chem. Chem. Phys.* **2013**, *15*, 2273–7.
- [200] H. Tsunoyama, N. Ichikuni, H. Sakurai, T. Tsukuda, *J. Am. Chem. Soc.* **2009**, *131*, 7086–93.
- [201] N. Almora-Barrios, I. Cano, P. W. N. M. van Leeuwen, N. López, *ACS Catal.* **2017**, *7*, 3949–3954.

- [202] I. Cano, M. A. Huertos, A. M. Chapman, G. Buntkowsky, T. Gutmann, P. B. Groszewicz, P. W. N. M. van Leeuwen, *J. Am. Chem. Soc.* **2015**, *137*, 7718–7727.
- [203] I. Cano, A. M. Chapman, A. Urakawa, P. W. van Leeuwen, *J. Am. Chem. Soc.* **2014**, *136*, 2520–8.
- [204] F. Zaera, *Langmuir* **1996**, *12*, 88–94.
- [205] H. M. Chase, T. J. McDonough, K. R. Overly, C. M. Laperle, *J. Phys. Org. Chem.* **2013**, *26*, 322–326.
- [206] P. J. Dyson, P. G. Jessop, *Catal. Sci. Technol.* **2016**, *6*, 3302–3316.
- [207] J. L. Davis, M. A. Barteau, *Surf. Sci.* **1989**, *208*, 383–403.
- [208] J. L. Davis, M. A. Barteau, *J. Am. Chem. Soc.* **2002**, *111*, 1782–1792.
- [209] D. A. Esan, M. Trenary, *Phys. Chem. Chem. Phys.* **2017**, *19*, 10870–10877.
- [210] D. Stacchiola, L. Burkholder, W. T. Tysoe, *J. Am. Chem. Soc.* **2002**, *124*, 8984–9.
- [211] I. Lee, F. Zaera, *J. Phys. Chem. B* **2005**, *109*, 12920–6.
- [212] O. Skoplyak, M. A. Barteau, J. G. Chen, *Surf. Sci.* **2008**, *602*, 3578–3587.
- [213] J. L. Davis, M. A. Barteau, *Surf. Sci.* **1990**, *235*, 235–248.
- [214] F. Madsen, I. Terpager, K. Olskær, J. Spanget-Larsen, *Chem. Phys.* **1992**, *165*, 351–360.
- [215] S. Attia, S. Schauermaun, *J. Phys. Chem. C* **2019**, *124*, 557–566.
- [216] J. J. Max, C. Chapados, *J. Chem. Phys.* **2005**, *122*, 14504.
- [217] J. J. Max, C. Chapados, *J. Chem. Phys.* **2009**, *130*, 124513.
- [218] J. C. de Jesús, F. Zaera, *Surf. Sci.* **1999**, *430*, 99–115.
- [219] M. E. Kordesch, W. Stenzel, H. Conrad, *Surf. Sci.* **1988**, *205*, 100–116.
- [220] M. E. Kordesch, T. Lindner, J. Somers, W. Stenzel, H. Conrad, A. M. Bradshaw, G. P. Williams, *Spectrochim. Acta A* **1987**, *43*, 1561–1566.
- [221] T. Szilágyi, *Appl. Surf. Sci.* **1988**, *35*, 19–26.
- [222] B. A. Sexton, N. R. Avery, *Surf. Sci.* **1983**, *129*, 21–36.
- [223] S. Semancik, G. L. Haller, J. T. Yates, *J. Chem. Phys.* **1983**, *78*, 6970–6981.
- [224] K. Murphy, S. Azad, D. W. Bennett, W. T. Tysoe, *Surf. Sci.* **2000**, *467*, 1–9.
- [225] N. R. Avery, T. W. Matheson, *Surf. Sci.* **1984**, *143*, 110–124.
- [226] Y. Ren, D. Esan, I. Waluyo, J. D. Krooswyk, M. Trenary, *J. Phys. Chem. C* **2017**, *121*, 9424–9432.

- [227] J. Raskó, J. Kiss, *Catal. Lett.* **2006**, *109*, 71–76.
- [228] E. C. Ou, P. A. Young, P. R. Norton, *Surf. Sci.* **1992**, *277*, 123–131.
- [229] S. Katano, E. Herceg, M. Trenary, Y. Kim, M. Kawai, *J. Phys. Chem. B* **2006**, *110*, 20344–9.
- [230] D. Jentz, H. Celio, P. Mills, M. Trenary, *Surf. Sci.* **1995**, *341*, 1–8.
- [231] D. Jentz, M. Trenary, X. D. Peng, P. Stair, *Surf. Sci.* **1995**, *341*, 282–294.
- [232] W. Erley, J. C. Hemminger, *Surf. Sci.* **1994**, *316*, L1025–L1030.
- [233] L. Vogt, E. Schulte, S. Collins, P. Quaino, *Top. Catal.* **2019**, *62*, 1076–1085.
- [234] J. Wang, Q. Tang, S. Jin, Y. Wang, Z. Yuan, Q. Chi, Z. Zhang, *New J. Chem.* **2020**, *44*, 549–555.
- [235] M. C. Schmidt, S. Attia, C. Schröder, A. K. Baumann, P. Pessier, S. Schaueremann, *J. Phys. Chem. C* **2020**, *124*, 14262–14271.
- [236] S. Attia, M. C. Schmidt, C. Schröder, P. Pessier, S. Schaueremann, *Angew. Chem. Int. Ed.* **2018**, *57*, 16659–16664.
- [237] S. Attia, M. C. Schmidt, C. Schröder, S. Schaueremann, *ACS Catal.* **2019**, *9*, 6882–6889.
- [238] S. Attia, M. C. Schmidt, C. Schröder, J. Weber, A. K. Baumann, S. Schaueremann, *J. Phys. Chem. C* **2019**, *123*, 29271–29277.
- [239] M. C. Schmidt, S. Attia, C. Schröder, A.-K. Baumann, S. Schaueremann, *J. Phys. Chem. C* **2021**, *125*, 19311–19324.
- [240] M. Lischka, C. Mosch, A. Groß, *Surf. Sci.* **2004**, *570*, 227–236.
- [241] M. J. Frisch, G. W. Trucks, H. B. Schlegel, G. E. Scuseria, M. A. Robb, J. R. Cheeseman, G. Scalmani, V. Barone, G. A. Petersson, H. Nakatsuji, X. Li, M. Caricato, A. V. Marenich, J. Bloino, B. G. Janesko, R. Gomperts, B. Mennucci, H. P. Hratchian, J. V. Ortiz, A. F. Izmaylov, J. L. Sonnenberg, Williams, F. Ding, F. Lipparini, F. Egidi, J. Goings, B. Peng, A. Petrone, T. Henderson, D. Ranasinghe, V. G. Zakrzewski, J. Gao, N. Rega, G. Zheng, W. Liang, M. Hada, M. Ehara, K. Toyota, R. Fukuda, J. Hasegawa, M. Ishida, T. Nakajima, Y. Honda, O. Kitao, H. Nakai, T. Vreven, K. Throssell, J. A. Montgomery Jr., J. E. Peralta, F. Ogliaro, M. J. Bearpark, J. J. Heyd, E. N. Brothers, K. N. Kudin, V. N. Staroverov, T. A. Keith, R. Kobayashi, J. Normand, K. Raghavachari, A. P. Rendell, J. C. Burant, S. S. Iyengar, J. Tomasi, M. Cossi, J. M. Millam, M. Klene, C. Adamo, R. Cammi, J. W. Ochterski, R. L. Martin, K. Morokuma, O. Farkas, J. B. Foresman, D. J. Fox, *Gaussian 16 Rev. C.01*, **2016**.
- [242] R. Dennington, T. A. Keith, J. M. Millam, *GaussView, Version 6.1*, **2016**.
- [243] A. Gambi, S. Giorgianni, A. Passerini, R. Visinoni, S. Ghersetti, *Spectrochim. Acta A* **1980**, *36*, 871–878.

- [244] M. Chen, N. Maeda, A. Baiker, J. Huang, *ACS Catal.* **2012**, *2*, 2007–2013.
- [245] F. Meemken, A. Baiker, S. Schenker, K. Hungerbuhler, *Chem. Eur. J.* **2014**, *20*, 1298–309.
- [246] R. C. Dunbar, D. T. Moore, J. Oomens, *J. Phys. Chem. A* **2006**, *110*, 8316–26.
- [247] J. Velasquez, E. D. Pillai, P. D. Carnegie, M. A. Duncan, *J. Phys. Chem. A* **2006**, *110*, 2325–30.
- [248] R. Thijs, T. Zeegers-Huyskens, *Spectrochim. Acta A* **1984**, *40*, 307–313.
- [249] C. Schröder, M. C. Schmidt, C. Witt, S. Attia, J. Weber, A.-K. Baumann, B. Hartke, S. Schaueremann, *J. Phys. Chem. C* **2020**, *124*, 28159–28168.
- [250] C. Witt, M.-C. Schmidt, C. Schröder, S. Schaueremann, B. Hartke, *J. Phys. Chem. C* **2021**, *125*, 26167–26179.
- [251] W. H. De Camp, *Chirality* **1989**, *1*, 2–6.
- [252] I. Coric, B. List, *Nature* **2012**, *483*, 315–9.
- [253] G. M. R. Tombo, D. Belluš, *Angew. Chem. Int. Ed.* **1991**, *30*, 1193–1215.
- [254] J. Botting, *Drug News Perspect.* **2002**, *15*, 604–611.
- [255] R. Kopf, D. Lorenz, E. Salewski, *Naunyn Schmiedebergs Arch. Pharmacol.* **1964**, *247*, 121–35.
- [256] A. M. Rouh, *Chem. Eng. News* **2010**, *82*, 47–62.
- [257] G. M. Schwab, F. Rost, L. Rudolph, *Kolloid-Z.* **1934**, *68*, 157–165.
- [258] R. L. Beamer, C. S. Fickling, J. H. Ewing, *J. Pharm. Sci.* **1967**, *56*, 1029–32.
- [259] R. L. Beamer, R. H. Belding, C. S. Fickling, *J. Pharm. Sci.* **1969**, *58*, 1142–4.
- [260] R. L. Beamer, R. H. Belding, C. S. Fickling, *J. Pharm. Sci.* **1969**, *58*, 1419–21.
- [261] K. Harada, *Naturwissenschaften* **1970**, *57*, 114–119.
- [262] D. S. Sholl, A. Asthagiri, T. D. Power, *J. Phys. Chem. B* **2001**, *105*, 4771–4782.
- [263] F. Zaera, *Chem. Soc. Rev.* **2017**, *46*, 7374–7398.
- [264] G. A. Attard, A. Ahmadi, J. Feliu, A. Rodes, E. Herrero, S. Blais, G. Jerkiewicz, *J. Phys. Chem. B* **1999**, *103*, 1381–1385.
- [265] G. A. Attard, *J. Phys. Chem. B* **2001**, *105*, 3158–3167.
- [266] A. D. Reinicker, A. J. Therrien, T. J. Lawton, R. Ali, E. C. Sykes, A. J. Gellman, *Chem. Commun.* **2016**, *52*, 11263–11266.
- [267] Y. Yun, A. J. Gellman, *Angew. Chem. Int. Ed.* **2013**, *52*, 3394–7.

- [268] S. F. Yuk, A. Asthagiri, *Surf. Sci.* **2014**, *629*, 28–34.
- [269] J. L. Fajin, J. R. Gomes, M. N. Cordeiro, *Langmuir* **2013**, *29*, 8856–64.
- [270] N. Jalili, N. Ansari, F. Viñes, F. Illas, F. Nazari, *J. Phys. Chem. C* **2014**, *118*, 1568–1575.
- [271] T. D. Power, A. Asthagiri, D. S. Sholl, *Langmuir* **2002**, *18*, 3737–3748.
- [272] A. Perosa, P. Tundo, M. Selva, *J. Mol. Catal. A: Chem.* **2002**, *180*, 169–175.
- [273] F. Zaera, *Chem. Rev.* **1995**, *95*, 2651–2693.
- [274] R. Döll, C. A. Gerken, M. A. Van Hove, G. A. Somorjai, *Surf. Sci.* **1997**, *374*, 151–161.
- [275] N. Sheppard, C. De La Cruz, *Catal. Today* **2001**, *70*, 3–13.
- [276] P. S. Cremer, X. Su, Y. R. Shen, G. A. Somorjai, *J. Am. Chem. Soc.* **1996**, *118*, 2942–2949.
- [277] H. Öfner, F. Zaera, *J. Phys. Chem. B* **1997**, *101*, 396–408.
- [278] W. S. Sim, T. C. Li, P. X. Yang, B. S. Yeo, *J. Am. Chem. Soc.* **2002**, *124*, 4970–1.
- [279] S. Spicher, S. Grimme, *Angew. Chem. Int. Ed.* **2020**, *59*, 15665–15673.
- [280] S. Grimme, C. Bannwarth, P. Shushkov, *J. Chem. Theory Comput.* **2017**, *13*, 1989–2009.
- [281] C. Bannwarth, S. Ehlert, S. Grimme, *J. Chem. Theory Comput.* **2019**, *15*, 1652–1671.
- [282] M. J. Kolb, A. L. Garden, C. Badan, J. A. Garrido Torres, E. Skulason, L. B. F. Juurlink, H. Jonsson, M. T. M. Koper, *Phys. Chem. Chem. Phys.* **2019**, *21*, 17142–17151.
- [283] V. Demers-Carpentier, P. H. McBreen, *J. Phys. Chem. C* **2011**, *115*, 6513–6520.
- [284] G. Goubert, A. M. H. Rasmussen, Y. Dong, M. N. Groves, P. H. McBreen, B. Hammer, *Surf. Sci.* **2014**, *629*, 123–131.
- [285] V. Demers-Carpentier, M.-A. Laliberté, Y. Pan, G. Mahieu, S. Lavoie, G. Goubert, B. Hammer, P. H. McBreen, *J. Phys. Chem. C* **2010**, *115*, 1355–1360.
- [286] S. Attia, E. J. Spadafora, M. C. Schmidt, C. Schröder, A. K. Baumann, S. Schauer-mann, *Phys. Chem. Chem. Phys.* **2020**, *22*, 15696–15706.

Danksagung

An erster Stelle möchte ich mich bei meiner Betreuerin, Prof. Dr. Swetlana Schaueremann für die Möglichkeit bedanken an diesen faszinierenden Forschungsapparaturen arbeiten zu können und über die Jahre hinweg äußerst gut betreut worden zu sein - und gleichzeitig ein außerordentliches Maß an freier Forschung zu haben.

Gleichermaßen sind viele aktive und ehemalige Kollegen zu nennen, ohne deren Hilfe diese Arbeit nie möglich gewesen wäre. Thank you, Smadar, for your introduction into surface science. You were really patient in teaching me with all this fancy UHV stuff. You did an amazing job :)

Ebenso danken möchte ich Marvin und Ann-Katrin, ohne deren Hilfe und Mitarbeit ich nicht so weit gekommen wäre. Ein großen Dank auch an die fleißigen Bachelor Philipp, Jan, Ole und Jann, die im Rahmen ihrer Arbeiten hier einen großen Beitrag zu den gewonnenen Forschungsergebnissen geleistet haben.

Vielen Dank, Christopher und Bernd, für die große Hilfe bei den theoretischen Untersuchungen zu EP und all die schönen Gespräche zu dem "was macht dieses Molekül auf der Oberfläche?"

Ich möchte mich auch bei Niklas, Tim, Andreas, Frank, Finn, Timo sowie allen anderen Kollegen bedanken, die in den vergangenen Jahren durch ihre Hilfe, Ratschläge oder einfach durch ihr Zuhören da waren.

Danke Herr König von und zu Thrun mir damals im Grundpraktikum die füsikalische Kämi nahezubringen – mit Recht sagtest du sinngemäß "das ist eigentlich schon ganz cool".

Vielen Dank auch an die Freunde und Verwandte, die mich in den letzten Jahren unterstützt haben diese Arbeit in der Form so fertigzustellen. Vor allem aber Steffi und Lilly, die mir insbesondere in der Schlussphase alles ermöglicht haben.

Dennis, bald geht's wieder los..

Zu guter letzt muss natürlich auch der Onzin-Kwaken Quatsch-Comedy-Verein aus Großherzogtum Jegum-Handewitt samt dem Schalmeienorchester erwähnt werden, ohne deren fortwährende Unterstützung in allen Lebenslagen kein Weiterkommen möglich sein wird.